Hideaki Takabe

The Physics of Laser Plasmas and Applications – Volume 2

Fluid Models and Atomic Physics of Plasmas

Springer

Springer Series in Plasma Science and Technology

Plasma Science and Technology covers all fundamental and applied aspects of what is referred to as the "fourth state of matter." Bringing together contributions from physics, the space sciences, engineering and the applied sciences, the topics covered range from the fundamental properties of plasma to its broad spectrum of applications in industry, energy technologies and healthcare.

Contributions to the book series on all aspects of plasma research and technology development are welcome. Particular emphasis in applications will be on high-temperature plasma phenomena, which are relevant to energy generation, and on low-temperature plasmas, which are used as a tool for industrial applications. This cross-disciplinary approach offers graduate-level readers as well as researchers and professionals in academia and industry vital new ideas and techniques for plasma applications.

Hideaki Takabe

The Physics of Laser Plasmas and Applications - Volume 2

Fluid Models and Atomic Physics of Plasmas

Springer

Hideaki Takabe
Institute of Laser Engineering
Osaka University
Suita, Osaka, Japan

Institute of Radiation Physics
Helmholtz Zentrum Dresden Rossendorf
Dresden, Germany

A 500 eV Planck radiation generated by spherical implosion of plastic shell with intense lasers is used to study the emission spectra from photo-ionized plasmas near Black Hole (Cygnus X-3) and neutron star (Vela X-1) [see Chap. 5]. (Reprinted by permission from Macmillan Publisher Ltd: copyright 1993. (Courtesy of S. Fujioka))

Preface

Volume 1 introduced the physics of laser-plasma interactions. There, the discussion assumed of a fully ionized plasma. The laser energy absorbed by the material is converted into random kinetic energy of electrons. In other words, it is the thermal energy of the electron population. Ions gain energy through inelastic Coulomb collisions with electrons. This is the physical mechanism of temperature relaxation.

If the laser intensity is sufficiently non-relativistic, the velocity distribution of the produced electrons and ions can be approximated as being in local thermodynamic equilibrium (LTE). In this case, the macroscopic behavior of the electron and ion groups can be treated by the fluid model. Fluid models are widely used to study plasma phenomena over long periods of time and over a wide spatial range.

Particle-in-Cell (PIC) simulations, cited many times in Volume 1, are now widely used to study the microscopic physics of laser-matter interactions, thanks to rapid advances in computer performance. However, the number of particles is still too large to study the whole picture of the plasma, and it is still difficult to follow the entire physical process with a computer. Therefore, fluid models with less degrees of freedom have been widely used to study the physics of plasmas in the laboratory, in space, and in the universe.

Roughly speaking, PIC is used to study microscopic plasma physics under idealized conditions, while fluid simulations are used to study global phenomena of plasma dynamics. Another reason why the fluid approximation equations are widely used is that they can be modified to model the physics of non-ideal plasmas, such as ionization and other atomic processes, non-local energy transport, nuclear reactions, magnetohydrodynamic phenomena, and so on. The fluid approximation also has the advantage that plasma behavior can be analyzed from the knowledge of historical fluid mechanics, in three dimension, and that fluid physics is easily understood intuitively because of familiar phenomena such as air and water.

In Volume 2, several plasma fluid equations are presented. We explain under what assumptions they were derived. The reader should choose with deep thought which equations are the simplest and good enough approximations for his or her research topic. Do not think about solving the fluid equations in the most precise

form. How simple and close to the truth the equations should be to start with will be a test of the reader's sense of physics. Rather, it is extremely difficult to find the necessary and sufficient basic equations and study the problem from the beginning. As you proceed with your research, please try to pursue the truth by simplifying the basic equations and then complicating them.

Specifically, as introduced in this book, starting from the two-fluid plasma model of electrons and ions, a variety of physics and its mathematics will be introduced for the following subjects. Magnetohydrodynamics, thermodynamics of shock waves and non-ideal dense plasmas, self-similarity solutions of nonlinear fluids, atomic processes such as ionization and recombination, non-local electron heat transport, X-ray energy transport and atomic physics, physics of quantum mechanical many-electron states in dense plasmas, and its comparison with experiments.

In this book, We introduce the above physics topics, intertwining them with astrophysics. However, in this book, We only introduce the case in which the spatial structure is one-dimensional: one-dimensional refers to physical phenomena limited to plane, cylindrical, and spherical symmetry. Therefore, the equations of the fluid model are described by mathematical solutions where the independent variables are (t, x) or (t, r). Furthermore, in many cases, one-dimensional solutions are obtained assuming stationarity in a coordinate system in motion. Knowing one-dimensional fluid plasma solutions is the foundation for analyzing complex plasma behavior. It is extremely important as basic knowledge.

More complex plasma fluid physics, such as when the one-dimensional solution has a structure to the remaining two-dimensional disturbances, or even when those disturbances grow and cause fluid instability phenomena, will be carefully explained in the following Volume 3. There, the physics of charged fluids, which generate electric and magnetic fields and are subject to these field forces, will be explained. In studying such science, we look back the physics studied on neutral fluids such as water and air. Naturally, the study of plasma fluid turbulence becomes important. We will consider this while learning about neutral fluid turbulence and mathematical methods.

This series consists of four volumes. Plasmas have high temperatures, so the mean free path is proportional to the square of the temperature. For individual particles, it is proportional to the fourth power of their velocity. Therefore, when studying the physics of high-temperature plasmas, the fluid approximation, which assumes that the plasma is in local thermal equilibrium and that the plasma state is determined only by the density, velocity, and temperature as a fluid, is no longer applicable. When high temperatures are attempted to be realized by shock waves, the high-speed component of the velocity distribution deviates from the Maxwell distribution. Plasmas in which such collisions are unlikely to occur are called "collisionless plasmas".

In Volume 4, we introduce the physics of collisionless plasmas by analyzing the time evolution of the velocity distribution function, rather than the fluid approximation. Collisionless shock waves, particle acceleration, and structure formation by self-induced electromagnetic fields are explained. While Volume 1 introduced the interaction between laser electromagnetic fields and charged particles, Volume 4

deals with plasmas that emerge when the plasma itself generates electric and magnetic fields due to instability, turbulence, and other factors, and charged particles interact with them as a result.

When I was a graduate student, he began to study and research fluid mechanics to study the physical mechanism of laser ablation of solid materials and the ablation pressure that forms shock waves in solids. I would like to thank Professor T. Taniuti for his guidance in plasma fluids. While promoting research as a young university faculty member with Professor K. Mima, I also began to study fluid instability and started the development of the physics-integrated implosion, code ILESTA at Osaka University. I would like to thank Professor Chiyoe Yamanaka for pushing me to develop such a physics-integrated code and giving me the opportunity to work with the physics experiment group of the Gekko XII experiment at Osaka University.

To compose a handmade implosion simulation code, I also had to study a lot of physics related to atomic physics and atomic processes. I also read many papers on astrophysics, and Professors F. L. Wang, D. Saltzman, T. Kato, T. Fujimoto, K. Takayanagi, I. Murakami, and R. M. More were good mentors and collaborators in my process of studying atomic physics and atomic processes.

Physics of high-density plasmas has been a challenging topic for me for many years. After retirement, I had the opportunity to do intensive research at HZDR in Dresden. Thanks to the invitation by Prof. R. Sauerbrey and Prof. T. Cowan, I was able to participate in the so-called High Density Energy Physics (HEDP) research with the European X-FEL at DESY in Hamburg. The work on warm dense matter (WDM) by the theoretical group (J. Vorberger) and the experimental group (D. Kraus) reminded me of what I learned from Prof. S. Ichimaru in the 1980s. I would like to thank everyone for supporting my research at HZDR. I had the opportunity to give a series of lectures there. The lecture notes helped me write chapters on physics of dense plasmas.

To study the three-dimensional evolution of such plasmas, complex thermodynamic states over a wide range of temperatures and densities must be modeled by hydrodynamic simulations. The physics models include, for example, effective charge (ionization degree), pressure due to ions and electrons, their respective internal energies, and opacity and emissivity of radiation. It is difficult to describe the details in this volume, but I would like to introduce the understanding I have acquired through my research career. In addition, several examples from recent research activities using X-FEL are given. Even for researchers in the field of engineering, it is my intention to introduce a minimum of physics so that the reader can understand the current state-of-the-art research by reading this book.

I would like to thank Prof. P. Chen for providing the environment that allowed me to continue and complete the writing of this textbook in Taipei after Dresden. I would also like to thank "Google Scholar" for helping me find many recent papers on the topics presented in this book. I was able to learn the latest results of the research in which I was once involved. It was a pleasure for the author to learn about the unflagging progress of the research. I would also like to express my gratitude to Dr. H. Niko of Springer, who helps the publication.

This book is not a review book. It would be cumbersome and confusing for the reader to list all the important original papers on the topics of each chapter. Therefore, I, in writing this book with an understanding of physics, have mainly cited papers that help the reader to understand physics more easily. In addition, I have cited the figures to reproduce diagrams that help readers to grasp the image of physics. Therefore, readers who wish to learn more about the subject should refer to the limitedly cited reference papers in this book for further study.

Osaka, Japan   Hideaki Takabe
July 31, 2023

Contents

Chapter 1
Introduction

Abstract A brief overview of the fluid model to describe most of the plasmas is given. Assuming the velocity distributions of electrons and ions are shifted Maxwellian distribution, plasmas can be described with fluid approximation regardless they are collisional or collisionless. The time evolution of laser plasmas is described with the fluid model with non-ideal equation of state, non-local electron transport, radiation transport, and so on. Modeling atomic state of plasma, effective charge, spectral opacity, and emissivity are calculated to couple with the energy equation of the electron fluid. As a reference to the plasma physics explained in this book, the physics scenario of laser fusion dynamics is used to know what kinds of physics become to couple from laser absorption to the fusion energy production through the implosion dynamics.

It is emphasized that the development of a physics-integrated code is important to study such laser-produced plasmas. Along with the advancement of technology for diagnostics and lasers, the analysis of the experimental data has helped the improvement of the physics models by comparing the experimental data to the corresponding simulations. Considering the technically limited number of implosion experiments with a huge laser facility, the advancement of the physics-integrated codes is becoming the main issue to increase the quality of analysis and design for better performance experiments. The progress of computer performance and advancement of experiments are now non-separable in complicated nonlinear systems such as plasma physics even within the hydrodynamic modeling of plasmas.

1.1 Fluid Model

As studied in Volume 1, intense lasers are used to heat the matter to produce high-temperature plasmas, where extremely high pressure is produced to compress the matter to a density higher than the solid densities. In studying the physics of laser-plasma interaction and the resultant heating of plasmas, the key physics was the mechanical dynamics of electron particles in the electric and magnetic fields of lasers.

Since the phenomena are so complicated, the particle-in-cell (PIC) simulation has been used widely as seen in Volume 1. The usage of the PIC codes is the direct way to study plasma physics in the case of the interaction with ultra-short and ultra-intense lasers, because the pulse duration is very short less than a pico-second (10^{-12} s) and the density of the interaction region is relatively low compared to solid density. Therefore, PIC simulation is a powerful tool for studying physics under reasonable modeling of the interacting plasma region during the laser pulse duration.

On the other hand, the laser-produced plasma dynamics in the range of more than a nano-second (10^{-9} s), is unable to study with the use of PIC codes the whole dynamics from the low-density region expanding to the vacuum to the compressed high-density region. It is required to model the laser-produced plasma with another mathematics.

The next precise way is to solve Boltzmann equations directly, while the particle distribution functions at each space and time are also a function of particle velocity or energy at each point. Its degree of freedom is infinity and it should be discussed how many numerical grids are affordable in solving Boltzmann equations computationally. Solving the Vlasov equation is equivalent to solving particle dynamics directly in PIC code for collisionless plasma. In general, however, thanks to the progress of computer capability, the PIC codes are widely used because of the simplicity of numerical methods and their numerical stability.

Instead of PIC or kinetic methods, the easier way to solve the physics is to model the plasma as fluids and use the basic equations for fluid dynamics. It is equivalent to assuming that the distribution function is **Maxwellian** locally with particle density n, flow velocity **u**, and temperature T,

$$f(\mathbf{v}, \mathbf{r}, t) = \frac{n}{(2\pi T/m)^{3/2}} e^{-\frac{m}{2T}(\mathbf{v} - \mathbf{u})^2} \tag{1.1}$$

In the fluid model, the basic fluid equations to n, **u**, and T are solved as functions of time and space (t, **r**).

Taking the moments of velocity, v^0, $\mathbf{v}$, and v^2 of the Boltzmann equation, it is well known that the fluid equations are obtained even for the ion and electron two-fluid system. Then, the basic equation to be solved are coupled partial differential equations for

Density n(**r**, t) or mass density ρ (**r**, t),
Flow velocity or mean velocity vector **u**(**r**, t),
Temperature T(**r**, t).

Note that depending on the time and space scale of the plasma phenomena, the ions and electrons are assumed to be different densities, velocities, and temperatures. When we are interested in a long time and space scale phenomena, one-fluid one-temperature or one-fluid two-temperature models are used. In discussing two-fluid models, it is usual to take into account the coupling with Maxwell equations, because charge separation and electric current produce electric and magnetic fields working new forces to electron and ion fluids.

The neutral fluid equations have a longer history than the Boltzmann equation. From the end of the seventeenth century, the analytical and algebraic aspects of mechanics were advanced, and the laws of conservation of mechanical quantities such as momentum, angular momentum, and energy were proposed, and the equations of motion were formulated.

In the eighteenth century, the consideration of mechanics was extended from point mass to systems with many points, i.e., continua such as rigid bodies and fluids, and the theory of mechanics was applied to them as well. By the middle of the eighteenth century, **Bernoulli's theorem**, the first fundamental law of fluids, was proposed, followed by **Euler's equations** of motion and **Lagrange's equations** of motion. This is said to be the birth of modern fluid mechanics.

1.2   Brief History of Fluid Dynamics

It is useful to give a general description of the development of fluid dynamics. Wikipedia is copied here since it is well-described. Fluid mechanics is the branch of physics concerned with the mechanics of fluids (liquids, gases, and plasmas) and the forces on them. It has applications in a wide range of disciplines, including mechanical, civil, chemical, and biomedical engineering, geophysics, oceanography, meteorology, astrophysics, biology, and plasmas.

It can be divided into fluid statics, the study of fluids at rest; and fluid dynamics, the study of the effect of forces on fluid motion. It is a branch of continuum mechanics, a subject that models matter without using the information that it is made out of atoms; that is, it models matter from a macroscopic viewpoint rather than from a microscopic one.

Fluid mechanics, especially fluid dynamics, is an active field of research, typically mathematically nonlinear and complex systems. Many problems are partly or wholly unsolved and are best addressed by numerical methods, typically using computers. A modern discipline called computational fluid dynamics (CFD), is devoted to this approach. Particle image velocimetry, an experimental method for visualizing and analyzing fluid flow, also takes advantage of the highly visual nature of fluid flow.

The study of fluid mechanics goes back at least to the days of ancient Greece when Archimedes investigated fluid statics and buoyancy and formulated his famous law known now as the Archimedes' principle, which was published in his work "On Floating Bodies" – generally considered to be the first major work on fluid mechanics. Rapid advancement in fluid mechanics began with Leonardo da Vinci (observations and experiments), Evangelista Torricelli (invented the barometer), Isaac Newton (investigated viscosity), and Blaise Pascal (researched hydrostatics, formulated Pascal's law), and was continued by Daniel Bernoulli with the introduction of mathematical fluid dynamics in "Hydrodynamica" (1739).

The inviscid flow was further analyzed by various mathematicians (Jean le Rond d'Alembert, Joseph Louis Lagrange, Pierre-Simon Laplace, Siméon Denis Poisson)

and viscous flow was explored by a multitude of engineers including Jean Léonard Marie Poiseuille and Gotthilf Hagen. Further mathematical justification was provided by Claude-Louis Navier and George Gabriel Stokes in the **Navier–Stokes equations** and boundary layers were investigated (Ludwig Prandtl, Theodore von Kármán), while various scientists such as Osborne Reynolds, Andrey Kolmogorov, and Geoffrey Ingram Taylor advanced the understanding of fluid viscosity and turbulence.

1.3 Compressible Fluid Plasma

Most of the classical fluid dynamics cited above are about incompressible fluid, where the fluid density is constant and flow velocity is slow. Compressible fluid dynamics starts to be studied in the field of aerodynamics. Once the flow velocity becomes near and higher than the sound velocity of the fluid, compressibility becomes essential. One of the pioneering good textbooks about compressible fluid dynamics is the book by Liepmann and Roshko [1]. Then, the compressible fluid in high temperature and high density is well described by a famous book by Zel'dovich and Raizer [2]. The shock wave structure of plasmas was studied precisely based on a two-fluid model including the charge separation effect in [3].

The book [2] is unique and highly related to the topics of shock waves and hydrodynamics of laser-produced plasma to be shown in the present book. It is noted, however, that the book is a good one for one-dimensional hydrodynamics, while almost no description of the hydrodynamic instabilities and resultant turbulent mixing is to be discusses in Volume 3. This is because such topics of hydrodynamic instabilities have been mainly developed after the publication of the book. The book "fluid dynamics" by Landau and Lifshitz [4] is also famous as a pioneering book of modern fluid mechanics, where the compressible fluids and stability of fluid dynamics are also discussed.

The study of the equation of state (EOS) of non-ideal matters and plasmas are not simple and self-consistent statistical physics should be studied. Plasma emits radiation in the X-ray region to affect the fluid dynamics via energy transport. The so-call **radiation-hydrodynamics** should be modeled as basic equations. In addition, electron transport becomes important and a simple diffusive approximation violates. This is because the laser energy is deposited dominantly near the cut-off density and the heated electrons transport their energy into a relatively cold region. Then, most of the energy is carried by high-energy electrons whose Coulomb mean-free path is proportional to the square of the kinetic energy. Suck non-local transport should be modeled in the fluid equations.

Different from most of the fluids cited above, the hydrodynamic equation is not appropriate to understand other plasma phenomena, because high-temperature plasma is almost collisionless and the velocity distribution function easily departs from Maxwell distribution in (1.1). A variety of plasma instabilities are induced when non-Maxwellian electrons or ions tend to be in a thermos-dynamics

equilibrium state after the growth of electromagnetic energy. For example, an electron beam is injected into plasma, and electro-static and electromagnetic waves are induced to grow their energies into a nonlinear stage where particle-field nonlinear interaction is essential. Such a phenomenon is in general to be studied by so-call kinetic theory of plasma, which will be given in Volume 4.

1.4   Hydrodynamics of Laser Fusion

The author researched the possibility of laser fusion and its related physics to apply to studying astrophysics with intense lasers in the laboratory. The starting point is to study physics-integrated radiation hydrodynamics of laser fusion as shown in Fig. 1.1 [5]. The engineering scenario – an optimistic scenario – for fusion energy production is shown in the array at the center. This concept of laser-driven implosion is proposed in 1972 by Nuckolls et al. [6].

   Why engineering (or optimistic) is because the physics scenario is assumed to be in spherical symmetry as schematically shown in Fig. 1.2. However, the physics in the laser fusion has been clarified to be not so simple through a lot of implosion experiments. In the laser-plasma interaction, energy loss by reflection and nonlinear physics of the interaction discussed in Volume 1 should be modeled. In general, the nonlinear interaction produced hot electrons to pre-heat the solid target, preventing the ideal hydrodynamic implosion.

   Electrons obtain energy from the laser and transport it to the ablation front. On the right side in Fig. 1.1, the non-ideal fluid physics is listed. The transport is not diffusive and anomalous physics should be considered because of non-local transport, radiation transport, and the effect of self-generated magnetic and electric fields. We need to study plasma turbulences as shown in Volume 4.

   After accelerating the fuel plasma in the in-flight phase, the kinetic energy is converted to the thermal energy to ignite a fusion reaction at the center of a spherical target as shown in Fig. 1.2. The compressed fuel should be controlled so that it consists of the central ignitor (red) and the surrounding main cold fuel (blue) as shown at "ignition" in Fig. 1.2. In such one-dimensional scenario, it is possible to obtain fusion energy production larger than 100 times the input laser energy. The fusion product of alpha particles works to induce the nuclear-burn of the main fuel. It should be noted that for generation of electric power with such high-gain laser fusion, very challenging implosion with the compressed fuel radius less than $1/30 \sim 1/50$ of the initial radius is required, very different from the image of the cartoon in Fig. 1.2.

   On the left in Fig. 1.1, on the other hand, the physical issues to be studied are listed regarding the multi-dimensional effect of the laser implosion process. In the direct-drive laser fusion scheme, non-uniformity of laser absorption energy flux on the target surface initiates uneven hydrodynamics. This is called the "imprint" of hydrodynamic instability. How the imprint is serious depends on the thermal transport and the equation of states of ablating plasma and shocked solid material.
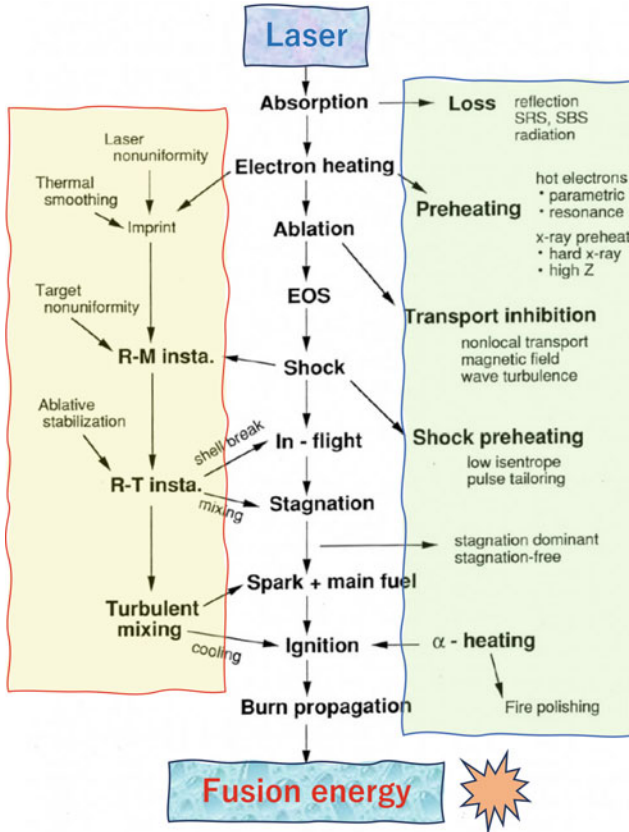
Fig. 1.1 The laser fusion physical scenario. The central scenario is the spherically symmetric implosion and burn scenario in fluid assumption. The nature is, however, not so kind to allow us to keep in one dimension and fluid assumption. The right-hand-side represents the importance of transport issues and high-energy electron production. Long range heating by alpha particles helps smoothing of the non-uniform core. The scenario on the left-hand-side is related to multi-dimensional effects. From instability to turbulence, challenging subjects will be described in Volume 3. Reprint with permission from Ref. [5]. Copyright by IAEA

Since the laser intensity is extremely high, the initial shock wave induces Richtmyer-Meshkov instability. In the in-flight and final stagnation phases, **Rayleigh-Taylor instability** becomes important as the instability prevents the engineering scenario of implosion. Linear instability, nonlinear physics, and finally material mixing by **turbulent mixing** are the critical issue to realize the fusion energy, while their physics are still under intensive study. One fortunate physical phenomenon is known as **ablative stabilization** of the classical Rayleigh-Taylor instability, where the ablation flow and heat conduction by electrons and radiation reduces the growth rate of the Rayleigh-Taylor instability at the ablation front. The
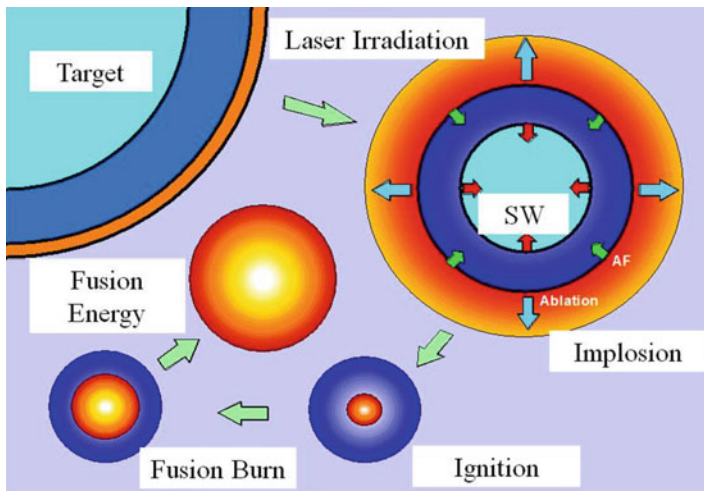
Fig. 1.2 Schematics of Engineering scenario of laser fusion. The target with ablator (orange) and frozen DT fuel (blue) are irradiated by many laser beams for implosion with shock waves. The fuel DT are required to squeeze about 30 times smaller radius to ignite the imploded fuel. Ignition is triggered and fusion product alpha particles heat whole the compressed fuel to produce about 100 times energy of input laser energy

physics of hydrodynamics instability and turbulent mixing will be shown in Volume 3.

A review on the direct drive laser fusion is given for example, by Craxton et al. in [7]. One of the top runners in the theory, computing, and experiments of direct-drive laser implosion and fusion research has been the Laboratory for Laser Energetics, Univ. of Rochester. The review paper has summarized most of the accomplishments in direct-drive laser fusion with the OMEGA laser facility including all the other activities from the beginning of laser fusion research. The most critical issue of laser fusion is the physics stemming from the multi-dimensional effect, and more detail of the implosion physics will be given in Volume 3.

1.5 Modeling Radiation-Hydrodynamics in Astrophysics

One of the most attractive applications of the physics of laser plasma is to study astrophysical phenomena in the laboratory. This is called "**laboratory astrophysics**". There are two points of view linking laser-generated plasma and astrophysics; that is, sameness and similarity. The sameness is that the physics are identical, and the similarity is that the physical phenomena or dynamics are similar in non-dimensional time and space. For example,

1. Sameness of physics

    (a) Ionization of plasmas, equation of state,
    (b) Opacity, emissivity
    (c) Nuclear reaction

2. Similarity of physics

    (a) Dynamical phenomena of compressible plasma fluids,
    (b) Non-equilibrium atomic processes,
    (c) Radiation transport, particle transport

The class (1) is easy to understand. For example, a laser fusion implosion experiment has achieved a plasma state comparable to the temperature and density of the Sun. The thermodynamic properties of astronomical objects can be studied in detail by generating small pieces of them in the laboratory. This is also the case of radiation properties like emission and absorption spectra of x-rays.

Class (2) is an attempt to elucidate various physics of compressible fluid phenomena, atomic processes, and so on by transforming time and space scales to the power of 10–20 (10^{10-20}) on the basis of a similarity law. It is possible to reduce the phenomena to the time scale of density ratio ($\sim 10^{20}$) from phenomena in astrophysics to those in the laboratory. Therefore, for example, we have considered the hydrodynamic similarity between laser implosion and supernova explosions.

It is too much to explain more about laboratory astrophysics and interested readers are recommended to refer to a review paper [8] and the references cited therein. The following ten topics are reviewed about how laser experiments are carried out to clarify the physics in Universe.

1. Equation of state experiment of high-energy-density plasmas compressed by shocks by lasers
2. Opacity measurement of hot-dense plasmas produced by lasers
3. Photo-ionized plasma experiment modeling Black-Hole binary system
4. Blast waves generated by intense lasers
5. Hydrodynamic instability and the physics of turbulent mixing
6. Magnetic reconnection experiments
7. Magnetic turbulence experiments
8. Collisionless shock mediated by Weibel instability and magnetic turbulence
9. Modeling cosmic-ray generation via relativistic laser and charged particle interaction
10. Electron-positron plasma generation by ultra-intense Lasers

In the present Volume 2, topics (1)–(4) will be discussed. A typical example to model photo-ionizing plasma near a black hole or neutron star is shown in the figure on the front page of the present book. By use of laser implosion, it is possible to generate Planckian radiation of radiation temperature 500 eV which is almost the same as from the surface of compact objects such as black holes or neutron stars [9]. On the right in the figure, a comparison of the measured spectrum in the model experiment and observed from the photo-ionized plasmas near the compact objects

are shown for silicon atoms to clarify the ionization process. The detail of this topic is described in Chap. 5.

1.6 Verification and Validation (V&V)

One of the typical approaches in studying the laser-plasmas is to focus the development of computer simulation code with all of related physics as mathematical models, which is called "**physics-integrated code**". In Fig. 1.3, the elements of the integrated code are listed in relation to each other. Mostly, all the elements couple in a nonlinear manner, and the performance of the simulation is sensitive to the most unreliable modeling of physics.

In the early time of research, one-dimensional integrated codes have been developed. It is because the computer performance was still low and multi-dimensional hydrodynamic simulation was not possible. At that time, physics modeling of laser heating, atomic physics, and equation of state were the main issues in modeling the physics as simply as possible so that it fits the computer capability at that time. Then, the modeling done already in astrophysics has been adapted to the laser fusion codes. The kinetic effect of radiation and particles has been newly installed because of the discrepancy in the experimental result from the simplified model used in astrophysics.

To upgrade the codes to two- and three-dimensions, we have to wait for the progress of the computer performance. This situation very resembles the case of the simulation of global warming. S. Manabe was awarded the Nobel Prize in physics in 2021 for "the physical modeling of Earth's climate, quantifying variability and reliably predicting global warming" [10]. His pioneering work is the temperature change on the earth's surface in one-dimensional thermal equilibrium of the
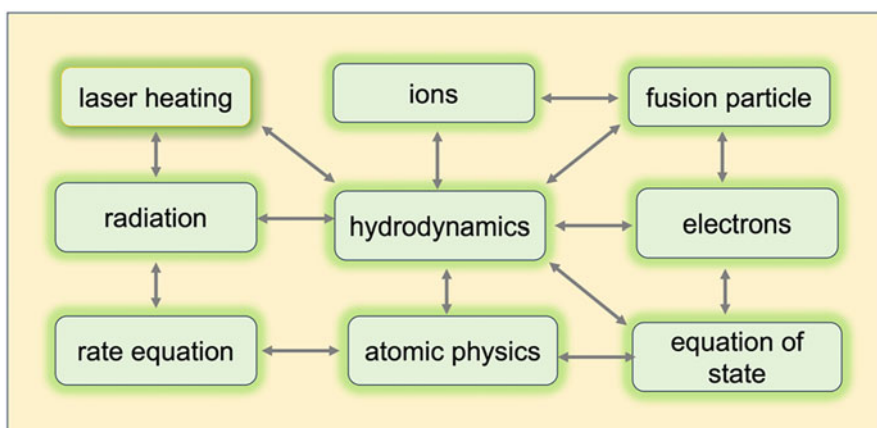
Fig. 1.3 Physics elements in the integrated code for laser fusion research. Note that now hydrodynamics is required to be of three-dimensional
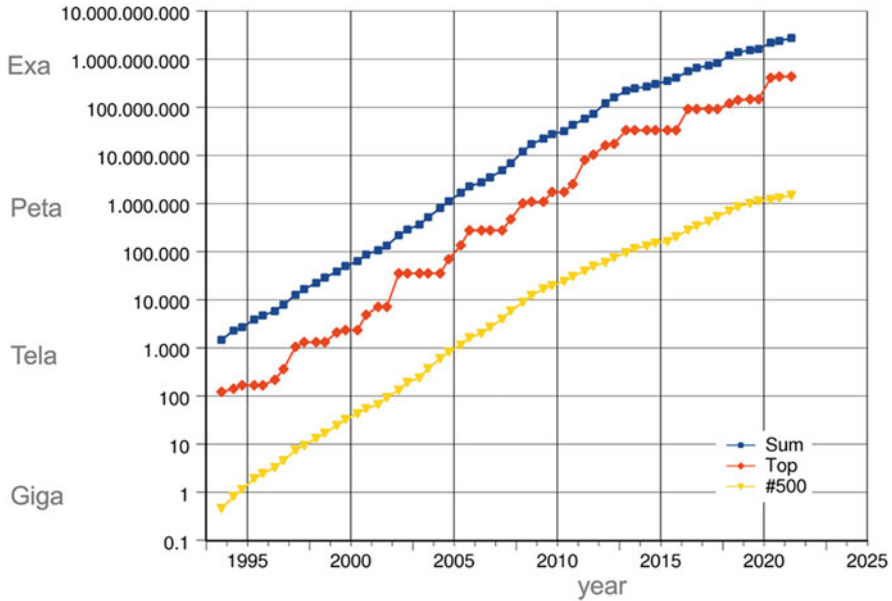
Fig. 1.4 Rapid growth of supercomputer performance, based on data from the top500.org website. The logarithmic *y*-axis shows performance in Giga flops. Combined performance of 500 largest supercomputers (blue). Fastest supercomputer (red). Supercomputer in 500th place (yellow). [From data of https://www.top500.org/]

atmosphere due to the increase of CO_2 gas in 1967. He has modeled many physics elements based on microphysics and developed one-dimensional code to solve nonlinear coupled systems. Such work has led the world to consider seriously about global warming and to decide on the carbon-neutral policy.

Thanks to the rapid progress of computer capability as shown in Fig. 1.4, now three-dimensional radiation-hydrodynamic codes become an essential tool to study the performance of implosion experiments and to design and predict better experiments. Multi-dimensional hydro-code also requires a heavy calculation of non-local transport, where the energy space needs multi-group transport. In addition, each physics model has been replaced by a new model with more sophisticated physics. It is noted that a magnetic field is generated in the multi-dimensional plasma fluid. Although its energy density is much less compared to the thermal energy, its effect on the energy transport coefficient of electrons is sensitive to alter the hydrodynamic phenomena.

It is surprising to know that the performance (speed) of supercomputers increased 10,000 times in the last 20 years. This means the increase of one order of performance (speed) has been accomplished every 5 years. This progress suggests that the research method has changed from mostly experimental data analysis to analysis with the physics-integrated codes in laser fusion research. At the same time, such code development verified with experimental data has been regarded to be beneficial for the improvement of astrophysics research.

Let us here consider more general importance of verification and validation of simulation codes and the collaboration with experiments [11]. Simulation models are increasingly being used to solve many problems and to aid in decision-making like the carbon-neutral policy. The developers and users of these models, the decision makers using information obtained from the results of these models, and the individuals affected by decisions based on such models are all rightly concerned with whether a model and its results are "correct". This concern is addressed through model **verification and validation (V&V)**.

Verification is the process of checking that software achieves its goal without any bugs. It is the process to ensure whether the program that is developed is right or not. It verifies whether the developed program fulfills the requirements that we have. Verification is static testing. Verification means "Are we building the code right?".

Validation is the process of checking whether the software product is up to the mark or in other words product has high-level requirements. It is the process of checking the validation of the code i.e., it checks what we are developing is the right to predict the experiments. It is the validation of actual and expected experimental products. Validation is dynamic testing. Validation means "Are we building the right code to explain and predict the product?". Here we can regard the product as the implosion experiments. If not right, further improvement of the physical models and/or finding new physics are required. It is of course that the integrated codes can't predict the real physics without checking with corresponding experimental results and model experiments, and continuous effort of improving the physics models.

The rapid progress of computer performance has made it possible to use computers for machine learning, neural network, big data analysis, statistical modeling, and so on. **Artificial intelligence (AI)** helps more advanced study of the integrated physics system. By activating the deep-neural network system shown in Fig. 1.5, it is advantageous for us to use wide knowledge of science and deep thinking to the input data. Such artificial intelligence starts to be used in many kinds of research, and its review has been published in the plasma physics field [12–17].

In the present volume, the physics of compressible hydrodynamics is introduced. The hydrodynamics is limited to only one-dimensional one, and multi-dimensional hydrodynamics will be studied in Volume 3. Atomic physics of plasma and the equation of the state of dense plasmas are explained as advanced models of plasma fluids as functions of density and temperature, including the case of non-local thermodynamic equilibrium (non-LTE) states. Most of the description is focused on theoretical physics, with which especially young researchers can obtain the image of physics in studying any kind of plasmas. Collisionless plasmas are also an interesting subject and are to be discussed in Volume 4.

1.7 Brief in Each Chapter

In Chap. 2, basic equations governing a variety of fluid models of plasmas are shown with simple explanations. In general, high-density plasmas are approximately modeled with neutral compressible fluid with heating and loss terms, and energy
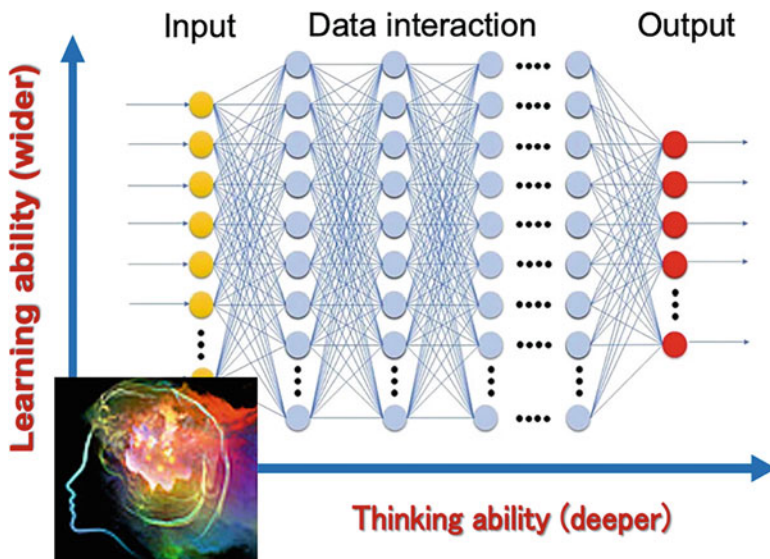
Fig. 1.5 Schematics of human brain and artificial intelligence. (Courtesy of TU Dresden)

transport terms. It is called "radiation-hydrodynamics". Although the plasma is assumed as a neutral fluid, the equation of state should cover from the cold solid material to an electron-degenerated high-density state. The generation of the magnetic field is also briefly explained and the properties of the magneto-hydrodynamic (MHD) equation are discussed. A variety of waves in plasmas are derived and the importance to know the waves is discussed.

In Chap. 3, the physics of shock waves is discussed. Laser-driven ablation plasma produces extremely-high pressure called "ablation pressure". Its physical mechanism is shown by relating to the slow combustion wave, namely the deflagration wave. The ablation pressure scaling law is obtained by solving a hydrodynamic equation in steady state assumption. Such simple theoretical results are compared to the data obtained in model experiments with intense lasers. The dynamics of plasma acceleration by the ablation pressure is also compared to the corresponding experiments with advanced diagnostics.

In Chap. 4, the time-dependent dynamics of laser plasmas is an essential issue to be studied and to be used for applications. It is needed to solve nonlinear partial differential equations even in one-dimensional assumptions. Especially, in spherical geometry, it is hard to find simple analytical solutions. However, it has been shown that the self-similar mathematical method provides a variety of analytical solutions as a function of self-similar variable $\xi \propto r/t^{\alpha}$, where r is the radius, t is time, and α is a constant found finally as an eigenvalue of the problem. Several examples are described there related to the implosion dynamics in spherical symmetric systems. It is important to know such self-similar solutions to obtain the physics image of the implosion and shock dynamics in a converging system.

In Chap. 5, atomic physics and the atomic process of partially ionized atoms are explained within an isolated atom or ion model. While re-reviewing the physics of the atomic structure of the multi-electron atomic system, the quantum physics of all atomic processes are also re-reviewed with intuitive images of the processes. It is not applicable to assume the atomic state of the laboratory plasmas is in the thermodynamic equilibrium (LTE) state, and the non-LTE atomic process should be considered. Photo-ionizing plasma is a typical example of a non-LTE atomic state, and its model experiment with intense laser is compared to the astrophysical plasmas.

In Chap. 6, it is emphasized that rapid heating of plasma by intense laser produces a steep temperature gradient, where the heat flux by the diffusion model is not applicable and the flux should be evaluated with the Fokker-Planck equation of electrons. This is because the plasma size is shorter than the mean free path of the electron component mostly transporting the heat flux. Different mathematical models have been proposed and compared to the Fokker-Planck simulations. The advanced modeling is explained and the importance for studying the direct-drive laser fusion is discussed. The progress of the improvement of the models is reviewed.

In Chap. 7, a brief review of the kinetics of radiation transport with many groups of photo energy is given. In this topic, the toughest job is to calculate the spectral opacity and emissivity, especially of partially ionized medium- and high-Z ions. Once the spectral line opacity becomes important in the radiation energy transport, the numerical modeling becomes complicated for optically thick plasmas. The density dependence of line profiles is discussed by paying attention to related microphysics. The same type of Boltzmann equation should be solved for neutrino transport in gravitationally collapsing supernova explosions of massive stars. Big computing of 3-D simulations is shown as a related topic of radiation transport.

In Chap. 8, the basic knowledge to study dense and non-so-high-temperature plasmas produced by laser shock waves in solid materials is described. In general, the ions are treated as isolated ones in plasma in the case of magnetically confined plasma, space plasma, and so on. As we know, condensed matter shows a many-body effect like band structure. This means with an increase in density and temperature, the many-body effect should be taken into account in any theoretical model and computation. Thanks to the progress of computing, it became possible to carry out "ab initio" calculations. The widely used model, Density Functional Theory (DFT), is briefly derived to prepare its application to the physics of equation of state and warm dense matter.

In Chap. 9, the physics of warm dense matter is discussed. A study of the equation of state with shock waves is introduced. The other method to study high-pressure physics with static high-pressure is also shown, and the long-standing physics of insulator-metal phase transition is discussed. The theory of strongly coupled plasma is studied backing to the old time when computer capability is not enough. It is shown that the warm dense mater can be studied precisely in experiments with X-ray Free-Electron-Lasers (XFEL) and precise theoretical analysis is introduced by the use of density-functional-theory.

References

1. H.W. Liepmann, A. Roshko, *Element of Gasdynamics* (Dover books, 1957)
2. Ya. B. Zel'dovich, Yu. P. Raizer, *Physics of Shock Waves and High Temperature Hydrodynamic Phenomena* (Dover, 2002)
3. M.Y. Jaffrin, R.F. Probstein, Structure of a plasma shock wave. Phys. Fluids **7**(10), 1658–1674 (1964)
4. L.D. Landau, E.M. Lifshitz, *Fluid Mechanics (Course of Theoretical Physics: Volume 6)*, 2nd edn. (Butterworth-Heinemann, Oxford, 1987)
5. H. Takabe, A historical perspective of developments in hydrodynamic instabilities, integrated codes and laboratory astrophysics. Nucl. Fusion **44**(12), S149 (2004)
6. J. Nuckolls et al., Laser compression of matter to super-high densities: Thermonuclear (CTR) applications. Nature **239**(5368), 139–142 (1972)
7. R.S. Craxton et al., Direct-drive inertial confinement fusion: A review. Phys. Plasmas. **22**, 110501 (2015)
8. H. Takabe, Y. Kuramitsu, Recent progress of laboratory astrophysics with intense lasers, High Power Laser Science and Engineering, vol. 9 (Cambridge University Press, 2021), p. e49
9. S. Fujioka et al., X-ray astronomy in the laboratory with a miniature compact object produced by laser-driven implosion. Nat. Phys. **5**, 821 (2009)
10. S. Manabe, A.J. Broccoli, *Beyond Global Warming: How Numerical Models Revealed the Secrets of Climate Change* (Princeton University Press, 2020). https://www.nobelprize.org/prizes/physics/2021/manabe/facts/
11. D. Post, L.G. Volta, Computational science demands a new paradigm. Phys. Today **58**(1), 35–41 (2005)
12. B.K. Speasr et al., Deep learning: A guide for practitioners in the physical sciences. Phys. Plasmas **25**, 080901 (2018)
13. P.W. Hatfield et al., The data-driven future of high-energy-density physics. Nature **593**, 351 (2021)
14. G. Kluth et al., Deep learning for NLTE spectral opacities. Phys. Plasmas **27**, 5 (2020)
15. J.A. Gaffney et al., Making inertial confinement fusion models more predictive. Phys. Plasmas **26**, 8 (2019)
16. V. Gopalaswamy et al., Using statistical modeling to predict and understand fusion experiments. Phys. Plasmas **28**, 12 (2021)
17. B.Z. Djordjević et al., Modeling laser-driven ion acceleration with deep learning. Phys. Plasmas **28**, 4 (2021)

Chapter 2
Basic Properties of Plasma in Fluid Model

Abstract If the spatial variation of plasma is longer than the particle mean free path and the time variation is sufficiently longer than the plasma Coulomb collision time, the plasma can be approximated as being in local thermal equilibrium (LTE) at any point (t, **r**). Then the velocity distribution functions of the particles become Maxwellian. In addition, assuming Maxwellian is also a good assumption in many cases even for collisionless plasmas such as high-temperature fusion plasmas. In the fluid model of plasmas, The plasmas can be described in terms of five variables characterizing local Maxwellian: the density n(t, **r**), flow velocity vector **u**(t,**r**), and temperature T(t, **r**). So, the mathematics used in fluid physics is widely applicable to studying plasma phenomena.

Although conventional fluids are neutral, plasma fluids of electrons and ions couple with electromagnetic fields. It is, therefore, necessary to solve Maxwell's equations simultaneously. It is also possible to approximate electrons and ions as two different fluids or as a single fluid in case-by-case. This requires an insight into what kind of physics is important in our problem.

After reviewing the basic equation of fluids, several fluid models for plasmas are shown. Especially, a variety of waves appears because of charged particle fluids are derived to know why waves are fundamental to knowing the plasma dynamics. The mathematical method to obtain the wave solutions as an initial value problem is explained as well as the meaning of the resultant dispersion relations.

Magneto-hydrodynamic equations (MHD) are derived to explain the effects of the Biermann battery, magnetic dynamo, etc. The relationship of magnetic field and vortex flow is studied. Resistive MHD is derived including the Nernst effect, which becomes important for the magnetic field in strong electron heat flux.

Finally, electromagnetic (EM) waves in magnetized plasmas are derived to see how to use for diagnostics in the laboratory and observation of wide range of electromagnetic waves from the Universe.

2.1   Introduction

The plasma is characterized by the collective motion of many charged particles through the Coulomb interaction. It is usually impossible to use the particle-in-cell (PIC) simulation to study a long-time and large-scale evolution of plasmas with many orders of magnitude differences in density and temperature in a system. It is more convenient to use the fluid approximation of plasmas by introducing macroscopic physical quantities, which are statistical averages of velocity moments of plasma particle velocity (momentum) distribution function.

In the history of the fluid model, Euler and Lagrange derived a mathematical model of fluid dynamics. By the middle of the eighteenth century, "Bernoulli's theorem," which is said to be the first fundamental law of hydrodynamics, was proposed, followed by "Euler's equation of motion" and "Lagrange's equation of motion," which are said to have given birth to modern fluid dynamics.

The fluid model has been applied to gas dynamics. In most cases, it is a good approximation to assume that the relatively high-density plasma such as laser plasma is neutral fluid in the local thermodynamic equilibrium (LTE). Note that the fluid approximation assumes the distribution function of electrons and ions are Maxwellian around their flow velocities, consequently, the so-called kinetic effects to be studied in Volume 4 can be neglected because they are not so important.

In this chapter, it is explained how plasma is approximated as fluid and what kind of basic equations are used for plasmas as fluids. It is not necessary to assume that the plasma is completely ionized gas and that the fluid equations are applicable to the plasmas with the ionization process progressing. The fluid equations are widely used for cases to study the dynamics of the plasmas in any state such as neutral gas, fluid, and even solid.

They are also collectively referred to as "continuum media". Then the image of plasma in this textbook will be very wide. In assuming the plasma as continuum media, another physical state such as gas, liquid, solid, strongly coupled plasma, etc. are also expressed as plasmas in the present textbook, case by case.

2.1.1   Coulomb Collision Relaxation Times

Ideal plasma consists of many ions and electrons, and they are interacting with the Coulomb force in collisional plasma or freely moving by thermal motion in the collisionless plasma case. If the distribution function of the ions and electrons is not and far from Maxwellian distributions, it is required to study the plasma based on the kinetic theory starting with the Vlasov equation. In the present Volume 2, however, the plasma is assumed to consist of the ions and electrons characterized by shifted Maxwellian distributions.

Fig. 2.1 Schematic of an electron scattering by Coulomb force of a heavy ion at the center
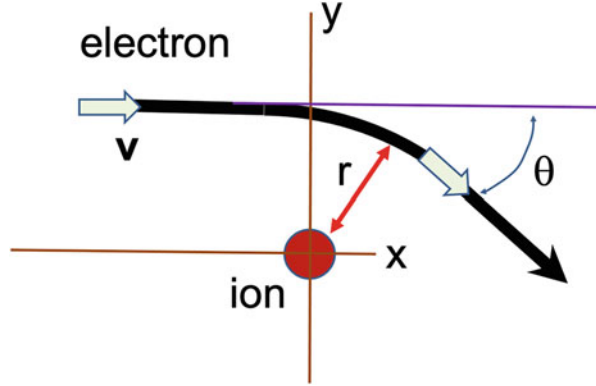
As shown in Fig. 2.1, the Coulomb collision cross-section for an electron with velocity **v** by the ion Coulomb force in plasma is intuitively derived as follows.

$$|\Delta(mv)|_y \approx \frac{Ze^2}{4\pi\varepsilon_0 r^2}\Delta t, \quad \Delta t \approx \frac{r}{v}, \tag{2.1}$$

where the strong interaction becomes effective when the electron kinetic energy of the electron is comparable to the Coulomb force by the ion. Set its radius r_c. Since this radius r_c is the effective distance for strong interaction, the Coulomb collision cross-section of the electron is evaluated as follows.

$$\sigma_c \sim \pi r_c^2 \propto \frac{Z^2}{v^4} \tag{2.2}$$

With use of this cross-section, the collision frequency, the inverse of collision time τ_c, is given as

$$\nu_c(v) = \frac{1}{\tau_c(v)} = n_i\sigma_c v \propto \frac{Z}{v^3}n_e \tag{2.3}$$

Note that the Coulomb collision time strongly depends on the electron velocity and it vanishes for high-velocity electrons. This is the case of the collisionless plasma for high-temperature and low-density plasmas, such as plasmas in magnetically confined fusion devices.

In evaluating the average collision time for the Maxwellian distribution of electrons, the velocity in (2.3) is replaced with the thermal velocity $v_e = (T_e/m)^{1/2}$. This is roughly equal to the distribution function relaxation time τ_e for the electron group. The derivation from (2.1) can also apply to the ion-ion Coulomb collision and the velocity dependence is the same as (2.3). So, roughly speaking the ion relaxation time $\tau_i \sim (v_e/v_i)^3 >> \tau_e$, where v_i is the ion thermal velocity.

However, the electro-ion energy (temperature) relaxation time τ_T (*has* roughly the following relation [1].

$$\tau_e << \tau_i << \tau_T \qquad (2.4)$$

The temperature relaxation time τ_T is roughly given as

$$\tau_T = \frac{m_i}{m_e} \tau_e \qquad (2.5)$$

Since τ_e is almost equal to the classical laser heating time as shown in [1], the temperature relaxation time is almost three orders of magnitude longer than the laser heating time, consequently, the ion temperature is much lower than the electron temperature in the laser heating region.

In the high-density and low-temperature regions such as near and in solid-density plasma, however, it is reasonable to assume a single temperature, $T_e = T_i = T$, and both electron and ion temperatures are equal and given as T. In assuming the plasma is a single fluid, the fluid model of the plasma can be developed by use of conventional fluid mechanics to neutral fluids like air, water, and even solids. Most of the regions of laser-driven plasmas such as shock waves and implosion dynamics in over the solid density are well described by the single temperature and neutral fluid model. Let us start with the basic property of such neutral fluids.

2.1.2 Fluid Model for Laser-Plasma

In this chapter, a variety of fluid assumptions and fluid equations are introduced to describe the fluid dynamics of laser-produced plasma. The models explained in this chapter are listed as.

One Fluid and One Temperature Fluid Model This is the traditional fluid equation to be applicable for the simplest case. The equation is the same as normal fluid, while the equation of state (EOS) from a wide range of temperature and density should be modeled in another way. This is because the pressure should be modeled from solids at room temperature where quantum physics is essential to the state of ionization and to the high-density state of strongly coupling plasma. In addition, electrons and radiation mainly x-rays, transfer the local energy in space. Such transports are modeled in general by heat conduction, while the conduction coefficient is a function of the temperature. In the case where the heat conductivity is proportional to the power of the temperature, it is possible to solve the heat wave analytically in some cases.

One Fluid and Two Temperature Fluid Model In laser-produced plasma, the plasma density and temperature change in time and space over many orders of magnitude. In the ablating and expanding region, the plasma density is relatively

low, so that it is better to assume the ions and electrons have different temperatures. In addition, absorbed laser energy near the critical density is carried to an over-dense region via electrons and radiation heat conductions. The equation of both temperatures, especially electron one should include such heat conduction terms. The first step is to model them with diffusion approximation, and so-called **Spitzer's heat conductivity** is included in the electron temperature equation. However, the diffusion model is not valid in any case of laser plasma and **non-local heat conduction** will be discussed in Chap. 6.

Two Fluid Equations It is hard to extend the above model to two fluids for electrons and ions. It is, however, general that two-fluid models are required to study the phenomena over the Debye length much shorter than the mean free path. It is not so bad to neglect to solve the energy equations and use some simple relation like isothermal or adiabatic relations. Since the attractive force by charge separation for two fluids is strong and the distance is about Debye length, the two-fluid model is applied to study plasma waves induced by charge separations. Laser propagation in plasma is affected only by electron motion and ions can be assumed at rest in high-frequency motions.

Mathematics for Wave Analysis For small perturbations in any type of fluid equations, it is general to obtain coupled partial differential equations providing wave phenomena. The basic equations are modified to coupled, algebraic equations after linearization, Fourier transformation, and Laplace transformation. It becomes clear by solving the wave equation as an initial value problem that why finding the poles of the **dispersion relation** is enough to discuss the waves in plasma. The waves in plasma are important to know how fast the energy of a local disturbance diffuses or propagates around via wave propagation. If there are many waves in a complicated plasma, how fast the plasma confinement breaks is predicted by knowing the fastest wave.

Magneto-hydrodynamic (MHD) Equations It is usual to use a strong magnetic field to confine plasmas. Even in laser-produced plasma, strong magnetic fields are produced. In most cases, macroscopic fluid dynamics is controlled by ion motion, but electrons are easily run in the plasma by electric and magnetic fields in the plasma. The fluid model for plasma in external and internal magnetic fields is the MHD model, where additionally the equations to the electric current and magnetic field should be coupled. In most case, the equation to the current is replaced with a generalized **Ohm's law**. Ideal MHD model for collisionless plasma and resistive MHD model including magnetic diffusion by resistivity and heat flux are derived.

MHD waves In strongly magnetized plasma, new waves due to the magnetic tension and pressure become important as the fastest waves. The former is called the Alfven wave and the latter is called the compressible **Alfven wave**. Of course, it is more complicated because the thermal pressure force couples with the compressional Alfven wave. In addition, circularly polarized-Alfven waves can carry the angular momentum of the plasma particles. So-called Alfven breaking by this

torsional Alfven wave plays an important role to carry out the angular momentum of accretion discs around the stellar objects in the Universe.

Electromagnetic Waves Electromagnetic waves are widely used in our life and also used for plasma experiments for measurement and probing plasmas. External magnetic fields modify dramatically the dispersion relation of the waves. In astrophysics, they are widely used to study the dynamics in the Universe by observing radio waves to gamma rays. It is also used to study the magnetic field in plasmas. The laser is electromagnetic wave with strong electric and magnetic fields. To know the properties of lasers in plasmas is a fundamental as studied in the book as well as well reviewed in Volume 1.

2.2 Neutral and Single Fluid Approximation of Plasma

2.2.1 Fluid Assumption

What is the fluid approximation? Consider a local fluid element, say in a volume with a unit mass, out of all fluid composed of many particles as one mass point. First, consider the equation of motion of this local fluid called a **fluid element**. This is the governing equation on the average flow velocity of the fluid element. At the same time, it is considered that the fluid element has internal energy as a small thermodynamic system, and a governing equation relating to its temperature is derived from the first law of the thermodynamics. In addition, the mass of the fluid element should be governed by the conservation relation.

It is useful to know the intuitive image of the fluid approximation. Since fluids such as water are packed closely with molecules, it is natural for the readers to imagine that the molecules of water in a certain volume move together like a large mass point. However, if this is the case of gas with a mean free path much longer than the intermolecular distance, the molecules that make up the unit mass volume of fluid will interchange with external particles from time to time. Then, the image of moving together is wrong. However, since fluid equations can be mathematically derived from the Boltzmann equation, it is enough to think that a continuous group of fluid fragments like a point mass is a mathematical concept.

However, the fluid approximation is reasonable only when the assumption of local thermal equilibrium is satisfied so that the velocity distribution function of particles made of fluid is close to Maxwellian. The same is true for the plasma. The mean free path of high-temperature plasma easily becomes longer than the plasma size. Still, the fluid equations are indeed appropriate mathematical models as long as the velocity distribution function of the plasma is close to the Maxwell distribution locally. This mathematics is shown in Appendix A.

Consider the thermodynamics of the fluid element. With the internal energy density set to ε, the first law of thermodynamics should be satisfied.

$$d\varepsilon = -PdV + dQ \tag{2.6}$$

Here, P is the pressure, $V = 1/\rho$ is the volume occupied by a unit mass (referred to as a **specific volume**), ρ is the mass density, and dQ indicates the amount of energy that flows into this volume as thermal energy by thermal conduction, heating, cooling, etc., and also the heat flowing out from the volume.

The fluid of the specific volume moves at the average flow velocity vector **u**. The equation of motion is inferred from the Newton equation,

$$\rho \frac{d}{dt}\boldsymbol{u} = \rho\boldsymbol{F} - \nabla P \tag{2.7}$$

Here, **F** is an external force. The difference from the Newton equation is that the force due to the pressure appears in (2.7). When molecules cannot move freely like in water and move as a whole locally, the pressure can be regarded as the average force by the surrounding fluid molecules acting on the surface of the specific volume. It is hard to understand intuitively the physics image, however, when the particles are freely moving in the volume like in the case of collisionless plasma. As explained later, the pressure is the momentum flux of the microscopic particles passing through the unit surface per unit time. The reason why this is added to the Newton equation as a slope of pressure will be explained after deriving it mathematically.

To analyze any fluid phenomenon, two other equations are necessary. One is the equation for mass density, the other is the form of the pressure P as a function of density and internal energy. The former is called the **equation of continuity** and the latter is called the **equation of state**, respectively. A fluid whose density hardly changes like water in our daily life is called an **incompressible fluid**. In this case, the density is unchanged, and the equation of continuity is not necessary. In studying the plasma produced by the high-intensity laser, however, it is easy to create the pressure of millions of atmospheres in the matters and the compression of even water is easy. In many cases in the laser-plasmas, it is necessary to consider the phenomena of compressive fluids whose density also changes dramatically.

The governing equation for the mass density is called the **equation of continuity** (the continuity equation) and is given by the following relation,

$$\frac{\partial \rho}{\partial t} + \nabla(\rho\boldsymbol{u}) = 0 \tag{2.8}$$

This is also called the **mass conservation law** of fluid. It is clear that (2.8) is written in the same partial differential equation as the energy conservation equation of the electromagnetic wave in Vol. 1. In (2.8), $\rho\boldsymbol{u}$ is the **mass density flux**.

Integrating (2.8) over an arbitrary volume V, the following relations are obtained.

$$\oint \frac{\partial \rho}{\partial t} dV = \frac{\partial}{\partial t} \left(\oint \rho dV \right) \tag{2.9}$$

$$\oint \nabla(\rho \boldsymbol{u}) dV = \oint \rho \boldsymbol{u} \cdot d\boldsymbol{S} \tag{2.10}$$

Here, (2.10) is the **Gauss theorem**. Then, (2.8) has the following relation in the integrated expression.

$$\frac{\partial}{\partial t} \left(\oint \rho dV \right) = - \oint \rho \boldsymbol{u} \cdot d\boldsymbol{S} \tag{2.11}$$

This indicates that the time change of the mass in any volume V is determined by the difference between the mass escaping from the volume surface and the mass flowing in. Therefore, total mass is kept constant when the volume V is taken to be the volume of the total system without any external mass flux.

As mathematically proved with (2.8), it can be shown in a general form.

$$\frac{\partial W}{\partial t} + \nabla \boldsymbol{Q} = 0 \tag{2.12}$$

This is a partial differential equation showing the **conservation relation** to a physical quantity W and its flux **Q**.

2.2.2   Basic Equations of Fluid Dynamics

There are two ways of expression of fluid equations. They are mathematically the same as explained later, while the concept of physical quantities is different:

1. Lagrange fluid equation
2. Euler fluid equation

These differences appear with difference on time derivative. **Lagrange** type is written with **total derivative** (d/dt), while **Euler** type is expressed with partial derivative ($\partial/\partial t$). Both are directly related as follows.

$$\frac{d}{dt} = \frac{\partial}{\partial t} + \boldsymbol{u} \cdot \nabla \tag{2.13}$$

Here, $\boldsymbol{u} \cdot \nabla$ is called the **convection term** of fluid, and it means the change of variables due to convective motion of fluid elements.

Fig. 2.2 Equi-contours of a fluid field $f(t, x)$ in one dimension in space. The solid line is trajectory of a fluid element. The total derivative, Lagrange derivative, has the relation with the fluid field in Euler coordinate. This figure shows the relation between Lagrangian and Euler time derivative intuitively
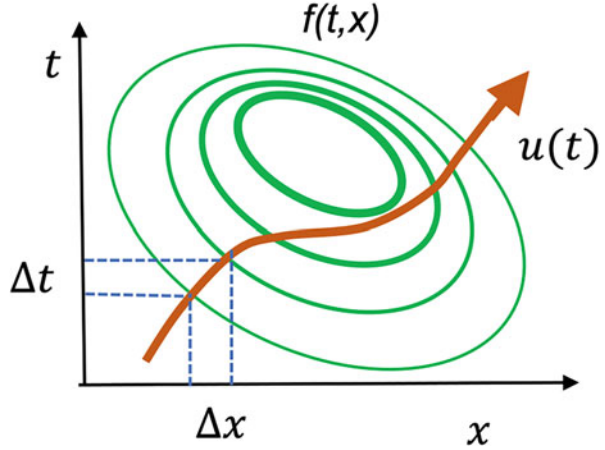
In Newton mechanics, the equation of motion is governed by the force applied to a point mass. On the other hand, the Maxwell equation is that governing physical quantities of electric and magnetic fields defined in a given space. There are two ways to formulate hydrodynamic equations as the former image, Lagrange type, and Euler type that defines the field variables such as velocity fields like the electric field. One can choose one of two types of fluid equations that is convenient for one's problem and mathematically easier to solve that problem.

The relationship between the two types can be understood from Fig. 2.2. The contour lines are equi-contours of a certain physical quantity (e.g.; the velocity in x-direction) obtained by solving a fluid equation, where the brown line is the x-trajectory of a fluid element. For the sake of simplicity, assume that space is only one dimension on the x axis and consider the physical quantity shown in Fig. 2.2 as $f(t, x)$. Then, the following relation can be obtained for small amounts Δx and Δt.

$$\Delta f = \frac{\partial f}{\partial t} \Delta t + \frac{\partial f}{\partial x} \Delta x \qquad (2.14)$$

This is rewritten to be

$$\frac{\Delta f}{\Delta t} = \frac{\partial f}{\partial t} + \frac{\Delta x}{\Delta t} \frac{\partial f}{\partial x} \qquad (2.15)$$

As can be seen in Fig. 2.2, since the local fluid moves in space, at the limit of $\Delta t \rightarrow 0$, (2.15) becomes,

$$\frac{df}{dt} = \frac{\partial f}{\partial t} + u_x \frac{\partial f}{\partial x} \qquad (2.16)$$

Therefore, it is clear that in the three-dimensional space (2.16) becomes (2.13).

When analyzing a fluid phenomenon, the Lagrange type of equation is easy to solve mathematically, and the image of physical results is also easy to grasp in some cases. For example, a one-dimensional compressible fluid is good example. However, when analyzing complicated flow or carrying out multidimensional computer simulation, the Euler type is generally easier to solve numerically.

In the fluid equation of the Lagrange type, (2.7) can be regarded as the equation of motion for the point mass, ρ. Since it also carries the thermodynamic quantities, from the expression (2.6) applied to the internal energy per unit mass of the fluid, the following energy equation can be derived.

$$\frac{d\varepsilon}{dt} = -P\frac{dV}{dt} + \frac{dQ}{dt} \tag{2.17}$$

Here, the specific volume

$$V = \frac{1}{\rho} \tag{2.18}$$

It is noted that (2.17) is rewritten after inserting (2.18) into (2.17) and using (2.8),

$$\frac{d\varepsilon}{dt} = -\frac{P}{\rho}\nabla u + \frac{dQ}{dt} \tag{2.19}$$

As a result, the following coupled equations are derived for the fluid equation in Lagrange type

$$\frac{d\rho}{dt} = -\rho\nabla \cdot u \text{ (Equation of continuity)} \tag{2.20}$$

$$\rho\frac{du}{dt} = -\nabla P + \rho F \text{ (Equation of motion)} \tag{2.21}$$

$$\frac{d\varepsilon}{dt} = -\frac{P}{\rho}\nabla u + \frac{dQ}{dt} \text{ (Energy equation)} \tag{2.22}$$

On the other hand, in the Euler type, the hydrodynamic variables are considered as the field quantities in the time and space (t, **r**). As like the Maxwell equations, the equation governing such field quantities is a partial differential equation. Therefore, (2.20) can be in the Euler type as follows.

$$\frac{\partial\rho}{\partial t} + \nabla(\rho u) = 0 \tag{2.23}$$

$$\rho\left(\frac{\partial}{\partial t} + u \cdot \nabla\right)u = -\nabla P + \rho F \tag{2.24}$$

$$\left(\frac{\partial}{\partial t} + \boldsymbol{u} \cdot \nabla\right)\varepsilon = -\frac{P}{\rho}\nabla\boldsymbol{u} + \frac{dQ}{dt} \tag{2.25}$$

It should be noted that the equations of (2.23, 2.24, and 2.25) differ significantly from that of the Maxwell equation; namely, the fluid equations are nonlinear equations. For example, the **nonlinearity** of fluid dynamics stems from the convection term:

$$\boldsymbol{u} \cdot \nabla\boldsymbol{u} \tag{2.26}$$

As the fluid velocity increases, the convective term cannot be neglected and it plays an important role in the formation of a unique structure like shock waves to be discussed in Chap. 3.

2.2.3 Conservation Relations

Three conservation equations can be derived from the fluid equations. Consider the case without the external source force **F** in (2.14) and heat Q in (2.25). The conservation of mass has already been shown in (2.8). Next is the fluid momentum density conservation law, which is obtained by adding two equations after multiplying (2.24) and (2.23) by the flow vector **u**.

$$\frac{\partial}{\partial t}(\rho\boldsymbol{u}) + \nabla\left(\rho\boldsymbol{u} \otimes \boldsymbol{u} + \overleftrightarrow{P}\right) = 0 \tag{2.27}$$

Here, the mathematical symbol "⊗" means in this case to create a three-dimensional tensor from three-dimensional vectors, whose (i, j) component is $u_i u_j$ in (2.27). This is called a **dyadic product** (tensor). The pressure was generally indicated in the form of a tensor in three-dimension. For the ideal gas, the pressure is a scalar and it can be considered that a scalar pressure is multiplied by a unit tensor in (2.27).

The third and final one is the energy conservation equation. The sum of the kinetic energy of the fluid flow and the thermodynamic internal energy should be conserved. By deriving an equation for each energy density for both, the total conservation form can be obtained after adding both equations. Specifically, multiplying (2.23) by $1/2u^2$, multiplying (2.24) by **u**, and multiplying them by (2.25) multiplied by density ρ give

$$\frac{\partial}{\partial t}\left(\frac{1}{2}\rho u^2 + \rho\varepsilon\right) + \nabla\left\{\left(\frac{1}{2}\rho u^2 + \rho\varepsilon + P\right)\boldsymbol{u}\right\} = 0 \tag{2.28}$$

Here, P is a scalar for the sake of simplicity. Even if the pressure is tensor, the tensor pressure can be easily written in the same form as (2.28). In gas dynamics, the **enthalpy** in the form is also introduced.

$$h = \varepsilon + \frac{P}{\rho} \tag{2.29}$$

As a result, it is found that the conservation form of the fluid equation consists of (2.8) for mass, (2.27) for momentum, and (2.28) for total energy. It is easily found that these three equations are in the form of standard conservation Eqs. (2.12).

2.2.4 Equation of State

In general, the external force **F** and heat exchange dQ are given in solving (2.20, 2.21, 2.22, 2.23, 2.24, and 2.25). Still, however, one another relation or equation is necessary in order to make the fluid equations in closed form. It is called the **equation of state** (**EOS**) and is a relation between internal energy ε and pressure P. The equation of state is usually given with a new thermodynamic quantity, temperature T, in the form

$$\begin{aligned} P &= P(\rho, T) \\ \varepsilon &= \varepsilon(\rho, T) \end{aligned} \tag{2.30}$$

In (2.22), the equation of energy can be transformed into the equation for temperature T, and the fluid equation can be solvable as a closed system of three equations for density ρ and flow velocity **u** (three-dimensional vector), and temperature T.

Except for the case of the ideal gas, how to calculate the equation of state (2.30) itself is a major research topic in the laser plasma. The matter changes from solid to liquid, neutral gas to plasma. In laser-plasma experiments, it is usually required to study strong shock waves and related phenomena, where the shock waves pass through the solid and change the overall states. In such a case, it is necessary to introduce an appropriate formula for the equation of state within the range of density and temperature over many orders of magnitude. It is also required to model the phase transitions, although the fluid approximation is still valid.

For the time being, the following EOS is assumed as the ideal gas for the fluid consisting of fully ionized ions with charge Z and electrons.

$$P = (Z + 1)n_i T \tag{2.31}$$

$$\varepsilon = \frac{(Z + 1)}{\gamma - 1} \frac{T}{M} \tag{2.32}$$

Here, T is expressed in units of energy including Boltzmann constant k_B. The unit of the electron volt (eV) is used in the present book for the temperature. In (2.31), n_i is the number density of ions and M is approximated by the ion mass, because the

electron mass can be neglected. In addition, γ in (2.32) is the **specific heat ratio**. Note that γ is given simply as a function of the degree of freedom of the particle dynamics, and given number of the freedom, N, the following relation is satisfied.

$$\gamma = \frac{N+2}{N} \tag{2.33}$$

If there are no internal degrees of freedom in all particles of the fluid and the particles freely fly in the x, y, and z spatial three dimensions, N = 3 and it is enough to set $\gamma = 5/3$.

2.2.5   Thermodynamic Consistency

If the laser intensity is not so high, the electrons on the solid surface are heated, the inside of the solid is heated by the heat conduction of electrons, and the temperature increases from the surface. When the temperature is high, the solid melts and undergoes a phase transition to a liquid state. Furthermore, the laser intensity is strong, and vaporization occurs from the liquid state when the temperature becomes high enough. Depending on the material, the phase transition proceeds while the gas and the liquid are mixed, and the state becomes a neutral gas state. Furthermore, as neutral gas absorbs laser photons, dissociation progresses and ionization starts. If the laser intensity is sufficiently strong and the Z-value of the solid is not so high, the material becomes in a completely ionized plasma state, and the temperature increases further. The microphysics of ionization and related processes will be discussed in Chap. 5.

This book must be useful for analyzing the plasma process, and the plasma in stars, including non-ideal plasma with a wide range of temperature and density regions. If the fluid equations are used to analyze and simulate from a solid state to an ideal plasma with reasonable mathematical model, the ideal gas equation of state alone is not sufficient. When a star is born from a molecular cloud and evolves in time, non-ideal plasma should be studied about molecular dissociation, ionization processes etc. Therefore, the thermodynamics and statistical mechanics for understanding general properties of the equation of state should be studied including phase transition.

When the system is in thermodynamic equilibrium, the equation of state is determined only by two state functions of the system, for example, temperature T and density ρ like (2.30). In general, the equation of state can be derived from the thermodynamic potential. It is known that **Helmholtz free energy** F (T, ρ) per unit mass of the system is defined with a function of only (T, ρ), and it satisfies the following relations.

$$S = -\frac{\partial F}{\partial T} \tag{2.34}$$

$$\varepsilon = F + TS = -T^2 \frac{\partial}{\partial T}\left(\frac{F}{T}\right) \tag{2.35}$$

$$P = -\frac{\partial F}{\partial V}, \qquad V = \frac{1}{\rho} \tag{2.36}$$

Here, S is an entropy per unit mass.

If F (T, ρ) is given, the equation of state is uniquely determined. At the same time, the following **thermodynamic consistency** is satisfied automatically.

$$\frac{\partial \varepsilon}{\partial V} = -P + T\frac{\partial P}{\partial T} \tag{2.37}$$

The relation (2.37) is obtained by partial differentiation of (2.35) with V, partial differentiation of (2.34) with V, and the change of the order of V and T. As can be seen from (2.37), it is not allowed to define P and ε independently. Given a function of pressure P, the internal energy ε must be uniquely determined by (2.37). When modeling the pressure P with some approximation, ε is necessary to be obtained from (2.37) by integrating with V.

What happens if the equation of state does not satisfy (2.37)? When in the Newton equation, a point mass moves from the initial point to the endpoint in a mechanical potential, the energy obtained by the point mass is given by the difference between the potential energies at both points. As same as this, if the equation of state does not satisfy (2.37), the amount of change in internal energy depends on which path in the two-dimensional space of (V, T) the system took to change. This contradicts the assumption that the physical quantity changes in the thermal equilibrium state. In the ideal gas equation of state (2.31, 2.32, and 2.33), both sides of (2.37) disappear, and it turns out that (2.37) is satisfied for arbitrary constant γ.

2.2.6 Cold Pressure

Intense lasers are also used to study the properties of matter at extremely high pressure. High-pressure physics by the use of lasers is now an important research field. For example, the physics of the insulator-metal phase transitions is intensively studied these days as will be discussed in Chap. 8. The pressure and internal energy of the matter compressed more than its solid density are mainly determined by the pressure due to the exchange interaction of electrons and the Coulomb repulsive force among electrons and ions for covariant bonding matter and electron degenerate pressure due to **Pauli exclusive principle** for the matter with many free electrons like metals. Such pressure at T = 0 is called the **cold pressure** P_c and it is only a function of the density ρ.

Fig. 2.3 The cold pressures of several materials commonly used as targets of laser plasma are plotted as function of density. Phase transition is clearly seen in the case of solid DT fusion fuel. Reprint with permission from Ref. [2]. Copyright 1998 by American Institute of Physics
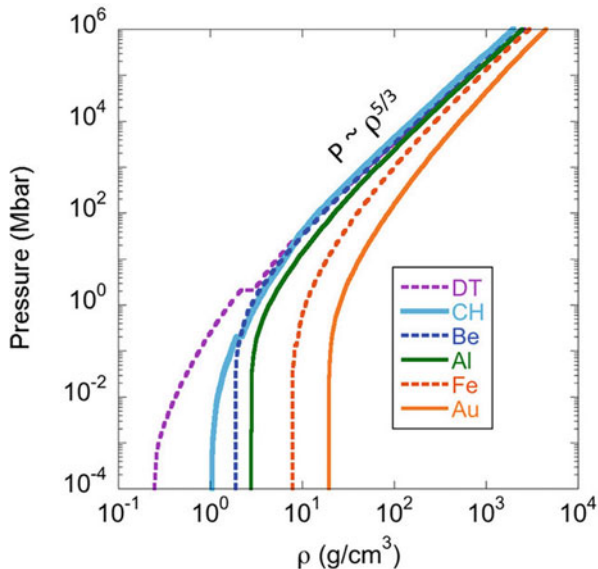
The functional form of the pressure of matter at high density can be written in the form.

$$P(\rho, T) = P_c(\rho) + P_t(\rho, T) \tag{2.38}$$

where P_t is the **thermal component** and $P_t = 0$ at $T = 0$. The cold pressures of several materials are plotted in Fig. 2.3 [2], where the pressure is equal to zero at the nominal solid density at $T = 0$. The cold pressure is plotted for DT fusion fuel, CH plastic, Be, Al aluminum, Fe iron, and Au gold, widely used for solid targets irradiated by intense lasers. The cold pressure is due to molecular bonding pressure and the electron **Fermi pressure** at density near and higher than the solid density.

Then, it is clear that the cold component of the pressure should be calculated with (2.37) as

$$\varepsilon_c(\rho) = \int \frac{P_c(\rho)}{\rho^2} d\rho \tag{2.39}$$

Of course, if one has the function of the cold internal energy, the cold pressure is obtained by the density derivative of the cold energy by (2.39).

In solving the hydrodynamic equations with such a cold pressure, it is important to modify the equation of energy (2.22) as follows. Then, the total internal energy should be in the form.

$$\varepsilon(\rho, T) = \varepsilon_c(\rho) + \varepsilon_t(\rho, T) \tag{2.40}$$

where ε_t is the thermal component derived from (2.37) with P_t in (2.38). Note then that the cold component satisfies the relation.

$$d\varepsilon_c = -P_c dV \tag{2.41}$$

(2.41) indicates that the cold components of pressure and internal energy in (2.17) cancel to disappear from the equation of energy. It is enough to insert only the thermal component of (2.38) and (2.40) into (2.17).

The energy equation is converted to the equation for the temperature as

$$\frac{d}{dt}\varepsilon_t(\rho, T) = \frac{\partial \varepsilon_t}{\partial T}\frac{dT}{dt} + \frac{\partial \varepsilon_t}{\partial V}\frac{dV}{dt} \tag{2.42}$$

Inserting (2.42) to (2.17) the equation to the temperature is obtained from (2.25) as

$$\frac{\partial \varepsilon_t}{\partial T}\frac{dT}{dt} = -\left(P_t + \frac{\partial \varepsilon_t}{\partial V}\right)\frac{dV}{dt} + \frac{dQ}{dt} = -T\frac{\partial P_t}{\partial T}\nabla \boldsymbol{u} + \frac{dQ}{dt} \tag{2.43}$$

In the case where the thermal component can be neglected and the pressure is only the function of the density, fluid equations are closed only with (2.23) and (2.24) and it is not necessary to solve (2.25). This is the case, for example, where the electron Fermi pressure is dominant in compression. It is also the case where the cold pressure by the ion Coulomb force is dominant in higher-density.

On the other hand, the adiabatic compression without the heat term $Q = 0$ in (2.43) provides the temperature as a function of only the density, consequently, it is not necessary to solve the energy equation explicitly. In some cases, it is assumed that the pressure does not depend on the temperature in hydrodynamic model such as star formation in astrophysics or the formation of a large-scale structure in the Universe. Such a simplified EOS is used to model that "entropy decreases in the process of formation of stars" taking account of heating by compression and energy loss due to radiation emission. Such a case is called a **polytrophic process** in thermodynamics. That is,

$$P = A\rho^n \tag{2.44}$$

where A is a constant coefficient and the pressure is proportional to the n-th power of the density. In general, the "n" is called a **polytrophic exponent.**

2.3 Sound Waves

To know the fundamental property of the fluids, the linear response of small perturbations in the fluid Eqs. (2.23, 2.24, and 2.25) is studied. It is well known that they give the relation of sound waves propagating in any continuous media.

Now, when a very weak disturbance is generated externally in steady state fluid whose physical quantities are described with a subscript "0". The physical quantities due to the disturbance are shown with a suffix "1", where they change as a function of space and time. The linearized continuity equation and momentum equation are derived as follows.

$$\frac{\partial}{\partial t}\rho_1 + \rho_0 \nabla \boldsymbol{u}_1 = 0 \tag{2.45}$$

$$\rho_0 \frac{\partial}{\partial t}\boldsymbol{u}_1 = -\left(\frac{\partial P}{\partial \rho}\right)_0 \nabla \rho_1 \tag{2.46}$$

where $\boldsymbol{u}_0 = 0$ has been assumed. The external force is also neglected here. In (2.46), it is assumed that $P = P(\rho)$.

Partial differentiation due to the density of pressure has a dimension of velocity squared, and the velocity (**sound velocity**) V_s of the sound wave propagating in the fluid can be defined as follows.

$$V_s = \sqrt{\left(\frac{\partial P}{\partial \rho}\right)}\Bigg|_{\rho=\rho_0} \tag{2.47}$$

where RHS is a constant value calculated with ρ_0 and P_0. By substituting (2.47) into (2.46), a partial differential equation of the second order for the density disturbance is obtained.

$$\left(\frac{\partial^2}{\partial t^2} - V_s^2 \nabla^2\right)\rho_1 = 0 \tag{2.48}$$

For simplicity, if the density perturbation is assumed to propagate in the x direction and there is no spatial change in the y and z directions, (2.48) becomes the form.

$$\left(\frac{\partial}{\partial t} + V_s \frac{\partial}{\partial x}\right)\left(\frac{\partial}{\partial t} - V_s \frac{\partial}{\partial x}\right)\rho_1 = 0 \tag{2.49}$$

Equation (2.49) gives the waves of the first term which propagates in the x direction at the velocity Vs and the wave which the second term propagates in the -x direction. The dispersion relation to the frequency ω and wavenumber $\boldsymbol{k}$ is easily calculated as

$$\omega^2 = V_s^2 k^2 \tag{2.50}$$

In our everyday conversation, the density and pressure disturbance of sound is sufficiently small, and the sound wave propagates at the sound velocity obtained by substituting the air density and pressure in (2.47). In fact, we open and close

the vocal cord membrane in the throat of the mouth and adjust the waveform of the pressure coming out of the mouth. This generates sound waves, and since the propagation speed of the sound waves is constant and independent of the wavelength as derived in (2.50), the pressure wave of the same waveform goes all the way. Therefore, as a vibration of the eardrum of the listener, the time change of the pressure wave is sensed, and the conversation sound is recognized.

This fact can be applied to the sound waves in solids, liquids, and gases. What is understood from (2.47) is that the sound velocity is related to the **bulk modulus B** defined as follows.

$$B = \rho_0 V_s{}^2 \tag{2.51}$$

The bulk modulus is the pressure to compress the matter to the density two times from the normal condition. It can be seen that the propagation speed of the sound wave is slower as it is easy to compress. In other words, in a continuous body regarded as **incompressible** such as a solid or a liquid which is difficult to compress in the everyday life. Since the density change due to pressure disturbance is almost as close as zero, the speed of sound is fast. That is, it can be seen that the incompressible fluid approximation is the limit of the infinite sound speed.

A typical example of the data of Bulk modulus is listed below. Shock waves produced by laser irradiation generate the pressure of more than Mega bar (10^6 atm.) and the physical property of highly compressed matter is studied.

water: 0.022×10^6 atm.,	carbon: 0.18×10^6 atm.,
aluminum: 0.75×10^6 atm.,	iron: 1.1×10^6 atm.,
polyethylene (CH): 0.04×10^6 atm.,	gold: 2.2×10^6 atm.,
air: 1 atm.,	solid hydrogen: 2000 atm.

The sound velocity is the most important physical parameter of any kind of fluid or continuous media. When the spontaneous release of high pressure happens due to some natural or artificial reason at a certain point in space, the sound waves play a role to relax the pressure in space. The sound waves also carry the energy around so that the pressure disturbance disappears as time goes on. Earthquake is due to the release or generation of huge energy underground and this energy is spread by the waves propagating in the ground with given velocities.

2.3.1   Wave Propagation in Spherical Geometry

It is useful to know how the waves propagate in the spherical geometry. At a far distance place from the initial disturbance, it can be assumed that the wave perturbation is spherically symmetric, and using the spherical Laplacian in (2.48), the wave equation becomes,

$$\frac{\partial^2}{\partial t^2} u_1 - \frac{1}{r^2} \frac{\partial}{\partial r} \left(r^2 \frac{\partial}{\partial r} \right) u_1 = 0 \tag{2.52}$$

Using the fact that the wave energy is conserved in propagation, it is expected that the energy flux satisfies the relation,

$$\frac{1}{2} \rho_0 u_1^2 V_s \times 4\pi r^2 = const. \tag{2.53}$$

This energy conservation relation suggests the functional structure of the perturbations as

$$u_1 = \frac{A}{r} e^{ikr - i\omega t} + \frac{B}{r} e^{ikr + i\omega t} \tag{2.54}$$

where A and B are constants determined by the initial condition. The first one is a spherical wave propagating outward, while the second one is that coming from the out to the center. If the wave source is released at the center, $B = 0$ is satisfied. It is clear that (2.54) satisfies the wave equation in spherical geometry. If there is no damping of the perturbations, the amplitude of the waves decreases in proportion to $1/r$ due to the spherical geometry effect.

2.3.2 Importance of Wave Analysis

Assume that some fluid is at rest and in a stationary state. Suppose, for example, an energy is released at a certain point in the stationary fluid. In the case of air, it is clear what happens when a firework explodes in the air. Then, we hear strong sounds generated by the explosion, and of course we enjoy the fireworks. This is analogous to the case of confined plasma. When some energy is released in some point of plasma, the energy disperses to the surrounding by waves. Even with a slight perturbation in the plasma, waves are excited, and they disperse energy and momentum in the plasma. Because of this reason, it is very important to investigate the wave property in the equilibrium plasma beforehand. If the amplitude of the waves is large, the plasma itself is destroyed.

The role of the waves in such equilibrium state is experienced in the case of the propagation of the **seismic wave** due to the **earthquake**. As shown in Fig. 2.4, when energy generation suddenly occurs at the seismic source, the energy propagates to the surface of the earth through seismic waves, tsunamis, etc. The seismic waves are longitudinal and transverse waves propagating from the epicenter. The longitudinal wave propagates by compressing the soil with the velocity of about 10,000 km/h (6 km/s). This is the sound wave in the soil material. The transverse wave arises due to the viscosity of soil and propagates at 5000 km/h (3 km/s).

The former longitudinal waves are called the P waves, and the transverse waves are called the S waves. Furthermore, when both waves reach the surface of the earth,
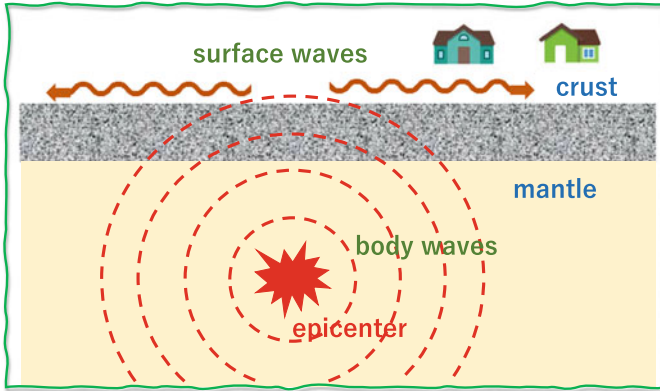
Fig. 2.4 Schematic of propagation of seismic waves from the energy source (epicenter). The longitudinal and transverse waves transport the energy of the earthquake to the surface of the earth. Once the waves arrive on the surface, the surface wave spread the energy over the wider area of the earth. To study the property of the waves of continuous media is important to know the energy transport by such a hydrodynamic motion

they will become surface waves propagating on the ground surface like the gravitational waves of the water surface explain in Volume 3. To issue an earthquake warning, the occurrence of an earthquake is detected by observing this P wave and S wave in advance. From the energy point of view, the waves act to disperse the energy soon after a huge energy such as a collapse of the ocean floor occurs locally.

It is the same in plasmas. Consider, for example, the case where the plasma ejected by the explosion of the Sun surface (solar flare) falls as the plasma energy from the outside into the plasma confined in the earth magnetosphere. The abruptly injected energy propagates in the Earth's magnetic field at high velocity by the **Alfven waves** discussed later. If the amplitude is too large, the plasma itself will be destroyed. When the plasma fluctuates greatly in the magnetic field, an electric field is generated, and electromagnetic waves are generated from the Maxwell equations. If this electric field is too strong, excessive current will flow in the circuit of the communication system and it will be destroyed. In order to predict such natural disasters, the research field of "space weather forecast" is promoted through collaboration between solar observation and numerical simulations.

2.3.3   Wave Optics and Metamaterial

For the readers, it is interesting to know more about another wave property of the sound waves. In Fig. 2.5, a **metamaterial** for sound wave is shown [3]. The scattering of a sound wave from the left on a rigid object at the center is shown on the left in Fig. 2.5. It is obvious that the wave is scattered due to the reflection by the object and interferometry makes the wave profile complex. The snapshot is the
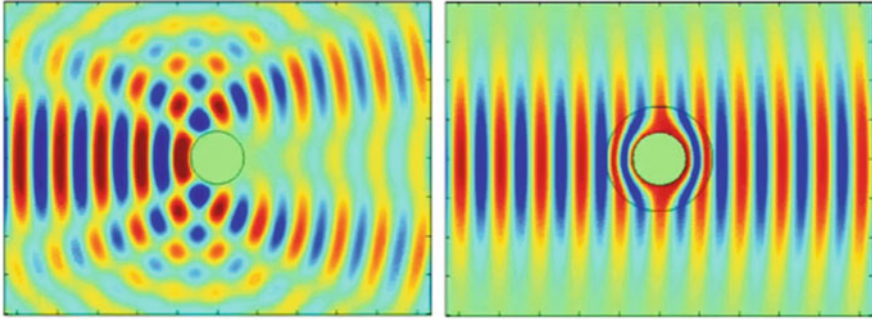
Fig. 2.5 A snapshot of the density contours of the sound wave scattered by an object. (**a**) is the case of scattering by a normal object, while (**b**) is by a meta-material with an additional shell around the object. Mathematical solution of the sound wave scattering allows almost no scattering object, and the object becomes transparent to the sound wave. Reprint with permission from Ref. [3]. Copyright 1998 by American Institute of Physics

density perturbation and quasi-specular reflection and deep shadow of the wave are observed in the right as the normal case. Surrounding the same object with an ideal cloaking shell, however, shows the absence of both reflection and shadow as shown on the right in Fig. 2.5. The wave power is transmitted around the metamaterial object with no losses and the existing of the object cannot be detected.

Such concept of metamaterial is also applicable to any kind of waves. This is the so-called stealth function, which can be applied to any wave, for example, the reflection of radio waves from an object can be avoided with the same idea to the electromagnetic waves.

2.4 Non-Ideal Fluid with Viscosity and Thermal Conduction

2.4.1 Viscosity and Reynolds Number

The ideal fluid has been assumed so far, and the effects such as molecular viscosity are ignored in the fluid equations. Also, we have ignored the heat conduction in the equation of energy. In any fluid dynamics with the non-uniformity of flow velocity and/or temperature, the viscosity and/or heat conduction should be evaluated at first whether they can be neglected.

Consider the fluid dynamics of weather and climate phenomena in our daily life. In summer, strong sunlight raises the temperature of the earth's surface. Heat conduction and convection phenomena in the air can cause the mirages. When this happens near the equator of the Pacific Ocean or the Atlantic Ocean, high temperature seawater evaporates, creating rising air flow, and typhoons and hurricanes are born by the Coriolis force stemming from the rotation of the Earth. In the typhoons

and hurricanes, small eddies grow finally to one large vortex while being influenced by viscosity and nonlinear effects. It is well known that the lower the center pressure, the larger the size.

In order to study the actual fluid phenomena, there are cases where three coupled equations of ideal fluid (2.23, 2.24, and 2.25) are not appropriate. It is necessary to consider the viscosity effect accompanying the spatial variation of the flow velocity in the equation of motion. The viscosity relaxes the spatial variation of fluid velocity and converts the flow kinetic energy to the internal energy of fluid (heat). This is the viscosity heating of fluid same as the frictional heating of a body in a simple mechanics.

In the equation of energy, in addition, when the temperature changes spatially, it is necessary to consider the transport of the internal energy. This is a corresponding phenomenon of the diffusion of internal energy. The continuity equation is an equation of mass conservation and can be used as it is. Taking into account these effects, the equation of motion in (2.21) and the equation of energy in (2.22) should be modified.

Derivation of the details of that viscosity force is complicated, so the following equation of motion with a scalar viscosity is used in this book without any mathematical derivation.

$$\rho \frac{d\boldsymbol{u}}{dt} = -\nabla P + \rho \boldsymbol{F} + \frac{4}{3}\mu\nabla^2\boldsymbol{u} - \mu\nabla\times\nabla\times\boldsymbol{u} \qquad (2.55)$$

This is **Navier-Stokes equation**. Here, μ is a **viscosity coefficient** and assumed to be constant. In (2.55), the first term of the viscosity is the diffusion of flow velocity with the **diffusion coefficient**

$$\nu = \frac{\mu}{\rho} \qquad (2.56)$$

The ν in (2.56) is called the **kinematic viscosity coefficient**. The last term on RHS in (2.55) is the force that makes the flow velocity variation in space smooth when the flow velocity changes in perpendicular to the direction of flow vector.

In many cases in fluid dynamics, **incompressible assumption** is used. For example, fluid dynamics of climate change and subsonic aircraft can be studied by neglecting the change of the density. In the **subsonic flow** the flow velocity is lower than the sound velocity and the density perturbation due to the motion of a body can be smoothed out by the sound waves. In the **supersonic flow**, **shock waves** to be described in Chap. 3 are generated, then, the **compressibility** becomes essential in the fluid dynamics. The motion of a submarine in the sea water is studied with the assumption of incompressibility. The **Navier-Stokes** equation is used for complicated fluid calculations such as a change from laminar flow to turbulent flow of the wind flow in our life. The incompressible Navier-Stokes equation is directly derived from (2.55).

$$\frac{\partial \boldsymbol{u}}{\partial t} + (\boldsymbol{u} \cdot \nabla)\boldsymbol{u} = -\nabla\left(\frac{P}{\rho}\right) + \nu\nabla^2\boldsymbol{u}, \boldsymbol{\nabla} \cdot \boldsymbol{u} = 0 \qquad (2.57)$$

In the incompressible case, it is enough to solve (2.57) instead of (2.20, 2.21, 2.22, 2.23, 2.24, and 2.25).

Change the equation of (2.57) to a non-dimensional form. For example, consider the wind flowing around a building. Assume that L is the typical length of the building, U is the typical speed of the wind, ρ is the density of the air, and P is the atmospheric pressure. Then, with a hat "~" (tilde) to the dimensionless quantities, the physical variables can be transferred to non-dimensional variables as follows.

$$\tilde{r} = \frac{r}{L}, \quad \tilde{t} = \frac{tU}{L}, \quad \tilde{\boldsymbol{u}} = \frac{\boldsymbol{u}}{U}, \quad \tilde{p} = \frac{P}{\rho U^2} \qquad (2.58)$$

Using these dimensionless variables, the Navier-Stokes Eq. (2.57) can be rewritten in non-dimensional form.

$$\frac{\partial \tilde{\boldsymbol{u}}}{\partial \tilde{t}} + \left(\tilde{\boldsymbol{u}} \cdot \tilde{\nabla}\right)\tilde{\boldsymbol{u}} = -\tilde{\nabla}\tilde{p} + \frac{1}{Re}\tilde{\nabla}^2\tilde{\boldsymbol{u}} \qquad (2.59)$$

Whatever the scale of fluid phenomenon, the fluid dynamic phenomenon governed by (2.59) depends only on the dimensionless parameter

$$Re = \frac{UL}{\nu} = \frac{\rho UL}{\mu} \qquad (2.60)$$

If the two fluid systems with different scales are similar, the fluids governed by (2.59) with the same value of "Re" has the same mathematical solution in the dimensionless form. This dimensionless quantity Re is an important value in discussing fluid turbulence and is called **Reynolds number**. For example, it is useful to calculate the value of Re in case of the wind around the building; for example, U = 10 m/s, L = 100 m, and air mean-free-path l $\left(\sim 20 \text{ Å}\right)$,

$$Re \approx \frac{UL}{\ell V_s} \approx \frac{10 m/s \times 100 m}{\left[\pi\left(2 \times 10^{-9}m\right)^2 \times 10^{25}m^{-3}\right]^{-1} \times 300 m/s} \approx 10^7 \qquad (2.61)$$

It is a very large number. Therefore, macroscopic fluid phenomena can be discussed by neglecting the effect of viscosity. It is noted, however, that the viscosity becomes essential in discussing fluid turbulences. The small vortexes in the turbulence disappear after transferring their kinetic energy to the thermal energy because of the viscosity.

The convection term $(\boldsymbol{u} \cdot \nabla)\boldsymbol{u}$ of the Navier-Stokes Eq. (2.57) is called the **inertia term** in the analysis of fluid turbulence. The term $\nu\nabla^2\boldsymbol{u}$ is a **viscosity term**. By inserting typical values in these terms, the inertia term is U^2/L and the viscosity term is $\nu U/L^2$, so the following relationship is satisfied

$$Re = \frac{UL}{\nu} = \frac{\text{(inertia term)}}{\text{(viscosity term)}} \tag{2.62}$$

This is the definition of Reynold number, but it is not an exact definition. In gas dynamic phenomena in our daily life, the Reynold number is very large as (2.61). In the case of the wing of an airplane, it is as large as $Re = 10^8$. Rather, it suggests that nonlinear effects (inertia term) often dominate phenomena in a variety of fluid and gas phenomena in our daily life.

In the case of non-dimensional Eq. (2.59), the solution depends only on Re number, if two systems are in a similar structure. In fluid turbulence it is known that turbulent energy flows from large vortices to small vortices in three-dimensional case due to inertia terms. The larger the Reynold number, the larger and smaller vortices coexist at the same location in the fluid turbulence.

Also, as the water or wind flows crossing a building of the cylinder structure changes its flow pattern according to the increase of the Reynold number due to the
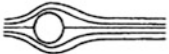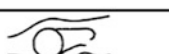
Reynolds number regime	Flow regime	Flow form	Flow characteristic
$Re \to 0$	Creeping flow		Steady, no wake
$3 - 4 < Re < 30 - 40$	Vortex pairs in wake		Steady, symmetric separation
$\frac{30}{40} < Re < \frac{80}{90}$	Onset of Karman vortex street		Laminar, unstable wake
$\frac{80}{90} < Re < \frac{150}{300}$	Pure Karman vortex street		Karman vortex street
$\frac{150}{300} < Re < \frac{10^5}{1.3 \cdot 10^5}$	Subcritical regime		Laminar, with vortex street instabilities
$\frac{10^5}{1.3 \cdot 10^5} < Re < 3.5 \cdot 10^6$	Critical regime		Laminar separation Turbulent reattachment Turbulent separation Turbulent wake
$3.5 \cdot 10^6 < Re$	Supercritical regime (transcritical)		Turbulent separation

Fig. 2.6 The flow pattern changes depending on the Reynold number of the system. The figure shows the flow forms and flow characteristic for the case where a laminar flow comes to the cylindrical obstacle with different Reynold numbers. It changes dramatically from laminar flow to turbulent flow. Preprint from Ref. [4] with kind permission from Springer Science + Business Media
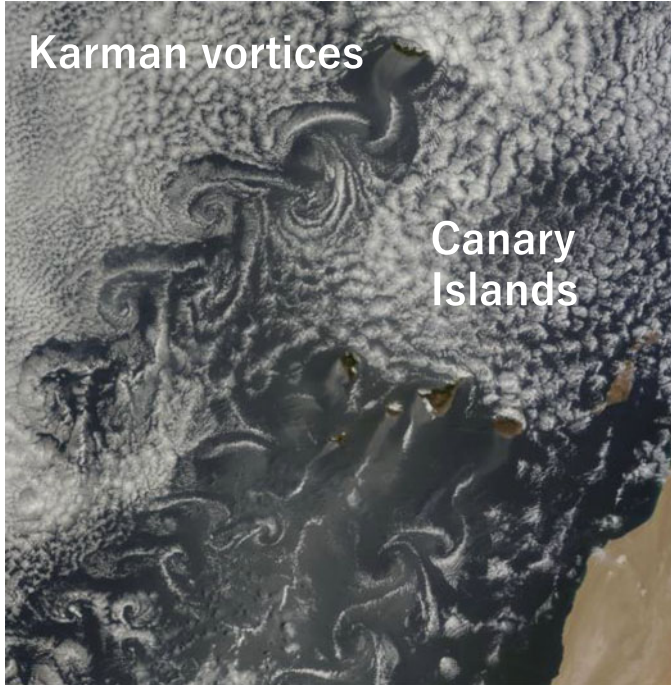
Fig. 2.7 Karman vortex in the nature. Canary Islands kick up Karman vortices, May 20, 2015. (NASA earth observatory)

increase of flow velocity. As shown in Fig. 2.6 [4], with increase of the flow velocity, the flow pattern is initially a laminar flow, peeling will occur next, the **Karman vortex** is formed, and it transits to turbulent flow. In Fig. 2.7, Karman vortices generated by the Canary Island are shown as a picture of clouds by a NASA weather satellite.

2.4.2 Wave Damping by Viscosity

It is clear intuitively that the viscosity plays a role to damp the amplitude of the sound waves. The wave equation including the viscosity in (2.48) is easily obtained to a Fourier component with k in the plane geometry.

$$\frac{\partial^2}{\partial t^2}u_1 + k^2\nu\frac{\partial}{\partial t}u_1 + k^2V_s{}^2 = 0 \qquad (2.63)$$

Since (2.63) is an equation of a harmonic oscillation, the second term corresponds to a friction or damping term. The dispersion relation of (2.63) is

$$\omega \approx \pm kV_s - i\frac{\nu}{2}k^2 \tag{2.64}$$

So, mathematically it is easy to confirm that the solution is proportional to the form,

$$exp(\mp ikV_s t)\, exp\left(-\frac{\nu}{2}k^2 t\right) \tag{2.65}$$

The term with a positive ν always damps the amplitude of the waves. It is informative to evaluate how large this damping is for the sound waves in the air. The vocal sound "do" is 260 Hz and the wavelength is about 1 m. The length of wave propagation L_d until the exponent of the damping reduces a factor ½ is estimated roughly,

$$L_d \approx \frac{V_s}{\nu k^2} \approx \frac{\lambda}{\ell}\frac{\lambda}{(2\pi)^2} >> \lambda \tag{2.66}$$

where λ is the wavelength, l is the air mean-free-path, and approximate relation $\nu \sim l V_s$ was used. Since the vocal sound wavelength is much longer than the molecular mean-free-path, viscos damping can be neglected for our vocal sound waves. Note that the spherical damping is dominant as shown in (2.54).

2.4.3 Thermal Conduction

Next, **thermal conduction** should be also included in the equation of energy in high temperature plasmas. This is a phenomenon in which internal energy is given from or deprived by the surrounding fluid to a local fluid due to heat transport. This is included in the term corresponding to dQ in (2.6). Therefore (2.22) is modified to the form

$$\frac{d\varepsilon}{dt} = -\frac{P}{\rho}\nabla\boldsymbol{u} + \frac{4}{3}\frac{\mu}{\rho}(\nabla\boldsymbol{u})^2 + \frac{1}{\rho}\nabla(\kappa\nabla T) \tag{2.67}$$

where κ is the **heat conduction coefficient** and the second term on RHS indicates that the flow kinetic energy is converted into heat energy by the viscosity. Thus, (2.67) shows a viscous term also appears in the energy eq. (2.22).

Under the condition that the density is constant and no flow in (2.67), it reduces to the equation of **temperature diffusion**. In plasmas without magnetic field, the electron thermal conduction is more important.

$$\frac{\partial T_e}{\partial t} = \nabla(\chi_e \nabla T_e) \tag{2.68}$$

Here, T_e is the electron temperature and χ_e is the **electron temperature diffusion coefficient**. In high-temperature plasmas, strong dependence of the Coulomb

collision time to the electron velocity shown in (2.3) results the Maxwellian averaged diffusion coefficient is proportional to

$$\chi_e \sim \ell_e v_e \propto T_e^{5/2} \tag{2.69}$$

Therefore, the temperature diffusion Eq. (2.68) is a nonlinear equation and Fourier decomposition method is not applicable.

Fortunately, it is well-known that as long as the temperature dependence is power law and the initial and boundary conditions are not complicated, the following self-similar method helps to reduce the partial differential equation to an ordinary differential equation, which is in general one-dimensional eigen-value problem [5].

2.4.4   Self-Similar Solution

Discuss a general case where the diffusion coefficient is given in the form.

$$\chi = aT^n \tag{2.70}$$

Here, "a" is a constant and "n" is a numerical value indicating the degree of nonlinearity. In general, n is often an integer or half integer.

In the case where fluid is heated to a high temperature locally before fluid moves, the heat conduction becomes important than the effect of the sound waves We investigate one-dimensional plane given by the following equation.

$$\frac{\partial}{\partial t} T = a \frac{\partial}{\partial x} \left(T^n \frac{\partial}{\partial x} T \right) \tag{2.71}$$

Let's solve (2.71) while explaining the mathematics of **self-similar solution**.

From the dimensional analysis of the Eq. (2.71), with the coordinates of the characteristic front of the **heat conduction wave** taken as x_f and the average temperature as T_a at the time t, (2.71) should satisfy the following dimensional relation.

$$aT_a^n \sim \frac{x_f^2}{t} \tag{2.72}$$

To solve this, it is required to impose an initial or boundary condition.

As an example, suppose that energy E_0 is instantaneously generated at x = 0. Then the law of conservation of energy is

$$E_0 = \frac{1}{\gamma - 1} \rho_0 \int_{-\infty}^{+\infty} T(t,x) dx \sim \frac{2}{\gamma - 1} \rho_0 T_a x_f = const. \tag{2.73}$$

where $1/(\gamma-1)$ is the heat capacity. Equation (2.73) suggests the relation.

$$T_a x_f \sim \frac{\gamma - 1}{2\rho_0} E_0 \equiv \alpha : \text{const.} \tag{2.74}$$

Inserting (2.74) to (2.72), the time dependence of the heat wave front is

$$x_f \sim (a\alpha^n t)^{\frac{1}{n+2}} \tag{2.75}$$

The average temperature is obtained by substituting (2.75) into (2.82),

$$T_a(t) \sim \left(\frac{\alpha^2}{at}\right)^{\frac{1}{n+2}} \tag{2.76}$$

The dimensionless variable ξ is introduced as follows.

$$\xi = \frac{x}{x_f(t)} \tag{2.77}$$

The temperature is given by introducing a dimensionless function $g(\xi)$,

$$T(t, x) = T_a(t) g(\xi) \tag{2.78}$$

The time and space differentiations are modified as.

$$\frac{\partial}{\partial t} T = -\frac{1}{n+2} \frac{T_a(t)}{t} \left(g + \xi \frac{dg}{d\xi} \right) \tag{2.79}$$

$$a \frac{\partial}{\partial x} \left(T^n \frac{\partial}{\partial x} T \right) = a \frac{T_a^{n+1}}{x_f^2} \frac{d}{d\xi} \left(g^n \frac{dg}{d\xi} \right) \tag{2.80}$$

Equation (2.71) becomes an ordinary differential equation after one integration as follows.

$$(n+2) g^n \frac{dg}{d\xi} + \xi g = 0 \tag{2.81}$$

where the integral constant is zero evaluated as $g(\xi) = 0$ at ξ infinity. This can be easily integrated, by assuming the value of at the wave-front ($\xi = \xi_0$) constant,

$$g(\xi) = \begin{cases} \beta \left[1 - \left(\frac{\xi}{\xi_0} \right)^2 \right]^{\frac{1}{n}} & |\xi| \leq \xi_0 \\ 0 & |\xi| \geq \xi_0 \end{cases} \tag{2.82}$$

Fig. 2.8 Time evolution of the nonlinear heat wave with $n = 5/2$, electron heat wave, in non-dimensional space and time. The nonlinearity makes the temperature profile being flat at high temperature region because of better conduction and steep profile near the front due to less conduction. In plotting the non-dimensional profile, we set $a = \alpha = \beta = \xi_0 = 1$ in (2.75), (2.76), (2.82) and (2.84) for normalized time $t = 1, 2, \ldots, 10$
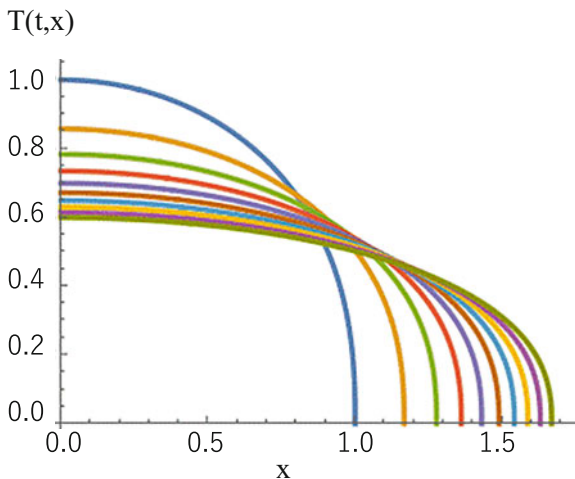
where β is a constant and is given as:

$$\beta = \left\{ \frac{n}{2(n+2)} \xi_0{}^2 \right\}^{1/n} \tag{2.83}$$

For the case of electron heat conduction with $n = 5/2$, the time evolution of temperature is shown in Fig. 2.8. As can be seen from the functional form of (2.82) with a large n, the wave front of heat conduction can be clearly defined unlike the case of linear diffusion with $n = 0$. Furthermore, the higher the temperature, the larger the thermal conductivity coefficient. The temperature profile is a flat shape rather than Gaussian for $n = 0$ case.

The solution is

$$T(t,x) = \beta \left(\frac{\alpha^2}{at} \right)^{\frac{1}{n+2}} g(\xi) \tag{2.84}$$

Note that the non-dimensional constant ξ_0 is not obtained yet. It is obtained so that the total energy is conserved as (2.73). Inserting (2.84) into the second term in (2.73), the total energy becomes E_0. In the case where the resultant ordinary differential equation is not analytically integrated, the problem becomes an eigen-value problem with numerical integration, where ξ_0 becomes the eigen-value.

It is useful to solve for the case of $n = 0$, well-known linear diffusion problem, with this self-similar method. It is a standard way to solve (2.71) by using Fourier transformation. However, it can be applicable only for the linear diffusion. As seen above, the self-similar method can be applied to nonlinear diffusion equations, too. As clear in (2.82), it is not straight forward in $n = 0$ case. With this self-similar method, (2.81) becomes

$$2\frac{dg}{d\xi} + \xi g = 0 \tag{2.85}$$

This can be easily solved to obtain the well-known solution.

$$T(t,x) \propto \frac{1}{\sqrt{at}} e^{-x^2/(at)} \tag{2.86}$$

Finally, let me explain the qualitative relationship between fluid motion and heat conduction waves. Generally, when rapid heating occurs on the surface of a solid, the speed of the heat conduction wave is very high, and the heat conduction wave propagates through the solid without fluid motion. Even in an insulator, free electrons increase at once by rapid heating, and a heat conduction wave propagates while ionizing atoms in the inside.

However, the speed of the heat conduction wave suddenly decreases as seen in (2.75), and when the speed becomes about the sound speed of the heated region, the movement of the ions such as strong sound waves and shock waves will accompany. After that, a structure of density and temperature, in which heat conduction and fluid motion are combined as almost stationary state, is formed as deflagration wave to be explained in Chap. 3.

Here, we showed how the self-similar method is powerful mathematics in solving a partial differential equation. The self-similar method has been applied to find analytical solutions of spherical implosion and explosion of compressible fluids driven by strong spherical shock waves. This topic will be studied in Chap. 4.

2.5 Incompressibility and Vortex

2.5.1 Incompressible Fluid

The **compressibility** of fluids and gases such as water and air are defined as

$$\eta = \frac{1}{B} = -\frac{1}{V}\frac{dV}{dP} = \frac{1}{\rho}\frac{d\rho}{dP} \tag{2.87}$$

The "B" is the bulk modulus defined in (2.51) and corresponds to the pressure required to compress the nominal density twice.

For incompressible fluids, the equation of continuity (2.20) can be replaced with the follow simple relation.

$$\nabla \cdot \boldsymbol{u} = 0 \tag{2.88}$$

Here, we introduce the definition of **vorticity** vector $\boldsymbol{\omega}$.

$$\boldsymbol{\omega} \equiv \nabla \times \boldsymbol{u} \tag{2.89}$$

In the case of incompressible and vortex-free flow ($\boldsymbol{\omega} = 0$), the flow velocity is defined with a potential (**velocity potential**), ϕ.

$$\nabla \times \boldsymbol{u} = 0 \quad \Rightarrow \quad \boldsymbol{u} = \nabla \phi \tag{2.90}$$

$$\nabla \cdot \boldsymbol{u} = 0 \quad \Rightarrow \quad \Delta \phi = 0 \tag{2.91}$$

Such flow is called the **potential flow**.

It is better to see the image of the relation between the vortex and velocity vector. Image the case where a vortex is located at the center in the cylindrical geometry. It is easy to see the structure of the flow velocity vector by use of the analogy between electric current and static magnetic field. For a static condition, The Ampere law in the Maxwell equations is

$$\nabla \times \boldsymbol{H} = \boldsymbol{j}, \qquad \boldsymbol{H} = \frac{\boldsymbol{B}}{\mu_0} \tag{2.92}$$

Regarding the electric current as vorticity, the magnetic field vector corresponds to the fluid flow velocity. In the case where the vortex is localized at the center, the absolute value of the flow velocity decreases in proportion to 1/r. This is well-known magnetic field distribution in the electromagnetism.

With a mathematical formula, Lagrange derivative of the flow velocity is rewritten as

$$\frac{d\boldsymbol{u}}{dt} = \frac{\partial \boldsymbol{u}}{\partial t} + \nabla \left(\frac{1}{2} u^2 \right) - \boldsymbol{u} \times \nabla \times \boldsymbol{u} \tag{2.93}$$

In the potential flow, from (2.93) and (2.90), the equation of motion (2.21) becomes.

$$\nabla \left(-\frac{\partial \phi}{\partial t} + \int \frac{dP}{\rho} + \frac{1}{2} |\nabla \phi|^2 + U \right) = 0 \tag{2.94}$$

Here, the external force is given as a potential force

$$\boldsymbol{F} = -\nabla U \tag{2.95}$$

From the Eq. (2.94), the following relation is found.

$$-\frac{\partial \phi}{\partial t} + \int \frac{dP}{\rho} + \frac{1}{2} |\nabla \phi|^2 + U = 0 \tag{2.96}$$

Here, RHS of (2.96) can be an arbitral function of time, f (t), but if we redefine the velocity potential like $\phi' = \phi - \int f(t)dt$, we can generalize that f (t) = 0. In a steady
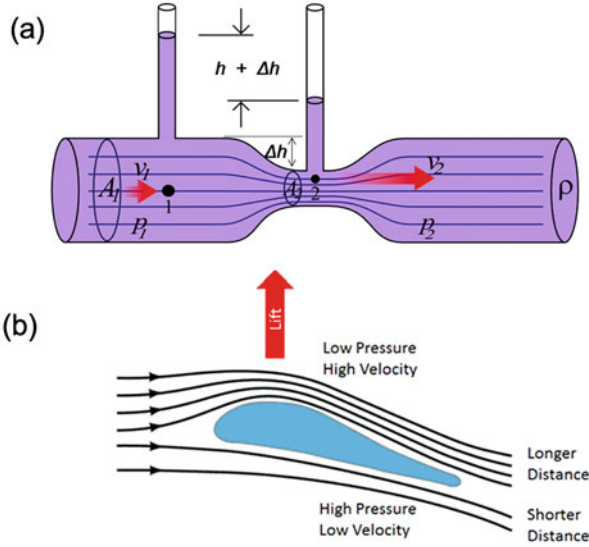
Fig. 2.9 Engineering application of Bernoulli's theorem. (**a**) The difference of the height indicated the difference of velocity. This is used to measure the speed of an airplane flying at subsonic velocity where incompressibility is good assumption. (**b**) is the principle of lift force of airplanes. Design the main wing structure so that the top is longer than the bottom, and the pressure of the air passing over the top is lower than the pressure below. When the airplane takes off, this pressure difference provides lift and helps the aircraft to climb

flow of incompressible and vortex-free fluids, therefore, the following relation should be satisfied.

$$\int \frac{dP}{\rho} + \frac{1}{2}u^2 + U = (\text{constant in space}) \tag{2.97}$$

The relation of (2.96) and (2.97) is called **Bernoulli's theorem**.

Using (2.97), a mechanical device for measuring the speed of flow velocity is designed as in Fig. 2.9a. This principle has been used to measure the speed of subsonic-aircrafts. As seen in Fig. 2.9b, the wing of an aircraft is designed so that the upper length is longer than the lower length, then the flow velocity is higher in the top of the wings and the pressure is lower. The difference of the pressure pushes the wings upward. This force is called the **lift force**.

2.5.2   Incompressibility Assumption

In most of the hydrodynamic phenomena, the **incompressible assumption** can be used and the problems become simpler than the compressible fluids. Then, the equation of continuity and equation of energy can be replaced by the incompressible

condition (2.88). In general, the incompressible Navier-Stokes Eq. (2.55) is only one equation to be solved by coupling with (2.88).

Let us consider the condition under which the assumption of incompressible fluid is appropriate. Evaluate the density perturbation $\delta\rho$ in a uniform fluid with density ρ_0. Induced velocity perturbation $\delta\mathbf{u}$, originated by the compressibility can be given as the same form in (2.45) and (2.46) as follows.

$$\frac{\partial}{\partial t}\,\delta\rho = -\rho_0 \nabla \delta\mathbf{u} \tag{2.98}$$

$$\frac{\partial}{\partial t}\,\delta\mathbf{u} = -\frac{1}{\rho_0}\nabla\delta P = -\frac{V_s^2}{\rho_0}\nabla\delta\rho \tag{2.99}$$

$$V_s^2 = \left(\frac{\partial P}{\partial \rho}\right) \tag{2.100}$$

where δP is an induced pressure perturbation and V_s is the sound velocity defined in (2.47). From (2.98) and (2.99), the following relation is obtained. Assuming $|\nabla| \approx 1/L$ and $|\partial/\partial t| \approx \tau$, the relation is obtained

$$\left|\frac{\delta\rho}{\rho_0}\right| \approx \frac{L}{\tau}\frac{|\delta\mathbf{u}|}{V_s^2} \tag{2.101}$$

It is clear from (2.101) that the density change by the compressibility can be neglected for the case with sufficiently high sound velocity V_s. For example, a car speed of 100 km/s is about $L/\tau \sim |\delta\mathbf{u}| \sim 0.1 V_s$ and the density perturbation is only 1%. In the case of a supersonic jet fighter with Mach number more than unity, the density perturbation roughly evaluated with (2.101) is more than unity, so that hydrodynamics should be solved as compressible fluid.

2.5.3   Vortex Equation

The following equation is obtained by taking the rotation of the equation of motion (2.57).

$$\frac{\partial}{\partial t}\boldsymbol{\omega} = \nabla \times (\boldsymbol{u} \times \boldsymbol{\omega}) + \frac{1}{\rho^2}\nabla\rho \times \nabla P + \frac{4}{3}\nu\nabla^2\boldsymbol{\omega} \tag{2.102}$$

This can be rewritten in the form.

$$\frac{\partial}{\partial t}\boldsymbol{\omega} + \boldsymbol{u}\cdot\nabla\boldsymbol{\omega} = (\boldsymbol{\omega}\cdot\nabla)\boldsymbol{u} - \boldsymbol{\omega}(\nabla\boldsymbol{u}) + \frac{1}{\rho^2}\nabla\rho \times \nabla P + \frac{4}{3}\nu\nabla^2\boldsymbol{\omega} \tag{2.103}$$

Here, $\boldsymbol{\omega}$ is the vorticity defined in (2.89).

The first term of RHS in (2.103) is a term that exists only in the case of three-dimensional flow, and a vortex localized in a certain region is stretched to the direction of vorticity vector by this term. In the three-dimensional fluid turbulence, the vortexes are cascaded to thin, long vortexes in the turbulence energy spectrum. This is called **cascade** in wavenumber space of the turbulence. As the vortex is elongated, the viscosity of the fourth term on RHS of (2.103) acts as a damping term of the vorticity. This is the effect of dissipation in which the kinetic energy of the vortex is converted into the thermal energy of the fluid.

The second term in (2.103) disappears in incompressible fluid. This term is the compressibility effect of amplifying the vorticity in the fluid as it is compressed. And, the third term is a source term for vortex generation. Note that it depends on the property of the **equation of state** (EOS). If pressure is only a function of the density, this term disappears.

Even with ideal fluid equation of state, vortexes are generated by this term. The third term in (2.103) is called the **baroclinic term**. In fluid dynamics, the **baroclinity** is a measure of the stratification in a fluid. A baroclinic atmosphere is one for which the density depends on both the temperature and the pressure; contrast this with **barotropic** atmosphere, for which the density depends only on the pressure. In atmospheric terms, the barotropic zones of the Earth are generally found in the central latitudes, or tropics, whereas the baroclinic areas are generally found in the mid-latitude/polar regions.

Let us see the difference of role of the first term of RHS of (2.103) in two- and three-dimensional vortices. The effect appears as the difference between a **tornado** and a **typhoon**. Our Earth's atmosphere is about 5 km as the thickness of the air fluid. Since a relatively small-scale vortex is subjected to the three-dimensional effect and becomes a thin and long vortex like a tornado. However, in the case of typhoon, the size of the vortex is as much as 1000 km compared to the atmosphere thickness of ~5 km, which is like a vortex in a very thin water in two-dimension. Therefore, the typhoon is a two-dimensional vortex and the first term on RHS of (2.103) does not work for the evolution of vortex. In fact, when examining the two-dimensional vortex turbulence, it turns out that the energy of the vortex moves in the wavenumber space from small to large wavenumber direction. This is called an **inverse cascade**.

To see explicitly the force to generate vortices on the surface of the earth, it is better to write the vortex equation in a rotating system with an angular momentum $\mathbf{\Omega}$. Then, Navier-Stokes Eq. (2.57) includes two new forces, since Newton equation is modified in this frame as

$$\frac{d\boldsymbol{v}}{dt} = \frac{\boldsymbol{F}}{m} + 2\boldsymbol{v} \times \mathbf{\Omega} - \mathbf{\Omega} \times (\mathbf{\Omega} \times \mathbf{r}) \qquad (2.104)$$

where the second and third terms in RHS are the **Coriolis** and centrifugal forces, respectively. Of course, $\mathbf{r}$ and $\mathbf{v}$ are those in the rotating coordinate. It is relatively simpler to solve Navier-Stokes equation in the rotating system with these two forces.
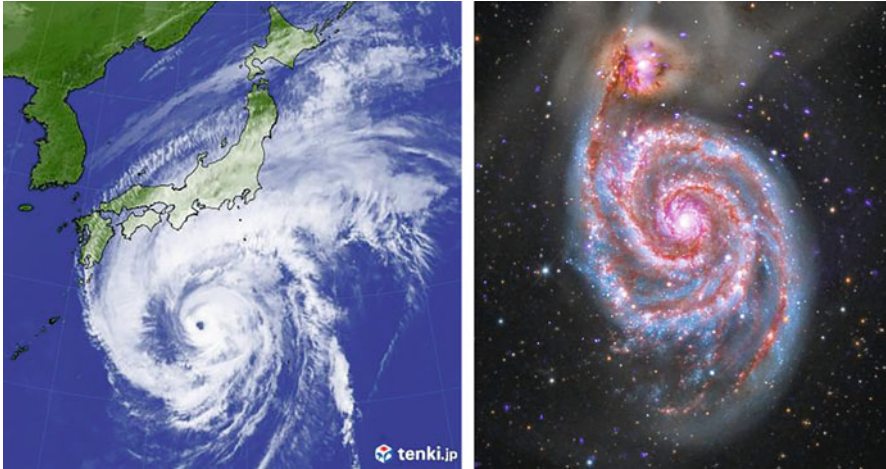
Fig. 2.10 A satellite picture of clouds by a typhoon attacking Japan islands (left, Courtesy of Tenki.jp), and X-ray image of the spiral Galaxy M51 taken by Chandra x-ray satellite by NASA (right by NASA/CXC/SAO)

It is easy to image the centrifugal force which is always perpendicular to the rotating axis ($\mathbf{\Omega}$-direction). The Coriolis force is easily understood with the analogy of Lorentz force. Regarding $2\mathbf{\Omega}$ is like an constant magnetic field vector in the z-direction in the cylindrical coordinate, the Coriolis force is the same mathematical form as the Lorentz force. For example, it is perpendicular force to the rising air in Summer to generate vortices due to Coriolis force.

A picture of clouds in a typhoon approaching to Japan and Korea is taken by a weather forecast satellite as shown in Fig. 2.10a. The vortex is enhanced on the way to the north by the Coriolis force. It is clearly seen the "eye" of the typhoon at the center.

It is interesting to compare the spiral motion of the typhoon to the spiral motion of a galaxy. A galaxy consists of about 100 billion starts, and it can be regarded as fluid. In general, galaxy is of pancake type structure and starts are rotating around the center of the galaxy with given angular momentum. In Fig. 2.10b, an observed x-ray image of the M51 galaxy is shown. The spiral motion of the stars in the galaxy is observed in the satellite image. The image suggests that the vorticity is localized at the center of the galaxy.

2.6   One-Fluid and Two-Temperature Fluid Model

It seems to be that a precise treatment of laser-plasma should be based on the two-fluid and two-temperature model identifying the ion and electron fluids. As shown in (2.4) and (2.5), the next better is the assumption of two temperatures but one fluid. Two fluid is required when the charge separation is important to affect the

fluid phenomena. This is the case near low density and high-temperature region like laser expanding plasma to be discussed in Chap. 3. The other case is the situation where the charge neutrality is satisfied, but the electron current is strong to generate strong magnetic field affecting the fluid dynamics. This is modeled by magneto-hydro-dynamics (MHD) fluid discussed later.

As described in Chap. 2 in Vol. 1, the velocity distribution of heated electrons becomes Maxwellian with an electron temperature T_e due to collisions between electrons, and the ions tend to be a Maxwell distribution with T_i relatively slowly, if the time scale of phenomena is longer than τ_e and τ_i in (2.4). However, it takes even longer time for both temperatures to have the same value as suggested in (2.5). In the case of laser heating, electron cyclotron heating, etc., the electrons in the plasma are heated from outside, and the ions are heated through the temperature relaxation process by the electron-ion Coulomb collision. Therefore, it is generally better to assume that the temperatures of electrons and ions are different in such plasmas.

In addition, plasma shock waves such as blast waves of supernova remnants heat the ions at the shock front, and the electrons slowly receive energy from the ions due to temperature relaxation. In the magnetic field confined plasma, when plasma is heated by a microwave source whose frequency is adjusted to resonate the ion cyclotron frequency, the ion temperature rises but the electron is heated slowly via the ion-electron collision.

Of course, if the time scale of the fluid dynamics is faster than the electron and ion relaxation times, there is no guarantee that the distribution functions are in Maxwellian. However, the fluid equation is much easier to solve compared to the Boltzmann equations directly. It is better to start with solving a plasma dynamic with the fluid model at first. Then, if some violation of fluid assumption is found in the solution, it is better to consider how to take into account the kinetic effect in the basic equation.

The one-fluid and two-temperature fluid model is widely used as the basic equation for studying the whole dynamics from laser heating to fusion burn in laser nuclear fusion implosion dynamics. The basic equations are derived from the two fluid equations given, for example, in the Babinski's book [6]. To assume charge neutrality, the scale length of the plasma fluid variation in space should be sufficiently longer than the Debye length. Then, one fluid approximation is reasonable, and the equation of continuity and the equation of motion are same as (2.20) and (2.21), respectively.

$$\frac{d\rho}{dt} = -\rho \nabla \boldsymbol{u} \tag{2.105}$$

$$\rho \frac{d\boldsymbol{u}}{dt} = -\nabla P \tag{2.106}$$

However, the energy equation should be formulated for the ion and electron fluids as separate thermodynamic systems. As important terms, the heat conductions, temperature relaxation, and energy source terms should be included. For example, S_e is the energy source by laser and radiation, and S_i is a source by the collisional heating by fusion-product particles. Then, both energy equations are written as,

$$\rho \frac{d\varepsilon_i}{dt} = -P_i \nabla \boldsymbol{u} - \nabla \boldsymbol{q}_i + Q_{ei} + S_i \qquad (2.107)$$

$$\rho \frac{d\varepsilon_e}{dt} = -P_e \nabla \boldsymbol{u} - \nabla \boldsymbol{q}_e - Q_{ei} + S_e \qquad (2.108)$$

Here, ε_i and ε_e are the internal energies per unit mass of ion and electron fluids, q_i and q_e are heat fluxes of ions and electrons, Q_{ei} is the **temperature relaxation** in unit time per unit mass from electrons to ions (or vice versa when Q_{ei} is negative). The S_i and S_e are terms of energy sources and losses due to other effects to ion and electron fluids, respectively. For example, when the thermal x-ray radiation exchanges energy with plasma, the term S_e should include the effects of heating and cooling by radiation. That term must be combined with an equation on radiation in a self-consistent way. In (2.107) and (2.108), the **thermal conduction coefficients** of ions and electrons, and the temperature relaxation term are given as follows [6].

$$\kappa_e = \alpha(Z) \frac{n_e T_e \tau_e}{m_e} \propto T_e^{\frac{5}{2}}, \quad \kappa_i = 3.9 \frac{n_i T_i \tau_i}{m_i} \propto T_i^{5/2} \qquad (2.109)$$

$$Q_{ei} = \frac{m_e}{m_i} \frac{T_e - T_i}{\tau_e} \qquad (2.110)$$

Here, τ_e is the relaxation time given in (2.4). The collision time due to the Coulomb collision is subtly changed depending on the ionization degree Z of the ions, so it is applied as a correction term $\alpha(Z)$ thereof. For example, $\alpha(Z) = 3.16$ for $Z = 1$, others are in Ref [6]. Note that the thermal conduction coefficient roughly given as (2.69) for electrons and the same form $l_i v_i$ for ions except numerical factors. It is found that the ion thermal conduction is much weaker than the electron thermal conduction even for the same temperature profile.

Note that the one-fluid, two temperature fluid model is the basic equations for an **integrated-physics code** for laser fusion simulation. Depending on the difference of problems, additional physics are included in the basic equations.

2.7 Two Fluid Equation of Plasma

For analyzing short time and short scale plasma phenomena, two-fluid plasma model is widely used. In a short time, plasma is in general collisionless and there is no time for the ions and electrons to become Maxwell distributions via the Coulomb collision. Nevertheless, the ion and electron particle distributions are assumed to be in Maxwellian, and they are described with fluid models like the neutral fluids. The mathematical proof of the fluid approximation is shown in Appendix-A.

In general, the energy equations to the ions and electrons are neglected for simplicity by assuming constant temperature or adiabatic response. For simplicity, consider the case of fully ionized hydrogen plasma. Extension to partially ionized

non-ideal plasma with other atomic and charge numbers is straightforward, if there is no need to be consistent with complicated atomic processes explained in Chap. 5.

Plasma consists of two kinds of charged particle groups whose masses are different by thousand times. Since the masses are very different, the ions behave separately as ion fluid and the electrons as electron fluid. Assume that both electrons and ions behave as the ideal fluid, and their degrees of freedom are only three-dimensional translational motions. Then, both equations of state are the same as (2.31) and (2.32) with N = 3 and γ = 5/3. Then, the following equations are obtained for the ion fluid, after setting the number density of ions n_i and setting its flow velocity and temperature to $\boldsymbol{u}_i$ and T_i.

$$\frac{\partial n_i}{\partial t} + \nabla(n_i \boldsymbol{u}_i) \quad = \quad 0 \tag{2.111}$$

$$m_i \left(\frac{\partial}{\partial t} + \boldsymbol{u}_i \cdot \nabla \right) \boldsymbol{u}_i = -\frac{1}{n_i} \nabla(n_i T_i) + e(\boldsymbol{E} + \boldsymbol{u}_i \times \boldsymbol{B}) - \frac{1}{n_i} \boldsymbol{R} \tag{2.112}$$

Both the ion and electron gases are the ideal gas and charged particle ions are affected by Lorentz force. The electron fluid follows the equations.

$$\frac{\partial n_e}{\partial t} + \nabla(n_e \boldsymbol{u}_e) \quad = \quad 0 \tag{2.113}$$

$$m_e \left(\frac{\partial}{\partial t} + \boldsymbol{u}_e \cdot \nabla \right) \boldsymbol{u}_e = -\frac{1}{n_e} \nabla(n_e T_e) - e(\boldsymbol{E} + \boldsymbol{u}_e \times \boldsymbol{B}) + \frac{1}{n_e} \boldsymbol{R} \tag{2.114}$$

Here, $\boldsymbol{R}$ is the force due to friction appearing when the velocities of the electron and the ion fluids are different, and is given as the following form [6].

$$\boldsymbol{R} = -\frac{m_e n_e}{\tau_{ei}} (\boldsymbol{u}_e - \boldsymbol{u}_i) \tag{2.115}$$

Note that both the viscosity and thermal conductions have been neglected above.

Electric and magnetic fields appearing in Lorentz force are not only imposed externally but also generated by the ion and electron fluid motions. The charge density ρ and current density $\boldsymbol{j}$ are defined as

$$\rho = en_i - en_e \quad \boldsymbol{j} = en_i \boldsymbol{u}_i - en_e \boldsymbol{u}_e \tag{2.116}$$

(2.116) should be used in solving the Maxwell equations.

$$\textbf{Faraday's Law} \nabla \times \boldsymbol{E} = -\frac{\partial \boldsymbol{B}}{\partial t} \tag{2.117}$$

$$\textbf{Ampere's Law } \frac{1}{\mu_0} \nabla \times \boldsymbol{B} = \boldsymbol{j} + \varepsilon_0 \frac{\partial \boldsymbol{E}}{\partial t} \tag{2.118}$$

$$\textbf{Poisson Equation } \varepsilon_0 \nabla \cdot \boldsymbol{E} = \rho \tag{2.119}$$

$$\textbf{Gauss law } \nabla \cdot \boldsymbol{B} = 0 \tag{2.120}$$

It is necessary to solve the fluid equations by coupling with the Maxwell equations at the same time self-consistently. This point is essential difference compared to the conventional fluid or gas with no charge, and soling any plasma physics is more complicated mathematically. So, when the computer appeared in the late 1940's, the researchers in plasma physics became a pioneer in computational physics even with fluid assumption of plasmas.

The basic equations were given above; however, it is not always necessary to couple all equations. For example, to investigate the phenomenon which is too fast for the ion fluid to follow, it is reasonable to keep the ions fixed and consider only the motion of the electron fluid. In a phenomenon, on the other hand, in which ions move slowly and the electrons just accompany them, the electron fluid follows the motion of the ion fluid. In such case, it is found the charge neutrality is good assumption without solving the electron equation.

Plasma shock wave structures are studied precisely by soling complete equations of two fluid and two temperature fluid equation [7]. They have solved structure of stationary plasma shock waves and studied the effects of charge separation, electron and ion heat conduction, temperature relaxation, viscosity, etc. The same kind of research was done in the book [5], where the details are given in Chap. 7. It is too much here to discuss such precise calculation consistently by solving all above fluid equations, so the reader interested are recommended to read such references.

2.7.1   Electron Plasma Waves

Typical waves in two fluid plasma driven by the electric field are the **electron plasma wave** and **ion acoustic wave**. The electron plasma wave is sustained by the electric field due to charge separation by the electron motion. So, the electron inertial force balances the force by the electric field and electron pressure. In this case, the ions can be assumed to be at rest, namely, the ions cannot move because of their larger mass.

To know the linear response of any plasma from an equilibrium state, small perturbations of physical quantities are considered after neglecting all nonlinear terms. This mathematical prescription is called "linearization". In the electron plasma wave, the linear perturbations are the following electron density, electron velocity, and electrostatic field.

$$n_{e1}, \quad \boldsymbol{u}_{e1}, \quad \boldsymbol{E}_1 \tag{2.121}$$

Then, the continuity Eq. (2.113) is linearized as

$$\frac{\partial}{\partial t} n_{e1} + n_{e0} \nabla \boldsymbol{u}_{e1} = 0 \tag{2.122}$$

The equation of motion of electrons (2.114) is linearized as

$$m_e \frac{\partial}{\partial t} \boldsymbol{u}_{e1} = -\frac{1}{n_{e0}} \nabla P_{e1} - e\boldsymbol{E}_1 \tag{2.123}$$

The Poisson Eq. (2.119) is linearized as

$$\nabla \boldsymbol{E}_1 = -\frac{e}{\varepsilon_0} n_{e1} \tag{2.124}$$

Assuming that the pressure is given in the form (2.31), the linearized pressure is

$$P_{e1} = \left(\frac{\partial P_e}{\partial n_e}\right) n_{e1} = \gamma T_e n_{e1} \tag{2.125}$$

where T_e is assumed to be given. In (2.125), the γ is evaluated so that the electron motion is one-dimensional adiabatic and $\gamma = 3$ from (2.33).

The dispersion relation to the **electron plasma waves** is easily obtained as

$$\omega^2 = \omega_{pe}^2 + 3v_e^2 k^2, \quad v_e = \sqrt{T_e/m_e} \tag{2.126}$$

where ω_{pe} is the **electron plasma frequency**, or simply called **plasma frequency** defined as

$$\omega_{pe} = \sqrt{\frac{e^2 n_e}{\varepsilon_0 m_e}} \tag{2.127}$$

In the cold plasma limit, the plasma waves tend to a simple oscillation

$$\omega^2 = \omega_{pe}^2 \tag{2.128}$$

This oscillation of electrons is called **plasma oscillation**. Note that ω_{pe} is a **resonance frequency** of the electrons in cold plasma.

2.7.2 Ion Acoustic Waves

If the time scale of the oscillation of perturbations is long enough, it is necessary to take account of the motion of ion fluid. The electric field due to the charge separation in slow time scale attracts the electrons, so that the electron fluid almost follows the motion of the ion fluid. Consider the electron and ion density perturbations are slightly different, while the electrons follow the ion fluid motion. Both fluids are coupled by the electrostatic field. Derive the equations for linear perturbations of the following four quantities.

$$n_{i1}, \quad \boldsymbol{u}_{i1}, \quad n_{e1}, \quad \boldsymbol{E}_1 \tag{2.129}$$

The linearized equation of (2.111) is given as

$$\frac{\partial}{\partial t} n_{i1} + n_{i0} \nabla \boldsymbol{u}_{i1} = 0 \tag{2.130}$$

Eq. (2.112) becomes

$$m_i \frac{\partial}{\partial t} \boldsymbol{u}_{i1} = -\frac{1}{n_{i0}} \nabla P_{i1} - e\boldsymbol{E}_1 \tag{2.131}$$

Then, in (2.114) it is possible to neglect the inertial term. Assume that the electric field should balance with the electron pressure force.

$$-\frac{1}{n_{e0}} \nabla P_{e1} - e\boldsymbol{E}_1 = 0 \tag{2.132}$$

The final relation is the Poisson Eq. (2.119).

$$\nabla \boldsymbol{E}_1 = \frac{e}{\varepsilon_0} (n_{i1} - n_{e1}) \tag{2.133}$$

After Fourier transformation, the ion density perturbation is found to have the following relation with the electron density perturbation.

$$n_{i1} = \left(1 + k^2 \lambda_{De}^2\right) n_{e1} \tag{2.134}$$

Note that both density perturbations are almost the same for small k, while the electron density does not follow the ion density for large k.

By solving the above coupled equations after Fourier-Laplace transformation, the dispersion relation of the **ion acoustic wave** or simply the **ion wave** is obtained.

$$\omega^2 = \frac{\gamma_i T_i}{m_i} + \frac{\gamma_e T_e}{m_i} \frac{1}{\left(1 + k^2 \lambda_{De}^2\right)}, \quad \gamma_i = \frac{5}{3}, \quad \gamma_e = 1 \tag{2.135}$$

where the ion fluid is adiabatic and the electron fluid is assumed to keep a constant temperature because of the dominant electron thermal conduction. It is usual that the most of plasmas have higher electron temperature compared to the ion one. (2.135) is usually written to be

$$\omega^2 = C_s^2 k^2 \frac{1}{1 + k^2 \lambda_{De}^2} \tag{2.136}$$

where C_s is the **ion acoustic velocity** defined by

$$C_s = \sqrt{\frac{\gamma_e T_e}{m_i}}, \tag{2.137}$$

The dispersion relation (2.136) is plotted in Fig. 2.11. It is noted that the ion acoustic wave phase velocity satisfies the relation.

$$v_i < \frac{\omega}{k} << v_e \tag{2.138}$$

Once this relation is not satisfied, the ion waves are damped by the kinetic effect, so-called **Landau damping**. The physics of Landau damping will be discussed in Volume 4.
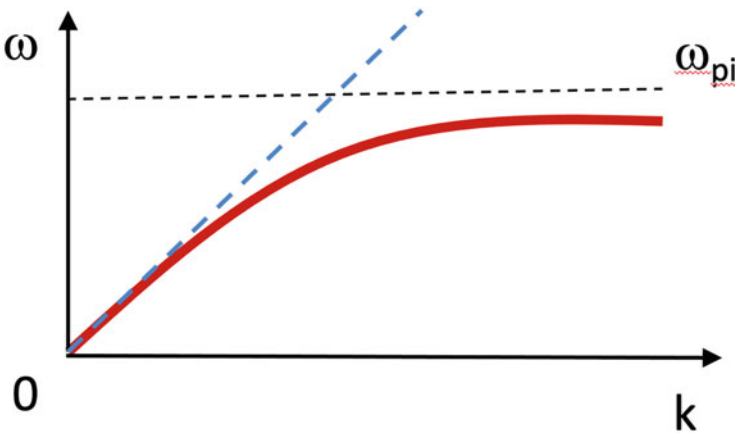
Fig. 2.11 The dispersion relation of the ion acoustic wave is plotted by the red line. It starts with a constant velocity at small k, while saturates at large k region

2.8   Mathematics for Wave Analysis

The waves in plasma produced by the motion of ions and electrons coupled with Maxwell equation have the same role as the seismic waves, the sound wave, etc. So, if there is a disturbance somewhere in the plasma, the induced waves carry energy so as to disperse the energy spatially and temporally. As the result, plasma confinement is prohibited in some cases. When the amplitude of the waves is sufficiently small, it can be analyzed as weak deviation from the equilibrium state. Then, the governing equations can be linearized, and it is enough to solve the linearized wave equations. **Fourier-Laplace transformation** has been used to obtain the wave dispersion relation, but any precise mathematics has not been explained, yet. To proof the mathematics, we start with the small vibration of an oscillator before the wave analysis. In the wave theory, it is standard to analyze using Fourier-Laplace expansion, and it is strait forward to use the mathematics of the analysis of such an oscillator.

2.8.1   Initial Value Problem of an Equation of Oscillation

First, let's solve exactly the initial value problem of the equation for a harmonic oscillator with a damping term by the Laplace's method. The equation of the harmonic oscillator with the eigen-frequency ω_0 and damping coefficient γ can be written as follows.

$$\frac{d^2x}{dt^2} + 2\gamma\frac{dx}{dt} + \omega_0^2 x = 0 \tag{2.139}$$

Multiplying (2.139) by $e^{i\omega t}$ and introducing time-integrated variables, Laplace transformation is carried out with the definition.

$$X(\omega) = \int_0^\infty x(t)e^{i\omega t}dt \tag{2.140}$$

It should be noted that even if $x(t)$ grows exponentially in time, $Im\,(\omega)$ should be a positive value so that this integral (2.140) must not diverge. Carrying out the Laplace transform of (2.139), the second term becomes

$$\int_0^\infty \frac{dx}{dt}e^{i\omega t}dt = xe^{i\omega t}\big|_0^\infty - i\omega X(\omega) = -x(0) - i\omega X(\omega) \tag{2.141}$$

The Laplace transform of the first derivative includes the initial value x (0). The second derivative is

$$\int_0^\infty \frac{d^2x}{dt^2} e^{i\omega t} dt = \frac{dx}{dt} e^{i\omega t}\Big|_0^\infty - i\omega \int_0^\infty \frac{dx}{dt} e^{i\omega t} dt = -\dot{x}(0) + i\omega x(0) - \omega^2 X(\omega) \quad (2.142)$$

This includes the first derivative at $t = 0$, $\dot{x}(0) = dx / dt$ $(t = 0)$.

If Laplace transform is performed accurately as mentioned above, Laplace transformed equation of (2.139) is given as

$$\left(\omega^2 + 2i\gamma\omega - \omega_0^2\right)X(\omega) = -\dot{x}(0) + (i\omega - 2\gamma)x(0) \quad (2.143)$$

LHS of (2.143) is factorized.

$$\left(\omega^2 + 2i\gamma\omega - \omega_0^2\right) = (\omega - \omega_1)(\omega - \omega_2) \quad (2.144)$$

Here,

$$\omega_1 = \sqrt{\omega_0^2 - \gamma^2} - i\gamma, \quad \omega_2 = -\sqrt{\omega_0^2 - \gamma^2} - i\gamma \quad (2.145)$$

Since $X(\omega)$ is given in (2.143), the Laplace inverse transformation is performed to give

$$x(t) = \frac{1}{2\pi} \int_{-\infty}^{+\infty} X(\omega)e^{-i\omega t} d\omega$$

$$= -\frac{\dot{x}(0)}{2\pi} \int_{-\infty}^{+\infty} \frac{e^{-i\omega t}}{(\omega - \omega_1)(\omega - \omega_2)} d\omega$$

$$+ \frac{x(0)}{2\pi} \int_{-\infty}^{+\infty} \frac{(i\omega - 2\gamma)e^{-i\omega t}}{(\omega - \omega_1)(\omega - \omega_2)} d\omega \quad (2.146)$$

Here, $1/2\pi$ of (2.146) is a normalization constant.

The integration of (2.146) is easily carried out with the **residue theorem** and **Cauchy's theorem**. For the sake of simplicity, the real part of the Eq. (2.145) is rewritten to be,

$$\Omega = \sqrt{\omega_0^2 - \gamma^2} \quad (2.147)$$

The integral of (2.146) has singular points $\omega = \omega_1$, ω_2. In the Laplace transform defined in (2.140), it was required that the imaginary part of ω should be positive and large enough so that the integral of (2.140) does not diverge. Now, in the integral of (2.146), take the value of Im (ω) is sufficiently large negative value and extend the integral to a closed curve (red) like Fig. 2.12. Then, according to the Cauchy's theorem, this line integral (2.140) is obtained by adding negative signs to the
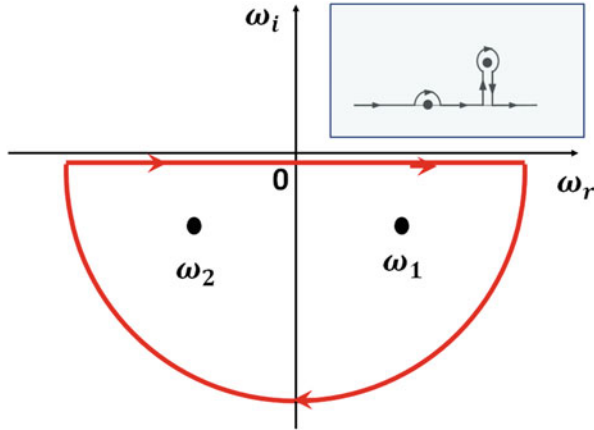
Fig. 2.12 The integration loop in the complex space for the inverse-integration of Laplace transformation. In the case of inverse-Laplace integration, it is necessary to down the integration line to the negative infinite circle for convergence of the integration. Then, it is found that Cauchy's theorem indicates that only the contribution by the pole remains in the loop integration. If there are roots with positive imaginary part like shown in the small box above, then the integration pass should be modified as shown in the small box. Then, we obtain exponentially growing solutions

residues from the two poles like in Fig. 2.12. It should be the direction of the clockwise. The first term on RHS of (2.146) is integrated.

$$-\frac{1}{2\pi}\int_{-\infty}^{+\infty}\frac{e^{-i\omega t}}{(\omega-\omega_1)(\omega-\omega_2)}d\omega = -\frac{ie^{-\gamma t}}{2\Omega}\left(e^{i\Omega t}-e^{-i\Omega t}\right)$$
$$=\frac{e^{-\gamma t}}{\Omega}sin(\Omega t) \tag{2.148}$$

The second term is

$$\frac{1}{2\pi}\int_{-\infty}^{+\infty}\frac{(i\omega-2\gamma)e^{-i\omega t}}{(\omega-\omega_1)(\omega-\omega_2)}d\omega = \frac{e^{-\gamma t}}{2}\left(e^{i\Omega t}+e^{-i\Omega t}\right)+\frac{i\gamma e^{-\gamma t}}{2\Omega}$$
$$\times\left(e^{i\Omega t}-e^{-i\Omega t}\right)=e^{-\gamma t}\left(cos(\Omega t)+\frac{\gamma}{\omega_3}sin(\Omega t)\right) \tag{2.149}$$

Finally, the solutions are obtained by substituting (2.148) and (2.149) into (2.146) as follows.

$$x(t)=e^{-\gamma t}\left[\frac{sin(\omega_3 t)}{\Omega}\dot{x}(0)+\left(cos(\Omega t)+\frac{\gamma}{\Omega}sin(\Omega t)\right)x(0)\right] \tag{2.150}$$

It is easy to confirm that the solution obtained in this way satisfies the initial condition.

In the absence of the damping term ($\gamma = 0$) the solution is simplified from (2.150).

$$x(t) = \dot{x}(0)\frac{sin(\omega_0 t)}{\omega_0} + x(0)\,cos(\omega_0 t) \tag{2.151}$$

The form of (2.151) is the general solution of the harmonic oscillator in the form.

$$x(t) = Asin(\omega_0 t) + Bcos(\omega_0 t) \tag{2.152}$$

The constants of A and B in (2.152) should be determined from initial conditions as (2.151).

The case of (2.139) is easy to solve even as an initial value problem as seen above. However, if the equation becomes higher order, third or fourth order differential one, it is hard to solve as above. Then, if the Laplace transform is used, the differential equations become algebraic equations, eventually resulting in a problem of finding poles in the Laplace inverse transformation. This is easy and useful as a general theory. This advantage is very powerful.

It is useful to know the case where the relation (2.144) has solutions with positive imaginary. Then, it is necessary to down the integration contour from above to below by avoiding the singular point as shown in the inlet at the top right in Fig. 2.12. In this case, the solution has a term exponentially growing in time. So, the change of the contour from the Laplace to inverse-Laplace transformation should be carried out by paying attention to the assumption for the convergence of the integral for t > 0.

2.8.2 Solving with Fourier-Laplace Method

Apply the Fourier decomposition to the equation for the electromagnetic waves in vacuum. The mathematics are the same for the sound waves, plasma waves and any other waves. Solve the initial value problem for the Fourier component of wavenumber **k**. The Laplace transform same as the harmonic oscillator is used for this Fourier mode. For simplicity, try to solve the one-dimensional problem of space with the x direction. The basic equation is

$$\left(\frac{\partial^2}{\partial t^2} - c^2\frac{\partial^2}{\partial x^2}\right)E = 0 \tag{2.153}$$

where c is the speed of light in vacuum. (2.153) is the same type of equation as (2.49) and expanded as,

$$\left(\frac{\partial}{\partial t} - c\frac{\partial}{\partial x}\right)\left(\frac{\partial}{\partial t} + c\frac{\partial}{\partial x}\right)E = 0 \tag{2.154}$$

It is clear (2.154) has the general solution.

$$E(t,x) = f(x - ct) + g(x + ct) \tag{2.155}$$

where f and g are arbitrary functions. The first term of (2.155) is the wave propagating to the right in the x axis, and the second term is the wave propagating to the left. Here, f and g are determined by the initial condition. Since (2.153) is a linear partial differential equation, the principle of superposition can be used. Then, the solution can be given in the form with the sum of the Fourier components.

$$E(t,x) = \sum_k E_k(t)e^{ikx} \tag{2.156}$$

Inserting (2.156) into (2.153), the following ordinary differential equations are obtained for each Fourier component.

$$\frac{d^2 E_k}{dt^2} + c^2 k^2 E_k = 0 \tag{2.157}$$

Assuming $\gamma = 0$ in (2.139) and $\omega_0^2 = c^2 k^2$ in (2.139), (2.157) is of the same form as the harmonic oscillator. Therefore, from (2.151) the solution to the initial value problem is obtained.

$$E_k(t) = \frac{dE_k(0)}{dt}\frac{sin(\omega_0 t)}{\omega_0} + E_k(0)\,cos(\omega_0 t) \tag{2.158}$$

The solution can be obtained with the Fourier decomposition of the initial condition.
   Inserting (2.158) to (2.156), the following form is obtained as the solution.

$$E(t,x) = \sum_k A_k e^{-ik(ct-x)} + \sum_k B_k e^{ik(ct+x)} \tag{2.159}$$

where A_k and B_k are given by the Fourier transformation of the initial condition.
   It is useful to know that partial differential equations can be solved as ordinary differential equations in the case of linear perturbations. Furthermore, solving the initial value problem of the Eq. (2.154) is nothing without finding the poles in closed curve of the Cauchy integral in the two-dimensional complex space. The solution has the form proportional to exp.$(-i\omega t)$, and its frequency and growth rate (or damping rate) are the real part and the imaginary part of the singular points, respectively.
   Therefore, the solution of the algebraic equation corresponding to the singular points can be symbolically expressed

$$\omega = \omega(\mathbf{k}) \tag{2.160}$$

The relation (2.160) is generally called a **dispersion relation**. For wavenumber **k**, the number of waves is equal to the number of singularities of the denominator of the Laplace inverse transformation. The number of singularities increases as the basic equations become more complicated. Electromagnetic waves are simple, second-order equations, but there are numerous waves in the plasma. Therefore, rather than directly solving the differential equation, it is better to use the Fourier-Laplace transform to obtain the algebraic equation of dispersion relation, for example, the dispersion relation of electromagnetic wave in the vacuum is simple as

$$\omega^2 = c^2 k^2 \tag{2.161}$$

In the case that the dispersion relation is a real function and has roots of complex, there is always a solution of wave growing in time. In such a case, the wave is said to be unstable. To find the instabilities in plasma is very common subject even in laser-produced plasmas as will be seen later.

2.9   Magneto-Hydrodynamic Equation of Plasma

An ion is much heavier than an electron. Therefore, the relatively slow change in the plasma dynamics is often determined by the inertial of the ions. In this case, electrons move in association with ions so as to avoid charge separation to form a strong electric field. However, since the high temperature plasma has a high electric conductivity, the electron flow keeps electric current even in weak electric field. Then, while maintaining charge neutrality, an electron current is generated, and it is better to regard that the ions move slowly with strong magnetic field due to the electron current.

In such a case, there is no need to solve the above two fluid equations separately. In general, the behavior of plasma is approximated by **Magneto-Hydro-Dynamics (MHD)** equation derived below. For example, in magnetic confined plasmas, we first study the confinement condition of plasma with use of the MHD equation. This MHD equation was derived by **H. Alfven**, awarded the Nobel Prize in Physics in 1970. His achievement is stated in the citation for this award, "fundamental research and discovery with magneto-hydrodynamics as meaningful application to various parts of plasma physics".

In recent years, observation technology has been advanced rapidly to provide details of the plasmas in the Universe. As the result, there is a movement to reconstruct astrophysics based on plasma physics, for example, the explosive phenomenon in the Universe. In the laser-plasma, the generation of magnetic field or coupling of external magnetic field has become an important topic mainly relating to l**aboratory astrophysics**, such as magnetic reconnection [8].

The MHD equation have been introduced as basic equation to describe space plasmas and magnetically confined plasma. The magnetic field is ubiquitous in the Universe. It is important to understand the approximation in obtaining MHD

equation and the property of the equation. The MHD equation is derived while explaining the derivation procedure and approximation.

Multiply (2.111) by m_e, multiply (2.113) by m_i, take the sum of both, and divide it by $(m_i + m_e)$. In derivation, charge neutrality $n_e/Z = n_i = n$ is assumed as explained above. Furthermore, the mass density and flow rate of the MHD fluid are introduced as

$$\rho = (m_i + m_e)n, \quad \boldsymbol{v} = \frac{m_i \boldsymbol{u}_i + m_e \boldsymbol{u_e}}{m_i + m_e} \tag{2.162}$$

Then, the mathematical process above gives

$$\rho \frac{\partial \boldsymbol{v}}{\partial t} = - \nabla P + \boldsymbol{j} \times \boldsymbol{B} \tag{2.163}$$

In obtaining (2.163), the convective term was neglected. MHD equation is applicable only when the flow velocity is sufficiently slow

$$|\boldsymbol{v} \cdot \nabla \boldsymbol{v}| < < \left| \frac{\partial \boldsymbol{v}}{\partial t} \right| \tag{2.164}$$

Next, the following equation is obtained by multiplying (2.112) by m_e, multiplying (2.114) by m_i, taking a difference and approximating $m_e < < m_i$.

$$\frac{\partial \boldsymbol{j}}{\partial t} = \frac{e^2 \rho}{m_i m_e} \left(\boldsymbol{E} + \boldsymbol{v} \times \boldsymbol{B} - \frac{\nu_{ei} m_e}{ne^2} \boldsymbol{j} \right) - \frac{e}{m_e} \boldsymbol{j} \times \boldsymbol{B} - \frac{e}{m_i} \nabla P_i + \frac{e}{m_e} \nabla P_e \tag{2.165}$$

Since the phenomenon is slow because of the heavy ions, it is reasonable to neglect LHS of (2.165) in what follows. Because of large mass ratio the term of P_i on the right side can also be ignored relative to the term with P_e. Then, (2.165) reduces to a **generalized Ohm's law**.

$$\boldsymbol{E} + \boldsymbol{v} \times \boldsymbol{B} = \frac{1}{\sigma_{ei}} \boldsymbol{j} + \frac{1}{en} (\boldsymbol{j} \times \boldsymbol{B} - \nabla P_e) \tag{2.166}$$

Here, σ_{ei} is the electric conductivity. The resistivity is $1/\sigma_{ei}$ and it stems from the Coulomb scattering of electrons by ions in plasma.

The first term of the parenthesis in the second term on RHS of (2.166) is called the **Hall effect**. This means if there is current flow under an external magnetic field, a potential difference appears in the vertical direction. The second term of the bracket on RHS of (2.166) shows the effect of **ambipolar electric field** which can be generated by electrons with large mobility to escape by the pressure gradient of electrons. Without magnetic field and pressure gradient in (2.166), it reduces to the well-known **Ohm's law** in the form.

$$\boldsymbol{j} = \sigma(\boldsymbol{E} + \boldsymbol{v} \times \boldsymbol{B}) \tag{2.167}$$

2.9.1 Biermann Battery Effect

Now, assume that (2.166) is an equation giving the electric field. It is necessary to formulate governing equations for the magnetic field and density for the completion of the coupled equations for MHD phenomena. It is clear that the equation for density is a continuity equation of (2.111) for the density (2.162).

$$\frac{\partial \rho}{\partial t} + \nabla (\rho \boldsymbol{v}) = 0 \qquad (2.168)$$

The equation governing the magnetic field is obtained by taking the rotation of (2.166) and using Maxwell Eq. (2.117).

$$\frac{\partial \boldsymbol{B}}{\partial t} = \nabla \times (\boldsymbol{v} \times \boldsymbol{B}) - \nabla \times \left(\frac{1}{\mu_0 \sigma_{ei}} \nabla \times \boldsymbol{B} \right) - \nabla \times \left(\frac{\boldsymbol{j} \times \boldsymbol{B}}{en} \right) + \nabla$$
$$\times \left(\frac{1}{en} \nabla P_e \right) \qquad (2.169)$$

This equation is the governing equation of the magnetic field and can be rewritten as a combination of three terms with **B** and one source term.

$$\frac{\partial \boldsymbol{B}}{\partial t} = \nabla \times (\boldsymbol{v} \times \boldsymbol{B}) - \nabla \times \left(\frac{1}{\mu_0 \sigma_{ei}} \nabla \times \boldsymbol{B} \right) - \nabla \times \left(\frac{\boldsymbol{j} \times \boldsymbol{B}}{en} \right) - \frac{1}{en} \nabla n \times \nabla T_e \quad (2.170)$$

The last term in (2.170) plays a role of source and sink of magnetic field. This term is called **Biermann battery effect** [9].

In laser plasma experiment, Biermann battery effect is used to generate magnetic fields to study, for example, **magnetic reconnection** physics [10, 11]. When a single intense laser, shown with the yellow arrow, irradiates a foil as shown in Fig. 2.13a, the produced plasma expands to the laser direction. Since the thermal conduction by electron is dominant and the electrons spread almost uniformly in the hemi-sphere, while the ions expand dominantly in the normal direction. Then, $\nabla n \times \nabla T_e$ term in (2.170) is produced like a torus (doughnut) shape as shown by blue in Fig. 2.13a. The surrounding arrows show charge current vector by expanding electrons.

With use of a short-pulse proton beam (E = 32.8 MeV) generated by an ultra-short laser pulse, a snapshot of the proton beam bending image is obtained as shown in Fig. 2.13b, where the dark image shows the region that the proton beams are bended by the magnetic field. The maximum strength of magnetic field is reported about 2 MG [10]. Note that the spatial size of Fig. 2.13b is about 1 mm and the life time of magnetic field is of the order of ns.

By use of such strong magnetic field, dynamics of magnetic reconnection has been studied. Two intense lasers are focused on an aluminum plate with separation distance of ~1 mm to produce the same two magnetic field structure. The bending of the proton particles is measured to evaluate the magnetic field profiles as shown in
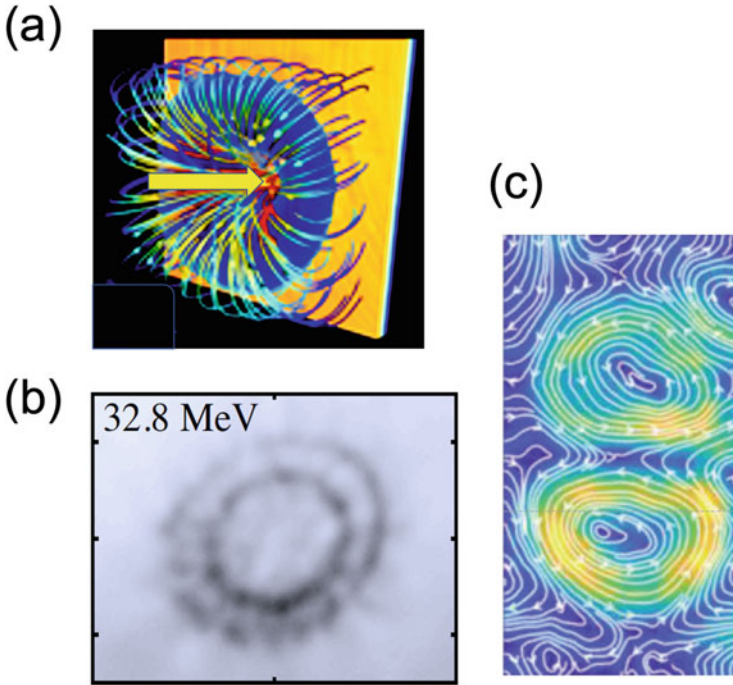
Fig. 2.13 Magnetic field generation in laser produced plasmas via Biermann battery effect. (**a**) Schematic of generation mechanism of magnetic field. A laser irradiated as yellow arrow at the center. (**b**) Proton back-light image of laser-produced magnetic field. (**c**) Magnetic lines overlapped on the proton back-light image to study magnetic reconnection in irradiating two lasers from the same direction. Reprint with permission from Refs. [10, 11]. Copyright 1998 by American Institute of Physics

Fig. 2.13c [11]. The lines are magnetic field line speculated with the proton image. Several snap shots are obtained to study the time evolution of topology of magnetic field.

2.9.2   Similarity of Vortex and Magnetic Fields

Let us discuss about the similarity of (2.169) to the equation of the vortex in neutral fluid (2.102). Except for the Hall effects, it is clear that both are mathematically same. In other words, if any vortexes seen in neutral fluid are generated in plasma, the plasma has electric current along the vortex flow, (see Fig. 2.14). Any vortex in plasma accompanies electric current, a relative motion of the electrons with respect to the ions, consequently, the magnetic field is generated. The vortex is a very important concept such as turbulence and turbulent transport in neutral fluid. In

Fig. 2.14 The relation of flow velocity and magnetic field induced by the vortex and electron current in two-dimensional space, respectively. In the neutral fluid, the vortex is generated by the baroclinic term. This means that if the fluid is conducting plasma, the generation of vorticity means the generation of magnetic field in plasma
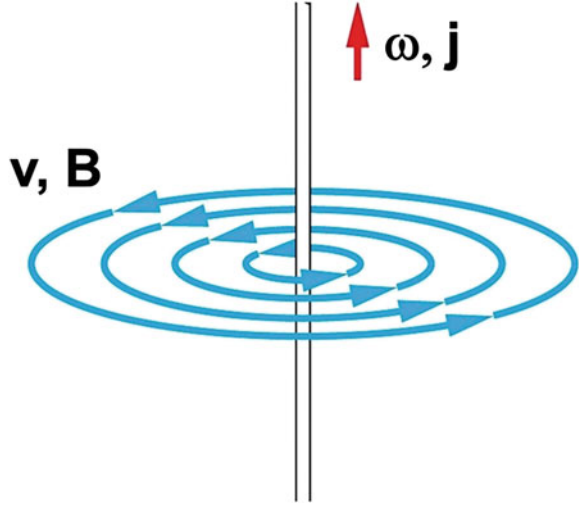
plasma, the transport of charged particles is strongly affected by magnetic field, as magnetic field turbulence is developed by vortexes.

Since MHD phenomena are generally discussed after neglecting the Hall effect or Biermann battery effect, the equation for the magnetic field is solved including the first two terms of (2.169). If the electric conductivity is also constant, the equation of (2.169) reduces to

$$\frac{\partial \boldsymbol{B}}{\partial t} = \nabla \times (\boldsymbol{v} \times \boldsymbol{B}) + \frac{1}{\sigma_{ei}\mu_0} \nabla^2 \boldsymbol{B} \qquad (2.171)$$

The first term on RHS is the convection term and the magnetic field winds around the plasma flow. The electric resistance of the plasma appears in the second term. In the case where the plasma resistivity cannot be neglected, the magnetic field diffuses in space, consequently, charged particles diffuse across the magnetic field. The diffusion of the charged particles is equivalent to the magnetic field diffusion through the plasma. The diffusion term disappears if the plasma is a perfect conductor, namely collisionless plasma.

In general, the diffusion term of magnetic field is regarded same as the Reynolds number (2.62) of the neutral fluid. The diffusion of magnetic field also plays a role in converting the magnetic field energy into the thermal energy of the plasma. Therefore, the **magnetic Reynolds number** in the MHD can be defined as the dimensionless quantity corresponding to the Reynolds number as follows.

$$R_m = \frac{(inertial\ term)}{(magnetic\ diffusion)} = \mu_0 \sigma_{ei} UL \qquad (2.172)$$

Here, U and L are a characteristic flow velocity and a size of plasma. For $R_m >> 1$ the plasma can be described with the **ideal MHD** equation to be explained below. In many of laser plasmas in the laboratory, R_m is not so large. On the other hand, the plasmas in the Universe have very large L and/or very low density, therefore, in either case $R_m \rightarrow \infty$ can be assumed. It is good enough to assume the ideal MHD for study of such plasmas.

2.9.3   Ideal MHD Plasma

When the diffusion coefficient of the magnetic field is dominated by the Coulomb scattering, the diffusion is not important relatively in the laboratory plasmas aiming for nuclear fusion at high temperature or in space plasmas with large scale. Therefore, the ideal plasma approximation in which the magnetic Reynolds number R_m is a very large means that the diffusion term can be neglected. However, in a phenomenon that is governed by dissipation such as magnetic reconnection on the solar surface, it is difficult to explain the observed dynamics by the classical diffusion only due to the Coulomb scattering. In such a case, be aware that the resistivity due to magnetic turbulence induced by plasma wave instabilities becomes dominant. Such resistivity is called **anomalous resistivity** and will be discussed in Vol. 4.

The basic equation for the magnetic field of the **ideal MHD** is (2.171) without resistivity.

$$\frac{\partial \boldsymbol{B}}{\partial t} = \nabla \times (\boldsymbol{v} \times \boldsymbol{B}) \tag{2.173}$$

Use the following mathematical relation to the convection term.

$$\nabla \times (\boldsymbol{v} \times \boldsymbol{B}) = (\boldsymbol{B} \cdot \nabla)\boldsymbol{v} - \boldsymbol{v} \cdot \nabla \boldsymbol{B} - \boldsymbol{B}\nabla \boldsymbol{v} \tag{2.174}$$

where the relation $\nabla \cdot \boldsymbol{B} = 0$ has been used. From the equation of continuity (2.168),

$$\nabla \cdot \boldsymbol{v} = -\frac{1}{\rho}\frac{d\rho}{dt} \tag{2.175}$$

Inserting (2.174) to (2.173) and replacing the second term on RHS of (2.174) to LHS of (2.173), a new relation is obtained.

$$\frac{d\boldsymbol{B}}{dt} = (\boldsymbol{B} \cdot \nabla)\boldsymbol{v} + \frac{\boldsymbol{B}}{\rho}\frac{d\rho}{dt} \tag{2.176}$$

This can be rewritten to be

$$\frac{d}{dt}\left(\frac{\boldsymbol{B}}{\rho}\right) = \left(\frac{\boldsymbol{B}}{\rho} \cdot \nabla\right)\boldsymbol{v} \tag{2.177}$$

It is found from (2.177) that when the flow is perpendicular to the magnetic field, RHS of (2.177) disappears and the quantity $\boldsymbol{B}/\rho$ is preserved along the plasma flow.

In addition, an equation of motion (2.163) is

$$\rho \frac{d\boldsymbol{v}}{dt} = \boldsymbol{j} \times \boldsymbol{B} - \nabla(P_e + P_i) \tag{2.178}$$

In (2.178), the first term on RHS is modified from Ampere's eq. (2.118) by neglecting the displacement current.

$$\boldsymbol{j} \times \boldsymbol{B} = \frac{1}{\mu_0}(\nabla \times \boldsymbol{B}) \times \boldsymbol{B} = -\nabla\left(\frac{B^2}{2\mu_0}\right) + \frac{1}{\mu_0}(\boldsymbol{B} \cdot \nabla)\boldsymbol{B} \tag{2.179}$$

This means that the force due to the magnetic field acts on the plasma as the **magnetic pressure** with the first term of RHS in (2.179) and the **magnetic tension** with the second term.

Here, the ideal MHD equation is closed with the three equations; namely, the equation of continuity (2.168), the equation for motion (2.178), and the equation for magnetic field (2.177). It is also necessary to give EOS for the pressure in (2.178). From the equation of motion, the ratio between the pressure due to the particles and that due to the magnetic field is a dimensionless quantity called **plasma β** value and is defined as.

$$\beta = \frac{(\text{plasma pressure})}{(\text{magnetic pressure})} = \frac{P_i + P_e}{\frac{B^2}{2\mu_0}} \tag{2.180}$$

Magnetic field confinement fusion machine such as **Tokamak** has β value of 1–2 percent. In order to extract energy by nuclear fusion and to put it into practical use, it is said that from the viewpoint of various losses, any fusion machine is necessary to have the β value more than 10%. Therefore, researches on **spherical Tokamak** with high β values are actively studied. Also, in the solar surface, the magnetic field is very strong, and plasma research focuses on physical phenomena in the so-called low beta (low-β) plasma. However, the laser produced plasma and the various plasmas in the Universe are in general high-beta (high-β) plasma. In high-β plasmas, the magnetic field influence on the charged particle transport becomes more important than the magnetic pressure.

It is useful to see the pressure form acting on MHD explicitly. Using the following relation to (2.179),

$$(\boldsymbol{B} \cdot \nabla)\boldsymbol{B} = \nabla(\boldsymbol{B} \otimes \boldsymbol{B}) \tag{2.181}$$

$$[\boldsymbol{B} \otimes \boldsymbol{B}]_{ij} \equiv B_i B_j$$

The conservation form of the momentum density is given from (2.178) in the form:

$$\frac{\partial}{\partial t}(\rho \boldsymbol{v}) + \nabla \left(\rho \boldsymbol{u} \otimes \boldsymbol{u} + \overset{\leftrightarrow}{\boldsymbol{T}} \right) = 0 \tag{2.182}$$

Here, the tensor $\overset{\leftrightarrow}{\boldsymbol{T}}$ is given to be

$$\overset{\leftrightarrow}{\boldsymbol{T}} = \left(P + \frac{B^2}{2\mu_0} \right) \overset{\leftrightarrow}{\boldsymbol{I}} - \frac{1}{\mu_0} \boldsymbol{B} \otimes \boldsymbol{B} \tag{2.183}$$

where $\overset{\leftrightarrow}{\boldsymbol{I}}$ is the unit tensor and P is the total pressure, $P = P_i + P_e$. The tensor of (2.183) is the total tensor pressure acting on the MHD fluid.

It is useful to show explicitly the component of the tensor:

$$T_{ik} = \left(P + \frac{B^2}{2\mu_0} \right) \delta_{ik} - \frac{B_i B_k}{\mu_0} \tag{2.184}$$

In the local frame in which the direction of the magnetic field is in the z-direction, $\overset{\leftrightarrow}{\boldsymbol{T}}$ can be given in the form.

$$\overset{\leftrightarrow}{\boldsymbol{T}} = \begin{bmatrix} P + \dfrac{B^2}{2\mu_0} & 0 & 0 \\ 0 & P + \dfrac{B^2}{2\mu_0} & 0 \\ 0 & 0 & P - \dfrac{B^2}{2\mu_0} \end{bmatrix} \tag{2.185}$$

As is clear from (2.185), the pressure by the magnetic field is in the perpendicular direction to the magnetic field vector. On the other hand, the tension works in the magnetic field direction as negative pressure. The magnetic field component in the z direction is physically.

(z-component by B)

$$= \left(\text{magnetic pressure} : \frac{B^2}{2\mu_0} \right) + \left(\text{magnetic tension} : -\frac{B^2}{\mu_0} \right) \tag{2.186}$$

Finally, the energy conservation equation of the MHD fluid is in the form.

$$\frac{\partial}{\partial t} U + \nabla \boldsymbol{S} = 0 \tag{2.187}$$

where the energy density U and the energy flux density **S** are

$$U = \frac{1}{2}\rho v^2 + \frac{1}{\gamma - 1}P + \frac{B^2}{2\mu_0} \qquad (2.188)$$

$$S = \left(\frac{1}{2}\rho v^2 + \frac{\gamma}{\gamma - 1}P\right)v + \frac{1}{\mu_0}\boldsymbol{B} \times (\boldsymbol{v} \times \boldsymbol{B}) \qquad (2.189)$$

In deriving (2.188) and (2.189), the ideal EOS for both particles have been assumed in the forms in (2.31) and (2.32) with the same specific heat γ, say $\gamma = 5/3$ for the fully ionized plasma.

2.9.4   Magnetic Dynamo Effect

Magnetic field grows even for the case without the source term like the Biermann battery effect in (2.170). Given fluid velocity field $\boldsymbol{v}(\boldsymbol{r})$ in (2.171), it has an eigen function $\boldsymbol{B}_0(\boldsymbol{r})$ in the form: $\boldsymbol{B}(\boldsymbol{r}, t) = \boldsymbol{B}_0(\boldsymbol{r}) \exp(\gamma t)$, where γ is the eigen value representing the growth rate of the magnetic field.

The principle of the growth of magnetic energy is explained intuitively like this. As explained in (2.186), the magnetic field has tension force and one need a work to stretch the magnetic field line in the direction of the magnetic vector. When the topology of flow field $\boldsymbol{v}(\boldsymbol{r})$ is complicated due to the convective motion in rotating plasma fluid system, for example, the conducting fluid inside the earth, plasma in the Sun, etc., the length of magnetic field line is possibly stretched by the convective motion, if the resistivity term in (2.171) is small enough, namely large R_m case.

In the case when the plasma pressure is much larger than the magnetic pressure, it is a good approximation to solve Navier-Stokes Eq. (2.57) independently from (2.171).

After solving NS equation and find almost stational convective motion, the eigenvalue problem with reasonable boundary condition is solve to obtain the form $\boldsymbol{B}_0(\boldsymbol{r}) \exp(\gamma t)$ for the linear stability analysis. Then, the nonlinear evolution can be studied by solving numerically (2.171). We may find the nonlinear saturation profile of the magnetic field, where magnetic field is always enhanced by the first term in (2.171) to balance the dissipation of the second term. This is the case of magnetic field of the earth and the Sun.

In Fig. 2.15, the magnetic field near the surface of the Sun observed via radiation emission by electrons in their cyclotron motions is shown [12]. Such strong magnetic field is originally produced by the magnetic dynamo effect in the deep inside of the Sun. It is clear that since the magnetized region has lower density than non-magnetized neighbor plasma, the magnetic field rises by the buoyancy. Figure 2.15 is a snap shot of such magnetic field appeared on the surface and will disappear later via the magnetic reconnection.

Fig. 2.15 The magnetic field near the surface of the Sun observed via radiation emission by electrons in cyclotron motions [12]. Credit: NASA NASA/TRACE

2.9.5   Plasma Confinement by Magnetic Field

Eq. (2.178) gives the condition of plasma confined in magnetic field. The basic equation to solve configurations of plasma and magnetic field in the state of force balance is given as,

$$\boldsymbol{j} \times \boldsymbol{B} = \nabla P, \quad \boldsymbol{j} = \frac{\nabla \times \boldsymbol{B}}{\mu_0}, \quad \nabla \cdot \boldsymbol{B} = 0 \tag{2.190}$$

To find a configuration of magnetic confinement device for collisionless fusion plasma, this ideal MHD equation should be solved at first. It is clear from the divergence-free property of magnetic field ($\nabla \cdot \boldsymbol{B} = 0$) that the solution should have **torus** topology as shown in Fig. 2.16. as represented by **Tokamak** machine.

   One of mathematically simple solution in an ideal one-dimension is the pinch plasma. To generate strong x-ray flux like that by lasers, **Z-pinch** machine driven by pulse power has been used [13]. The Z-machine has a solution of (2.190) with assuming one-dimensional cylindrical symmetric geometry, where **j** in the z-direction and **B** in the azimuthal direction. Then, (2.178) reduces to the.

$$\frac{dP(r)}{dr} + \frac{B_\theta(r)}{\mu_0 r} \frac{d}{dr}[rB_\theta(r)] = 0 \tag{2.191}$$

Then, (2.191) can be rewritten to be the force balance relation,

$$\frac{d}{dr}\left(P + \frac{B_0^2}{2\mu_0}\right) + \frac{B_0^2}{\mu_0 r} = 0 \tag{2.192}$$

Equation (2.192) represents that the pressure force by plasma and magnetic field balances with the tension force of magnetic field in (2.184). Solving (2.191), the

Fig. 2.16 Optimum
structure of MHD solution,
torus
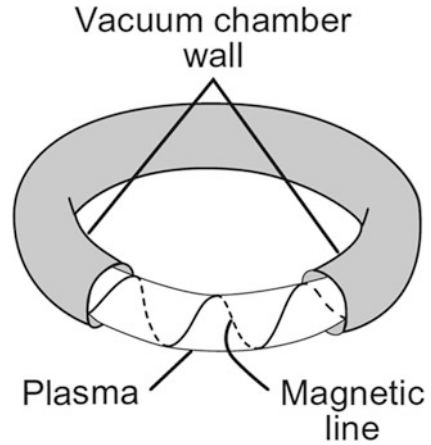
Fig. 2.17 Normalized
pressure and magnetic field
profiles of ideal
one-dimensional Z-pinch
solution
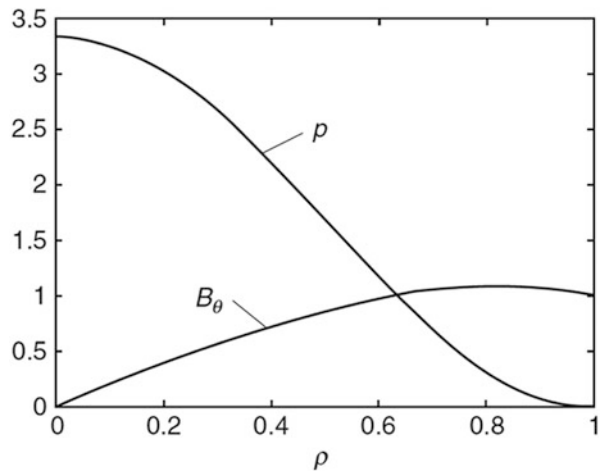
normalized profile of the magnetic field $B_\theta(r)$ and pressure P(r) of the Z-pinch is
shown in Fig. 2.17. The magnetic field is normalized by the value at the outer radius
($\rho = 1$) and the pressure is normalized by the magnetic pressure at $\rho = 1$. The size of
the radius is arbitrary as shown with the normalized radius ρ.

The wire-array Z-machine is used to study the possibility of **MagLIF** (magnetic
laser inertial fusion) with combination of Z-pinch compression and laser heating
[14]. Combining the magnetic field in the compression phase, the particle heat
conduction can be reduced to relax the fuel ignition condition. It is well known,
however, that the Z-pinch plasma confinement is unstable to perturbation from the
cylindrical symmetry of the plasma and magnetic field, and MHD stability has to be
studied.

2.9.6   Resistive MHD in Strong Heat Flux

In high-density plasmas produced by lasers or Z-pinch, the ideal MHD is not appropriate to describe the dynamics of magnetic field and fluid phenomena. In the case where strong heat flow in proportion to $-\nabla T$ is important to the fluid dynamics, (2.179) is not an appropriate relation. This is because in deriving (2.179), we have assumed that the distribution function is Maxwellian with electron flow velocity $\mathbf{u}_e$ defined in (2.116).

In laser produced plasma, the heat flow carries the absorbed laser energy to the over-dense region, and the temperature is non-uniform in space. In such a case, the distribution function is not isotropic and it deforms in the direction of the heat flow. In general, it is enough to consider the heat flux by the electrons and the following discussion is done for the electron distribution function $f_e(\mathbf{v}, \mathbf{x}, t)$.

As will be seen in Chap. 6, the heat flux formula like (2.109) is derived by starting with Boltzmann equation. We follow the formulation given in [15]. The Boltzmann equation with a simplified **Krook collision operator** is given in the form.

$$\frac{\partial f_e}{\partial t} + \mathbf{v} \cdot \nabla f_e - \frac{e}{m}(\mathbf{E} + \mathbf{v} \times \mathbf{B}) \cdot \frac{\partial f_e}{\partial \mathbf{v}} = -\nu_{ei}(f_e - f_M) \tag{2.193}$$

where f_M is the local Maxwell distribution with n_e and T_e. Consider that (2.190) is in the local frame of the ion motion. The collision frequency ν_{ei} due to Coulomb collision of electrons by ions is given in (2.3).

Note that the collision frequency is a function of the electron velocity. In the standard way to solve (2.193) is the perturbation method, where the gradient length of T_e is assumed much longer than the electron mean-free-path. Then, it is assumed that

$$f_e = f_0 + \boldsymbol{f}_1 \cdot \frac{\boldsymbol{v}}{v} \tag{2.194}$$

where $\boldsymbol{f}_1$ is a vector function and small enough compared to f_0. Assuming f_0 is Maxwellian f_M and inserting (2.194) into (2.193), the equation to the perturbed distribution function is obtained.

$$\frac{\partial f_1}{\partial t} + \mathbf{v} \cdot \nabla f_0 - \frac{e}{m}\mathbf{E} \cdot \frac{\partial f_0}{\partial \mathbf{v}} - \frac{e}{m}\mathbf{B} \times f_1 = -\nu_{ei}f_1 \tag{2.195}$$

In general, the perturbation of the distribution consists of the two terms due to the mean flow and the temperature gradient. When both are in the x-direction, the $\boldsymbol{f}_1$ has only x-component and it can be expressed in the form:

$$f_1 = a_1\boldsymbol{j} + a_2\boldsymbol{q}_T \tag{2.196}$$

where $\mathbf{j}$ is the electric current and $\mathbf{q}_T$ is the heat flux by electrons. In (2.195), a_1 and a_2 are constants. When the heat flux is neglected and in addition the velocity dependence in ν_{ei} of (2.3) is neglected in (2.195), (2.166) is obtained by taking the velocity moment of (2.195).

However, when the heat flux term is included, the v^3 moment of ν_{ei} should be considered. Then, the generalized Ohm's law is obtained after neglecting the time dependence in the form.

$$\mathbf{E} + \mathbf{v} \times \mathbf{B} = \frac{\mathbf{j}}{\sigma*} + \frac{1}{en_e}(\mathbf{j} \times \mathbf{B} - \nabla P_e) - \frac{1}{e}\nabla T_e - \frac{2}{5}\frac{\mathbf{q}_e \times \mathbf{B}}{P_e} \tag{2.197}$$

where $\sigma* = 5/2\sigma$ with σ in (2.166). The factor 5/2 stems from the v^3 dependence of the collision frequency ν_{ei}. The last two terms on RHS in (2.197) appear due to the heat flux proportional to ∇T_e. Note that the heat flux $\mathbf{q}_e$ in (2.197) is not equal to the $\mathbf{q}_T$ in (2.192). Since the energy is also carried by the plasma flow and $\mathbf{q}_e$ is purely heat flux remaining only for $\mathbf{j} = 0$. It is shown in [15]

$$\mathbf{q}_e \approx \mathbf{q}_T - \frac{5}{2}\frac{T_e}{e}\mathbf{j} = -\kappa_e \nabla T_e \tag{2.198}$$

In order to keep the fundamental structure of the Ohm's law as (2.166), it is required to derive the structure of $\mathbf{j}/\sigma$ term. In the real case, the Coulomb collision frequency is proportional to v^{-3} and σ in (2.166) should be replaced with $\sigma* = 5/2\sigma$. With inclusion of v-dependence of the Coulomb collision frequency, the Hall term is found to have two terms. One is proportional to the current and the other is proportional to the heat flux. So, consistently, the Hall term is given as the total convection flow velocity as

$$\mathbf{u}_B = -\frac{\mathbf{j}}{en_e} + \frac{2}{5}\frac{\mathbf{q}_e}{P_e} \tag{2.199}$$

This term is called the **Nernst effect**. The importance of the Nernst effect in laser ablation plasma was pointed out in [15].

2.10 MHD Waves

Consider linear perturbations of the ideal MHD equation. The underlying formula is the equation of motion for the velocity of the magnetized fluid (2.163) and the eq. (2.173) for the magnetic field. Suppose that a stationary plasma is confined by an external magnetic field $\mathbf{B}_0$. For example, consider the plasma trapped in the earth's magnetic field. Before linearizing, the following operation is applied to (2.173).

$$\nabla \times (\boldsymbol{v} \times \boldsymbol{B}) = (\boldsymbol{B} \cdot \nabla)\boldsymbol{v} - (\boldsymbol{v} \cdot \nabla)\boldsymbol{B} + \boldsymbol{v}(\nabla \cdot \boldsymbol{B}) - \boldsymbol{B}(\nabla \cdot \boldsymbol{v}) \tag{2.200}$$

Since from the Maxwell equation$\nabla \cdot \boldsymbol{B} = 0$, three terms remain in (2.200). Then, the basic equations are

$$\rho \frac{d}{dt}\boldsymbol{v} = \frac{1}{\mu_0}(\nabla \times \boldsymbol{B}) \times \boldsymbol{B} \tag{2.201}$$

$$\frac{\partial}{\partial t}\boldsymbol{B} = (\boldsymbol{B} \cdot \nabla)\boldsymbol{v} - (\boldsymbol{v} \cdot \nabla)\boldsymbol{B} - \boldsymbol{B}(\nabla \cdot \boldsymbol{v}) \tag{2.202}$$

Assume the form of the linear perturbations of the magnetic field and velocity as

$$\boldsymbol{B} = \boldsymbol{B}_0 + \boldsymbol{B}_1 \tag{2.203}$$

$$\boldsymbol{v} = \boldsymbol{v}_0 + \boldsymbol{v}_1 \tag{2.204}$$

Linearize Eqs. (2.201) and (2.202), and assume the plasma is at rest, namely $\boldsymbol{v}_0 = 0$. Consider that the perturbation is assumed to be incompressible $\nabla \cdot \boldsymbol{v} = 0$. Then, the basic equations for the linear components are

$$\rho_0 \frac{\partial}{\partial t}\boldsymbol{v}_1 = \frac{1}{\mu_0}\left\{(\nabla \times \boldsymbol{B}_1) \times \boldsymbol{B}_0 + (\nabla \times \boldsymbol{B}_0) \times \boldsymbol{B}_1\right\} \tag{2.205}$$

$$\frac{\partial}{\partial t}\boldsymbol{B}_1 = (\boldsymbol{B}_0 \cdot \nabla)\boldsymbol{v}_1 - (\boldsymbol{v}_1 \cdot \nabla)\boldsymbol{B}_0 \tag{2.206}$$

Since the current producing the external magnetic field $\mathbf{B}_0$ is outside the plasma, the second term of the parenthesis in (2.205) does not exist in the plasma.

Consider two cases separately, namely the wave propagates parallel or perpendicular to the external magnetic field. Waves propagating to the parallel direction are called **Alfven waves**, and in the perpendicular case they are called **magnetic sonic waves** or **compressible Alfven waves**.

2.10.1 Alfven Waves

Let's use the Fourier decomposition to the linear perturbations and find the dispersion relation of the wave with wave number **k**. First, the incompressibility is assumed for the case where the vibration is perpendicular to the magnetic field and the wave number **k** is in the direction of the magnetic field. The direction of the external magnetic field is the z-axis direction as shown in Fig. 2.18. First of all, in the simple case, assuming that the wave number is in the z direction ($\theta = 0$) and the wave oscillation is in the x direction, both (2.205) and (2.206) remain only the x component as follows.

Fig. 2.18 The definition of
the coordinate to study the
waves in the constant
external magnetic field in
the z-direction
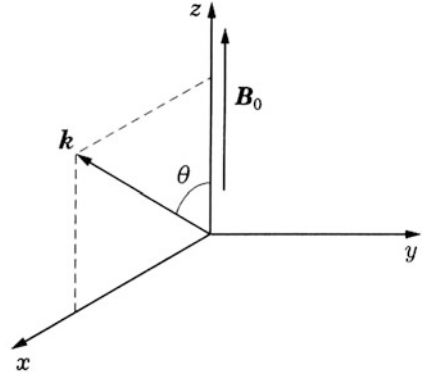
$$\rho_0 \frac{\partial}{\partial t} v_1 = \frac{B_0}{\mu_0} \frac{\partial}{\partial z} B_1 \tag{2.207}$$

$$\frac{\partial}{\partial t} B_1 = B_0 \frac{\partial}{\partial z} v_1 \tag{2.208}$$

By taking $\partial/\partial t$ for (2.207) and substituting (2.208) into (2.207), the following wave equation is obtained.

$$\frac{\partial^2}{\partial t^2} v_1 - V_A{}^2 \frac{\partial}{\partial z} v_1 = 0 \tag{2.209}$$

Here, V_A is called the **Alfven velocity**. The Alfven velocity is defined as follows.

$$V_A = \sqrt{\frac{B_0^2}{\mu_0 \rho_0}} \tag{2.210}$$

This velocity is the value obtained by dividing the tension of the magnetic field of (2.186) by the mass density. As in the image shown in Fig. 2.19, it is a wave caused by the ions wound around the magnetic field vibrating due to the tension of the magnetic field. It is the same as the acoustic of the strings of a guitar. The acoustic sound becomes higher when the string is strongly tensioned (strong magnetic field), the thicker the string (the higher the ion density), the lower the acoustic sound is.

Since the propagation velocity of the Alfven wave is constant, the dispersion relation of the Alfven waves is

$$\omega^2 = V_A{}^2 k^2 \tag{2.211}$$

Fig. 2.19 A schematic of the perturbed magnetic field and ions in cyclotron motion following the deformed magnetic field line
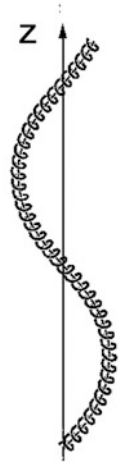
It is important to note that if the plasma is low-β plasma confined by some external magnetic field, the Alfven speed is faster than the sound waves in (2.47) and ion acoustic waves (2.137). Therefore, energy spontaneously generated in the plasma is dominantly carried by the Alfven waves.

It is informative to obtain (2.211) by the energy principle. Let us find the change of the magnetic energy due to the sinusoidal distortion of the magnetic field δW_B and the kinetic energy for the ions around the magnetic field δW_k over one wavelength $\lambda = 2\pi/k$. As displacing $\xi(x,t) = \xi_0(t) \sin(kz)$ in the perpendicular direction of the background magnetic field, the following energies are defined.

$$\delta W_B = (tension) \times (elongated\ length\ of\ the\ magnetic\ field)$$

$$\delta W_k = (kinetic\ energy\ of\ oscillation.)$$

Both are easily calculated to be the following forms per one wavelength

$$\delta W_B = \frac{B_0^2}{\mu_0} \left\{ \int_0^\lambda \sqrt{1 + \left(\frac{\partial \xi}{\partial z}\right)^2}\, dz - \lambda \right\} = \frac{\lambda}{4} (k\xi_0)^2 \frac{B_0^2}{\mu_0} \tag{2.212}$$

$$\delta W_k = \int_0^\lambda \frac{1}{2} \rho_0 \left(\frac{d\xi}{dt}\right)^2 dz = \frac{\lambda}{4} \rho_0 \left(\frac{d\xi_0}{dt}\right)^2 \tag{2.213}$$

Here, **Lagrangian** is defined by considering ξ_0 as the generalized coordinate. Then, by solving the Euler-Lagrange equation, a simple oscillator equation can be derived. The frequency is easily obtained

$$\omega^2 = k^2 V_A^{\,2} \tag{2.214}$$

2.10.2   *Compressive Alfven Wave (Magneto Acoustic Waves)*

Consider longitudinal waves propagating perpendicularly to the magnetic field. In this case, of course, since it is compressible, the pressure term of the eq. (2.178) also remains as the effect of finite temperature. The external magnetic field is the z direction as shown in Fig. 2.18, the oscillation is the x direction, and the wave number **k** is also in the x direction ($\theta = \pi/2$). Then, the compressibility comes out, so the basic equations are (2.168), (2.178), and (2.173).

As a new perturbation, density perturbation arises from the compressibility.

$$\rho = \rho_0 + \rho_1 \tag{2.215}$$

By inserting (2.215), (2.203), and (2.204) into the three basic equations and linearizing them, the following linearized equations are obtained.

$$\frac{\partial}{\partial t}\rho_1 + \rho_0 \frac{\partial}{\partial x}v_1 = 0 \tag{2.216}$$

$$\rho_0 \frac{\partial}{\partial t}v_1 = -C_S^2 \frac{\partial}{\partial x}\rho_1 - \frac{B_0}{\mu_0}\frac{\partial}{\partial x}B_1 \tag{2.217}$$

$$\frac{\partial}{\partial t}B_1 = -B_0 \frac{\partial}{\partial x}v_1 \tag{2.218}$$

By taking the time differentiation of (2.217) and using (2.216) and (2.218), a partial differential equation of the second order is obtained.

$$\frac{\partial^2}{\partial t^2}v_1 - V_S^2 \frac{\partial^2}{\partial x^2}v_1 - V_A^2 \frac{\partial^2}{\partial x^2}v_1 = 0 \tag{2.219}$$

Here, V_s is the sound velocity defined in (2.47). The dispersion relationship is easily obtained from (2.219) as

$$\omega^2 = k^2 \left(V_A^2 + V_S^2\right) \tag{2.220}$$

This is a wave called the **magneto acoustic wave**. When a compressional wave is generated in the direction perpendicular to the magnetic field, the density perturbation is oscillated by not only the magnetic pressure but also the pressure of the plasma. This is the reason of the name, magneto acoustic waves. For the case without thermal pressure, this wave is called the **compressional Alfven wave**.

The difference of the magnetic field displacement of the wave of (2.214) and that of (2.220) is clear. Although the Alfven waves are transverse wave and the displacement of the magnetic field is perpendicular to the propagation direction of the wave, the compressive Alfven wave is the same as the ion acoustic wave and it is a

longitudinal wave. Since the magnetic pressure also contributes to the restoring force, the propagation velocity is faster than the ion acoustic waves.

2.10.3 Ion Acoustic Wave and Three Waves

We investigated the longitudinal and transverse waves, but there is a wave which receives restoring force by the pressure propagating in the magnetic field direction. Since the motion is parallel to the magnetic field, the force due to the magnetic field can be neglected (same as in the case without the magnetic field). Neglecting the magnetic field in (2.71), the following wave equation is obtained.

$$\frac{\partial^2}{\partial t^2} v_1 - V_S{}^2 \frac{\partial^2}{\partial x^2} v_1 = 0 \tag{2.221}$$

This is the same as the acoustic wave given at (2.48). Note that inclusion of charge separation effect, the dispersion relation of the ion acoustic waves (2.135) is reproduced.

Therefore, we had already three waves. The waves propagating along the magnetic field are the **Alfven wave** (transverse wave) and **ion acoustic wave** (longitudinal wave). The wave propagating perpendicular to the magnetic field is the **magneto acoustic wave** (longitudinal wave).

Then, what kind of waves can propagate obliquely to the magnetic field? Does the ion acoustic wave change continuously to the magneto acoustic wave? Or may it be a mixed wave of longitudinal and transverse waves?

The basic equations are (2.168), (2.173), and (2.178). Assume that the arbitrary perturbations are given in the linearized forms and the angle that the wave number **k** forms with the magnetic field is θ as shown in Fig. 2.20. The oscillation component in the y-direction is transverse wave and the dispersion relation is

$$\omega^2 = k^2 V_A{}^2 \cos^2\theta \tag{2.222}$$

This is an obliquely propagating Alfven wave. At the same time there are two waves oscillating in the (x, z) plane, and after a bit messy calculation the dispersion relation can be found in the form.

$$\omega^4 - k^2\left(V_S{}^2 + V_A{}^2\right)\omega^2 + k^4 V_S{}^2 V_A{}^2 \cos^2\theta = 0 \tag{2.223}$$

This can be easily solved and the dispersion relation is obtained as follows

$$\frac{\omega^2}{k^2} = \frac{\left(V_S{}^2 + V_A{}^2\right)}{2} \pm \sqrt{\left(V_S{}^2 + V_A{}^2\right)^2 - 4V_S{}^2 V_A{}^2 \cos^2\theta} \tag{2.224}$$

Fig. 2.20 The phase
velocities of three waves
induced by ion oscillations
in an external magnetic
field, called Friedrichs
diagram. The "f" represents
fast magneto-acoustic wave
(fast wave), "a" Alfven
wave, and "s" slow
magneto-acoustic wave
(slow wave)
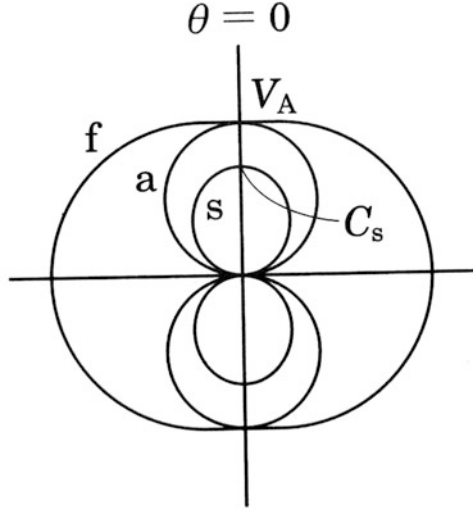
In the case where the magnetic pressure is higher than the plasma pressure (lowβ)
such as the earth's magnetosphere, the sun, and the magnetic confinement fusion
device $V_A > V_S (= C_S$ in Fig. 2.20), the angular dependence of the phase velocity is
shown in Fig. 2.20. As can be seen from (2.222) and (2.224), there are three waves at
an arbitrary angle, two waves degenerate at $\theta = 0$, and at $\theta = \pi/2$ the waves are only
the magneto acoustic waves. In Fig. 2.20, the "f" represents the fast magneto
acoustic wave (**fast mode**), "a" the Alfven wave, and "s" the slow magnetic acoustic
wave (**slow mode**). This diagram is refereed to **Friedrichs diagram**.

2.10.4 Torsional Alfven Wave

The circularly polarized Alfven waves couple with the angular momentum of
plasma. This is important as a physical mechanism for releasing the angular momen-
tum of **the accretion disk** in baby stars or planets. Consider an accretion disk with
magnetic field as shown in Fig. 2.21. The accretion disk is modeled with a pan cake
structure where the plasma is differentially rotating.

$$\boldsymbol{v} = r\Omega(r, z, t)\boldsymbol{e}_\phi \tag{2.225}$$

The magnetic field is assumed axially symmetric and is considered to be composed
of two components: a poloidal component (z-direction) and a toroidal component
(ϕ-direction).

$$\boldsymbol{B} = \boldsymbol{B}_p(r, z, t) + B_\phi(r, z, t)\boldsymbol{e}_\phi \tag{2.226}$$

The magnetic field is substituted into (2.202) to find the following relations.

Fig. 2.21 A schematic image of cut-view of accretion disk and external magnetic field. The accretion disk is plasma and the strong interaction between the plasma and magnetic field is expected
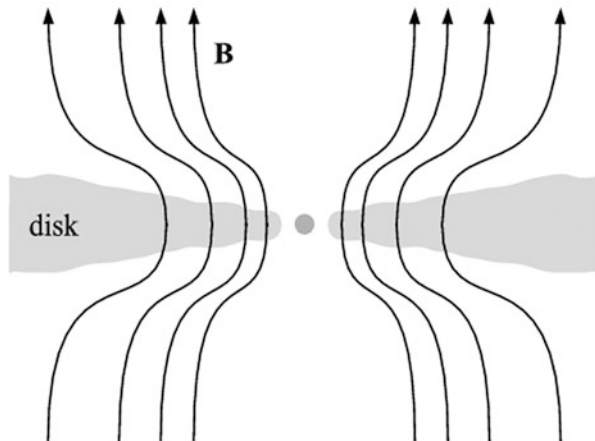
$$\frac{\partial \boldsymbol{B}_p}{\partial t} = 0 \qquad (2.227)$$

$$\frac{\partial B_\phi}{\partial t} = r\boldsymbol{B}_p \cdot \nabla \Omega \qquad (2.228)$$

Here, on RHS of (2.228), only the first term on the right side of (2.202) remains, and the second two terms disappear.The condition to keep stationary rotation (2.228) required the relation.

$$\boldsymbol{B}_p \cdot \nabla \Omega = 0 \qquad (2.229)$$

This is called **Ferraro's theorem** for a homogeneous rotation. If the magnetic field rotates at different angular velocities in the z-direction, the magnetic field twists and the rotation energy of plasma, that is, the angular momentum of plasma is converted into the energy of the magnetic field. However, since there is tension in the magnetic field, it should attempt to extract its twist outside the disc and to become a uniform magnetic field in the z-direction. The twist of the magnetic field is due to the angular momentum of the plasma of the disk, and the tension of the magnetic field transports the angular momentum by the **torsional Alfven wave** (explained below) outside the disk.

Furthermore, inserting (2.225) and (2.226) into the equation of motion (2.201) leads

$$(\nabla \times \boldsymbol{B}) \times \boldsymbol{B} = (\boldsymbol{B} \cdot \nabla)\boldsymbol{B} \qquad (2.230)$$

Then, (2.201) becomes the following equation

$$\rho r \frac{\partial}{\partial t} \Omega = \frac{1}{\mu_0} B_p \frac{\partial}{\partial z} B_\phi \qquad (2.231)$$

Here, the convection term of (2.201) automatically disappears as follows.

$$\mathbf{v} \cdot \nabla \mathbf{v} = 0 \qquad (2.232)$$

Substituting (2.228) into (2.230) leads the following wave equation

$$\frac{\partial^2}{\partial t^2} \Omega - V_{A,p}{}^2 \frac{\partial^2}{\partial z^2} \Omega = 0 \qquad (2.233)$$

Here, $V_{A,p}$ is the Alfven velocity due to the poloidal magnetic field. As can be seen from the derivation above, there is no linearization, therefore, the displacement in the z direction with respect to an arbitrary amplitude is transported outside the accretion disk at the Alfven velocity. As a result, the poloidal component of the magnetic field tries to keep the linear shape. (2.233) is the wave equation for the "**torsional Alfven wave**".

The accretion disk shown in Fig. 2.21 is formed by the plasmas falling to the gravitational center with rotating motion. The rotation motion is not of a constant angular momentum Ω in radial direction. Such differential rotation is known to induce the **magneto-rotational instability (MRI)** [16], and turbulent magnetic field is generated. The turbulent magnetic field enhances the transport of the matter falling to the central gravity, namely angular momentum of the matter transport. It is interesting to point out that a large-scale experiment plans to be carried out with a cylinder box filled with high-temperature liquid sodium (liquid metal) under differential rotation as shown in Fig. 2.22 [17]. Since the normal fluid in the differential rotating system, called **Taylor-Couette flow**, is unstable to fast rotating condition, the magnetic field is amplified by the dynamo effect as shown in Sect. 2.9.

2.11 Electromagnetic Wave in Magnetic Field

The hydrodynamic equations are the most useful ones to find the dynamical physics in many kinds of plasmas from the laboratory to the Universe. The physics of electromagnetic (EM) waves discussed here are usually used to measure, diagnose, or observe different kinds and different scales of plasmas. Of course, intense-lasers have been used to generate plasmas as shown in Volume 1. Strong microwaves are also used to heat magnetically confined plasma and processing plasmas [18]. In general, however, the electromagnetic waves due to electron current in plasmas are relatively high-frequency and the ions with larger mass cannot follow the electron motions. Since the most of fluid motions of plasmas are driven by the ion motions and the electromagnetic waves stemming from the electron motions do not couple with the fluid motions explained above.

Fig. 2.22 A structure of sodium liquid experiment to study MRI by differential rotations. Reprint with permission from Ref. [17]. Copyright 1998 by American Physical Society
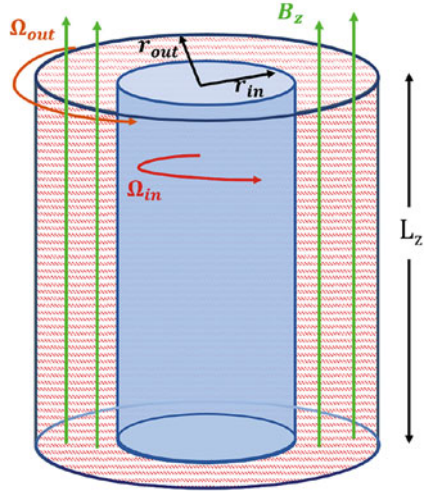
However, EM waves propagates not only in plasmas but also in vacuum. Therefore, EM waves are convenient waves for observing and investigating any plasmas. It is useful to know the fundamental property of the electromagnetic waves in plasmas. Some examples of applications for measurement and observation of plasmas are discussed here.

2.11.1 EM Waves in Plasmas

Electromagnetic waves are widely used for diagnostics of plasmas in the laboratory and observation of the Universe. In astronomy, the electromagnetic waves of wide range of wavelength have been observed to study energetic dynamics in the Universe. Since magnetic field is ubiquitous in Universe, it is also important to know the property of the electromagnetic waves in external magnetic field.

Maxwell equations provides the propagation of the electromagnetic waves in plasmas with the following simple equation as shown in Chap. 2.2.1 in Volume 1.

$$\left(\frac{\partial^2}{\partial t^2} - c^2\nabla^2\right)\boldsymbol{E} = -\frac{1}{\varepsilon_0}\frac{\partial}{\partial t}\boldsymbol{j} \tag{2.234}$$

where $\boldsymbol{E}$ is the electric field of the electromagnetic waves and $\boldsymbol{j}$ is an plasma current induced by $\boldsymbol{E}$. It was already shown in Volume 1 that the dispersion relation of the electromagnetic waves in plasma is given as

$$\omega^2 = \omega_{pe}^2 + c^2 k^2 \tag{2.235}$$

where ω_{pe} is the plasma frequency defined as

$$\omega_{pe}^2 = \frac{e^2 n_e}{\varepsilon_0 m} \tag{2.236}$$

Here, n_e is the electron density. Note that $\omega_{pe}^2 \propto m^{-1}$, the inverse of an electron mass. In Fig. 2.23 the dispersion relation is plotted with the solid line and with the dotted line of the light in vacuum.

The dispersion relation (2.235) indicates that the density of plasma with a size L can be measured from the phase shift of laser beams after passing through the plasma. By use of **holographic interferometry** technique, the density profile of an exploding foil heated by the other intense laser irradiated from the left is observed as shown in Fig. 2.24 [19]. The black-and-white stripe pattern shows the phase change due to the different densities of the measured light propagating in the expanding plasma.

The **refraction index** N is a function of density.

$$N \equiv \frac{c}{\frac{\omega}{k}} \leq 1 \tag{2.237}$$

This is used to obtain shadow image of plasmas. It is clear that the sharp density change reflects laser light impinging with a shallow angle. This property can be used to measure the spatial density structure of plasma shock waves etc. In Fig. 2.25, double exposure shadow images of laser-produced blast waves and the turbulence behind are shown [20].

Fig. 2.23 Dispersion relation of electromagnetic field in plasma
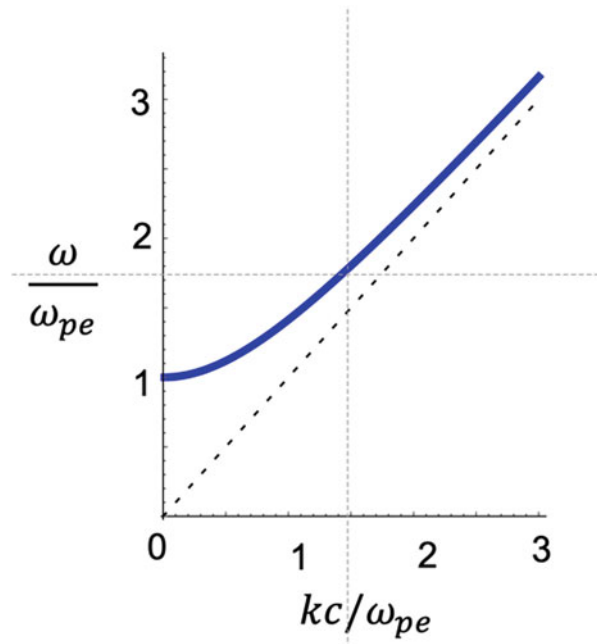
Fig. 2.24 A snapshot of holographic interferometry image of exploding foil. Reprint with permission from Ref. [19]. Copyright 1998 by American Physical Society
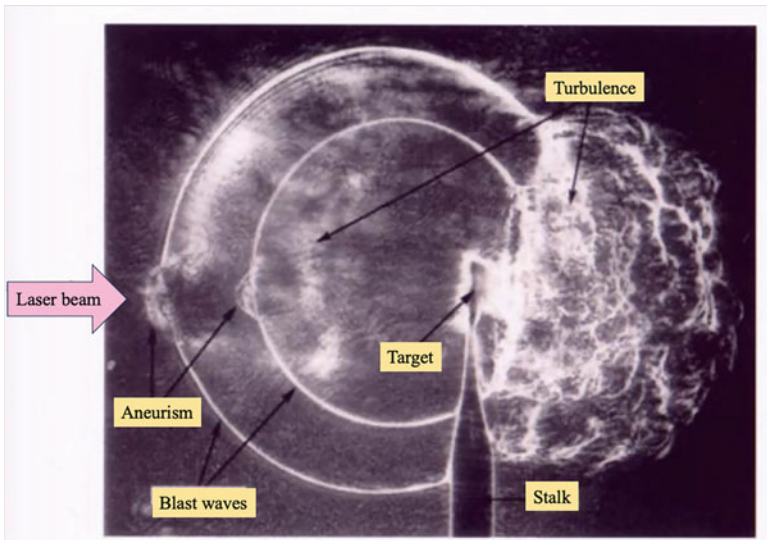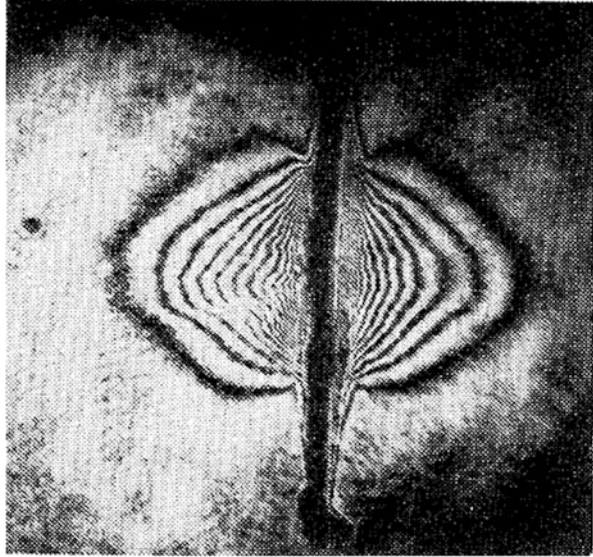
Fig. 2.25 Double exposure image of laser produced blast wave in nitrogen gas. Laser irradiates from left on aluminum target. Reprint from Ref. [20] with kind permission from Springer Science + Business Media. (Courtesy of B. Ripin.)

The **dispersion measure (DM)** defined as follows is also used to speculate the distance of a radio pulse source from a far distant space at L.

$$DM = \int_0^L n_e dx \qquad (2.238)$$
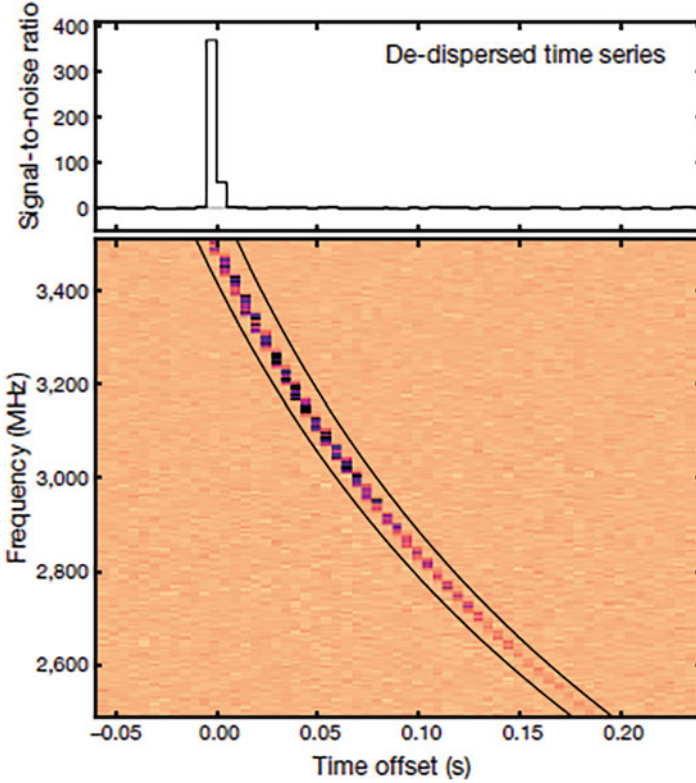
Fig. 2.26 Fast radio burst (FRB) signal observed in 2016. Time evolution of frequency. Reprinted by permission from Macmillan Publisher Ltd: Ref. [22], copyright 1993

For example, a radio pulse with high energy flux was observed near GHz radio wave at first in 2007. After this discovery of such a short radio pulse, the events are now called **FRB (Fast Radio Burst)** [21]. In Fig. 2.26, the signal of FRB 121102 observed in 2016 is shown [22]. Time–frequency data extracted from phased VLA visibilities at the burst location shows the ν^{-2} dispersive sweep of the burst. The solid black lines illustrate the expected sweep for DM = 558 pc cm^{-3}. The de-dispersed light curve is projected to the upper panel. The colour scale indicates the flux density.

The group velocity v_g of the electromagnetic waves in plasma with electron density n_e is

$$v_g = c \left(1 - \frac{\omega_{pe}^2}{\omega^2}\right)^{1/2} \tag{2.239}$$

This relation explains the reason of the delay of low frequency part. The time-delay of low frequency to high frequency ($\omega_L - \omega_H$) is obtained approximately for low-density plasma as

$$v_g \approx c \left(1 - \frac{1}{2} \frac{e^2}{\varepsilon_0 m} \frac{n_e}{\omega^2} \right) \tag{2.240}$$

$$\Delta t = \frac{L}{\Delta v_g} = \frac{1}{2} \frac{e^2}{\varepsilon_0 m} \left(\frac{1}{\omega_L^2} - \frac{1}{\omega_H^2} \right) DM \tag{2.241}$$

The pulse delay in Fig. 2.26 is used to evaluate the distance of the energy source of the burst, and it is found that DM is 558 cm^{-3}pc, which is about 12 times higher than the DM of the Milky Way galaxy. It is concluded that the energy source, which is not explained theoretically yet, is located at cosmological distance.

2.11.2   Electromagnetic Waves from Magnetized Plasmas

The dispersion relation is modified depending on how the induced current is related to the electric field of the electromagnetic waves. When the external magnetic field is applied or exists in plasmas, the electron motion is affected by the Lorentz force and the electric current is modified from the case without B-field given in (2.234). We have already studied the case of ion fluid motions driving MHD waves in external magnetic field in Sect. 2.10. It is in general the electromagnetic waves don't affect the MHD dynamics.

It is better to consider two idealistic cases; one is when the EM wave propagates along with the magnetic field (Fig. 2.27), and the other is when EM wave propagates perpendicular to the magnetic field. This knowledge can be applicable to the general

Fig. 2.27 Electric field of EM wave propagating to $\mathbf{B_0}$ or $- \mathbf{B_0}$ direction
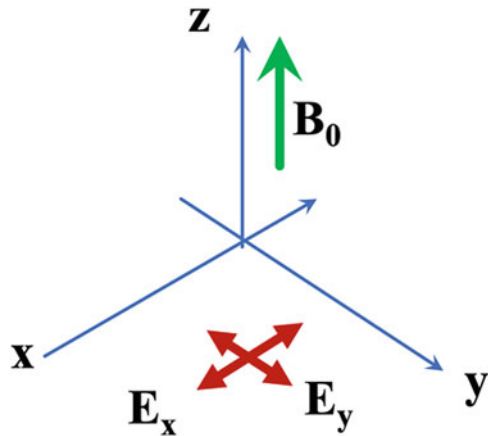
case when EM wave propagates with an arbitrary angle to the magnetic field, although it is not discussed here.

Let us derive the induced current beginning with equation of motion of an electron.

$$m\frac{d}{dt}\mathbf{v} = -e(\mathbf{E} + \mathbf{v} \times \mathbf{B})$$ (2.242)

Estimate the effect of magnetic field by assuming that the magnetic force is weak enough compared to the force by **E**. Then, the perturbation method gives a simple relation

$$\left|\frac{\mathbf{v} \times \mathbf{B}}{\mathbf{E}}\right| \sim \frac{\omega_{ce}}{\omega}, \quad \omega_{ce} = \frac{eB}{m}$$ (2.243)

where ω_{ce} is the electron cyclotron frequency. Namely, low frequency mode is strongly modified with ω near or lower than ω_{ce}. We consider here the case where EM wave propagates along the magnetic field, then, it is required to obtain coupled equations for the EM electric fields in x- and y-directions as in Fig. 2.27.

Here, we don't derive the dispersion relation because it needs a long calculation, and the readers wishing to know are recommended to refer to, e.g. [23]. There dispersion relation is the fourth order to ω in the form.

$$\left(\omega^2 - c^2 k^2 - \alpha\right)^2 - \alpha^2 \frac{\omega_{ce}^2}{\omega^2} = 0$$ (2.244)

$$\alpha = \frac{\omega_{pe}^2}{1 - \omega_{ce}^2/\omega^2}$$ (2.245)

The dispersion relation (2.244) gives two independent modes. They are circularly polarized EM waves. The electric field of EM waves rotates to the right and left directions of magnetic field vector. Assuming that the magnetic field is in the z-direction and the rotating electric field with (k, ω) in (x, y) plane, two dispersion relations are obtained.

[R-wave] for the mode $E_x + iE_y$:

$$\omega^2 = c^2 k^2 + \frac{\omega_{pe}^2}{1 - \omega_{ce}/\omega}$$ (2.246)

[L-wave] for the mode $E_x - iE_y$:

$$\omega^2 = c^2 k^2 + \frac{\omega_{pe}^2}{1 + \omega_{ce}/\omega}$$ (2.247)

The real part of the electric field of the R-wave, $Re(E_x + iE_y)$, is given as

$$E = A\left[\cos(kx - \omega t + \varphi)i_x + \sin(kx - \omega t + \varphi)i_y\right] \tag{2.248}$$

where i_x and i_y are the unit vectors in x- and y- directions, and A and φ are constants.

It is clear that the L-wave has the negative sign for the second term (y-component) in (2.238). That is, the electric field vector of the R-wave rotates to the right, facing the z-direction, and the L-wave rotates to the left.

Note that the difference is only the sign of the denominators. Intuitively, we can image from (2.235) and (2.246) that the effect of magnetic field is regarded to assuming that the **effective mass** of electrons is given as

$$m_{eff} = \left(1 \mp \frac{\omega_{ce}}{\omega}\right)m \tag{2.249}$$

It is easy to know that the dispersion relation of the L-wave is given with that same as in Fig. 2.23 with the plasma frequency with the effective mass of "+" sign in (2.249). The **cut-off density** effectively decreases in the magnetic field. This means EM wave can propagates in the plasmas with less density than the nominal cut-off density, if there is a strong external magnetic field.

On the other hand, the R-wave has higher cut-off density for $\omega_{ce} < \omega$, and a new mode appears for low frequency EM wave with $\omega_{ce} < \omega$ as shown in Fig. 2.28 for the case of $\omega_{ce}/\omega_{pe} = 0.5$. In the case of $\omega = \omega_{ce}$, what happens is the **resonance of EM**

Fig. 2.28 Dispersion relation of the R-wave for the case with $\omega_{ce} = 0.5\omega_{pe}$. The dashed lines are asymptotic of $\omega = \omega_{ce}$ and $\omega = ck$
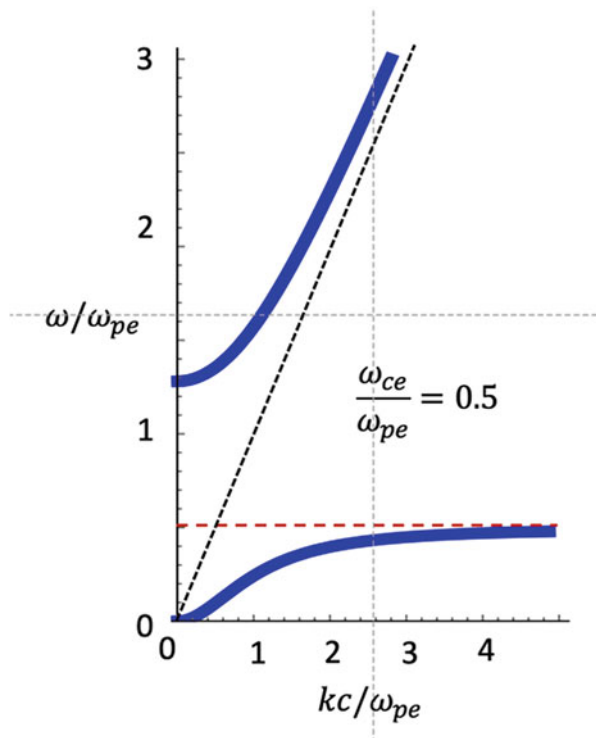
wave and electron cyclotron motion. Then, the detail analysis gives the absorption of EM wave energy by the electron motion and the electron orbits continuously becomes larger in time. This resonance is used to heat electrons confined in strong magnetic field.

It is important to know that thanks to the electron cyclotron motion, the electric field of EM wave is maintained even in the density higher than the nominal cut-off density. The R-wave in the region $\omega < \omega_{ce}$ is called "**whistler wave**".

For the density n_e $[cm^{-3}]$ and magnetic field B [Gauss] units, both frequencies are.

$$\omega_{pe} = 5.6 \times 10^4 \sqrt{n_e} \ \left[s^{-1} \right]$$

$$\omega_{ce} = 1.8 \times 10^7 B \ \left[s^{-1} \right]$$

2.11.3   Faraday Rotation

It is well-known that when linearly polarized EM wave propagates along an external magnetic field, the polarization angle rotates because of the difference of dispersion relations of the R and L waves as shown in Fig. 2.29 [24]. Since the linearly polarized EM wave propagates as two circularly polarized waves of the R and L waves with different phase velocity, the combined EM with have a different angle of
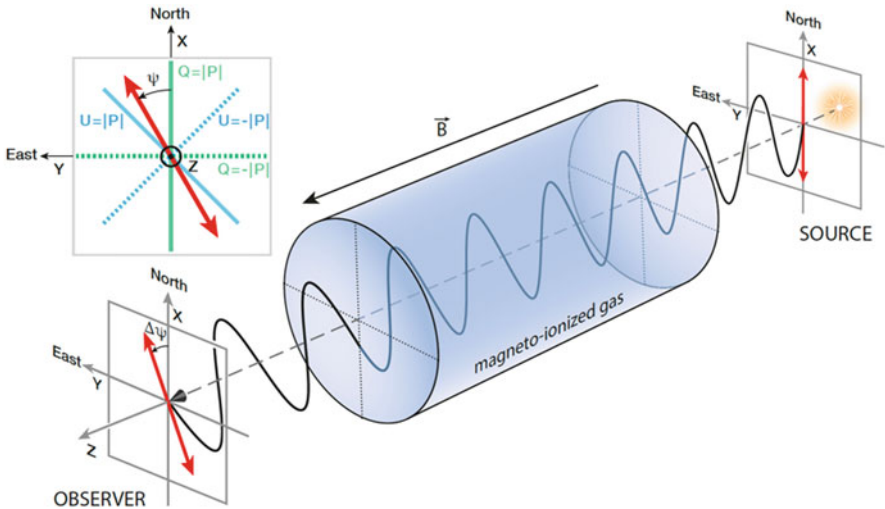
Fig. 2.29 The principle of Faraday rotation of linearly polarized EM wave traveling along magnetic field. The rotation angle is proportional to the Faraday rotation measure. Reprinted with permission from Ref. [24]. Copyright 1998 by Oxford University Press

polarization, when it goes out from the magnetized plasma. This phenomenon is called **Faraday rotation** in magnetized plasma. This effect was discovered by **M. Faraday** in 1845 with light propagating through magnetized glass.

The Faraday rotation has been used to measure the self-generated magnetic field in laser produced plasmas [25]. Irradiating a linearly polarized laser for diagnostic purpose like the case of Fig. 2.27, the shift of the polarization direction after the passage of magnetized plasma gives the information of the magnetic field in the plasma. The magnetic field is generated via **Biermann battery effect** in the laser-plasma as shown in Sect. 2.9. It was found that magnetic field of Mega Gauss is produced. It is noted, however, that the plasma β-value in (2.180) is still higher than unity, roughly $\beta \sim 100$. Since the laser plasma is small, but high-energy density, such strong magnetic field is produced during a short time of ns.

In Fig. 2.26, the polarization of the observed radio wave changes as a function of frequency. This fact can be used to evaluate the average magnetic field strength in the long path from the source. The principle is simple. For a give frequency ω, the difference of wavenumber, $\Delta k (\Delta k \ll k)$, of (2.246) and (2.247) is calculated to be,

$$\Delta k \approx \frac{\omega_{pe}^2}{\omega^2} \frac{\omega_{ce}}{c} \tag{2.250}$$

Integrating Δk over the propagation length L, the phase shift $\Delta \Phi$ is expressed in the form

$$\Delta \Phi = \int_0^L \Delta k dx = \frac{e^3}{\varepsilon_0 cm^2 \omega^2} \int_0^L n_e B_{\parallel} dx \equiv RM\lambda^2 \ [rad] \tag{2.251}$$

where $B_{\parallel}$ is the parallel magnetic field and λ is the wavelength. **RM** in (2.251) is called the **Faraday rotation measure**.

In the case where EM wave propagates perpendicular to external magnetic field, there are two modes depending on the polarization direction. For the case of E-field is parallel to the magnetic field, no magnetic effect appears because $\boldsymbol{v} \times \boldsymbol{B} = 0$ in (2.242) and the dispersion relation is given by (2.235). This mode is called the **ordinary wave**. On the other hand, when the polarization is perpendicular to the B-field, $\boldsymbol{v} \times \boldsymbol{B}$ term modify the EM propagation, and Lorentz force induces the plasma motion in **k** direction to couple with the electrostatic modes. This mode is called the **extraordinary wave**. The detail analysis is given, for example, in [23].

2.11.4 EM Waves from Magnetized Plasmas

A variety of EM waves from the radio waves to the γ-rays is generated by plasma electron motions in the Universe. **Synchrotron emission** of EM wave by highly relativistic electrons are strong EM sources. In Fig. 2.30, a schematic of the

Fig. 2.30 Schematics of synchrotron radiation emission from a highly-relativistic electron rotating in magnetic field. The radiation is linearly polarized and the observed frequency is up-shifted by relativistic effect. Reprinted with permission from Ref. [26]. Copyright 1998 by Oxford University Press
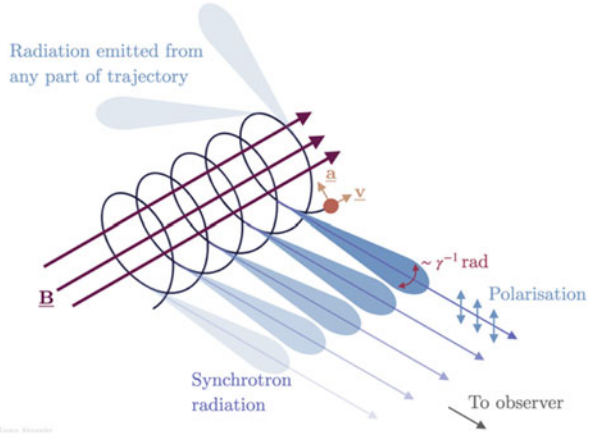
mechanism of the emission is shown [26]. The radiation is emitted in the case where a charged particle is in accelerating motion as shown by Larmor. It is called the **Larmor emission** in non-relativistic electron case and the radiation is emitted dominantly in the direction perpendicular to the acceleration vector. In relativistic motion, it is called the **synchrotron emission**. The emission angle becomes narrow in proportion to $1/\gamma$, where γ is the Lorentz factor of a rotating electron. This is called **relativistic beaming** as discussed in Chap. 5 in Vol. 1. So, the emitted synchrotron frequency is up-shifted as $\omega = \omega_{ce}\gamma^2$. This means radio waves emitting from non-relativistic electrons becomes x-ray for highly relativistic electrons.

Supernova remnants (SNRs) are known to be a candidate where high-energy cosmic rays are generated by the shock waves (blast waves) produced by supernova explosion. Note that the detail physics of blast waves will be discussed in Chap. 4. The SNR of the supernova-1006 which exploded almost 1000 years ago is well studied with the radio to gamma-ray obserbation. The x-ray image shows a clear evidence of the particle acceleration in the vicinity of the blast wave front. With evaluated strength of magnetic field in μG range, it is speculated that highly relativistic electrons (up to 10^{15} eV) are emitting x-rays.

Since the synchrotron radiation is linearly polarized, the direction of magnetic field is speculated by the polarization measurement of radio wave. Assuming the magnetic field is given externally, and the structure is globally uniform in the SNR. The **degree of polarization** P is defined as

$$P \equiv \frac{I_{pol}}{I} \tag{2.252}$$

where I_{pol} is the intensity of polarized EM component and I is the total intensity. As seen in the distribution of the degree of polarization in Fig. 2.31, left-top and right-bottom are highly polarized [27]. From the distribution of the local polarization directions observed, it is concluded that the SN1006 has a large-scale magnetic field along the line from left-top to right-bottom [27].

Fig. 2.31 Observed image of the degree of polarization of radio emission from SNR 1006 remnant. Reprinted with permission from Ref. [27]. Copyright by American Astronomical Society
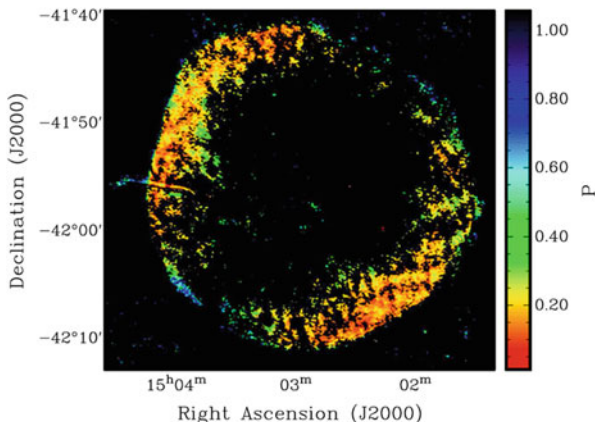
Appendix-A: Fluid Approximation of Plasma

Basic equations to describe microscopic to macroscopic phenomena have been proposed in plasma physics so that they provide the essence of physics with the reduction of the degree of freedom. They leave only the degree of freedom as small as possible. Of course, it is better to solve the following **Vlasov equations** to ion and electron velocity distribution functions $f_\alpha(\mathbf{v})$ (α: ion or electron) as will be discussed in Volume 4 to study higher-freedom phenomena of laser-plasma.

$$\frac{\partial f_\alpha}{\partial t} + \mathbf{v} \cdot \frac{\partial f_\alpha}{\partial \mathbf{r}} + \frac{q}{m}(\mathbf{E} + \mathbf{v} \times \mathbf{B}) \cdot \frac{\partial f_\alpha}{\partial \mathbf{v}} = 0 \tag{2.A-1}$$

where q and m are charge and mass of ion or electron, respectively.

Except for the case where the distribution functions are very far from shifted-Maxwellian, the fluid approximation of plasma is often adopted instead of Vlasov equation because of less freedom in the basic equations. Such a fluid is called "**electromagnetic fluid**" or "**magneto-hydrodynamic fluid**". As a matter of course, such modeling may cause loss of the physics that should originally appear. This point which cannot be derived by fluid model will be explained in relation to the **Landau damping** later.

In the case of neutral fluids, the mean free path is sufficiently shorter than the change length of the physical quantities and collision time is much shorter than the time scale of fluid changes. This means the distribution function in Boltzmann equation is well described with a local **Maxwell distribution**. Then, the collision term to appear in (2.A-1) in Boltzmann equation should also disappear mathematically. In such frequently colliding particle system like molecular gas, the velocity dependence of the distribution function is given with local Maxwell distribution and as seen below the fluid model is very reliable.

The same fluid model is used to describe plasmas regardless of collision dominant or not. Within the assumption of local Maxwellian, the velocity moment equations of

Vlasov equation give the fluid equations as show below. The fluid variables are defined by the velocity moments.

$$\text{Density} : n(t, \boldsymbol{r}) = \int_{-\infty}^{\infty} f d\boldsymbol{v} \tag{2.A-2}$$

$$\text{Flow rate} : \boldsymbol{u}(t, \boldsymbol{r}) = \frac{1}{n} \int_{-\infty}^{\infty} \boldsymbol{v} f d\boldsymbol{v} \tag{2.A-3}$$

$$\text{Temperature} : T(t, \boldsymbol{r}) = \frac{2}{3} \frac{1}{n} \int_{-\infty}^{\infty} \frac{1}{2} m(\boldsymbol{v} - \boldsymbol{u})^2 f d\boldsymbol{v} \tag{2.A-4}$$

$$\text{Heat flux} : \boldsymbol{q}(t, \boldsymbol{r}) = \int_{-\infty}^{\infty} \frac{1}{2} m(\boldsymbol{v} - \boldsymbol{u})^2 (\boldsymbol{v} - \boldsymbol{u}) f d\boldsymbol{v} \tag{2.A-5}$$

Here, we assumed charged particles have no internal degrees of freedom and the specific heat ratio $C_p/C_v = \gamma = 5/3$ for simplicity. We defined the third moment of velocity in (2.A-5). In the case of the Maxwell distribution, the velocity distribution function is shifted by the mean flow velocity **u** and spreads with the width T of the temperature.

It is clear that (2.A-4) corresponds to the fact that the average kinetic energy per particle is 3/2 T. Maxwell distribution function is isotropic around $\mathbf{v} = \mathbf{u}$, and the heat flux $\mathbf{q} = 0$. This means if we can derive such moment equations for the unknown variables n, **u**, T, it is closed coupled equations and be principally possible to be solved. These equations are the basic equations for fluids.

There is no guarantee, however, that the plasma is collisionless and the velocity distribution function is close to the Maxwell distribution. The plasma distribution function may be determined by its production process, interaction with the confining wall, and so on. However, it is empirically proofed that in many cases the distribution can be approximated with the shifted Maxwell distribution. Although there is no theoretical validity to approximate plasmas as fluids, the fluid model is widely used instead of Vlasov kinetic model for more simplicity in mathematical treatment. If the deviation from Maxwellian is small enough, the heat flux **q**, viscosity etc. can be approximated proportional to the gradients of fluid quantities. The electron heat flux given in (2.A-5) will be derived later in Chap. 6.

Let's derive mathematically the equation of continuity and the equation of motion by taking the velocity moments of the Vlasov equation. First, the zeroth order moment is obtained by integrating (2.A-1) directly by **v.** The integral of the first term and the second term of Vlasov equation are simple. Although it seems that the integral value remains in the third term because of the force of $\boldsymbol{v} \times \boldsymbol{B}$, the actual integration disappears because v_i is not included in the i-component of $\boldsymbol{v} \times \boldsymbol{B}$ in actual calculation. Therefore, it reduces to

$$\frac{\partial n}{\partial t} + \nabla(n\boldsymbol{u}) \quad = \quad 0 \tag{2.A-6}$$

Next, integrate by multiplying (2.A-1) by the vector **v**. Calculate the i (= x, y, or z) component. The first term is simple. The following **v'** which is the velocity spread from the mean velocity **u** is defined for integrating the second term as (2.A-4).

$$v = u + v^{'} \qquad (2.\text{A-7})$$

The product with **v** is the vector and its i component of the second term of (2.A-1) is

$$\frac{\partial}{\partial x_j}\left(\int v_i v_j f d\boldsymbol{v}\right) = \frac{\partial}{\partial x_j}\left(nu_i u_j\right) + \frac{\partial}{\partial x_j}\left(\int v_i' v_j' f d\boldsymbol{v}\right) \qquad (2.\text{A-8})$$

Note that when a subscript that indicates a coordinate appears twice, such as j, it means to take the sum of the three components x, y, and z with respect to j. Such notation is called **Einstein notation**. The pressure is generated on the second term on the RHS of (2.A-8). Since the Maxwell distribution is isotropic in the velocity space around the mean velocity **u**, the second term in (2.A-8) reduces to

$$\int v_i' v_j' f d\boldsymbol{v} = nT\delta_{ij} \qquad (2.\text{A-9})$$

Here, δ_{ij} is the Kronecker delta, $\delta_{ij} = 1$ for i = j, and $\delta_{ij} = 0$ for otherwise. When the distribution function is isotropic, the pressure is a scalar. In general, the pressure is tensor unless the distribution function is isotropic.

The calculation of the force term of Vlasov equation is not so simple. Calculate the x component and calculate the y and z components in the same way. Multiply the third term of Vlasov equation by v_x and integrating it in v_x, v_y, and v_z space, the following is obtained.

$$\iiint dv_x dv_y dv_z v_x \frac{F_j}{m} \frac{\partial f}{\partial v_j} = \iint \frac{F_x}{m} dv_y dv_z \int v_x \frac{\partial f}{\partial v_x} dv_x \qquad (2.\text{A-10})$$

Here, we can put F_x out of the integral over v_x in (2.A-10). This is possible because Lorentz force of $\mathbf{F} = q\,(\mathbf{E} + \mathbf{v} \times \mathbf{B})$, **E** does not depend on v_x and the x component of $\mathbf{v} \times \mathbf{B}$ does not depend on v_x. Carrying out the same mathematics for y and z components, it is clear the same logics works. The integral with respect to v_x in (2.A-10) is executed by using partial integral. With integration over v_y and v_z. Then, the x component of the velocity moments of the third term of Vlasov Eq. (2.A-1) is obtained. By performing the same calculation for v_y and v_z as well, we obtain all three components.

From the above mathematics, the flowing equation of motion is obtained.

$$m\left(\frac{\partial}{\partial t} + \boldsymbol{u} \cdot \nabla\right)\boldsymbol{u} = -\frac{1}{n}\nabla P + q(\boldsymbol{E} + \boldsymbol{u} \times \boldsymbol{B}) \qquad (2.\text{A-11})$$

Here, P is pressure, $P = nT$.

The second moment of velocity gives an equation for temperature T, but let's omit the derivation in the text. In the phenomenon that thermal conduction is important and it can be assumed that the temperature T is a constant, the fluid equation is closed only by (2.A-6) and (2.A-11).

The fluid approximation of plasma is the same as neutral fluid equations except for the force by the electromagnetic field Therefore, knowledge of fluid dynamics is fundamental for studying various phenomena of plasmas. In some cases, the plasma may be regarded as a neutral fluid and analysis becomes simpler.

Since the same procedure from Vlasov equation to fluid model is applicable to electron and ion distribution functions. Through such procedure, the basic equations for two fluid model can be obtained following the mathematics shown above.

Finally, it is noted that

1. Plasma phenomena of electron and ion particles can be well studied with two fluid model for electrons and ions by coupling with Maxwell equations. This is correct only when each particle is in thermodynamic equilibrium with Maxwell velocity distribution function.
2. The fluid model cannot provide the phenomenon of Landau damping. In **Landau damping**, only a small number of particles satisfying the resonant condition interact with electrostatic or electromagnetic waves. This is important physics appearing in plasmas. In addition, if the velocity distribution function is very far from a shifted-Maxwellian distribution in collisionless condition, a variety of new phenomena unpredicted with the fluid model appear in plasma as will be shown in Volume 4.

References

1. H. Takabe, *The physics of laser plasmas and applications—Volume 1* (Springer, 2020) Chapter 2
2. D.S. Montgomery et al., Design considerations for indirectly driven double shell capsules. Phys. Plasmas **25**, 092706 (2018)
3. C. Shen, et al. Acoustic metacages for sound shielding with steady air flow. J. Appl. Phys. 123.12 (2018): 124501.
4. H. Schlichting, K. Gersten, *Boundary-Layer Theory*, 9th edn. (Springer, 2017)
5. Y. B. Zel'dovich, Y. P. Raiser, *Physics of Shock Waves and High-Temperature Hydrodynamic Phenomena"*, Vols. 1 & 2 (Academic Press, New York, 1966 and 1967), Chap. 10.
6. S. I. Braginskii, *Transport Process in a Plasma*, in *Review of Plasma Physics*, Ed by M. A. Leontovich (Consultants Bureau, 1965), Vol. 1; E. M. Epperlein M. G. Hains, *Transport in laser-produced plasmas*, Phys. Fluids 29, 1029 (1988): Blancard, Christophe, Jean Clérouin, and Gérald Faussurier. Electron-ion temperature relaxation in hydrogen plasmas. High Energ. Dens. Phys. 9.2 (2013): 247–250.
7. M.Y. Jaffrin, R.F. Probstein, Structure of a plasma shock wave. Phys. Fluids **7**, 2.964 (1658)
8. H. Takabe and Y. Kuramitsu, "Recent progress of laboratory astrophysics with intense lasers," High Power Laser Sci. Eng. 9, E49 (2021)
9. M. Kulsrud, et al., The protogalactic origin for cosmic magnetic fields, Astro. Phys. J., 480: 481 (1997).; Shukla, Nitin, et al. "Interplay between the Weibel instability and the Biermann battery in realistic laser-solid interactions." Phys. Rev Res 2.2 (2020): 023129.

10. P. T. Campbell, et al. "Magnetic signatures of radiation-driven double ablation fronts." Phys. Rev. Lett. 125.14 (2020): 145001.
11. C.A.J. Palmer et al., Field reconstruction from proton radiography of intense laser driven magnetic reconnection. Phys. Plasmas **26**(8), 083109 (2019)
12. https://nso.edu/for-public/sun-science/coronal-loops/
13. S.A. Slutz et al., Pulsed-power-driven cylindrical liner implosions of laser preheated fuel magnetized with an axial field. Phys. Plasmas **17**, 056303 (2010)
14. J.R. Davies et al., Laser-driven magnetized liner inertial fusion. Phys. Plasmas **24**, 062701 (2017)
15. M.G. Haines, Heat flux effects in Ohm's law. Plasma Physics Control. Fusion **28**, 1705 (1986) A. Nishiguchi, T. Yabe, and M. G. Haines, *Nernst effect in laser-produced plasmas*, Phys. Fluids 28, 3683 (1985)
16. S. A. Balbus, J. F. Hawley. A powerful local shear instability in weakly magnetized disks. I-Linear analysis. II-Nonlinear evolution. Astrophys J 376 (1991): 214–233.
17. A. Mishra, G. Mamatsashvili, F. Stefani, Nonlinear evolution of magnetorotational instability in a magnetized Taylor-Couette flow: Scaling properties and relation to upcoming DRESDYN-MRI experiment. Phys. Rev. Fluids **8**(8), 083902 (2023)
18. S. Shinohara, *High-Density Helicon Plasma Science: From Basics to Applications* (Springer Nature, 2023)
19. M.D. Rosen et al., Exploding-foil technique for achieving a soft x-ray laser. Phys. Rev. Lett. **54**(2), 106 (1985)
20. B. Ripin et al., *Physics of Laser-Produced Interstreaming Plasmas in Laser Interaction and Related Plasma Phenomena Vol 7* (Plenum Press, New York, 1986)
21. E. Petroff, J.W.T. Hessels, D.R. Lorimer, Fast radio bursts. Astron. Astrophys. Rev. **27**, 1–75 (2019).; Petroff, E., J. W. T. Hessels, and D. R. Lorimer. "Fast radio bursts at the dawn of the 2020s." *The Astronomy and Astrophysics Review* 30.1 (2022): 2
22. S. Chatterjee et al., A direct localization of a fast radio burst and its host. Nature **541**(7635), 58–61 (2017)
23. F.F. Chen, *Introduction to Plasma Physics* (Springer Science & Business Media, 2012)
24. K. Ferrière, J.L. West, T.R. Jaffe, The correct sense of Faraday rotation. Mon. Not. R. Astron. Soc. **507**(4), 4968–4982 (2021)
25. J.A. Stamper, Review on spontaneous magnetic fields in laser-produced plasmas: phenomena and measurements. Laser Part Beams **9**(4), 841–862 (1991)
26. https://www.wikiwand.com/en/Synchrotron_radiation
27. E.M. Reynoso, J.P. Hughes, D.A. Moffett, On the radio polarization signature of efficient and inefficient particle acceleration in supernova remnant SN 1006. Astron J **145**(4), 104 (2013)

Chapter 3
Shock Waves and Ablation Dynamics

Abstract When an intense laser is irradiated on a solid target, the laser energy is absorbed on the surface so that the material becomes plasma to expand into the vacuum region. Through the laser-plasma interaction, the laser energy heats the expanding region spreading by its sound velocity. As the result the expanding region has the temperature ~ 1 keV and the pressure reaches 100 Mbar (10TPa). Since the laser is absorbed near relatively high density ($\sim$cut-off density), the plasma can be assumed to be in LTE and hydrodynamic description is acceptable.

The surface pressure called ablation pressure drives strong shock waves in the solid material as if the solid is almost gas. The shock wave physics is briefly reviewed to use the Rankin-Hugoniot (RH) relation, although detail studied is needed for the equation of state of the compressed matter. By use of the ablation pressure, it is possible to accelerate a thin material to higher velocity like a rocket propulsion.

One dimensional hydrodynamics is reviewed for steady state and time dependent dynamics within the ideal fluid assumption. Deflagration and detonation waves are also explained as jump condition with energy deposition. The laser implosion dynamics is compered between stationary solutions, computational results, and the experimental data. The importance of validation of simulation codes is discussed.

3.1   Introduction

Intense lasers have been used to generate high pressure (~ 10–100 Mbar) and high material ablation velocity (~ 100–$10,000$ km/s) from solid target surface. With such parameters, even any solid materials are easily compressed by a shock wave generated on the surface by abrupt energy deposition and/or heating by laser energy absorption as seen in Volume 1. The Coulomb mean free path of hydrogen plasma is about 1 μm for 1 keV at the cut-off density of laser with its wavelength 0.35 μm, which is the third harmonics of glass laser and widely used to study energetic phenomena driven by intense lasers.

Therefore, it is acceptable to model the dynamical phenomena driven by laser heating with hydrodynamic model explained in Chap. 2. For detail or precise study of the plasma, atomic process explained in this book becomes important, while the theoretical study is in general carried out with help of computer simulations. Study here the basic principle of laser-driven plasmas, which can be studied without details of transport physics given later in this book.

In the present chapter, let us study a variety of analytical solutions of hydrodynamic phenomena generated in laser-produced plasmas. Here, we assume the laser produced plasma is governed by the classical one-fluid and one-temperature equations given in. In some case, we decouple the energy equation by assuming a constant temperature, adiabatic, given pressure, and so on. In some case, the heat conduction in the energy equation plays important role.

It is usually in these days that one can easily run an integrated hydrodynamic simulation code for laser plasma to compare the result to corresponding experimental result and others. In analyzing the experimental data directly or with help of such simulations, it is difficult to understand the plasma physically without the knowledge of plasma hydrodynamics. At first, one has to have enough knowledge about one-dimensional hydrodynamics of compressible fluid plasma. As good text books, the author recommend Refs [1, 2] for further study of the physics of compressible fluid dynamics.

Relating to the laser-plasma hydrodynamic phenomena, we can enumerate several analytical solutions found in a long history of hydrodynamics. In addition, we have to know some special solutions found in the history of laser plasma study. All of the solutions to be explained here are idealized one-dimensional solutions by assuming jump condition, stationary state, and self-similarity. The basic fluid equations are partial differential ones, but algebraic relations are obtained in the jump case such as a shock jump. In the stationary or self-similarity case, one can reduces the fluid equations to ordinary differential equations. Then, it is possible to solve analytically or numerically under one-dimensionally symmetric space. By combining these solutions, we can imagine the physics happening in the experiment or multi-dimensional simulation code. This is the reason why we have to study one-dimensional hydrodynamics of compressible fluid at first.

As we see here, a jump condition of fluid provides the relation between upstream and down-stream in a shock wave. If the energy is generated at the jump surface by a chemical reaction, the shock wave may change to a detonation wave, and the rarefactive jump is also physically possible foe entropy increase by chemical reaction . This is called deflagration wave (flame of candle, for example). The deflagration by laser heating maintains the ablated plasma expansion to the vacuum. The laser energy is absorbed at relatively lower density than the solid, and the electron and/or radiation energy transfer keep the solid surface ablation as schematically shown in Fig. 3.1.

Then, the pressure of the ablation, ablation pressure, is extremely high to keep the shock wave propagating in the solid or keep accelerating the finite thickness target. This is called "ablative acceleration". The shocked material is accelerated by rocket propulsion mechanism toward target center for a spherical fusion capsule. We can

Fig. 3.1 Schematics of time evolution of solid matter density and temperature. (**a**) before laser irradiation. (**b**) the laser energy is absorbed on the solid surface. The heat wave penetrates into the solid surface without hydrodynamic motion. (**c**) Rapid increase of the pressure in the surface area drives a shock wave going inside and expanding wave to the vacuum region
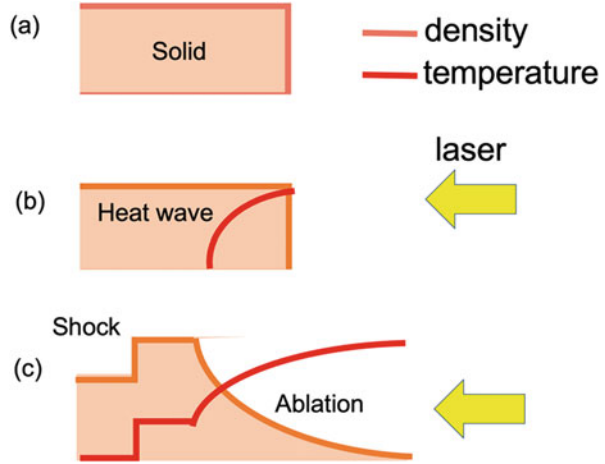
find a stationary solution of ablation structure to know its profiles as see later. This can be used to study the detail of the stability as will be shown in Vol. 3.

Finally, one-dimensional compressible hydrodynamics is also studied to know the Laval nozzle. The principle of jet engine is mentioned to relate the physics of ablation acceleration of nuclear fusion targets by intense laser irradiation.

3.2 Nonlinear Waves and Shock Waves

In Chap. 2, the linear analysis of the sound wave has been discussed. How the physics will change if the amplitude of the sound wave is high and nonlinear term cannot be neglected. Let's consider a wave propagating to the right that satisfies the first term of (2.49) for simplicity. Such a wave propagating in only one direction is called a **simple wave**. Keeping the nonlinear convection term in (2.46) as in (2.24) and deriving a simple wave relation for velocity perturbation u_1, the following is obtained.

$$\frac{\partial}{\partial t}u_1 + (V_s + u_1)\frac{\partial}{\partial x}u_1 = 0 \tag{3.1}$$

A nonlinear term by the convection

$$u_1\frac{\partial u_1}{\partial x}$$

is added to the sound wave propagation equation. Consider to solve (3.1) under the initial condition at t = 0. Assume the initial wave velocity profile u_1 is as shown at the left edge in Fig. 3.2. The large part of u_1 propagates faster than the other part, and soon after the wave front becomes sharp to overlap at one point as shown with the
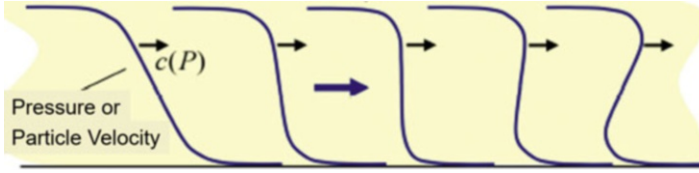
Fig. 3.2 Mathematical solution of nonlinear sinusoidal wave with viscosity

wave form at the center in Fig. 3.2, Mathematically, the wave solution becomes a multivalued function as shown on the right. Such multivalued functions are not allowed physically. Actually, (2.46) inherently ignores the physics that becomes important when the velocity profile becomes sharp. It is the viscosity due to collision between micro particles in the fluid and Coulomb collisions in plasmas.

With the effect of viscosity, (2.46) becomes the **Navier-Stokes equation** (2.55). Therefore, it is physically reasonable to add the viscosity term to (3.1). Then, the equation will be given. In the frame moving with the sound velocity, $x = V_s t$ is easily derived as

$$\frac{\partial}{\partial t} u_1 + u_1 \frac{\partial}{\partial x} u_1 = \mu \frac{\partial^2}{\partial x^2} u_1 \tag{3.2}$$

This equation is called the **Burgers equation.** It is known that (3.2) has a shock wave solution in stationary sate. Note that the shock wave travels with additional velocity depending on the strength of the shock.

The shock front has a narrow region where the flow velocity changes due to the balance between fluid nonlinearity and viscosity. When the wave front becomes steep with nonlinearity, the viscosity term adjusts the gradient. This can be seen from the fact that RHS of (3.2) is in the form of diffusion. In microscopic view, when the flow velocity becomes steeps, it shows that the kinetic energy of the flow velocity is converted to the thermal energy by the collision between the molecules. Therefore, the entropy increases at the wave front from the upstream and down-stream. This is called **shock wave heating**.

Although the Burgers equation is a nonlinear partial differential equation, it can be transformed to a linear equation by **Cole-Hopf transformation**. For this purpose, introduce new variable ϕ

$$u_1 = -2\mu \frac{1}{\phi} \frac{\partial \phi}{\partial x} \tag{3.3}$$

Inserting (3.3) into (3.2), the following new equation to ϕ is obtained.

$$\frac{\partial}{\partial x}\left(\frac{1}{\phi} \frac{\partial \phi}{\partial t}\right) = \mu \frac{\partial}{\partial x}\left(\frac{1}{\phi} \frac{\partial^2 \phi}{\partial x^2}\right) \tag{3.4}$$

Integrating (3.4) with x, a linear equation to the new variable ϕ is obtained

$$\frac{\partial \phi}{\partial t} = \mu \frac{\partial^2 \phi}{\partial x^2} + f(t)\phi \qquad (3.5)$$

Here, $f(t)$ is an arbitrary function of time, and it is possible to set $f(t) = 0$. Then, the Eq. (3.5) becomes the following diffusion equation.

$$\frac{\partial \phi}{\partial t} = \mu \frac{\partial^2 \phi}{\partial x^2} \qquad (3.6)$$

Since the RHS in (3.2) is small at the beginning (the initial condition in Fig. 3.2), the two terms on the LHS in (3.2) balance. As the slope of the wave front increases, the first term on LHS and RHS become balanced in (3.2). Since this is a diffusion equation, the amplitude of ϕ finally becomes small and it becomes flat and finishes Note that if the initial condistion is not sinusoidal but like $u_1(0,x) = -\tanh(x/L)$ with a large value of L, one can see the time evolution of $u_1(t,x)$ to form a stationally shock wave, where the thickness of the shock front is deteremined as stationary solution of (3.2).

3.3   Shock Wave Jump Relation

In order to obtain more realistic relation to the shock waves it is required to solve the fluid equations in (20, 21, and 22) consistently. If there are no external force and no external energy source, it is possible to obtain the jump relation between the upstream and down-stream of the shock wave front. It is required to solve the fluid equation in the frame moving with the shock front. In this frame, the stationary state of a shock propagation can be assumed. To solve the jump relation or continuity relation in the shock frame is found to be mathematical relation between the given upstream condition and the solved downstream condition for a given strength of the shock wave. Such algebraic equations giving the jump relation is called **Ranking-Hugoniot relation.**

In many cases, it is possible to neglect the structure of the shock front being of order of mean-free-path. However, its structure becomes important in high-temperature plasma, since the Coulomb mean free path is proportional to the square of the temperature. In the plasma described with two-temperature model as shown in Chap. 2, it is known that the electron heat conduction and temperature relaxation make the shock structure about one hundred times wider than the length of Coulomb collision mean free path [1, 3]. When the length of such structure becomes the size of the fluid system, we have to consider the kinetic effect and solve Fokker-Planck equation to the plasma shock structure. It is also shown that the concentration of multi-species ion plasma is modified by the force of electric field produced by the abrupt change of pressure.

3.3.1 Rnaking-Hugoniot Relation

The Burgers Eq. (3.2) giving the solution of the shock wave is an equation special-ized for a simple wave. Let's find the relation of the shock wave exactly from the neutral fluid equations. Ignoring the wave front of the shock wave, that is, the region where the nonlinearity and the viscosity are balanced (narrow range of about the mean free path), the basic equations for the one-dimensional plane flow are derived from (2.23), (2.24), and (2.25) by neglecting external force and heating. The viscosity and conductivity are also neglected, since the physical quantities are constant in both sides of the shock front. These three equations can be rewritten as conservative equations as follows.

$$\frac{\partial}{\partial t}\rho + \frac{\partial}{\partial x}(\rho u) = 0 \tag{3.7}$$

$$\frac{\partial}{\partial t}(\rho u) + \frac{\partial}{\partial x}(\rho u^2 + P) = 0 \tag{3.8}$$

$$\frac{\partial}{\partial t}\left(\varepsilon + \frac{1}{2}\rho u^2\right) + \frac{\partial}{\partial x}\left[\left(\varepsilon + P + \frac{1}{2}\rho u^2\right)u\right] = 0 \tag{3.9}$$

Equation (3.8) is obtained by multiplying (3.7) by u and adding it to (2.24). Equation (3.9) can be derived by multiplying (3.7) by $1/2u^2$, adding it to (3.8) multiplied by u, and adding it to (2.25).

Let's consider a shock wave propagating to the left according to the custom. The Eqs. (3.7, 3.8, and 3.9) remain the same even in the system moving with the shock wave front, but the flow velocity becomes the velocity seen in the moving frame. Assume that the fluid is stationary and no time variation. In Fig. 3.3, the flow, and the change of variables across the shock front are schematically shown. The flowing fluid passes through the shock front and the deceleration of flow by the pressure accompanies the compression of flow. Since the viscosity and conduction are given by the spatial differentiation of the physical quantity, the spatially integrated relation of (3.7, 3.8, and 3.9) is sufficient for the jump relation of the shock wave.
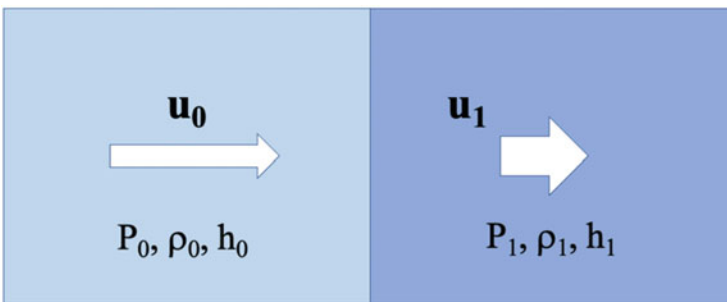
Fig. 3.3 Physical quantities in the upstream and downstream of a shock front

Ignore the time derivative and require the conservation from the upstream (subscript 0 to the physical quantities) to the downstream (subscript 1 to the physical quantities). Spatial integration of (3.7, 3.8, and 3.9) gives the following relations.

$$\rho_0 u_0 = \rho_1 u_1 \tag{3.10}$$

$$\rho_0 u_0^2 + P_0 = \rho_1 u_1^2 + P_1 \tag{3.11}$$

$$\left(\varepsilon_0 + P_0 + \frac{1}{2}\rho_0 u_0^2\right)u_0 = \left(\varepsilon_1 + P_1 + \frac{1}{2}\rho_1 u_1^2\right)u_1 \tag{3.12}$$

These relations should be transformed into more easily understandable relations. It is natural to assume that the density ρ_0 and pressure P_0 of the front of the shock wave are given. Then, let the physical quantity that determines the strength of the shock wave be the pressure P_1 in the shocked region. As the equation of state, the ideal gas of (2.31) and (2.32) is assumed. Then, since (3.10, 3.11, and 3.12) has three unknowns and three relations, it can be solved. The relation of the pressure P_1 on the shocked region and the reciprocal (referred to as **specific volume**) of the density of the shocked region $V_1 = 1/\rho_1$ can be derived as follows.

$$\frac{P_1}{P_0} = \frac{(\gamma+1)V_0 - (\gamma-1)V_1}{(\gamma+1)V_1 - (\gamma-1)V_0} \tag{3.13}$$

This relation is referred to as **Rankin-Hugoniot (RH) relation**. The curve given by (3.13) is also called **Hugoniot curve** or **shock wave curve**. This relation is shown with the line "RH" in Fig. 3.4. for the case with $\gamma = 5/3$. The line with "P" is the **adiabatic curve** (also referred as **Poisson curve**) and shows the relation ($P \propto V^{-\gamma}$)

Fig. 3.4 The Ranking-Hugoniot (RH) relation for a shock wave and Poisson relation (P) giving the adiabatic change
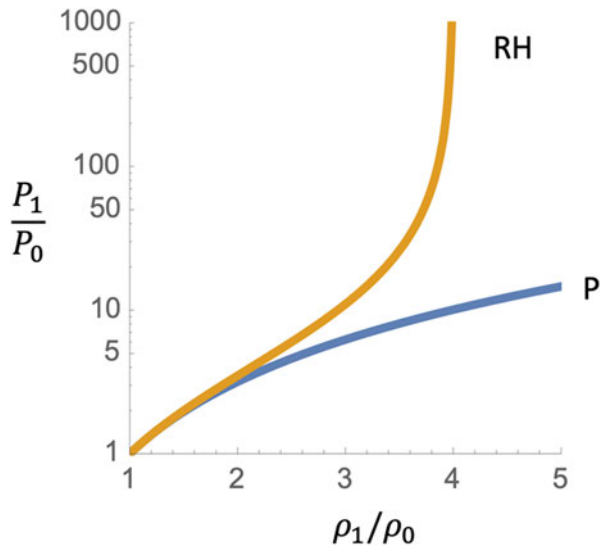
for constant entropy. It is noted that the RH relation is along with the adiabatic curve for a weak shock and the entropy increases clearly near $\rho_1 \sim 2\rho_0$. This indicates that it is possible to compress fluid almost adiabatically by designing the compression with a series of shock wave production. This is called adiabatic compression by pressure tailoring.

First, let's explain the characteristics of the shock wave curve. At the limit of $P_1 \to \infty$, there is the limited value for V_1, and its value can be obtained from eq. (3.13) as follows.

$$V_1 = \frac{\gamma - 1}{\gamma + 1} V_0, \quad \rho_1 = \frac{\gamma + 1}{\gamma - 1} \rho_0 \tag{3.14}$$

In the case that the degree of freedom of the gas heated by the shock wave is N, from (2.33) the maximum compression rate is

$$\left. \frac{\rho_1}{\rho_0} \right|_{max} = N + 1 \tag{3.15}$$

For gases of monoatomic molecules moving three-dimensionally, the compression ratio is four times. The reason why the compression ratio increases as the degree of freedom increases is as follows. The shock wave is heated by converting kinetic energy to the internal energy.

How is the increase of the internal energy due to such energy conversion? For example, in diatomic molecule gas such as N_2 and O_2, the degree of freedom has three dimensions of translational motion and two dimensions of vibration and rotation of molecules, totaling 5 degrees of freedom. The five degree obtains energy, while only three degree of the translational motion contributes to the pressure. Therefore, even at the same speed, the temperature rise in the shocked region is only 3/5 times of the monoatomic molecule case. Since the pressure on the right side must support the ram pressure on the left side in (3.11), the density of the diatomic gas has to increase to maintain the pressure balance. This is also true when the ionization or phase transition happens at the shock front, the density jump depends on the details of equation of state.

The relation of the flow velocities is obtained from (3.10, 3.11, and 3.12) in the form.

$$u_0{}^2 = \frac{V_0}{2} [(\gamma - 1)P_0 + (\gamma + 1)P_1] \tag{3.16}$$

$$u_1{}^2 = \frac{V_0}{2} \frac{[(\gamma + 1)P_0 + (\gamma - 1)P_1]^2}{[(\gamma - 1)P_0 + (\gamma + 1)P_1]} \tag{3.17}$$

As clear from Fig. 3.4, the shock wave curve is above the adiabatic curve for $V_1 < V_0$, indicating that the entropy increases through the shock wave surface. Although $V_1 > V_0$ is mathematically possible, it is not physically permitted in the

normal ideal gas. This is because the entropy decreases across the discontinuous surface without any energy leakage from the shock front.

The dimensionless number characterizing the strength of the shock wave is the **Mach number**. The Mach number is the flow velocity divided by the sound velocity. In general, the Mach number M of a shock wave is defined as the value obtained by dividing the speed of the shock wave by the speed of sound ahead of the wave front.

$$M = \frac{u_0}{V_S}, \quad V_S = \sqrt{\gamma \frac{P_0}{\rho_0}} \tag{3.18}$$

The sound velocity given in (2.47) can be easily obtained in the ideal gas as above. Note that the Mach number M is always greater than unity.

When the temperature rises due to the shock wave is extremely high, for example, the molecular gas is dissociated and ionized to be in a plasma state as its atomic process will be explained in Chap. 5. This phenomenon is called **shock wave ionization**. Let's look for the relation when the molecule of the main constituent is completely ionized by the shock wave like air, diatomic molecules. Let γ_0 be the specific heat ratio of the molecular gas, and γ_1 be the specific heat ratio of the plasma of the shock wave backside ionized completely. In the extremely strong shock waves, we can ignore both the pressure and the internal energy in the shock wave front, so we can see that all γ in (3.13) is good for γ_1. The compression ratio is determined only by the specific heat ratio of the rear side. However, note that (3.12) does not include the energy needed for the dissociation and ionization is not considered. It should be modeled.

The above discussion is clear in comparing Hugoniot curve of (3.13) with $\gamma_1 = 5/3$ to the experimental result for the liquid hydrogen shown in Fig. 3.5 [4] In Fig. 3.5, the orange line is RH curve for $\gamma = 5/3$, while the marks with error bars are

Fig. 3.5 Shock Hugoniot data of liquid deuterium from an experiment and other experiments and theoretical curve. The orange curve is that from ideal RH relation. Reprint with permission from Ref. [4]. Copyright 1998 by American Physical Society
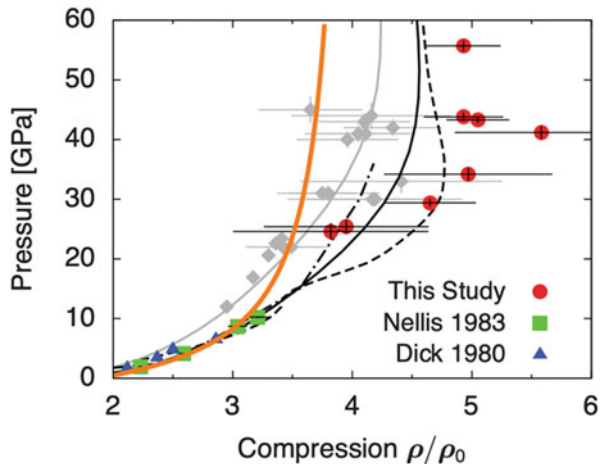
experimental data. The black lines are theoretical curves. It is suggested that the effective γ decreases around 30 GPa (0.3 Mbar), namely more freedom such as dissociation etc. increase the number of freedom N, [$\gamma = (N + 2)/N$].

3.3.2   Structure of Shock Waves

The jump relation by Ranking-Hugoniot tells us nothing about the transition region of two states. In the case of neutral fluid, it is determined as the diffusive structure by the viscosity in general. It is well-know that the physical quantities continuously vary from the front region to the shocked region with a typical with of the molecular mean-free-path, which is very thin in the air and gases on grand. Of course, it is different for a very strong shock wave generated by the space shuttle in the re-entry to the earth atmosphere. In such a case, the kinetic effect apart from the local Maxwellian assumption should be solved to determine the structure; namely, Boltzmann equation has to be solved to obtain the detail of the shock structure.

The structure of the shock wave in the jump region, call hereafter it the **shock front structure**, in fully ionized plasmas was studied [3]. The stationary shock solution is solved with two fluid equations in (2.111, 2.112, 2.113, and 2.114) by coupling with two temperature energy Eqs. (2.107) and (2.108). In order to solve the steady state fluid equations, it is studied to find the property of the singularities in (velocity, temperature) space. The integration starts from the **node point** of the upstream region to the **saddle point** of the downstream region [3]. Such integration is demanded, because the plasma shock wave at high Mach-number has wide range of parameters. They are Debye length, Coulomb collision mean-free-path, dominant electron heat wave structure, and slow temperature relaxation between electrons and ions.

The details of the shock front structures are given in [3] for a variety of Mach number. The shock wave picture is measured in an experiment with use of optical imaging of the shock in gas, where the shadow of the probe light shows the region where the refractive index changes abruptly in space such as shock front. The shadow image of a bullet in the air is shown in Fig. 3.6. The bullet is flying from left to right at supersonic speed in the air. A strong shock wave is generated in front of the bullet, and it is also seen a turbulent flow behind the bullet. Since the radius of the bullet is small, the shock front shows the structure of a bow, and such shock wave is called a **bow shock**.

Extremely high-pressure generated by intense lasers on a variety of solid materials allows us to study the shock waves in high-density matters. The progress of femto-second diagnostics by **X-FEL (X-ray Free Electron Laser)** made it possible to visualize the shock structure propagating in solid matters. Since the x-rays can propagate in matter whose density is higher than solid densities in general, it is possible to use the ultra-short pulse x-rays for the imaging diagnostics.

The temporal evolution of a shock wave in diamond is measured, yielding detailed information on shock dynamics, such as the shock velocity, the shock

Fig. 3.6 An optical shadow image of a bullet flying in the air with supersonic velocity. The shock wave is generated in front of the bullet as well as both sides. Such shockwave is called a bow shock
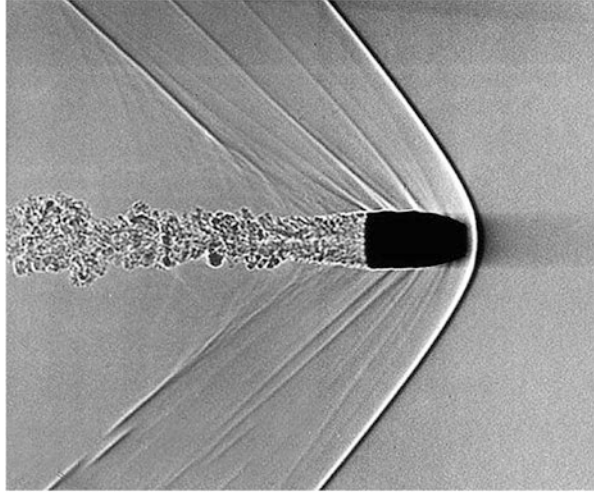
front width, and the local compression of the material [5]. It is reported that an intense laser with 150 ps pulse width and energy 130 mJ is focused on solid diamond at intensity of 10^{13} W/cm^2. The compression wave with density change of 10% (1.2 ns) and shock front width of 1 μm is observed as shown in Fig. 3.7. The XFEL pulse duration is 50 fs and the spatial resolution of the image is 0.5 μm. The progress of diagnostics has made it possible to study the shock wave, equation of state, and related physical properties in high-density plasmas.

It is shown for example at p. 474 in Ref. [1] that the thickness of the shock front obtained by solving equation with the viscosity is given in the form.

$$\delta \sim l_0 \frac{M}{M^2 - 1} \tag{3.19}$$

where l_0 is the mean free path in the upstream region and M is the Mach number of the shock wave. Note that the collision cross-section σ is constant in the mean-free path proportional $1/n\sigma$.

To study the detail of the shock wave structure in high-density not only in single solid but also mixture material such as DT (deuterium-tritium), plastic CH (carbon-hydrogen), and so on, the fluid model is not appropriate, and the kinetic equation should be solved. The first trial to apply suck kinetic model to obtain the shock structure has been done by Mott-Smith as indicated at page. 476 in Ref. [1], where the structure is solved by assuming a linear combination of bi-Maxwellian of those in both constant regions. As more advance theoretical study, **Fokker-Planck code** is used to study not only the structure, but also the change of concentration due to local electric field in the shock front layer [6].

In the Fokker-Planck simulation in [6], the electrons are solved with fluid assumption, while the ions are solved with Fokker-Planck equations with Coulomb
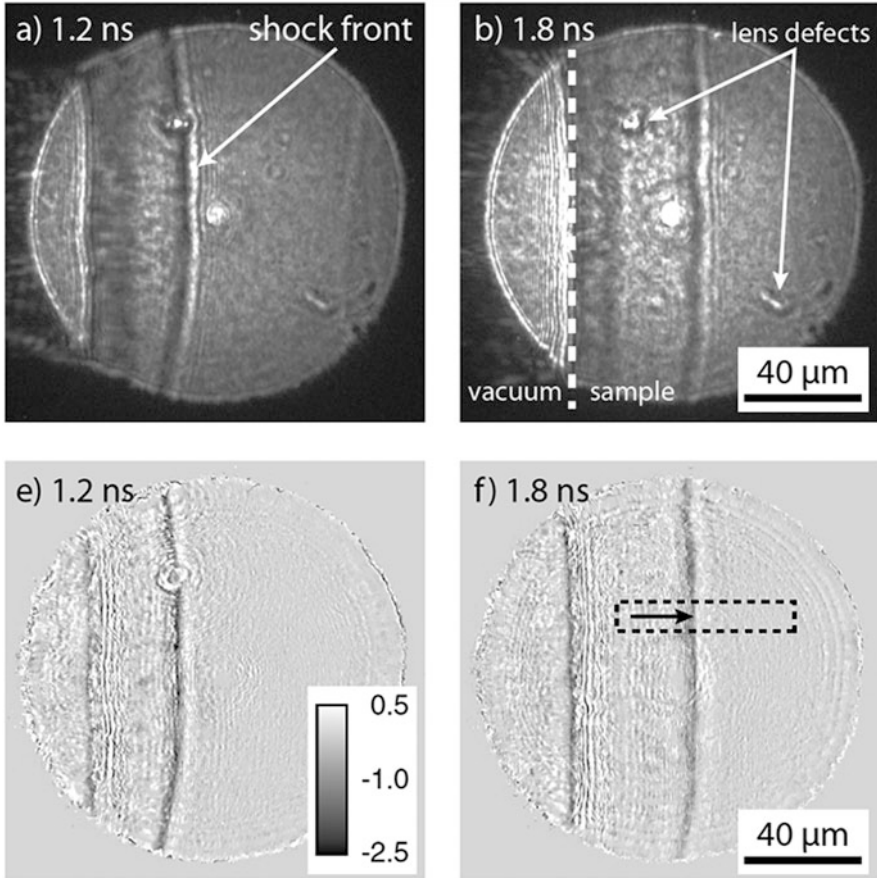
Fig. 3.7 X-ray shadow images of a shock wave propagating in a diamond at 1.2 and 1.8 ns. The shock wave is generated by an intense laser. The two images below are the corresponding images after eliminating the back ground from the above two images. Reprinted by permission from Macmillan Publisher Ltd: Ref. [5], copyright 1993

collisions between ions themselves and with electrons. In the collisional shock wave, the ion kinetic energy is converted to the thermal energy only via ion-ion collisional process and the ion viscosity determined the structure of ion density and temperature near the shock front. This thickness of the density variation of the ions at a shock front is roughly given as (3.19), although the mean-free-path of plasma strongly depends on the temperature.

As shown in Chap. 2.2, ion and electron mean-free paths are the same except Z and m_i dependence, while the diffusion coefficient is proportional to the product of the mean-free-path and the thermal velocity. Therefore, the electrons diffuse about $\sqrt{m_i/m_e}$ times wider than the ion-mean-free path. The electrons are heated via temperature relaxation after the abrupt heating of ions by viscosity; however, it is
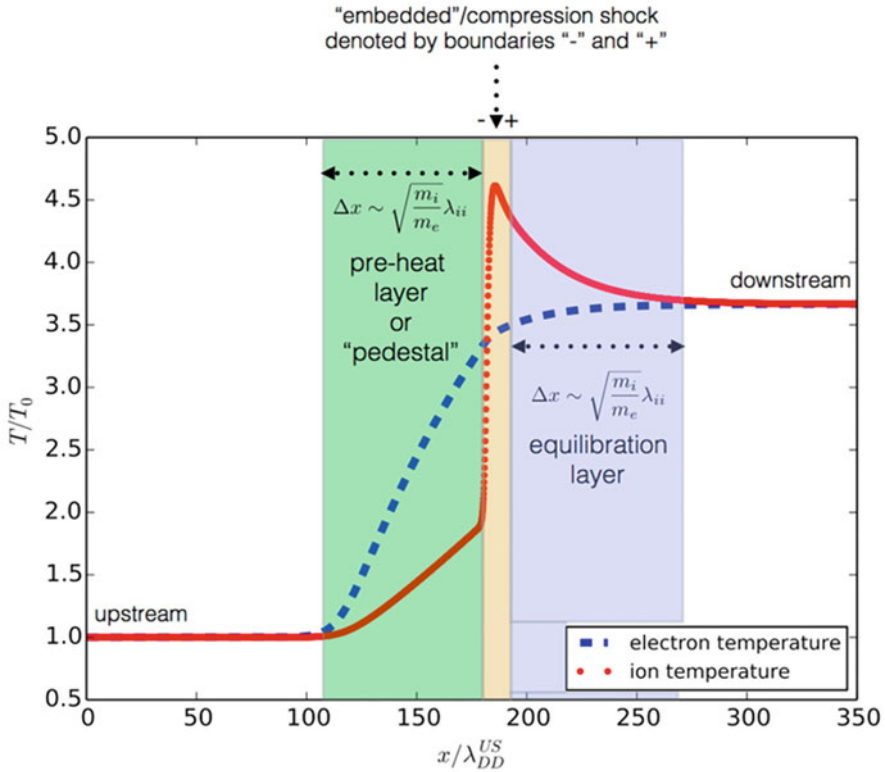
Fig. 3.8 Shock wave structure obtained by solving Fokker-Planck equations to multi-ion components with Coulomb collision effect. The electrons are assumed to be fluid. The red is the ion temperature profile and the blue is electron temperature one. Reprint with permission from Ref. [6]. Copyright 1998 by American Physical Society

slow process. As the result, a strong plasma shock structure is given like as shown in Fig. 3.8 [6]. It consists of very sharp ion temperature and density jump with the thickness of the ion mean free path, and electron heat wave tongue in front of the ion jump and the temperature relaxation region behind the ion jump.

In the Fokker-Planck calculation of Fig. 3.8, it is also found that strong electrostatic field is generated to cause nonuniform concentration of D and T ions in space [6]. The electric field is produced due to density and temperature gradients in the shock front. Since the electron inertial is much smaller than the ions, it is possible to neglect the electron inertial term in (2.114) to obtain the relation.

$$eE + \frac{1}{n_e} \frac{\partial}{\partial x}(n_e T_e) = 0 \tag{3.20}$$

At the shock front the density and temperature of electrons increases abruptly and a strong electric field is generated from high to low pressure direction. Note that the almost charge neutrality is kept between electron and ion fluids and the change separation appears over the distance of Debye length characterized by the higher temperature. It is concluded that due to the difference of the Z/m_i in (2.112) for not hydrogen, but the mixture of deuterium and tritium, the component with larger Z/m_i (D^+) shifts in the front region from the shocked region by the strong electric field, causing the change of concentration of multi-component ion plasma. This effect cannot be neglected in the fusion reaction of DT mixture fuel.

It is noted that we have assumed the simple equation of state even for dense plasmas so far. As will be discussed in Chap. 9, the **equation of state (EOS)** of matters near and over the solid density is not ideal (not simple), and EOS including many body interaction such as strongly coupling should be studied. In higher density and relatively lower temperature, the quantum effects also play important role in the thermodynamic properties. In some case, the phase transition occurs by a shock wave. In the phase transition, the latent or dissolved heat appear as energy release or absorption modifying the Ranking-Hugoniot relation.

3.4 Deflagration and Detonation Waves

3.4.1 Jump Relation with Energy Source

As described above, the discontinuous wave fronts where the density decreases from the upstream to the downstream cannot exist physically as long as the basic equations, (3.7), (3.8), and (3.9). This is because the entropy decreases from the upstream to the downstream of the jump. However, for example, if any chemical combustion or nuclear burning occur on the wave front, to increase the entropy at the jump layer, a solution of decreasing density is physically permitted. Such jump waves are called **deflagration wave**. In our surroundings, a good example is **combustion waves.**

When energy is generated in the wave front, the energy W generated per unit time and unit area appears in LHS of (3.12). Then, the relation (3.13) is modified as.

$$\frac{P_1}{P_0} = \frac{(\gamma + 1) - (\gamma - 1)V_1/V_0 + 2W/(J_0 V_0)}{(\gamma + 1)V_1/V_0 - (\gamma - 1)} \tag{3.21}$$

Here, $J_0 = n_0 u_0$ is the fluid particle flux. For a given value W, the relation (3.21) is plotted in the (P, V) plane with thick solid line in Fig. 3.9. Note that there is no physical region between the points A and B because the value $J_0^2 < 0$. For reference, the adiabatic curve with the entropy $S = S_0$ (constant) of the upstream region is also plotted as "P" (Poisson curve), the curve of S_0.

Fig. 3.9 The deflagration and detonation curve from the upstream (V_0, P_0) to the downstream
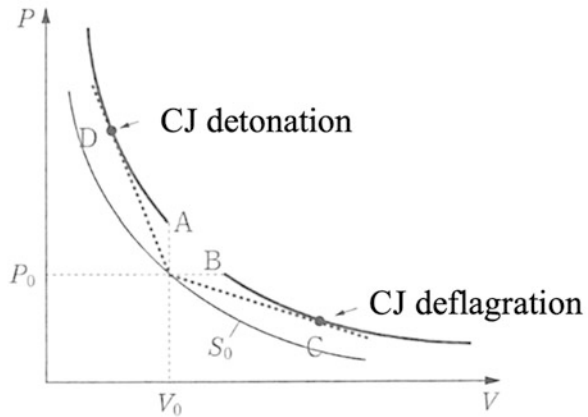
The physically meaningful solution is limited to the solution that transitions from the upstream (V_0, P_0) to the right point C, or the solution that to the left point D. The jump that transitions from the upstream to the right C is called **deflagration wave**. Since the propagation speed of the deflagration wave is slower than the sound speed in the upstream, a shock wave is generated in the upstream region by the pressure generation due to the energy release by combustion. On the other hand, the transition to compressible region D is called **detonation wave**.

3.4.2   Deflagration Waves

The basic structure of deflagration wave is shown in Fig. 3.10. The essential property of the deflagration is the same as those by chemical reaction, nuclear reaction, and laser heating in the critical region. The chemical and nuclear reaction rates are proportional to the higher power of the temperature; therefor, rapid heating happens when the temperature reaches the reaction temperature. Then, energy is generated in relatively narrow region as shown in Fig. 3.10. The same structure is also seen in the combustion waves in the jet and rocket engines. Energy is locally released in the region "b" in Fig. 3.10, and its energy is transported to the left conduction zone "a" by heat conduction. This is the basic structure of the deflagration waves and the heated gas by the reaction in the zone b tends to expand to relatively low-density region in the space or into the vacuum. The reaction of the exhaust of the expanding gas produces high pressure to generate shock waves toward left or sequential pulses of sound wave to accelerate the left region, for example, rocket propulsion.

As can be seen in Fig. 3.9, the pressure hardly changes and the density drops due to the temperature distribution controlled by heat conduction. However, since heat conduction is not so high in a chemical reaction, the thermal conduction region "a" is not so wide and it looks as a sharp surface. The dimensionless quantity $Z = a/b$ is

Fig. 3.10 Schematic of the deflagration wave. Chemical reaction takes place as "H" and thermal conduction penetrates temperature as "T". The fuel density drops as "C"

C: Fuel concentration
T: Temperature
H: Heating rate
a: Conduction zone
b: Reaction zone
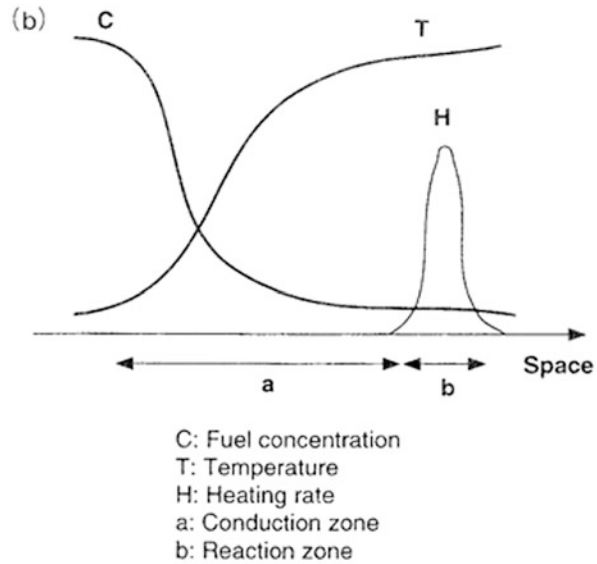
called the **Zel'dovich numbe**r. As shown below the thickness of the conduction zone "a" is relatively thin compraed to the size of the system.

It is well know that the deflagration wave driven by the internal reaction is unstable to the rippling of the burning front [2]. Therefore, it cannot remain as one-dimensional combustion wave for a long time and the burning front easily becomes unstable to increase the reaction front surface. The increase of the surface leads the increase of the enegy production rate to strength the shock wave in the front and finally the deflagration changes to the detonation to be described below. This explanation seems contradict against the stable frame of candle. The density of the wax from the solid to after-burn decreases along the flow. Thanks to the gravitation force, the candle can keep such a stable flame.

The deflagration wave produced by heating with laser has also the same structure. The heating region concentrates on the cutoff density of the laser, and the absorbed energy is transported to the left side by nonlinear electronic heat conduction, almost the same as Fig. 3.10. In Fig. 3.11, a snap shot of laser-deflagration is shown with 1-D hydro-simulation, when a thin flat plastic plate is irradiated with intense laser. This is obtained with the single-fluid, two-temperature fluid Eqs. (2.105, 2.106, 2.107, and 2.108).

The density is the highest in the wave front of thermal conduction (**ablation surface**). This is because the target is accelerating to the left by the **ablation pressure**, and the effective gravity (inertial force) is to the right direction. Due to the nonlinearity of the electron heat conduction, the ablating plasma rapidly expands. Since only the electrons are heated by laser, the electron temperature reaches 3 keV, but ions are heated up to about the half of the electron fluid by the temperature

Fig. 3.11 A deflagration structure, called as ablation structure in general, calculated by one-dimensional implosion code showing compressed shell and heat conduction region
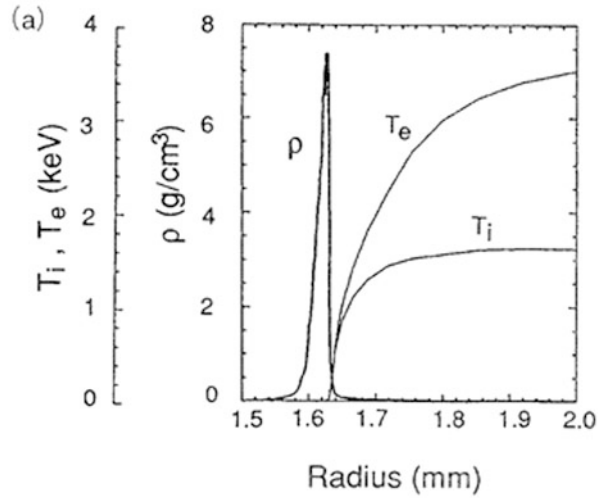
Fig. 3.12 A candle is a typical example of the deflagration wave

relaxation process. This wave front instability is very important for stable acceleration of the targets, and will be discussed in Volume 3.

The flame of candle in Fig. 3.12 is a slowly combusting wave in 3-D. It is famous Michael Faraday's "**The Chemical History of a Candle**" [7]. He mentioned in 1850 as follows.

There is not a law under which any part of this universe is governed which does not come into play and is touched upon in these phenomena. There is no better, there is no more open door by which you can enter into the study of natural philosophy than by considering the physical phenomena of a candle.

Deflagration wave is important to know the mechanism of ablation pressure sustained by laser absorption in the expanding plasma. It is useful hear remind the science of a candle. Consider the mechanism that keeps a candle burning. Solid wax is heated by its own flame, melts and rises with decrease of the density by buoyancy (In Fig. 3.10, from solid wax of "C" to the zone "a"). When evaporated wax reaches the temperature of reaction (region "b"), it starts chemical reaction and fire appears. That reaction heat is what maintains the light as a flame.

The density of the wax expands from solid to vapor, and then expands further as it becomes even hotter as a result of the chemical reaction. We can regard the solid wax is the upstream state, and the flame heated by the chemical reaction corresponds to the downstream state. The zone "a" is the conduction zone, while it is assumed a jump from up- to down-stream. When we consider a flame that continues to burn in one dimension, it satisfies the discontinuity condition for the deflagration wave as shown below.

It is better to point out essential difference of deflagration waves between the chemical reaction and laser ablation surface. The combustion front of chemical reaction is unstable to two/three-dimensional deformation of the front, because the energy release rate increases as the area of the surface increases by the deformation. The energy release is due to the reaction of the fluid itself. On the other hand, in the laser heating deflagration, the energy input rate is not affected by the deformation of the ablation surface, and no instability is induced. In the case of ablation front, the instability is due to the inertial force. This is called Rayleigh-Taylor instability as will be study in Volume 3.

3.4.3 Detonation Waves

On the other hand, the wave that transitions to the left "D" in Fig. 3.9 is supersonic to the upstream fluid. Such a burning wave is an explosive combustion and it is called a **detonation wave**. Detonation waves are often seen in movies such as explosives. Since the temperature increased by the shock wave compression is higher than the ignition temperature of the explosive, the chemical reaction is taken place on the shock wave front and the energy is explosively released. This is an explosion phenomenon. The engine of the car uses the explosion pressure to run the car. The gasoline and air are injected to mix for chemical reaction into the piston, and the ignition is sputtered by a spark plug. Then, a detonation wave is generated from that point, and high pressure is generated. This pressure pushes down the cylinder and converts its work into kinetic energy of mechanical rotation of car wheels.

A schematic of the pressure and temperature profile of the detonation wave in a tube is shown in Fig. 3.13 [8]. The shock wave heats and compress the front to reach the ignition temperature of the fuel-air mixed gas (or unreacted explosive). Then, the chemical reaction heats the reaction zone to keep the shock propagation. The maximum temperature point in Fig. 3.13 corresponds to the point "D" in Fig. 3.9. Behind the reaction zone, low density expansion zone follows to continue the burned gas zone, which works strong pressure to the left wall.
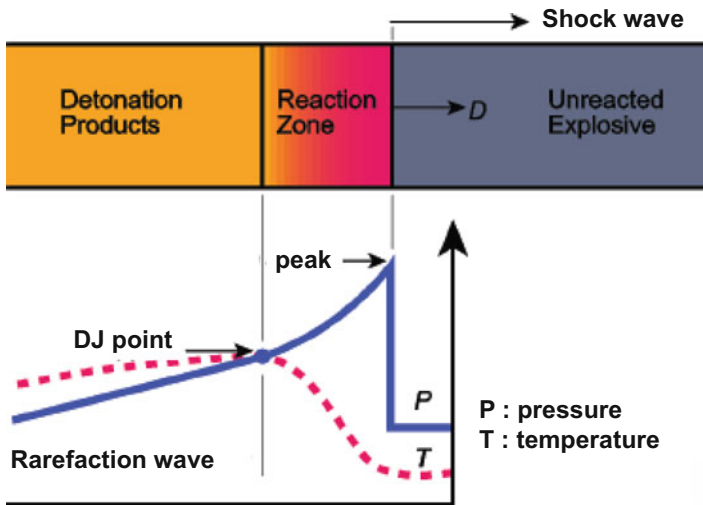
Fig. 3.13 A schematic of the pressure and temperature profiles of a detonation wave in a tube [8]. (Courtesy of Dr. Minchinton)

It is well known that as mentioned above, the deflagration front of chemical reaction is hydrodynamically unstable. It is called **Landau-Darrius instability** and the deflagration front distorts to have fractal structure. Then, as the front surface (area in 3-D) increases, the energy generation rate due to the chemical reaction increases. Since the deflagration is subsonic and the strong sound wave or shock wave is formed in front of the deflagration wave. As the result, the increase of reaction energy enhances the strength of the shock. At the stage when the temperature becomes high enough to ignite the fuel, the deflagration wave transits to the detonation wave. This is called **deflagration-detonation transition (DDT)**.

In Fig. 3.14, the temperature and pressure evolution around the time of DDT is shown from 2-D computer simulation of chemically-reacting gas [9]. In this case the deflagration wave is deformed by the boundary protruding at the center in the figure, it is seen that a reflected shock with higher pressure and temperature is generated at $t = 10.48$ ms. This reflected stronger shock wave locally ignites the fuel to change the burning to the detonation. The burning speed after this time increases dramatically and the temperature and pressure increased globally after DDT occurs.

3.4.4 Supernova Ia DDT

The physics of **supernova type Ia** explosion observed in space is thought to be a carbon nuclear burning type explosion, in which a **white dwarf (WD)** explodes by nuclear burning [10]. A white dwarf, the mother body of type Ia supernova
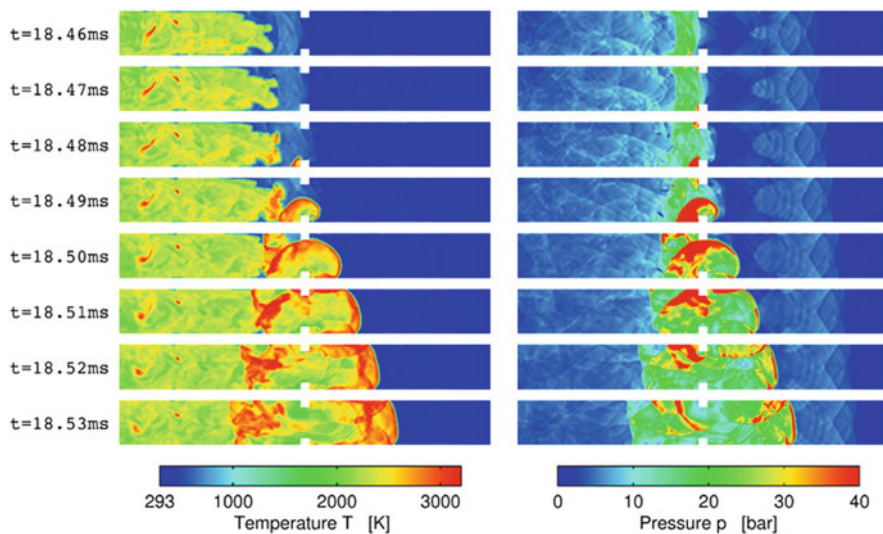
Fig. 3.14 The time evolution of temperature and pressure showing the deflagration to ignite to change to a detonation by edge reflected shock heating [9]. From Journal of Combustion

explosion, is one of a binary system with a companion star, usually a main sequence star. The mass of the white dwarf is increases in time by peeling mass from the surface of the companion star with strong gravity. Before its mass reaches the critical mass of **Chandrasekhar limit** (approximately 1.4 times the solar mass), the gravity of WD is sustained by the Fermi pressure of the non-relativistic electrons.

However, the mass approaches the critical mass, the Fermi energy of the electrons near the center of WD becomes more than mc^2. The density dependence of the pressure shifts from the non-relativistic case of $\rho^{5/3}$ to the relativistic one of $\rho^{4/3}$, namely Fermi pressure becomes relatively soft. Then, the white dwarf cannot withstand further mass increase. As the result, the center of the white dwarf collapses to be higher temperature and higher density to ignite the nuclear fusion of carbon burning.

Since the mass of the white dwarf at the time of explosion is determined by the Chandrasekhar mass, it can be considered that the explosion energy is almost constant for Type Ia supernovae. Since the explosion itself becomes brighter than a galaxy typically consisting of 100 billions of starts, it becomes a standard light source from a far distant Universe. Observation data have impacted the argument of cosmology such as whether the universe is open or closed. At the present time, it is concluded from the observation of type Ia supernovae that the universe is further accelerating with increase of the expansion velocity. This fact concluded the universe is expanded by the **dark energy**, consisting of 70% of the energy in Universe.

A simple physical scenario of type Ia supernova explosion is as follows. The main components of white dwarfs before explosion are carbon and oxygen. If the
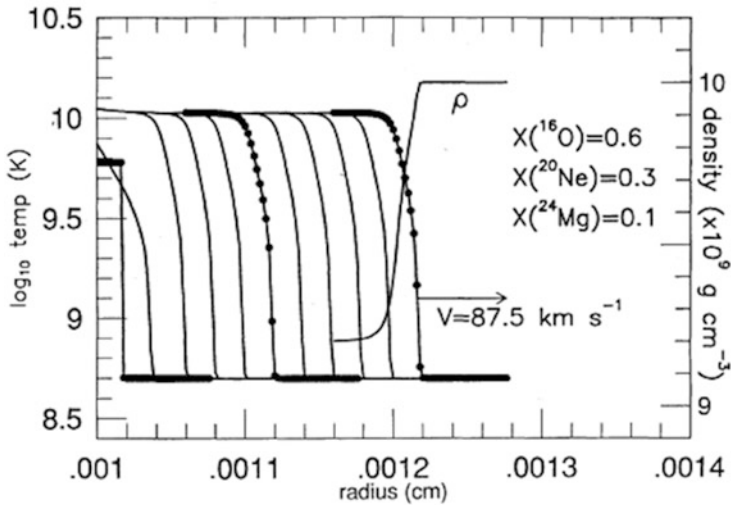
Fig. 3.15 One-dimensional thermonuclear deflagration wave propagating near the center of a white dwarf characterized with extremely high-density and electron Fermi pressure. Reprinted with permission from Ref. [11]. Copyright by American Astronomical Society

temperature near the center exceeds several hundred keV, nuclear fusion reaction of carbon and oxygen occurs. However, the pressure rises caused by the nuclear reaction is still smaller than the degenerate pressure of the electrons, so the deflagration front does not explosively spread, propagating as a weak combustion wave. In Fig. 3.15, the one-dimensional simulation is shown for the propagation of the nuclear burning wave in the density 10^{10} g/cm^3 [11]. It is surprising to know that the thickness of the wave is extremely small compared to the size of the white dwarf of thousands of kilometers.

If the wave front remains spherically symmetric, the stars will expand due to shock waves ahead of the deflagration wave, nuclear combustion will be terminated by this expansion. The nuclear deflagration front is hydrodynamically unstable same as chemical reaction, the deflagration front grows as fractal structure. As a result, the area of the deflagration front becomes many times larger than $4\pi R^2$, where R is the average radius of the deflagration front. Then, the nuclear reaction energy released in unit time increases in proportion to the increase in area of the front, the shock wave is intensified.

When the temperature rise due to this shock wave exceeds the temperature at which the nuclear reaction takes place as shown in Fig. 3.13, the nuclear reaction transits to the detonation wave. Such a combustion scenario is called a delayed detonation model in astrophysics. Among the heavy elements in the universe, it is believed that the iron is mainly nuclear synthesized by type Ia supernovae. In the above scenario, unstable nuclear nickel 56 is produced by carbon and oxygen nuclear fusion and ^{56}Ni nuclear decays eventually to the iron in the universe.

3.5 Rarefaction Waves

A shock wave is generated by pushing its boundary by a piston. On the other hand, we have no stationary solution of the case when the piston moves to the opposite direction. If the piston disappears abruptly, the fluid expands into the vacuum with its sound velocity. As it is already mentioned, the rarefactive shock wave is not physically acceptable and it is required to find time-dependent solution of such expanding wave. Such solution is called **rarefaction wave.** It is well known that it is given by a self-similar solution. Here we consider two cases; one is adiabatic rarefaction wave and the other is rarefaction wave that expands isothermally due to overwhelming heat conduction. For the sake of simplicity, we assume that the fluid is initially located in the vacuum at t = 0.

Without viscosity and external force and assuming one-dimensional plane geometry, (2.23) and (2.24) can be written as follows.

$$\frac{\partial \rho}{\partial t} + \rho \frac{\partial u}{\partial x} + u \frac{\partial \rho}{\partial x} = 0 \tag{3.22}$$

$$\frac{\partial u}{\partial t} + u \frac{\partial u}{\partial x} + \frac{V_s^2}{\rho} \frac{\partial \rho}{\partial x} = 0 \tag{3.23}$$

We try to find **self-similar solution** and reduce (3.22) and (3.23) to coupled ordinary differential equations according to the method explained in Chap. 2. From the dimensional analysis of (3.22) and (3.23), it is found that there is only one dimensionless variable ξ defined to be

$$\xi = \frac{1}{c_0} \frac{x}{t} \tag{3.24}$$

Here c_0 is the sound velocity at t = 0 defined as

$$c_0 = \sqrt{\frac{\partial P}{\partial \rho}} \Bigg|_{\rho = \rho_0} \tag{3.25}$$

Here ρ_0 is the initial density.

Let us assume that the solution of (3.22) and (3.23) can be written in the forms

$$\rho = \rho_0 R(\xi), \quad u = c_0 U(\xi), \quad V_s = c_0 V(\xi) \tag{3.26}$$

Then, using relations

$$\frac{\partial \xi}{\partial t} = -\frac{\xi}{c_0 t}, \quad \frac{\partial \xi}{\partial x} = -\frac{1}{c_0 t} \tag{3.27}$$

Equations (3.22) and (3.23) can be transformed to the following coupled ordinary differential equations.

$$(U - \xi)R' + RU' = 0 \tag{3.28}$$

$$(U - \xi)U' + V^2 \frac{1}{R} R' = 0 \tag{3.29}$$

Here, the superscript $(')$ represents the ordinary differentiation by ξ. For (3.28) and (3.29) to have a non-trivial solution, the determinant which can be made with the coefficients of differentiated variables needs to be zero. From this condition, the following relations are obtained.

$$(U - \xi)^2 = V^2 \tag{3.30}$$

$$U = \xi \pm V \tag{3.31}$$

For the case where the fluid is only in the region of $0 < x$ initially, the expansion front called as a rarefaction wave propagates in the fluid. This solution corresponds to the plus sign of (3.31).

3.5.1 Adiabatic Rarefaction Wave

The fluid expands adiabatically into the vacuum. Under the adiabatic condition the following relationship is satisfied.

$$V = R^{\frac{(\gamma-1)}{2}} \tag{3.32}$$

With use of (3.31), (3.29) can be modified like

$$\frac{2}{\gamma - 1} \frac{d}{d\xi} \left\{ R^{(\gamma-1)/2} \right\} = \frac{dU}{d\xi} \tag{3.33}$$

Integrating this equation with the condition $U = 0$ at $R = 1$, the density profile is obtained.

$$R = \left\{ \frac{\gamma - 1}{2} \left(\frac{2}{\gamma - 1} - U \right) \right\}^{\frac{2}{(\gamma-1)}} \tag{3.34}$$

The condition $U = 0$ at $R = 1$ is the point which propagating to the minus x-direction with the sound velocity c_0 and this corresponds to the front of the rarefaction wave.

In the moving frame with the rarefaction front, we take the plus solution of (3.31)

$$U = \xi + V \tag{3.35}$$

Inserting (3.32) and (3.34 to 3.35), the flow velocity is obtained.

$$U = \frac{2}{\gamma + 1}(\xi + 1) \tag{3.36}$$

Since U = 0 at the rear of the rarefaction wave, the normalized coordinate ξ should be $\xi = -1$, namely it is also clear that at this point the following relation is also satisfied.

$$R(-1) = V(-1) = 1 \tag{3.37}$$

In the present case of adiabatic expansion, the rarefaction wave expands with a finite velocity into vacuum and the expansion velocity of this front u_f and its ξ value ξ_f are given by setting R = 0 in (3.34) as

$$u_f = \frac{2}{\gamma - 1}c_0 \tag{3.38}$$

$$\xi_f = \frac{\gamma + 1}{\gamma - 1} \tag{3.39}$$

This expansion front velocity can be explained physically as follows. The fluid flow is driven by enthalpy h. Namely, the enthalpy is converted to the kinetic energy of the flow:

$$h \rightarrow \frac{1}{2}u^2 \tag{3.40}$$

Inserting the initial value of the enthalpy gives

$$u_{max} = \frac{2}{\gamma - 1}c_0 \tag{3.41}$$

Such intuitive way gives the prediction of the solution (3.38).

Here we have solved mathematics for the rarefaction wave and the solution of (3.22) and (3.23) is given from (3.36) and (3.34) as

$$u(t,x) = \frac{2}{\gamma + 1}\left(\frac{x}{t} + c_0\right) \tag{3.42}$$

Fig. 3.16 A snap shot of density and velocity profiles of an adiabatic rarefaction wave
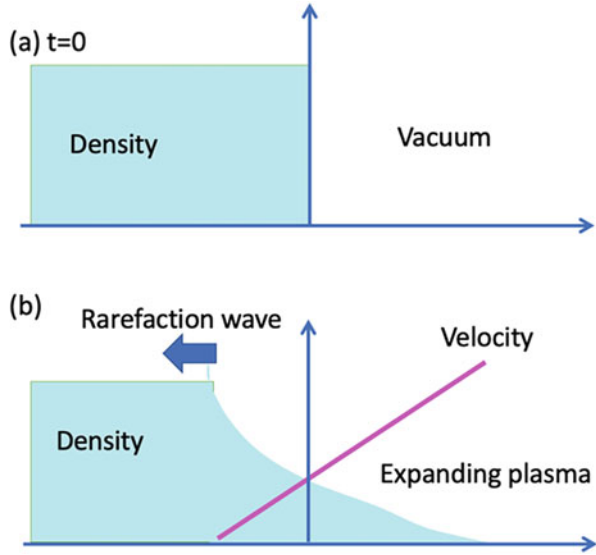
$$\rho(t,x) = \rho_0 \left\{ 1 - \frac{\gamma - 1}{\gamma + 1} \left(\frac{x}{c_0 t} + 1 \right) \right\}^{\frac{2}{(\gamma - 1)}} \tag{3.43}$$

It should be noted that the solutions are valid only for the region of the rarefaction wave defined by

$$-1 < \frac{x}{c_0 t} < \frac{\gamma + 1}{\gamma - 1} \tag{3.44}$$

The density and velocity profiles at a given time is plotted in Fig. 3.16.

3.5.2 Isothermal Rarefaction Wave

As the degree of freedom increases, the specific heat ratio γ approaches unity, and as apparent from (3.38), the rarefaction wave spreads to infinity. However, when expanding while heating from the outside and keeping the initial temperature, the above analytical solution cannot be applied. **Isothermal** is possible, for example, by irradiating a solid surface with a high intensity laser, bringing it to a high-pressure state, and when a rarefaction wave is generated in the direction of laser irradiation in the vacuum. Because the electron heat conduction is dominant in the rarefaction region, the rarefaction wave expands while the temperature is almost uniform. It is useful to find an analytical solution for such a rarefaction wave. In this case as well, a self-similar solution exists.

The basic equations are same as (3.22, 3.23, 3.24, 3.25, 3.26, and 3.27) except (3.26). Then, (3.26) should be modified like

$$\rho = \rho_0 R(\xi), \quad u = c_0 U(\xi), \quad V_s = c_0 : const. \tag{3.45}$$

Although it is impossible to use (3.32) and (3.33), (3.30) gives the flow velocity.

$$U = \xi + 1 \tag{3.46}$$

Then, (3.28) and (3.29) turn out the same equation as

$$U' + \frac{1}{R} R' = 0 \tag{3.47}$$

This equation can be solved easily to give

$$R = e^{-U} \tag{3.48}$$

This gives the density profile as

$$R = e^{-U} \quad \rightarrow \quad \rho = \rho_0 e^{-(\xi+1)} \tag{3.49}$$

This profiles are plotted in Fig. 3.16. The front of the rarefaction wave is $U = 0$ at $\xi = -1$.

In order to maintain such an isothermal rarefaction wave, it is necessary to constantly supply energy to the rarefaction wave from the outside. This is because the temperature does not change and the internal energy does not change, so it is necessary to constantly supply the increment of the kinetic energy obtained by the rarefaction wave as heat. Let's calculate the rate of energy increase per unit time. Assuming that the energy increase rate is given as an energy flux Q from the outside,

$$Q = \frac{d}{dt} \int_{-c_0}^{\infty} \left(\frac{1}{2} \rho u^2 + \frac{1}{\gamma - 1} P \right) dx \tag{3.50}$$

Inserting the solution above and change the integral with self-similar coordinate, (3.50) becomes

$$Q = \rho_0 c_0^2 \int_{-1}^{\infty} \left(\frac{1}{2} R U^2 + \frac{1}{\gamma - 1} R \right) d\xi \tag{3.51}$$

With the change of variable

$$y = \xi + 1 \tag{3.52}$$

(3.52) reduces to

$$Q = \rho_0 c_0{}^3 \int_0^{\infty} \left(\frac{1}{2} y^2 e^{-y} + \frac{1}{\gamma - 1} e^{-y} \right) dy \qquad (3.53)$$

The integration of (3.53) is done easily to obtain

$$Q = \frac{\gamma + 1}{\gamma - 1} \rho_0 c_0{}^3 \qquad (3.54)$$

Note that the coefficient of Q is 4 for $\gamma = 5/3$.

3.5.3   Shock Tube

Now, we knew that there is no jump solution with decreasing density along the flow, but the density decreases as the time-dependent rarefaction wave. The experiments of shock waves in gas have been carried out, for example, using the **shock tube** shown in Fig. 3.17. The cylindrical tube is divided into two parts by a thin film (diaphragm) and each pressure is set to a different pressure. When the thin film is burned out with a laser or the like, high-pressure gas expands to push the low-pressure part, and a shock wave is formed in the low-pressure part. However, in such experiments, only shock waves with a pressure jump of at most several atmospheres are possible to be generated. Therefore, a very strong shock wave was generated by high-explosives and so on. By using a high intensity laser to irradiate on gas or solid, it is now possible to generate high pressure more 10 times the **bulk modulus** B defined in (2.51). To study the high-pressure physics as to be discussed later, typically the diamond anvil cell for static high pressure or lasers are used to study the dynamical high-pressure property of solid material, such as internal state of the earth and planets.

3.6   Ablation Pressure and Ablative Acceleration

3.6.1   Ablation Structure

Instead of the energy production by chemical reactions, the energy increase by intense laser can also keep the deflagration wave. In the case of Chapman-Jouguet deflagration wave, the exhaust velocity is the sound velocity at the rear of the deflagration wave. In the chemical reactions, the reacted molecule gas may have the temperature of the molecular bonding energy, namely T ~ 0.1 eV. Since the intense-laser can deposit much large amount of energy in the deflagration region, we
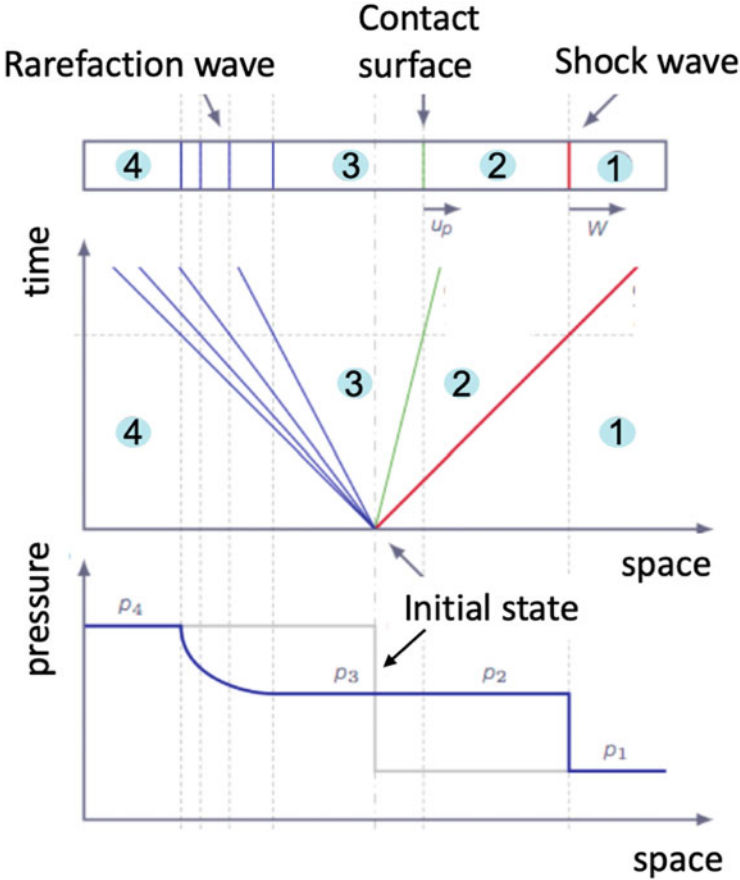
Fig. 3.17 A schematics of shock tube. Pressure is initially different in both gases. The boundary of the gases is opened to shock wave travel to the right and the rarefaction wave goes to the left. Their trajectories ate plotted in above with a snap shot on the top

can expect the temperature of more than 1 keV as seen below. Such high-temperature exhaust plasma can accelerate any matter to the velocity of sound speed, namely $v \sim 3 \times 10^7$ *cm/s* as we already saw in Fig. 3.18.

Consider a simple structure of the deflagration wave produced and maintained by constant heating of the ablating plasma by an intense laser. Assume that a stationary deflagration with a shock wave in the over-dense solid target and iso-thermal rarefaction wave into the vacuum region.

In Fig. 3.18a, the schematics of the trajectories of the shock front, deflagration zone, and the front of the rarefaction wave is plotted. The dashed line is a fluid particle trajectory from solid, shocked region, deflagration to the rarefaction wave. In the shocked region, fluids are accelerated to the left by the ablation pressure. The pressure generated by the deflagration is called **ablation pressure**.

Fig. 3.18 Schematics of a laser driven shock wave and ablation of a solid target. (**a**) The time evolution of shock and deflagration waves. (**b**) The snapshot of density, temperatures, and flow velocity at the time t_1. The broken curve in (a) represents a path of a fluid element
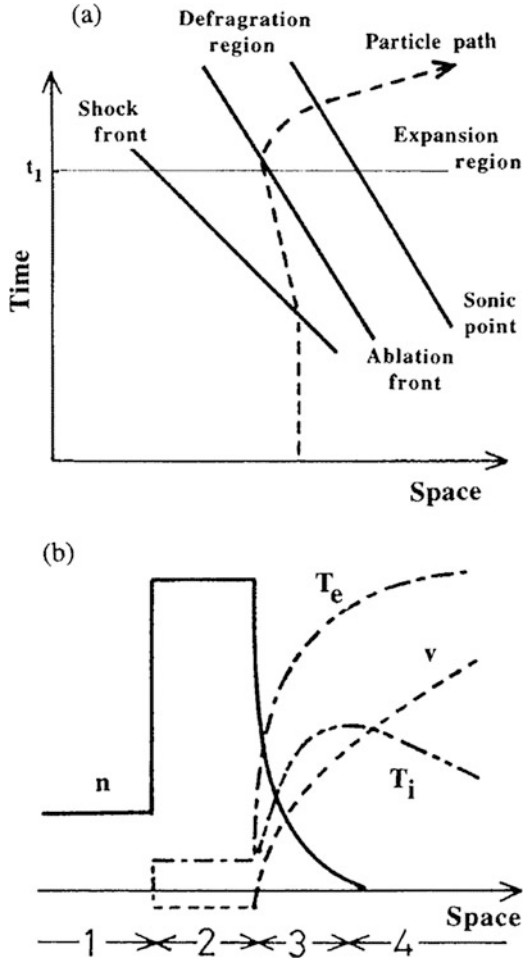
In Fig. 3.18b, the rough snap shot at $t = t_1$ is drawn. The density (n) increases by the shock compression in the Zone-2, dramatically decreases in the deflation zone-3, and exponentially decreases in the Zone-4. The temperature increases by shock heating in Zone-2, abruptly increases in Zone-3 by electron heat conduction, and keeps almost constant in the expansion Zone-4. In two-temperature model [12], the ion fluid is heated by Coulomb collision in the subsonic Zone-3, while to be cool down in the expansion Zone-4 as roughly indicated in Fig. 3.18b.

The jump condition of the shock wave, ablation front, and the expansion into the vacuum region are shown as (V, P) diagram in Fig. 3.19. Fluid particles are compressed and accelerated forward by the shock wave from the point 1 to 2 and encounter the ablation surface. Then, they are heated in the direction of vacuum and accelerated as shown from point 2 to 3. After the passage of the Chapman-Jouguet
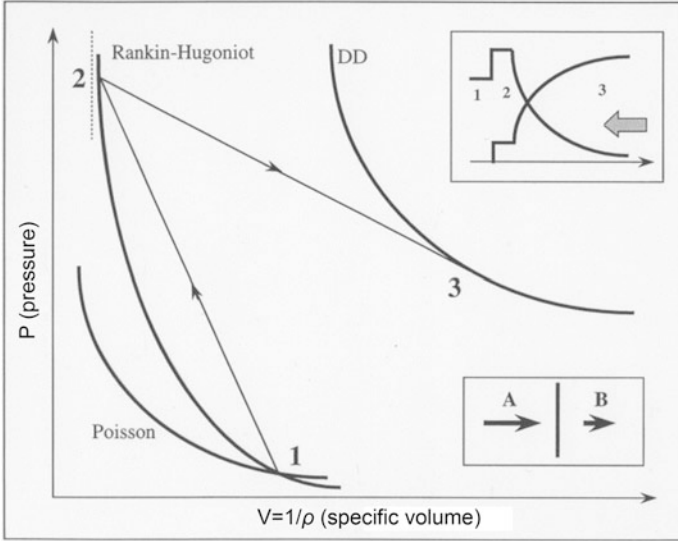
Fig. 3.19 The P-V diagram for the two jumps of the shock wave and the following deflagration wave driven by laser heating. The density and temperature profiles are schematically shown in the inlet figure

(CJ) deflagration point 3, the particles are exhausted as the rarefaction wave into the vacuum. This is the same mechanism as rocket exhaust. The difference is that the rocket fuel is a chemical reaction and can only produce exhaust speeds on the order of 10 km/s, but with laser ablation it can be more than 1000 km/s.

Let's calculate the laser heating energy needed to keep such almost stationary deflagration structure. The dominant energy is used to heat the exhausting plasma from the Chapman-Jouguet point and to heating the rarefaction wave expanding to the vacuum. The electron heat conduction penetrates in the deflagration structure and keeps the ablation of the dense material. Assuming the deflagration structure is stationary state, the inward heat flux is carried out as the ablation energy. We neglect the energy increase in the shocked region because it is a small fraction compared to the laser energy input. The energy flows out constantly into the rarefaction wave through the Chapman-Jouguet point.

3.6.2 Ablation Pressure

It is assumed that the rarefaction region has very good electron heat conduction and the temperature is constant in space. As derived in (3.54), energy flux required to maintain the isothermal rarefaction wave is evaluated to be,

$$\frac{dE_{abl}}{dt} \approx 4PC_s|_{CJ} \tag{3.55}$$

Here, the right side is evaluated with the values at the CJ point of the ablation structure. Requiring that the laser must supply this energy, the relationship between laser absorption intensity and ablation pressure can be obtained.

By balancing the energy of the absorbed laser with the energy of (3.55), the scaling law of the following ablation pressure P_{abl} can be obtained. We use the fact that the pressure on the ablation surface is almost twice the pressure at the CJ point [12]. It is also assumed that the laser (wavelength is λ *in μm* unit) is absorbed at the critical density point. Then, the ablation pressure P_{abl} is calculated to be.

$$P_{abl} \approx 12\left(\frac{I_{14}}{\lambda_{\mu m}}\right)^{2/3} \quad [Mbar] \tag{3.56}$$

Here, it is assumed that the CJ point of the ablation is the cut-off density point of the laser, and I_{14} is the absorbed laser intensity in the unit of 10^{14} *W/cm^2*. In early time of laser plasma experiment, the ablation pressure has been measured with foil targets as shown in Fig. 3.20 by four different laser wavelengths [13]. It is noted that shorter wavelength laser generates higher ablation pressure up to ~100 Mbar. The theoretical scaling law of (3.56) can well explain the experimental results.

By solving the stationary solution, the mass flow velocity J_0 flowing into the ablation region can also be obtained. It is called **mass ablation rate** $\dot{m}$ and given as

$$\dot{m} \approx 1.5 \times 10^5 \left(\frac{I_{14}}{(\lambda_{\mu m})^4}\right)^{1/3} \quad [g/(cm^2 s)] \tag{3.57}$$

In Fig. 3.21, the experimental data are plotted for the cases of three different wavelength lasers [14]. It is seen that the theoretical result can explain the experimental data. Note that the mass ablation rate is important value to estimating the ablative stabilization to reduce the hydrodynamic instability of implosion. So, shorter wavelength is better from this point. The ablative stabilization will be discussed in Volume 3.

3.6.3   Rocket Model

By using the relation of ablation pressure obtained above, we can derive an equation for acceleration of an object (thin foil) of finite mass by laser ablation pressure. This is called a "**rocket model**" and corresponds to a simple evaluation of rocket design. Now, when the thin foil is moving at the velocity V(t), the following relation is obtained with the mass of the accelerating part ahead of the ablation front as M (t).
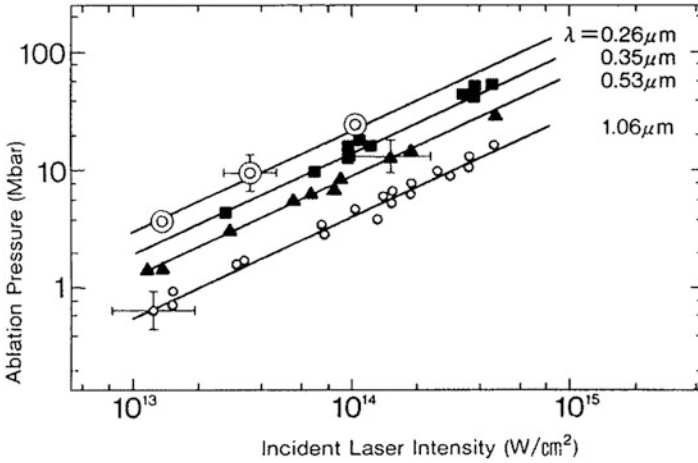
Fig. 3.20 Ablation pressure as functions of laser intensity and its wavelength. The data are obtained in early time of laser plasma research. Reprinted with permission from Ref. [13]. Copyright by Institute of Physics
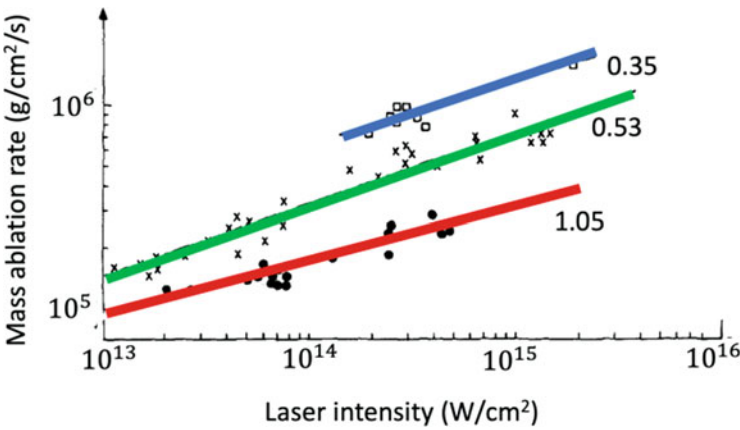
Fig. 3.21 Mass ablation frate at the ablation front as functions of laser intensity and laser wavelength. The data are obtained in early time of laser plasma research. Reprint from Ref. [14]. Copyright 2012, with permission from Elsevier

$$M\frac{dV}{dt} = P_{abl} \tag{3.58}$$

Since mass decreases with the rate given in (), the following is given

$$M(t) = M_0 - \dot{m}t \tag{3.59}$$

where M_0 is the initial mass. Assuming that $\dot{m}$ and P_{abl} are constant, the Eq. (3.58) can be integrated and the following relation is obtained.

$$V = V_0 \ln\left(\frac{1}{\varepsilon}\right)$$

$$\varepsilon = 1 - \frac{t}{\tau_0} \quad\left(= \frac{M(t)}{M_0}\right) \tag{3.60}$$

where

$$V_0 = P_{abl}/\dot{m} \approx 2C_s, \quad \tau_0 = M_0/\dot{m} \tag{3.61}$$

(3.60) show that the velocity is only a function of the remaining mass. V_0 is a value about two times the sound velocity at the CJ point, C_s. That is, the maximum speed is determined by how high the temperature can be achieved in the deflagration. Acceleration distance can be calculated,

$$d = d_0(1 - \varepsilon + \varepsilon \ln\varepsilon) \tag{3.62}$$

where

$$d_0 = V_0\tau_0 \tag{3.63}$$

As a result of acceleration, the fraction of the input energy to the kinetic energy is called **hydrodynamic efficiency** η_H.

$$\eta_H \equiv \frac{\frac{1}{2}MV^2}{E_{ab}} = \eta_0 \frac{\varepsilon(\ln\varepsilon)^2}{1 - \varepsilon} \tag{3.64}$$

With absorbed laser intensity I_{ab}, the non-dimensional coefficient η_0 is given to be

$$\eta_0 = \frac{(P_{abl})^2}{2\dot{m}I_{ab}} \tag{3.65}$$

Figure 3.22 shows the dependence of η_H/η_0 upon ε found in (3.65). The value of η_0 is 1/2 for the isothermal from CJ point to vacuum. Therefore, it can be $\eta_h = 0.3$ at maximum for $\varepsilon \approx 30$ %. Accordingly, if the thin foil is accelerated to ablate about 80%, the mass of the foil can be accelerated to about 1.6 times the sound velocity of the CJ point with an energy efficiency of 30 to 40%.

For example, even if the sound velocity at the C-J point is low, the rocket which fly to the space must escape from the earth's gravity and fly far. This is called the Earth escape velocity and its value is about 11.2 km/s (40,300 km/h). In the reaction of chemical fuel, the maximum sound velocity does not exceed this value. Therefore, by designing the final mass of the rocket is small, the escape speed can be achieved.

Fig. 3.22 Normalized
rocket kinetic energy
efficiency as a function of
the mass ablation fraction
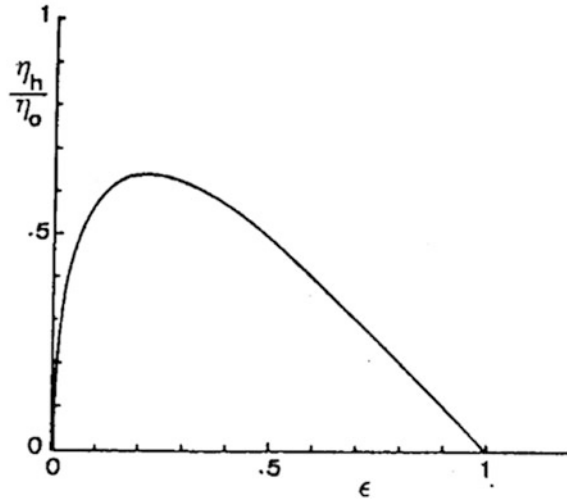
This corresponds to the fact that the spacecraft part flying into space is a very small
tip part compared to the main body at the time of launch.

3.7 Ablation Structure in Acceleration Phase

In the early stage of laser fusion experiments, so called **glass-micro-balloon (GMB)**
has been used as a spherical capsule to confine deuterium-tritium mixture fusion fuel
gas [15]. Even for a very thin shell glass, it is seen that the glass is ablated by the
laser heating explained in Chap. 2 (Vol. 1). The ablation pressure drives the shock
waves and acceleration of the glass plasma to further accelerating the fuel by the
shock waves. An example of one-dimensional simulation of the implosion dynamics
of such a GMB is shown in Fig. 3.23.

In the radius-time diagram, the lines are fluid Lagrange grids and totally,
160 grids are used. The line crossing the grids is the trajectory of the cut-off density.
The details of the parameters are given in Ref. [15]. A gaussian shape pulse is
irradiated with about 10 kJ energy of green lasers. The top on the right is the time
evolution of electron temperature and the bottom is the plasma density at 6 timings
shown with arrows on the right in the r-t diagram. The ablation pressure generates a
shock wave to accelerate the glass plasma and heat and compress the DT fuel
plasma. It is seen that almost stationary ablation structure is propagating to the
center of the target.
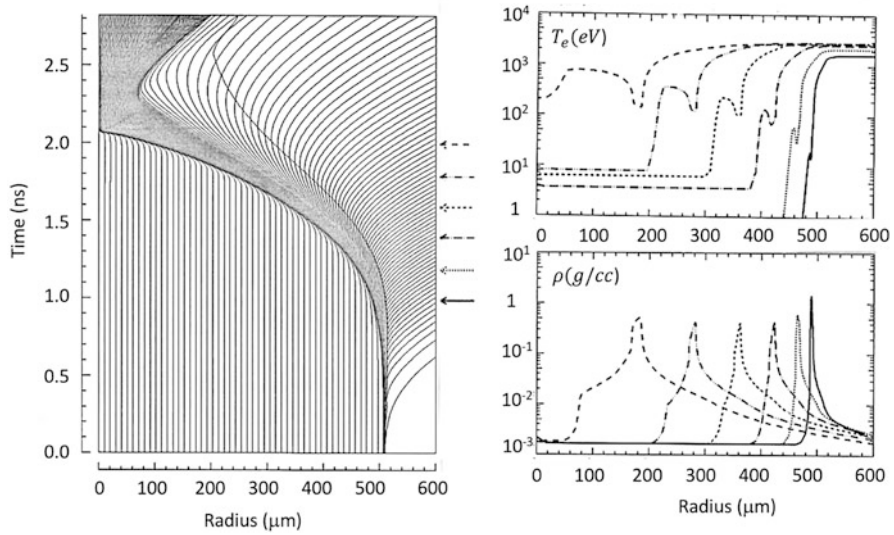
Fig. 3.23 The radius-time diagram of the Lagrange fluid trajectories obtained with one-dimensional implosion code. A thin shell glass micro-balloon filled with DT fuel is imploded by laser irradiation to generate fusion neutrons. The snap shots at six different time indicated the r-t diagram are plotted on the right for electron temperature and density

3.7.1   Stationary Accelerating Ablation Front

To precisely study the hydrodynamic stability of such ablation structure, stationary accelerating ablation structure has been used in spherical geometry as the back-ground implosion dynamics [16]. One-fluid one-temperature hydrodynamic equations in spherical geometry have been used including the nonlinear thermal conduction. When the equations are normalized by the physical quantities at the CJ point of the deflagration wave, the normalized equations governing the stationary solution are as follows [16].

$$\frac{\partial}{\partial \tilde{r}}\left(\tilde{r}^2 \tilde{\rho}_0 \tilde{u}_0\right) = 0 \tag{3.66}$$

$$\tilde{\rho}_0 \tilde{u}_0 \frac{\partial}{\partial \tilde{r}} \tilde{u}_0 = -\frac{\partial}{\partial \tilde{r}} \tilde{P}_0 + G\tilde{\rho}_0 \tag{3.67}$$

$$\frac{3}{2}\tilde{\rho}_0 \tilde{u}_0 \frac{\partial}{\partial \tilde{r}} \tilde{T}_0 = -\frac{\tilde{P}_0}{\tilde{r}^2}\frac{\partial}{\partial \tilde{r}}\left(\tilde{r}^2 \tilde{u}_0\right) + \frac{K_0}{\tilde{r}^2}\frac{\partial}{\partial \tilde{r}}\left(\tilde{r}^2 \tilde{T}_0^{5/2}\frac{\partial}{\partial \tilde{r}} \tilde{T}_0\right), \tag{3.68}$$

where G is the normalized gravity given by the inertial force. Here, $\tilde{\rho}_0, \tilde{u}_0, \tilde{T}_0$ are normalized density, flow velocity, and temperature, respectively, and they are functions only of normalized spatial coordinate $\tilde{r}$. Normalized physical quantities are defined as follows using the physical quantities at the CJ sonic point.

$$\tilde{\rho}_0 = \frac{\rho_0}{\rho_s}, \quad \tilde{u}_0 = \frac{u_0}{C_s}, \quad \tilde{T}_0 = \frac{T_0}{T_s}$$

$$\tilde{r} = r/r_s, \quad \tilde{t} = t/(r_s/C_s) \tag{3.69}$$

Here, $\tilde{\rho}_0, \tilde{u}_0, \tilde{T}_0$ are the unity at the sonic point of ablation. C_s is the sound velocity at the sonic point where $\tilde{u}_0 = u_0/C_s = 1$ is satisfied. Here, we also showed the normalized time to be used in the stability analysis in Vol. 3.

In normalizing as above, the following two dimensionless coefficients appeared.

$$G = \frac{g r_s}{C_s^2}, \quad K_0 = \frac{K(T = T_s)}{\rho_s C_s r_s A^{-1}} \tag{3.70}$$

Here, the numerator of the definition of K_0 is the thermal conduction coefficient at the sonic point, and A is the atomic number of the matter.

Equations (3.66, 3.67, and 3.68) are integrated numerically from the CJ sonic point toward the upstream side. For a given value of G, we obtain the following density ratio R_ρ by varying the value of K_0.

$$R_\rho = \frac{\rho_a}{\rho_s} = \frac{(density\ at\ ablation\ front)}{(density\ at\ sonic\ point)} \tag{3.71}$$

Regards this value as the eigenvalue of the integration, by changing the value of K_0.

The resultant density profiles are shown in Fig. 3.24 for the fixed density ratio $R_\rho = 50$ and five different G [16]. It seems that the ablation front is discontinuous; however, the profiles are all continuous. This is because the heat conduction
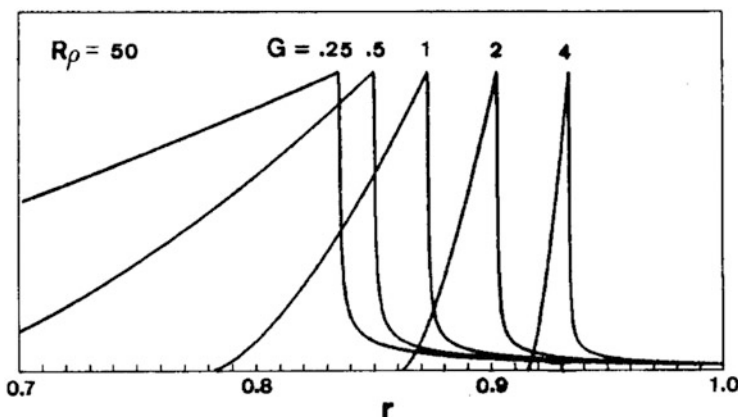

Fig. 3.24 Stationary solution of compressed shell and expanding ablation profiles driven by Spitzer's nonlinear heat conduction from the right boundary of the sonic point. Each profile is obtained for a fixed density ratio of 50 and different strength of the inertial force. Reprint with permission from Ref. [16]. Copyright 1998 by American Institute of Physics

coefficient is proportional to the 5/2-th power of the temperature, so it has a steep structure as shown in Fig. 2.8.

The density profile in the left of the ablation front decreases rapidly as G increases. The thin shell GMB, the density profile in Fig. 3.23 is like the case with large G. The spatial structure of the compressed region is like the Earth's atmosphere due to the gravity. In addition, when passing through that surface, the plasma is rapidly heated by the electron heat conduction, resulting in a dramatically varying structure. Namely, the density sharply decreases and temperature increases drastically. This is a typical profile of laser heating ablation. Note that the ablation profile is sensitive to the energy transport physics. As mentioned in Chap. 6 the profile changes for the case that the nonlocal electron transport and/or radiation one is dominant in the deflagration region.

3.8 Implosion Dynamics and Ablation Profiles in Experiments

3.8.1 Implosion Dynamics

The dynamics of implosion has been measured experimentally by the framing camera of the self-emitting x-ray as shown in Fig. 3.25. In the implosion experiment, a CH polymer polystyrene micro-balloon of radius 226 μm and the thickness 8 μm is irradiated with a squared laser pulse of 1.6 ns width with a picket fence of 0.2 ns and the main pulse of 1,6 ns 0.4 ns after the picket pulse. The laser wavelength is 0.53 μm. The time evolution of x-rat emitting mainly from the imploding high-density shell plasma and the heated fuel gas at the final compression time are measured as shown at the right in Fig. 3.25. The x-ray emission is also calculated for the corresponding implosion with one-dimensional hydrodynamic simulation code ILESTA-1D [15]. It was confirmed that the implosion dynamics agrees well, while the final strong x-ray emission by heated fuel plasma in the stagnation phase is not clearly observed in the experiment. This is due to the hydrodynamic instability in the final stagnation phase.

The implosion diagnostic image shown in Fig. 3.25 is rather old and the diagnostics of small scale and short time has progressed rapidly. More precision technique, for example, has demonstrated the measurement of self-emission x-ray shadowgraph, which provides a method to measure the ablation-front trajectory and low-mode nonuniformity of a target imploded by directly illuminating a fusion capsule with laser beams [17]. The technique uses time-resolved images of soft x-rays (>1 keV) emitted from the coronal plasma of the target imaged onto an x-ray framing camera to determine the position of the ablation front. This method has been used to accurately measure the ablation-front radius, image-to-image timing, and absolute timing. Angular averaging of the images provides an average radius measurement and an error in velocity of 3%. This technique
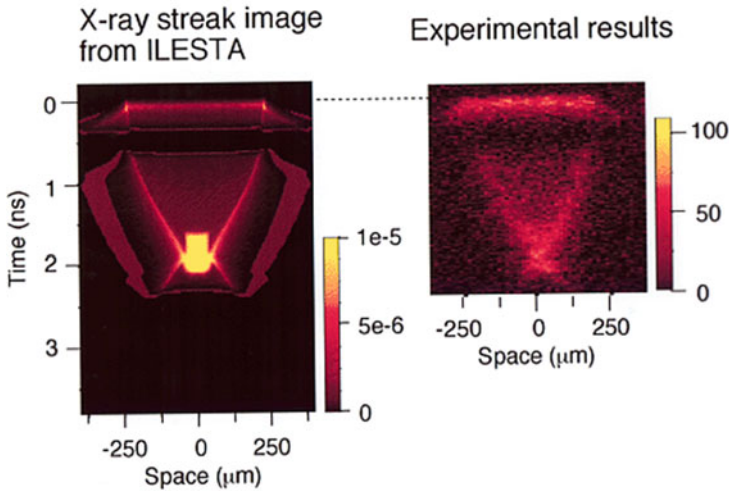
Fig. 3.25 Implosion dynamics of a spherical shell target with DD fuel. Both images show x-ray self-emission obtained with one-dimensional simulation and from the experiment in the same condition. The global image is same, while the final compression is very week in the experiment, suggesting hydrodynamic instability in the stagnation phase

has already been used as the diagnostics of implosion experiments at the Omega Laser Facility and the National Ignition Facility.

The experimental data can be used widely in the laser-produced plasmas to **verify and validate (V&V)** the physics-integrated simulation codes. The simulation code should be improved by checking its prediction via comparison with corresponding experiments.

In Fig. 3.26, the series of the x-ray self-emission images from an implosion experiment is shown at the top. Each image is time integrated over ~40 ps, and interstrip timing is ~250 ps. The clear green circles are the surface of ablation front. The implosion is done with 19.6 kJ laser of 60 beams OMEGA facility. The target has an 867.8 μm outer diameter with a 26.8 μm thick CH ablator covered by 0.1 μm of aluminum and filled with deuterium at 10.5 atm. The laser pulse shape is plotted in Fig. 3.26a with the solid line. It has one 100-ps picket pulse to set the initial condition of target implosion, and the step-like main pulse of 2 ns duration.

The trajectory of the ablation front is compared to the corresponding one-dimensional integrated code LILAC. The dashed line is the trajectory from LILAC simulation and the red marks are taken from the experiment data shown on the top. The imploding ablation front velocity is also compared in Fig. 3.26b. The maximum velocity is ~2×10^7 cm/s, well reproduced in LILAC code. The discrepancy in the early phase is due to the sensitivity of modeling target material with fluid approximation. It is clear in both comparisons that the simulation code well reproduces the trajectory, meaning that the energetics of the implosion dynamics is predictable with LILAC code.
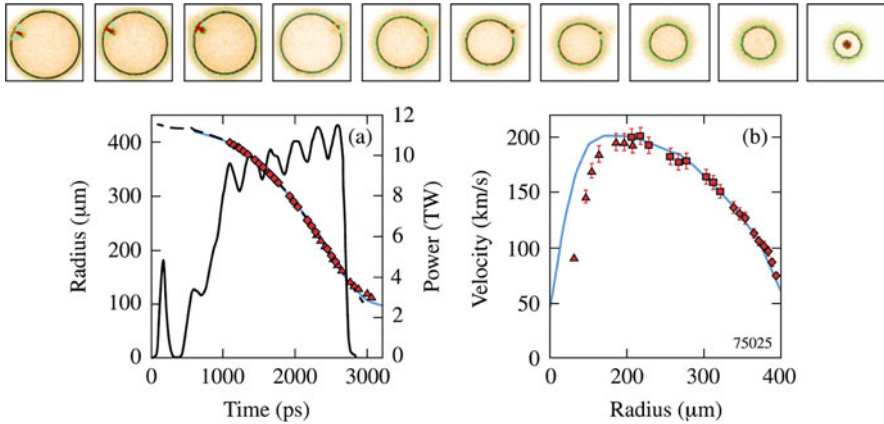
Fig. 3.26 The top: Sequential photographs of self-emitting x-ray from ablation fronts imploding by laser irradiation. (**a**): Time evolution of laser intensity and the trajectory of ablation front. The red marks are experimental data and the dashed line is from simulation. (**b**): The velocity of the ablation front from data with red mark and the blue line from simulation. Reprinted with permission from Ref. [17]. Copyright by Cambridge University Press

3.8.2 Back Light Imaging

By use of external x-ray source more precise distribution of the density can be measured. This method is called **X-ray back-lighting.** To measure the density profile, plane target is used. The target is C + H polymer polystyrene. The thickness is 40 μm and the width is 200 μm. The main drive-laser is irradiated on the target surface. At the same time, another laser irradiates the titanium plate of 20 μm to produce a small titanium plasma near the target. Filtering x-rays so that only the x-ray of narrow energy band around 4.85 keV can transmit through the C + H plasma from the side, the shadow image of the accelerating foil plasma is measured. The spatial distribution of the transmission intensity as a function of time can be obtained with a high-speed X-ray camera and the data are processed to the time evolution of the density distribution. The principle is simple. Electrons in K shell of carbon (C) in the C + H plasma absorb X rays coming from the titanium plasma. With the known energy of X-ray (=4.85 keV), the absorption coefficient (=19.72 cm^2/g), and the initial width of the foil 200 μm, it is easy to obtain the density from the ratio of transmission. With such data the spatial distribution of density has been obtained experimentally as shown in Fig. 3.27 [18].

The experimental time evolution of the foil acceleration dynamics and that obtained with the ILESTA-1D code are compared. The trajectories of the foil ablation front and rear surface are plotted for experimental data (marks with error bars) and ILESTA-1D (dashed and dash dot lines) for the density of 0.5 g/cm^3. The trajectory of the center of mass is also plotted to compare. The ablation surface starts to move downward before 1 ns, and the shock wave is produced at the same time.
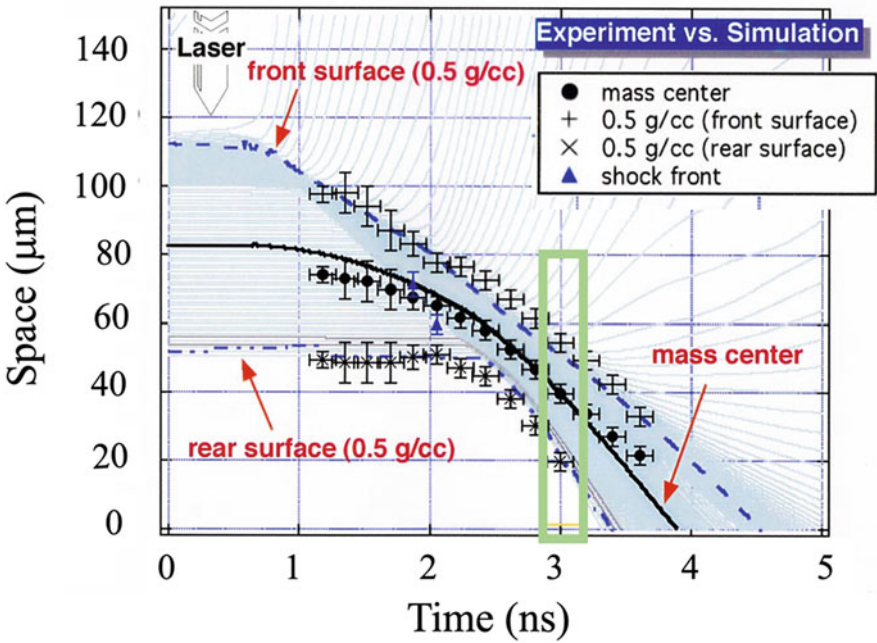
Fig. 3.27 R-T diagram from experiment and ILESTA code. The black marks are taken from time evolution of x-ray backlighting measurement. The mass center is plotted with black line. The flow lines of Lagrangian meshes from 1-D ILESTA code are plotted with water color lines. Reprint with permission from Ref. [18]. Copyright 1998 by American Institute of Physics

The shock wave reaches the rear surface around 2.2 ns, and a rarefaction wave having the initial velocity of the shocked region expands downward. In detail, the rarefaction wave propagates upward in Fig. 3.27 to the ablation surface. Then, gradually the density profile becomes a steady acceleration density one as shown in Fig. 3.24. As can be seen from this comparison, the experiment can be well reproduced with sufficient precision, and this code is widely used in the Japanese laser plasma community as the standard code for design and proposal of experiments and further analysis after a variety of experiments.

In Fig. 3.28 the density distribution of the experiment and two simulations are plotted for the time of 3 ns in Fig. 3.27. In the simulations, the results are shown for two cases with the diffusion model (Spitzer-Harm: SH) or kinetic model (Fokker-Planck equation: FP) as discussed later soon. In the present experiment, the laser intensity is relatively low at 7×10^{13} W/cm^2, and the wavelength is short as 0.35 μm of the third harmonics. It is seen that the diffusion approximation sufficiently reproduces experimental data in this case.
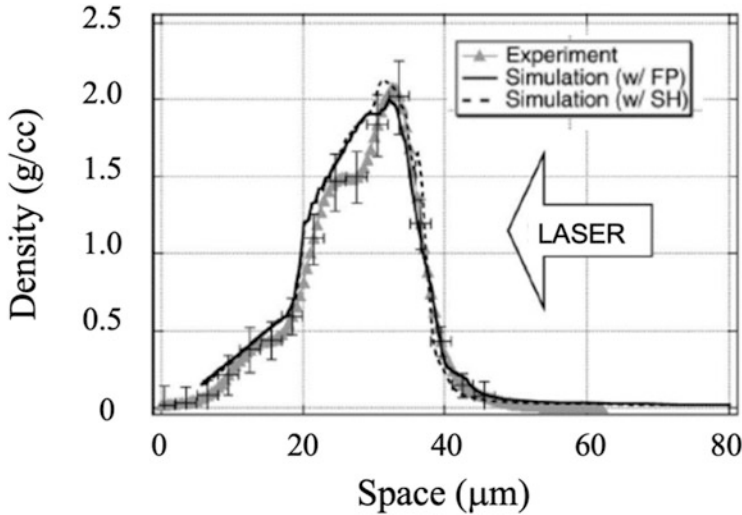
Fig. 3.28 The snap shot of the density profile around t = 3 ns in Fig. 3.27 is shown from experimental data with error bars, comparing to the corresponding simulation profile with solid line. Reprint with permission from Ref. [18]. Copyright 1998 by American Institute of Physics

3.8.3   Hydrodynamics of the Final Compression

In Fig. 3.29 a stretched view of the compression phase of the radius-time diagram of Fig. 3.23 is shown. After the shock front collides at the central singular point, the shock wave is reflected to decelerate the following fuel gas to stagnate the DT fuel plasma. Then, it collides at the boundary of high-density glass plasma and reflected toward the center again. Since the reflected shock becomes higher pressure via energy conversion from fluid kinetic energy to the thermal energy, the temperature and pressure of the fuel gas increases more to decelerate the glass plasma to finally push back outward as seen in Fig. 3.29. Of course, the assumption of one-dimensional spherical symmetry is too idealistic. It is natural to think that the lower-density fuel plasma cannot decelerate the heavier glass plasma and the glass plasma may penetrate directly to the central region repelling the DT fuel plasma. As the result, the fuel plasma cannot obtain enough pressure work by the glass plasma not to be heated up to enhance fusion reaction. Such physics is called hydrodynamic instability and mixing. Material mixing by hydrodynamic instability in the stagnation phase is critical issue to explain the experimental results as shown in for example [15]. The instability and resultant turbulent mixing will be studied and discussed later. However, it is informative to know more about one-dimensional hydrodynamics in the final compression phase as shown in Fig. 3.29.

Fig. 3.29 A stretched r-t diagram near the final compression of Fig. 3.23. When the shock wave collides the center, a reflected shock is generated to propagate outward to collide the contact surface with the falling glass shell plasma. This shock is again reflected by the higher density of the glass plasma by gaining energy from the kinetic energy of the glass plasma. This shock compress and heat further the DT plasma to enhance the DT fusion yield
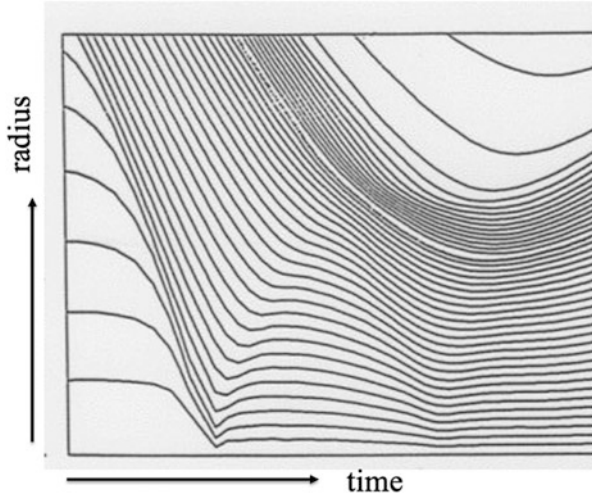
3.9   Ablation and Nozzle

3.9.1   Laser Ablation by Heat Conduction

It is useful to know a general property of the stationary ablation structure as shown in Fig. 3.18 driven by nonlinear electron heat wave, whose (P, V) diagram is plotted in Fig. 3.19. Let us consider for the case of plane geometry. From (2.23) and (2.27), the following two conservation relations are obtained.

$$\rho u = J_0 : const. \tag{3.72}$$

$$\rho u^2 + P = 2P_0 : const., \tag{3.73}$$

where the constants are given by the values at the sonic point defined with the subscript "0" as

$$u_0^2 = \frac{P_0}{\rho_0} \tag{3.74}$$

Chapman-Jouguet deflagration wave is given by knowing how to obtain the structure connecting from subsonic region to the sonic point.

Let us discuss the structure in normalized flow velocity $U = u/u_0$ and normalized temperature $T = (P/P_0)/(\rho/\rho_0)$. From (3.72) and (3.73), the following simple relation is derived.

$$T = -(U-1)^2 + 1 \tag{3.75}$$

Note that this relation gives a monotonic increase of the flow velocity in the subsonic region and requires the temperature is maximum at the sonic point (U = 1).

$$dT = -2(U-1)dU \tag{3.76}$$

In the case of laser ablation structure, the electron heat conduction determines the structure. So, the ablation structure depends on the physics of energy transport. In the case of diffusion-type heat conduction, the temperature change is managed by heat flux Q

$$Q(x) = -K(x)\frac{\partial T}{\partial x} \tag{3.77}$$

Therefore, the absorbed laser energy must supply this heat flux at the sonic point $x = x_0$ with the laser heating rate S in the form.

$$\frac{\partial}{\partial x}Q = S\delta(x-x_0) \tag{3.78}$$

This assumption allows the solution continues to increase the flow velocity and expands to the vacuum region as the isothermal rarefaction wave.

When we assume the stationary state even for the supersonic region, the temperature must go down in the supersonic region as given in solution (3.75). This is not realistic model for the ablation structure expanding into the vacuum. As a simple model, it is appropriate to assume that the stationary deflagration wave is continuously connects the iso-thermal rarefaction wave.

Such one-dimensional stationary model can be applicable by changing the size of the one-dimensional geometry like a nozzle and spherical geometry as seen below.

3.9.2 Laval Nozzle

It is well-known that even with one-dimensional flow, but if the flow is in a nozzle with the cross-sectional area changing in space, it is possible to obtain a solution continuously transiting the sonic point from subsonic to supersonic. In this case, we have another valuable the cross-sectional area A(x). Then, (3.72) is replaced by the following relation.

$$\rho u A = const. \tag{3.79}$$

In the present case, we have to use Bernoulli relation of steady state flow (2.97) to compressible flow given as

$$\frac{1}{2}u^2 + \int \frac{dP}{\rho} = const. \tag{3.80}$$

Introducing the sound speed "a" and local Mach number M defined as

$$a^2 \equiv \frac{dP}{d\rho}, \qquad M = \frac{u}{a} \tag{3.81}$$

Then, (3.80) is rewritten as

$$\frac{d\rho}{\rho} = -M^2 \frac{du}{u} \tag{3.82}$$

This indicates that the density decreases along with the increase of the flow velocity. It is possible to change (3.79) as

$$\frac{d\rho}{\rho} + \frac{du}{u} + \frac{dA}{A} = 0 \tag{3.83}$$

Then, the following relation is obtained.

$$\left(1 - M^2\right)\frac{du}{u} = -\frac{dA}{A} \tag{3.84}$$

This indicates that in the subsonic region (M < 1), the flow velocity increases with the decrease of the pipe size A, and the flow comes to the sonic point by keeping increase if A is minimum value at the sonic point M = 1. Then, in the supersonic region, the increase of flow velocity is maintained by increasing the size of the pipe. Such pipe is called **Laval nozzle** as shown in Fig. 3.30.

It is useful to estimate how high supersonic flow velocity of gas is generated as the maximum. Let us assume that the high-pressure with very low velocity flow is generated out of the subsonic edge in Fig. 3.30. Assuming that the gas is adiabatic and $P \propto \rho^\gamma$ is satisfied. Then, (3.80) at the left boundary should conserve to reduce the relation.

$$u_{max} = \sqrt{\frac{2}{\gamma - 1}} V_s(x_0) \tag{3.85}$$

where $V_s(x_0)$ is the sound velocity at the left boundary. Roughly speaking, the sound velocity increases with the temperature, increase of the gas temperature injecting to Laval nozzle gives higher exhausting velocity. In the jet engine, the fuel combustion in front of the nozzle increases the temperature of the gas to increase the pressure and the temperature to covert the heating energy to the large momentum flow. The total momentum flux is proportional to $\rho u A u$. Increase of $\rho u A$ and exhausts with u_{max} gives us the maximum propulsion force.

Fig. 3.30 Structure of a Laval nozzle and flow velocity changing from subsonic to supersonic
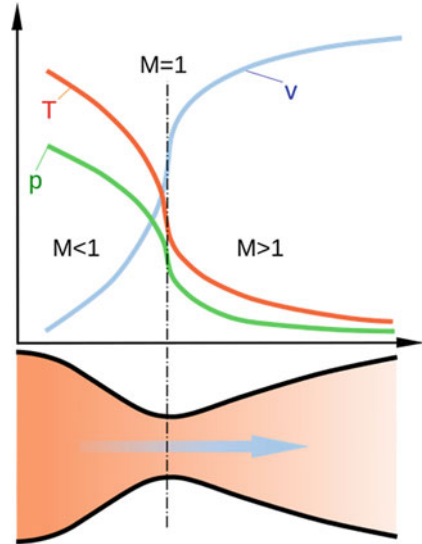
Gas jet generated with such Laval nozzle is widely used for laser-plasma experiments. In the laser wake-field acceleration of charged particles, ultra-intense-short pulse laser propagates in low density gas and the gas jet is used to provides such almost constant density gas. The gas is spontaneously ionized when the laser interacts with the gas atom and plasma waves are generated as a wake of laser passage. In Fig. 3.31 an example of the gas density profile after the exhaust from the gas jet nozzle is shown. It is expected to give an almost constant density plasma in a vacuum chamber [19].

3.9.3   Solar Wind (Parker Solution)

Although the temperature of the sun surface is about 6000 degrees, there is a corona region whose temperature is one million degrees in the outer layer, and plasma always flows out into outer space from the surface. This is called **solar wind.** The same thing happens with other stars, which is called **stellar wind**. Generally, hydrogen, helium and other heavy elements are ejected from the sun surface. It is huge amount of one million tons per second, and the solar wind is falling against the earth as well. The speed of the solar wind is as high as 300 to 900 km/s. The temperature is about 10 to one million degrees.

Regarding solar wind, Parker elucidated the above Laval nozzle idea by applying it to solar wind. He has chosen the effect of spreading the cross-sectional area A to the spherical shape, and that $M = 1$ is gives with the radius at which the deceleration effect by the Sun gravity successfully transitions from subsonic to supersonic.
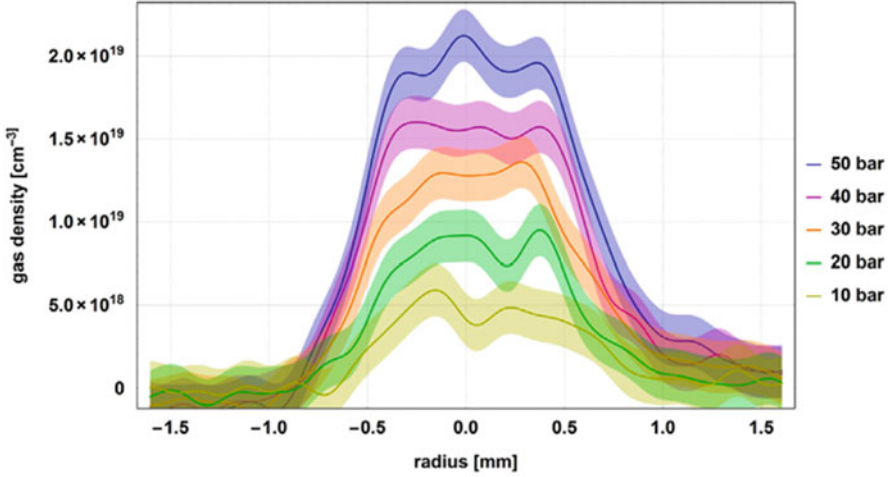
(a) Helium gas density profile.

Fig. 3.31 A typical experimental data of gas density ejected from the exit of gas jet nozzle for use to laser wake-field acceleration experiment. Reprint from Ref. [19]. Copyright 2012, with permission from Elsevier

Let's follow the **Parker's solution**. First, the equation of continuity is

$$4\pi r^2 \rho u = const. = \left| \frac{dM}{dt} \right| \tag{3.86}$$

where M is the mass of the sun. We assume that the temperature of the solar wind is constant (T: constant). Then, the pressure is proportional to the density, and the sound speed a is also constant as

$$a^2 = \frac{P}{\rho} = const. \tag{3.87}$$

Then, the equation of motion is

$$u \frac{du}{dr} = -\frac{a^2}{\rho} \frac{d\rho}{dr} - \frac{GM}{r^2} \tag{3.88}$$

Differentiation of (3.86) gives

$$2\frac{dr}{r} + \frac{d\rho}{\rho} + \frac{du}{u} = 0 \tag{3.89}$$

Substituting this into (3.88) and erasing $d\rho$ yields the following equation. 。

Fig. 3.32 The velocity-radius diagram to obtain the solution of the solar wind generated on the sun surface as subsonic flow to pass the sonic point to accelerate to supersonic. The integration path passing the saddle point provides uniquely the physically acceptable solution. Reprint from Ref. [20] with kind permission from Springer Science + Business Media
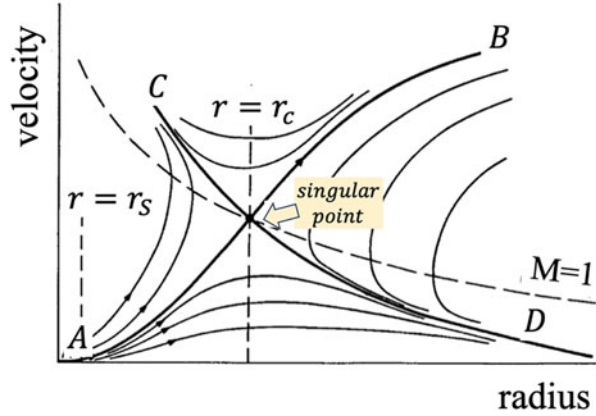
$$\left(M^2 - 1\right)\frac{1}{u}\frac{du}{dr} = \frac{2}{r}\left(1 - \frac{r_c}{r}\right) \tag{3.90}$$

$$r_c = \frac{GM}{2a^2} \tag{3.91}$$

Here, r_c is the point at which the solar wind becomes sonic speed. When a typical value is entered, it is about 2.5 times the sun radius.

Finally, it is useful to note about mathematics in obtaining the solution of Laval nozzle and the solar wind. It is easily found that for example, for a given temperature, numerical integration to the radius r cannot be extended to the supersonic region. As shown in Fig. 3.32, most of the integral solution of (3.90) cannot pass the sonic point, because the sonic point is mathematically singular point [20]. In general, it is recommended to find the pass from the sonic point to give physically reasonable solution at the solar surface and the infinity.

3.9.4 Singularity and Saddle Points

Now, in the case of Laval nozzle, an analytical solution has been shown already, but here we show that there exists a solution in which a differential equation having a singularity at the sonic point in (3.90) continues from subsonic to supersonic. For that purpose, we investigate the properties of differential curves at singular point $(r = r_c, u = a)$.

There are two types of singularities: **saddle** and **node points.** With a saddle point, the integral curve is uniquely determined in two-directional space in (3.90), but not uniquely determined if it is a node. It is understood that this sonic point is a saddle point, and there are two integral curves connecting from subsonic to supersonic speed. Let us see the mathematics below.

Now, we study mathematical properties of the singular point in (3.90)

$$r = r_c + \delta r \tag{3.92}$$

$$u = a + \delta u \tag{3.93}$$

Then, Taylor expansion (3.90) is carried out with (3.91) and (3.92) to make (3.90) linearized equation around the singular pint.

$$\frac{du}{dr} = 2\left(\frac{a}{r_c}\right)^2 \frac{\delta r}{\delta u} \tag{3.94}$$

The small deviations should be on the integral lines, namely

$$\frac{\delta u}{\delta r} = \frac{du}{dr} \tag{3.95}$$

So, after all, the integral from the singular point must have the slope of the following two directions.

$$\frac{du}{dr} = \pm \sqrt{2}\,\frac{a}{r_c} \tag{3.96}$$

The actual integral curve is as shown the thick solid line A-B in Fig. 3.32. The line C-D is non-physical integration path.

In Fig. 3.32, the solar wind solution increases from subsonic to supersonic with radius, which corresponds to the solution of + sign in (3.96). Another integral curve is Bondi's solution (1952) representing spherically symmetric **accretion flow**. The fundamental Eqs. (3.86) and (3.87) are the same, although the sign of the flow velocity is negative, namely matters fall on the surface of stars. The stationary solution of the so-called accretion flow, in which matters are accumulated from the surroundings, can be obtained at the same time. Actually, accretion is not spherical symmetry in the universe, in the case of a binary star system a white dwarf peels off the surface of a companion star and become heavier. In such a case, it is of a form of disk and it has an angular momentum at the same time. It rotates around the white dwarf and loses its angular momentum with viscosity and accretes matters on the surface of the white dwarf. Therefore, note that the Bondi solution is a very rough approximate solution.

References

1. Y.B. Zel'dovich, Y.P. Raizer, *Physics of Shock Waves and High Temperature Hydrodynamic Phenomena* (Dover, 2002)
2. L.D. Landau, E.M. Lifshitz, *Fluid Mechanics (Course of Theoretical Physics: Volume 6)*, 2nd edn. (Butterworth-Heinemann, Oxford, 1987)

3. M.Y. Jaffrin, R.F. Probstein, Structure of a plasma shock wave. Phys. Fluids **7**(10), 1658–1674 (1964)
4. T. Sano et al., Laser-shock compression and Hugoniot measurements of liquid hydrogen to 55 GPa. Phys. Rev. B **83**(5), 054117 (2011)
5. A. Schropp et al., Imaging shock waves in diamond with both high temporal and spatial resolution at an XFEL. Sci. Rep. **5**, 11089 (2015). https://doi.org/10.1038/srep11089
6. B.D. Keenan, Deciphering the kinetic structure of multi-ion plasma shocks. Phys. Rev. E **96**, 053203 (2017)
7. M. Emden, M. Gerwig, Can Faraday's the chemical history of a candle inform the teaching of experimentation? An hermeneutic approach for teaching scientific inquiry from a proven historical exemplar. Sci. & Educ. **29**(3), 589–616 (2020)
8. A. Minchinton, On the influence of fundamental detonics on blasting practice, in *11th International Symposium On Rock Fragmentation By Blasting* (2015)
9. F. Ettner, K. G. Vollmer, T. Sattelmayer, Numerical simulation of the deflagration-to-detonation transition in inhomogeneous mixtures, J. Combust., Article ID 686347, 15 pages, (2014) https://doi.org/10.1155/2014/686347
10. F. Röpke, K. Friedrich, S.A. Sim, Models for type Ia supernovae and related astrophysical transients. Space Sci. Rev. **214**, 1–17 (2018)
11. X. Timmes, S.E. Woosley, The conductive propagation of nuc;ear flames I. Degernerate C+O and O+Ne+Mg white dwarfs. Astrophys. J. **396**(649) (1992)
12. H. Takabe, K. Nishihara, T. Taniuti, Deflagration waves in laser compression. I. J. Phys. Soc. Jpn. **45**(6), 2001–2008 (1978)
13. G.H. McCall, Laser-driven implosion experiments. Plasma Phys **25.3**, 237 (1983)
14. T.J. Goldsack et al., The variation of mass ablation rate with laser wavelength and target geometry. Opt. Commun. **42**(1), 55–59 (1982)
15. H. Takabe et al., Scalings of implosion experiments for high neutron yield. Phys. Fluids **31**, 2884 (1988)
16. H. Takabe et al., Self-consistent growth rate of the Rayleigh–Taylor instability in an ablatively, accelerating plasma. Phys. Fluids **28**(3676) (1985) Phys. Fluids, 26, 2299 (1983)
17. D.T. Michel et al., Measurements of the ablation-front trajectory and low-mode nonuniformity in direct-drive implosions using x-ray self-emission shadowgraph, High Power Laser Sci Eng, (2015), 3, e19, 8 pages
18. S. Fujioka et al., First observation of density profile in directly laser-driven polystyrene targets for ablative Rayleigh–Taylor instability research. Phys. Plasmas **10**, 4784 (2003)
19. J.P. Couperus, Tomographic characterization of gas-jet targets for laser wake-field acceleration. Nucl. Instrum. Methods Phys. Res. **A830**, 504–509 (2016)
20. M.M. Echim, J. Lemaire, O. Lie-Svendsen, A review on solar wind modeling: kinetic and fluid aspects. Surv. Geophys **32**, 1–70 (2011)

Chapter 4
Self-Similar Solutions of Compressible Fluids

Abstract Strong shock waves are used to compress and heat any matters in the laboratory. The ablation pressure by intense laser is used to compress even solid matters. In plane geometry, it is easier to design multi-shocks to compress the matters, while it is more beneficial to use the spherical compression. No simple solutions are available to know the trajectories of shocks in one-dimensional spherical symmetry. Here we see several analytical solutions with the self-similar method. The method is to find new governing solution of ordinary differential equation from partial differential fluid equations. The self-similar method is known before the birth of computer.

The blast wave is the most famous one. Here, we review the basic method to derive several self-similar solutions allowing the spherical implosion, useful to laser driven implosion. The isobaric solution provides uniform pressure and spark-main fuel structure, and isochoric solution gives us uniform density profile at the maximum compression. It is shown that even including thermal conduction, it is possible to find a solution of ablation structure. This is an extended solution more appropriate compared to the steady state solutions shown in the previous chapter.

The blast waves are widely used from laser experiments to supernova remnants (SNRs). SNRs are blast waves driven by the matters exploding by supernova explosion. A self-similar solution with forward and reverse shock waves is found to explain many observation data of SNRs. A numerical simulation shows that the solution of ejecta-driven shock changes from Chevalier's self-similar solution to the other Sedov-Taylor one. The self-similarity is one of the key physics controlling nonlinear hydrodynamic equations.

4.1 Introduction

4.1.1 Strong Shock Reflection

Consider strong shock limit where $P_1 \gg P_0$ and P_0 can be neglected in the Ranking-Hugoniot relation in (3.13). In the case of irradiation of intense laser on solid matters,

this limit is possible to be realized. However, as we see in Fig. 2.3, the equation of state (EOS) is not ideal. This means an effective specific heat γ is a function of density and pressure even in LTE. For example, aluminum is almost incompressible up to the 100 kBar (1 Bar $= 10^5$ Pa) and it becomes compressible over a few hundred k-Bar. The solid matters are hard because of Coulomb repulsive force in lower pressure than the Bulk modulus shown in Chap. 2. Over this pressure, most of solids have the dominant pressure of electron Fermi pressure. The Fermi pressure P_F is proportional to the density as $P_F \propto \rho^{5/3}$.

Neglecting P_0, (3.16) gives the following scaling of achievable pressure by stagnation of a shock wave by a rigid boundary as shown in Fig. 4.1.

$$P_1 \approx \rho_0 u_0^2 \tag{4.1}$$

The following simple formula is obtained

$$P\,[Mbar] = \frac{\rho_0}{[g/cm^3]} \left\{ \frac{u_0}{[10^6 cm/s]} \right\}^2 \tag{4.2}$$

If we can compress and accelerate a matter to the density of 100 g/cm^3 and the velocity of $3 \times 10^7 cm/s$, an extremely high pressure around 100 Gbar can be achieved by the stagnation. It is hard to realize such initial condition with ρ_0 and u_0 in plane geometry, but the following idea is used.
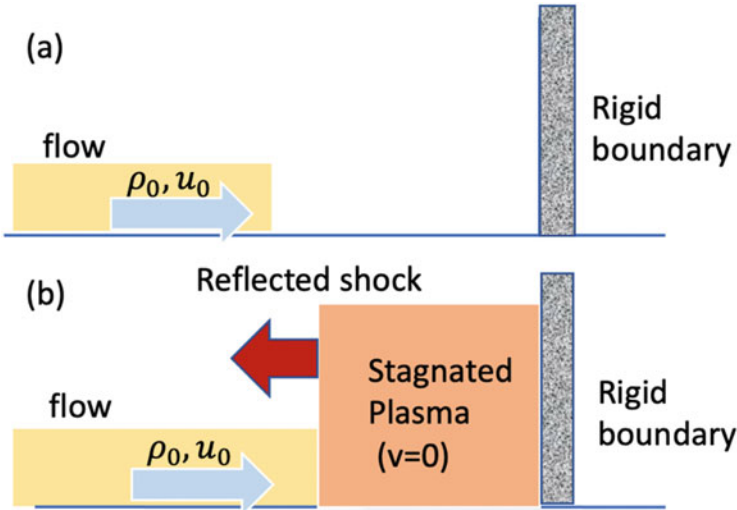
Fig. 4.1 The kinetic energy of fluid flow is converted to the thermal energy by collision with a rig wall. The density increases in the reflecting shock wave, but it is limited by the RH relation in plane geometry

4.1.2 Tailored Compression

Even in plane geometry, however, it is possible to compress matters to extremely high-density by use of multi shock waves, namely sequential shock compression. In Fig. 3.4, we have seen that the Ranking-Hugoniot curve is almost the same curve as the adiabatic curve for lower compression case. So, if we can shape the pressure to make shock waves so that each shock wave is that of compression of about two-times the density of the rear of the previous shock wave, it is possible to compress plasma under almost adiabatic condition.

In Fig. 4.2, this tailored pressure compression is shown in x-t diagram (a) and a snap shot of the density at a time t_s is plotted on the right (b). In this hydrodynamics, all shock waves are designed to arrive at x = 0 at the time of maximum compression (t_m). The initial shock trajectory is plotted with blue and the sequential shocks are plotted with yellow lines in (a). Since a shock is always stronger than the front shock, the generated shock velocity is faster than the front one. If we can increase the number of shocks, it is equivalent to the adiabatic compression and the maximum density is proportional to the available maximum pressure. By use of a finite strength shock for the first one (blue), the adiabatic compression is possible with the entropy determined by the first shock wave.

Of course, the design of the tailored compression is not so simple mainly because of non-ideal equation of state. As shown in Fig. 3.5, the phase transition from solid to plasma has complicated process with an effectively different freedom of physical condition. It has been carried out to study the equation of state of shocked solid materials theoretically, computationally, and experimentally. This issue will be discussed in this text later.
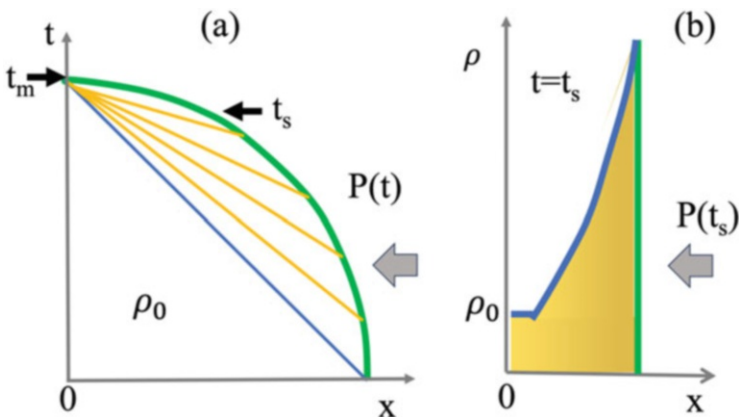
Fig. 4.2 Schematics of tailored pressure for almost adiabatic compression in plane geometry. After the first shock wave shown in blue, many subsequent shock waves are generated. The density profile becomes like (**b**) at t = t_s. The maximum density is expected at t = t_m

4.1.3 Hollow Shell Implosion

When an intense laser irradiates a solid material, it is possible to generate ~100 Mbar of so-called ablation pressure on the surface of a spherical target for nuclear fusion experiment shown, for example, in Fig. 4.3a. By use of spherical convergence geometry, it is possible to enhance the density and pressure. It is, however, hard to evaluate the effect of the spherical geometry, because as shown in Fig. 4.3b, the compressed and accelerated plasma of DT ice by shock waves is decelerated by the decrease of the surface shown with blue arrows ($\propto r^2$), depending on the thickness of the shell and its pressure. In addition, self-pressure works to expands the shell as green force in Fig. 4.3b to reduce the density. It is true that we can achieve higher compression and extreme pressure if the thickness of the plasma shell is thin enough and the pressure is as low as possible, namely keeping low entropy state. As shown in Fig. 2.3, the lowest pressure at higher density is given by Fermi pressure and it is impossible to keep the pressure lower than the Fermi pressure. The Fermi pressure decelerate the shell velocity and force to expand the shell as shown in Fig. 4.3b.

Therefore, it is not clear how the accelerated matter by shock waves converges toward the central singularity point. Theoretical guideline of the spherical effect on the shock dynamics is given as **self-similar solution** of the ideal fluid equations. This is explained in this Chapter.

To obtain the image of one-dimensional fluid dynamics of laser implosion, one example obtained with the physics-integrated implosion code ILESTA [1] is shown for the case of a hollow plastic shell implosion. In Fig. 4.4, time evolution of fluid

Fig. 4.3 (**a**) A cut-view of a typical target structure of spherical laser fusion implosion. The ablator is irradiated by intense laser to generate the ablation pressure to compress the fusion fuel DT ice at the center of the target. The gas is residual gas with low pressure. (**b**) is the time the DT plasma is imploded near the center. It feels the force as shown with blue and green arrows
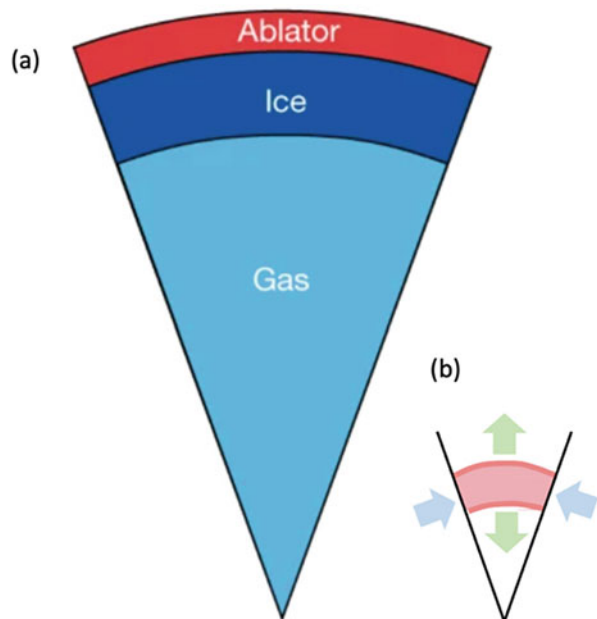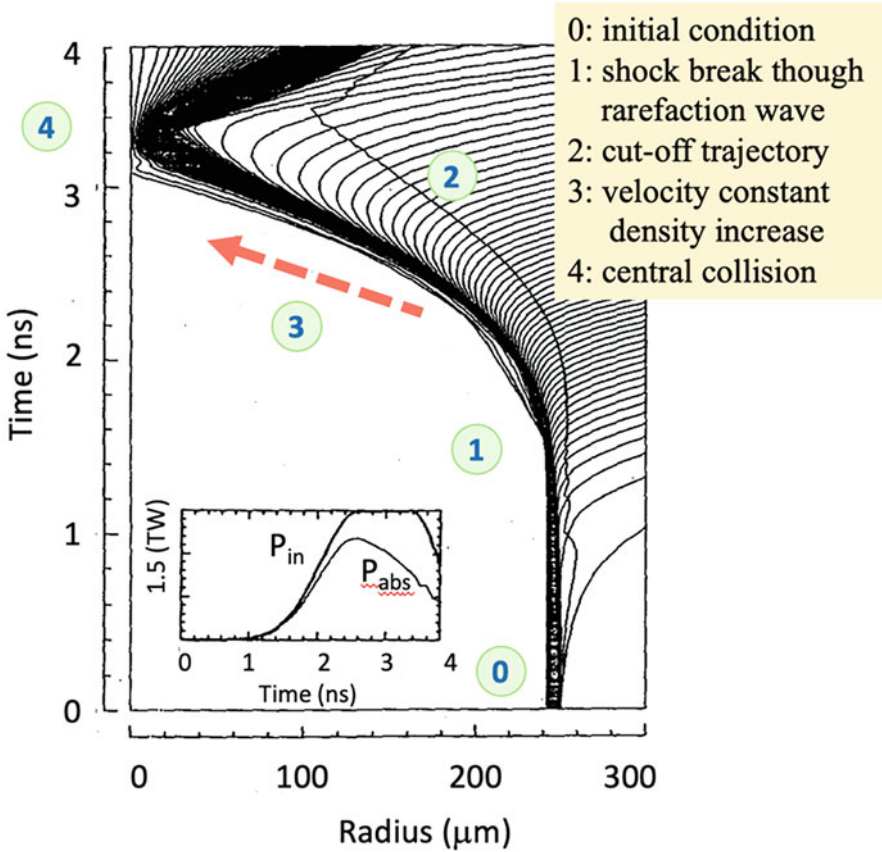
Fig. 4.4 RT-diagram of dynamics of fluid elements in one-dimensional spherical implosion simulation. Plastic hollow shell is imploded by the laser power shown in the inlet

elements (Lagrangian trajectories) is plotted in radius and time diagram. A thin plastic shell (CH) of diameter 500 μm and thickness of 10 μm is irradiated by green laser ($\lambda_L = 0.53\mu m$) with energy of 8 kJ. The shapes of input (P_{in}) and the absorbed (P_{abs}) pulses are plotted in the inlet figure.

In Fig. 4.4, the initial shock wave arrives at the rear-side of the shell at the point (1). The shock breaks through the shell and the shocked plasma expands as the rarefaction wave. The trajectory of the laser cut-off density is plotted with the line (2). As seen in the inlet, the peak of absorbed laser power is around t = 2.5 ns, and the shell plasma keeps to shrink toward the center of the target. The mean velocity of the plasma shell is kept almost constant and it is estimated to be $u_0 \approx 3 \times 10^7 cm/s$.

In Fig. 4.5, the trajectories of all fluid elements are plotted in the density and pressure diagram, where the cold curve of plastic shown with the blue dashed line from (0) to (1) is taken from Fig. 2.3. The initial condition of the simulation is all below the point (0). Since the laser intensity increases continuously, the plastic of
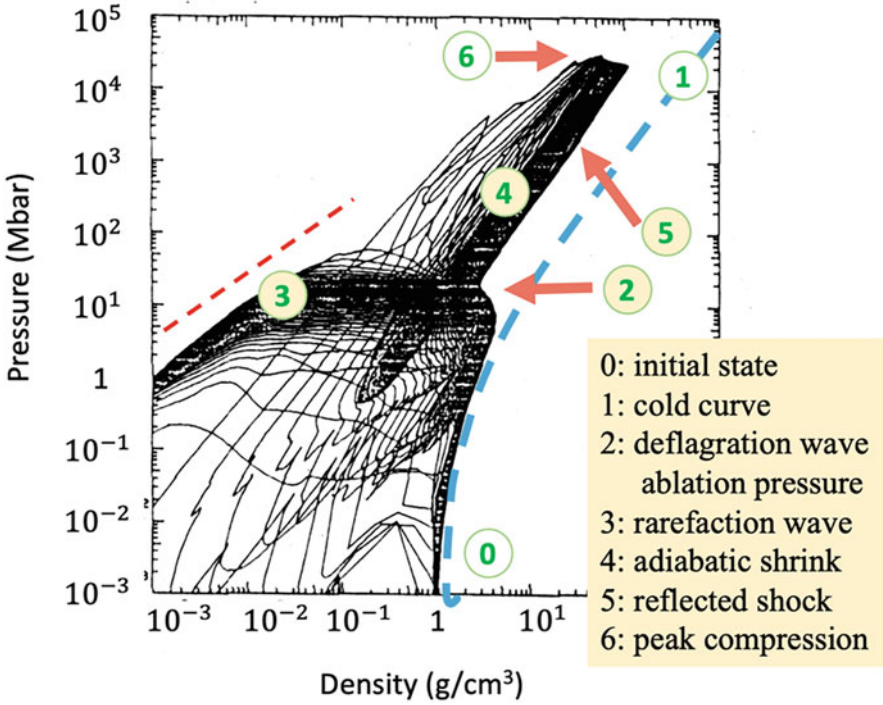
Fig. 4.5 Time evolution of all fluid elements in Fig. 4.4 are plotted in density-pressure diagram. The initial condition is near the point (0). The blue dashed line is the cold curve. The red dashed cure is a constant temperature line

solid CH is compressed almost adiabatically. The outer plastic is then ablated into vacuum, while it decreases the density more than two order of magnitude from the point (2) to (3). Note that the pressure is kept almost constant as the characteristic of the deflagration wave. This pressure is the ablation pressure to be discussed soon. It is seen that the ablation pressure is about 20 ~ 30 Mbar in Fig. 4.5. After the exhaust of plasma in the deflagration wave, the rarefaction wave expands to the vacuum while keeping a constant temperature, where the red dashed line is the constant temperature line ($P \propto \rho$) in Fig. 4.5.

In the present simulation, the radiation preheat by d doped silicon is included. The radiation pre-heat increases the entropy of the plastic shell plasma. As the shrink of the shell radius, the density increases in the phase of the point (4) thanks to the effect of compression by the spherical convergence. The density increases from (2) to (5), then a strong shock wave generated at the center converted the shell kinetic energy to the compression energy as shown from the point (5) to (6). It is found that from (2) to (5) the compression is almost adiabatic and its **adiabat α** defined as

$$P = \alpha P_c \tag{4.3}$$

is about $\alpha = 8$ in (2)–(5) and $\alpha = 10$ at the maximum density.

In the final convergence of the kinetic energy to the thermal energy, the maximum pressure is obtained in the simulation. By use of the velocity u_0 and density ρ_0 in the simulation, the point (5) in Fig. 4.5, rough evaluation (4.2) gives the pressure as

$$P = 27 \ [Gbar] \text{ for } \rho_0 = 30 \ [g/cc] \tag{4.4}$$

The simulation resulted the maximum pressure of about 40 Gbar, higher than the value above due to the spherical effect. As seen at the point (6) the density profile of the maximum pressure is clear to have a structure with the density from 30 to 100 g/cc. This is because the center of the core is the part initially expanded by the shock at the time (1) in Fig. 4.4 and its entropy increases higher by the second shock at 2.4 ns. This means the final core has the central spark of high-temperature and the surrounding of high-density region automatically. The isobaric profile is commonly seen in the self-similar solution to be discussed later.

It is well-known that to achieve the extremely high-pressure for nuclear fusion ignition, so-called **tailored pulse** is required [2]. Also, the implosion dynamics should be designed so that the DT ice plasma region in Fig. 4.3 is protected from the entropy increase by shock wave and radiation pre-heat. The material of the ablator should be selected by taking account that it does not emit x-ray radiation or it should be shielded by some idea. As the case of Fig. 4.4, the radiation pre-heat prohibited the low-adiabat compression of the adiabat, $\alpha < 2\sim3$.

The hydrodynamic stability of implosion is very critical especially for thin-shell and low-adiabatic implosion. This means that to achieve expected high-density compression, it is required to develop three-dimensional hydrodynamics code with important physics integrated in the code. For example, HYDRA and ASTER are used as the standard three-dimensional integrated codes [3, 4], respectively At least two-dimensional simulation code is necessary to analyze the implosion experiments from which we can obtain limit data indirectly. The hydrodynamic instability of implosion is hot topics and to be discussed in details in Volume 3.

4.1.4   Analytic Solution of Spherical Implosion

Any kind of computer simulation code should be verified through comparing to the code with the corresponding experiment. The comparison has been carried out for a simple part of the plasma dynamics as explained in the previous chapter. Since the implosion dynamics with help of the singularity of spherical geometry is important to the application of high-energy-density physics in laser plasma, it is useful to know some analytic solutions of spherical dynamics. Possible idealistic solutions have been found by altering the time and space dependent partial differential equations to coupled ordinary differential equations. This method is to find self-similar solution by finding the similarity variable.

In the previous chapter, we studied analytic solutions with the steady state assumption in the appropriate moving frame. In the present chapter, on the other

hand, we will review the self-similar solutions describing spherical implosion and explosion dynamics. It is also shown that a self-similar solution is also found to the time dependent ablation structure under the idealized boundary condition.

4.2 Basic Equations for Self-Similar Solutions

Try to study the physics of spherical compression by a strong shock wave propagating from the outer sphere in a uniform density fluid. It is surprising to know that theoretical works were published in early time by **Guderley**, Landau, others as described in the books Chap. XII in [5] and Chap. 6.7 in [6], where the method of self-similar-solution has been used to reduce nonlinear partial differential equations to ordinary differential equations as an eigen value problem. They obtained approximate analytical solution, and the mathematical method is described in [5, 6]. The hydrodynamic stability of the Guderley solution is studied in [7], where the property of the Guderley solution is numerically solved to obtain the solution. The Guderley solution gives the fluid dynamics in the converging phase of shock wave and the fluid dynamics after the shock reflection at the center, the singular point. It is reasonable to expect the geometrical effect, namely the shocked matter moves toward the center to be compressed and heated adiabatically by the geometrical effect and the central singularity effect.

Of course, the spherically symmetric hydrodynamics is naive assumption and there is no proof that the spherical symmetry can be reasonably achieved even with highly precision technology. This is a big issue to be discussed relating to the laser fusion in Volume 3. The present understanding is that it is not possible because of the hydrodynamics instability and turbulent mixing generated by the thermal noise on the target and pressure nonuniformity by laser ablation as will be discussed later. But, analytical solution such as self-similar solution is very useful to know the fluid dynamics in such extreme condition. The solution can be used to verify the accuracy of the hydrodynamic simulation code under idealized condition.

4.2.1 Self-Similar Solutions

Compression of matters with shock waves can be evaluated by using the RH relations and rarefaction wave in the plane geometry. It is not trivial to predict the propagation of shock wave in the spherical geometry, because time dependent geometry effects on the shock front continuously change the density, flow velocity, and pressure in time, in space as well. In solving an idealized nonlinear coupled equations, so-called the method of **self-similar solution** has been applied in many cases. The type of the fluid dynamics consists of two-types [8].

1. Implosion and collapsing cavities
2. Converging and diverging shocks

Following Refs. [6, 9], let us summarize the solutions useful for relating to the laser implosion.

The self-similar solution is based on the dimensional analysis of the basic equations as we have already shown a simple case of the nonlinear heat conduction in Chap. 2. In what follows, we consider only the case of adiabatic dynamics except shock jump surface. Including the shock front in the self-similar solutions, the strong jump limit is assumed to connect two different self-similar solutions. Note that the adiabatic assumption means that the entropy $S = P/\rho^\gamma$ is constant in time for each fluid particle, while the spatial variation of S(r) is allowed as initial condition.

Let us follow the notation in [9]. The basic equations are (2.20) – (2.22) with $Q = 0$, namely adiabatic condition $dS/dt = 0$ is assumed. In the spherical geometry, the equations are given in Euler description as

$$\frac{\partial \rho}{\partial t} + \frac{\partial}{\partial r}(\rho u) + \frac{2\rho u}{r} = 0 \tag{4.5}$$

$$\frac{\partial u}{\partial t} + u\frac{\partial u}{\partial r} + \frac{1}{\gamma\rho}\frac{\partial}{\partial r}(\rho c^2) = 0 \tag{4.6}$$

$$\frac{\partial c}{\partial t} + u\frac{\partial c}{\partial r} + \frac{\gamma - 1}{2}c\left(\frac{\partial u}{\partial r} + \frac{2u}{r}\right) = 0 \tag{4.7}$$

where c is the sound velocity.

$$c^2 = \gamma\frac{P}{\rho} \tag{4.8}$$

We take the **similarity variable** ξ with an unknown constant α in the form.

$$\xi = \frac{r}{|t|^\alpha} \tag{4.9}$$

Note that ξ is non-dimensional variable with use of typical time t_0 ($t \to t/t_0$) and r_0 ($r \to r/r_0$) to be defined in applying the solutions to some real problem [6, 9].

Assume the following solution from the dimensional analysis.

$$u(r, t) = \alpha\frac{r}{t}U(\xi) \tag{4.10}$$

$$c(t, r) = \alpha\frac{r}{t}C(\xi) \tag{4.11}$$

$$\rho(r, t) = \rho_0 r^\kappa N(\xi) \tag{4.12}$$

Note that α and κ are constants and α is the eigen value as see below. In the analysis, the constant α is determined like an eigen value to obtain any expected solution of $U(\xi)$ and $C(\xi)$, while the parameter κ is given so that the density profile is reasonable as expected. As we see soon, for a given test value of α, we can obtain the function $U(\xi)$ and $C(\xi)$ satisfying an appropriate boundary condition in the case of collapsing cavities. In the shock case, the jump relation connects the solution of $U(\xi)$ and $C(\xi)$ from subsonic to supersonic points.

Inserting (4.10, 4.11, and 4.12) to (4.5, 4.6, and 4.7) and using the simple relations

$$\frac{\partial f(\xi)}{\partial t} = -\alpha \frac{\xi}{t} \frac{df(\xi)}{d\xi}, \; \frac{\partial f(\xi)}{\partial r} = \frac{\xi}{t} \frac{df(\xi)}{d\xi} \tag{4.13}$$

Then, (4.6) and (4.7) are reduced to the following two ordinary differential equations and one conservation relation [6],

$$\frac{dU}{d(ln\xi)} = \frac{G(U, C)}{D(U, C)} \tag{4.14}$$

$$\frac{dC}{d(ln\xi)} = \frac{F(U, C)}{D(U, C)} \tag{4.15}$$

where

$$D(V, C) = C^2 - (1 - U)^2 \tag{4.16}$$

$F(U, C)$
$$= C \left\{ (1 - U)\left(\frac{1}{\alpha} - U\right) + U[\lambda + (\gamma - 1)(U - 1)] - C^2 + \frac{\varepsilon}{2\gamma} \frac{C^2}{U - 1} \right\} \tag{4.17}$$

$$G(U, C) = U(1 - U)\left(\frac{1}{\alpha} - U\right) - C^2[3U + (\kappa - 2\lambda)/\gamma] \tag{4.18}$$

$$\lambda = \frac{1}{\alpha} - 1, \; \varepsilon = \kappa(\gamma - 1) + 2\lambda \tag{4.19}$$

And the conservation law provides the density profile as follows.

$$N(\xi) = K_3 \left(\alpha \xi^{1/\alpha} C\right)^A (1 - U)^B, \tag{4.20}$$

$$A = \frac{\mu(\kappa + 3)}{\beta}, \; B = \frac{(\kappa + \mu\lambda)}{\beta}, \; \mu = \frac{2}{(\gamma - 1)}, \beta = 3 - \mu\lambda \tag{4.21}$$

where K_3 is constant.

These equations are used by **Guderley** to solve the shock wave converging to the center and reflected by the center in the spherical geometry [9]. It is amazing to know

that he solved this problem in 1942 [9]. Almost the same time, **Taylor and Sedov** has independently solved the problem of the blast wave, which is the shock dynamics of point source explosion in air [10–12]. In this chapter, let us briefly review the two cases relating to the laser-driven implosions and blast waves. The first one is isobaric and isochoric implosion, and the second one is Taylor-Sedov explosion.

4.3 Self-Similar Implosion (Isobaric)

The mathematical method proposed by Guderley is applied to obtain an implosion dynamics to form almost constant pressure with higher temperature at the center behind the reflected shock wave at the maximum compression time [13]. The basic equations are (4.5, 4.6, and 4.7). In the implosion phase, we find the solution with the density like Fig. 4.2b, while spatial profile of the entropy increasing from the rear to the front of the imploding shell, so that the high-temperature with relatively low-density central core is expected. The free parameter of κ in (4.12) is set $\kappa = 3$.

The general properties of coupled differential Eqs. (4.14) and (4.15) is studied. At first

$$D = 0, \ C = -U + 1 \ and \ U - 1 \tag{4.22}$$

$D = 0$ gives a singularity condition. Integrating (4.14) and (4.15) on these lines, the derivative of U and C diverges except for $G = 0$ *and* $F = 0$. This means if we can find the point in the (U, C) plane where $G = F = 0$, the integration can be proceeded normally. This point is also a singular point (S).

Solving the algebraic couple equations

$$G(U, C; \alpha) = 0 \tag{4.23}$$

$$F(U, C; \alpha) = 0 \tag{4.24}$$

on the line (4.22), it is possible to obtain the singular point (S) in a form.

$$\alpha = \alpha(U_s, C_s) \tag{4.25}$$

In the isobaric implosion [13], it is found that $\alpha = 0.7$ gives the expected solution with reasonable profiles. In finding the exponent as an eigen value problem, the following integral is solved in (U, C) space with a trial value of α from (4.25).

$$\frac{dU}{dC} = \frac{G(U, C; \alpha)}{F(U, C; \alpha)} \tag{4.26}$$

Fig. 4.6 The integral trajectories to allow the self-similar solution of isobaric implosion and explosion dynamics in (U, C) space. The implosion (t < 0) is in U > 0 region and explosion (t > 0) is in U < 0 region. Reprinted with permission from Ref. [6]. Copyright 1998 by Oxford University Press
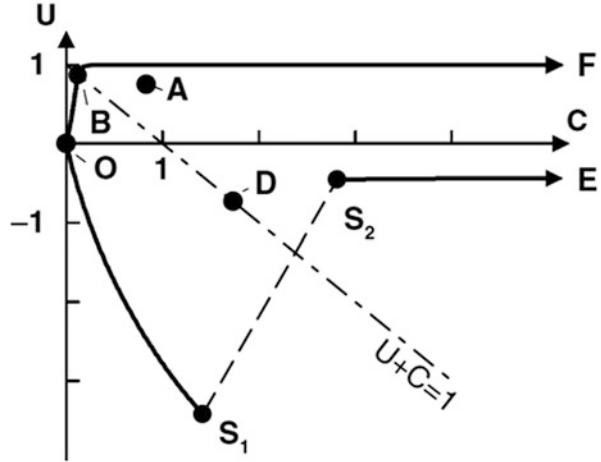
It is concluded in [13] that the integration path of implosion phase (t < 0) and explosion phase (t > 0) should take the path as shown in Fig. 4.6. The point B and D are the singular points.

In the implosion phase (t < 0), the integration path from F ($r \rightarrow 0$) to B to O ($r \rightarrow \infty$) gives the solution. In the explosion phase (t > 0), the high-temperature central core is $E(r \rightarrow 0)$ to the rear of the reflection shock S_1 to the state in front of the shock wave S_2 connecting to the central high-temperature core E ($r \rightarrow 0$). Note that the velocity is defined as in (4.10) and U > 0 in t < 0 means the velocity is negative, namely in implosion phase. For t > 0, the strong shock jump from the RH relation is assumed, and the fluid is strongly decelerated by the shock from $U \approx -3.5$ to $U \approx -0.5$.

It is important to know the properties of the singular points in (U, C) plane. It is easily found that the singular point B in Fig. 4.6 is the **saddle point** and the integration path can cross the singular line (4.22) only the path shown in a stretched view Fig. 4.7 near the singular point B. It shows a general property of integration paths started from different points in (U, C) plane. The point B is indicated as the point S, the saddle point in Fig. 4.7. We found that this is the same as the saddle point in Fig. 3.32.

On the other hand, the singular point of O, where U = C = 0 is the other type of singular point. It is a **node point.** Near the node point, all integral paths converge to the node point or all paths can start all direction from the node point. In the present isobaric implosion, the solution should be an integral path from the point O to smoothly transit the singular point B on the saddle path shown with orange in Fig. 4.7. Then, all normalized functions, $U(\xi)$, $C(\xi)$, and $N(\xi)$ are obtained by numerically integrating (4.14) and (4.15).

Fig. 4.7 A schematic of a saddle point in the integration paths in two-dimensional space. The integration path can smoothly continue over the saddle point as the orange line
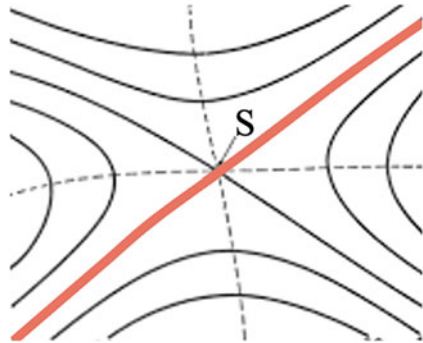
Fig. 4.8 The density profiles given by the self-similar solution for the isobaric implosion. Reprint with permission from Ref. [13]. Copyright 1998 by American Physical Society
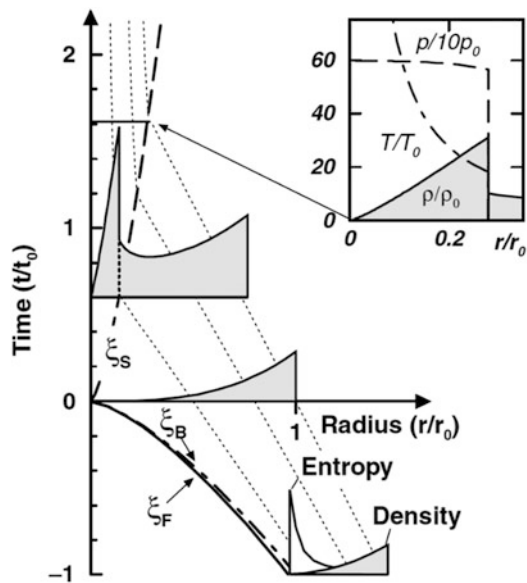
The time evolution of the density profile is given as shown in Fig. 4.8 [13]. Note that the solution is a hollow shell with the front $\xi_F = 0.96$ and the shock front $\xi_S = 0.198$. Their trajectories are plotted with the dashed lines, $r(t) = |t|^\alpha \xi$, where $\xi = \xi_F$ and ξ_S. To make the central hot spark, the density and entropy profiles in the implosion phase is assumed at $t = -1$ as shown in Fig, 4.8. At the time of void closure ($t = 0$), the solution continues to the explosion phase ($t > 0$). A strong shock wave traveling to the outward is generated in the still-imploding fluid. The spatial profiles of the density, temperature, and pressure after the implosion are shown in the inset figure at $t = 1.6$. So-called isobaric central ignition profile is formed.

4.4 Guderley Self-Similar Solution

The Guderley solution is also an implosion dynamics. The difference from the above is that in the implosion phase, a strong shock wave is assumed to travel in a uniform gas ($\kappa = 0$). Then, it is found that the eigen-value is $\alpha = 0.688$ [9].

In this case, the self-similar solution starts from the shock front ($\xi = 1$). The imploding shock front is the point "A" in Fig. 4.6 obtained by the RH relation for strong shock limit. The integral path has to come to the singular point (saddle point) on the line $U + C = 1$ same as the previous case. The integration path goes to the point "O". In the explosion phase, it takes the path in negative U and jump from "S_1" in the negative U to "S_2" in the positive U, then it goes to the large C region in Fig. 4.6.

In Fig. 4.9, the time evolution of the density in (r, t) space is shown. The density behind the converging shock wave increases with the radius because of spherical geometry effect. The density becomes flat at t = 0 with negative velocity, but $U = 0$ *in* $0 < \xi < 1$. Then, the reflected shock is produced and propagates to have the snap shot at t = 1 in Fig. 4.9. The maximum density is $32\rho_0$.

It is noted that hydrodynamic stability is studied to this Guderley solution numerically. It is reported that the 3-D perturbation at the shock front oscillates and relatively stable to the hydrodynamics instability [7].

Fig. 4.9 The density profiles given by the self-similar solution of converging shock wave in gas with constant density in spherical geometry, Guderley solution. Reprinted with permission from Ref. [6]. Copyright 1998 by Oxford University Press
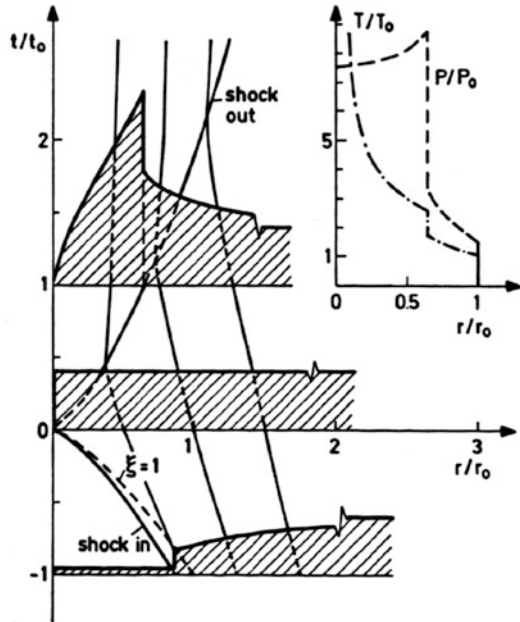
4.5 Isochoric Implosion

In Ref. [14], a self-similar implosion to provide with a uniform density profile behind the reflected shock is tried to find. This is the modification of the above isobaric implosion, and such uniform density is called "**isochoric**", **isochoric implosion**. The initial condition of the entropy is almost null at the front with finite implosion velocity. This indicates that the front point ($\xi = 1$) should be (U, C) = (1, 0). Then, the integration path has to pass the saddle point on U + C = 1 in Fig. 4.6 to converge to the point "O".

In the explosion phase (t > 0), the shock wave travel outward while keeping high-density behind the shock. We find a solution that the produced shock propagates outward with falling fluid in front and compressed fluid behind. In Ref. [14], the solution is found by starting the mathematical definition used in Ref. [8], where the similarity variable $x = t/r^{\lambda}$. This corresponds to $\alpha = 1/\lambda$ in the form of $\xi = r/t^{\alpha}$.

From the asymptotic solution given in [6], κ is found to be given as a function of $\alpha = 1/\lambda$ in the form.

$$\kappa = 2(1/\alpha + 1)/(\gamma - 1) \tag{4.27}$$

This relation is obtained by requiring the density is flat in the asymptotic relation at t = 0. The eigen-value $\alpha = 0.789$ is obtained. Then, the density profile must be steep as $\kappa = 6.801$ to allow very low adiabat at the front.

The time evolution of the density from the resultant self-similar solution is plotted in Fig. 4.10 for the implosion phase (left) and explosion phase (right). About 400 times the initial density is achieved with almost flat profile.

In this paper, the authors tried to find the target design so that the high-density compression is approximately realized by laser irradiation on a spherical target. They try to find the laser pulse shape for a standard laser fusion target shown in Fig. 4.11. To form the initial condition with U, C, and N profiles in Fig. 4.10, one Mbar pressure is loaded at the DT ice surface neat t = 10 ns. The optimized radius-time evolution of all fluid elements obtained with HYDRA code is plotted in Fig. 4.12
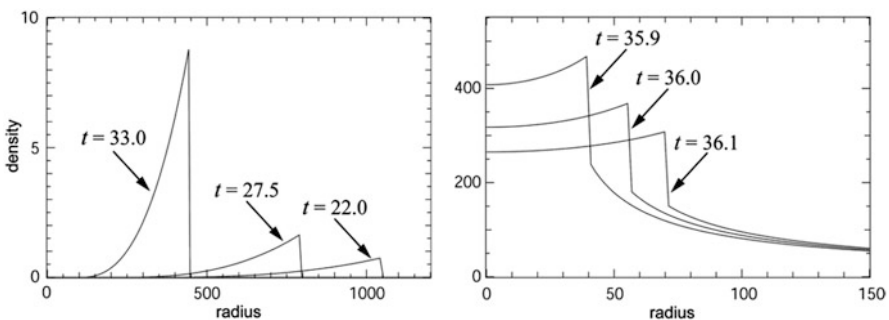
Fig. 4.10 Time evolution of isochoric implosion (left) and explosion (right) based on a self-similar solution. Reprinted with permission from Ref. [14]. Copyright by IAEA

Fig. 4.11 The optimized target structure to realize an isochoric implosion with HYDRA 1-D simulation code. Reprinted with permission from Ref. [14]. Copyright by IAEA
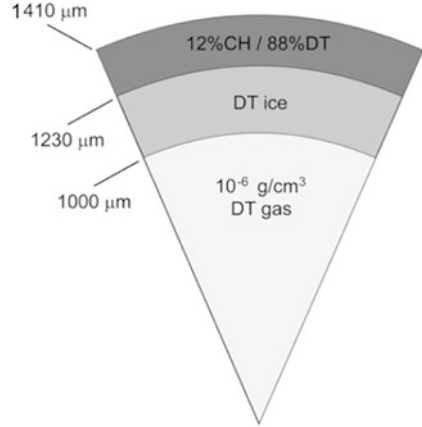
Fig. 4.12 Flow diagram and the pressure history of the optimized implosion to realize the isochoric density profile after the maximum compression. Reprinted with permission from Ref. [14]. Copyright by IAEA
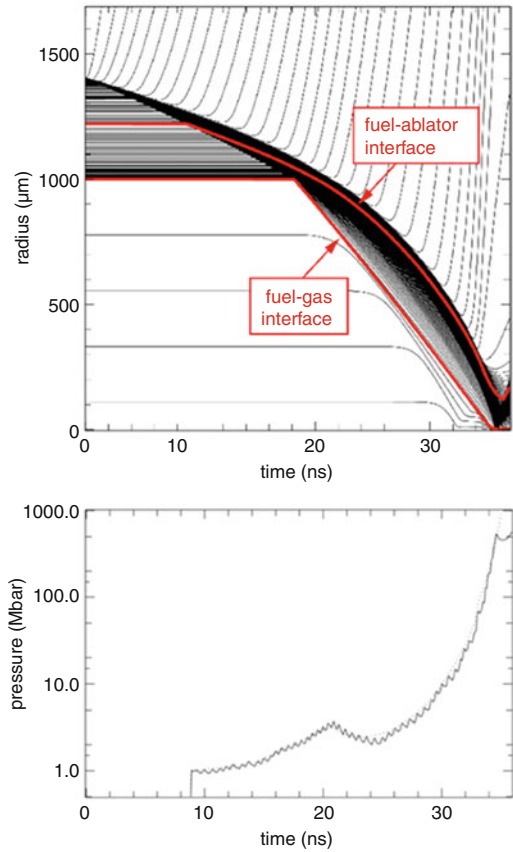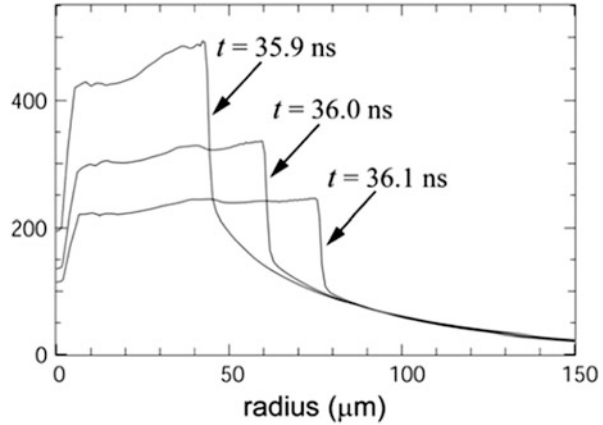
with the time evolution of corresponding pressure at the out surface of the DT ice. To keep the pressure reproduces the self-similar solution, 700 Mbar pressure is generated at the end of the optimized tailored laser pulse.

The initial shock wave travels in the ablator and collides the DT ice surface (t = 10 ns). Then, the rarefaction wave starts to expand to the inside of the shell around t = 19 ns to decrease the density like in Fig. 4.12. The rarefaction wave front comes to the DT ice surface to decrease the pressure near t = 20 ns. With continuous increase of laser power, the pressure increases to keep the self-similar solution. It is impossible to control the evolution after t > 0 in the self-similar solution. Actually, HYDRA simulation gave the density evolution after the shock formation as shown in Fig. 4.13. It is clear that almost the same profile as the self-similar solution in Fig. 4.10 is realized. The optimized laser pulse shape is given in [14], which is a highly tailored pulse with intensity from ~3 × 10^{12} to ~4 × 10^{15} *W/cm^2*. It is concluded that this isochoric implosion can be designed with the total laser energy of ~500 kJ.

4.6 Self-Similar Solution – Homogeneous Dynamics

In early time of laser fusion research, adiabatic self-similar solutions have been studied for the implosion and the final stagnation phases. R. **Kidder** has published a series of papers to show self-similar solutions of hydrodynamics of spherical implosion by tailored adiabatic compression [15]. Such solution is called **homogeneous adiabatic flow**. Hydrodynamic stability is also studied to the self-similar solution of implosion. The solution is applied to study the physics of ignition and nuclear burn as a pioneering work in laser fusion [16]. The homogeneous adiabatic flow is also applied to model the stagnation dynamics near the maximum compression of implosion [17] to study the hydrodynamic stability of the final compression phase.

Both of self-similar solutions are important to study the dynamics of implosion and analytically study the stability of the solutions. The self-similar solution and its stability analysis can be useful not only to design the implosion dynamics but also to use the **verification and validation** (V&V). The self-similar solutions to be discussed here is obtained by the method of variable separation, not using the similarity variable in (4.9). The mathematics to obtain the self-similar solutions in this case is easier than the previous case, since the solution is adiabatic and not necessary to take into account the jump by shock wave.

Here, two different self-similar solutions are derived for adiabatic assumption, Namely, it is possible to apply any cases with different spatial distribution of entropy for each fluid element in the imploding or stagnating plasmas. The solution of the stagnation dynamics is explained at first to derive the equations, and the implosion dynamics is explained by use of the same equation with different separation constant.

4.6.1   Stagnation Dynamics

The self-similar solutions for the spherical geometry studied so far always have singularity at t = 0 and we allow the fact that the solutions diverge to infinity. Of course, such divergence is allowed only mathematically and we have to consider neglected physics such as thermal conduction, viscosity, etc. We assume, however, that even such non-adiabatic physics plays important role near t = 0, the solution will be approximately continuous over the time t = 0.

In laser plasmas, another type of self-similar solution is used to describe the final implosion phase, so-called stagnation phase [1]. This solution models the hydrodynamics seen in Fig. 3.29. This self-similar method is introduced to model supernova explosion hydrodynamics [18]. In this case, the similarity variable in the form of (4.9) is not assumed, but ordinary differential equation is found by the mathematical method of separation of variables. Instead of Euler type basic equations in (2.23, 2.24, and 2.25), Lagrangian type Eqs. (2.20, 2.21, and 2.22) is used to obtain the trajectory of each fluid element $R(t, r_0)$, where r_0 is Lagrange coordinate of each fluid element. So, the density $\rho(t, r)$, flow velocity $u(t, r)$, and pressure $P(t, r)$ are assumed in a functional form of $A(r_0)B(t)$. This means the Lagrangian coordinate r_0 corresponds to the similarity variable ξ.

In spherical one-dimensional system, Lagrangian type Eqs. (2.20, 2.21, and 2.22) without the force and heat source can be given in the form with the Lagrangian coordinate $R(t, r_0)$,

$$\frac{d}{dt}\rho + \frac{\rho}{R^2}\frac{\partial}{\partial R}\left(R^2 u\right) = 0 \tag{4.28}$$

$$\rho \frac{d}{dt}u = -\frac{\partial}{\partial R}P \tag{4.29}$$

$$\frac{d}{dt}(P \rho^{-\gamma}) = 0 \tag{4.30}$$

The radius R is the radius of fluid element located at $r = r_0$ at $t = 0$ and defined as

$$\frac{d}{dt}R = u \tag{4.31}$$

The time evolution of the radius of a fluid element is defined with the scale function $F(t)$, corresponding to the above $B(t)$. We try to model the stagnation dynamics shown in Fig. 3.29. Smoothing the shock traveling effect in the stagnation dynamics, it is possible to obtain the functional form of F(t) so that the kinetic energy is converted to the thermal pressure to re-bounce the converging dynamics to our-ward.

Setting $t = 0$ at the maximum compression and the radius of each fluid element to be ξ, the time dependence of each Lagrange mesh is defined as

$$R(t, \xi) = \xi F(t) \tag{4.32}$$

Then, $F(t = 0) = 1$ is required.

It is easily to derive the following relation from conservation law of mass and entropy.

$$\rho(t, \xi) = \Phi(\xi)F(t)^{-3} \tag{4.33}$$

$$P(t, \xi) = \Pi(\xi)F(t)^{-3\gamma} \tag{4.34}$$

where $\Phi(\xi)$ and $\Pi(\xi)$ are the profiles of density and pressure at $t = 0$. For the case of deceleration to the center, the equation to the time evolution is derived from (4.29) in the form.

$$F^{3\gamma - 2}\frac{d^2}{dt^2}F = \frac{1}{\tau^2} \tag{4.35}$$

where τ is a characteristic time constant for the stagnation dynamics. It is order of nano-sec in laser implosion and sec in supernova explosion.

We can assume any reasonable density profile $\Phi(\xi)$ at the maximum compression, while the pressure should satisfy the force balance relation,

$$\frac{d}{d\xi}\Pi(\xi) = -\frac{\xi}{\tau^2}\Phi(\xi) \tag{4.36}$$

It is easy to solve (4.35) and for the case with $\gamma = 5/3$, we obtain.

Fig. 4.14 Normalized t-r
diagram of fluid elements in
the deceleration phase,
where t = 0 is the maximum
compression
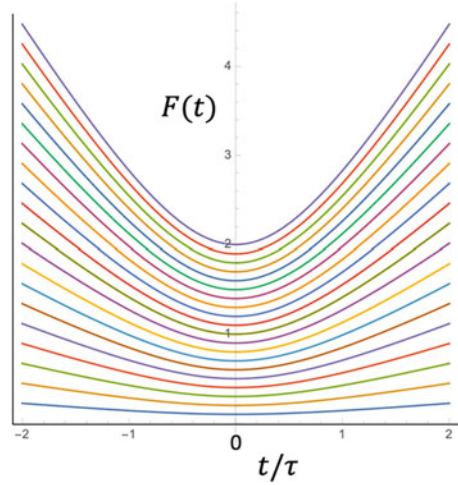
$$F(t) = \left\{ 1 + \left(\frac{t}{\tau}\right)^2 \right\}^{1/2} \tag{4.37}$$

One can easily confirm that this $F(t)$ is a good approximation of the dynamics of the
contact surface in Fig. 3.29. It provides approximate model for convergence (t < 0)
and expansion (t > 0) as shown in $[t/\tau, F(t)]$ diagram (t-r diagram) in Fig. 4.14.

4.6.2 Kidder's Implosion Dynamics

In 1974, just after the proposal of tailored implosion for laser fusion by Nuckolls
et al., Kidder proposed to use a self-similar solution for theoretical design of laser
implosion to achieve extremely high-density [16]. It is the theory of homogeneous
isentropic compression and its application to laser fusion. Homogeneous compres-
sion indicates that the target material with any layered structure converges uniformly
with a constant entropy S given as the initial condition. The solution allows any
entropy distribution in space.

The equations are same from (4.28) to (4.34), while the variable separation
constant in (4.35) has negative sign and (4.37) becomes as follow.

$$F(t) = \left\{ 1 - \left(\frac{t}{\tau}\right)^2 \right\}^{1/2} \tag{4.38}$$

(4.38) is rewritten in the relation of circle in $(t/\tau, F)$

$$F^2 + (t/\tau)^2 = 1 \tag{4.39}$$

It is clear that the fluid is at rest at the beginning, t = 0, and $dF/dt \rightarrow \infty$ at $t/\tau = 1$.

Fig. 4.15 Normalized t-r diagram of fluid elements in uniform implosion dynamics
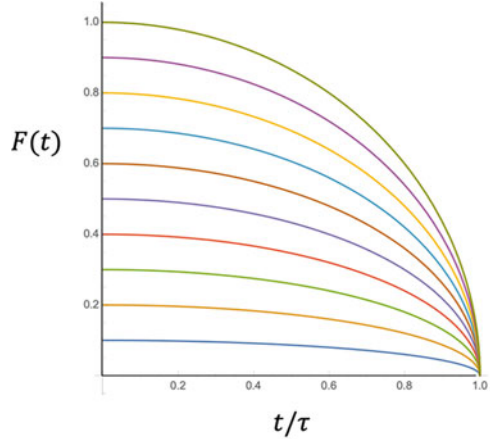
At the maximum compression, $t = \tau$, implosion velocity becomes infinity and all fluid elements converge at the central singular point. Of course, this is mathematical solution and density of (4.33) and pressure (4.34) becomes infinity.

In Fig. 4.15, virtual trajectories of fluid elements located in normalized space, ξ/R_0, is plotted, where R_0 is the initial radius of target and τ is regarded as the implosion time. This solution can be applicable to any density profile at t = 0, for a spherical solid ball, gas target, shell target, and so on. The application of the solution to laser fusion experiment, the critical issues are

1. How to generate the initial condition satisfying (4.36).
2. How high-density can be achieved even if the finite maximum pressure is demanded.
3. How to generate the ablation pressure as shown in Fig. 4.12.

Kidder has applied the solution of a hollow shell DT target to study the possible scenario, such as required laser pulse shape and its total energy, for demonstration of ignition, burn, and fusion energy production [19].

4.7   Self-Similar Solution of Ablation Dynamics

It is already shown that the deflagration and isothermal rarefaction waves are generated, when an intense laser is absorbed by solid target. Then, it is assumed that the deflagration wave is in stationary state. It is better if we can find an self-similar solution of the ablation structure valid to describe the time evolution of ablation plasma. The author found the self-similar solution of the ablation dynamics to the basic equations of one-fluid two-temperature fluid model [20], while the paper was published in Japanese. Therefore, I would like to show the self-similar solution

for the ablating plasma. The nonlinear electron heat conduction and electron-ion temperature relaxation are included within the ideal plasma assumption.

We assume that the plasma is fully ionized with ion charge Z and its mass m_i. We solve (2.105, 2.106, 2.107, and 2.108) to the ion number density n, velocity u, and ion and electron temperatures, T_i and T_e. The specific heat ratio $\gamma = 5/3$ is assumed. Then, $\rho = m_i n$, $\varepsilon_i = 3/2(T_i/m_i)$, $\varepsilon_e = 3/2(ZT_e/m_i)$. We try to find a self-similar solution in the plane geometry in the x-coordinate. Then, it is possible to reduce them to the following four coupled equations after neglecting source terms and ion thermal conduction much smaller than electron one.

$$\frac{\partial n}{\partial t} + \frac{\partial (nu)}{\partial x} = 0 \tag{4.40}$$

$$\frac{\partial u}{\partial t} + u\frac{\partial u}{\partial x} + \frac{1}{m_i n}\frac{\partial}{\partial x}\left[n(ZT_e + T_i)\right] = 0 \tag{4.41}$$

$$\frac{\partial T_i}{\partial t} + u\frac{\partial T_i}{\partial x} + \frac{2}{3}T_i\frac{\partial u}{\partial x} - \nu_0\frac{n(T_e - T_i)}{T_e^{\frac{3}{2}}} = 0 \tag{4.42}$$

$$\frac{\partial T_e}{\partial t} + u\frac{\partial T_e}{\partial x} + \frac{2}{3}T_e\frac{\partial u}{\partial x} + \nu_0\frac{n(T_e - T_i)}{ZT_e^{\frac{3}{2}}} - \frac{2}{3n}K_0\frac{\partial}{\partial x}\left(T_e^{\frac{5}{2}}\frac{\partial}{\partial x}T_e\right) = 0 \tag{4.43}$$

where ν_0 *and* K_0 are physical constants defined in (2.109) and (2.110) with Coulomb log. In the following calculations we solve the case with $Z = 1$ and $ln\Lambda = 10$ for simplicity.

It is important to note that if we try to find the solution with a given density at the ablation front, it is hard to obtain the self-similar solution because the density is fixed by this condition. Instead, we use the property of the ablation front that the density, velocity, and temperature profiles are very steep and the ablation structure may not be affected even if we adopt an ideal condition. The mass ablation rate, nu, and ablation pressure, nT_e and nT_i, are finite, while n is infinity and u, T_e, and T_i are null. This assumption is acceptable as seen, for example, in Figs. 3.23 and 2.24. Therefore, we find a self-similar solution satisfying the conditions.

$$\begin{cases} n = \infty, & u, T_e, T_i = 0 \\ nu, n(T_e + T_i) : finite \end{cases} at\ x = 0 \tag{4.44}$$

4.7.1   Dimensional Analysis

The dimensional analysis of (4.40)–(4.43) requires the following dependence to the coordinate x and time t.

$$u \sim \frac{x}{t}, \ T_e, T_i \sim \left(\frac{x}{t}\right)^2 \tag{4.45}$$

In the present analysis, the temperature relaxation and electron thermal conduction by Coulomb binary collision are determined by the collision time discussed in Sect. 2.1. They both are function of the collision frequency ν in the form.

$$\nu \propto \frac{n}{T_e^{3/2}} \tag{4.46}$$

Since (4.40) and (4.41) are homogeneous to the density n, (4.46) gives the dimension of the density n as the condition that a self-similar solution is possible. Inserting $\nu \sim 1/t$ to (4.46), it is found that the density should be proportional in the form.

$$n \sim \frac{x^3}{t^4} \tag{4.47}$$

We introduce the similarity variable ξ same as (4.9).

$$\xi = \frac{x}{t^\alpha} \tag{4.48}$$

Then, we can assume the following functional form.

$$n = K_0 m_i^{5/2} t^{3\alpha - 4} g(\xi) \tag{4.49}$$

$$u = t^{\alpha - 1} v(\xi) \tag{4.50}$$

$$T_i = m_i t^{2(\alpha - 1)} \tau_i(\xi) \tag{4.51}$$

$$T_e = m_i t^{2(\alpha - 1)} \tau_e(\xi) \tag{4.52}$$

Inserting (4.49, 4.50, 4.51, and 4.52) into (4.40, 4.41, 4.42, and 4.43), the following coupled ordinary differential equations are obtained.

$$(v - \alpha\xi)g' + [v' + (3\alpha - 4)]g = 0 \tag{4.53}$$

$$(v - \alpha\xi)v' + \frac{1}{g}[g(\tau_e + \tau_i)]' + (\alpha - 1)v = 0 \tag{4.54}$$

$$(v - \alpha\xi)\tau_i' + \left[\frac{2}{3}v' + 2(\alpha - 1)\right]\tau_i - \mu_0 \frac{g(\tau_e - \tau_i)}{\tau_e^{3/2}} = 0 \tag{4.55}$$

$$(v - \alpha\xi)(\tau_e + \tau_i)' + \left[\frac{2}{3}v' + 2(\alpha - 1)\right](\tau_e + \tau_i) - \frac{2}{3g}\left(\tau_e^{\frac{5}{2}}\tau_e'\right)' = 0 \tag{4.56}$$

where the dash $(')$ means the derivative by ξ. In (4.55), $\mu_0 = m_i K_0 \nu_0 \ (=6.417)$.

4.7.2   Integration

We have to solve the coupled Eqs. (4.53, 4.54, 4.55, and 4.56) by starting from the boundary shown in (4.44). To numerically integrate them, approximated analytic solutions are necessary near the ablation front (x = 0). By use of the approximate boundary condition (4.44), (4.53, 4.54, 4.55, and 4.56) reduce to the following equations for $\xi \approx 0$.

$$vg = J_0 : const. \tag{4.57}$$

$$g(\tau_e + \tau_i) = P_0 : const. \tag{4.58}$$

$$\tau_e = \tau_i \tag{4.59}$$

$$v(\tau_e + \tau_i)' + \frac{2}{3}v'(\tau_e + \tau_i) - \frac{2}{3g}\left(\tau_e^{\frac{5}{2}}\tau_e'\right)' = 0 \tag{4.60}$$

It is possible to set $J_0 = 1$ by re-scaling the definition of ξ, but P_0 should be determined so that the solution is acceptable. As we see below, the constant P_0 is determined as the eigen-value problem so that the solution satisfies the boundary condition at large ξ point.

Now, it is possible to solve (4.60) for $\xi \ll 1$, and the following relation is obtained.

$$\tau_e = \tau_i = \left(\frac{25}{2}\xi\right)^{2/5} \tag{4.61}$$

$$g = 1/v = \frac{P_0}{2}\left(\frac{25}{2}\xi\right)^{-2/5} \tag{4.62}$$

Consider an asymptotic solution for $\xi \to \infty$. Since we are interested in a solution with finite total energy of the ablation plasmas, namely the heat flux from $\xi \to \infty$ should be finite.

$$\tau_e^{\frac{5}{2}}\tau_e' = S_0 \ (\xi \to \infty) \tag{4.63}$$

where S_0 is a constant to be determined after integration. The boundary condition (4.63) is satisfied with the asymptotic solution of the electron temperature.

$$\tau_e \propto \xi^{\frac{2}{7}}, \ \tau_i = 0 \ (\xi \to \infty) \tag{4.64}$$

Consider how the integration path is determined by refereeing the same type of plane of Fig. 4.6. In the present case, we consider the velocity and temperature diagram (V, T) as defined below.

$$g(\xi) = \frac{\Gamma(\xi)}{\xi}, \; v(\xi) = \xi V(\xi), \; \tau_e(\xi) + \tau_i(\xi) = \xi^2 T(\xi) \qquad (4.65)$$

Transform (4.53) and (4.54) to the coupled equations for the new variables.

$$(V - \alpha)\frac{dln\Gamma}{dln\xi} + \frac{dV}{dln\xi} = 4(1 - \alpha) \qquad (4.66)$$

$$T\frac{dln\Gamma}{dln\xi} + (V - \alpha)\frac{dV}{dln\xi} = -\frac{d}{d\xi}(\xi T) - (V - 1)V \qquad (4.67)$$

Consider the property of (4.66) and (4.67) in the asymptotic limit ($\xi \to \infty$). From the asymptotic relation of (4.64), T and the pressure term in (4.67) vanishes.

$$T \propto \xi^{-12/7}, \frac{d}{d\xi}(\xi T) \propto \xi^{-12/7} \to 0 \; (\xi \to \infty) \qquad (4.68)$$

Eliminating the velocity derivative term in (4.66) and (4.67), we obtain the following equation to the density.

$$\frac{dln\Gamma}{dln\xi} = \frac{(V - 1)V + 4(1 - \alpha)(V - \alpha)}{(V - \alpha)^2 - T} \qquad (4.69)$$

To satisfy the rarefaction wave condition that the density decreases monotonically with increase of ξ.

$$\frac{dln\Gamma}{dln\xi} < 0 \; (\xi \to \infty) \qquad (4.70)$$

For the case with $\alpha > 9/8$, the numerator is positive for any value of V and the condition (4.70) requires

$$T > (V - \alpha)^2 \qquad (4.71)$$

In this case, the physically reasonable solution is possible only when the integration path from subsonic near ablation front continuously goes to supersonic region of asymptotic flow with the path shown with the dashed lines in Fig. 4.16 This requirement gives unique solution for a given α (>9/8). It is also clear from () that the density decreases exponentially for $\xi \to \infty$. It is also possible to obtain the solution with exponential decay for $1 < \alpha < 9/8$.

On the other hand, self-similar solution for $\alpha < 1$, from (4.49, 4.50, 4.51, and 4.52) it is clear that at t = 0,

$$T_e, T_i, u \to \infty \qquad (4.72)$$

Fig. 4.16 Similarity functions velocity and temperature. From both boundary conditions, the integration path is found to take the path shown with dotted line to converge the singular point (α, 0)
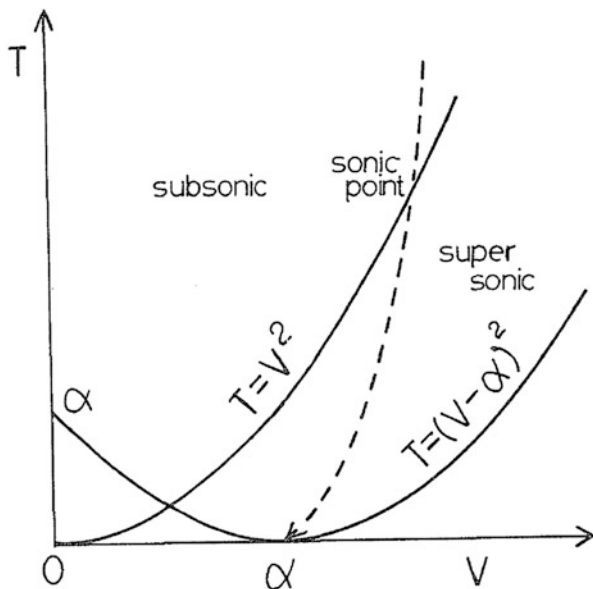
The solution has singularity at t = 0. It is important to know that the solutions of implosion dynamics of the self-similar solutions in this Chapter have been obtained with $\alpha < 1$.

In [20], further new variables are introduced to solve (4.53, 4.54, 4.55, and 4.56) numerically with functions of slowly varying in the $ln\xi$-ccoordinate, but we skip discussing this method here.

4.7.3 Classical Absorption Case ($\alpha = 5/4$)

Although the heat flux is deposited near the critical surface, for example, short wavelength laser is irradiated with not so high-intensity, where the classical absorption is dominant process to hear the electron. Here we assume that the heat flux coming from $\xi \rightarrow \infty$ is approximately equal to the laser energy flux. The heat flux is given as

$$Q = K_0 T_e^{5/2} \frac{\partial}{\partial x} T_e \propto t^{6\alpha - 7} S_0 \tag{4.73}$$

where S_0 is defined in (4.63) and obtained after solving the self-similar solution. It is clear that we can obtain the solution for the constant energy deposition for the case with $\alpha = 7/6$. In Ref. [20], the classical absorption for DT plasma is assumed to

Fig. 4.17 A self-similar solution of laser ablation plasma for the case of $\alpha = 5/4$ corresponding to the classical absorption of a constant intensity laser irradiation. The self-similar solution can be found by assuming that the density is infinite and the others are null in the moving frame, while the product pressure and mass ablation rate are kept finite. The profiles are normalized density (g), flow velocity (v), electron and ion temperatures (τ_e, τ_i) and electron heat flux (S)
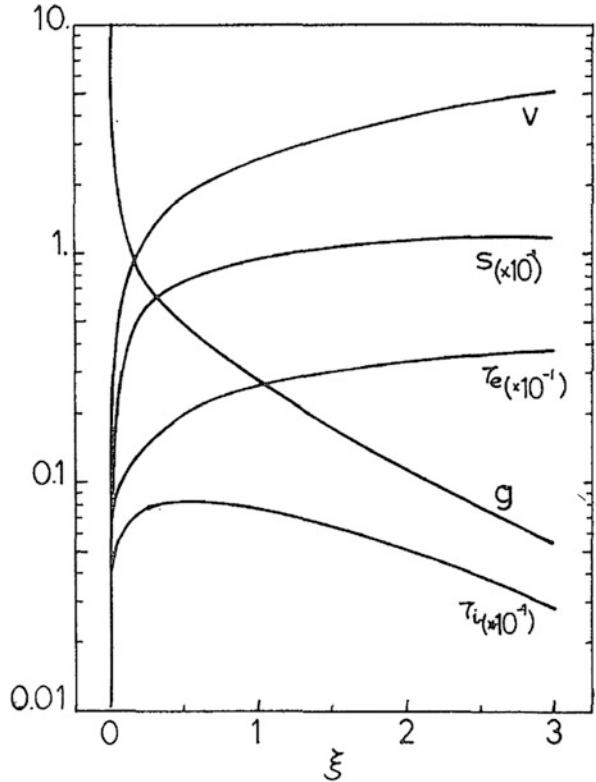
evaluate the absorbing power for a constant laser intensity. It is shown that $\alpha = 5/4$ is approximated [20].

In Fig. 4.17, nondimensional ablation structure is shown after solving the eigen value problem to the normalized pressure P_0. It is found that $P_0 = 2.7227$. This is regarded better solution than the stationary solution shown in the previous chapter, while the self-similar solution gives approximately the same scaling laws for the ablation pressure and so on as a function of absorbed laser intensity within our interest for laser plasmas.

4.8 Blast Wave (Taylor-Sedov Solution)

After the implosion and energy concentration at the compressed small central area, it is also important to know how this energy spreads hydrodynamically in space spherically. It is surprising that with some idealization of the problem, it is possible to find another self-similar solution as mentioned above. This is well known as the one-dimensional mathematical solution in spherically symmetry when a point

energy source is released spontaneously at the center (r = 0). This is called a **blast wave** and a spherical wave with a strong shock front propagating outward.

It is well summarized on a brief history of study of the blast wave in Ref. [21], so let us follow the description. A blast wave follows the rapid and localized release of a large amount of energy in a medium. The physics community got seasonably interested in the dynamics of such shocks in air in the early 1940s. Taylor [10], von Neumann [12] and Sedov [11] independently understood that, because of the global conservation of mass and energy, the extension R of the blast had to grow with time like a power law (time)$^\alpha$ with $\alpha = 2/5$ [or 2/(N + 2) in dimension N. From a few publicly available snapshots of the blast at different times, Taylor could estimate within 10% the strength of the Trinity detonation in 1945, at the time classified information [22].

Remarkably, the hydrodynamic description of the flow inside the blast, now known as the **Taylor–von Neumann– Sedov solution** (or **Taylor-Sedov solution**), is self-similar in time, depending only on the rescaled radial distance r = R(t). This similarity is of the first kind [22], i.e., driven by global invariants, and all exponents can be derived by dimensional analysis. This solution found widespread relevance beyond its initial realm, notably in plasma physics to describe **laser-induced shocks** and in astrophysics for the evolution of **supernova remnants**.

When the energy of the explosion is E_0 and the density of the surrounding gas of uniform density is ρ_0, the basic equations are one-dimensional equations of (4.5, 4.6, and 4.7). In this case, a strong shock wave propagates in the gas. Since the total energy of blast wave should conserve, the dimensional analysis requires the relation:

$$E_0 \sim \rho u^2 r^3 \tag{4.74}$$

Inserting (4.10, 4.11, and 4.12) into (4.74), the similarity valuable is obtained as

$$\alpha = \frac{2}{5}, \ \xi = \left(\frac{\rho_0}{E_0}\right)^{1/5} \frac{r}{t^{2/5}} \tag{4.75}$$

Here uniform density K = 0 is assumed.

The radius of the strong shock wave front is defined as

$$R(t) = \xi_0 \left(\frac{E_0}{\rho_0}\right)^{1/5} t^{2/5} \tag{4.76}$$

where ξ_0 gives the shock front and ξ_0 is the eigenvalue of this mathematical problem.

The equations to be solved are the same as (4.14) and (4.15). In the present case, the eigen value of the consistent solution is determined so that the following energy conservation is satisfied.

$$E_0 = \int_0^R 4\pi r^2 \rho \left(\varepsilon + \frac{u^2}{2}\right) dr \tag{4.77}$$
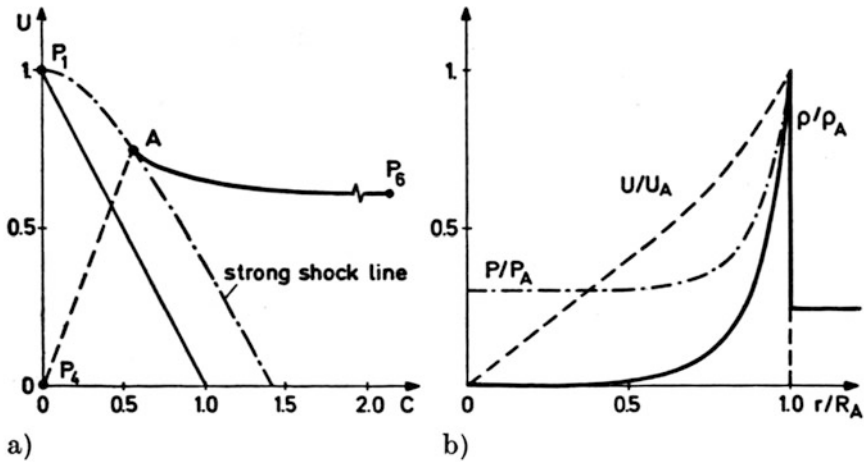
Fig. 4.18 (**a**) Taylor-Sedov solution for a strong point explosion in the U, C plane. Parameters:$\gamma = 5/3$, $\alpha = 2/5$, $K = 0$. (**b**) Density ρ, pressure P and velocity U of the Taylor-Sedov solution as a function of radius r. The label A denotes the values at the shock front. Reprinted with permission from Ref. [6]. Copyright 1998 by Oxford University Press

The integration path in (U, C) plane is shown in Fig. 4.18a [9]. In this case, the shock RH relation allows to jump over the singular curve and the point A in Fig. 4.18a is found to satisfy (3.13). The shocked region finally goes to the node singular point $(U, C) = (0, \infty)$ as shown in the Fig. 4.18a.

The normalized blast wave profile is obtained in Fig. 4.18b. Three quantities abruptly increase at the shock front and the velocity and density disappear at the center. Note that the temperature becomes infinity at the center, and the product pressure of the density and temperature is kept finite.

The calculation has been done with computer, however, in the former Soviet Union where there was no computer, surprisingly Sedov analytically solved the problem and found the eigenvalue. The approximate analytical solution of the eigenvalue is given in the form in [23].

$$\xi_0 = \left[\frac{75(\gamma - 1)(\gamma + 1)^2}{16\pi(3\gamma - 1)} \right]^{1/5} \tag{4.78}$$

The value agrees well with the numerical calculation values by Taylor. In Table 4.1, both results are compared for three different specific heat γ. Both gives reasonable γ-dependence. For the case with large γ, the internal freedom of the gas is at most $N = 3$ (x, y, z translational motions) and $\gamma = (N + 2)/N$ gives $\gamma = 5/3$. Additional freedoms like molecular rotation and vibration yields $N = 5$ and $\gamma = 7/5 = 1.4$. Increase of freedom means more need for thermal energy for all freedoms and the

fraction of the energy going to the shock kinetic energy decreases. The decrease of the eigen-value in Table indicates the shock speed gets slow.

It should be noted that both results give the eigen-value is almost equal to unity and this result encourages us in comparing some experimental result to the theoretical self-similarity. Only with the dimensional analysis, it is reasonable to assume $\xi_0 = 1$ for an approximate solution. Without solving the complicated equations for the spatial profile, it is possible to compare with the experimental data.

Let's calculate the energy partition ratio of the self-similar solution. The fractional ratio of the thermal energy and kinetic flow energy to the explosive energies does not change in time. Although thermal energy escapes as energy such as radiation, kinetic energy is preserved and spreads to space. That proportion is obtained with the following integration

$$F = \frac{\int_0^R 4\pi r^2 \rho \varepsilon \, dr}{\int_0^R 4\pi r^2 \rho \frac{u^2}{2} \, dr} \tag{4.79}$$

The result is obtained as.

$$F \quad = 6.1 \ (\gamma = 1.2), \quad = 3.5 \ (\gamma = 1.4), \quad = 2.5 \ (\gamma = 5/3) \tag{4.80}$$

The ratio of conversion to the internal energy increases as γ approaches unity. The physical reason is clear as already mentions regarding to the Table 4.1. It was $\gamma = (N + 2)/N$, where N is the internal degree of freedom of gas. The greater the degree of internal freedom, the lower the proportion of compatible energy going to the flow kinetic energy.

Let's itemize the features of this solution.

1. Flow velocity is null and the gradient of pressure is also null at the center (r = 0) to satisfy the boundary condition. As the result, the density is also zero at the center.
2. Because the pressure is finite at the center, it turns out that the temperature diverges to infinity.
3. When the blast wave arrives, the delta function-like force $-\partial P/\partial r$ works outward, while the opposite-directional force toward the center works immediately. After a while the force disappears.
4. The solution shows that the temperature becomes infinity at the center cannot happen physically. This is because there is a self-similar solution only by neglecting heat conduction. In fact, in the early time of explosion radiative heat

Table 4.1 The eigen value of self-similar solutions depends on the value of the specific heat γ

$\gamma \rightarrow \xi_0$	Sedov (analytic)	Taylor (numerical)
5/3 = 1.66	1.27	1.15
1.4	1.16	1.03
1.03	0.72	0.897

conduction waves such as X-rays (this is historically called **fireball**) spread and blast wave is generated after a while.

5. Self-similar solution is not applicable at any time, but because the blast wave ionizes surrounding gas, it will cool down while losing energy by radiation such as X-rays from partial ionized plasma. As the density of the blast wave front is higher, it is easier to cool, so the pressure at the front decreases and the kinetic energy is accumulated near the front and shocked matter expands like a shell.

4.9   Laser Blast Wave and Dissipation

4.9.1   Laser Experiments

By focusing and irradiating high-intensity short-pulse laser to a solid target surface placed in gas, the ablating plasma from the solid creates a clean blast wave in the gas as shown in Fig. 4.19a, where the blast wave image is taken by the darkfield shadow imaging [24]. Nd glass laser of 200 J and 5 ns pulse is irradiated on a foil to heat up about 1 keV. The gas is nitrogen gas of 5-torr, and the laser is irradiated from the right. The laser-irradiated target is an aluminum plate. It is measured that the ablating plasma expands with the velocity of 700 km/s. The shock wave is collisional shocks and the white ring in Fig. 4.19a is due to the refraction of the diagnostic laser beam at the shock front with abrupt electron density jump.

In Fig. 4.20, the measured radius of the blast wave is plotted as a function of time. It is seen that for t = 6–18 ns the front moves at a constant velocity corresponding to
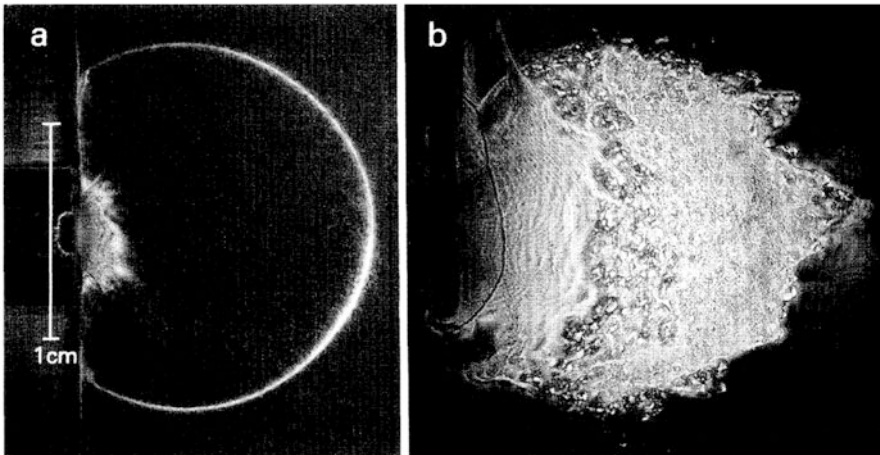
Fig. 4.19 Blast waves produced by laser irradiation on solid target in gas. (**a**) the case with nitrogen gas. This is a case of energy conserving blast wave. (**b**) the same experiment but the gas is higher Z xenon. Due to radiation energy loss, the blast wave front becomes unstable to hydrodynamic instability. Reprint with permission from Ref. [23]. Copyright 1998 by American Physical Society
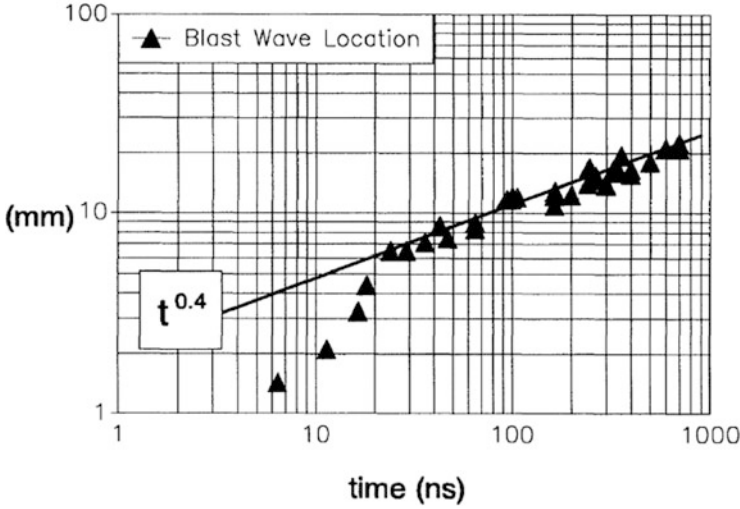
Fig. 4.20 Time evolution of the blast wave front from early ejecta motion to the phase of Taylor-Sedov blast wave for a long duration. Reprint with permission from Ref. [23]. Copyright 1998 by American Physical Society

the velocity of the ablating plasma, a blast wave not yet having formed. Around 25 ns it is clear that the blast wave velocity change to the time dependence given by the blast wave in (4.76) in proportion to $t^{-2/5}$. As we see later, the early time evolution may be a blast wave induced by the ejecta-driven, where the ejecta means the ablating plasma.

In the case of the nitrogen gas, it is evaluated that the specific heat $\gamma = 1.3 \pm 0.1$. On the other hand, when the same blast wave experiment is carried out in xenon gas, the image in Fig. 4.19b is measured. This is due to an instability of radiative blast wave predicted relating to astrophysical objects. It is concluded in Ref. [25] that because of the radiation cooling effect, the effective specific heat becomes lower than the previous nitrogen case, $\gamma = 1.06 \pm 0.02$. This is the experimental evidence that the blast wave is unstable for $\gamma < 1.2$. This is called **Vishiniac instability.**

For a variety of energy sources, the self-similar solution of the blast wave can be plotted on a single space of pressure and the scale range parameter S as shown below. From (4.76) and (4.74) with dimensional relation $\rho u^2 \sim P$, it is easy to derive the following functional relation after eliminating the time.

$$P = \frac{A}{S^3}, \ S = \frac{R}{(E_0)^{1/3}} \tag{4.81}$$

where A is a numerical constant of for a given γ and S is the scaled range parameter. In Fig. 4.21, the data from NRL experiment and NIF laser with 10 kJ irradiations are plotted with orange and green solid circles in (P, S) diagram [26]. For comparison to

Fig. 4.21 Scaling law for the pressure at the blast wave front as a function of the scaled rage parameter. Three different scale experiments from laser, high explosive, and nuclear explosive are found to be in the same scaling law. Reprint with permission from Ref. [26]. Copyright 1998 by American Institute of Physics
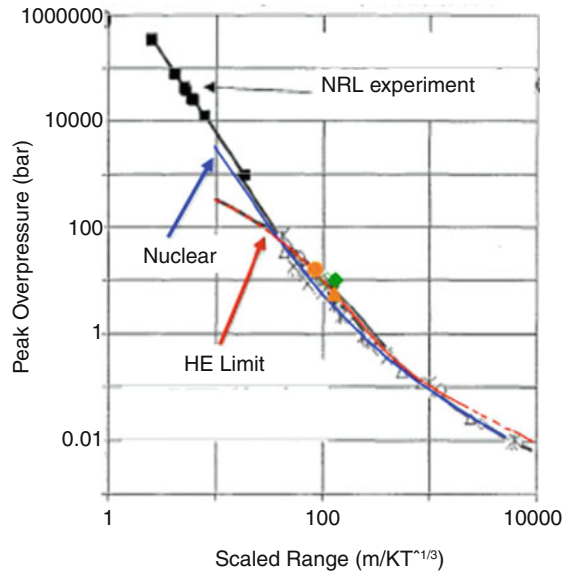
another type of blast wave, those produced by high-explosive and nuclear explosion are also shown with red dashed and solid blue lines. For comparison of extremely different energy explosion, the radius is in unit of meter and energy is in the unit of kiloton of TNT ($KT = 4 \times 10^{12}$ J). It is found that for small S the relation ($P \propto S^{-3}$) is satisfied, while in large S region the relation tends to another relation ($P \propto S^{-1}$). Note that A $\sim 10^7$ in these units with the value of NRL laser experiment (S, P) = (10, 10,000).

Although the explosion energy in Fig. 4.21 varies from 100 [J] to one [KT], while the change of S is about 4×10^{-4} in (energy)$^{-3}$ and the radius of the same pressure for the laser blast wave of 1 cm as seen in Fig. 4.19 is 27 m in KT blast wave.

4.9.2   Dissipative Blast Waves

The radiation loss from shocked plasma decreases the temperature of the plasma and the pressure also decreases. Note that the self-similarity relation of Taylor-Sedov blast wave is first derived from the dimensional analysis of the system with the energy conservation relation. Namely,

$$E_0 \propto \rho_0 D^2 r^d \propto \frac{r^{d+2}}{t^2} \tag{4.82}$$

where d is the dimension of the system. The power law dependence on the system dimension is given as

$$R(t) \propto t^{\alpha}, \tag{4.83}$$

$$\alpha = 2/(d+2) \tag{4.84}$$

The power $\alpha = 2/5$ (3-D, spherical), $=1/2$ (2-D, cylindrical), $= 2/3$ (1-D, planar).

The blasts caused by an intense explosion seen above like Taylor-Sedov blast wave are the prototypical example of self-similarity driven by conservation laws. In dissipative media, however, the energy conservation is violated, yet it is known that a distinctive self-similar solution appears. It hinges on the decoupling of random and coherent motion permitted by a broad class of dissipative mechanisms. This enforces a peculiar, layered structure in the shock as shown in [21]. It has been derived by the full hydrodynamic solution, validated by a microscopic approach based on molecular dynamics simulations.

When the thermal energy of the blast wave escapes or dissipates from the system by any process, for example, radiation loss, the blast wave changes from the energy conservative solution to the momentum conservation one. The dimensional analysis in this case is given as

$$M_0 \propto \rho_0 D r^d \propto \frac{r^{d+1}}{t} \tag{4.85}$$

where M_0 is the total momentum of the expanding matter and α in (4.84) is given as

$$\alpha = 1/(d+1) \tag{4.86}$$

In [21], the particle dynamics is solved by molecular dynamics simulation for a model system of granular gas consisting of identical spherical grains with the same radius and mass, where inelastic binary collisions conserve momentum but dissipate kinetic energy. The physical property of the results does not depend on specific dissipation mechanisms. In Fig. 4.22, the density, velocity, and temperature profiles are plotted as a function of the normalized radius. The cross marks with "Cons." are the results of the energy conservation case of the Taylor-Sedov solution, while the open circles with "Dissip." are the results obtained with the molecular dynamic simulation. The temperature decreases due to the dissipation inducing the increase of the density to keep the pressure jump at the blast wave.

In Fig. 4.22, the orange zone is the shock front, and the next zone is cooling region. After the zone, cold fluid zone shown with the two dashed lines follows. Since the velocity is kept high after the shock front, the central fluid easily flows the cold fluid to generate the cavity region after the thin shell structure of the dissipative blast wave. In Fig. 4.22, the solid lines are theoretical curves obtained from the fluid equations by modeling a dissipation term proportional to the product of the density and temperature [21].

More general model of cooling blast wave has been solved by assuming homogeneous self-similar cooling in the equation of energy. It is mathematically shown that for assuming the radius of the shock front of the blast wave, $R(t) \propto t^{\alpha}$, there is
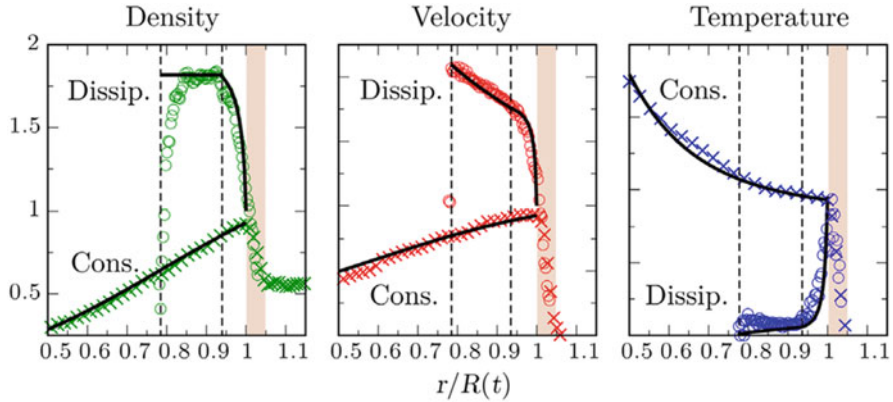
Fig. 4.22 The simulation result of a dissipative blast wave is shown with solid circles in a self-similar evolution. The corresponding Taylor-Sedov solution is also plotted with cross marks. Strong dissipation in the shocked region leads the solution from energy conservative one (Taylor-Sedov) to momentum conservative self-similar solution. Reprint with permission from Ref. [21]. Copyright 1998 by American Physical Society

self-similar solution physically reasonable for a given α in the rage $\alpha = 1/4 \sim 2/5$ as given above for spherically symmetric case [27]. The power law of the blast radius α is also called a **deceleration parameter**.

4.9.3   Radiation Effect on Blast Waves

Let us consider the case where the radiation cooling by Bremsstrahlung and radiative recombination becomes important in the blast wave evolution. It is known that the both cooling rates are roughly proportional to the density times the square root of the electron temperature. So, the above dissipation model can be applicable to predict that the same type of the momentum conserving blast wave becomes dominant after the Taylor-Sedov blast wave and the power law of the time evolution of the blast wave radius changes from $\alpha = 2/5$ to $1/4$ for spherical geometry ($d = 3$).

The study of blast waves produced by intense lasers in gases has also been done in the laboratory with better diagnostic instruments. A systematic scan of laser produced blast waves was performed and the structure of blast waves was examined over a wide range of drive laser energy. Lasers with energies ranging from 10–1000 J irradiating a pin target in either xenon or nitrogen gas, creating a spherical blast wave [28].

A strongly radiating blast wave in xenon gas is observed while blast waves in nitrogen more closely approximate a pure Taylor–Sedov wave as already seen in Fig. 4.19. Radiation emitted from the hot expanding shell ionizs the gas ahead of the shock wave, leading to a **radiative ionization precursor**. The precursor is the same

as the preheating tongue in case of electron preheating in shock structure as show in Fig. 3.8. Furthermore, energy loss by radiation in an optically thin system will increase the rate of deceleration of the blast wave.

These blast waves exhibit significant energy loss through radiation while propagating in xenon as evidenced by interferometric imaging revealing radiative precursors and deceleration parameter α well below those of an energy-conserving wave. Thinning of the blast wave shell from radiative cooling is observed through comparison of shocks launched in gases of differing atomic number. **Shell thinning** is also measured in cylindrical geometry ($N = 2$), when the gas density is altered, indicating the influence of conditions within the pre-shock medium [29]. These results are compared with radiative-hydrodynamic simulations.

One-dimensional simulations of blast wave evolution in xenon were carried out using a radiation hydrodynamics code in which radiation transport was calculated using a multi-group implicit Monte Carlo (IMC) technique, and the individual plasma components are treated in LTE. Figure 4.23 shows the simulated radial profiles of the electron density compared with the experimental data at different times in the blast wave evolution [29]. This discrepancy is likely a result of non-LTE effects associated with the ion fluid since the ions typically take several nanoseconds to thermalize. The radiative precursor is larger for the higher density in agreement with the experimental profile but extends further ahead of the shock than measured.

This indicates that in the precursor region the code does not accurately model the physics because of a significant departure from LTE caused by the detailed atomic physics of the radiating shock. The lower deceleration parameter of $\alpha = 0.44$ compared with $\alpha = 0.47$ with high density. Such effect of non-LTE atomic process has been studied with use of the **collisional radiative equilibrium (CRE)** code the physics, where CRE will be discussed later. The previous experimental data [29] is analyzed with CRE non-LTE code and it concluded that non-LTE code can explain the experimental data [30].

Fig. 4.23 Time evolution of the electron density of a cylindrical blast wave generated by laser irradiation in gas. The dotted lines are corresponding simulation result with radiation transport. Reprint from Ref. [29] with permission from Institute of Physics
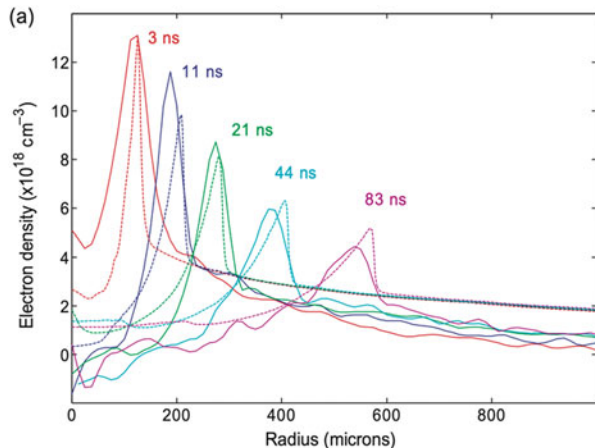
4.10   Blast Waves in Supernova Remnants

4.10.1   Supernova Remnants (SNRs)

The blast wave generated by an explosion of supernova is very important for study of astrophysics mainly related to the heavy element production in Universe. There are a variety of types of the supernova explosions. Most of they are classified as **Type Ia** and **Type II** the explosion mechanisms of which are very different, but the explosion energies are almost the same as 10^{44} [J]. It is surprising to know that this energy can be imagined by comparing to the rest mass energy of the Sun, $Mc^2 = 2 \times 10^{47}$ [J], where the mass of the Sun is $M = 2 \times 10^{33}$ [g] and c is the speed of light.

In Type-Ia, the explosion energy is produced by nuclear fusion reactions in a white dwarf as explained in Fig. 3.15. On the other hand, Type II supernova explosion is triggered by gravitational collapse of massive start and the energy of about 10^{46} [J] is generated as the energy of neutrinos. Since the mean free path of the neutrinos is much larger than the column density of the star, only 1% of the neutrino energy is converted to the matter explosion energy.

After such supernova explosions, the matter of exploded star and the surrounding gas continue to emit a wide range of electromagnetic waves over then of thousand years. Such remnant of the supernova explosion is called **supernova remnant (SNR)**. In Fig. 4.24, X-ray image of the supernova remnant **SN1006** is shown, where the image was taken by the x-ray satellite **Chandra** [31]. Its explosion was recorded many places in 1006. The detail of this remnant is given, for example, in

Fig. 4.24 The x-ray emission image of the supernova 1006 observed by Chandra x-ray satellite (NASA). Reprint from Ref. [31] with kind permission from Springer Science + Business Media

10 arcmin
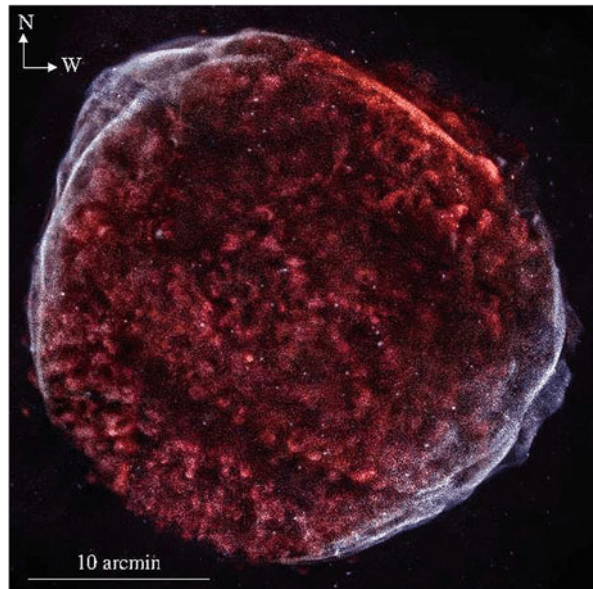
[31]. Its distance from the Earth is about 7200 light-years ($\sim 7 \times 10^{16}$ km). SN1006 was the brightest supernova (SN) witnessed in the human history. As of 1000 years later, it stands out as an ideal laboratory to study Type Ia supernova and the shocks in supernova remnants.

Three-dimensional supernova explosions have been studied for a variety of so-called **progenitors** (stars before explosion). According to [32], the density structure of progenitor of Type II is given approximately in the power law form,

$$\rho(r) = \rho_0 \left(\frac{r}{r_0} \right)^{-3} \tag{4.87}$$

where $\rho_0 = 10^{10}$ [g/cm^3] *and* $r_0 = 10^7$ [cm]. The surface of the star has about $r = 10^{13}$ [cm] and $\rho(r) = 10^{-8}$ [g/cm^3]. The shock wave generated inside the propagates to propagate outward and in the idealistic limit like the power law density profile, we can also find a self-similar solution of the shock propagation as described at p. 812 in [5].

In [32], the averaged shock wave velocity is shown to be about 10^4 km/s, 3% of the speed of light. So, roughly speaking, the shock wave arrives at the surface of the progenitor after 3 h, then the star starts to shine. Once the shock front arrives at the surface of the star, the shocked material expands in a low density **inter-stellar medium (ISM)**. This is the same as the free expansion of the ablation plasma by laser irradiation as seen in Fig. 4.20, where free expansion is measured until about 20 ns and then the self-similar blast wave was generated. Since the density ratio of the expanding material called "**ejecta**" to the density in ISM is extremely high, the ejecting material pushes the ISM with the same velocity. This is because the velocity of the ejecta is faster than the sound velocity of compressed ISM in front of the contact surface. Such pushing is called "**snowplow**".

In Fig. 4.25, one-dimensional simulation of the gravitational collapsing supernova 1987A is shown [33]. Note that the surface of the progenitor has a sharp density drop at the surface because of strong stellar wind. In the figure, the stage numbers correspond to the time since explosion as (0) t = 0 s; (1) 8.96 s; (2) 1.67×10^2 s; (3) 1.06×10^3 s; (4) 3.33×10^3 s; (5) 7.46×10^3 s. It is seen that the shock wave arrives at the center around 2 h. The density profile at the time of the shock arrival at the surface is almost flat profile and due to the expansion, this density decreases as the volume of the matter increases with the expansion velocity of 10,000 km/s. Then, the snowplow continues for a long time.

It is said that such a snowplow phase continues until the total mass of snowplowed gas becomes almost the same mass of the effective ejecta M.

$$\frac{4}{3} \pi R^3 \rho_{ISM} = M \tag{4.88}$$

where ρ_{ISM} is the mass density of ISM. Assuming the ejecta is expanding with the velocity 10^4 km/s, ρ_{ISM} as one hydrogen per cm^3, and demanding the mass M is
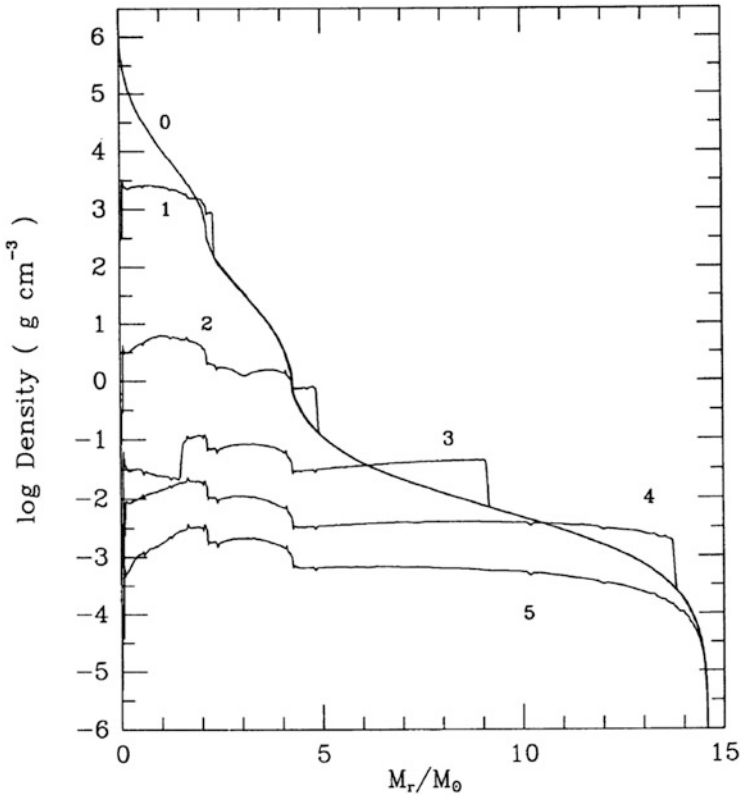
Fig. 4.25 Time evolution of the density profiles as a function of mass from the center. The shock wave is generated at t = 0. The stage numbers correspond to the time since explosion as (0) t = 0 s; (1) 8.96 s; (2) 1.67×10^2 s; (3) 1.06×10^3 s; (4) 3.33×10^3 s; (5) 7.46×10^3 s. Around the time of 2 h, the shock wave arrives at the surface of the star to start shining. Reprinted with permission from Ref. [33]. Copyright by American Astronomical Society

equal to the solar mass, then the timing to satisfy (4.88) is easily evaluated as about 200 years. Note that this simple value is too early as see below. It takes long time to detach the ejecting material and the autonomous propagation of the blast wave as the self-similar solution. This is because the density of the ejecting material is very high compare to the density of ISM.

The snow-plowed gas forms Sedov-Taylor self-similar blast wave after the deceleration of the contact surface begins. At the same time, the deceleration of the front region of the ejecting material pushes the following ejecta material to produce a **reverse shock wave** propagating toward the central region, where the density increase. This is unstable scheme to hydrodynamic instability. The Rayleigh-Taylor instability of the contact surface has been studied to compare the observation images.

It is noted that the velocity of the collisionless shock of SN1006 in Fig. 4.24 is $U_s = 3000$ km/s evaluated through the observation over 11 years. Typical values for the SNRs are given in [34] and (t, R_{sh}, U_{sh}) = (100, 2, 8000), (1000, 5, 2000), (10,000, 12.5, 500), where t is the time after explosion in the unit of years, R_{sh} is the shock front radius in units of pc ($= 3.1 \times 10^{16}$ m) and U_{sh} is the velocity of the shock front in units of km/s, respectively.

In Fig. 4.24, the spatial x-ray image of SN1006 near the sharp shock front has been analyzed in detail relating to the physics of cosmic-ray generation and confinement near the shock surface by magnetic field [35]. The typical temperature and density at the rear of the shock front is $T_i \sim 15$ keV ($T_e \sim 0.5$–1 keV) and the number density $n_i \sim 1$ cm^{-3} and the corresponding proton Coulomb mean free path is estimated to be 4×10^{17} m (= 41 light years). The diameter of SN1006 is about 3×10^{17} m (= 32 light years). The shock front width which is here defined to be that of the sharp intensity front in Fig. 4.24 is about 1.2×10^{15} m (=0.12 light years) [35]. As a result, it is concluded that the thickness of the shock front of SN1006 SNR is less than 1% of the radius and the Coulomb mean free path is 400 times longer than the shock front thickness, namely, the shock should be the collisionless shock.

Most of the shock waves are collisionless in Universe. To demonstrate the formation of collisionless shock with intense lasers, a model experiment was proposed [36]. With use of NIF and OMEGA lasers, the collisionless shock generation has been demonstrated experimentally with use of counter streaming ablation plasma [37, 38]. The magnetic field is generated by Weibel instability and the collisionless shock wave is generated after the nonlinear amplification of magnetic field.

In studying such collisionless shock waves, it is possible to use most of the hydrodynamics relations such as Ranking-Hugoniot relation except the shock wave structure. Instead of the particle collisions, Larmor motion of charge particles in turbulent magnetic field plays the role of dissipation. For example, a proton Larmor radius with a velocity of 10^3 km/s in the 3μG magnetic field is 3×10^7 m, extremely shorter than the radius of SNR and even shorter than the front thickness of the x-ray image, where the magnetic field in ISM is about $1 \sim 10$ μG.

It should be noted that the big and essential difference of the SNR shocks compared with the laser-driven shocks seen above is not the difference in the energy, the difference of 42 orders of magnitude, but the difference in physics. The shock wave of the SNRs is a collisionless plasma shock, but the laser shock wave is in general the collisional hydrodynamic shock wave. In the laser shock, the mean free path is almost the same as the thickness of the shock front. In addition, the collisionless shock accompanies the electric and magnetic fields which play an essential role in accelerating the charged particle, namely, the origin of cosmic rays [38].

Finally, let us evaluate the scale range parameter S in (4.81) for SN1006 blast wave. Assume the explosion energy is 10^{44} [J] and its radius 3×10^{17} [m], we obtain the value of $S \sim 10^7$ [m/KT$^{1/3}$]. The pressure of the blast wave is evaluated roughly as $P \sim 4 \times \rho_{ISM}(U_{Sh})^2$. Then we obtain $P \sim 10^{-12}$[atm] and the pressure evaluated with $A = 10^7$ is $P \sim 10^{-14}$[atm]. They are different of two orders of magnitudes and main cause of the difference is over estimate of the radius due to rapid expansion in the

early snow-plow phase with expansion velocity of 10,000 km/s. The point is very far right in Fig. 4.21. This is because of extremely low pressure of ISM gas. It is not so bad evaluation. Note that the self-similar solution assumed adiabatic condition, while in later time around 100,000 years, it is said that the radiation cooling effect as shown below becomes important and the blast wave front continue to expand as a thin shell structure.

4.10.2   Self-Similar Solution of SNRs

We see that the blast waves of SNRs are ejecta-driven blast wave and not the point-energy driven one like laser-driven blast wave seen in Fig. 4.19a. It is, however, surprising that even in such a case, **Chevalier** has found a group of self-similar solutions including the whole structure of expanding ejecta, reverse-shock, and blast wave propagating outward [39]. The mathematical method is almost the same as Sect. 4.2.

The ejecting matter is assumed to have the density profile in the radial direction like r^{-n} initially, where n is a given constant. Assuming a uniform expansion, the time and spatial evolution of the ejecta density profile is given in the form;

$$\rho \propto t^{-3}(r/t)^{-n} \tag{4.89}$$

where t^{-3} is due to uniform expansion and r/t is due to the assumption of constant velocity to each Lagrange fluid. The density profile of the surrounding gas (ISM) is assumed in the form.

$$\rho \propto r^{-s} \tag{4.90}$$

where s is a given constant. It is mentioned in [39] that Type-I supernovae are given for $(n, s) = (7,0)$, while Type II is better for $s = 2$ modeling the expanding envelope by the wind.

Since the time dependence of the radius of the contact surface, $R_c(t)$ should be the same for both in (4.89) and (4.90). Inserting $R_c(t)$ in the both and requiring both density has the same time dependence, it is easy to obtain the time dependence of $R_c(t)$ in the form.

$$R_c(t) = A t^{(n-3)/(n-s)} \tag{4.91}$$

where A is a constant. Note that in the case of $(n, s) = (5, 0)$, $R_c(t) \propto t^{2/5}$ and it is the case of Sedov-Taylor solution and it is studied the case $n > 5$ for $s = 0$. In this case, the expansion velocity is faster than the case of $n = 5$ due to the ejector snow plow effect.
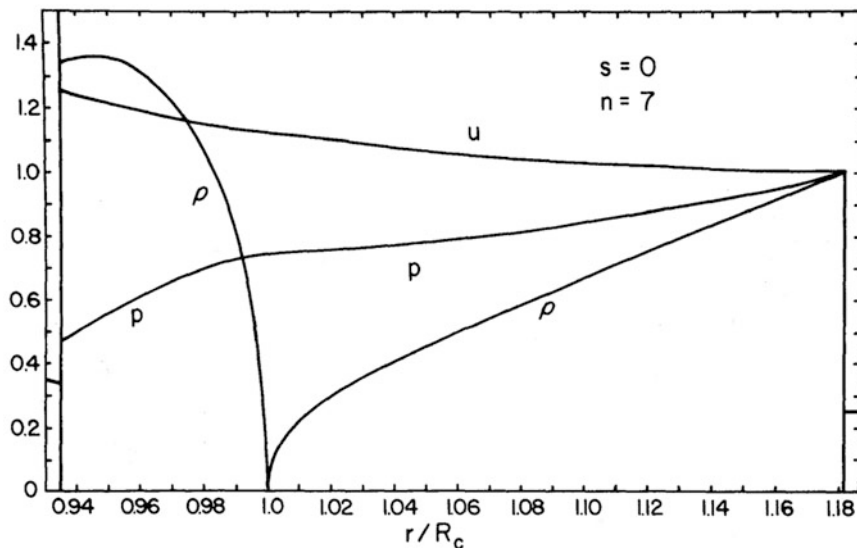
Fig. 4.26 Self-similar solutions of density, pressure, and velocity of the ejector-dominant blast wave of a typical Type Ia supernova remnant. The radius $r = R_c$ is the contact surface. The radii of the reverse shock front and the blast wave are 0.935 and 1.181. Reprinted with permission from ref. [39]. Copyright by American Astronomical Society

In Fig. 4.26, dimensionless profiles of the density (ρ), pressure (p), and velocity (u) profiles of the self-similar solution are plotted in the normalized coordinate, $r/R_c(t)$. The radii of the reverse shock front and the blast wave are 0.935 and 1.181. The velocity is almost uniform, while the density changes rapidly around the contact surface.

Consider an applicability of the ejecta-driven self-similar solution. It is clear that the mass of the ejecta (4.89) diverges near $r = 0$, while the total mass of the supernova ejecta is limited, for example, about the solar mass in Type I supernova explosion. It is clear that when the effective ejecta mass becomes near the solar mass, the present self-similar solution is not applicable. The ejecta velocity will reduce due to the energy transfer to the blast wave. It is clear that the total kinetic energy of the blast wave region E_{BW} can be shown as

$$E_{BW} \propto \left(\frac{dR_c}{dt}\right)^2 R_c^3 \propto t^{6/7}$$

It is reasonable to consider that after the present solution breaks down, the blast wave continues expanding by following Sedov-Taylor solution as far as the adiabatic flow is assumed.
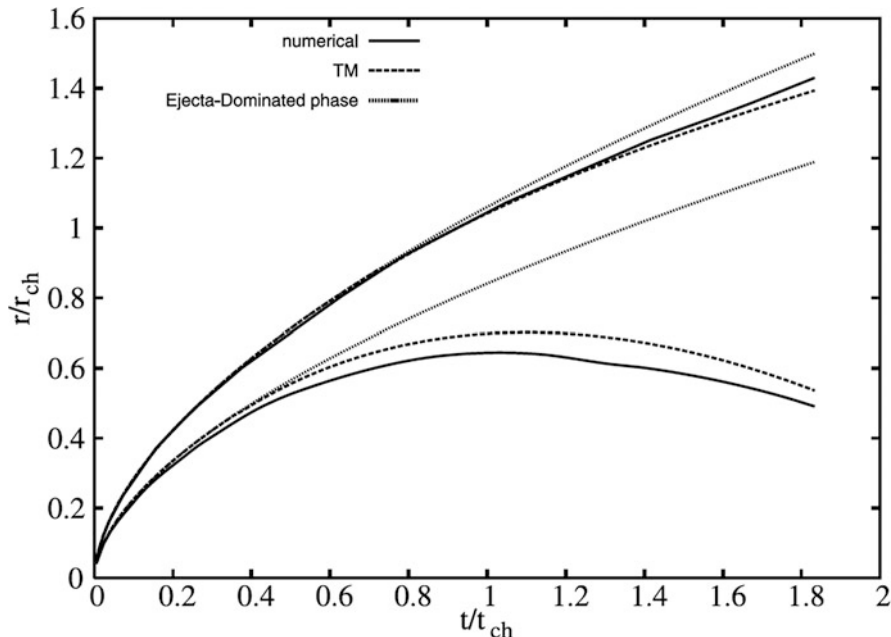
Fig. 4.27 The simulation result of time evolution of two shock fronts are plotted with the black solid lines. The shock fronts of the present ejector-driven self-similar solution are plotted with gray solid lines. The dotted two lines are analytic solution [40]. *Credit*: Fraschetti, Federico, et al., *A&A, 515, A104, 2010, reproduced with permission © ESO*

The trajectories of a blast wave (forward shock front; R_{BW}) and the reverse shock front (R_{RS}) were shown for further study with 3-D hydrodynamic simulation and one-dimensional result of radius-time evolution is plotted in Fig. 4.27 [40], where $(n, s) = (7,0)$ and $\gamma = 5/3$. The characteristic time (t_{ch}) and radius (r_{ch}) is calculated so that the ejected mass becomes the same as the mass of the shocked gas (ISM) [41].

In Fig. 4.27, the simulation result of time evolution of (R_{BW}, R_{RS}) are plotted with the black solid lines. The present ejector-driven self-similar solution is plotted with gray solid lines. The dotted two lines are analytic solution. It can be said that the ejector-driven phase is over before $t = t_{ch}$, while the dynamics in the early phase ($t < t_{ch}$) well agrees with the simulation. Since the mass of the ejector is limited, the R_{RS} travels toward the center after t_{ch}. After t_{ch}, R_{BW} becomes slower to fit to Sedov-Taylor solution.

In Fig. 4.28, the time evolution of the density profiles obtained by the simulation is plotted as a function of the radius normalized by $R_{BW}(t)$, where $t_{ch} = 1950$ years. In the figures, the ejector-dominant solution and Sedov-Taylor solution are also plotted with thin red lines. It is clearly seen that the simulation profiles smoothly transit around $t = t_{ch}$.
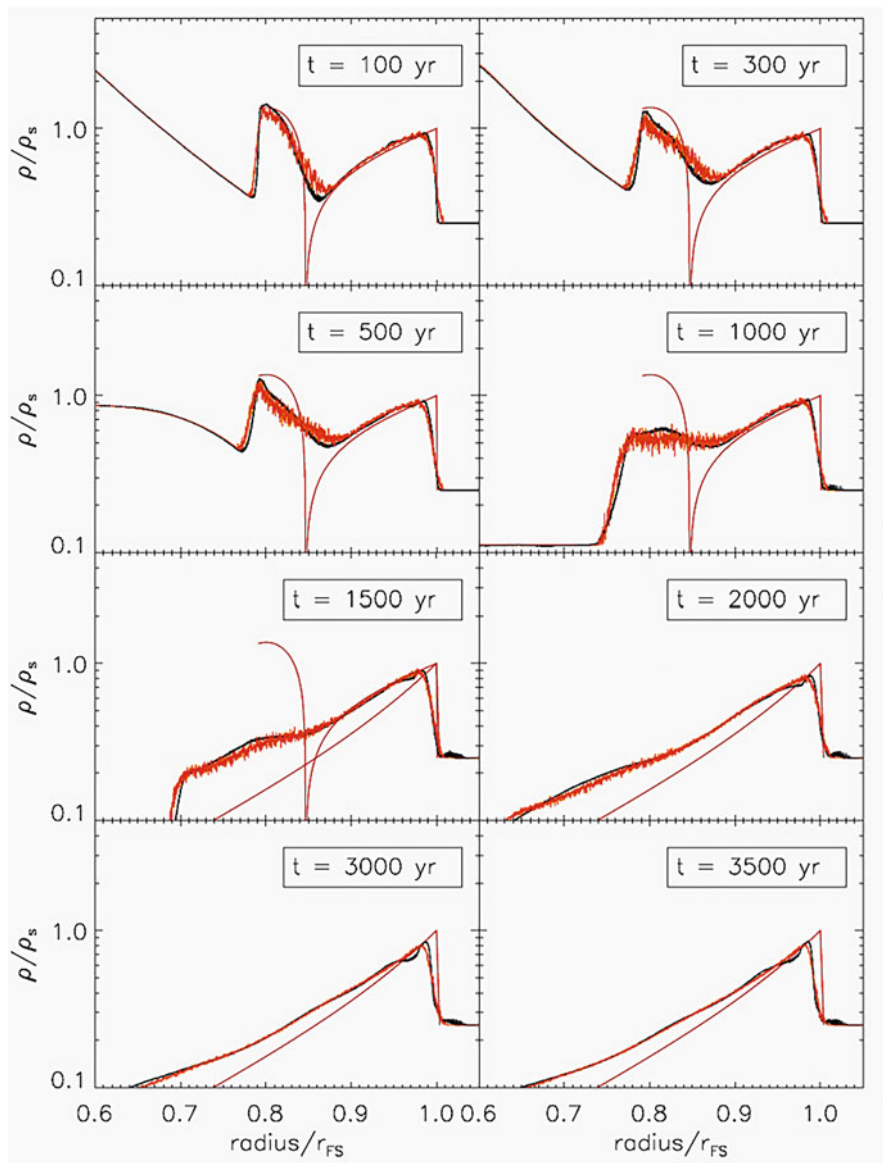
Fig. 4.28 The simulation result of time evolution of density profiles. The thin red lines show the present and Taylor-Sedov blast wave solutions [40]. *Credit*: Fraschetti, Federico, et al., *A&A, 515, A104, 2010, reproduced with permission* © ESO

It is clear that the contact surface is unstable to Rayleigh-Taylor instability in the ejector-driven phase seen in Figs. 4.26 and 4.28. Since $R_c(t) \propto t^{4/7}$ and the contact surface is kept decelerating by the pressure gradient force. Three-dimensional

Fig. 4.29 X-ray image of
Tycho SNR by Chandra
x-ray satellite [NASA]
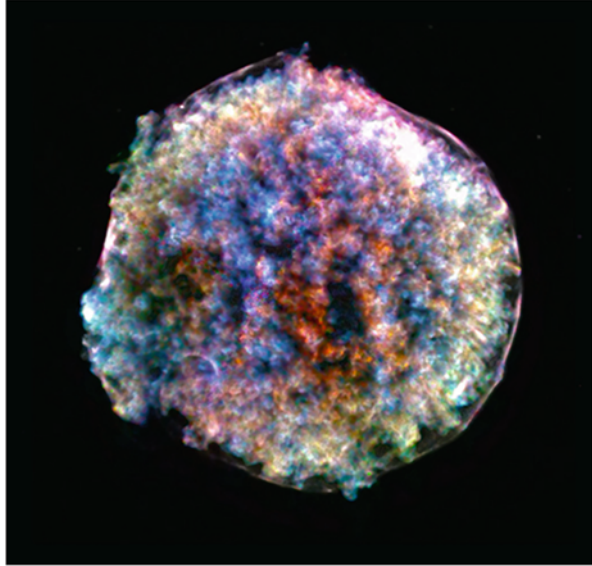
simulation has been done to study the physics of observation data, for example
in [40]. In Fig. 4.29, X-ray image of **Tycho SNR** observed by Chandra x-ray satellite
is shown. Very different of SN1006, Tycho SNR is sure to be affected by Rayleigh-
Taylor instability. It is concluded that the growth of Rayleigh-Taylor instability is
rather independent of the seeding by the non-uniformity in the explosion
phase [42]. It is out of the topics in the present volume and to be discussed in later
chapters.

Finally, it is useful to point out that the self-similar solution is studied in many
situations in astrophysics. Even with the gravitational force, self-similar solution of
star formation was found to explain the time evolution of gravitational collapse of
molecular cloud. A famous solution is called the **Larson-Penston** (LP) type simi-
larity solution [43]. Such star formation has been studied also with computational
method to compare with the self-similar solutions. The LP assumed that in early
phase of contraction the proto-star is optically thin and the radiation cooling makes
the system uniform temperature in time evolution.

Numerical simulation with reasonable opacity of the cloud and radiation transport
has been carried out [43]. The time evolution of the density, temperature and velocity
are compared to the LP solution to find the good agreement in the early phase before
the density approaches about 10^{20} cm^3 over more than ten-order of magnitude
evolution. In Fig. 4.30, the simulation result is shown for density, temperature,
velocity and hydrogen molecule concentration distribution for time from 0 to 7 tim-
ings [43]. It is confirmed that the density and velocity profiles are well explained
with LP solution up to the time of 5. After the time 5, the dissociation of hydrogen
molecule makes the system relatively optically thick system to apart from the LP
self-similar solution.
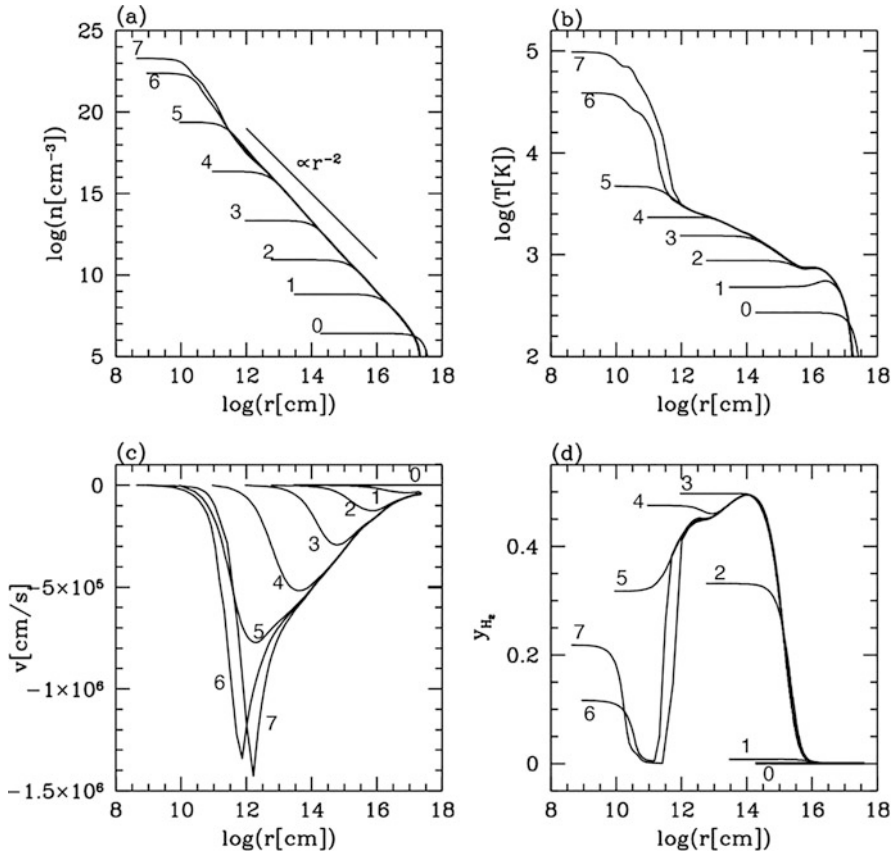
Fig. 4.30 Simulation result of star formation starting from low-density molecular cloud in self-gravitational system. The self-similar solution by Larson-Penston agreed well in the early stage. Reprinted with permission from Ref. [43]. Copyright by American Astronomical Society

References

1. H. Takabe et al., Scalings of implosion experiments for high neutron yield. Phys. Fluids **31**, 2884 (1988)
2. J.H. Nuckolls Contributions to the genesis and progress of ICF. In: *Inertial confinement nuclear fusion: A historical approach by its pioneers* (2007): 1–48
3. M.M. Marinak et al., Three-dimensional simulations of Nova high growth factor capsule implosion experiments. Phys. Plasmas **3**(5), 2070–2076 (1996)
4. I.V. Igumenshchev et al., Three-dimensional modeling of direct-drive cryogenic implosions on OMEGA. Phys. Plasmas **23**(5), 052702 (2016)
5. Y.B. Zel'dovich, Y.P. Raizer, *Physics of Shock Waves and High Temperature Hydrodynamic Phenomena* (Dover, 2002)
6. S. Atzeni, J. Meyer-ter-Vehn, *The Physics of Inertial Fusion* (Clarendon Press, Oxford, 2004)

7. M. Murakami, J. Sanz, Y. Iwamoto, Stability of spherical converging shock wave. Phys. Plasmas **22**, 072703 (2015)
8. R.B. Lazarus, Self-similar solutions for converging shocks and collapsing cavities. SIAM J. Numer. Anal. **18**(2), 316–371 (1981)
9. J. Meyer-ter-Vehn, C. Schalk, Selfsimilar spherical compression waves in gas dynamics. Zeitschrift für Naturforschung A **37**(8), 954–970 (1982)
10. G. Taylor, Proc. R. Soc. A **201**, 159 (1950) 201, 175 (1950)
11. L.I. Sedov, J. Appl. Math. Mech. **10**, 241 (1946)
12. J. von Neumann, *Collected Works*, vol VI (Pergamon Press, Oxford, 1963), p. 218
13. A. Kemp, J. Meyer-ter-Vehn, S. Atzeni, Stagnation pressure of imploding shells and ignition energy scaling of inertial confinement fusion targets. Phys. Rev. Lett. **86**(15), 3336 (2001)
14. D.S. Clark, M. Tabak, A self-similar isochoric implosion for fast ignition. Nucl Fusion **47**(9), 1147 (2007)
15. R.E. Kidder, Theory of homogeneous isentropic compression and its application to laser fusion. Nucl Fusion **14**(1), 53 (1974)
16. R.E. Kidder, *Laser Fusion: The First Ten Years 1962–1972. No. UCRL-BOOK-222681* (Lawrence Livermore National Lab.(LLNL), Livermore, 2006)
17. F. Hattori, H. Takabe, K. Mima, Rayleigh–Taylor instability in a spherically stagnating system. Phys. Fluids **29**(5), 1719–1724 (1986)
18. I.B. Bernstein, L. David, Rayleigh-Taylor instability of a self-similar spherical expansion. Astrophys J **225**(1), 633–640 (1978)
19. R.E. Kidder, Laser-driven isentropic hollow-shell implosions: the problem of ignition. Nucl. Fusion **19**(2), 223 (1979)
20. H. Takabe, T. Yabe, K. Nishihara, Ablation and compression mechanism in laser fusion plasmas (an approach with self-similar solutions). Rev. Laser Eng. **7**(4), 394–400 (1979). https://doi.org/10.2184/lsj.7.394
21. M. Barbier, D. Villamaina, E. Trizac, Blast dynamics in a dissipative gas. Phys. Rev. Letts. **115**, 214301 (2015)
22. G.I. Barenblatt, *Scaling, Self-Similarity, and Intermediate Asymptotics* (Cambridge University Press, Cambridge, UK, 1996)
23. J. Grun et al., Instability of Taylor-Sedov blast waves propagating through a uniform gas. Phys. Rev. Letts. **66**, 2738 (1991)
24. J. Grun et al., Laser–plasma simulations of astrophysical phenomena and novel applications to semiconductor annealing. Laser Part. Beams **21**, 529–534 (2003)
25. J. Grun et al., Observation of high-pressure blast-wave Decursors. Appl. Phys. Lett. **59**, 246 (1991)
26. K.B. Fournier et al., A geophysical shock and air blast simulator at the national ignition facility. Rev. Sci. Instrum. **85**, 095119 (2014)
27. A. Gintrand et al., Self-similar dynamics of radiative blast waves. Phys. Fluids **32**, 016105 (2020)
28. A.D. Edens, T. Ditmire, et al., Study of high Mach number laser driven blast waves. Phys. Plasmas **11**, 4968 (2004)
29. J. Osterhoff et al., Radiative shell thinning in intense laser-driven blast waves. New J. Phys. **11**, 023022 (2009)
30. R.H.H. Scott et al., Modeling radiative-shocks created by laser–cluster interactions. Phys. Plasmas **27**, 033301 (2020)
31. S. Katsuda, *Supernova of 1006 (G327.6+14.6)*, in *Handbook of Supernovae*, ed. by A.W. Alsabti, P. Murdin, (Springer International Publishing AG, 2017)
32. A. Wongwathanarat, E. Müller, H.-T. Janka, Three-dimensional simulations of Core-collapse supernovae: From shock revival to shock breakout. Astron. Astrophys. **577**, A48 (2015)
33. T. Shigeyama, K. Nomoto, Theoretical light curve of SN 1987A and mixing of hydrogen and nickel in the ejecta. Astrophys. J. **360**, 242 (1990)

34. F.D. Seward, P.A. Charles, *Exploring the X-Ray Universe*, 2nd edn. (Cambridge University Press, 2012)
35. A. Bamba et al., Small-scale structure of SN 1006 shock with Chandra observations. Astrophys. J. **589**, 827 (2003)
36. T.N. Kato, H. Takabe, Nonrelativistic collisionless shocks in weakly magnetized electron-ion plasmas: two-dimensional particle-in-cell simulation of perpendicular shock. Astrophys. J. **721**(828) (2010)
37. H. Takabe et al., High-Mach number collisionless shock and photo-ionized non-LTE plasma for laboratory astrophysics with intense lasers. Plasma Phys. Control Fusion **50**, 124057 (2008)
38. F. Fiuza et al., Electron acceleration in laboratory-produced turbulent collisionless shocks. Nat. Phys. **16**, 916–920 (2020)
39. R.A. Chevalier, Self-similar solutions for the interaction of stellar ejecta with an external medium. Astrophys. J. **258**(1), 790–797 (1982) Research supported by the University of Virginia 258 (1982): 790–797
40. F. Fraschetti et al., Simulation of the growth of the 3D Rayleigh-Taylor instability in supernova remnants using an expanding reference frame. Astron Astrophys **515**, A104 (2010)
41. X. Tang, R.A. Chevalier, Shock evolution in non-radiative supernova remnants. Mon. Not. R. Astron. Soc. **465**(4), 3793–3802 (2017)
42. G. Ferrand et al., From supernova to supernova remnant: Comparison of thermonuclear explosion models. Astrophys. J. **906**(2), 93 (2021)
43. K. Omukai, R. Nishi, Formation of primordial protostars. Astrophys. J. **508**(1), 141 (1998)

Chapter 5
Atomic Process in Plasmas

Abstract When a high-intensity laser is irradiated onto a solid gold (Z = 79), half of the electrons is partially ionized. The multi-electron structure of such ions is not obvious. Quantum mechanics of multi-electron systems and calculations of ionization statistics are required. In this chapter, the electrons in the ion are approximated to be bound in a spherically symmetric mean field, and the isolated atom is studied.

The Hartree-Hock (HF) equation, which accurately describes atoms in many-electron systems, can be solved, but it is a daunting task. For this purpose, simple but error-prone approximations have been used, such as the HULLAC and OPAL codes, which use the para-potential method instead of a rigorous description of the HF. It is an intuitive and easy-to-understand approximation.

Once the quantum state of the bound electrons can be calculated, the statistical distribution of ionization can be obtained by solving the Saha equation for thermal equilibrium. The threshold of ionization (continuum lowering) is determined. The calculation of such an ionic structure is presented. Due to the high temperature of the plasma, interaction with thermal radiation and free electrons cause excitation, ionization, and the reverse process. Calculations of these processes will be presented.

Applications of the rate equations will be explained. In the recently introduced X-ray laser (XFEL) heating, free electrons are also non-equilibrium (non-Maxwellian). This chapter begins with a review of hydrogen and helium atoms, and then introduces the topics of atomic physics and processes from the laboratory to the universe.

5.1 Introduction

In order to solve the hydrodynamic equation of partially ionized plasma, it is necessary to determine charge distribution and average charge of plasma ions. The equation of states, transport coefficients and so on are very sensitive to the charge state. In solving a time evolution of plasma, the charge state changes in time. Under a certain condition, the local thermodynamic equilibrium (LTE) is good approximation, while the other condition requires analysis based on some non-LTE atomic

process model. In general, laser produced plasma requires such non-LTE analysis to determine the charge distribution.

The charge distribution in LTE is given by solving well-known Saha relation. However, we have to know about the quantum states of bound electrons in all charge state ions in advance. Lasers irradiate not only low-Z materials, but also medium-Z and high-Z materials and the calculation of the quantum states themselves is a hard job. In the history of development of quantum mechanics, numerical methods to solve such quantum state of many electron system have been developed [1, 2].

Alongside development of such methods, a variety of simplified models have also been studied intensively. When we need only the charge state in a given condition, it is not necessary to solve Hartree-Fock equation with Slater matrix as shown in such textbooks. However, spectroscopic analysis and radiation transport demand data base obtained by such sophisticated calculation. Before going to details of the atomic model, we are required to speculate how detail atomic data are required in our specified plasma to be studied.

In non-LTE plasma we have to solve dynamics of ionization, recombination, excitation, and de-excitation. All of such processes depend on the quantum state of bound electrons. The cross section of each process σ has to be solved with quantum mechanics [3, 4]. In general, we use the perturbation method to solve Schrodinger equation. Except for special case with XFEL as we see later, it is a good approximation to assume the free electrons are in Maxwell distribution. Then, the velocity averaged rate (frequency) of the collisional atomic process is given for the corresponding cross section $\sigma(v)$ in the form.

$$\nu = \langle n\sigma(v)v \rangle, \tag{5.1}$$

where $\langle \rangle$ represents to take average with Maxwell distribution.

Then, we can formulate so-called **rate equation** to the population of each quantum state of all ions. It can be expressed by a relational expression that seems simple as follows.

$$\frac{dN_m^\varsigma}{dt} = \sum_{k \neq m, \eta \neq \varsigma} \left(-\nu_{mk}^{\varsigma\eta} N_m^\varsigma + \nu_{km}^{\eta\varsigma} N_k^\eta \right) \tag{5.2}$$

where N_m^ς represents the number of ions with the quantum state of bound electrons m and charge ζ. Of course, their numbers increase abruptly with the increase of atomic number Z of plasma or how detail atomic states we take account of. The first term on RHS gives the loss of N_m^ς due to the transition of $(\varsigma \to \eta)$ and $(m \to k)$, while the second term gives the increase due to the transition of $(\eta \to \varsigma)$ and $(k \to m)$. How many quantum states of bound electrons should be included strongly depends on how precise analysis are required. How we can reduce this task depends on modeling of atomic structure. Note that such a rate equation has been widely used in many different sciences; not only natural but also social sciences.

In plasma physics, so-called **collisional radiative model (CRM)** of rate equation is widely used for solving atomic process of non-LTE plasma [5]. Such codes are applied to study Astrophysical objects. The details of photo-ionized plasmas in Universe and laboratory are explained. The principle of masers and lasers are also shown with rate equations as described later. The masers and lasers are also observed in Universe.

Finally, interdisciplinary topics governed by rate equations are briefly described. Nucleosynthesis in Big-Bang and supernova explosion, Lorentz model giving chaos of weather, and virus infection are explained by showing how such rate equations are used in different natural and social sciences.

5.2   Saha Equilibrium of Charge State

In the region where the temperature is low and the density is moderately high, the collision effect by free electrons is dominant for excitation, ionization, de-excitation, and recombination even if the radiation field is very weak compared to Planckian distribution. In such a case, the ionization state of the plasma is realized while locally achieving thermal equilibrium. Such thermodynamically equilibrium (LTE) ionization distribution is called **Saha equilibrium** after the name of the Indian astronomer Meghnad Saha (1893–1956), who first proposed the equation for calculating the distribution of ions in different charge state in LTE.

Let us derive an equation of Saha equilibrium, which is coupled equations of the ionization distribution in the thermal equilibrium state. Here, the partition function Z is defined by **Helmholtz's free energy** F and is given in the form

$$F = -kT \ln Z \qquad (5.3)$$

For example, when the system is made of different types of gases (ions and electrons of different charges in the case of plasma) and their number are $N_1, N_2, \ldots$, the total **partition function** Z of the system is divided into individual partition functions Z_1, Z_2, in the form

$$Z = \frac{Z_1^{N_1}}{N_1!} \cdot \frac{Z_2^{N_2}}{N_2!} \cdot \ldots \qquad (5.4)$$

Here, the partition function for N_1 particles is defined as

$$Z = \sum_n g_n e^{-\frac{E_n}{kT}} \qquad (5.5)$$

The partition function is defined to be the sum of all possible quantum states for each particle system. Note that g_n, E_n are the degeneracy (number of states) and the intrinsic energy of all quantum states that the N_1 particle can take.

Inserting (5.5) into (5.4) and using the following Stirling formula,

$$N! = \left(\frac{N}{e}\right)^N \tag{5.6}$$

where "e" is the base of natural logarithm. The free energy of the formula (5.3) is obtained to be

$$F = -N_1 kT \ln\left(\frac{Z_1 e}{N_1}\right) - N_2 kT \ln\left(\frac{Z_2 e}{N_2}\right) - \dots \tag{5.7}$$

Now let's consider ionization equilibrium. In the partially ionized state, various ionic states coexist from the neutral state to the completely ionized state of the same atom. A partial ionized plasma can be thought of as a group of ions with different charge numbers. Let Z be the atomic number of the neutral atom, we obtain

$$F = -\sum_{\zeta=0}^{\zeta=Z} N_\zeta kT \ln\left(\frac{Z_\zeta e}{N_\zeta}\right) - N_e kT \ln\left(\frac{Z_e e}{N_e}\right) \tag{5.8}$$

Here, ζ is the number of ionized electrons. The charge is Z_ζ and number is N_ζ. The second term of Eq. (5.8) is a term due to free electrons. When the volume of plasma is V, the partition function is given to be

$$Z_e = 2\left(\frac{mkT}{2\pi\hbar^2}\right)^{3/2} V \tag{5.9}$$

It is clear in thermal equilibrium that the Helmholtz free energy F in (5.8) should take the minimum value. That is, if the ions in the ionization state are replaced with some ions, the following relationship holds.

$$\delta N_\zeta = -\delta N_{\zeta+1} = -\delta N_e \tag{5.10}$$

At the same time $\delta F = 0$ should also be satisfied. From this condition and (5.8), we obtain the relation

$$\frac{N_{\zeta+1} N_e}{N_\zeta} = \frac{Z_{\zeta+1} Z_e}{Z_\zeta} \tag{5.11}$$

Defining the number density, $n_e = N_e/V$, $n_\zeta = N_\zeta/V$, (5.11) can be written

$$\frac{n_{\zeta+1} n_e}{n_\zeta} = 2\frac{Z_{\zeta+1}}{Z_\zeta}\left(\frac{mkT}{2\pi\hbar^2}\right)^{3/2} \tag{5.12}$$

This is the basic formula by Saha.

Here, we introduce a new function of the energy u_ζ and the ionization state as follows

$$Z_\zeta = e^{-\frac{E_0^\zeta}{kT}} \sum_{n=0} g_n^\zeta e^{-\frac{E_n^\zeta - E_0^\zeta}{kT}} = e^{-\frac{E_0^\zeta}{kT}} u_\zeta \qquad (5.13)$$

Then, the Eq. (5.12) is

$$\frac{n_{\zeta+1} n_e}{n_\zeta} = 2 \frac{u_{\zeta+1}}{u_\zeta} \left(\frac{mkT}{2\pi\hbar^2} \right)^{3/2} e^{-\frac{I_{\zeta+1}}{kT}} \qquad (5.14)$$

$$I_{\zeta+1} = E_0^{\zeta+1} - E_0^\zeta \qquad (5.15)$$

Here, (5.15) is the ionization energy from the ionized state ζ to $\zeta + 1$.

Now, how is the internal excited state of each ion and its number of states determined? If it is hydrogen, the number of states is $2n^2$ and the energy level is simple. However, it is not simple how high n be included as bound states, because the upper n states may be free state due to the perturbation by the ions surrounding. If we think that every ion is in the ground state, we can calculate the number of states if Z is small, so the above equation seems to be solvable. However, it is necessary to consider the excited state in the partially ionized plasma in the case where the density is high and the temperature is not so high. Also, there are many states in the shell of the same main quantum number, and when a part is clogged, there is degeneracy. In that case what should one do? Although the charge distribution of thermal equilibrium state in Saha's equation seems to be apparent at first glance, the reality needs more detailed and lengthy study. Such ionization level lowering will be discussed in Chaps. 8 and 9 in detail.

Equation (5.14) is a nonlinear algebraic equation that can be solved by considering the conservation law of the number of electrons and the number of ions. The result will be different depending on how to calculate the internal quantum state of each ion state. An example of charge state distribution as a function of temperature is shown in Fig. 5.1 for the characteristic density when aluminum foil is irradiated with intense laser, where simple energy levels are used. The ion density is 10^{18} cm^{-3} and temperature are from 10 eV to 10 keV. In thermodynamic equilibrium, complete ionization occurs when the temperature exceeds 1 keV. The charge state 11+ is seen in the wide temperature range is because a higher energy (temperature) of electrons is necessary for stripping off more from the bound state because ions are in a helium-like closed shell state.

Now, let us also discuss for widely seen ionization situation in laboratory discharge experiment. When the temperature is sufficiently low, at most one electron is ionized. Try to find an approximate Saha relation exactly applied to hydrogen atoms and approximately used for any atoms. In one electron ionization state, (5.14) closes only in the case of $\zeta = 0$. Since $n_e = n_1$ at the same time, if we define ionization degree as $\alpha = n_e/n$, $n = n_0 + n_1$, we obtain the one relation

Fig. 5.1 An example of
charge state distribution as a
function of temperature is
shown for the characteristic
density when aluminum foil
is irradiated with intense
laser, where simple energy
levels are used in solving
Saha equation. The ion
density is 10^{18} cm^{-3} and
temperature is from 10 eV to
10 keV
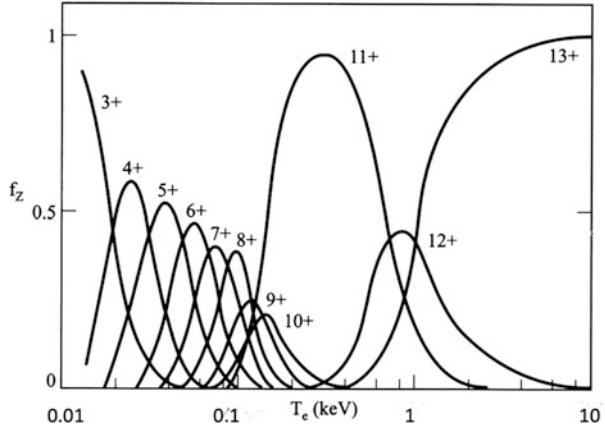
$$\frac{\alpha^2}{1-\alpha} = \frac{2}{n}\frac{u_1}{u_0}\left(\frac{mkT}{2\pi\hbar^2}\right)^{3/2} e^{-\frac{I}{kT}} \tag{5.16}$$

This is an exact relation for hydrogen, but an approximate relation for other ions. It
can be applicable in the limit of $I/kT \ll 1$ and $\alpha \ll 1$. Let us see the ionization degree
when the ionization is triggered. With the condition $\alpha \ll 1$, the following density
dependence is obtained from (5.16)

$$\alpha \propto \frac{1}{\sqrt{n}} \tag{5.17}$$

Even at the same temperature, the lower the density, the higher the degree of
ionization. Physical reasons can be intuitively explained in the following two ways.

1. Considering from the number of states, the number of bound states does not
   depend strongly on density, but as the space between atoms spreads wider, the
   number of identical energy states of free electrons increases proportionally to the
   volume. Therefore, many electrons gather in the free-state with a large number of
   states.
2. In the space where the density is extremely low($n = 1$ cm^{-3}), it is found that even
   if the temperature is extremely low the hydrogen is completely ionized from
   (5.16). This is because if free electrons collide with neutral atoms and collision
   ionization occurs, the probability that other free electrons are captured by hydro-
   gen ions are extremely low. Therefore, the free electrons will freely travel around
   the vacuum for a long time without encountering ions.

5.3   Quantum States of Atoms

In the plasma generation process, excitation and ionization of atoms by radiation absorption and electron collisions should be considered as elementary process. Moreover, it is necessary to understand quantum-mechanical interaction of atoms, electrons and photons, such as de-excitation, recombination, which is the reverse process of the above-mentioned elementary process. In some cases, it is necessary to calculate mathematical models with complicated atomic structures. To grasp the background knowledge of such atomic process, we will need to briefly review quantum mechanics and perturbation theory. However, we only discuss the quantum mechanics which is the foundation to study the atomic process in plasmas.

In order to study atomic physics, a multi-electron wave equation is the basis. Quantum mechanics can be easily derived by the principle of correspondence with classical mechanics.

5.3.1   Hydrogen Atom

Let us show time-dependent Schrodinger equation for the wave function $\phi(\mathbf{r},t)$ of a single electron system i.e., Hydrogen atom for a given spherical potential $U(\mathbf{r})$.

$$H \ = \frac{\mathbf{p}^2}{2m} + U = E \tag{5.18}$$

$$\mathbf{p} = i\hbar\nabla, \qquad E = -i\hbar\frac{\partial}{\partial t} \tag{5.19}$$

$$\left[-\frac{\hbar^2}{2m}\nabla^2 + U(\mathbf{r})\right]\phi(t,\mathbf{r}) = -i\hbar\frac{\partial}{\partial t}\phi(t,\mathbf{r}) \tag{5.20}$$

As is well known, the steady state solution of this equation is obtained by placing the conserved energy E

$$\phi(t,\mathbf{r}) = \psi(\mathbf{r})e^{-i\omega t}, \qquad \omega = E/\hbar \tag{5.21}$$

$$\left[-\frac{\hbar^2}{2m}\nabla^2 + U(\mathbf{r})\right]\psi(\mathbf{r}) = E\psi(\mathbf{r}) \tag{5.22}$$

This equation can be transformed into ordinary differential equations for r by a method such as the separation of variables. At that time, it can be seen that the three quantities of intrinsic energy, orbital angular momentum, and magnetic angular momentum cannot be taken as continuous values and are quantized as a separation constant.

Let's see why Schrodinger was able to arrive at (5.20). Naturally, without the predecessor work of analytical mechanics and electromagnetism, he never got to his idea. Analytical mechanics proves that geometric optics and wave optics can be connected by "introducing the concept of mechanics into the concept of wave" that the action function on the mass point of the Hamilton-Jacobi equation corresponds to the phase function of the wave. At the same time the boundary value problem of the Maxwell equation, for example, about the propagation of electromagnetic waves in a waveguide, it was found that the eigenvalue problem should be solved, and it was known that a specific frequency can exist only as a propagation solution. This is a concept conforming to Bohr's quantum hypothesis. At the same time, wave hypothesis of electron by de Broglie reminds us of the dynamic representation of wave optics. In this way academics clearly shows the birth of quantum mechanics that how to successfully adopt concepts of other fields and open up by giving new interpretations when challenging new discipline.

Hydrogen is the simplest atom binding one electron by the Coulomb force of a proton. The solution is the foundation for considering complex atoms, so let us review it briefly here. In the case of electrons bound to a hydrogen nucleus, the potential is a function of the radius coordinate r only in the form

$$U(r) = -\frac{e^2}{4\pi\varepsilon_0 r} \tag{5.23}$$

Three eigenvalues appear when substituting (5.23) into (5.22) and solving it by separating the variables, and the wave function is found to be in the form with three eigenvalues n, ℓ, m.

$$\psi(\mathbf{r}, \sigma) = R_{n\ell}(r) Y_\ell^m(\theta, \varphi) \chi_{m_s}(\sigma) \tag{5.24}$$

Here, $R_{n\ell}(r)$ the **radial wave function**, $Y_\ell^m(\theta, \varphi)$ is a **spherical harmonic function.** Note that the spherical harmonic function is an eigen-function satisfying the boundary condition in Fourier decomposition in the two-dimensional space on the surface of a sphere. For the convenience of multi-electron atom, the **spin function** $\chi_{m_s}(\sigma)$ is also introduced.

It is well known that the eigenvalue of energy is given in the form

$$E_n = -13.6\frac{1}{n^2} \ \ (eV) \tag{5.25}$$

Here, the reason why the energy eigenvalue depends only on the principal quantum number n is that the potential of (5.23) is mathematically special and **accidental degeneracy** with respect to the orbital quantum number l appears. For example, when there is shielding by the electrons of the inner shell like an alkali metal, the energy of the electrons of the outermost shell does not degenerate. The energy level of the outermost shell electron of a lithium atom is shown in Fig. 5.2. Since there are
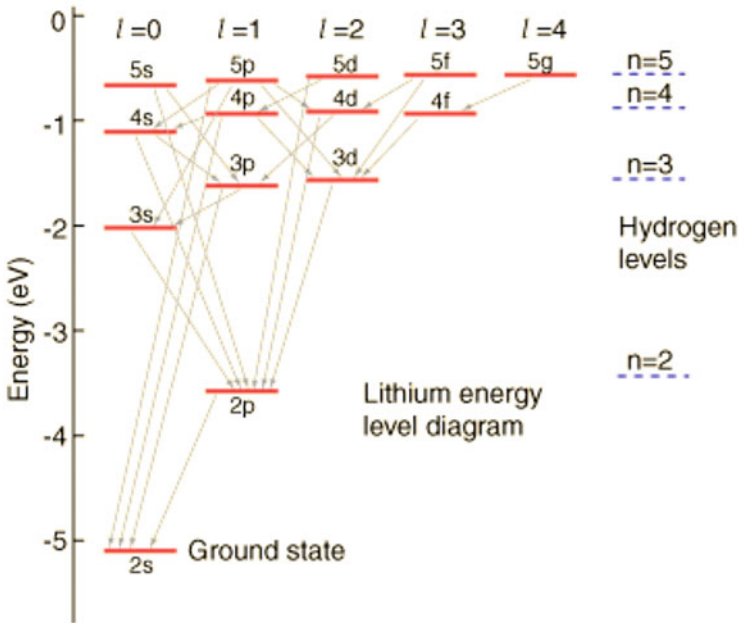
Fig. 5.2 The energy level of the outermost shell electron of a lithium atom

two electrons in the 1s state, there are two different energy levels 2s and 2p in n = 2 state. Because of the spread of the wave function of two electrons in 1s state, the wave function of 2s of lithium shrinks more than 2s of hydrogen, and consequently the energy becomes deeper. Because of the spread of the charge distribution of the two electrons of 1s, the effective potential becomes different from (5.23) and the accidental degeneracy disappears.

The number of quantum states of a hydrogen atom is $2n^2$ for each principal quantum state with its energy in (5.25). It is clear the sum of all of quantum states (n = 0~∞) diverges. In calculating Saha equilibrium for hydrogen plasma, it is necessary to avoid this divergence. Pay attention to the orbit radius of the wave function of n in the form:

$$r_n = a_B \frac{n^2}{Z} \tag{5.26}$$

where a_B is the **Bohr radius** (=0.53 A). It is clear that the orbit becomes larger with the increase of n. In plasma, an ion is surrounded by many other ions, and the free electrons also shields the nuclear charge at the center. Both effects make the large orbit electron be out of the attractive force by the nucleus and it is rather a free electron. This fact is schematically shown in Fig. 5.3, where outer orbits of bound electrons overlap with those of adjacent atoms.

Fig. 5.3 In plasma, an ion is surrounded by many other ions, and the free electrons also shields the nuclear charge at the center. Both effects make the large orbit electron be out of the attractive force by the nucleus and it is rather a free electron

Electron impacts

Photon emission, absorption

Excitation of bound electrons

Outer shells crushed by adjacent atoms

Disordered environment (fluid)

Pressure ionized electrons

Atomic continuum

Bound electrons

IP depression

Continuum lowering

Plasma continuum
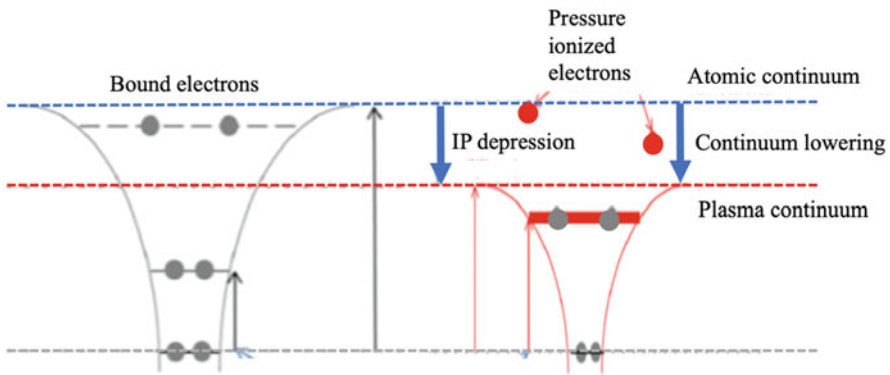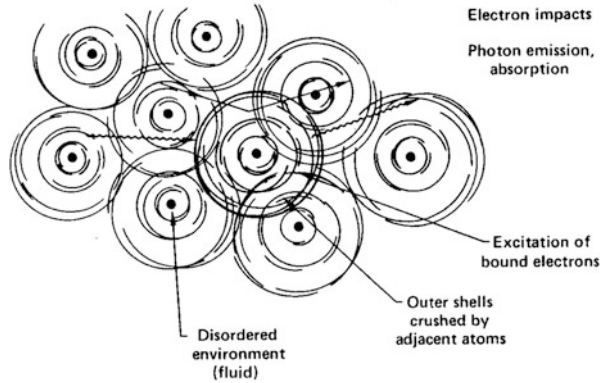
Fig. 5.4 The potential and bound states of an isolated atom are shown on the left. They must be modified like a plot in red as an atom embedded in plasma shown on the right. The electrons at higher energy levels becomes free electrons. As the result, the Coulomb field is shielded by such electrons disappears to make the potential structure sallower. Such modification is especially important in high-density plasma

Then, as shown in Fig. 5.4, the potential and bound states of an isolated atom must be modified like a plot in red as an atom embedded in plasma. The electrons at higher energy levels becomes free electrons. As the result, charge shielding by such electrons disappears to make the potential structure sallower. Such modification is especially important in high-density plasma. If it is possible to evaluate the average number of the maximum n as n*, using this as the maximum value of n in (5.5) and (5.13) makes it possible to solve the Saha Eq. (5.14) for hydrogen plasma. Such physics is called **ionization potential lowering** to be discussed later in the next chapter. As shown in Fig. 5.5, the effect of the lowering is clearly seen in the observed emission spectrum from hydrogen pellet injection into magnetically confined plasma. It is clear that line emissions from only three excited levels are observed, namely n* = 4 is inferred.

Fig. 5.5 The effect of the
ionization potential
lowering is clearly seen in
the observed emission
spectrum from hydrogen
pellet injection into
magnetically confined
plasma. It is clear that line
emissions from only three
excited levels are observed
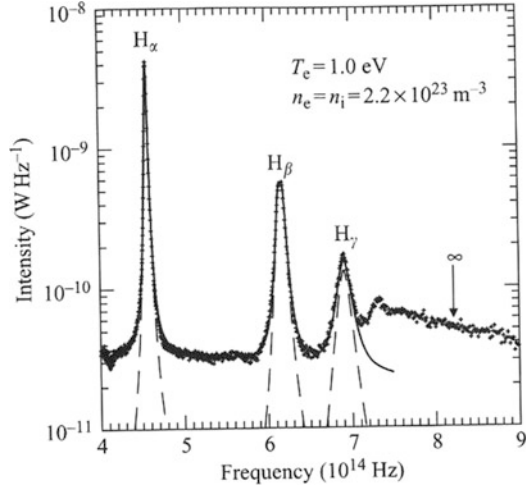
5.3.2   Helium Atom

The property of **electron spin** and Paul's **exclusive principle** is not considered in a
hydrogen atom, while it becomes essential in the atom having more than one
electron. This is because Pauli principle prohibits two electrons are in the same
quantum state including the spin state.

   The Hamiltonian of a **helium-like** atom is

$$H(\mathbf{r}_1, \mathbf{r}_2) = -\frac{\hbar^2}{2m_e}\left(\nabla_{\mathbf{r}_1}^2 + \nabla_{\mathbf{r}_2}^2\right) - \frac{Ze^2}{4\pi\varepsilon_0}\left(\frac{1}{r_1} + \frac{1}{r_2}\right) + \frac{e^2}{4\pi\varepsilon_0}\frac{1}{r_{12}} \qquad (5.27)$$

The first term is the kinetic energy of two electron whose coordinates are $\mathbf{r}_1$ and $\mathbf{r}_2$.
The second one is the attractive force by the nucleus. The third one is Coulomb
repulsive term between two electrons, where $|\mathbf{r}_1 - \mathbf{r}_2| = r_{12}$.

   It is known that Fermi particles like electrons should have the **anti-symmetry**
wave function. Describe two particle wave function as

$$\Psi(\mathbf{r}_1, \sigma_1; \mathbf{r}_2, \sigma_2) = \Psi(\tau_1, \tau_2) \qquad (5.28)$$

where τ is a simplified notation of $\mathbf{r}$ and σ. The function Ψ is called spin-orbitals. The
anti-symmetry condition requires

$$\Psi(\tau_1, \tau_2) = -\Psi(\tau_2, \tau_1) \qquad (5.29)$$

This requirement indicates that just a product of two single electron wave function cannot be a total wave function, where two electrons are in the quantum states a and b, the two-electron wave function are in the form.

$$\Psi(\tau_1, \tau_2) = \frac{1}{\sqrt{2}} \{\varphi_a(\tau_1)\varphi_b(\tau_2) - \varphi_a(\tau_2)\varphi_b(\tau_1)\} \tag{5.30}$$

Inserting (5.30) into Schrodinger equation with Hamiltonian (5.28), the total energy of two electrons is given in the form:

$$E = E_1 + E_2 + J_{12} + K_{12} \tag{5.31}$$

where E_1 and E_2 are a single electron energy given by hydrogen like binding energy.

$$E_1 + E_2 = -Z^2\{E_H(1) + E_H(2)\} \tag{5.32}$$

J_{12} in (5.31) is Coulomb interaction energy of two electrons and defined by

$$\begin{aligned} J_{12} = & \int \varphi_a{}^*(\tau_1)\varphi_b{}^*(\tau_2) \frac{e^2}{4\pi\varepsilon_0} \frac{1}{r_{12}} \varphi_a(\tau_1)\varphi_b(\tau_2)d\tau_1 d\tau_2 \\ = & \int |\varphi_a(\tau_1)|^2 \frac{e^2}{4\pi\varepsilon_0} \frac{1}{r_{12}} |\varphi_b(\tau_2)|^2 d\tau_1 d\tau_2 \end{aligned} \tag{5.33}$$

On the other hand, K_{12} in (5.31) is the **exchange interaction** energy

$$K_{12} = \iint \varphi_a{}^*(\tau_2)\varphi_b{}^*(\tau_1) \frac{e^2}{4\pi\varepsilon_0} \frac{1}{r_{12}} \varphi_a(\tau_1)\varphi_b(\tau_2)d\tau_1 d\tau_2 \tag{5.34}$$

Note that K_{12} is null when the spins are anti-direction, while K_{12} is finite only when the spins are in the same direction. It is clear that the total energy is lower when the spins are anti-direction for $K_{12} > 0$ for same direction, but $K_{12} = 0$ for anti-direction.

The energy diagram of helium atom is shown in Fig. 5.6. The left is for spins in anti-direction, while the right is for the spins in the same direction. The former is called **para-helium** ($S = 0$) and the latter is called **ortho-helium** ($S = 1$), where S is the sum of spins and $S = 0$ is called **singlet** and $S = 1$ is **triplets**, because $S = 1$ has three quantum state of $\mathbf{S} = -1$, 0, and 1.

5.3.3   Many-Electron Atom

In the case of atoms with many bound electrons, there are several approaches to obtain the atomic structure numerically, depending on how precisely the bound
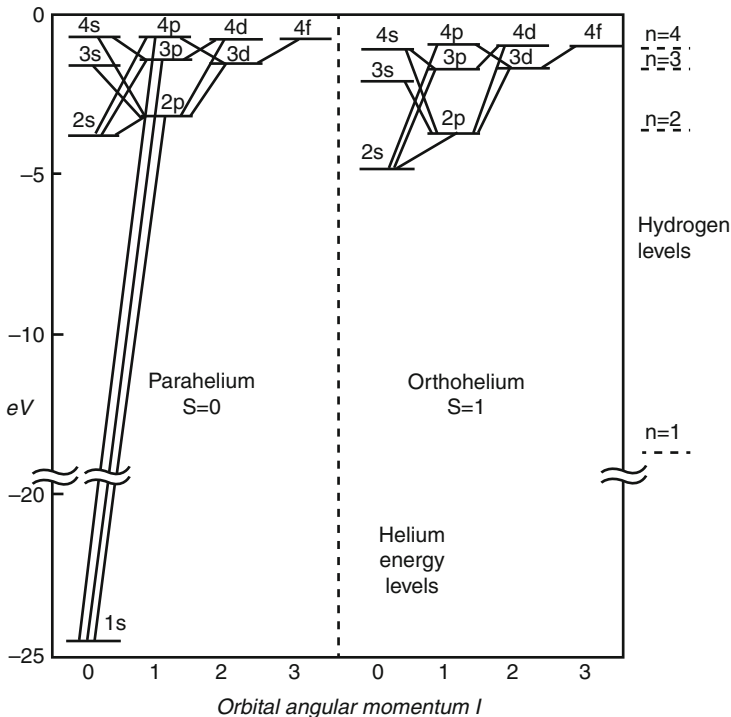
Fig. 5.6 The energy diagram of a helium atom

states should be calculated. The Hamiltonian for an atom or ion with atomic number Z with N bound electrons is given as

$$
H = -\frac{\hbar^2}{2m_e}\sum_i^N \nabla^2_{\mathbf{r}_i} + \frac{e^2}{4\pi\varepsilon_0}\left[-\sum_i^N \frac{Z}{r_i} + \frac{1}{2}\sum_i^N\sum_{j\neq i}^N \frac{1}{|\mathbf{r}_i - \mathbf{r}_j|}\right] \tag{5.35}
$$
$$
= T_e + V_{ne} + V_{ee}
$$

The first term is total electron kinetic energy, the second is Coulomb attraction energy by the nucleus, the third is electron-electron Coulomb interaction energy.

The basic strategy to solve (5.35) is to assume the configuration of N electrons. This means to define the quantum state of N electrons with the principal quantum number and the orbital angular momentum quantum number (n, l). For example, when six electrons are bound in an ion, the configuration of the ground state is represented as $(1s)^2(2s)^2(2p)^2$, with spectroscopic notation for l-state (s, p, d, f, g, h... for l = 0, 1, 2, 3, 4, 5, ...). This is an approximate expression of N-electron quantum state. Note that the closed shells of 1s and 2s are omitted from the

expression in the above case, in general, and given as $2p^2$. The potential force to each electron is also assumed to be spherically symmetric. This is called **central field approximation.** Then, the total wave function is assumed to be given by the combination of the function in (5.66) for assumed configuration of N-electrons [1, 2].

The standard numerical method of atomic structure calculation is **Hartree-Fock (HF) method**. The total wave function is assumed to be given by **Slater matrix** so that the total wave function is anti-symmetric. In this method, an iterative calculation is required until the numerical solution finally converges. Sometimes, just the production of N single wave functions is also used as the total wave function and this method is called **Hartree method**. This method is simpler as numeric method than the Hartree-Fock method, but no exchange interaction is included. Numerical data base obtained with Hartree-Fock calculation may be used to solve Saha equation for multi-electron ions of medium- and high-Z atom plasma. However, it is too much just for obtaining the effective charge distribution. As we see later, more simplified atomic structure model is used for plasma hydrodynamic simulations. As seen in the case of helium atom, the exchange interaction gives different energy spectrum depending on the spins of N electrons.

It is troublesome numerically to obtain the final radial wave functions of many electron system because of the iteration conversion process. Historically, more convenient way has been developed. It is **parametric potential (para-potential) method** [6]. So-called opacity codes have been developed to study the radiation transport in high-temperature plasma such as inside stellar objects and laboratory plasmas. As seen below, the opacity calculation demands reasonable atomic structure data. The number of atomic configurations is very huge in relatively mid and high Z atoms, it is convenient if a good approximate model is available to obtain the data of radial distribution functions in many configurations.

The well-known opacity codes, **OPAL** [7] and **HULLAC** [8] have been developed with the parametric potential method. When discussing the effective potentials in OPAL, for example, the electron configurations are assumed with two components. The first component is a "parent" configuration consisting of all the electrons in a given configuration except one. The excluded electron defines the second component or "running" electron. The parent configuration defines the effective potential for all the subshells available to the running electron. In order to incorporate the shell structure of the parent while retaining an analytic Fourier transform, OPAL introduced a potential with one **Yukawa term** for each occupied shell in the parent configuration.

$$V(r) = \frac{e}{4\pi\varepsilon_0 r}\left[(Z - \nu) + \sum_{n=1}^{n*} N_n e^{-\alpha_n r}\right] \qquad (5.36)$$

where

$$\nu = \sum_{n=1}^{n*} N_n \tag{5.37}$$

is the number of electrons for the parent ion, N_n the number of electrons in the shell with principal quantum number n, n* the maximum value of n for the parent configuration, and α_n the screening parameter for electrons in the shell n having principal quantum number n.

$$\alpha_n(\zeta, \nu) = (\zeta + 1)\left[a_0(\nu) + \frac{a_1(\nu)}{\zeta} + \frac{a_2(\nu)}{\zeta^2}\right] \tag{5.38}$$

where

$$\zeta = Z - \nu \tag{5.39}$$

The table of $\{a_i(\nu), i = 0, 1, 2\}$ are given in Ref. [6] and i = 3 is also given. These constants are obtained so that the results are optimized by comparing to the data of Dirac-Fock calculation. Relativistic version of Hartree-Fock. One electron wave function is calculated with Dirac equation in the potential (5.36). Note that some constants are also optimized to reproduce corresponding experimental data.

It is largely due to the improvement of the capability of the computer that such detailed calculation has become possible. However, simple model of atomic structure is demanded for direct coupling of radiation transport in the integrated hydrodynamic code.

5.3.4   Term Splitting

As shown in Fig. 5.7, the ion with one excited electron with a configuration p^3s^1 has the average energy for the configuration, splitting to three via exchange interaction and to six levels by **L-S coupling**. The energy levels given by the total wave function depend on the total orbital angular momentum **L** and total spin **S**. Each LS term is $(2L + 1)(2S + 1)$-fold degenerate, where

$$\mathbf{L} = \sum_i l_i, \quad \mathbf{S} = \sum_i s_i \tag{5.40}$$

It may be shown that the splitting of the configuration depends on L and S. The energy levels which are characterized by certain values of L and S are called **terms**
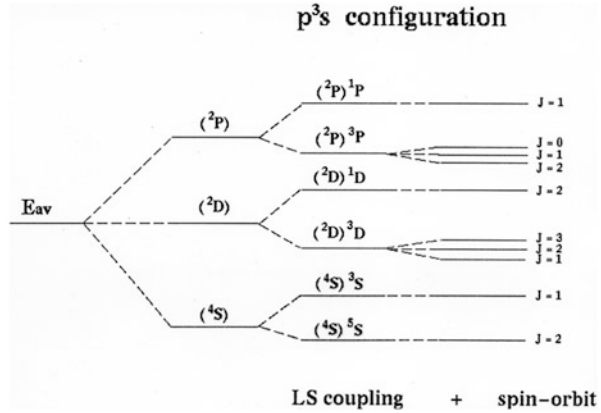
Fig. 5.7 An ion with one
excited electron with a
configuration p^3s^1 has the
average energy for the
configuration, splitting to
three via exchange
interaction and to six levels
by L-S coupling. The energy
levels given by the total
wave function depend on the
total orbital angular
momentum **L** and
total spin **S**

and the splitting is called **term splitting**. The coupling of angular momenta of
individual electrons to a resulting orbital angular momentum and spin is referred
to as **LS-coupling** or **Russell-Saunders coupling.**

Since the term splitting depends on L and S, the total electron state referred to as
configuration state functions (CSFs) are shown as the combination of orbitals and LS
coupling term in the form.

$$\Psi\left(\gamma^{(2S+1)}L\right)$$

where γ represents the orbital and S and L are the total spin and angular momentum.
For example, the ground state of six electrons has the following two CSFs for anti-
spin or parallel spin in 2p state.

$$1s^2 2s^2 2p^{2\,1}P \quad \text{or} \quad 1s^2 2s^2 2p^{2\,3}P$$

For the case of helium atom in Fig. 5.6, the parahelium and ortho-helium in $S = 0$
and $S = 3$ states, respectively.

It is almost enough to determine the quantum state of multi-electron atoms or ions
by Hartree-Fock methods. However, the details of line group structure become
important for analyzing experimental spectroscopic data and/or computation of
radiation hydrodynamics when the line radiation transport heats non-locally cold
plasma region. It is required to improve by adding the spin-orbit interaction in
Hamiltonian as follows.

$$H = T_e + V_{ne} + V_{ee} + V_{so} \tag{5.41}$$

where the **spin orbit interaction** is given in the form [1, 2].

$$V_{so} = a_{so} \sum_{i}^{N} \frac{1}{r_i} \frac{\partial V(r_i)}{\partial r_i} l_i \cdot s_i, \qquad a_{so} = \frac{\mu_B}{\hbar m_e c^2} \qquad (5.42)$$

The energy levels of atomic electrons are affected by the sum of the interaction between the electron spin magnetic moment and the current due to orbital angular momentum of each electron. It can be visualized as a magnetic field caused by the electron's orbital motion interacting with the spin magnetic moment of the electron. This effective magnetic field can be expressed in terms of the electron orbital angular momentum. Therefore, the energy levels have more fine structure and the number of energy levels becomes very huge when high-Z ions are considered.

Finally, schematic diagram of the lowest configuration of a neutral neon atom is shown in Fig. 5.8. The levels of each configuration lie within the limited energy range shown by the corresponding colored blocks (bands). This suggests that if the line width is broader than the separation of fine structure, it is possible to model all as a band, while if the width is narrower, it is required to identify the fine structure depending on what physics should remain in our model.

Fig. 5.8 Schematic diagram of the lowest configuration of a neutral neon atom. The levels of each configuration lie within the limited energy range shown by the corresponding shaded block
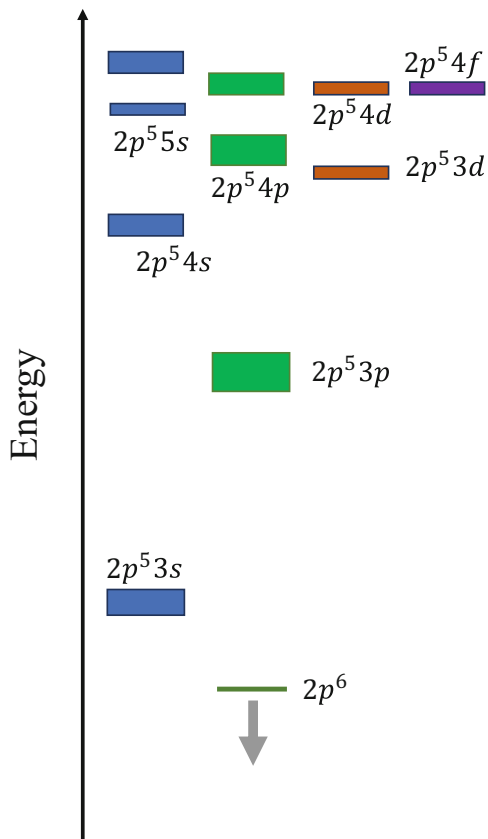
5.4   Quantum Theory of Electron Transitions

It is a fundamental of quantum mechanics to study the physics of atom-photon interaction based on the perturbation method. It is also a good example of mathematical physics on the perturbation theory. Try to derive the mathematics of transition of an electron in N-electron atom or ion, when a weak external perturbation is impacted on the bound electrons. Assume that the external one is due to a photon or an electron with its energy E_0 and its wave function is given in the form.

$$V_{ex}(t, \mathbf{r}) = a_0 e^{-i\omega_0 t + i\mathbf{k}_0 \cdot \mathbf{r}} \tag{5.43}$$

where $\omega_0 = E_0/\hbar$. Note that the wavenumber k_0 has the following relation with the energy, respectively,

$$\begin{aligned} \omega &= ck \qquad \text{(photon)} \\ \omega &= \frac{\hbar}{2m_e} k^2 \quad \text{(electron)} \end{aligned} \tag{5.44}$$

The total wave function of the initial bound electrons is $\Psi_i(\tau)$, where "i" means the initial state and τ indicate all coordinates of electrons. In addition, the total wave function of final state after transition is $\Psi_f(\tau)$, where "f" means the final state.

Assume that the perturbation is weak and the transition is slow enough as adiabatic transition, namely it is possible to assume that the wave function during the transition is approximated as a liner combination of the two states with time-dependent coefficients.

$$\Psi(t, \tau) = C_i(t)\Psi_i + C_f(t)\Psi_f \tag{5.45}$$

Of course, the conservation relation should be satisfied.

$$|C_i|^2 + |C_f|^2 = 1 \tag{5.46}$$

The initial and final wave functions are stationary ones and satisfy the Schrodinger equation.

$$-i\hbar \frac{\partial}{\partial t} \Psi(t, \tau) = H_0(\tau)\Psi(t, \tau) \tag{5.47}$$

where H_0 is Hamiltonian given in (5.37) for N-electron atom. The initial and final states $\Psi_i(\tau)$ and $\Psi_f(\tau)$ are eigen sates of (5.22) for N-electron Schrodinger equation. In addition to H_0, the perturbation potential energy (5.43) is included in time dependent Schrodinger equation. Assume that the wave function in the transition

phase is given by the form (5.45). Then the Schrodinger equation for the perturbation terms is given as

$$-i\hbar\frac{\partial}{\partial t}[C_i(t)\Psi_i + C_f(t)\Psi_f] = V_{ex}(t,\boldsymbol{\tau})[C_i(t)\Psi_i + C_f(t)\Psi_f] \tag{5.48}$$

Integrating (5.48) by all coordinate $\boldsymbol{\tau}$ after the product by the complex conjugate of the final state Ψ_f^*, the following relation is obtained.

$$-i\hbar\frac{\partial}{\partial t}[C_f(t)] = C_i(t)\int \Psi_f^* V_{ex}(t,\boldsymbol{\tau})\Psi_i d\boldsymbol{\tau} + C_f(t)\int \Psi_f^* V_{ex}(t,\boldsymbol{\tau})\Psi_f d\boldsymbol{\tau} \tag{5.49}$$

Note that the transition is given by the change of electron configuration. For example, consider the initial state is the oxygen ground state and the final state is one of the following two.

$$1s^2 2s^2 2p^4 \rightarrow 1s^2 2s^2 2p^3 nd \tag{5.50}$$

$$1s^2 2s^2 2p^4 \rightarrow 1s2s^2 2p^3 np \tag{5.51}$$

(5.50) is the transition of an outer shell electron, while (5.50) is the inner-shell electron transition. It is possible to integrate (5.49) by $\boldsymbol{\tau}$ except for the transiting electron coordinate **r**. (5.49) becomes the integral to one electron wave function (φ_i, φ_f).

$$\frac{dC_f}{dt} = i\frac{a_0}{\hbar}e^{i\Delta\omega t}\int \varphi_i^* e^{i\mathbf{k_0}\cdot\mathbf{r}}\varphi_f d\mathbf{r} = \alpha_{if}e^{i\Delta\omega t} \tag{5.52}$$

where

$$\Delta\omega = (\omega_i - \omega_f) - \omega_0 \tag{5.53}$$

$$\alpha_{if} = i\frac{a_0}{\hbar}\int \varphi_i^* e^{i\mathbf{k_0}\cdot\mathbf{r}}\varphi_f d\mathbf{r} \tag{5.54}$$

In deriving (5.52), it is assumed that $C_i = 1$. The second term in (5.49) is neglected because of the rapidly oscillating term with small C_f at the beginning, and only the first term remains because of resonance.

$$C_f(t) = \alpha_{if}\frac{e^{i\Delta\omega t} - 1}{i\Delta\omega} \tag{5.55}$$

Therefore, the probability of the j state is near the time origin

$$|C_f|^2 = C_f^* C_f = |\alpha_{if}|^2 \frac{2(1 - \cos \Delta\omega t)}{(\Delta\omega)^2} \tag{5.56}$$

As can be seen from the uncertainty principle, the energy level has a finite width and it is necessary to integrate over the frequency ω for obtaining the transition probability of electrons. Then, changing variables like

$$\Delta\omega t = \xi = 2x \tag{5.57}$$

and using the relation

$$\int_{-\infty}^{\infty} \frac{1 - \cos \xi}{\xi^2} d\xi = \int_{-\infty}^{\infty} \frac{\sin^2 x}{x^2} dx = \pi \tag{5.58}$$

The following solution is obtained.

$$|C_f|^2 = \nu_{if} t, \qquad \nu_{if} = 2\pi |\alpha_{if}|^2 \tag{5.59}$$

where ν_{if} is the **transition probability** (in unit of s^{-1}).

5.5 Photo-excitation and Ionization

Calculate the transition probability by photon interaction. As mentioned in Vol. 1, Hamiltonian of an electron including interaction with photon in the vacuum is given in the form [9]

$$H = \frac{P_c^2}{2m} = \frac{(p + eA)^2}{2m} = H_0 + \frac{e}{m} p \cdot A + \frac{e^2}{m} A^2,$$
$$H_0 = \frac{p^2}{2m} \tag{5.60}$$

where A is the vector potential of photon field. Assume that only one electron interacts with the photon for the transition and the other electrons are not necessary to consider in the following analysis. Use the following corresponding relation of the operators.

$$E \to i\hbar \frac{\partial}{\partial t}, \qquad p \to -i\hbar \nabla \tag{5.61}$$

Then, Schrodinger equation is obtained as

$$i\hbar \frac{\partial}{\partial t}\Psi = \left[H_0 + i\hbar \frac{e}{m}\mathbf{A}\cdot\nabla + \frac{e^2}{2m}\mathbf{A}^2\right]\Psi \tag{5.62}$$

It is clear that the second term on RHS is linear perturbation and the third term is non-linear perturbation. Here, the analysis is limited to the case of the linear theory and the third term is neglected. Assume that the vector potential is due to plane electromagnetic wave polarized in the x-direction.

$$\mathbf{A}(t,\mathbf{r}) = A_0\mathbf{i}_x e^{-i(\omega_0 t - \mathbf{k}_0\mathbf{r})} \tag{5.63}$$

Comparing (5.43) and (5.62), the assumed coefficient a_0 is in the present case found to be an operator.

$$a_0 e^{i\mathbf{k}_0\cdot\mathbf{r}} = -i\hbar \frac{e}{m}A_0 e^{i\mathbf{k}_0\cdot\mathbf{r}}\mathbf{i}_x\cdot\nabla \tag{5.64}$$

In order to calculate α_{if} in (5.54), we have to calculate

$$\alpha_{if} = \frac{e}{m}A_0\langle i|e^{i\mathbf{k}_0\cdot\mathbf{r}}\mathbf{i}_x\cdot\nabla|f\rangle \tag{5.65}$$

It is not easy to directly integrate (5.65). Let's examine the relationship between the photon energy and the energy level of electrons. In the case of hydrogen, the wave function of electrons is at most the extent of the Bohr radius. However, its energy level is about 10 eV, and the wave number of the photon with energy of 10 eV is $k = 8 \times 10^4$ cm^{-1}. This is because of the difference of the dispersion relation shown in (5.44). Therefore, the exponent of (5.65) is very small such as

$$\langle k_0 r\rangle \sim 10^{-3} \tag{5.66}$$

This means it is possible to use Taylor expansion.

$$e^{i\mathbf{k}_0\cdot\mathbf{r}} \approx 1 + i\mathbf{k}_0\cdot\mathbf{r} + \frac{1}{2}(\mathbf{k}_0\cdot\mathbf{r})^2 + \dots . \tag{5.67}$$

When only the first term unity is taken, the wavelength of the radiation field corresponds to an infinite. Such assumption is called **dipole approximation**. The second term in (5.67) gives **electric quadrupole transition** and **magnetic dipolar transition**, while they are neglected in the following analysis.

5.5.1   Dipole Transition Matrix Element

In integrating (5.65), the corresponding relation is used.

$$-i\hbar\nabla = \mathbf{p} = m\frac{d\mathbf{r}}{dt} = -im\omega\mathbf{r} \qquad (5.68)$$

(5.65) is rewritten by setting ω in (5.68) as ω_{if}.

$$\alpha_{if} = \frac{e}{\hbar}A_0\omega_{if}\langle i|x|f\rangle \qquad (5.69)$$

In general, the transition from i to j defines the **dipole matrix element** as.

$$\mathbf{r}_{ij} = \langle i|\mathbf{r}|j\rangle \qquad (5.70)$$

The matrix of (5.65) is its x component of (5.70). The value of the matrix element is large as the overlapping of the wave functions of i and j becomes stronger. The one electron wave function is possible to be given in the form (5.66). The radial distribution of the electron, $rR(r)$ can be imaged from that of an electron in hydrogen atom in Fig. 5.9. It is seen that the closer the principal quantum number is, the stronger the overlapping in (5.70). However, note that the integral on θ and φ in (2.97) gives the **selection rule** to be explained later.

Since the electric field $E_0 = \omega_0 A_0$, (5.65) is shown as

$$|\alpha_{if}|^2 = \frac{e^2}{\hbar^2}E_0^2|x_{if}|^2 \qquad (5.71)$$

Now, since the polarization direction is along x, the transition probability is symmetric around the x axis and θ is the angle formed by $\mathbf{r}$ and the x axis, $x = r\cos\theta$

$$\begin{aligned}\frac{1}{\tau_{if}} &= \nu_{if} = \frac{4}{3}\frac{\pi^2}{c\hbar^2}\left(\frac{e^2}{4\pi\varepsilon_0}\right)I(\omega)|\mathbf{r}_{if}|^2, \\ I(\omega) &= \frac{1}{2}\varepsilon_0 c\omega^2 A_0^2\end{aligned} \qquad (5.72)$$

Here, $I(\omega)$ is the photon energy flux overlap with the transition energy spectrum and the relationship $\langle\cos^2\theta\rangle = 1/2$ is used. Consequently, τ_{if} represents the transition time. When the number density of atoms or ions with the same configuration of the initial state is n_i, the transition cross section σ_{if} is given by the relation.

$$\nu_{if} = n_i\sigma_{if} \qquad (5.73)$$

Fig. 5.9 The radial
distributions of an electron,
rR(r), of a hydrogen atom
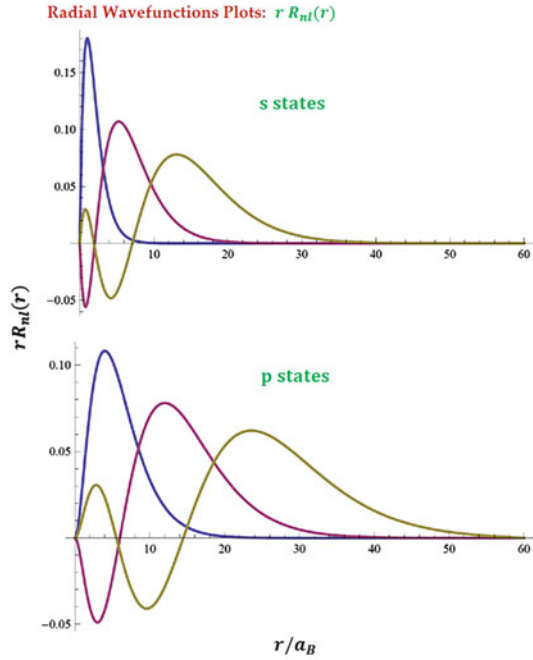
5.5.2   Einstein's A, B Coefficients

(5.72) gives coefficients of absorption and emission due to induced process, but in fact there is **spontaneous emission** process that cannot be solved by the above perturbation theory. Consider two energy levels as a simple quantum system. The upper level is indicated by 2, and the lower level is indicated by 1. Then, considering the three processes shown in Fig. 5.10, the number of the state 1 (N_1), evolves according to the following coupled equation.

$$\frac{dN_1}{dt} = A_{21}N_2 + B_{21}I(\omega)N_2 - B_{12}I(\omega)N_1 \tag{5.74}$$

At the same time, a similar equation governs the evolution of N_2. Here, A is the spontaneous emission coefficient, which is derived from the fact that the state other than the ground level is unstable and has a finite lifetime. Then, B_{21} and B_{12} indicate induced emission coefficient and absorption coefficient, respectively.

When both atoms and radiation fields are completely in thermal equilibrium, the right side of Eq. (5.74) must be balanced. In other words, when the photon field is Planck distribution (see Appendix) and the electron population is Boltzmann distribution, the detail balance relation should be satisfied.

Fig. 5.10 Energy diagram of two-level system showing absorption, spontaneous emission, and stimulated emission

(a) Absorption   (b) Spontaneous emission

(c) Simulated emission
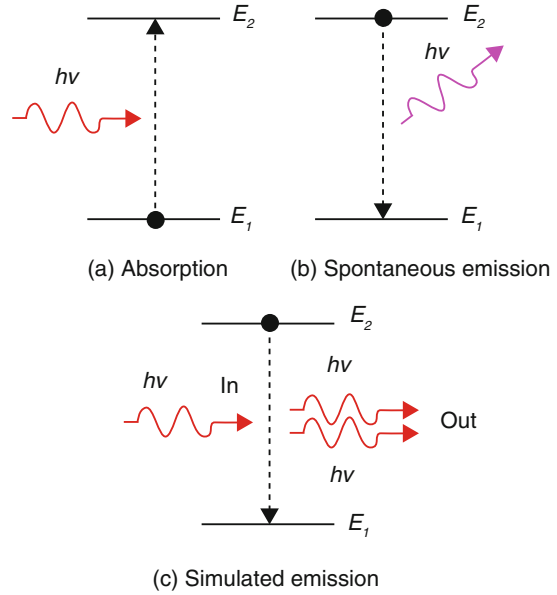
$$A_{21}N_2 + B_{21}I(\omega)N_2 - B_{12}I(\omega)N_1 = 0 \tag{5.75}$$

where $I(\omega) =$ (Planck distribution).

$$B_T(\nu) = \frac{2h\nu^3/c^2}{\exp(h\nu/T) - 1} \tag{5.76}$$

The electron equilibrium population should satisfy the relation

$$\frac{N_2}{N_1} = \frac{g_2}{g_1} \exp\left(-\frac{E_2 - E_1}{k_B T}\right) \tag{5.77}$$

It is noted that B_{12} has already been given by (5.72), so it is possible to explicitly obtain the remaining B_{21} and A_{21} from the three simultaneous equations. Equation (5.72) gives B_{12} as follows

$$B_{12} = \frac{2}{3}\frac{\pi}{\hbar^2}\left(\frac{e^2}{4\pi\varepsilon_0}\right)|\mathbf{r}_{12}|^2 \tag{5.78}$$

Using (5.78), B_{21} and A_{21} are obtained as follows.

$$B_{21} = \frac{g_1}{g_2}B_{12}, \tag{5.79}$$

B_{12} and A_{21} are written as

$$A_{21} = \frac{2h\nu^3}{c^2} B_{21} \qquad (5.80)$$

Since the three coefficients are proportional to the dipole moment, we introduce a dimensionless quantity of order of unity called **oscillator strength**

$$f_{ij} = \frac{2m\omega}{3h} |\mathbf{r}_{ij}|^2 \qquad (5.81)$$

Then, the spontaneous emission coefficient is given in [10].

$$A_{21} = 8.0 \times 10^9 \left(\frac{\hbar\omega}{13.6\,\mathrm{eV}} \right)^2 f_{21} \quad \mathrm{s}^{-1} \qquad (5.82)$$

In order to estimate the size of f_{ij} intuitively, rewrite (5.81) as

$$f_{12} = \frac{2}{3} \frac{\hbar\omega}{E_0} \frac{|\mathbf{r}_{12}|^2}{a_B^2}, \qquad (5.83)$$

where E_0 is the energy of hydrogen ground state.

We found that Einstein's A and B coefficients are proportional to the oscillator strength. From the integral in the spherical coordinates in the calculation of the oscillator strength, it is found that the **selection rule** is derived. What remains is the integral of radial direction r. Radial wave function is a solution oscillating to positive and negative except for the ground state (Fig. 5.9). It is clear that when the principal quantum numbers of $|1\rangle$ and $|2\rangle$ states are too far each other, the integral becomes that of positive and negative oscillating functions and becomes smaller. Oscillator strength takes a large value when both principal quantum numbers are close to each other. In addition, it can be expected that the larger $\hbar\omega/E_0$ in (5.83) the value of $|\mathbf{r}_{12}|^2/a_0^2$ the smaller. In fact, the magnitude of the oscillator strength is a constant value, and in the case of hydrogen atoms, it is known to be as shown in Table 5.1 [10].

In addition, the following **sum rule** called **Fermi's golden rule** is satisfied.

$$\sum_j f_{ij} = 1 \qquad (5.84)$$

Note that the summation of (5.84) represents all states for the complete system, including free electron states.

Table 5.1 Oscillator strength of hydrogen atom. The values are for the principal quantum number $n = 1$–5 [10]. The positive values are the absorption oscillator strength and the negative ones the emission oscillator strength. The larger values mean easier transition from the initial state to the final state

initial	1s	2s	2p		3s	3p		3d	
final	*np*	*np*	*ns*	*nd*	*np*	*ns*	*nd*	*np*	*nf*
n=1	–	–	-0.139	–	–	-0.026	–	–	–
2	0.4162	–	–	–	-0.041	-0.145	–	-0.417	–
3	0.0791	0.349	0.014	0.696	–	–	–	–	–
4	0.0290	0.1028	0.003	0.122	0.484	0.012	0.619	0.011	1.016
5	0.0139	0.0419	0.001	0.044	0.121	0.007	0.139	0.002	0.156

5.5.3   Selection Rule

Carry out the integration of (5.70). As is well known each Cartesian coordinate is transferred to the spherical coordinate as follows,

$$
\begin{aligned}
x &= r \sin\theta \cos\varphi \\
y &= r \sin\theta \sin\varphi \\
y &= r \cos\theta
\end{aligned}
\tag{5.85}
$$

The spherical harmonics in (5.24) is defined as

$$
Y_\ell^m(\theta, \varphi) = P_\ell^m(\theta)e^{im\varphi}
\tag{5.86}
$$

where P_l^m is Legendre fold function. The integral (5.70) by θ coordinate has the following form,

$$
\int_{-1}^{1} \xi P_\ell^m(\xi) P_{\ell'}^{m'}(\xi) d\xi
\tag{5.87}
$$

Legendre fold function has a formula.

$$
\xi P_\ell^m(\xi) = \frac{\ell + m}{2\ell + 1} P_{\ell-1}^m(\xi) + \frac{\ell - m + 1}{2\ell + 1} P_{\ell+1}^m(\xi)
\tag{5.88}
$$

Inserting (5.88) into (5.87), it is easy to show that the integral has finite value only for the case,

$$
\Delta\ell = \pm 1
\tag{5.89}
$$

In addition, the integral to φ coordinate requires the following selection rule, too.

$$\Delta m = 0, \pm 1 \tag{5.90}$$

5.6   Photo Excitation and De-excitation

In case where ions are partially ionized, spontaneous transition from the upper-level q to the lower-level p has been derived in (5.78). Rewriting it with the oscillator strength of radiation $f_{p,q}$, we obtain

$$A(q, p) = \frac{e^2 \omega^2}{2\pi mc^3 \varepsilon_0} \frac{g(p)}{g(q)} f_{p,q} \quad [s^{-1}] \tag{5.91}$$

Here, $g(p)$ and $g(q)$ are the number of states at the levels p and q, respectively. The oscillator strength $f_{q,p}$ of radiation emission is related to the **absorption oscillator strength** $f_{p,q}$ as follows.

$$f_{q,p} = \frac{g(p)}{g(q)} f_{p,q} \tag{5.92}$$

Regarding the oscillator strength of absorption in the case of hydrogen, there is a classical expression by Kramers (p. 269 in [10]),

$$f_{p,q} = \frac{2^6}{3\sqrt{3}\pi} \frac{1}{2p^5} \frac{1}{q^3} \frac{1}{(p^{-2} - q^{-2})^3} g_{bb} \tag{5.93}$$

Here, g_{bb} is a **gaunt factor**, which is a correction factor for matching with quantum mechanically accurate calculation. The subscript "bb" means a transition from a bound state to a bound state.

It is valuable to note a simple property of $f_{p,q}$. For a given p, $f_{p,q}$ becomes smaller in proportion to q^{-3} for larger q. In addition, the oscillator strength between higher levels such as $f_{p,p+1}$ tends to the following form.

$$f_{p,p+1} \simeq (p + 1)/5 \tag{5.94}$$

Let's find the photo excitation cross section. From the relation (5.72), we see that the reciprocal of the transition time from p to q is $B_{p,q}I(\omega)$. This should be equal to $\rho(\omega)\sigma$ where $\rho(\omega)$ is the number density of photons at thermal equilibrium (Planck distribution) and we obtain the cross section of spontaneous emission.

$$\sigma(p,q) = \frac{1}{4} \frac{c^3 h^2}{(\hbar\omega)^2} A(q,p) \tag{5.95}$$

Figure 5.11 shows the p and q dependence of A (q, p).

The cross section of the **photo de-excitation** is automatically obtained from the relation of detailed balance by using the cross section of the photo excitation. In thermodynamic equilibrium condition, RHS of (5.74) should balance, namely (5.75) should be satisfied. This is called the **principle of detailed balance**. That is, if the cross-section of photo-excitation is given, the cross-section of photo de-excitation in the reverse process should be automatically determined with use of (5.77) and (5.78). We insert Planckian intensity distribution into (5.74), and we use the relation (5.76). If we put these relationships into (5.74), we obtain the photo de-excitation cross section.

$$\sigma(q,p) = B_{q,p} B_T(\omega) \tag{5.96}$$

Here, $B_T(\omega)$ is energy flux of the Planck distribution define by $\hbar\omega c \rho(\omega)$ and (5.76). $B_{q,p}$ in (5.96) is obtained by using (5.77).

Fig. 5.11 The p and q dependence of Einstein's A coefficient A (q, p) [4]. Reprinted with kind permission by T. Fujimoto
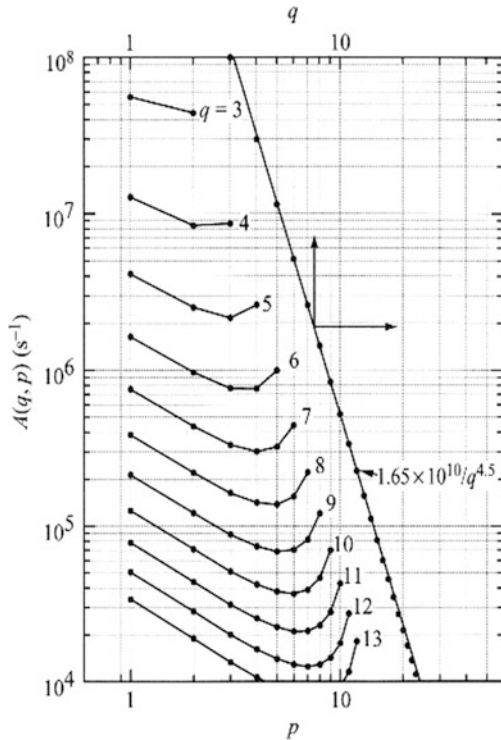
5.7   Photoionization and Photo-recombination

Let's calculate the cross section of photoionization where a photon interacts an atom and one electron becomes free electron by absorption of photon energy. The way of thinking is the same as in the above photo-excitation case, and this time we think about the transition including the electron free state from the bound state. We have to start with finding the wave function of free electron whose energy derived from Schrodinger equation is positive and the wave function is infinitely spread. This results in a wave function including the spherical Bessel function derived by the scattering problem. However, as the calculation becomes complicated, let's calculate the cross-section within **Born approximation** here. In Born approximation, free electron is assumed plane wave and is written in the following normalized form

$$\psi_f = \left(\frac{1}{2\pi}\right)^{3/2} e^{i\mathbf{k}\mathbf{r}} \tag{5.97}$$

That energy is

$$E_f = \frac{\hbar^2 k^2}{2m} \tag{5.98}$$

Consider the photo-ionization cross section for the case where the initially bound electron $|i\rangle$ is ionized and becomes a final state of free electron $|f\rangle$. Then, as has been derived in (5.65), we obtain the following form as the transition probability

$$\alpha_{if} = \frac{e}{m} A_0 \langle i | e^{-i\mathbf{k}\cdot\mathbf{r}} \mathbf{e}_p \cdot \nabla | f \rangle \tag{5.99}$$

Try to integrate (5.99) explicitly by assuming the case of $|i\rangle$ being the 1s of a hydrogen atom. The radial wave function of the hydrogen 1s is given as

$$\psi_i = \left(\frac{1}{\pi a_0^3}\right)^{1/2} e^{-r/a_0} \tag{5.100}$$

Inserting (5.100) and (5.97) into (5.99), the integration is easily carried out with assumption of the dipole approximation (5.67) in the form.

$$\int e^{-r/a_0} e^{-i\mathbf{k}\cdot\mathbf{r}} d\mathbf{r} = \frac{8\pi}{a_0 \left(a_0^{-2} + k_f^2\right)^2} \tag{5.101}$$

With use of (5.101), the cross section (5.73) for photo-ionization is derived to be the following form.

$$\sigma(\omega) = 32\alpha \frac{\hbar}{m\omega a_0^5} \frac{k_f^2}{\left(a_0^{-2} + k_f^2\right)^4} \int \cos^2\theta d\Omega \tag{5.102}$$

where θ is the angle formed by the polarization direction of light and the direction of the wave number of free electrons. In (5.100) α is the fine-structure constant.

$$\alpha = \frac{e^2}{2\varepsilon_0 hc} = 1/137 \tag{5.103}$$

Note that in deriving (5.102) we have assumed the wave number of free electrons is short, that is, the energy of light is sufficiently larger than the binding energy of the ground state;

$$k_f >> \frac{1}{a_0} \tag{5.104}$$

In addition, (5.102) can be written for any hydrogen-like ions of atomic number Z in the form,

$$\sigma(\omega) = \frac{128\pi}{3}\alpha\frac{\hbar}{m\omega}\left(\frac{Z}{k_f a_0}\right)^5 \tag{5.105}$$

(5.105) can be written finally as follows.

$$\sigma(\omega) = \frac{16\sqrt{2}\pi}{3}\alpha\left(\frac{Z}{a_0}\right)^5\left(\frac{\hbar}{m\omega}\right)^{7/2} \tag{5.106}$$

As you can see in (5.106), the photo-ionization cross section strongly depends on the photon energy.

The above calculation can be also expressed using the concept of the absorption oscillator strength in the free state $f_{p,\varepsilon}$. Assuming that the energy of incident light is $h\nu$, the cross-section of photoionization is analytically obtained with respect to hydrogen-like case. Ionization cross section can be written with the oscillator strength $f_{p,\varepsilon}$ in the form;

$$\sigma_{p,\varepsilon}(\nu) = \frac{e^2}{4mc\varepsilon_0}\frac{df_{p,\varepsilon}}{d\nu} \tag{5.107}$$

Here, $f_{p,\varepsilon}$ is the continuous absorption oscillator strength for the transition from the bound state p to a free state with kinetic energy ε. In the case of hydrogen atoms, the expression of $f_{p,\theta}$ in (5.93) can be used and extended to the bound-free transition. Replacing the final state to free state as $q \rightarrow i\kappa$, a pure imaginary number, we obtain the following form;

$$f_{p,\kappa} = \frac{2^6}{3\sqrt{3\pi}} \frac{1}{2p^5} \frac{1}{\kappa^3} \frac{1}{(p^{-2} + \kappa^{-2})^3} g_{bf} \qquad (5.108)$$

where κ should satisfy the energy conservation relation

$$h\nu = z^2 R\left(\frac{1}{p^2} + \frac{1}{\kappa^2}\right) \qquad (5.109)$$

where R is the Rydberg constant ($=13.6$ eV), and z is equal to 1 in the case of hydrogen and the charge number of the hydrogen-like ion. About the hydrogen-like atom whose charge number is z and who has one-electron in the s-state, we have the following relation.

$$df_{p,\varepsilon} = f_{p,\kappa}d\kappa = f_{p,\kappa}\frac{h\kappa^3}{2z^2 R}d\nu \qquad (5.110)$$

Using (5.110) the photoionization collision cross section is given

$$\sigma_{p,\varepsilon}(\nu) = \alpha\pi\frac{2^6}{3\sqrt{3}}\left(\frac{p^2 a_B}{z}\right)^2 \frac{1}{p^3}\left(\frac{z^2 R/p^2}{h\nu}\right)^3 g_{bf} \qquad (5.111)$$

Here, α is the fine structure constant ($=1/137$). This equation is equivalent to (5.107). When considering the case of a hydrogen atom and looking for the value at the point of $h\nu = R$, the cross section of the ground state ($p = 1$) is calculated

$$\sigma = 7 \times 10^{-18} \quad [cm^2]$$

For the case of hydrogen, the photoionization cross section is shown in Fig. 5.12. In the log-log figure, the straight line is a power law as given in (5.111). The following features are known for the cross section.

1. There is a threshold for $h\nu$ for photoionization, requiring the photon energy more than the ionization energy
2. Photo-ionization cross section from the s-state is proportional to $1/(h\nu)^3$
3. For higher energy photon, the photo-ionization cross section is larger for the lower energy level transition as seen in Fig. 5.12.

Regarding the iron atom (Fe), the photoionization coefficient from the K shell of iron is shown in Fig. 5.13 as a function of photon energy. As can be seen from Fig. 5.12, the ionization cross section is maximum at the threshold of photon energy, and abruptly decreases by the power of energy as the energy increases. Another characteristic feature is that as shown in Fig. 5.13. the ionization cross section from the grand state 1s hardly depends on ionization state. In other words, when high energy photons are incident on atoms with high-Z value, it is necessary to always consider **inner shell ionization.**

Fig. 5.12 The
photoionization cross
section of a hydrogen
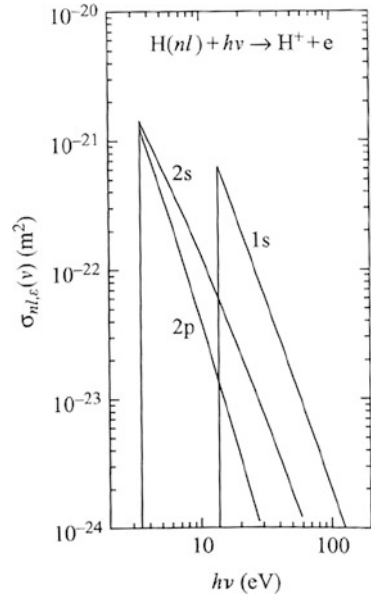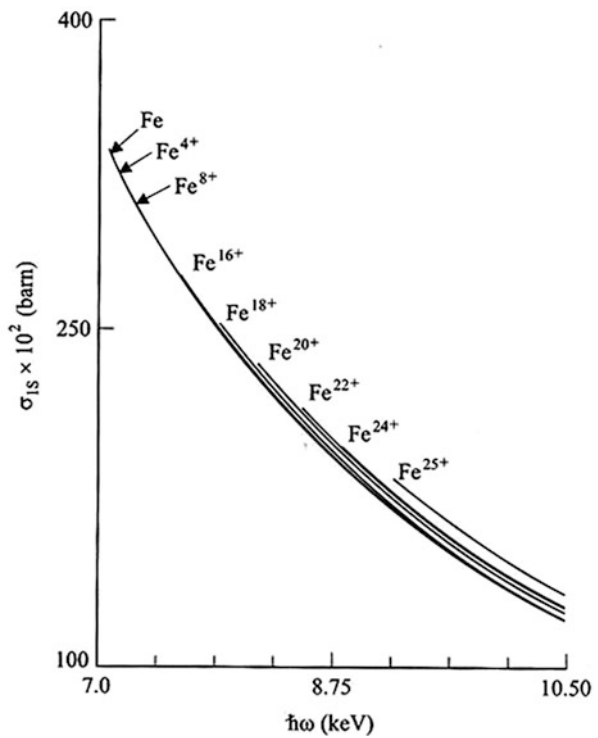atom [4]. Reprinted with
kind permission by
T. Fujimoto

Fig. 5.13 The
photoionization coefficient
from the K shell of iron is
shown as a function of
photon energy [3].
Reprinted with kind
permission by D. Salzmann

As evidenced by the discussion above, when a photon energy high enough to ionize 1s-electron, the 1s electron is ionized predominantly even if there are 2s electrons. Since the photo-ionization cross section is larger for the inner shell, it can be seen that the inner shell ionization is dominant. In this way, photoionization plasma needs to be modeled by taking account of the ionization progresses after the inner shell vacancy is produced.

Now, photo recombination, which is the reverse process of the photoionization, is an elementary process in which a free electron is captured to a bound state (quantum state m) to release the excess energy as a photon. The problem is a two-body problem in terms of quantum mechanics; a plane wave (5.97) of the free electron is defined as an initial state of (5.99). However, the cross section of the photo-recombination is easily obtained by considering the detail balance relation in the thermodynamic equilibrium state.

5.8   Quantum Theory of Electron Impact on Atom

In plasma high energy electrons play important role in ionizing and recombining the ions via electron impact. They are called collisional ionization and recombination, respectively. Most of plasma temperature is low compared to mc^2 and non-relativistic analysis is enough to obtain the cross sections of such processes. The situation is the same in the cases of excitation and de-excitation as well. Therefore, the following analysis is limited to the non-relativistic case. It is, however, noted that the highly relativistic electron beam produced by accelerators have been used as diagnostic tool to study the structure of nuclei and quarks inside nuclei [9]. This is because the de-Broglie wavelength of impacting electron can resonate with the size of nucleus and elementary particles. So, the following analysis to be done by stating with Schrodinger equation can be easily extended to the relativistic case, if Dirac equation is instead used as the basic equation.

Consider the case where free electrons collide to ionize or excite atoms or ions. This is called **electron impact excitation** or **ionization**. Precise calculation requires computation using wave function of free electrons distorted by the atomic field, and analytical handling is complicated. It is now possible to solve almost exact equations in detail with computers.

The cross section of the collisional excitation is shown in Fig. 5.14 for helium atoms in the para-helium ground state already explained in Fig. 5.6. As can be seen from the Fig. 5.14, the probability of transition to the p-state is the largest, and it is also possible for transition to 2s which is the optically forbidden. It is also noted that the cross section decreases as the transition to the higher energy levels. Unlike photoionization, the cross section gradually increases from the threshold energy, and when the energy is about three times the threshold energy, the cross section becomes maximum, and thereafter decreases with the power of energy as determined by the Born approximation described later.

Fig. 5.14 The cross
sections of the collisional
excitation of helium atoms
from the para-helium
ground state as a function of
an impacting electron
kinetic energy
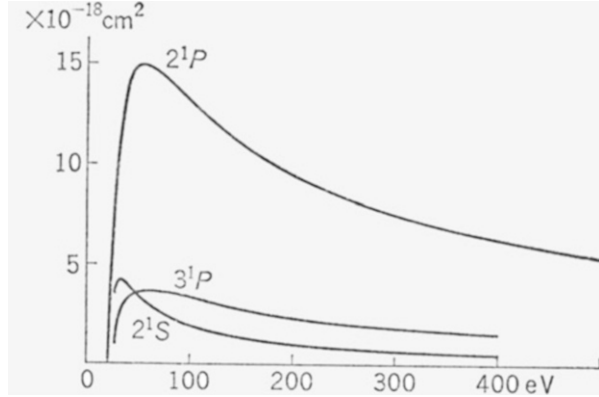
Different from the photoionization, in the electron collision, the ionization cross
section of the outermost shell electron is largest, and bound electrons are peeling
from the outside. It is also important to note that the photo-ionization cross section is
of the order of barn ($=10^{-24}$ cm^2), whereas the electron impact ionization cross
section is on the order of 10^{-16} cm^2. Although it is not very meaningful to compare
the cross section in Fig. 5.13 and one in Fig. 5.14, it is insufficient by comparison
only with the cross sections. It is required to compare the ionization rates

$$\nu = \langle n\sigma v \rangle \tag{5.112}$$

should be compared, taking average of the number of photons and photo energy
distribution for the photo-ionization or the number of electrons and electron energy
distribution in the electron impact ionization. In comparing the both ionization rates,
it is necessary to evaluate the plasma temperature, density and optical depth etc. The
optical depth is needed to evaluate if the photon density and energy distribution is
close to the Planck distribution.

With sizes like normal laboratory plasma the density of photons is much lower
than in Planck distribution and such plasma is called "**optically thin plasma**".
However, in huge plasmas like in the sun, radiation can be considered Planck
distribution. Even in a laboratory plasma for example, when heating material with
a high Z such as gold (Au: Z = 79) or uranium (U: Z = 92) with a high intensity
laser, the radiation field is close to Planck distribution with the temperature of
hundreds of eV.

The collisional ionization cross section of argon when peeling off electrons one
by one is shown in Fig. 5.15. It can be seen that as the bound electrons are ionized
and the ionization energy increases, the ionization cross section decreases. This can
be interpreted intuitively that the interaction with free electrons becomes less likely
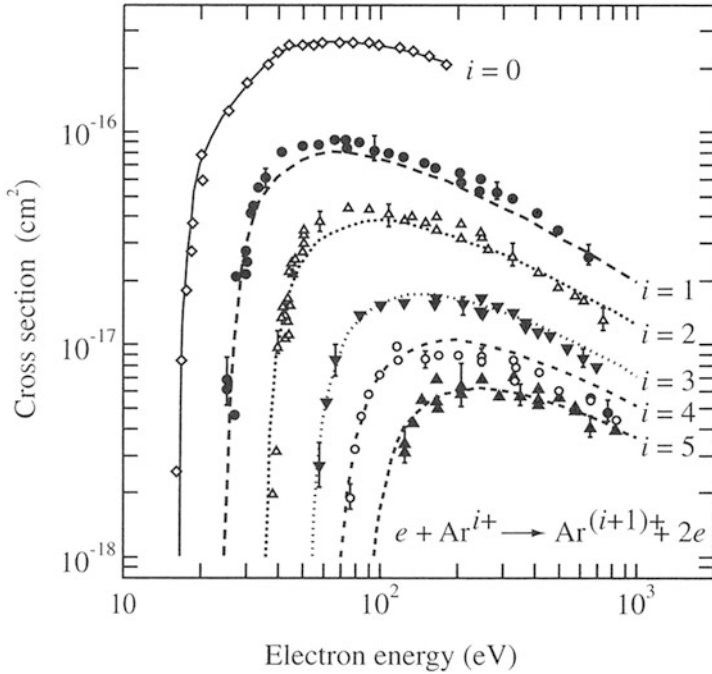as the wave function of bound electrons becomes smaller.

Fig. 5.15 The collisional ionization cross sections of argon when peeling off electrons one by one from neutral atom

5.8.1 Electron Impact to Atom

Consider the case where an electron collides on a neutral atom. There are three cases in the phenomena; elastic collision, electron collisional excitation, and electron impact ionization. These three processes are important elementary processes in plasma generation, plasma heating, and plasma transport. In plasma generation in a discharge tube, neutral atom excitation and plasma formation are the most basic atomic processes. This physics needs to be quantum mechanically analyzed, and the quantum scattering is the base for analysis.

Now let $\mathbf{r}_a$ be the coordinates of electrons subjected to excitation and ionization within the target atom, and denote with $\mathbf{r}$ the coordinates of the impact electron. The Schrödinger equation for a steady state where such phenomena continue is

$$\left\{ -\frac{\hbar^2}{2m}\nabla^2 + H_a(\mathbf{r}_a) + V(\mathbf{r}_a, \mathbf{r}) - E \right\} \Psi(\mathbf{r}_a, \mathbf{r}) = 0 \qquad (5.113)$$

Here, E is the total energy of the atom and the free electron. The general solution of (5.113) is given by expanding the $\mathbf{r}_a$ dependence of the wave function by eigenfunctions, so that we obtain the following multi electron wave function solution.

$$\Psi(\mathbf{r}_a, \mathbf{r}) = \sum_{\alpha} F_\alpha(\mathbf{r}) \varphi_\alpha(\mathbf{r}_a) \tag{5.114}$$

$$H_a(\mathbf{r}_a) \varphi_\alpha(\mathbf{r}_a) = E_\alpha \varphi_\alpha(\mathbf{r}_a) \tag{5.115}$$

Here, $\varphi_\alpha(\mathbf{r}_a)$ is the complete orthogonal functions to the Hamiltonian $H_a(\mathbf{r}_a)$ including all free electron eigen states. Substituting (5.114) into (5.113) and using the relation of (5.115), (5.113) becomes a simple form. Then, multiplying $\varphi_\alpha^*(\mathbf{r}_a)$ to the resultant form of (5.113) the following relation is obtained.

$$\left(\nabla^2 + k_\alpha^2\right) F_\alpha(\mathbf{r}) = \sum_{\beta} U_{\alpha\beta}(\mathbf{r}) F_\beta(\mathbf{r}) \tag{5.116}$$

where

$$k_\alpha^2 = \frac{2m}{\hbar^2}(E - E_\alpha) \tag{5.117}$$

$$U_{\alpha\beta}(\mathbf{r}) = \frac{2m}{\hbar^2} \int \varphi_\alpha^*(\mathbf{r}_a) V(\mathbf{r}_a, \mathbf{r}) \varphi_\beta(\mathbf{r}_a) d\mathbf{r}_a \tag{5.118}$$

We think that the initial state of the electron in the atom is constantly excited to the eigenstate α (α can also be in the continuous state). Then, when there is a free electron sufficiently far from the atom before the impact, it is possible to assume the wave function of the two electrons before the impact is given by

$$\Psi^0(\mathbf{r}_a, \mathbf{r}) = \exp(i\mathbf{k}_0 \cdot \mathbf{r}) \varphi_0(\mathbf{r}_a) \tag{5.119}$$

As the two electrons interact in the atomic potential, the bound-bound electron transit from the initial state to the eigen-state α of the bounded electron. The free electron becomes a spherical scattering state with the center of the atom as the origin. Therefore, the wave function of the free electron is described as

$$F_\alpha(\mathbf{r}) \rightarrow \delta_{\alpha 0} \exp(i\mathbf{k}_0 \cdot \mathbf{r}) + \frac{1}{r} f(0 \rightarrow \alpha; \theta, \varphi) \exp(i\mathbf{k}_\alpha \cdot \mathbf{r}) \tag{5.120}$$

Multiply (5.120) by the ratio of the electron flow velocity, that is, the wave number ratio, and integrate (5.120) over all angles. Then, the following equation can be obtained as the collisional cross section where the bound electron is excited as $|0\rangle \rightarrow |\alpha\rangle$ and at the same time the free electron is scattered.

$$\sigma(0 \rightarrow \alpha) = \frac{k_\alpha}{k_0} \int \int |f(0 \rightarrow \alpha; \theta, \varphi)|^2 \sin\theta d\theta d\varphi \tag{5.121}$$

(5.121) is the cross-section of **elastic scattering**.

Based on the perturbation theory to find the solution of (5.121), so-called **Born approximation** is used. That is, (5.120) is assumed to be expanded as

$$F_\alpha = F_\alpha^{(0)} + F_\alpha^{(1)} + F_\alpha^{(2)} + \ldots \tag{5.122}$$

In this approximation, the term $V(\mathbf{r}_a, \mathbf{r})$ in (5.113) is regarded a perturbation term. Then the first order equation is given

$$\left(\nabla^2 + k_\alpha^2\right)F_\alpha^{(1)} = \sum_\beta U_{\alpha\beta}(\mathbf{r})F_\beta^{(0)}(\mathbf{r}) \tag{5.123}$$

In addition, the following form is also assumed.

$$F_\alpha^{(0)}(\mathbf{r}) = \delta_{\alpha 0}\exp(i\mathbf{k}_0 \cdot \mathbf{r}) \tag{5.124}$$

Then, RHS of (5.123) is given. It is noted that Green function method is usually used to solve (5.116) exactly [9].

The collision cross section in the case of elastic collision is shown in Fig. 5.16. Its value is, of course, a function of the energy of the colliding electrons. It is useful to note that it is larger than the cross-section of "**inelastic collision**" such as collisional excitation and collision ionization.

As shown in Fig. 5.15, the ionization energy has the threshold value for the impact ionization cross section and the cross section abruptly increases. It takes the maximum value at about 2–3 times the threshold energy, and thereafter suddenly decreases. The detailed calculations of (5.121) are given in more specialized books, but a comparison between the results of Born approximation and experimental

Fig. 5.16 Elastic collision cross sections for Ar, Kr, and Xe neutral atoms as a function of impacting electron velocity. Note that such elastic collision cross section is larger than the cross-section of "inelastic collision" such as collisional excitation and collision ionization
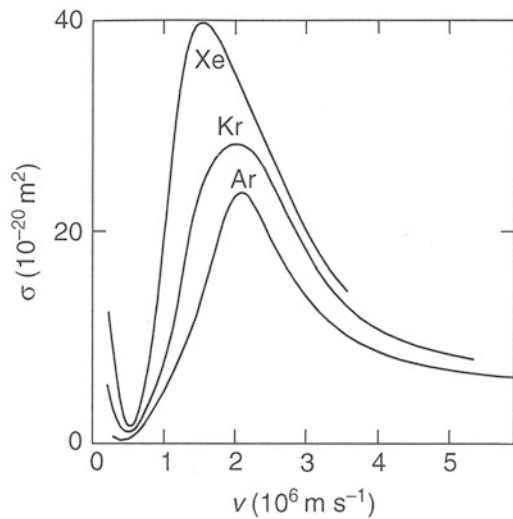
Fig. 5.17 Elastic collision cross section obtained theoretically by Born approximation compared to the experimental value for the case of hydrogen atom. The horizontal and vertical axis are impacting electron momentum and collision cross sections in arbitrary units, respectively. It is seen that the theory can predict well the experiment. Reproduced from ref. [9] by permission of Person education
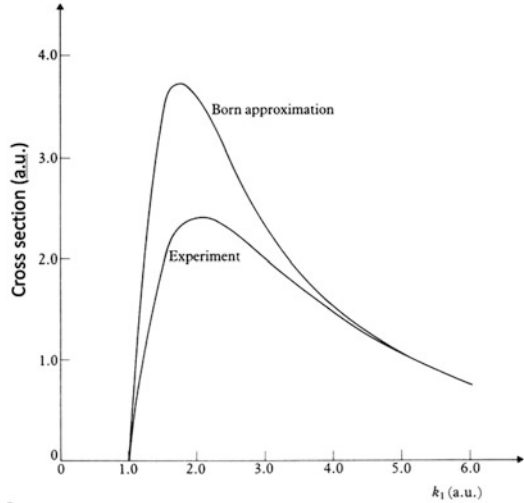
values is shown for the case of hydrogen in Fig. 5.17 [9]. Even when Born approximation is used, impact ionization of hydrogen can be obtained with such degree of accuracy. The Born approximation is appropriate at the high energy limit of the colliding electron, but the height of the peak of the cross section in the vicinity of the threshold is only about 1.5 times different. It is surprising to note that the properties of the curve are well reproduced.

5.8.2   Elastic Scattering

Let us calculate the cross-section of the elastic collision. Since the coordinate dependence of (5.113) can be fixed for $\mathbf{r}_a$, the wave function can be obtained by solving an equation for one electron wave function $F_0(\mathbf{r})$ in the form of (5.120). Partial wave expansion, which is Fourier transformation of any function axially symmetric, is applied to the scattering component as

$$F_0(\mathbf{r}) = \frac{1}{r} \sum_{\ell} A_{\ell} u_{\ell}(r) P_{\ell}(\cos\theta) \tag{5.125}$$

where P_{ℓ} is a normalized Legendre function.

By multiplying P_{ℓ} to (5.113) and integrating it over the angle, the following equation is obtained after the separation of variables.

$$\frac{d^2 u_{\ell}}{dr^2} + \left\{ k_0^2 - V(r) - \frac{\ell(\ell+1)}{r^2} \right\} u_{\ell} = 0 \tag{5.126}$$

Consider the properties of the solution of (5.126) intuitively without solving. Since the effective range of V (r) is of the order of Angstrom (10^{-8} cm), the inside of the parentheses in (5.126) becomes negative for large values of ℓ. In other words, it can be considered that there is only a small component of ℓ in scattering of low energy electrons. It is also clear that the increase of the free electron energy, large angle scattering described with large numbers of ℓ appears. It is noted that the **partial waves** with $\ell = 1, 2, 3$ are called s-wave, p-wave, d-wave. Since the s-wave has no ℓ-dependency, it shows isotropic scattering. The asymptotic solution of Eq. (5.126) at large radius is known to be

$$u_\ell(r)_{r \to \infty} \to \frac{1}{k_0} \sin\left(k_0 r - \frac{1}{2}\ell\pi + \eta_\ell\right) \qquad (5.127)$$

Here, η_ℓ is the "**phase shift**" due to scattering for the partial wave with angular quantum number ℓ. By placing (5.127) in (5.121), the scattering cross section can be found as follows.

$$\sigma = \frac{4\pi}{k_0^2} \sum_{\ell=0}^{\infty} (2\ell + 1) \sin^2\eta_\ell \qquad (5.128)$$

In the scattering of low energy electrons only a small number of partial waves appear with lower ℓ numbers. This fact suggests that the phase shift of larger l number is near $n\pi$, where n is an integer. Especially when it is less than 1 eV, only s-wave appears. It is also known that the phase shift becomes $n\pi$ at certain electron energy. Then, the scattering cross section of (5.128) becomes extremely small. This phenomenon is called the **Ramsauer effect**. In Fig. 5.16, elastic collision cross section by the noble gas is shown. It is seen that Ramsauer effect clearly appears at the low-speed part.

In Vol. 1, the scattering of an electron in Coulomb field by classical mechanics was solved to find the formula of **Rutherford scattering**. Let's compare the same electron scattering due to bare hydrogen nucleus (proton) to that obtained by the quantum mechanical analysis. The same problem can be solved exactly as the scattering problem described above. The scattering cross section thereof agrees with the classical Rutherford scattering one in the form [9].

$$\sigma = \left(\frac{e^2}{4\pi\varepsilon_0 mv^2}\right)^2 \frac{1}{4\sin^2(\theta/2)} \qquad (5.129)$$

It is useful to note that such quantum scattering of electron beam is applied to study a nuclear structure of many nuclei. In this case the potential force is due to not only Coulomb force but also nuclear force is inserted in (5.113). Historically, such electron beam measurement has been used to identify the particle distribution of nucleus and quarks in nucleon [11]. Note that in the case of relativistic electron scattering measurement by nuclei, the spin effect of electron and nucleus becomes

important and the cross-section (5.129) is modified to Mott scattering cross-section as shown in this chapter [11]. With the increase of Lorentz factor β to unity, the scattering angle becomes narrower than Rutherford scattering (5.129). The Motto formula is the relativistic quantum scattering derived by stating with Dirac equation.

### 5.8.3   Electron Collision De-excitation and Recombination

Solving (5.113), the cross sections of the collisional excitation and de-excitation are obtained. As clear in the above formulation, the bound state wave function transits from the initial state $\langle i| = \langle 0|$ to the final state $\langle f| = \langle \alpha|$ in (5.118). Such an inelastic collision, the wavenumber of the scattered electron k_0 in (5.120) should be replaced with k_α in (5.117).

However, recombination due to electron collision cannot be described by the formulation above with only one electron scattering wave. It is necessary to formulate for two electron scattered wave after the ionization. This is a **three-body problem**, it is hard to deal with quantum mechanically. The detail mathematics is out of the scope of the book.

If the cross sections of the electron collision excitation and electron impact ionization are calculated, the electron collision de-excitation and electron collisional recombination can be obtained. This principle is called the **detail balance** requiring that the latter two reversal process should balance in each when the thermodynamic equilibrium is established in plasma. Then, the distribution function of free electrons is Maxwellian.

The measured cross sections of the elastic, collisional-excitation, and collisional ionization are shown in Fig. 5.18 for the case of neutral argon gas as a function of impacting electron energy. When increasing the energy of electrons, firstly elastic

Fig. 5.18 The cross sections of elastic, collisional excitation, and collisional ionization as function of impacting electron kinetic energy for an argon atom
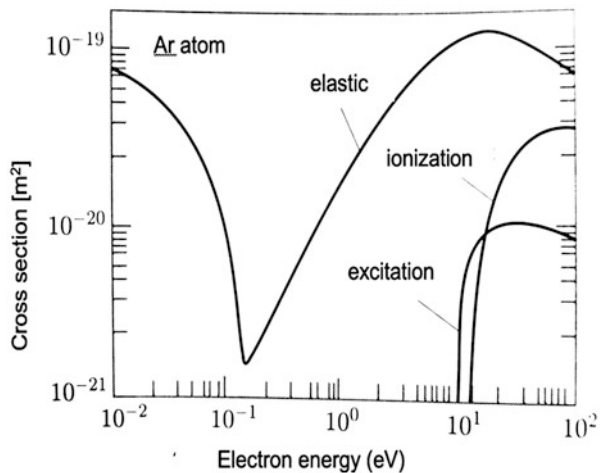
scattering is dominant, excitation occurs from the point where electron energy exceeds the threshold, and then electron impact ionization becomes dominant in further high energy region. By injection of high-energy electron beams to any neutral gas, it is possible to generate plasma.

5.9   Atomic Process in Maxwellian Free Electrons

Even if we have some detail database via computation about photon and electron atomic processes, it is hard job to chase the time evolution of all atomic states. This is because the atomic process cross sections discussed are functions of photon energy and electron kinetic energy. If the photon field is not Planck distribution or the free electron energy distribution is not Maxwellian, the atomic process demands a huge computation. This resembles to the case why the hydrodynamic approximation is used to study the macroscopic plasma dynamics, instead of solving kinetic equation to the velocity distribution.

Most of the plasma analysis, the free electron distribution is assumed to be Maxwellian, even when the electron distribution in the bound state is not necessarily Boltzmann distribution. Regarding the photon energy distribution, it is usual that the photon field is neglected in laboratory plasmas, while it is assumed Planckian in stellar objects. This is valid by evaluating the optical thickness of the plasmas. Most of laboratory plasmas are optically thin except for the plasma of high-Z atom like gold.

It is useful to summarize the atomic processes to be taken into account for studying the physics of laboratory and astrophysical plasmas. It is also necessary to include the free-free radiation (called **Bremsstrahlung** radiation) and free-free absorption (**inverse-Bremsstrahlung**) already discussed in Vol. 1.

1. Photo excitation
2. Photo de-excitation (spontaneous and stimulated emission)
3. Photo-ionization
4. Photo-recombination
5. Electron collisional excitation
6. Electron collisional de-excitation
7. Electron impact ionization
8. Electron collisional recombination (two-electron recombination):
9. Bremsstrahlung radiation
10. Inverse-Bremsstrahlung (absorption):

In the photo excitation, we need to know the detailed distribution of atomic energy levels and line-profile of radiation emission and absorption. The line profile in frequency space is determined by synthesized effects such as **natural width**, **Doppler broadening**, **Stark broadening**. Especially the theory of Stark broadening at high density plasma is still the theme of the forefront of research. The discussion is relatively simple if the photon distribution is Planckian. However, in the laboratory

plasma and the interstellar plasma whose density is relatively low, the radiation spectrum in plasma is generally very different from Planck distribution. Therefore, usually the photo-ionization and excitation process are neglected in determining the atomic states in plasma.

Assume that the plasma is close to the thermodynamic equilibrium state and the electron velocity distribution is Maxwellian. Then, the number of atomic process for an ion per unit time and unit volume, ν is given as an averaged value over the free electron velocity distribution.

$$\nu = \langle n\sigma v \rangle \tag{5.130}$$

Here, n is the number density of atoms or ions, v is the velocity of electrons, σ is the velocity-dependent cross section, and $\langle \rangle$ means to take average value with the electron velocity distribution. Considering that n can be put out from the averaging and the free electrons have a Maxwell distribution of the temperature T, then

$$\nu = n \int \sigma v f_M(v) dv = 4\pi \left(\frac{m}{2\pi T} \right)^{3/2} \int v^3 \sigma(v) \exp\left(-\frac{mv^2}{2T} \right) dv \tag{5.131}$$

Converting (5.131) to the integral to the kinetic energy $\varepsilon = \frac{1}{2}mv^2$, the followings is obtained

$$\chi = \frac{\nu}{n} = \frac{2^{3/2}\sqrt{m}}{\sqrt{\pi}T^{3/2}} \int_0^\infty \varepsilon^{3/2}\sigma(\varepsilon) \exp\left(-\frac{\varepsilon}{T} \right) d\varepsilon \tag{5.132}$$

where χ is called **rate coefficient**. It is found that the rate coefficient for excitation and ionization due to electron collision is a function only of temperature.

The coefficients of the atomic process involving the collision by free electrons are obtained by substituting the cross section as a function of electron energy into (5.132) and performing integration. However, it should be noted that the velocity distribution function of free electrons is limited to Maxwell distribution. For example, in the case of impact ionization, as shown in Fig. 5.15, the cross-section of the integrand of (5.132) is a function that rapidly rises from the ionization energy. However, Maxwell distribution has the shape as shown in Fig. 5.19, which has the maximum value. When the temperature is low, the tail component of the Maxwell distribution contributes greatly to those products as shown in Fig. 5.19. It is noted that depending on generation and heating process, plasma is not necessarily Maxwell distribution. Particularly, since the tail component of the velocity distribution is often elongated, it is better approximated by the Maxwellian distribution with two temperatures. It should keep in mind in using to the average values. It is useful to note that nuclear reaction cross sections such as DT fusion reaction also have strong dependence on the particle energy and the corresponding integrand in (5.132) has a peak called **Gamow peak**.
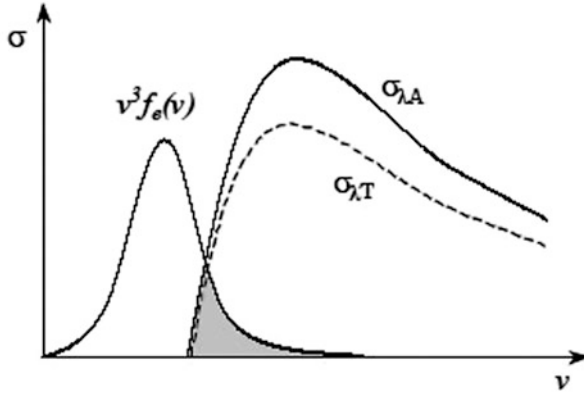
Fig. 5.19 Maxwellian averaged cross section in the case of impact ionization (see Fig. 5.15). The cross-section rapidly rises from the ionization energy like σ_A or σ_T, while Maxwell distribution has the shape like $v^2 f_e(v)$ as shown in the figure. When the temperature is relatively low, only the high-energy component of the Maxwell distribution contributes greatly to the averaged cross sections

The following point should also be noted. The electron velocity distribution has been assumed to be isotropic (spherically symmetric in speed space). However, when energy transport is strong in a certain direction, or when electrons confined by magnetic field are heated, the distribution function may become anisotropic. When ions in such plasma are excited by free electrons in an anisotropic velocity distribution, it is known that the excited quantum state can be biased, and line emission via transition to the ground state by spontaneous emission is polarized. The science field for studying physics of polarized emission is called "**polarization spectroscopy**", and studies are progressing with space physics observations and laboratory plasmas. Polarization spectroscopy is used as a method to investigate the structure of the magnetic field, especially in the universe.

5.9.1 Rate Coefficient of Electron Collision Excitation

The rate coefficient of velocity-averaged electron collisional excitation is

$$
\begin{aligned}
\chi_{m,n} &= \langle \sigma_{m,n} v \rangle \\
&\approx 16\pi \left(\frac{2\pi E_H}{3m} \right)^{\frac{1}{2}} a_0^2 f_{m,n} \frac{E_H}{E_{m,n}} \left(\frac{E_H}{T} \right)^{\frac{1}{2}} g_{m,n} \exp\left(-\frac{E_{m,n}}{T} \right)
\end{aligned}
\tag{5.133}
$$

Here, $m < n$, $E_H = 13.6\,\text{eV} = R$ (Rydberg constant), a_0 is the Bohr radius, $g_{m,n}$ is the gaunt factor. $f_{m,n}$ is the oscillator strength of the absorption defined in (5.83). (5.133) reduces to

$$\nu_{m,n}^{bb} = n_e \langle \sigma_{m,n} v \rangle = 4.3 \times 10^{-6} f_{m,n} \frac{n_e}{T_{eV}^{3/2}} \frac{T}{E_{m,n}} \exp\left(-\frac{E_{m,n}}{T}\right) \quad [s^{-1}] \qquad (5.134)$$

Here, Gaunt factor $g_{mn} = 0.275$ was used as approximate value.

5.9.2   Rate Coefficient of Electron Impact Ionization

The impact ionization coefficient (5.67) can be calculated in principle by setting the initial state to be bound electrons in atoms and the wave function after collision to be a plane wave (free electron) in a certain direction. However, it is easier to start with the formula by Thomson (1912) that has been used historically as the simplest expression given in (6.83) in [12].

$$\sigma_{m,c} = 4\pi a_0^2 \left(\frac{E_H}{E}\right)^2 \left(\frac{E}{E_{m,c}} - 1\right) \qquad (5.135)$$

where E is the electron kinetic energy and E_{mc} is the ionization energy from the bound state $\langle m|$. When this ionization cross section is multiplied by the Maxwell, the following rate is obtained after the integration.

$$\begin{aligned} \chi &= \langle \sigma_{m,c} v \rangle \\ &= 8\pi a_0^2 \left(\frac{2E_H}{\pi m}\right)^{1/2} \left(\frac{E_H}{E_{m,c}}\right)^{3/2} \beta^{-1/2} \left[\beta e^{-\beta} - \beta E_1(\beta)\right] \end{aligned} \qquad (5.136)$$

where

$$\beta = \frac{E_{m,c}}{T} \qquad (5.137)$$

The definition of E_1 and the approximate expression for the large value of β are

$$E_1(\beta) = \int_\beta^\infty \frac{e^{-x}}{x} dx = e^{-\beta}\left(\frac{1}{\beta} - \frac{1}{\beta^2} + \cdots\right) \qquad (5.138)$$

Using (5.138), (5.136) becomes

$$\chi_{m,c} = 8\pi a_0^2 \left(\frac{2E_H}{\pi m}\right)^{1/2} \left(\frac{E_H}{E_{m,c}}\right)^{3/2} \beta^{-1/2} e^{-\beta} \qquad (5.139)$$

As a more precise expression, Lotz has obtained the following formula fitted well with one-electron data of high Z [3].

$$\chi_{m,c} = 8\pi a_0^2 \left(\frac{2E_H}{\pi m}\right)^{1/2} \left(\frac{E_H}{E_{m,c}}\right)^{3/2} \beta^{-1/2} \left[0.69e^{-\beta} f(\beta)\right] \tag{5.140}$$

where

$$f(\beta) = \beta e^{\beta} E_1(\beta) \tag{5.141}$$

This function varies from 0.34 to 0.90 for $\beta = 1/4$ to 8. Here, if you obtain the rate coefficient of impact ionization after inserting the values into (5.139), the impact ionization frequency is

$$\nu_{m,c}^{bf} = 2.15 \times 10^{-6} T_{eV}^{-3/2} n_e \beta^{-2} e^{-\beta} \quad \left[s^{-1}\right] \tag{5.142}$$

5.9.3   Detailed Balance and Collisional Rates

The rate coefficient of collisional de-excitation is obtained from the rate coefficient of collisional excitation based on the detailed balance. The governing equation for transition of bound electrons due to electron collision with respect to the quantum states m and n can be written as follows.

$$\frac{dN_m}{dt} = -\frac{dN_n}{dt} = \nu_{n,m}^{bb} N_n - \nu_{m,n}^{bb} N_m \tag{5.143}$$

This relation should be balanced in the thermal equilibrium state. Using the rate coefficient of (5.134), the following is obtained.

$$\begin{aligned}
\nu_{n,m}^{bb} &= \frac{N_m}{N_n} \nu_{m,n}^{bb} \\
&= \frac{g_m}{g_n} e^{E_n - E_m} \nu_{m,n}^{bb}
\end{aligned} \tag{5.144}$$

Now, in collisional recombination coefficient is also derived from the detailed balance, using the impact ionization coefficient. In case of the high-density state, it becomes necessary to use the Fermi-Dirac distribution for electrons, but here the rate coefficient at the limit of low density satisfying the condition, $-\mu/T > > 1$, is obtained as follows from the detailed balance with (5.139).

$$\nu_{cm}^{fb} = 3.55 \times 10^{-28} g_m \frac{n_e^2}{T_{eV}^3} \beta^{-2} \quad \left[s^{-1}\right] \tag{5.145}$$

5.9.4   Rate Coefficient of Photo-recombination

The rate coefficient of photo recombination is obtained from the rate coefficient of photoionization in the local thermal equilibrium (LTE) state where photo distribution is Planckian. In LTE, the ionization cross section of (5.107) needs to be averaged by the radiation field of the Planck distribution. Planck distribution is a function of the temperature. The coefficient of optical recombination averaged by the energy distribution of electrons and photons is a function of only the quantum state of bound electrons in the ion.

When the cross section of photo-recombination is calculated from the detailed balance, the general theory is very complicated. Limit the study to the case only when a captured electron forms a hydrogen-like ion of charge state z from the charge state z-1. Write the photo recombination cross section as $\sigma_{\varepsilon,p}$, where the suffix indicates that ε is the kinetic energy of a free electron and that the free electron emits a photon of energy $h\nu$ and is captured in the state of the principal quantum number p. The following energy conservation should be satisfied.

$$h\nu = \frac{1}{2}mv^2 + \frac{z^2 I_H}{p^2}, \quad \varepsilon = \frac{1}{2}mv^2 \tag{5.146}$$

In LTE, the rate coefficient of photoionization given by (5.107) needs to be equal to the rate coefficient of photo recombination given by $\sigma_{\varepsilon,p}$, namely the relation becomes as follows using the Planck distribution.

$$n_0^{\zeta+1} n_e f_M(v) dvv \sigma_{\varepsilon,0} = \sum_p n_p^\zeta \rho_\nu d\nu c \sigma_{p,\varepsilon} \left(1 - e^{-h\nu/T}\right) \tag{5.147}$$

Here, f_M is the normalized Maxwell distribution, and ρ_ν is the photon density of the Planck distribution. The last parenthesis on R is a term for subtracting the number of photons by stimulated emission. In addition, the relationship $d\nu/(vdv) = h/m$ is satisfied by (5.146).

The cross section of photo recombination is obtained from (5.147) as follows

$$\sigma_{\varepsilon,0} = \sum_p \frac{n_p^\zeta}{n_0^{\zeta+1} n_e} \frac{m}{h} \frac{\rho_\nu c}{f_M(v)} \left(1 - e^{-h\nu/T}\right) \sigma_{p,\varepsilon} \tag{5.148}$$

where ρ_ν is given by (B2.3), and f_M is (B1.19). The first term of (5.148) is given by Saha's solution found in (5.14). Inserting the constants to (5.148), it is shown as

$$\sigma_{\varepsilon,0} = 2.8 \times 10^{-21} \frac{z^2}{\varepsilon_{eV}} \varphi\left(\frac{z^2 I_H}{\varepsilon}\right) \quad [\text{cm}^2] \tag{5.149}$$

The dimensionless function $\varphi(x)$ is a constant of order unity only depending on the principal quantum number. For the case where $p = 1$ contributes the most, its value is about 1, and (5.149) is approximated as follows

$$\sigma_{\varepsilon,0} \approx 3 \times 10^{-21} \frac{Z^2}{\varepsilon_{eV}} \qquad \left[cm^2 \right] \qquad (5.150)$$

5.10   Bremsstrahlung Emission and Absorption

Via collisions of free electrons with ions, photons are emitted. Since the above atomic processes via photons are important to be installed in the radiation hydrodynamic simulation to be discussed later, it is better to study the radiation process via free-free electron interaction. This photo-emission is called **Bremsstrahlung**. The reverse process contributes photo-absorption by free electrons. Note that this process is very important as classical absorption of laser photons as studied in Vol. 1. Calculate the cross-sections of Bremsstrahlung and its inverse process. Do not calculate strictly, try intuitive derivation, and finally match numerical coefficients to the exact solutions. Keep in mind that an electron is accelerated by an ion.

The charged particles under acceleration radiates electromagnetic waves. The electric dipole **p** has the following relationship for charged particles 1 and 2:

$$\mathbf{p} = e_1 \mathbf{r}_1 + e_2 \mathbf{r}_2 = \mu \left(\frac{e_1}{m_1} - \frac{e_2}{m_2} \right) \mathbf{r} \qquad (5.151)$$

Here, μ is the reduced mass, and **r** is the inter-particle distance. As can be seen, dipole radiation does not occur in collisions between electrons. Radiation emission by two electrons can be made by quadrupole effect. Consider radiation emitted when an electron collides at high speed with an iron of electric charge Z via Coulomb force. Then, electron is decelerated to run away from the ion.

In the case of the collision parameter b introduced in Chap. 2 and the typical acceleration is

$$|\ddot{\mathbf{r}}| = \alpha = \frac{1}{m} \frac{e^2 Z}{4\pi\varepsilon_0 b^2} \qquad (5.152)$$

Also, the time interval to feel acceleration force is

$$\Delta t = \frac{2\pi b}{v} \qquad (5.153)$$

Therefore, the energy radiated by one collision is

$$\Delta E = P\Delta t = \frac{\pi}{4c^3\varepsilon_0} \left(\frac{e^2 Z}{4\pi\varepsilon_0 m}\right)^2 \frac{1}{vb^3} \tag{5.154}$$

where P is the power of Larmor radiation emission.

Introduce a new physical quantity q_ν defined as

$$dq_\nu = \Delta E \times 2\pi bdb \tag{5.155}$$

Note that this has dimensions of (energy) × (area). Assuming that the reciprocal of the frequency ν of the light emitted is roughly equal to Δt in (5.153), the following relation is obtained after inserting (5.154) to (5.155).

$$dq_\nu = \frac{e^6 Z^2}{32m^2 c^3 \varepsilon_0^3} \frac{1}{v^2} d\nu \tag{5.156}$$

This is a rough calculation. It is known that the exact coefficient is larger by $4/\sqrt{3} = 2.3$ after solving the trajectory mathematically,

$$dq_\nu = \frac{e^6 Z^2}{8\sqrt{3}m^2 c^3 \varepsilon_0^3} \frac{1}{v^2} d\nu \tag{5.157}$$

For a given free electron distribution f (v), the energy radiated per unit time, volume, and frequency is

$$n_i n_e f(v) dv v dq_\nu(\nu) \tag{5.158}$$

The minimum velocity v_m at which electrons are not captured by ion is

$$\frac{1}{2} m v_m^{\ 2} = h\nu \tag{5.159}$$

Maxwell distribution of temperature T is

$$f(v)dv = \sqrt{\frac{2}{\pi}} \left(\frac{m}{T}\right)^{3/2} v^2 e^{-\frac{mv^2}{2T}} dv \tag{5.160}$$

Integrate Eq. (5.159) from the minimum velocity v_m in (5.159), the spectral emission is obtained.

$$J_\nu d\nu = n_i n_e \int_{v_m}^{\infty} f(v')dv'v' dq_\nu(v') \tag{5.161}$$

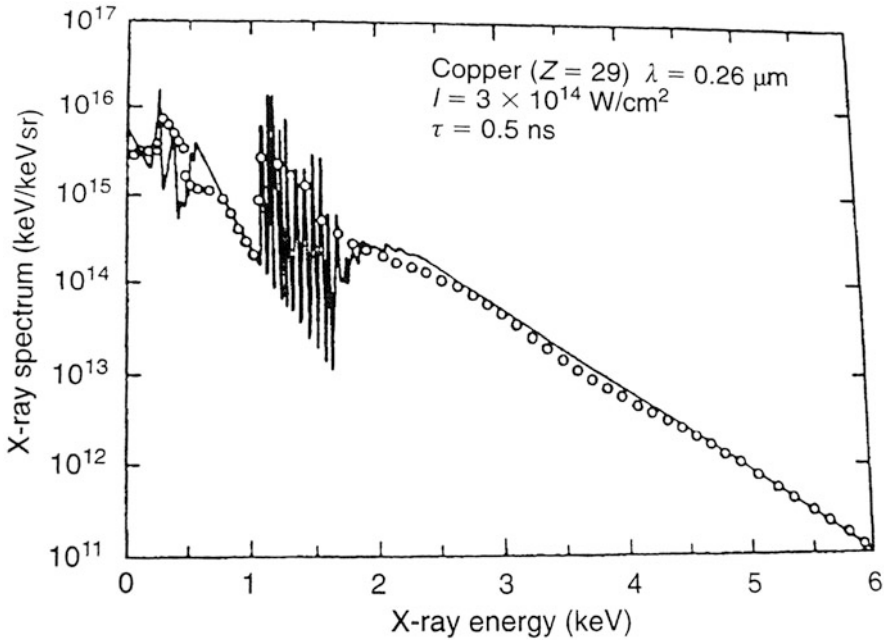Inserting (5.160) and (5.157) to (5.161), the spectral emission power is obtained.

Fig. 5.20 Bremsstrahlung emission spectrum shows a straight line in the semi-logarithmic graph in the experimental data. Reproduced from Ref. [13] by permission of John Wiley & Sons Ltd

$$J_\nu d\nu = \frac{1}{4}\left(\frac{2}{3\pi mT}\right)^{1/2}\frac{e^6 Z^2}{mc^3 \varepsilon_0^2}e^{-\frac{h\nu}{T}}d\nu \qquad (5.162)$$

This is the energy spectrum of Bremsstrahlung emission of plasma from unit volume and unit time.

(5.162) indicated that Bremsstrahlung shows a straight line in the semi-logarithmic graph as shown in the experimental data of Fig. 5.20 [13]. Since this inclination represents temperature, it is used for temperature measurement of optically thin plasma. By integrating over the spectrum, the radiant energy per unit time and unit volume can be obtained as follows.

$$J = \int_0^\infty J_\nu d\nu = 1.7 \times 10^{-26} Z^2 n_e n_i \sqrt{T_{eV}} \quad \left[W/cm^3\right] \qquad (5.163)$$

where n_e and n_i is in unit of cm^{-3} and T is in eV unit.

Now, consider the absorption coefficient by the **inverse-Bremsstrahlung** process. From the detail balance, the photo-absorption by free electrons in the Planck distribution should balance with the emission of (5.158). That is

$$n_i n_e U_{\nu,P} d\nu f(v) c d v a_\nu \left(1 - e^{-h\nu/T}\right) \tag{5.164}$$

Here, a_ν is the spectral absorption coefficient, $U_{\nu,P}$ is Planck distribution, which is defined as

$$U_{\nu,P} = h\nu\rho_\nu \tag{5.165}$$

The last term in Eq. (5.164) is required due to stimulated emission effect.

The energy conservation relation is given as

$$\frac{1}{2}mv'^2 = \frac{1}{2}mv^2 + h\nu \tag{5.166}$$

where v and v′ are the electron velocity after and before the photon absorption, respectively. Define the emission cross section σ_ν by

$$dq_\nu = h\nu d\sigma_\nu \tag{5.167}$$

The spectral absorption coefficient is shown as

$$a_\nu = \frac{c^2 v'^2}{8\pi\nu^2 v} \frac{d\sigma_\nu}{d\nu} \tag{5.168}$$

This is the absorption coefficient of the inverse-bremsstrahlung. With use of (5.167) and (5.157), the spectral absorption coefficient is obtained.

$$a_\nu = \frac{e^6 Z^2}{64\sqrt{3}\pi^2 h c m^2 \varepsilon_0^3 \nu^3 v} \tag{5.169}$$

This was derived by Kramers in 1923. When this is integrated with respect to the Maxwell distribution, the absorption coefficient is obtained.

$$K_\nu = 4.1 \times 10^{-37} Z^2 \frac{n_e n_i}{T_{eV}^{7/2} x^3} \quad [\text{cm}^{-1}], \quad x = \frac{h\nu}{T} \tag{5.170}$$

Here, the densities are in units of $[\text{cm}^{-3}]$.

5.11   Rate Equations

In general, the ionization and excitation of each ion at a local point should be solved as a function of time, because such processes have typical times to be some steady sate. As we have seen in this chapter, the reaction rates are calculated when the

physical values of electrons and ions are gives with the information of photon fields in the case of local thermodynamic equilibrium being satisfied. It is useful to note that rate equations to be explained here are widely solved in many different kinds of problems. Of course, the time evolution of atomic process in plasma is a good example, while we can enumerate the following physical phenomena, where different rate equations with corresponding reaction cross sections control the phenomena, while they are the same or similar form mathematically.

Different rate equation manages the phenomena in chemical reactions, nuclear reactions, spread of infectious diseases, and so on. It is known that the big bang produces the light elements up to He and Li during the first several minutes as shown in Fig. 5.21. This is called the big bang nuclear-synthesis. Since the Universe starts from a point by phase transition of vacuum state and extremely high-energy Universe starts to expand and cooled rapidly. Then, the density also decreased rapidly, the rate equation to the nuclear fusion processes of all elements provides the time evolution given in Fig. 5.21. The heavier elements than He and Li are produced mainly inside stars using long time. Relating to the hydrodynamic instabilities to be studied in Vol. 3, the supernova explosions are known to be the place where heavy elements such as irons are produced in extremely high-temperature and density conditions.

It is useful to obtain the feeling about the difference of chemical, atomic, and nuclear reactions. It is clear that each of three becomes important at the difference temperature. Chemical reaction is via bonding of different molecules whose binding energy is roughly 0.1–1 eV. Considering the effect of the contribution of tail component shown in Fig. 5.19, most of chemical reactions become dominant around the temperature of T = 0.01–0.1 eV, namely room temperature to thousands of degrees. The atomic reactions studied in details above are characterized by the electron binding energy in ion. Of course, it depends on ionization stage and
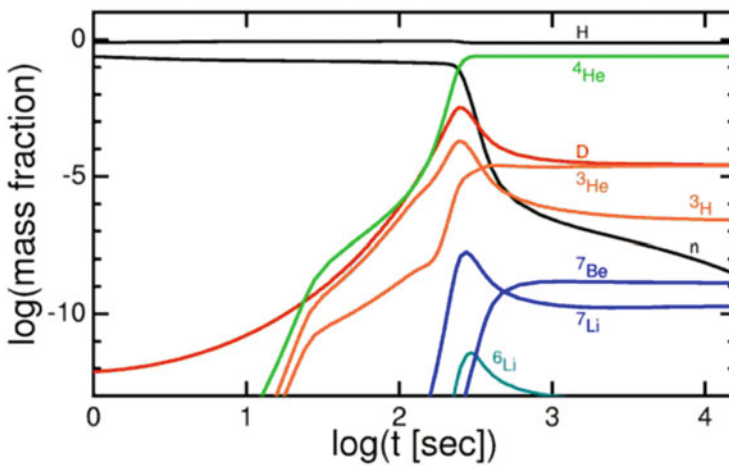

Fig. 5.21 Time evolution of the big-bang nucleosynthesis

Z-number of an ion, while the binding energy is in the range of 10 eV–1 keV. Therefore, when the plasma temperature is approaching to the binding energy, many atomic reactions take place.

Nuclear reaction is evaluated by the binding energy of nucleus. It is roughly about 1 MeV. Therefore, the temperature approaches to 10–100 eV, the nuclear reactions should be considered. Of course, whether such reactions may be dominant or not is strongly depends on the density. Since the reaction cross section is the orders of the size of molecule for chemical, atom for atomic, and nucleus for nuclear reactions. It is useful to have idea about how large their sizes. Molecule is about 10 Å (10^{-7} cm), atom 1 Å (10^{-8} cm), and nucleus 1 fm (10^{-13} cm). It is clear that the reaction cross section proportional to the square of radius is very small for the nuclear reaction and extremely-high density or extremely long time is required for substantial reaction. Such nuclear reaction is usually possible only in stars with high-density-high-temperature.

Three coupled nonlinear rate equations known as the Lorentz equation is famous to give chaotic variation of three quantities as a function of time with selection of coefficients of the rates in the equation. Rate equation is rather simple compared to, for example, hydrodynamic equations described in the previous chapter. The chaos and stochasticity in the Lorentz equation is interesting subject, while let us study the rate equations of atomic process by assuming that there are no chaotic phenomena.

In order to analyze the process of plasma formation from gas, it is necessary to solve the temporal evolution of excitation and ionization of gas atoms by free electrons and radiation. Then, the de-excitation and recombination are also treated self-consistently. The equation governing the temporal evolution is called **rate equation** for atomic processes. In general, we have to consider many atomic processes as schematically shown in Fig. 5.22. Consider here only the atomic process due to particles, while the atomic processes induced by external photons are neglected. This assumption is acceptable for most of plasmas in laboratory, namely optically thin plasma. It is also good approximation of plasmas in space whose density is low enough.

Consider an ion. Let the ionization degree be ζ and the quantum state of the bound electrons be m. The rate equation for the number of the ions in that state (N_m^ζ) is given as the sum of seven elementary processes in the form including only the electron collision process as follows

$$\frac{dN_m^\zeta}{dt} = -A_1 + A_2 \tag{5.171}$$

$$A_1 = \left(\sum_{n>m} \nu_{m,n}^{bb} + \sum_{k<m} \nu_{m,k}^{bb} + \sum_j \nu_{m,j}^{bf} \right) N_m^\zeta \tag{5.172}$$

$$A_2 = \sum_{n>m} \nu_{n,m}^{bb} N_n^\zeta + \sum_{k<m} \nu_{k,m}^{bb} N_k^\zeta + \sum_j \nu_{j,m}^{fb} N_j^{\zeta+1} + \sum_j \nu_{j,m}^{bf} N_j^{\zeta-1} \tag{5.173}$$
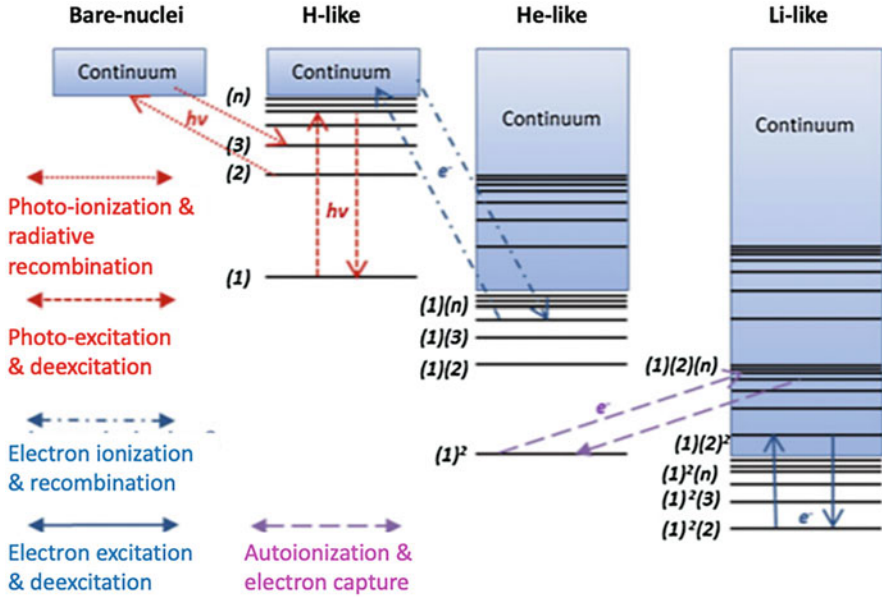
Fig. 5.22 Basic atomic processes to be solved in rate equation in laser plasma, where only single electron excitation is included for a simple atomic model with each configuration depending only on the principal quantum number, n. Reprint from Ref. [5] with kind permission from Springer Science + Business Media

Fig. 5.23 Atomic processes to m; going-out (5.3) and coming-in (4, 5, 6, 7) to the quantum sate m of an ion with charge state ζ
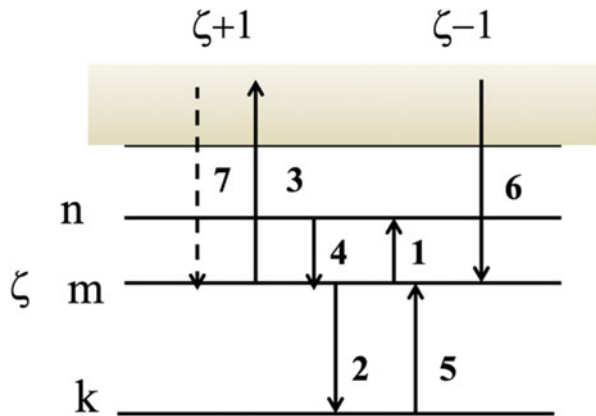
Here, A_1 is a homogeneous term, showing the transitions indicated as 1, 2, and 3 schematically shown in Fig. 5.23. In other words, it is a term by which an ion transits from the state of N_m^ζ to another state by collision excitation, de-excitation, and impact ionization. In contrast, A_2 in (5.173) shows the elementary processes 4, 5, 6, and 7 of Chap. 5.9 and are shown in Fig. 5.23. This shows a term in which the

state of ions changes to N_m^ζ due to de-excitation, excitation, recombination, and ionization.

Since the term due to radiation is not considered here, RHS of (5.171) is easy to understand by comparing with Fig. 5.23. While it will be explained later about the case with the effect by photons, it is useful to study the property of the solutions of (5.171). In such a case, the ionization state should be in the detail balance at the stationary state in (5.171) and the solution becomes the same as Saha solution (5.14).

How to solve the time evolution of ionization with (5.171). Given all eigen-state data of the bound states, (5.171) looks like a homogeneous coupled equation to the variables N_m^ζ. If so, it is easy to solve (5.171) by obtaining the eigen-values of the determinant for the matrix. However, (5.171) is not a linear equation to N_m^ζ. The rate coefficients are functions of the free electron density n_e, and it is given so that the charge neutrality is satisfied. Therefore, it is necessary to solve (5.171) numerically with the iteration method.

5.11.1   Corona Equilibrium (CE)

The Saha equilibrium is relatively easier to calculate the charge distribution of ions by using some atomic structure model for partially ionized atoms. The LTE assumption is, however, applicable to the limited cases such as the inside of the sun or low temperature plasmas. In general, plasmas in laboratory and observed plasma in the universe are rather of thermodynamically non-equilibrium (**non-LTE**) in many cases. However, solving the rate equation including all atomic processes requires a special computation technique and super-computing. Historically, non-LTE steady state models have been proposed. Typical examples of **corona equilibrium (CE)** model and **collisional radiative equilibrium (CRE)** model being used widely are explained below.

The corona equilibrium (CE) model stems from the corona plasma of the sun, far extended plasma from the surface of the Sun as shown in white in Fig. 5.24 [14]. The CE model can be applied to the plasma characterized by extremely low density, optically thin, and high temperature. It is assumed that all bound states are in the ground states. This is because the lifetimes of the excited states are relatively short compared to the time scale of the collisional excitation. Therefore, the bound states of partially ionized atoms have only one quantum state for each. The photo-effects are all neglected.

In the CE model, it is enough to solve a steady state by leaving only the three terms in the rate Eq. (5.171). Then, (5.171, 5.172, and 5.173) are approximated as

$$\frac{dN_0^\zeta}{dt} = -C_1 + C_2 \tag{5.174}$$

Fig. 5.24 Large scale
corona over the surface of
the Sun [14]. (NASA)

$$C_1 = \nu_C^{bf} N_0^\zeta \tag{5.175}$$

$$C_2 = \nu_R^{fb} N_0^{\zeta+1} + \nu_C^{bf} N_0^{\zeta-1} \tag{5.176}$$

Here, C_1 is the electron impact ionization, the first term of C_2 is the radiative recombination, and the second term is the electron impact ionization. The impact ionization coefficient is proportional to the electron density, and the radiative recombination coefficient is also proportional to the electron density. Therefore, the equilibrium solution of Eq. (5.174) is a function only of temperature and does not depend on the density. If the plasma is low density and high temperature, the ionization state becomes corona equilibrium (CE).

For example, in the universe, the interstellar plasma can be described by CE plasma, and the magnetically confined plasmas can be also modeled with CR plasma. Even in laser plasma, the corona equilibrium will be seen when the expansion plasma becomes sufficiently low density. Figure 5.25 shows the temperature dependence of the charge distribution of aluminum in the corona equilibrium (CE). The density is 10^{18} cm^{-3}, four order of less than LTE case in Fig. 5.1. It can be seen less ionization in CE compared to LTE.

It is important to know that observing the line emission from CE plasma can be used to identify the plasma temperature as follows. Consider the line of hydrogen 2p-1s transition. Since the ground state of hydrogen atom is $N_0 = N_{1s}$ in (5.174).
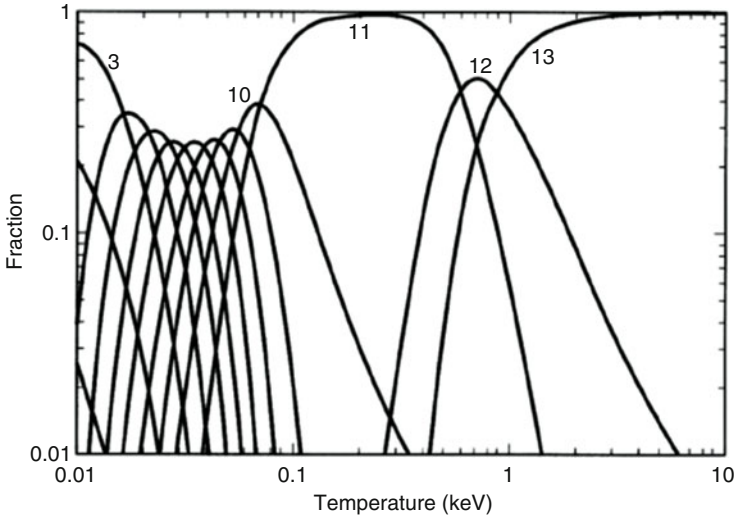
Fig. 5.25 Temperature dependence of the charge distribution of aluminum plasma in the corona equilibrium (CE). The density is 10^{18} cm^{-3}
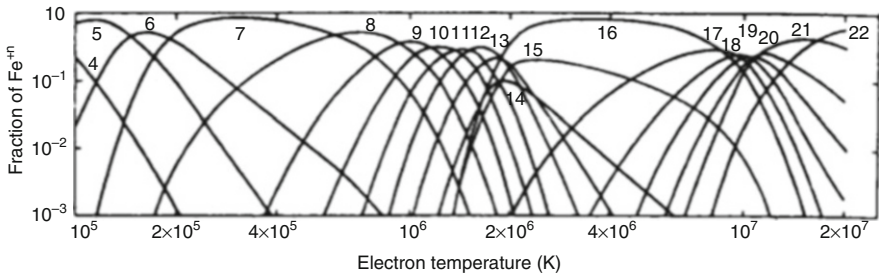

Fig. 5.26 Charge distribution of the corona equilibrium of iron (Fe), the most abundant metal element in the universe. Reprint from Ref. [15] with kind permission from Cambridge University Press

Using the electron collision excitation coefficient (5.134), the intensity of the Lyman α line of 2p-1s transition is found to be proportional to the excitation rate to 2p as

$$\frac{dN_{2p}}{dt} = \left(\nu^{bb}_{1s,2p} N_{1s} \right)_{coll} \tag{5.177}$$

The amount of Lyman α radiation emitted from the unit area in unit time can be known by identifying the product of the density and depth by another method. Then, (5.177) is the relation to measure the plasma temperature.

Figure 5.26 shows the corona equilibrium of iron (Fe), the most abundant metal element in the universe [15]. The temperature of the photosphere of the sun is 6000 K (about 0.6 eV), but the temperature of the corona plasma outside is as high as 1 keV evaluated with CE model. It corresponds to the temperature at the right end of the horizontal axis in Fig. 5.26. There is no conclusion on why the corona plasma, which is downstream of the plasma flow from the sun, has a higher temperature than the upstream by three orders of magnitude. For example, some theory suggests many micro-magnetic **reconnections** are taken place in the corona and the energy of the magnetic field is converted to the thermal energy of the plasma.

5.11.2   *Collisional Radiative Model (CRM)*

Time development of ion charge and atomic structure distribution in plasma has been studied by solving the rate equations without the radiation field. Adding the radiative decay terms in (5.171, 5.172, and 5.173), the time evolution of dynamic plasma can be solved, for example, by coupling with hydrodynamic code. Such atomic process is called **collisional radiative** model (CRM). This code can be extended to study the radiation effect on the atomic process by coupling with radiation transport with detail photons spectrum. Most of the study can be done by including radiative recombination and photo-ionized plasma has been studied [16].

In the case of long-time evolution of plasma like those in Universe and magnetic confinement, stationary state assumption is valid. Such model of CRM is called **collisional radiative equilibrium (CRE)**. The CRE connects continuously between LTE and CE plasma atomic state. As shown in Fig. 5.27 [16], CRE model tends to Saha equilibrium at the high-density limit and CE at the low density and high temperature limit. Since the CRE model without radiation pumping is a function of temperature and density, it is widely used for laser plasmas and radiation-hydrodynamic computations for optically-thin condition. In the CRE model without radiation, the following assumptions are adopted.

1. Since the radiation intensity is weak enough compared to the Planck radiation, the excitation and ionization due to radiative process are neglected.
2. Including all except for the above two, the stationary solutions of (5.171) are solved as functions of given temperature and density.

In the plasma where the time scale of the rate coefficients of all atomic processes is sufficiently faster than the time scale of the change of plasma, for example, the time scale of fluid plasma change, quasi-steady state is satisfied. Then, CRE becomes the solution of the rate equation. So, the comparison of the time scale is important. The temporal evolution of the ionization or recombination becomes important as follows.

Ionizing Plasma   When the interstellar gas is abruptly heated by a shock wave such as a blast wave of a supernova explosion, it takes time for the heated plasma to reach the equilibrium. Meanwhile, ionization progresses gradually. It is referred to as
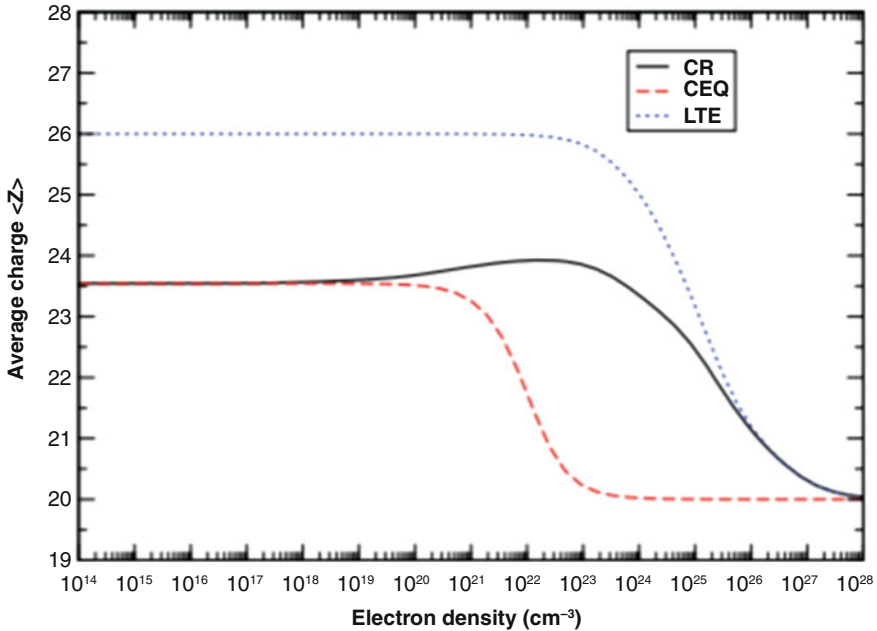
Fig. 5.27 Comparison of three steady state equilibrium atomic process models. The CRE connects continuously to the LTE and CE in the low density and high-density limits. Reprint from Ref. [5] with kind permission from Springer Science + Business Media

ionizing plasma. It is considered that ionization progresses due to the collisions of free electrons, so unless the product of density and time (nt) is not less than a certain value, it does not settle to the equilibrium state. In the interstellar space, the density is extremely low, so that the equilibrium time will be tens of thousands of years.

Recombining Plasma   When high temperature plasma is suddenly cooled, such as by expanding into a vacuum like solar wind from the corona plasma and laser produced plasma, recombination progresses slowly far from thermal equilibrium or corona equilibrium. Since the probability of transition to the quantum state of the outer shell having a high energy level is high in collisional recombination, the distribution of the bound electrons of the ion may be larger in the upper level. This is called the **negative temperature** state, and in such a plasma, as explained in the following section, maser or laser amplification by induced emission becomes possible.

It is important to note that for the purpose to couple with radiation hydrodynamic code, it is better to solve the rate equations with less atomic states. If the average charge state is well predicted with such a simple model, it is better to install such a model in the integrated code to solve time dependent ionization. It is, however, important to compare radiation emission spectra with many experiments, it is

required to know the detail atomic data as seen in Fig. 5.7. It is clever way if it is possible to reproduce the detail energy levels and the other radiation transport related data from the simple atomic model. Such research has been done, for example, based on simple screened hydrogen model [17]. It has been developed to be able to study spectroscopic data with laser-plasma experiments.

5.12   Masers and Lasers

5.12.1   Principle of Laser and Maser

The principle of laser and maser using different energy transitions of atoms in solids and gases is based on the rate equation of the atomic and molecular states of matters. For simplicity, consider a system of atomic bound states consisting of four levels as shown in Fig. 5.28. The Level 1 is the ground state and Level 4 is assumed to have many levels like conduction band in solid. Such a system is called a four-level system, and electrons move between levels. Assume that the Level 4 to Level 3 is a non-radiative transition, that is, thermal relaxation occurs due to the influence of, for example the phonons or surrounding electrons. Then the rate equation for such four levels is

$$\frac{dN_1}{dt} = -\nu_{14}N_1 + (\nu_{21} + A_{21} + S_{21})N_2 \tag{5.178}$$

$$\frac{dN_3}{dt} = \nu_{23}N_2 - (\nu_{32} + A_{32})N_3 + S_{43}N_4 \tag{5.179}$$

$$\frac{dN_4}{dt} = \nu_{14}N_1 - (\nu_{41} + A_{41} + S_{43})N_4 \tag{5.180}$$

$$N_2 = N - (N_1 + N_3 + N_4) \tag{5.181}$$

Here, ν_{mn} is the transition probability from state m to state n. In the solid laser, a strong light source from the outside excites from the Levels 1 to 4 in Fig. 5.28. In the above equations, the coefficient of photo-excitation by external light is set in the rate coefficient ν_{14}, A_{mn} is the spontaneous decay coefficient, and S_{mn} represents the relaxation rate by interaction with the degree of freedom in the solid such as lattice vibration. (5.181) is the conservation equation of the number of electrons.

Steady state (d/dt = 0) should be realized if the strong light source for laser excitation is continuously irradiated to this atomic system. When the third and fourth terms on RHS of (5.179) are large, and if the first and fourth terms are balanced in (5.180), the following equation is obtained.
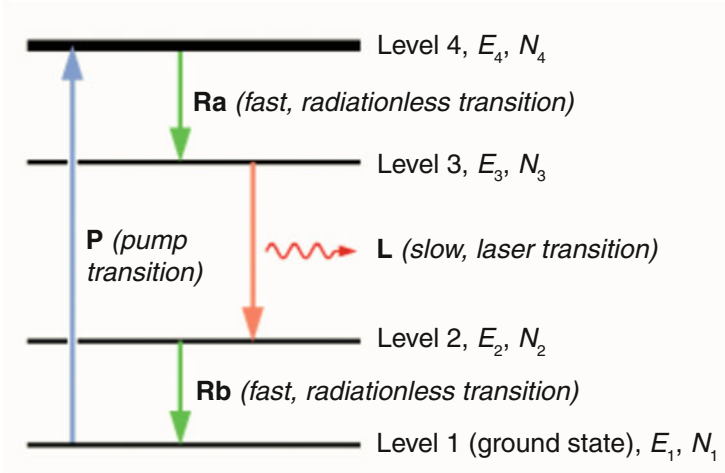
Fig. 5.28 Schematics of excitation by external photon for laser emission in a typical four-level atom

$$\frac{dN_3}{dt} = \nu_{14}N_1 - A_{32}N_3 \tag{5.182}$$

In the steady state,

$$\frac{N_3}{N_1} = \frac{\nu_{14}}{A_{32}} \tag{5.183}$$

If there is no pumping light source and the material is in thermal equilibrium, the following relation should be satisfied.

$$\frac{N_3}{N_1} = \frac{g_3}{g_1} \exp\left(-\frac{\Delta E_{31}}{T}\right) \tag{5.184}$$

However, if the photo-excitation by the external source is strong and the spontaneous emission coefficient is relatively small, the following relation may be satisfied.

$$\frac{N_3}{N_1} \frac{g_1}{g_3} > 1 \tag{5.185}$$

In other words, a "**negative temperature**" state of temperature $T < 0$ is realized by the definition of (5.184). This is called "**population inversion**". This also indicates that the population inversion is also realized between the Levels 3 and 2 in Fig. 5.28. When passing light with the energy of $h\nu = \Delta E_{32}$, the light is amplified due to the stimulated emission. In addition, the light is amplified to keep coherency (same phase) in the amplification process. In gas media, electron beam may be also used to

generate a population inversion via the electron collisional excitation. For example, this method is adopted for a carbon dioxide (CO_2) gas laser with a wavelength of 10.6 μm which is widely used for industrial purpose. The energy levels of the vibration of the carbon dioxide molecule are used for laser emission.

5.12.2   Masers and Lasers in Universe

C. Towns, an awardee of the Nobel Prize in Physics in 1964 for the invention of the principle of laser and maser, has moved to the field of radio astronomy in 1967, and in 1968 his group discovered the maser emission of water molecules coming from Orion constellation [18]. Strong infrared emission from stars creates the population inversion in the rotational levels of the water molecules around young-age stars and high intensity radio waves are generated via induced emission. The maser is coherent emission of microwave due to excited molecule. H_2O (water) maser and SiO masers are typical examples. The former mainly stems from the star-birth region, while the latter is from star-death region.

In 1992 water molecule maser from the Active Galaxy M 106 (NGC 4258) was observed [19]. This observation concluded from the spatial distribution of maser source that there is a black hole with a mass of 36 million times the solar mass at the center. The maser source molecules are excited by the light emitted by plasma falling into the black hole, and the population inversion is maintained. The maser's energy is likely to reach 210 times the total energy emitting from the sun's surface. The spatial variation of the Doppler shift of the maser light was identified to be Kepler motion with which the mass of super-massive Black Hole was inferred.

It is also reported that strong ultra-violet laser is observed by Hubble Space Telescope (HST), and it can be interpreted theoretically due to the population inversion of a four-level atom of Fe II [20]. The observed line was 250 nm, in the UV spectrum of gas closed to the η-Carina, the most active and luminous star in the Galaxy. It is inferred that accidental wavelength coincidence between a strong line of the most abundant elements (H, He) and Fe II absorption line makes the photo-excitation possible. The image of laser emission from the gas pumped by the η-Carina is shown in Fig. 5.29.

Note that the induced emission in Universe is not the same as lasers and masers in laboratory. The induced emission in Universe is so-called amplified spontaneous emission (ASE) of radiation. In lasers in laboratory is designed so that a seed light pass through the media with population inversion and the emission is controlled.

It is impressive to copy the words by Towns in [18]. "Both masers and lasers have been in the universe for billions of years. I didn't have to invent them. As is clear from this example, there must be many more and more secrets hidden in the universe."

Fig. 5.29 The image of
laser emission by amplified
spontaneous emission from
the gas pumped by extreme
photons in the η-Carina.
(NASA)
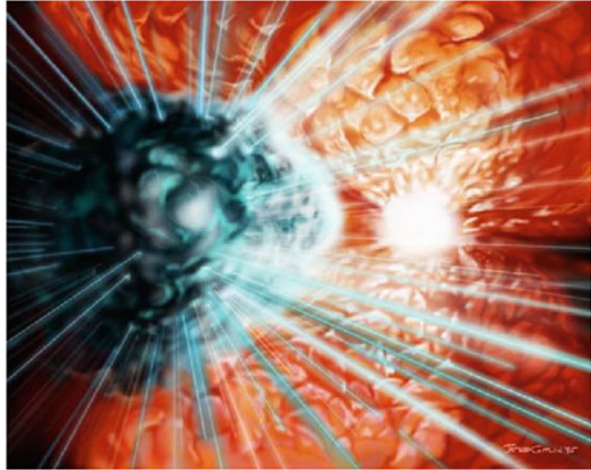
5.13   Photo-ionized Plasma

Photo-ionized plasmas in Universe emits non-thermal spectra being observed by
telescopes for wide range of photon-energy. Especially line emissions from relatively
cold objects in space are mainly due to photo-ionization by hot compact objects in the
vicinity of line-emitting large objects. Therefore, study of photo-ionized plasma and
spectrum from such a plasma is important to study the compact object such as black-
holes, neutron-stars, white dwarfs, etc. In this section, the observation of photo-
ionized plasmas in Universe is briefly introduced and x-ray photo-ionized plasma
experiments in laboratory as model experiment for space is also reviewed.

5.13.1   Planetary Nebula

In the space, the **planetary nebulae** (PN) are observed, many of which newly found
by Hubble Space Telescope (HST). The image of NGC7009 is shown in Fig. 5.30.
The colorful images of the planetary nebulae are not powered by the ultraviolet lights
from the central white dwarf. It excites and ionized the surrounding gas to keep the
emission. It emits intrinsic emission lines in the process of recombination and
de-excitation to the ground state. They are emission nebula consisting of an
expanding, glowing shell of ionized gas ejected from red giant stars late in their
lives. The term "planetary nebula" is a misnomer because they are unrelated to
planets or exoplanets. The term originates from the planet-like round shape of these
nebulae observed by astronomers through early telescopes. Though the modern
interpretation is different, the old term is still used.

   All planetary nebulae form at the end of the life of a star of intermediate mass,
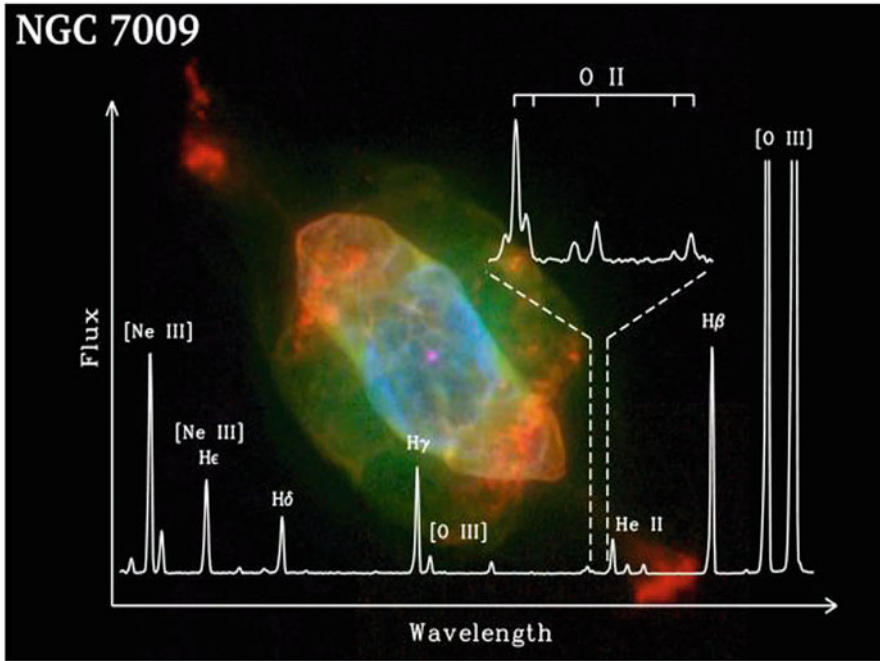about 1–8 solar masses. It is expected that the Sun will form a planetary nebula at the

Fig. 5.30 Emission image and spectra of a planetary nebula NGC7009, a photo-excited plasma in Universe [21]. (NASA)

end of its life cycle [20]. They are a relatively short-lived phenomenon, lasting perhaps a few tens of thousands of years, compared to considerably longer phases of stellar evolution. Once all of the red giant's atmosphere has been dissipated, energetic ultraviolet radiation from the exposed hot luminous core, called a planetary nebula nucleus ionizes the ejected material. Absorbed ultraviolet light then energizes the shell of nebulous gas around the central star, causing it to appear as a brightly colorful planetary nebula.

It is noted that many forbidden line emissions are observed, because the density is very low and almost no collisional de-excitations are taken place. As the result, the long life-time metastable states decay via higher order effect in (5.67). The lines indicated with the brackets like [Ne III] in Fig. 5.30 are the forbidden lines within the dipole transitions. X-ray lines from planetary nebulae are observed [21].

5.13.2   XFEL and Inner-Shell Ionization

X-ray free-electron lasers (XFELs) have been used to develop new science with coherent hard x-rays. After accelerating electron beams relativistic, coherent x-rays are generated and amplified in passing through a magnetic undulator device. For
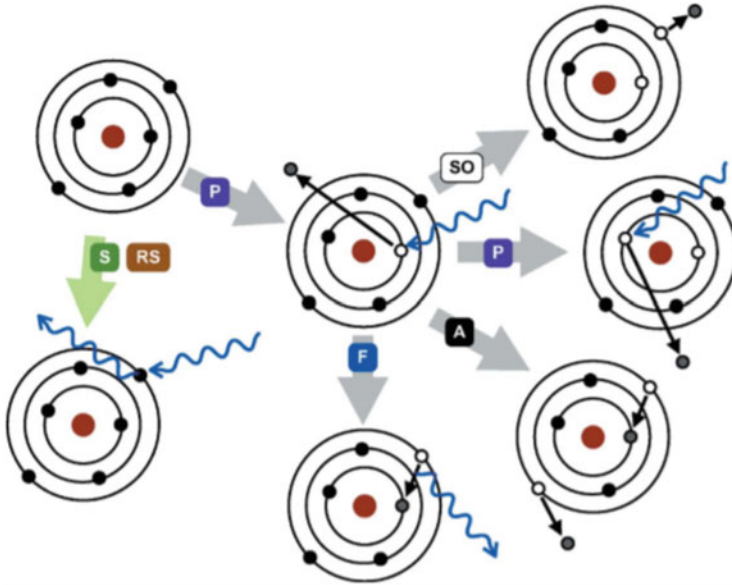
Fig. 5.31 Diagrams of X-ray-induced physical processes treated by XATOM. P photoionization, A Auger (Coster–Kronig) decay, F fluorescence, SO shake-off, S Rayleigh and Compton X-ray scattering, RS resonant elastic X-ray scattering. Reprint from Ref. [23] with kind permission from Springer Science + Business Media

example, European-XFEL [22] has output of 3–25 keV with focused intensity of 10^{17-18} W/cm^2 for 2–100 fs pulse. It is 3 mJ at 5 keV with 10^{10} photons/pulse. Such x-ray is strong enough to study the inner-shell ionization process of high-Z atoms. When the ionization potential is lower than the XFEL energy, the inner-shell ionization is dominant in the atomic process.

As we see in Fig. 5.12, 1s electron in K-shell is dominantly ionized, while 2s and 2p electrons are dominantly ionized if the ionization potential of K-shell is larger than the x-ray energy. When a vacancy is produced in such an inner shell, it is known that the subsequent process is Auger decay or fluorescence process. The atomic process induced by such inner-shell ionization is schematically shown in Fig. 5.31 [23]. In order to analyze experimental results, all rate coefficients are calculated by developing XATOM code, the details of the code are given in [23]. In obtaining the orbital wave functions, Hartree-Fock-Slater method is used in the code.

In particular, XATOM is designed for describing complex interactions between atoms and intense XFEL pulses. During the XFEL–atom interaction, if single-photon absorption is saturated, multiphoton absorption occurs via a sequence of single-photon ionization and accompanying relaxation processes like fluorescence and Auger decay. The X-ray multiphoton absorption usually yields highly charged states, involving a variety of different multiple-hole states. XATOM calculates atomic data – orbitals and orbital energies, and cross sections and rates for X-ray-

induced processes – for all individual electronic configurations, including multiple-hole states, of arbitrary atomic species. More detail description of the theory of atomic photo-effect is given in [24].

Since the x-ray intensity is high, deep inner-shell multiphoton ionization has been observed experimentally [25]. In the experiment XFEL-SACLA was used to irradiate neutral xenon (Xe) gas to measure the multiply ionized Xe ions. At highest charged ions of Xe^{26+} have been observed. The ionization process was theoretically studied to obtain a model shown in Fig. 5.32. It is one typical pathway yielding Xe^{24+} [25]. The plot illustrates that the total energy of the system varies in the course of the ionization steps. After L-shell photoionization (blue arrows), the energetically excited core-hole state relaxes via a series of Auger and Coster-Kronig decays (green arrows), and/or fluorescence (yellow arrows). Note that another photoionization occurs before the atom fully relaxes to the ground configuration. We find it useful to view the multiphoton multiple ionization dynamics occurring in a single atom in terms of quantum evaporation of electrons: x rays heat up the atomic system to highly excited states, and then the system relaxes primarily by emitting electrons with characteristic energies. The excess energy is shared among the electrons via electron-electron collisions, resulting in the ejection of 24 electrons in total. For each photoionization. Note that this multi-photon process is not the nonlinear process discussed in Vol 1 regarding multi-photon ionization by intense lasers, but liner process sequence in one pulse.

The population inversion and subsequent x-ray laser phenomenon have been demonstrating with the inner-shell photo-ionization by XFEL-LCLS at SLAC [26]. There have been a lot of studies on x-ray lasers in laboratory with use of
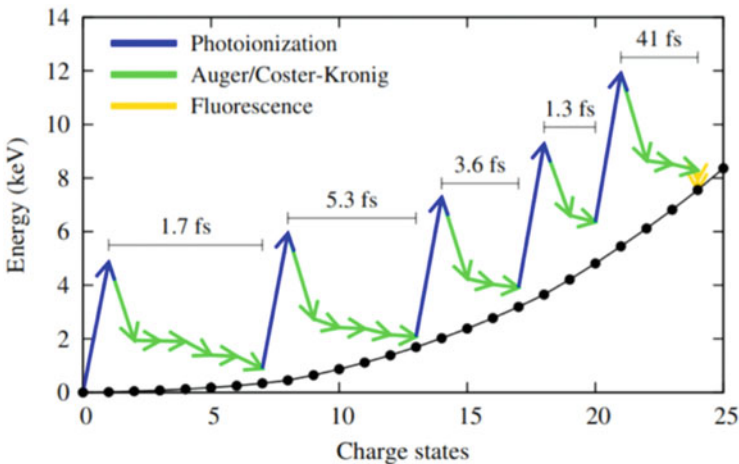

Fig. 5.32 An exemplary pathway of multiphoton multiple ionization of Xe at 5.5 keV. The black solid line with dots indicates the ground-configuration energy for given charge states, and the energy of neutral Xe is set to zero. Reprint with permission from Ref. [25]. Copyright 1998 by American Physical Society
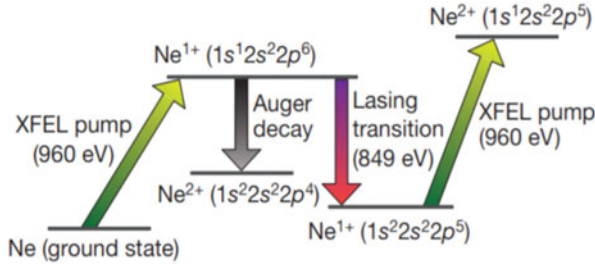
Fig. 5.33 Level scheme. Population inversion of the 1s 1 2s 2 2p6 -to-1s 2 2s 2 2p5 transition is created by K-shell photo-ionization of neutral neon. The Auger decay time of the inverted state (2.4 fs) dominates the kinetics of the system in the small-signal-gain regime. The lower lasing state is depleted by K-shell photo-ionization. Reprint from Ref. [26] with kind permission from Springer Nature Publ.

plasma as briefly shown below. XFEL made it possible to pump new atomic X-ray lasers with ultrashort pulse duration, extreme spectral brightness and full temporal coherence. X-ray laser in keV energy regime based on atomic population inversion and driven by rapid K-shell photo-ionization are demonstrated using pulses from an XFEL through the physical process shown in Fig. 5.33 [26]. A population inversion of the Kα transition is experimentally demonstrated in singly ionized neon at x-ray energy of 849 eV. Strong amplified spontaneous emission is observed from the end of the excited plasma. This resulted in femtosecond-duration, high-intensity X-ray pulses of much shorter wavelength and greater brilliance than achieved with previous atomic X-ray lasers.

It is useful to briefly describe about x-ray laser research before the XFEL era. X-ray spectroscopy is one of the most powerful diagnostics in laser plasma from the beginning of research. H. Griem gave a review on diagnostics and modeling of dense plasma, emphasizing density and temperature measurements [27]. Most of the x-ray laser pumping has been studied for the case of collisional excitation scheme in laser produced plasma, while the energy conversion efficiency was very low in UV range, say ~60 eV.

Since the XFEL x-ray source is mono-energetics and photo-ionization plays essential role to generate free electrons from target atoms, it is not appropriate to assume the free electrons have Maxwell distribution during the short time of x-ray pulse. Time-dependent calculations of electron energy distribution functions (EEDF) in the presence of intense XFEL radiation have been studied computationally by solving Boltzmann equation of free electrons. The code is coupled with atomic codes for photo-ionization and related atomic processes. The condition of simulation is that argon gas of atomic number density 1.6×10^{19} cm^{-3} is irradiated by a pulse duration of 40 fs, intensity 2×10^{17} W/cm^2 XFEL with x-ray photon energy of 1.07 keV. In Fig. 5.34, the time evolution of the free electron distribution functions is shown from 1 fs to 40 fs [28].
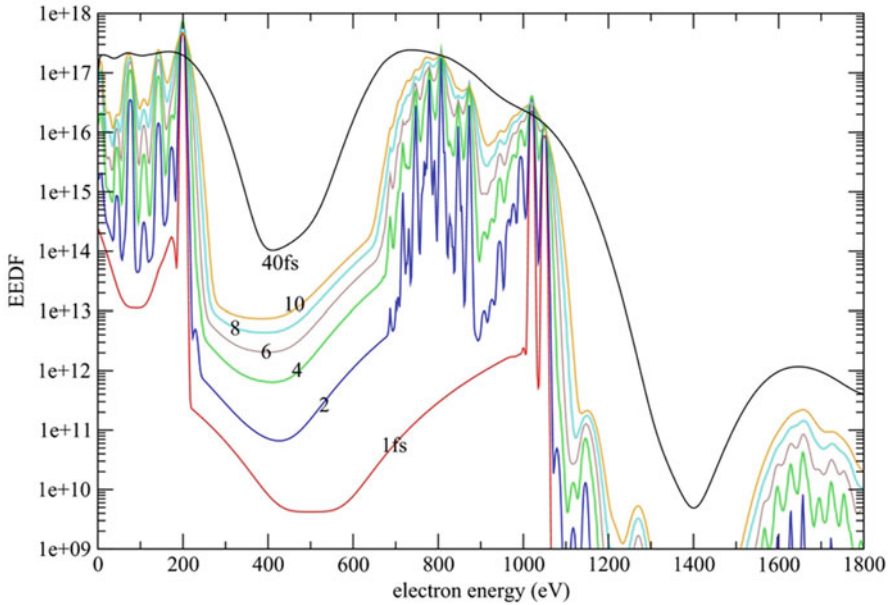
Fig. 5.34 Time evolution of free electron distribution in argon gas of atomic number density 1.6×10^{19} cm^{-3} irradiated by a pulse duration of 40 fs, intensity 2×10^{17} W/cm^2 XFEL with x-ray photon energy of 1.07 keV. Time evolution is shown from 1 fs to 40 fs. The distribution function is far from Maxwellian. Reprint from Ref. [28] with permission from Institute of Physics Publ

At 1 ps, the peak of EEDF is located at the excess energy of K-shell ionization of neutral atom around 200 eV. Then, the peak around 700–900 eV is due to electrons ejected by Auger process. As time increases and the ionization potential increases in ionized argon, the photo-ionized electrons appear in the energy spectrum lower than 200 eV. In Fig. 5.35 long time evolution after x-ray irradiation is shown [28]. It is clear that it takes about 2 ps so that the free electron is thermalized to be Maxwellian. Simulation was also carried out for the case of irradiation of black-body radiation of the radiation temperature $T_r = 100 \sim 300$ eV [29]. FEDF is relatively smooth compared to the XFEL irradiation case.

5.13.3   *Photo-ionization in X-Ray Binary*

It is very challenging to study photo-ionized plasma, because it is hard to produce black-body radiation with radiation temperature more than 100 eV in laboratory to ionize very abundant atom such as Si, Fe, etc. with atomic numbers more than 10. However, such bright radiation sources in x-ray regime have been observed in Universe with x-ray satellites such as ASCA, Suzaku (Japan), Chandra (US), Newton (EU). In studying compact objects such as black-holes, neutron stars, and
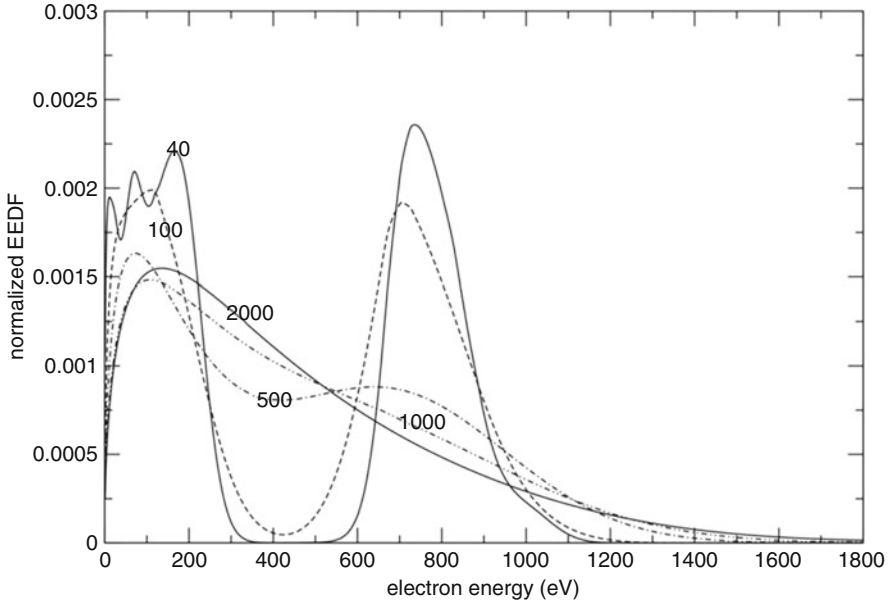
Fig. 5.35 Long time evolution of electron distribution function after Fig. 5.34 by XFEL irradiation. It is clear that it takes about 2 ps so that the free electron is thermalized to be Maxwellian. Reprint from Ref. [28] with permission from Institute of Physics Publ

white dwarfs, binary system made of such a compact star and a normal star emits strong x-rays with witch the property of compact objects can be studied with use of x-ray spectra etc. I order to analyze the observed x-ray spectrum, modeling of photo-ionized plasma is essential. Such simulation codes should be verified and validated via comparison with appropriate experiment in laboratory. Here, the topics of photo-ionized plasma in Universe and related laboratory experiments are reviewed. Always, the computational modeling is discussed by comparing to both of the observational and experimental data.

The photo excitation and ionization processes become important in a variety of astrophysical phenomena. A familiar photo-ionized plasma is clearly observed by telescope as the edge of neutral hydrogen in clouds with H_a line emissions. For example, **Eagle Nebula** boundary observed is the surface where the photo-ionization by UV radiation generated by massive stars nearby. The UV light ionizes molecular cloud to ionize neutral hydrogen atoms to be proton, HII. This region is called **HII region** [30]. HII region is related to the birth of many stars in the molecular clouds.

On the other hand, photo-ionization of so-called metal in universe, where metal means higher Z atoms than most abundant H and He. Since high-Z ions emits x-ray line emissions, they are good targets to be observed to study the physics of very energetic radiation source. Cygnus X-1 and **Cygnus X3** are well known x-ray binary
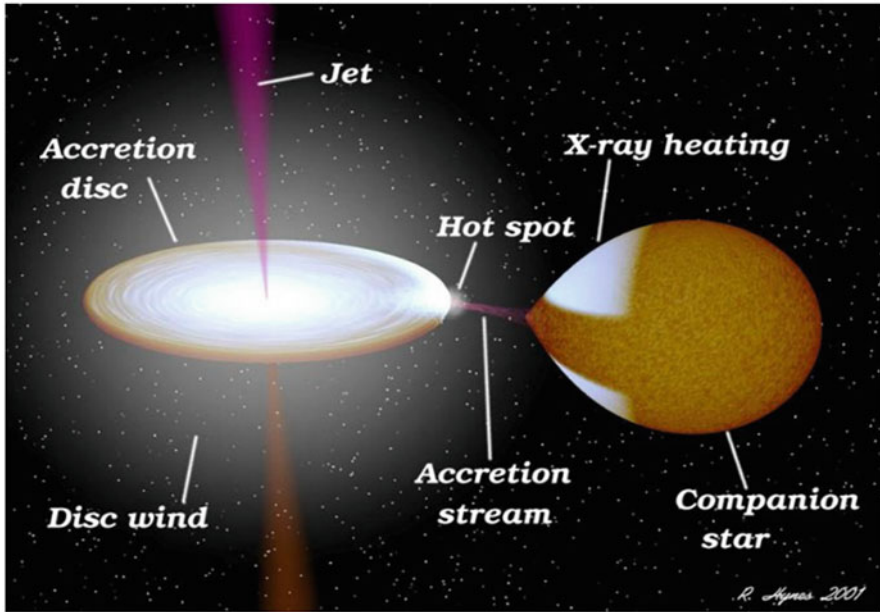
Fig. 5.36 A schematic of x-ray binary system consisting of a compact object and a main sequence star. (Image by NASA)

[31]. They are located around 7.4 kpc (20 k light years), however emitting very luminous x-rays. The schematic of such a binary system is shown in Fig. 5.36. The companion star is a massive normal star with very high-mass stellar wind to donate the matter to the compact object. Since the matter has angular momentum to form the accretion disc around the compact object. Since the compact object like black-hole absorb the mass via strong gravitation, the matter of accretion disc is continuously falls into the black hole. During the process losing the angular momentum, the excess energy heats the matter and the matter near the compact object becomes extremely high temperature plasma emitting almost Planckian radiation. The radiation temperature becomes almost 1 keV and the radiation photo-ionized the accreting plasma and the surface of the companion star whose radius is much larger than the compact one. In case of Cygnus X3, the binary system is rotating around the center of mass with 4.8 h period.

How the plasma is strongly affected by photo-ionization in atomic process is measured with the **photo-ionization parameter** ξ defined by

$$\xi = \frac{L}{n_e R^2} \quad [\text{erg/cm/s}] \tag{5.186}$$

where L is the total luminosity of the compact object and R is the radius of the most x-ray emitting plasma region of the accretion disk by photo-ionization. The n_e is the

electron density to measure the photo-recombination. This (5.186) is a rough estimation of the ratio of the photo-ionization rate to the photo-recombination rate, namely.

$$R = \frac{\langle \sigma_{pi} n_p c \rangle}{\langle \sigma_{pr} n_e v \rangle} \propto \frac{I_p}{n_e} \tag{5.187}$$

In (5.187), the photo-ionization and photo-recombination cross sections are of course dependent on each transition, while neglecting this difference. In addition, the photo-ionization also depends on the photon spectrum $n_p(\nu)$. After neglecting such dependencies, roughly speaking the radiation intensity divided by the electron density would be a good measure of the effect of photo-ionization in plasma. Note that our photo-ionization plasma can be realized when the condition $\xi \gg 1$ is satisfied in the unit of (5.186).

In a detail analysis of the spectra from Cygnus X-3 has been done [32]. In order to analyze the data, the ionization parameter should be identified. The XSTAR code for photoionization equilibrium model with a 1.72 keV Planck radiation temperature illumination spectrum is used. In the XSTAR code, atomic process is coupled with energy balance relation to determine electron temperature consistently. Note that XSTAR code is well developed but is zero-dimensional model, no spatial structure, and radiation transport is not included in the code. This becomes important in laboratory experiments as mentioned below. In Fig. 5.37, the charge state
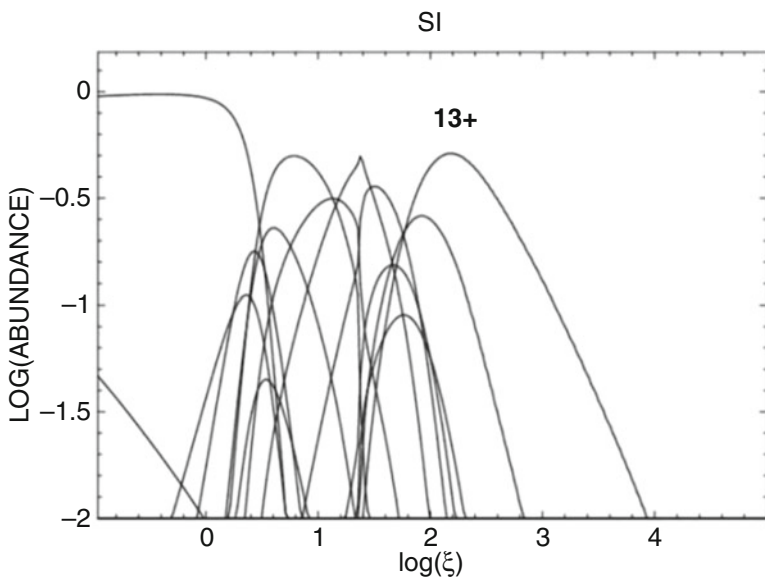

Fig. 5.37 Charge distribution of silicon atom as a function of the ionization parameter ξ. Reprinted with permission from Ref. [32]. Copyright by American Astronomical Society

distribution as a function of the ionization parameter ξ is plotted. It is seen that around $\xi = 10^2$ the abundance of He-like silicon has the peak. The bright emission of He-like silicon Kα line suggests the ionization parameter $\xi \sim 10^2$ for Cygnus 3 binary system. It is also concluded that the density must be higher than 10^{12} cm^{-3} in the region responsible for most of the emission.

The electron temperature obtained from the energy balance relation is also calculated. It is about 20 eV at $\xi \sim 10^2$. This is lowest estimation of the temperature of photo-ionized plasma, because the plasma is assumed to be optically thin and the emitted radiation due to photo-recombination and photo de-excitation are assumed all escape from the system. This may be due to the fact that the specification of the spatial profile of the binary plasma system is very tuff.

In Fig. 5.38, the observed line emissions from H-like and He-like silicon ions (Si XIV and Si XIII) are shown. The brightest line near 2 keV is from Kα line of H-like silicon. The line-like peaks from He-like silicon are also observed near 1.85 keV. In photo-ionized plasma, it is usual to observe three lines around 1.83–1.88 keV [33]. They are evaluated to be by the resonance (r), inter-combination (i), and forbidden (f) lines as indicated in Fig. 5.38. In Fig. 5.39, such three different
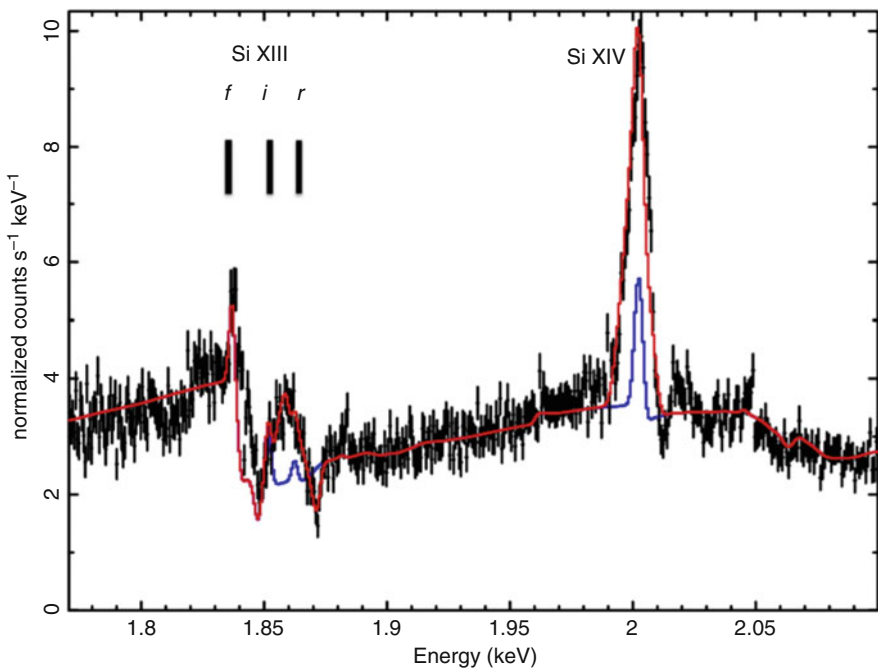

Fig. 5.38 The observed line emissions from H-like and He-like silicon ions (Si XIV and Si XIII) . The brightest line near 2 keV is from Kα line of H-like silicon. The line-like peaks from He-like silicon are also observed near 1.85 keV. The resonance (r), inter-combination (i), and forbidden (f) lines are speculated. Reprinted with permission from Ref. [32]. Copyright by American Astronomical Society
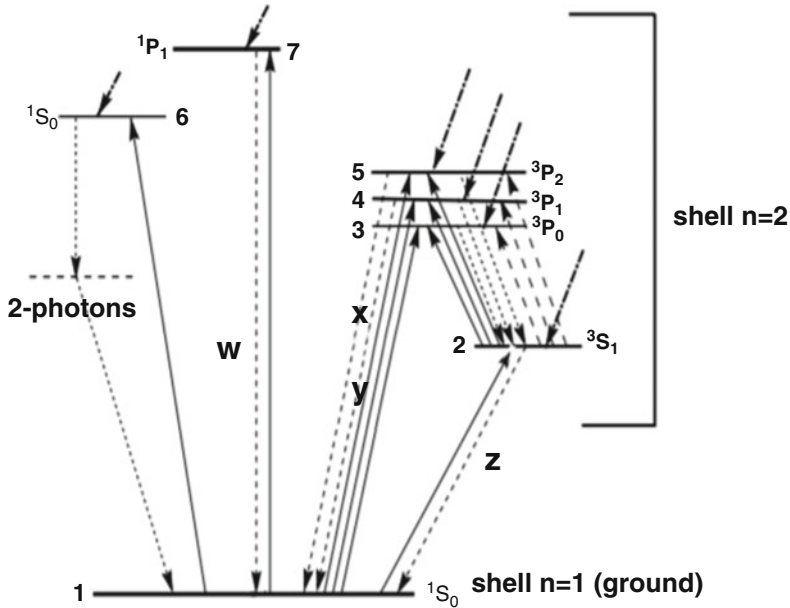
Fig. 5.39 The three different line transitions in Fig. 5.38 are shown for helium-like ions, where w, (x,y), and z correspond to the resonance (r), inter-combination (i), and forbidden (f) transitions [34]. *Credit*: D. Porquet, et al., *A&A,376, 1113, 2001, reproduced with permission* © *ESO*

line transitions are shown for helium-like ions, where w, (x,y), and z correspond to the resonance, inter-combination, and forbidden transitions [34]. The forbidden lines are possibly observed from plasma in low density as we saw in the planetary nebulae in Fig. 5.30.

In Fig. 5.38, the model calculation with only the photo-ionized plasma at rest gives the blue spectrum, being very different intensity profile near all lines. The red spectrum, on the other hand, is given by taking account additionally the wind plasma component from the surface of the companion normal star [32]. It is complicated to explain the physical reason and recommended to refer the paper by Kallman et al. Even in such a case, we have to consider many atomic processes as schematically shown in Fig. 5.22.

Active Galactic Nuclei (AGN) [31] extremely far from our Galaxy are strong X-ray source in the deep sky, and about 70% of x-ray observed from far from our Galaxy are inferred from many AGNs. The physical process of x-ray generation is the same as x-ray binary in our Galaxy, namely from accretion disk. However, the accreting matter is absorbed by a huge black-hole with mass of 10^6–10^{10} solar mass. Some of them also observed as maser source as described previously. The x-ray spectra from AGNs have been observed and studied for example in [35]. Theoretical models are fitted to the observed optical/UV spectra and the maximum accretion disk temperature was always about 2 eV. However, the observed x-ray spectrum has a

power law in high-energy region because of the non-thermal process in complicated geometry near the center of the massive black-hole and accretion disk. So, effective ionization parameter to silicon is relatively high.

A possibility of x-ray laser emission from such Planckian radiation pumping was studied theoretically by us [36]. We have asked ourselves whether x-ray lasers can exist in Astrophysical objects. As a model, we used the 1s2p $^1P_1$ populations in He-like ions, which are generated by K-shell photo-ionization of Li-like ions as typically observed in X-ray binaries as mentioned above. Although we have fixed to Planckian radiation source, it is concluded that it is difficult to produce population inversion for this transition. If the low energy part of Planckian radiation is absorbed in the atmosphere of a companion star, it may be possible to produce such population inversion inside the star near the surface. We are required to study more about the condition of x-ray binary or other candidates where such a condition is realized.

5.13.4   Photo-ionized Plasmas in Laboratory

The photo-ionized plasmas are model experiment of x-ray binary system, while there are several differences due to limit of laboratory plasma. One is time dependence of atomic state, second is expanding flow of plasma, the third is optical depth especially of line radiation transport. Of course, the radiation source such as more than 1 keV radiation temperature is not possible in laboratory so far. However, photo-ionized plasma itself is an interesting problem from view point of atomic process, opacity, line profile modeling, radiation transfer, and so on.

The photo-ionized plasma has been studied for looking for better coupling with the absorbing plasma in hohlraum targets, where laser energy is converted to radiation energy to be absorbed by fusion pellet in the hohlraum. In the National Ignition Facility (NIF) ignition campaign, almost Planckian radiation with radiation temperature $T_r = 250$–300 eV has been used for implosions under the absorption of laser energy of 0.8 ~ 1.1 M Joule [37]. The radiation continues for about 5 ns and it is expected that the photo-ionized plasma is almost in steady-state. Z-pinch machine is demonstrated to be an intense x-ray sources and proposed to be also applicable to study the physics of photo-ionized plasma in Universe [38]

Preliminary design and experiments of photo-ionized plasma were reported for the cases with Z-pinch [39] and laser induced gold cavity [40] radiations. The radiation temperature is in the rage of 80 ~ 200 eV. The absorption and emission spectroscopy of such photo-ionized plasma have been studied. In addition, scalability to very low-density plasma in Universe was also discussed. Application of such photo-ionized experiments to astrophysics has been discussed internationally [41] and The Z Astrophysical Plasma Properties (ZAPP) collaboration has been initiated for applying the Z-pinch for a variety of astrophysical model experiments [42].

Precise experimental result is first reported for Z-pinch photo-ionization plasma, where the Z-pinch radiation spectrum was observed and the radiation temperature was measured to be 165 eV [43]. Charge distribution of photo-ionized iron plasma
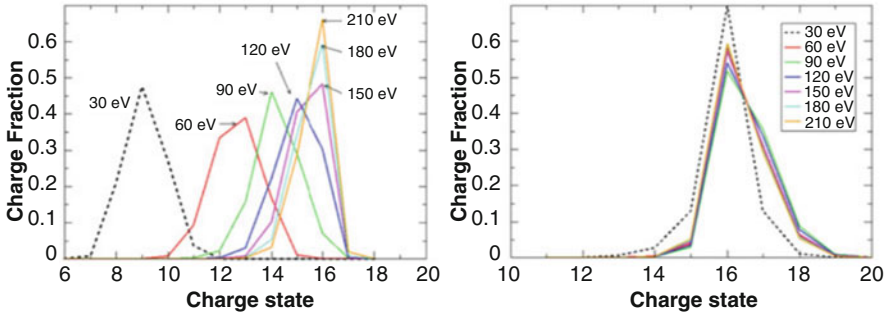
Fig. 5.40 Charge distribution calculated for photo-ionization experiment with Z-machine. The left is without radiation and the right is with external radiation heating, where the temperature is the plasma temperature. It is clear that charge distribution is insensitive to the iron plasma temperature for more than 150 eV in this experimental condition. Reprint with permission from Ref. [17]. Copyright 1998 by American Physical Society. Reprint from Ref. [43] with kind permission from Springer Science + Business Media

observed in the experiment is compared with three different atomic process codes including photo-ionization. Two of them are standard codes to analyze the photo-ionization plasma emission spectrum compared to X-ray satellite data, while the third one is FLYCHK mentioned in [17]. It is noted that the absorption spectra have been compared to the detail line profiles predicted with HULLAC code. And the resultant charge distribution was compared to three codes. It is found that the averaged charge is $<Z> = 16$ and three codes well fit to the experimental data [43]. In Fig. 5.40, the charge distributions are shown for the case assuming a constant temperature of iron plasma [17, 43]. The left is without external radiation source, while the right is with external radiation heating, where the temperature is the plasma temperature. It is clear that charge distribution is insensitive to the iron plasma temperature for more than 150 eV in this experimental condition.

It is speculated that compared to AGN x-ray flux, the x-ray flux for contributing silicon photo-ionization is almost the same as that obtained by Z-pinch x-ray with $T_r = 165$ eV [44]. The absorption spectra and emission spectra have been analyzed with two different codes. For the condition measured in Z-pinch experiment, both codes result over ionization of Si^{+9} and Si^{+8} the absorption spectrum show almost the L-shell electrons are already photo-ionized and only two electrons remain. In the computational model, the inner-shell ionization from M-shell and subsequent Auger process may be overestimated. It is suggested that so-called resonant Auger destruction (RAD) are over-estimated in the codes [44].

In order to relate such laboratory experiment to the binary system observation, higher radiation has been generated by use of radiation from an imploded spherical target. By use of Gekko-XII laser system, twelve beams irradiate a target to generate almost 0.5 keV radiation temperature. Total energy of 4 kJ with pulse duration of 1.2 ns at green light (0.53 μm) are impinged on a plastic target with the diameter 505 μm and thickness 6.4 μm [33]. Although the pulse duration of the radiation is
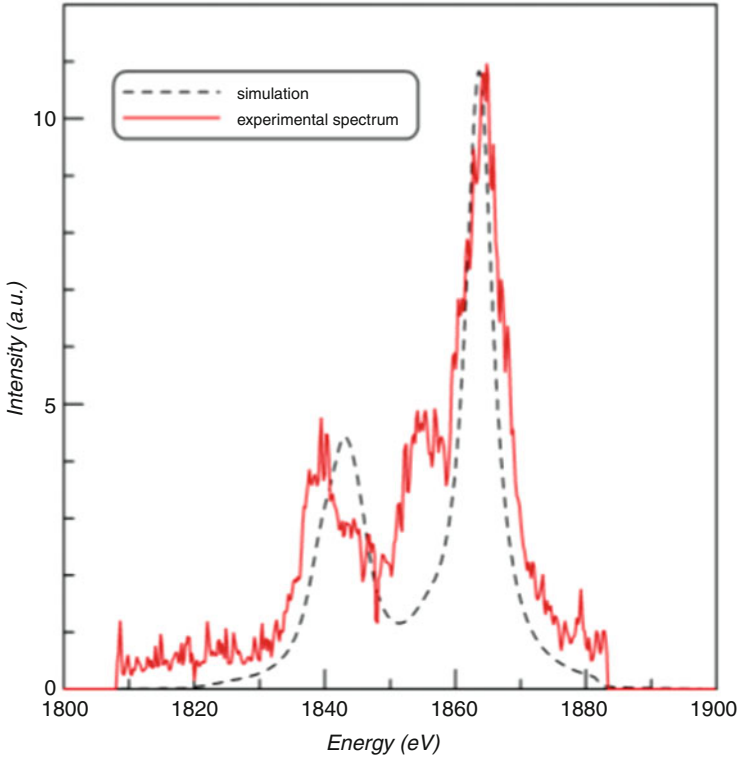
Fig. 5.41 Comparison of experimental spectrum and time-dependent numerical spectrum for photo-ionization experiment. The time dependent simulation for the experiment cannot reproduce this hump given in the experimental spectrum. Reprinted with permission from Ref. [45]. Copyright by American Astronomical Society

160 ps, it is enough time to generate He-like silicon with the density $n_e = 10^{20}$ cm^{-3} located near the imploded core. Observation data from Cygnus X3 and Vela-X1are compared to the experimental data for the line emissions from He-like silicon [33]. The line inferred as the forbidden transitions only expected in low density astrophysical plasma [32] is also observed. However, time dependent simulation for the experiment cannot reproduce this hump in spectrum as shown in Fig. 5.41 [45]. On the other hand, this hump is generated in computation in [46, 47], although strength of three humps are not reproduced. It is still an open question.

The inter-combination line (1s^2 ^{1}S-1s2p ^{3}P and 1s^2 ^{1}S-1s2p ^{3}P) is strengthened by satellite lines from the Li-like species which has similar energies. Namely, 1s^{2}3p-1s2p3p transition has energy around 1.855 keV. So-called satellite lines of Li-like ions.

Mancini et al. [48] has carried out sophisticated computer simulation with Boltzmann code for free electrons used in [29]. The Boltzmann code is coupled with radiation hydrodynamic code. It is shown that photo-excitation is very

important to control radiation cooling rate and the evaluated electron temperature is found to be lower than predicted by CLOUDY and XSTAR codes. In addition, high-energy tail component generated by photo-ionization affects the population of excited state enhancing the radiation cooling rate.

Appendix-B: Thermal Equilibrium Statistical Mechanics

Plasma consists of a large number of particles. Even with a super-computer, it is not possible to follow the motions of all particles in systems in laboratory or in space. We need to use statistical mechanics to describe any macroscopic dynamics of such plasmas. Here, the minimum knowledge of the statistical mechanics is reviewed on the topics that will be required to study plasma physics in the present book.

B-1 Boltzmann Distribution

Assume that many particles exist in an isolated system. Consider that the number of the particles N is sufficiently large, while exchanging energy and momentum inside the system. In the system, each particle energy is quantized and each energy state is symbolically indicated as a k-state. Assume that n_1 particles in state 1, n_2 in state 2, n_i in state i and all the particles are somewhere in a certain energy state. Then, the probability for the system takes the combination of P $(n_1, n_2,,,, n_i,,,,)$ in each energy state is

$$P(n_1, n_2, \cdots, n_i, \cdots) = p(n_1)p(n_2)\cdots p(n_i)\cdots \tag{B1.1}$$

Here, p (n_i) is the number of combinations where n_i particles exist in i state. That is, p (n_i) obviously

$$p(n_i) = C_n^{n_i} = \frac{n!}{n_i!(n - n_i)!} \tag{B1.2}$$

Calculating p (n_i) from 1 to subsequent number, and using the fact that the second term of the denominator cancels with the numerator of the next number, the probability is obtained as follows.

$$P(n_1, n_2, \cdots, n_i, \cdots) = A\frac{n!}{\prod n_i!} \tag{B1.3}$$

Here, Π means to take the product for all i. In (B1.3), A is a normalization constant.

Let's find the distribution when the combination of the arrangement of the number of particles in each energy state is the maximum. For that purpose, we use the following **Stirling formula.**

$$ln(n!) \approx \int_0^n ln(x)dx \tag{B1.4}$$

Then, we write $\bar{n}_i$ the number of i states where P in (B1.1) is the maximum value. Carrying out the Taylor expansion around the number of particles in each state with the maximum probability, and using (B1.2) and (B1.3), we obtain

$$ln\, P(n_1, n_2, \cdots, n_i, \cdots) = ln\, P(\bar{n}_1, \bar{n}_2, \cdots, \bar{n}_i, \cdots) - \sum_i ln(\bar{n}_i)\delta n_i \tag{B1.5}$$

Here, δn_i with the energy E_i is the deviation from the maximum probability and they have to satisfy the following constraint conditions.

$$\sum_i \delta n_i = 0, \quad \sum_i E_i \delta n_i = 0 \tag{B1.6}$$

(B1.6) are the condition of particle number and energy conservations, respectively.

The first term on RHS of (B1.5) is a constant value.

Also, around the maximum probability the first derivative needs to disappear. With combination of the restrictive condition (B1.6), the following relation should be satisfied.

$$\sum_i \left(ln(\bar{n}_i) - ln\, C + \frac{E_i}{T}\right)\delta n_i = 0 \tag{B1.7}$$

where C and T are constants to be determined for convenience later. In the vicinity of the maximum probability, (B1.7) requires that the inside of the parentheses be balanced, so the following relational expression is obtained

$$\bar{n}_i = C exp\left(-\frac{E_i}{T}\right) \tag{B1.8}$$

Here, C is determined so that the number of all particles is N. T is the temperature of the system, multiplied by the Boltzmann constant and is a unit of energy. (B1.8) shows just the **Boltzmann distribution**. Any particles that weakly interact in a system should be Boltzmann distribution in the thermal equilibrium.

It was assumed above that each energy state has one particle at most, but it is easy to extend the case where the energy state is degenerate or even continuous. If the eigen-state "i" is degenerate with g_i, the distribution function is modified as

$$\bar{n}_i = C g_i\, exp\left(-\frac{E_i}{T}\right) \tag{B1.9}$$

Maxwell Distribution

Maxwell derived the velocity distribution of gas system by assuming that there must be a steady state velocity distribution for many particles in gas (1860). Using the Boltzmann distribution given in (B1.9), it is easy to derive **Maxwell distribution** for freely moving particles in gas and plasma. Note that the number of states changes depending on how to define the freedom, say one, two, or three-dimension in space. Maxwell distribution is that for freely moving particles system of Boltzmann distribution, so it is also called **Maxwell-Boltzmann distribution**.

For the sake of simplicity, assume that plasma particles only move in the x direction in one dimension. Let's assume that the plasma is trapped in the potential of length L which correspond the size of box containing the particles. Then, the energy state of the free particle is discretized, and the wave function of electron or ion must satisfy the following condition.

$$\psi = sin\left(\frac{p_x L}{\hbar}\right), \ \frac{p_x L}{\hbar} = \pi k \ (\text{k : integer}) \tag{B1.10}$$

It is clear that the number of states of one-dimensional free particles is equally spaced in the velocity (momentum) space. Therefore, the number of states is constant. From this fact, the velocity distribution function of the plasma particles with free thermal motion is given by (B1.8).

$$f(v_x) = C exp\left(-\frac{m v_x^2}{2T}\right) \tag{B1.11}$$

Using the relation of integration;

$$\int_{-\infty}^{\infty} e^{-\alpha x^2} dx = \left(\frac{\pi}{\alpha}\right)^{1/2} \tag{B1.12}$$

The velocity distribution function of free particles in one-dimensional space is

$$f(v_x) = \left(\frac{m}{2\pi T}\right)^{1/2} exp\left(-\frac{m v_x^2}{2T}\right) \tag{B1.13}$$

This is a **Gaussian distribution**, and its dispersion shows thermal spread.

In three dimensions, the upper one-dimensional distribution is used also in the y and z directions, and it is obtained by taking three products. However, note that in that case, it is the probability of finding particles in the volume of the velocity space $dv_x dv_y dv_z$. Since it can be considered that there is no anisotropy of the distribution function in the thermal equilibrium state, the distribution function is spherically symmetric in the velocity space. It should be only a function of the absolute value of the velocity

$$v^2 = v_x{}^2 + v_y{}^2 + v_x{}^2 \qquad\qquad (B1.14)$$

Then, we can write a three-dimensional velocity distribution as a function of v. Note that the number of states increases with v. That is, using the spherical coordinates of the velocity space

$$g(v) = 4\pi v^2 dv \qquad\qquad (B1.15)$$

Using (B1.9), the velocity distribution function is obtained as

$$f(v) = 4\pi \left(\frac{m}{2\pi T}\right)^{3/2} v^2 \, exp\left(-\frac{mv^2}{2T}\right) \qquad\qquad (B1.16)$$

Here, the normalization constant is obtained with the following relation

$$\int_0^\infty x^2 e^{-\alpha x^2} dx = \frac{\pi^{1/2}}{4\alpha^{3/2}} \qquad\qquad (B1.17)$$

Since the relation $1/2mv^2 = \varepsilon$ is satisfied, the distribution function for the kinetic energy ε is also derived from (B1.16). The change of variables must be done in the integral system of the distribution. That is

$$mvdv = d\varepsilon \rightarrow dv = \frac{1}{\sqrt{2m}} \frac{d\varepsilon}{\sqrt{\varepsilon}} \qquad\qquad (B1.18)$$

By rewriting (B1.16) with use of (B1.18), the energy distribution function is obtained as a function of kinetic energy.

$$f(\varepsilon) = \frac{2}{\sqrt{\pi}T^{3/2}} \sqrt{\varepsilon} \, exp\left(-\frac{\varepsilon}{T}\right) \qquad\qquad (B1.19)$$

Note that, as is well known, the number of states increases proportionally to $\sqrt{\varepsilon}$ for free electrons in plasma or solid.

B-2 Bose-Einstein Distribution and Planck Distribution

Particles with spin integer or zero are allowed to stay as many as in one quantum state. The distribution function at this time can be easily obtained as follows. (B1.9) is the probability that particles of quantum state i exist. It is enough to add the probability that particles 1, 2, and 3, exits at the same energy state. By use of the probability

$$x_i = exp\left(\frac{\mu - E_i}{T}\right) \tag{B2.1}$$

The probability in this case is

$$p(x_i) = x_i + x_i^2 + x_i^3 + \ldots\ldots$$
$$= \frac{x_i}{1 - x_i} = \frac{1}{1 - exp\left(\frac{E_i - \mu}{T}\right)} \tag{B2.2}$$

Here, μ can be regarded as a normalized constant determined from particle density.

Planck Distribution

The energy distribution of the radiation field in thermal equilibrium with the substance at the temperature T is Planck distribution. Photon is a Bose particle of spin 1. The number density of photons of energy hν can be described as follows with use of (B2.2).

$$\rho(\nu) = \frac{8\pi}{c^3}\nu^2 \frac{1}{e^{\frac{h\nu}{T}} - 1} = \frac{8\pi}{c^3} \frac{\nu^2 e^{\frac{-h\nu}{T}}}{1 - e^{\frac{-h\nu}{T}}} \tag{B2.3}$$

In order to derive (B2.3), we first need to calculate the number of states of photons with energy hν.. Let us assume that the radiation field is in thermal equilibrium in a square cavity of its length L. The photons, which are electromagnetic waves, are quantized so that the electric field has a node at the boundary. Then the wavenumber of allowed photon is calculated simply

$$k_x = \frac{\pi n}{L}, \quad n = 0, 1, 2, \cdots \tag{B2.4}$$

The wavenumbers should be quantized. By applying this relation also in the y and z directions, we can see that the number of state is a function of only the absolute value k of the wavenumber. Calculating the volume of photons (k, k + dk) in k space and set it as g (k)dk, we obtain

$$g(k)dk = \frac{1}{V}\left(\frac{L}{\pi}\right)^3 \times \frac{\pi}{2}k^2 dk = \frac{k^2 dk}{2\pi^2} \tag{B2.5}$$

where V is the volume of system and $V = L^3$. Furthermore, since electromagnetic waves are transverse waves and the degree of freedom of polarization direction is 2 which should be multiplied to (B2.5). Using the frequency ν of photons instead of wavenumber,

$$k = \frac{2\pi\nu}{c} \tag{B2.6}$$

Then, (B2.5) becomes

$$g(\nu)d\nu = \frac{8\pi\nu^2 d\nu}{c^3} \tag{B2.7}$$

There was a classical theory of Rayleigh-Jeans until Planck distribution was found. They considered the photons in the cavity as having an energy of T as an average per photon from the energy equilibrium distribution and the energy distribution of photons was considered to be the value multiplied by T to (B2.7). However, it is obvious that it diverges in the area of large ν.

The probability of having energy E_i is

$$P_i = \frac{e^{\frac{-E_i}{k_B T}}}{\sum_i e^{\frac{-E_i}{k_B T}}} \tag{B2.8}$$

In the classical image, the photon field has not been determined that the state of ν has the energy of $h\nu$, and the photon field is quantized in the harmonic oscillator field of the classical frequency ν. Then, the energy level is shown with integer n,

$$E_i = \left(n + \frac{1}{2}\right)h\nu \tag{B2.9}$$

where we neglect the contribution from $n = 0$, since it is the energy determined by the uncertainty principle and cannot be observed. Among the small set of this frequency ν, the probability is found to be

$$P_n = \frac{\left(e^{-\frac{h\nu}{k_B T}}\right)^n}{\sum_{n=1}^{\infty} \left(e^{-\frac{h\nu}{k_B T}}\right)^n} = \left(e^{-\frac{h\nu}{k_B T}}\right)^n \left(1 - e^{-\frac{h\nu}{k_B T}}\right) \tag{B2.10}$$

And the average energy of photons of frequency ν is

$$\bar{\varepsilon} = \sum_{n=1}^{\infty} P_n n h\nu = \frac{h\nu}{e^{\frac{h\nu}{k_B T}} - 1} \tag{B2.11}$$

By multiplying (B2.11) with (B2.7), the photon number density between frequencies $(\nu, \nu + d\nu)$ is obtained to be

$$\rho(\nu)d\nu = \frac{8\pi}{c^3}\nu^2 \frac{1}{e^{\frac{h\nu}{T}} - 1} d\nu \tag{B2.12}$$
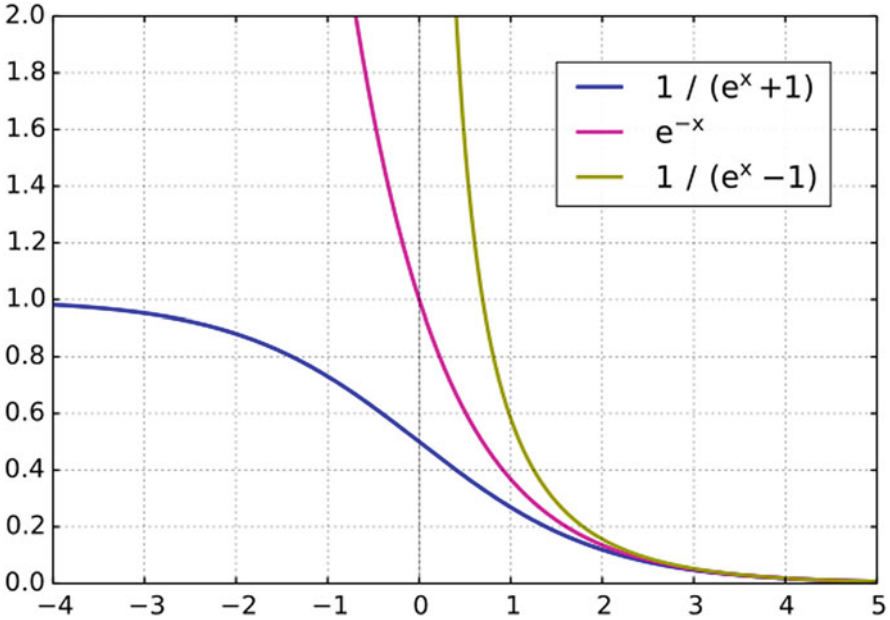
(B2.12) is the Planck radiation distribution.

Fig. B.1 Bose-Einstein, (gold) Boltzmann, (red) and Fermi-Dirac (blue) distributions ($\mu = 0$)

B-3 Fermi-Dirac Distribution

Only one particle can exist in the same quantum state for spin-half particles; they are for example, electrons, protons, and neutrons. It is due to Pauli's exclusion principle. Even in plasma, the density becomes high enough, such as inside the white dwarf, the free electrons degenerate. The electrons in accelerating fuel should be controlled degenerate in laser fusion. In such degenerate plasma, free electrons have average energy of Fermi energy although the temperature is relatively low. Let's obtain such Fermi-Dirac distribution in a simple way.

The idea is the same as in the case of the Bose-Einstein distribution, but in the state of energy E_i only one electron can exist. Since the probability that n particles exist is proportional to x_i^n, the probability of existence in the quantum state $|i\rangle$ is obtained as follows using (B2.1) where the probability in the case of no particle and one particle at the state should be denominator

$$p(x_i) = \frac{x_i}{1 + x_i} \tag{B3.1}$$

(B3.1) can be rewritten to the Fermi-Dirac distribution

$$p(E_i) = \frac{1}{1 + exp\left(\frac{E_i - \mu}{T}\right)} \tag{B3.2}$$

The three distribution functions are plotted for $\mu = 0$ in Fig. B.1.

Fermi Energy

Inside metals free electrons are running around even at a relatively low temperature. Fermi particles such as electrons with $T = 0$ and density n are distributed in the form of a step function in Fig. B.1. The maximum energy is called Fermi energy E_F. Derive the Fermi energy E_F.

   Apply the calculation of photons (B2.5) to electrons waves, assume $T = 0$, and the wavenumber space is filled up to k_F. Since the degree of freedom of the electron's spin is 2, the number of electrons of the Fermi sphere is

$$n = 2 \int_0^{k_F} g(k)dk = \frac{1}{3\pi^2} k_F^3 \tag{B3.3}$$

Using this k_F, Fermi energy is

White Dwarf Stars in M4   HST · WFPC2
PRC95-32 · ST ScI OPO · August 28, 1995 · H. Bond (ST ScI), NASA
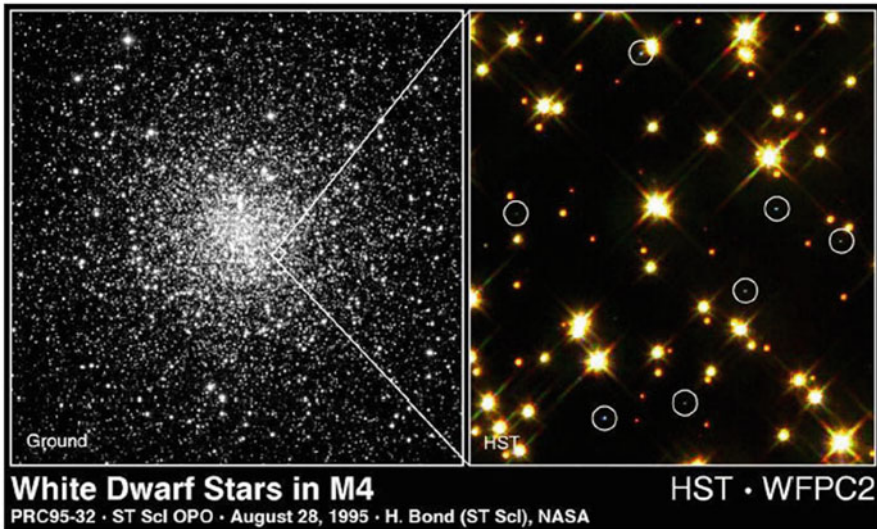
Fig. B.2 Observation image of an old galaxy and several white dwarfs are seen in the stretched view (in all circles). Image by HST, NASA

$$E_F = \frac{(\hbar k_F)^2}{2m} = \frac{\hbar^2}{2m}\left(3\pi^2 n\right)^{2/3}$$

$$E_F = 3.3 \times 10^{-15}\left(n\left[cm^{-3}\right]\right)^{2/3}[eV] \tag{B3.4}$$

The average energy of Fermi particles is calculated as

$$\langle E_F \rangle = \frac{2\int_0^{k_F}\frac{\hbar^2}{2m}k^2 g(k)dk}{n} = \frac{3}{5}E_F \tag{B3.5}$$

The typical values of Fermi energy are as follows.

1. **Metal:** The number density of metal free electrons is given with $n = 10^{22}$ to ^{23} [cm^{-3}] in the solid state. (B3.4) gives

$$E_F = 2 \sim 10\ eV \tag{B3.6}$$

2. **White dwarf:** A white dwarf is a star with about solar mass and sustained by balance between the degenerate pressure of electrons and self-gravity. The electrons are almost completely degenerate. It is a compact star of the size of the Earth. It has been observed in an old galaxy as shown in Fig. B.2. Several white dwarfs are shown in a stretched view on the right and they are encircled by white circles. Since a solar mass is in the radius of the Earth, a typical electron density is $n = 10^{30}$ [cm^{-3}] (about $\rho = 10^6$ [g/cm^3]). Fermi energy at such a high density is

$$E_F \approx 3 \times 10^5\ eV = 0.3\ MeV \tag{B3.7}$$

3. **Nucleus:** The inverse of the volume of a proton is $n = 10^{37}$ [cm^{-3}], and the size of the nucleus is decided by balancing of the degenerate pressure of the nucleon and the strong force There. Therefore, using this density and the mass of protons, Fermi energy is

$$E_F \approx 3 \times 10^7\ eV = 30\ MeV \tag{B3.8}$$

4. **Neutron star:** A neutron star is a compact star left at the center, when a massive star gravitationally collapses and type II supernova explosion occurs. It is a compact object whose radius is about 10 km and mass is about the solar mass. A typical density is 2×10^{14} g/cm^3, namely the size of cubic sugar is about the total weight of 7 billion people in the world. This number density is $n = 10^{38}$ [cm^{-3}], and its Fermi energy is

$$E_F \approx 1 \times 10^9 \; eV = 1 GeV \tag{B3.9}$$

Consider the case of a binary star where a white dwarf forms a binary star with the main sequence star. The mass of the white dwarfs increases with time due to mass accretion from the surface of the companion star. As already seen above, Fermi energy (B3.7) is about the rest mass energy of an electron; therefore, it is necessary to consider the relativistic effect as the white dwarf mass increases. The gravitational force can be supported by non-relativistic electron degeneration pressure. However, it is necessary to consider the fact that the pressure is the momentum flux density per unit area

$$P_F = npv \tag{B3.10}$$

where p is the average momentum of electrons, v is the average velocity of electron. In non-relativistic cases

$$p = \sqrt{2mE_F}, \quad v = p/m$$
$$P_F \; \alpha \; n^{5/3} \tag{B3.11}$$
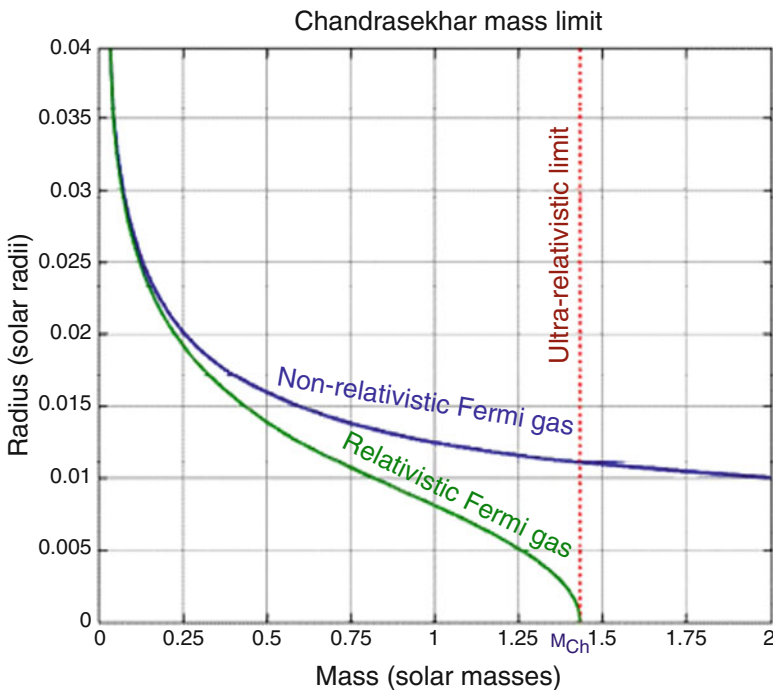
Fig. B.3 The radius of white dwarfs with different mass. Non-relativistic case gives physical solutions, while relativistic Fermi pressure cannot sustain the gravity for the case with more than Chandrasekhar mass

And the density-dependency is strong. This 5/3 power law prevents the collapse due to self-gravity. However, as the mass increases in time, the density further increases and the electrons become relativistic degenerate. In this case, since the speed of the particle flux is limited by the speed of light, the pressure dependence on the density is weakened. In other words, the star becomes "soft" at the dense central region, since the relativistic Fermi pressure is

$$p = \sqrt{2mE_F}, \quad v = c$$
$$P_F \ \alpha \ n^{4/3} \tag{B3.12}$$

It is found that the hydrostatic solution of a white dwarf is not obtained in the relativistic region where the pressure depends on the power of 4/3 of density. Namely, gravitational collapse should be taken place near the central point as mass increases.

When the gravitational collapse happens near the center of the star, the main component of the star, carbon and oxygen, starts thermonuclear reaction. The produced thermal energy explodes the white dwarf. Such phenomenon is the **Type Ia supernova explosion**. The explosion is believed to occur when the mass exceeds the critical mass (this is called **Chandrasekhar critical mass**, 1.26 times the solar mass with a simple calculation, which is estimated to be about 1.44 times recently). In Fig. B.3, the radius of a white dwarf obtained with the equation of state with no relativistic effect and relativistic effect is plotted as a function of the total mass of the white dwarf. It is clear that taking account of the relativistic effect, there is no steady state solution of such white dwarf. Therefore, it is considered that the mass at the time of explosion is constant and the luminosity from Type Ia supernovae is also equal. Due to such reason, it can be used as the standard light source of the universe.

References

1. C.F. Fischer, T. Brage, P. Jonsson, *Computational Atomic Structure* (Institute of Physics, 1997)
2. R.D. Cowan, *The Theory of Atomic Structure and Spectra* (University of California, Berkeley, 1981)
3. D. Salzmann, *Atomic Physics in Hot Plasmas* (Oxford University Press, 1998)
4. T. Fujimoto, *Plasma Spectroscopy* (Oxford Science Publication, 2004); H. R. Griem, *Principle of Plasma Spectroscopy*, (Cambridge University Press, 1997)
5. Y. Ralchenko, *Modern Methods in Collisional-Radiative Modeling of Plasmas* (Springer, 2016)
6. F.J. Roger, Analytic electron-ion effective potentials for Z≤55. Phys. Rev. A **25**, 1008 (1981); F. J. Roger et al., Parametric potential method for generating atomic data, Phys. Rev. A 38, 5007 (1988)
7. C.A. Iglesias, Iron-group opacities for B stars. NMRAS **450**, 2 (2015)
8. A. Bar-Shalom, M. Krapisch, J. Oreg, HULLAC, an integrated computer package for atomic processes in plasmas. J. Quant. Spec. Rad. Transfer **71**, 169 (2001)
9. B.H. Branden, C.J. Joachain, *Quantum Mechanics* (Pearson Education, 2000). Chap. 13
10. H.A. Bethe, E.E. Salpeter, *Quantum Mechanics of One-and Two-Electron Atoms* (Dover Publication, 1957)

11. B. Povh et al., *Particles and Nuclei* (Springer, 2008)
12. Ya B. Zel'dovich, Yu P. Raiser, *Physics of Shock Waves and High-Temperature Hydrodynamic Phenomena*", Vols. 1 & 2 (Academic Press, New York, 1966 and 67)
13. I.C.E. Turce, J.B. Dance, *X-rays from Laser Plasmas* (Wiley, 1998)
14. H. Shiwaku et al., Published: July 31, 2018 https://doi.org/10.1371/journal.pone.0199955 Fig. 3 Corona of the Sun.
15. A. Dalgarno, D. Layzer (eds.), *Spectroscopy of Astrophysical Plasmas* (Cambridge University Press, 1987)
16. C.J. Fontes, J. Colgan, J. Abdallah Jr, *Self-consistent Large-Scale Collisional-Radiative Modeling,* Chap. 2 at p. 17 in Ref. [5].
17. H.-K. Chung, S.B. Hansen and H.A. Scott, *Generalized Collisional Radiative Model Using Screened Hydrogenic Levels*. Chap. 3 in Ref. [5]; H. K. Chung et al., High Energy Density Physics 1, 3 (2005)
18. C.H. Towns, *How the Laser Happened: Adventures of a Scientist* (Oxford University Press, 1999)
19. N. Nakai et al., Extremely-high-velocity H_2O maser emission in the galaxy NGC4258. Nature **361**, 45 (1993); M. Miyoshi et al., Collisional pumping of SiO masers in evolved stars, Nature 371, 395 (1994)
20. S. Johansson, V.S. Letokhov, Radiative cycle with stimulated emission from atoms and ions in an astrophysical plasma. Phys. Rev. Lett. **90**, 011101 (2003)
21. M.A. Guerrero, X-ray shaping of planetary nebulae. Galaxies MDPI **6**(3), 98 (2018). https://doi.org/10.3390/galaxies6030098
22. European X-FEL, https://www.xfel.eu
23. Z. Jurek et al., XMDYN and XATOM: Versatile simulation tools for quantitative modeling of X-ray free-electron laser induced dynamics of matter. J. Appl. Crystallogr. **49**, 1048–1056 (2016)
24. L. Sabbatucci, F. Salvat, Theory and calculation of the atomic photo effect. Radiation. Phys. Chem. **121**, 122 (2016)
25. H. Fukuzawa et al., Deep inner-Shell multiphoton ionization by intense X-ray free-electron laser pulses. Phys. Rev. Lett. **110**, 173005 (2013)
26. N. Rohringer et al., Atomic inner-shell X-ray laser at 1.46 nano-metres pumped by an X-ray free-electron laser. Nature **481**, 488 (2012)
27. H.R. Griem, Plasma spectroscopy in inertial confinement fusion and soft x-ray laser research. Phys. Fluids B **4**, 2346 (1992)
28. J. Abdallah, J. Colgan, N. Rohringer, Time-dependent calculations of electron energy distribution functions for neon gas in the presence of intense XFEL radiation. J. Phys. B Atomic Mol. Phys. **46**, 235004 (2013)
29. J. Abdallah, J. Colgan, Time-dependent calculations of electron energy distribution functions for cold argon gas in the presence of intense black-body radiation. J. Phys. B Atomic Mol. Phys. **45**, 035701 (2012)
30. A. Mizuta, Formation of pillars at the boundaries between H II regions and molecular clouds. Astrophys. J. **647**, 1151–1158 (2006)
31. F.D. Seward, P.A. Chales, *Exploring the X-ray Universe*, 2nd edn. (Cambridge University Press, 2010) Chap. 11 X-ray binaries
32. T. Kallman et al., Photoionization emission models for the Cyg X-3 X-ray Spectrum. Astrophys. J. **874**, 51 (2019)
33. S. Fujioka et al., X-ray astronomy in the laboratory with a miniature compact object produced by laser-driven implosion. Nat. Phys. **5**, 821 (2009)
34. D. Porquet et al., Line ratios for helium-like ions: Applications to collision-dominated plasmas. A&A **376**, 1113 (2001)
35. Page 277 in Ref. [31]; B. Czerny et al., Universal spectral shape of high accretion rate AGN. A&A **412**, 317 (2003); J. Mao et al., Anatomy of the AGN in NGC 5548 IX. Photoionized emission features in the soft X-ray spectra, A&A 612, A18 (2018)

36. D. Saltzmann, H. Takabe, Can X-ray lasers exist in astrophysical objects? Publ. Astron. Soc. Japan **63**, 727 (2011)
37. J. Lindl et al., Review of the National Ignition Campaign 2009–2012. Phys. Plasmas. **21**, 020501 (2014)
38. M.K. Matzen, Z pinches as intense x-ray sources for high-energy density physics applications. Phys. Plasmas. **4**, 1519 (1997)
39. J.E. Baily et al., J. Quant. Spec. Rad. Transfer **71**, 157 (2001)
40. H. Takabe, Laboratory astrophysics with intense lasers, Prog. Their. Phys. Suppl., 143, 2020 (2001); Y. Morita et al., J. Quant. Spec. Rad. Transfer 71, 517 (2001)
41. R.C. Mancini et al., Accretion disk dynamics, photoionized plasmas, and stellar opacities. Phys. Plasmas. **16**, 041001 (2009)
42. G.A. Rochau et al., ZAPP: The Z astrophysical plasma properties collaboration. Phys. Plasmas **21**, 056308 (2014)
43. M.E. Foord et al., Charge-state distribution and Doppler effect in an expanding photoionized plasma. Phys. Rev. Lett. **93**, 055002 (2004)
44. G.P. Loisel et al., Benchmark experiment for photoionized plasma emission from accretion-powered X-ray sources. Phys. Rev. Lett. **119**, 075001 (2017)
45. F.-L. Wang et al., Calculation of Photoionized plasmas with a detailed-configuration-accounting atomic model. Astrophys. J. **706**(598) (2009)
46. E. Hill and S. Rose, Physics of Plasmas, 17, 10331 (2010)
47. Z. Wu et al., Time-dependent simulation of the spectrum from a photoionized Si plasma. HEDP **23**, 153 (2017)
48. R.C. Mancini et al., X-ray heating and electron temperature of laboratory photoionized plasmas. Phys. Rev. E **101**, 051201(R) (2020)

Chapter 6
Non-local Transport of Electrons in Plasmas

Abstract Since plasma is high temperature and the charge particles are running with high temperature, for example, at 1 keV, about the velocity of 10^9 (electron) and 2×10^7 (ion) [cm/s]. Since Coulomb mean-free-path is proportional to (*velocity*)^4, higher velocity component transfers its energy over a long distance without Coulomb collision. This is usually called as "non-local transport" and the traditional diffusion model in neutral gas cannot be applicable. In laser plasma, the locally heated electron thermal energy is transported into cold over-dense region non-locally. The best way to solve such problem is to solve Fokker-Planck equation, while it is time consuming and some theoretical models have been proposed and studied over the last four decades. The physics of such models are explained here and most recent model SNB is shown and compared to experiments. The difficulty of transport of charges particles such as electrons is how to include the effect of electrostatic field and magnetic field self-consistently.

6.1 Spitzer-Harm Diffusion Model

6.1.1 Model Equation for Diffusion

Consider a simple equation describing time evolution of temperature. Assume that the particles carry the energy of plasma proportional to the temperature T. The plasma particles, mainly electrons, are assumed to be in random walk over every time interval Δt. The probability of the displacement during the time interval Δx is given as the probability density $W(\Delta x, \Delta t)$. Then, the time evolution of the distribution of the temperature T is governed by

$$T(x,t) = \int_{-\infty}^{\infty} W(\Delta x, \Delta t) T(x - \Delta x, t - \Delta t) d(\Delta x) \qquad (6.1)$$

Note that for simplicity Δt is assumed constant.

Under the condition that the spatial variation of T is gentle enough, (6.1) can be approximated with Taylor expansion to reduce to the form.

$$T(x-\Delta x, t-\Delta t) = T(x,t) - \Delta x \frac{\partial T}{\partial x} + \frac{1}{2}(\Delta x)^2 \frac{\partial^2 T}{\partial x^2} + \cdots \qquad (6.2)$$

In (6.1), the **probability function** W(Δx, Δt) is normalized,

$$\int_{-\infty}^{\infty} W(\Delta x, \Delta t) d(\Delta x) = 1 \qquad (6.3)$$

It is also reasonable to assume that W(Δx, Δt) is an even function of Δx.

Inserting (6.2) to (6.1), the following diffusion equation is obtained.

$$\frac{\partial}{\partial t} T = \frac{\partial}{\partial x}\left(\chi \frac{\partial}{\partial x} T\right),$$

$$\chi = \frac{1}{2\Delta t} \int_{-\infty}^{\infty} W(\Delta x)(\Delta x)^2 d(\Delta x) \qquad (6.4)$$

$$\chi = \frac{1}{2} v \Delta x \Rightarrow \chi \approx \frac{\left\langle (\Delta x)^2 \right\rangle}{\Delta t}$$

where $< >$ represents the ensemble average and we assumed that the space integral of T should be conserved.

$$\int_{-\infty}^{\infty} T(x,t) dx = Q : const. \qquad (6.5)$$

This diffusion approximation is valid only when the following condition is satisfied.

$$\left|\frac{\Delta x}{T} \frac{\partial T}{\partial x}\right| \equiv \frac{\Delta x}{L_T} < < 1 \qquad (6.6)$$

where L_T is the scale length of the gradient of T.

Let us consider that (6.4) is the energy diffusion by electron motion in plasma, the heat flux by the electron thermal motion should be in the form.

$$q_e = \frac{3}{2} n_e \chi(T_e) \nabla T_e \approx n_e v_e \lambda_e \nabla T_e = q_{FS} \frac{\lambda_e}{L_T} \qquad (6.7)$$

where $v_e = (T_e/m)^{1/2}$, λ_e is the electron average mean-free-path, and q_{FS} is the **free streaming heat flux** defined by

$$q_{FS} = n_e v_e T_e \qquad (6.8)$$

The free-streaming heat flux is the maximum of the heat flux by all electron of Maxwell distribution in one–direction. If we integrate the heat flux it is 0.6 times the free streaming flux.

In a historical paper by Spitzer-Harm [1], the mathematical formula of the electron heat conduction in fully ionized plasma was derived by starting with Fokker-Planck equation as we see soon. Its mathematical form is derived from the above simple model. Since the mean-free-path has the following relation,

$$\lambda_e \propto \frac{T_e^2}{n_e} \tag{6.9}$$

The **Spitzer-Harm heat flux** q_{SH} is given from (6.4).

$$q_e \equiv q_{SH} = -\kappa_0 T_e^{5/2} \nabla T_e \tag{6.10}$$

where κ_0 is a constant. This heat flux is already shown in (2.109). The heat flux of (6.10) has been widely used to describe the electron energy transport.

6.1.2   Flux Limit

In the early time 1970s of laser plasma research, it was found that the flux (6.7) is limited by the maximum much less than (6.8) and so-called **flux limiter** is proposed an ad hock method to be installed in simulation codes [2]. The flux-limiter was widely used in hydrodynamic simulations, because the temperature of the laser heated region becomes low without the flux-limiter to give higher absorption rate of laser via classical absorption as suggested in Chap. 2 in Volume 1. In the case where the flux-limiter is adopted in the simulation code, the heat flux propagating to higher density region is limited and the electron temperature in the absorption region becomes higher, consequently the absorption rate is suppressed.

In laser produced plasmas, for example, it has been well recognized that a simple diffusive expression of electron transport given in (2.109) cannot be applicable. The phenomenon has been called **flux-limit**. In physics integrated computer simulation based on hydrodynamic description the flux-limiter f was artificially installed in order to avoid higher absorption rate and hydrodynamic efficiency.

$$q_L = f q_{FS}, \tag{6.11}$$

where f was evaluated to be 0.03–0.1 according to the difference of experiments. In hydrodynamic simulations, the following hear flus was modeled.

Fig. 6.1 Bremsstrahlung
x-ray emission spectrum
obtained in a laser produced
plasma experiment (solid
circles). The time integrated
spectrum has been
compared to hydrodynamic
simulation results with
different flux limiters.
Spitzer-Harm diffusion
model ($f = \infty$) is far from
the experimental spectrum,
while with smaller flux
limiter the data can be
explained computationally.
Strong flux limitation was
suggested in the early time
from such comparison.
Reprint with permission
from Ref. [2]. Copyright
1998 by American Physical
Society
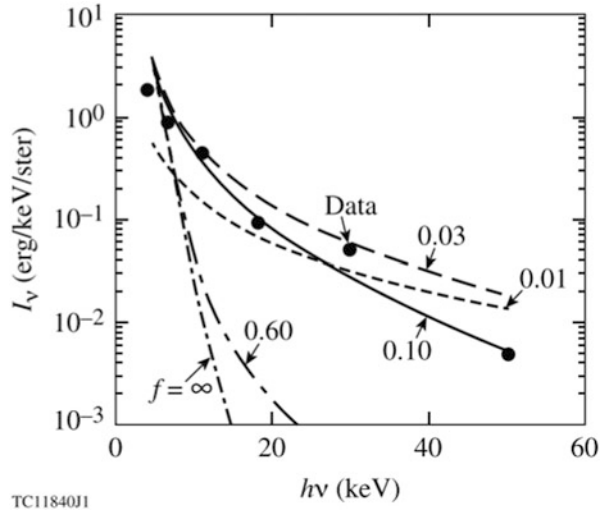
$$q_{eff} = min(q_{FL}, q_{SH}) \tag{6.12}$$

or

$$q_{eff} = \frac{q_{SH} \cdot q_L}{q_{SH} + q_L}, \tag{6.13}$$

Then, the heat flow is small enough the **Spitzer-Harm diffusion** formula is used, but
it is designed to limited by the limited flux.

In Fig. 6.1, calculated Bremsstrahlung emission spectrum I_ν versus photon energy
$h\nu$ for different value of the flux limiter f is compared to the experimental data (solid
circles). It is clear that simulation without the flux limiter results very low temper-
ature in the Bremsstrahlung emission, while as the flux limiter increase hard x-ray
emission reproduced as shown in Fig. 6.1. It is too early to conclude that in the
experiment the flux is limited as $f = 0.01$–0.03. Such comparison of simulation to a
variety of experimental results, however, had required to improve the mathematical
model of the diffusion by electron heat conduction in high-intensity laser plasma
interacting plasmas.

6.1.3   Mathematical Derivation of Spitzer-Harm Diffusion

In order to know the reason for the flux limit and the limiting condition of the validity
of the diffusion approximation (6.10), let us repeat the mathematical process for
deriving the diffusion model for the electron heat conduction.

Mathematical derivation of **Spitzer's heat flux** can be done by starting with the following kinetic equation of Vlasov equation with **Krook collision operator**.

$$\frac{\partial}{\partial t}f + \mathbf{v} \cdot \nabla f - \frac{e}{m}\mathbf{E} \cdot \frac{\partial}{\partial v}f = -\nu_c(f - f_M) \tag{6.14}$$

where $\mathbf{E}$ is electrostatic field generated by charge separation due to electron motion by heat flux and f_M is local Maxwell distribution. The collision frequency ν_c is due to electron-ion and electron-electron collisions to be fixed so that they are derived by Fokker-Planck equation as a function of velocity as shown later.

In solving (6.14), space dependence is assumed one-dimensional in the x-direction and the velocity distribution function is assumed to consist of two terms; the isotropic component and the small anisotropic component.

$$f(x, v, \mu) = f_0(x, v) + \mu f_1(x, v) \tag{6.15}$$

$$\mu = cos\theta_v \tag{6.16}$$

where f_0 and f_1 are functions of only the absolute value of the velocity in $\mathbf{v}$-space. The angle dependence of the velocity space is assumed only by θ_v, velocity angle along the x-direction as shown in Fig. 6.2. Inserting (6.15) to (6.14) yields

$$\frac{\partial}{\partial x}[v\mu(f_0 + \mu f_1)] - \frac{e}{m}E\frac{\partial}{\partial v}[\mu(f_0 + \mu f_1)]$$
$$+ \frac{e}{m}E\frac{1 - \mu^2}{v}f_1 = -\frac{v}{\lambda_c}(f_0 - f_M + \mu f_1) \tag{6.17}$$

where $\lambda_c = v/\nu_c$ is an effective mean free path for electrons with the velocity v.

Fig. 6.2 Schematics of electron velocity distribution function to be modeled for Fokker-Planck equation, where non-uniformity of temperature is assumed to be in the x-direction and the velocity distribution is axially symmetric along the x-velocity axis. Space one-dimension and velocity space two-dimension are assumed
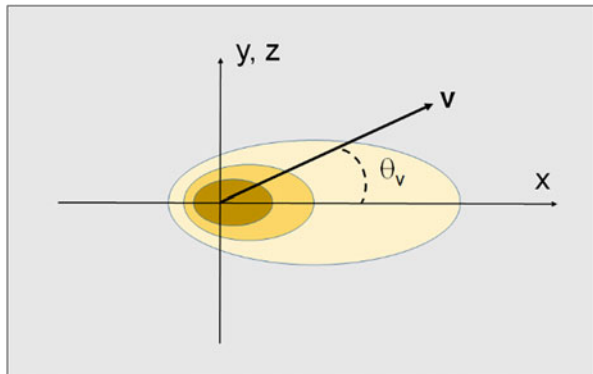
Taking the moment of velocity angle $\int_{-1}^{1} d\mu$ of (6.17), the first order distribution function is obtained as

$$
\begin{aligned}
f_1 &= -\lambda_c \left(\frac{\partial}{\partial x} - \frac{e}{m} \frac{E}{v} \frac{\partial}{\partial v} \right) f_M \\
&= -\frac{\lambda_c}{T_e} \left[eE + \frac{1}{2} \left(\frac{mv^2}{T_e} - 3 \right) \frac{\partial T_e}{\partial x} \right] f_M
\end{aligned}
\tag{6.18}
$$

where f_0 is assumed to be a local Maxwellian f_M and the density is assumed to be uniform.

The electron current density is defined as

$$
j_e = -e \int v_x f d^3 v = -\frac{4\pi e}{3} \int_0^\infty v^3 f_1 dv
\tag{6.19}
$$

Inserting (6.18) into (6.19), the current density is obtained in the form.

$$
j_e = \sigma E - \beta \frac{dT_e}{dx}
\tag{6.20}
$$

where σ is the **electron conductivity** and β is the coefficient of **thermal current**. Note that the coefficients σ and β are functions of the temperature. Once there is a current flow in one-dimensional system, charge separation takes place. It is better to assume that this charge separation is induces the return current to keep the current neutral condition. Requiring the current neutral condition, the electric field is given in the form.

$$
E = \frac{\beta}{\sigma} \frac{dT_e}{dx}
\tag{6.21}
$$

The electron heat flux is calculated as follows.

$$
q_e = \frac{m}{2} \int v^2 v_x f d^3 v = \frac{4\pi m}{6} \int_0^\infty v^5 f_1 dv
\tag{6.22}
$$

Inserting (6.18) into (6.22) and eliminating E with (6.21), the heat flux (6.22) can be obtained in the form.

$$
q_e = \gamma j_e - K_e \frac{dT_e}{dx}
\tag{6.23}
$$

where γ is a constant and K_e is the electron heat conduction coefficient. Requiring the current neutral condition, the electron heat flux is given in the form:

$$
q_e = -K_e \nabla T_e
\tag{6.24}
$$

In the precise calculation including electron and ion contribution to the effective mean-free path in (6.18), the heat flux derived by Spitzer-Harm has the following form [3].

$$\boldsymbol{q}_{SH} = -\frac{128(Z + 0.24)}{3\pi(Z + 4.2)} \lambda_{SH} n_e v_e \nabla T_e \tag{6.25}$$

where λ_{SH} is the Spitzer-Harm mean free path,

$$\lambda_{SH} = \frac{3}{4\sqrt{2\pi}Z} \frac{1}{n_e b_0^2 ln\Lambda} \tag{6.26}$$

where the Coulomb impact radius defined in Chap. 2 in Volume 1 is given as b_0 satisfying the relation.

$$\frac{e^2}{4\pi\varepsilon_0 b_0} = mv_e^2 = T_e \tag{6.27}$$

In (6.25), the Z is the charge state for partially ionized plasma and the Z-dependence of the coefficient stems from the different ratio between the electron and ion contribution to Coulomb scattering. It is useful to express the form (6.25) as

$$q_{SH} = -a_0 \frac{\lambda_{SH}}{L_T} q_{FS} \tag{6.28}$$

where a_0 is the coefficient in (6.25) and q_{FS} is called **free-streaming flux** defined as

$$q_{FS} = n_e T_e v_e \tag{6.29}$$

This free-streaming energy flux is frequently used as normalization value for electron heat flux. This is almost the maximum flux by the half of Maxwell distribution. So, any model for heat flux cannot be larger than q_{FS}. This indicates that the mean-free-path should be much shorter than the temperature gradient scale L_T defined in (6.6).

It is useful to note that the maximum electron heat flux is in general much smaller than the free-streaming flux for example as seen in Fig. 6.1. This is because the strong heat flux induces the electrostatic field inhibiting the large heat flow goes to one direction. The charge separation is very important to reduce the heat flux compared to the free-streaming value. This is not the case for charge neutral particles like photons as will be explained later in this Chapter. In the case of photon emission, it is easily seen near the plasma boundary that almost all photons flow freely in one direction.

6.1.4   Breakdown of Diffusion Approximation

We have to be careful that Spitzer-Harm diffusion formula of the electron heat flux derived in (6.24) has been obtained in (6.18) with the assumption that

$$f_0 \gg |f_1| \tag{6.30}$$

Inserting (6.21) into (6.18) it is possible directly evaluate the condition (6.30) for f_0 being Maxwellian.

$$\frac{f_1}{f_M} = \frac{\lambda_c(v_e)}{L_T}\left(\frac{v}{v_e}\right)^4\left[\left(\frac{v}{\sqrt{2}v_e}\right)^2 - 4\right] \tag{6.31}$$

where L_T is the gradient scale defined in (6.6).

It is clear that the distribution function becomes negative for the case of $|f_1/f_0| > 1$. The velocity dependent heat flux $v^5 f_1$ in (6.22) is found to have its maximum at $v = 3.4 v_e$. Since the heat flux is the integral of large power of the velocity, the maximum heat flux is mainly due to the electrons with the velocity more than the thermal velocity. The effective mean free path of such electrons is $(3.4)^4 \sim 10^2$ time longer than the SH mean free path in (6.26). Inserting $v = 3.4 v_e$ to (6.31), it is found that the perturbation of the distribution become larger than the Maxwell distribution $|f_1/f_0| > 1$ at the value of the mean free path.

$$\frac{\lambda_c(v_e)}{L_T} \cong 4 \times 10^{-3} \tag{6.32}$$

This means that the SH heat conduction model cannot be applicable for the temerature gradient shorter than that in (6.32). This is usual case of laser produced plasma, where laser heating energy is carried by heated electrons from near the cut-off density to the solid density surface. It is essential to model the heat flux in another way.

6.2   Vlasov-Fokker-Planck Equation

6.2.1   Boltzmann Equation

Boltzmann equation is a kinetic equation of particles under collisional process. It is well known that in case of highly ionized plasma Coulomb collision between ions and electrons can be approximated by Fokker-Planck differential form. It is better, however, to start from Boltzmann equation to show what approximation are used to

derive Fokker-Planck equation to study the electron energy transport in laser pro-
duced plasma. See Appendix-C.

Boltzmann equation is non-linear integral-differential equation and time-
consuming computation is required to solve numerically. **Boltzmann equation** for
Coulomb collision system in plasma is formally given to be:

$$\frac{\partial f}{\partial t} + \boldsymbol{v} \cdot \frac{\partial f}{\partial \boldsymbol{r}} - \frac{e}{m} \boldsymbol{E} \cdot \frac{\partial}{\partial \boldsymbol{v}} f = \left(\frac{df}{dt}\right)_{coll} = \left.\frac{df}{dt}\right|_{ei} + \left.\frac{df}{dt}\right|_{ee} \tag{6.33}$$

In RHS in (6.33), the collision terms of electrons with ions and with electrons are
shown in the first and second terms, respectively.

Derive the collision term with assumption that only binary collision is enough to
derive the collision term. Then, assume that binary collision changes the velocities of
two particles before and after the collision. Consider the collision term of the
electron distribution function with velocity $\boldsymbol{v}$ changes its velocity to $\boldsymbol{v}$' by the
collision of electron or ion with velocity $\boldsymbol{v}_s$ changing it to $\boldsymbol{v}_s$' after the collision. In
what follows the subscribe "s" represents the both cases of collision with ion and
electron.

$$\{\boldsymbol{v}, \boldsymbol{v}_s\} \rightarrow \{\boldsymbol{v}', \boldsymbol{v}'_s\} \tag{6.34}$$

The differential cross section of such binary collision $\sigma_s(\boldsymbol{\Omega})$ is given as the function
of the relative orientation of the vectors $\boldsymbol{v}$-$\boldsymbol{v}_s$ and $\boldsymbol{v}'$-$\boldsymbol{v}_s'$, the unit vector of which is
defined as $\boldsymbol{\Omega}$. Of course, the functional form, σ_s depends on the collision opponent is
an electron or an ion. Then, it is easy to understand that the collision term is given in
the form.

$$\left(\frac{df}{dt}\right)_{coll} = \sum_{s=i,e} \int d\boldsymbol{\Omega} \int d\boldsymbol{v}_s \sigma_s(\boldsymbol{\Omega}) |\boldsymbol{v} - \boldsymbol{v}_s| \left(f'f'_s - ff_s\right) \tag{6.35}$$

In (6.35),

$$\begin{aligned} f &\equiv f(\boldsymbol{r}, \boldsymbol{v}, t), \quad f' \equiv f(\boldsymbol{r}, \boldsymbol{v}', t) \\ f_s &\equiv f_s(\boldsymbol{r}, \boldsymbol{v}_s, t), \quad f_s{}' \equiv f_s(\boldsymbol{r}, \boldsymbol{v}'_s, t) \end{aligned} \tag{6.36}$$

The collision term (6.33) gives the change of the distribution function f after the
collision with another or same particle with distribution f_s at the point $\boldsymbol{r}$ and time
t. The term f' f_s' represents the gain to $\boldsymbol{v}$ from $\boldsymbol{v}$' due to the collision with $\boldsymbol{v}_s$'. On the
other hand, the term ff_s represents the loss from $\boldsymbol{v}$ from $\boldsymbol{v}$· after the collision with a
particle with the velocity $\boldsymbol{v}_s$. Integrating by $\boldsymbol{v}_s$ provides all contribution from the
particle in plasma at ($\boldsymbol{r}$,t) position by the other electrons and ions. Since the integrand
should be the collision frequency, it is proportional to $\sigma_s(\boldsymbol{\Omega})|\boldsymbol{v} - \boldsymbol{v}_s|$. The scattering
cross section is given by Rutherford scattering formula.

6.2.2 Taylor Expansion of Collision Term

In the Coulomb scattering, the velocity change $|\Delta \mathbf{v}|$ by one binary collision is sufficiently smaller than the velocity $|\mathbf{v}|$. In such case, Boltzmann equation of (6.33) can be expanded with the small velocity change. When the probability density of the small change of $\Delta \mathbf{v}$ due to the scattering of the distribution of $\mathbf{v}$ is $W(\mathbf{v}, \Delta \mathbf{v})$, the following relation holds

$$f(\mathbf{v}, \mathbf{r}, t + \Delta t) = \int f(\mathbf{v} - \Delta \mathbf{v}, \mathbf{r}, t) W(\mathbf{v} - \Delta \mathbf{v}, \Delta \mathbf{v}) d(\Delta \mathbf{v}) \qquad (6.37)$$

It is important to note the physical difference of (6.1) and (6.33). In case of random walk in real space (6.1), the mean random step $<\Delta x>$ can be easily break the condition for approximation (6.6) and the breakdown of the diffusion approximation appears as in Spitzer-Harm model. However, the random scattering in the velocity space is always valid as long as Coulomb scattering is considered. So, it is expected that Taylor expansion of (6.37) is applicable even to the case with steep temperature gradients. This is because the velocity change in most of Coulomb scattering is due to small angle scattering.

In what follows, only the change of distribution function of electrons by the small angle scattering is formulated for simplicity. Assuming small angle scattering and considering that the distribution function change with short time interval Δt, (6.37) reduces to the Taylor expansion form to Δt and $\Delta \mathbf{v}$ in the form.

$$
\begin{aligned}
f(\mathbf{v}, \mathbf{r}, t + \Delta t) \; = \; \int f(\mathbf{v}, \mathbf{r}, t) W(\mathbf{v}, \Delta \mathbf{v}) - \Delta \mathbf{v} \cdot \frac{\partial}{\partial \mathbf{v}} [f(\mathbf{v}, \mathbf{r}, t) W(\mathbf{v}, \Delta \mathbf{v})] \\
+ \frac{1}{2} \sum_i \sum_k \Delta v_i \Delta v_k \frac{\partial^2}{\partial v_i \partial v_k} [f(\mathbf{v}, \mathbf{r}, t) W(\mathbf{v}, \Delta \mathbf{v})] \; d(\Delta \mathbf{v})
\end{aligned}
$$

$$(6.38)$$

From (6.38) the collision term in a differential form to Coulomb interacting system is obtained.

$$\left(\frac{df}{dt}\right)_{coll} = \frac{\partial}{\partial v_i} \left[\left\langle \frac{\Delta v_i}{\Delta t} \right\rangle f(\mathbf{v}, \mathbf{r}, t) \right] + \frac{1}{2} \sum_i \sum_k \frac{\partial^2}{\partial v_i \partial v_k} \left[\left\langle \frac{\Delta v_i \Delta v_k}{\Delta t} \right\rangle f(\mathbf{v}, \mathbf{r}, t) \right] \quad (6.39)$$

where $< \; >$ represents the ensemble average of the terms. In case of one-dimension in the real space, the velocity space can be approximated axial symmetric with the axis of the inhomogeneous direction as shown in Fig. 6.2. The velocity space is two-dimensional in the cylindrical coordinate system (v_r, θ_v). The characteristics of Fokker-Planck equation are as follows:

1. The distribution function never becomes negative,
2. The equation satisfies the conservation of particle, momentum, and energy locally.
3. It satisfies Boltzmann's H-theorem. Even starting from any distribution function, the final distribution function becomes Maxwellian in LTE condition.

6.2.3 Derivation of Fokker-Planck (FP) Equation

What Fokker-Planck (FP) equation says is that any random force in Brownian motion reduces to the combination of the friction term and diffusion term.

After a long algebra shown in [4, 5], FP equation is found to have the following form.

$$\left(\frac{\partial}{\partial t}f\right)_{coll} = -\Gamma\frac{\partial}{\partial v_k}\left(\frac{\partial H}{\partial v_k}f\right) + \frac{1}{2}\Gamma\frac{\partial^2}{\partial v_k\partial v_j}\left(\frac{\partial^2 G}{\partial v_k\partial v_j}f\right) \qquad (6.40)$$

where G is derived from Rutherford scattering cross section and H and G are given as

$$\Gamma = \frac{Z^2 e^4}{4\pi\varepsilon_0^2 m^2}\,ln\,\Lambda \qquad (6.41)$$

$$H(\mathbf{v}) = Z_s^2\left(\frac{m+m_s}{m_s}\right)\int\frac{f_s(\mathbf{v}_s)}{|\mathbf{v}-\mathbf{v}_s|}d\mathbf{v}_s \qquad (6.42)$$

$$G(\mathbf{v}) = Z_s^2\int f_s(\mathbf{v}_s)|\mathbf{v}-\mathbf{v}_s|d\mathbf{v}_s \qquad (6.43)$$

It is noted that the definition H and G are called the **Rosenbluth potentials** [6].

It is known that the first term of RHS in (6.40) is the dynamical friction and the second one is the diffusion term in the velocity space. The Fokker-Planck equation assumes only the scattering by the binary Coulomb collision, therefore, in the system of two kind of particles like fully-ionized ions and electrons, we have to solve the equation for electron distribution function changing in time by scattering due to electron-electron (e-e), electron-ion (e-i). It is noted that in the case of e-e scattering, (6.40) is a nonlinear equation to the distribution function.

6.2.4 Linearized FP Model

It is time consuming to solve exactly (6.40) at each time step in FP computer simulation. It is better to consider some approximation to make numerical method

much easier in solving (6.40). For the present problem of electron heat transport, the following two assumptions can be adopted.

1. In the collision with the ions, it is assumed that $m_i >> m_e$ and energy transfer between electron and ions is neglected. This means the ions are regarded to be particles at rest. Then, the ion collision contributes to only the momentum change and no energy change of scattered electrons.
2. The nonlinear term in calculation of H and G in (6.42) and (6.43) are assumed by replacing f_s is local Maxwell distribution. In addition, $|v - v_s|$ is replaced with $\mathbf{v}$ in the both definitions. This is valid because the electron heat transport is sensitive to the collision of large v component by the electron with lower energy.

The 1st and 2nd derivatives in velocity space (6.40) can be separated to the changes in the absolute value of v (energy) and the scattering to perpendicular direction without changing energy. The former is only due to electron-electron scattering and the latter is due to both. It is possible to separate them into two parts as shown below.

The scattering term can be given as

$$\left.\frac{df}{dt}\right|_{ei,ee} = \sum_{s=i,e} \frac{\partial}{\partial v_\perp}\left(D_s \frac{\partial}{\partial v_\perp}f\right) \tag{6.44}$$

$$\left.\frac{df}{dt}\right|_{ee} = \frac{\partial}{\partial v_\parallel}\left(F_e f + D_e \frac{\partial}{\partial v_\parallel}f\right) \tag{6.45}$$

In what follows, the distribution function is assume to be cylindrically symmetric in the velocity space along the x-direction, where the plasma parameters change in space locally in the x-direction.

By use of Taylor expansion with care of the fact that hear flux is due to high velocity component, while the collisions are mainly with electrons with relatively low velocity, the following approximated linear form of Fokker-Planck equation is obtained

$$\frac{\partial}{\partial t}f + v\mu\frac{\partial}{\partial x}f - \frac{e}{m}E\left(\mu\frac{\partial}{\partial v} + \frac{1-\mu^2}{v}\frac{\partial}{\partial \mu}\right)f$$
$$= \frac{v}{2\lambda_S(v)}\left\{\frac{\partial}{\partial \mu}(1-\mu^2)\frac{\partial}{\partial \mu}f\right\} + \frac{v^2}{\lambda_f(v)}\left(\frac{\partial}{\partial v}\frac{v_e^2}{v}\frac{\partial}{\partial v} + \frac{\partial}{\partial v}\right)f \tag{6.46}$$

The angle of the velocity space is replaced with a definition

$$\mu = \cos\theta \tag{6.47}$$

It is noted that the following formula was used in (6.46).

$$\frac{\partial}{\partial v_x} = \mu \frac{\partial}{\partial v} + (1 - \mu^2) v^{-1} \frac{\partial}{\partial \mu} \tag{6.48}$$

In the RHS of (6.46), the first term is the effective mean free path by scattering.

$$\lambda_S(v) = \frac{m^2 v^4}{4\pi n_e (Z+1) e^4 \, ln \Lambda} \tag{6.49}$$

This is due to the scattering of electrons by ions and background electrons. The second term is due to the frictional force among electrons.

$$\lambda_f(v) = \frac{m^2 v^4}{4\pi n_e e^4 \, ln \Lambda} \left[= (Z+1)\lambda_S(v)\right] \tag{6.50}$$

It is mathematically clear that the 1st term in RHS of (6.46) is diffusion in angular space without energy change, while the 2nd term is the change in v-space with change of energy. It is noted that the RHS of (6.46) disappears when the electron distribution function is a Maxwellian distribution with thermal velocity v_e. The second term in (6.46) is derived by assuming that the counter electrons are in local Maxwellian.

In order to check the validity of several heat conduction models, it has been done to solve directly the FP equation numerically as reference case. The property that the Legendre functions is the eigen function of 1st term of RHS of (6.46) has been well used. The distribution function is expanded by **Legendre polynomial** as follows:

$$f = \sum_{n=0}^{N} f_n(x, v, t) P_n(\mu) \tag{6.51}$$

Inserting (6.51) into (6.46) and using the following mathematical formula to Legendre function.

$$\mu P_n = \frac{1}{2n+1} \left[(n+1)P_{n+1} + nP_{n+1}\right]$$
$$(\mu^2 - 1)\frac{\partial}{\partial \mu} P_n = n(\mu P_n - P_{n-1}) \tag{6.52}$$
$$\frac{\partial}{\partial \mu}\left\{(1-\mu^2)\frac{\partial}{\partial \mu}P_n\right\} = -n(n+1)P_n$$

It is possible to make (6.46) as functions only proportional to Legendre function regarding the terms including μ. Comparing the term proportional to the same order of Legendre functions, the following coupled equations are obtained.

$$
\frac{\partial}{\partial t} f_n + v \frac{\partial}{\partial x} \left(\frac{n}{2n-1} f_{n-1} + \frac{n+1}{2n+3} f_{n+1} \right)
$$
$$
- \frac{e}{m} E \left[\frac{n}{n-1} \left(\frac{\partial f_{n-1}}{\partial v} - \frac{n-1}{v} f_{n-1} \right) + \frac{n+1}{2n+3} \left(\frac{\partial f_{n-1}}{\partial v} + (n+2) \frac{f_{n+1}}{v} \right) \right]
$$
$$
= - \frac{v}{2\lambda_S(v)} n(n+1) f_n + \frac{v^2}{\lambda_f(v)} \left(\frac{\partial}{\partial v} \frac{v_e^2}{v} \frac{\partial}{\partial v} + \frac{\partial}{\partial v} \right) f_n
$$

$$(6.53)$$

This can be numerically solved by coupling with Poisson equation.

$$
\varepsilon_0 \frac{dE}{dx} = 4\pi e n_e \left(\int f d^3 \mathbf{v} - 1 \right) \tag{6.54}
$$

FP equation shown in (6.53) looks like linear coupled equations for f_n ($n = 0 \sim n_{max}$), where n_{max} is the maximum number of n to be solved. However, the electrostatic field generated by the electron heat flux is given by the sum of all Legendre component f_n, consequently for example some iterative process is required to obtain at each time step consistently. In addition, very fast oscillation by plasma waves is also generated by charge separation. In order to weaken such oscillation effect, some idea is required in numerically solving (6.53) and (6.54).

FP Eq. (6.53) has been solved numerically with numerically reducing the plasma oscillation frequency [7]. The plasma is initially uniform in density and temperature. The temperature in the region around the one boundary is quickly heated to 4 times, and the time progress of heat flux and temperature have been calculated. The Legendre components up to $n = 8$ have been solved in (6.53). In addition, Poisson equation is solved with an artificial fraction r = .0011 as a factor in RHS in (6.54). Plots of temperature $<v^2>$ and heat flux $<v^2 v_x>$ as function s of space x at three different times are shown in Fig. 6.3. It is seen that the heat flux is maximum near the heated region and the heat flux propagates from the left to the right in time.

In Fig. 6.4, the calculated heat flux is plotted at two typical time with symbols (x) and (o) as functions of the local temperature gradient length L (=L_T) normalized by the local mean free path λ. The hear flux Q by FP calculation is normalized by the local free streaming flux $Q_f = q_{FS}$ defined by (6.8) in the vertical axis. In Fig. 6.4, the solid line is the relation of heat flux by SH model (6.24). It is found that the heat flux is saturated around 0.1 q_{FL} for $\lambda/L_T < 0.01$ in the FP calculation. In the next paper by Bell, he has carried out FP simulation for the density and temperature profile more realistic to the laser ablation plasma. He found the flux limitation of about f = 0.03 for $\lambda/L_T < 0.01$ [8].

It is noted that the flux limit factor in Fig. 6.1 seems to be f = 0.02–0.01 for the best fit to the experiment, but the flux limiter is an ad hoc parameter and a different limiter may happen depending on the plasma parameters. These fact means SH diffusion model is not acceptable even in a simple model for the sharp temperature gradient satisfying $\lambda/L_T < 0.01$, and it is required to derive another heat flux model easily installable into hydrodynamic simulation code. This will be discussed soon.
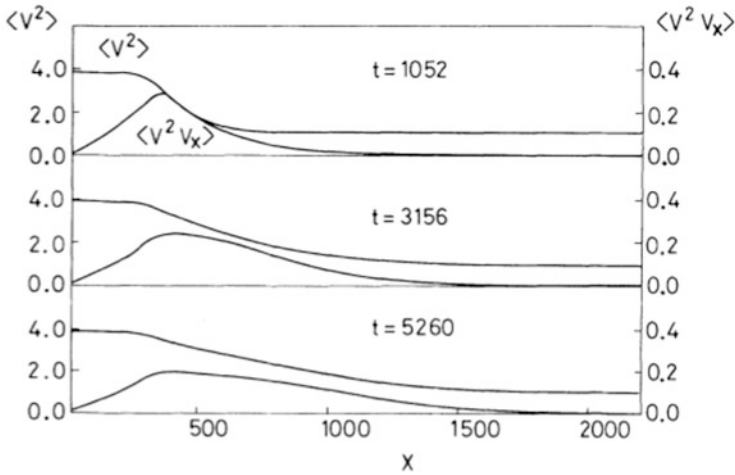
Fig. 6.3 Time evolution of an effective temperature $\langle v^2 \rangle$ and heat flux $\langle v^2 v_x \rangle$ obtained by a model simulation for Fokker-Planck equation of electron in constant density. At the left boundary, the effective temperature is kept four times of that at the right boundary. The heat wave propagates from the left to right. Reprint with permission from Ref. [7]. Copyright 1998 by American Physical Society
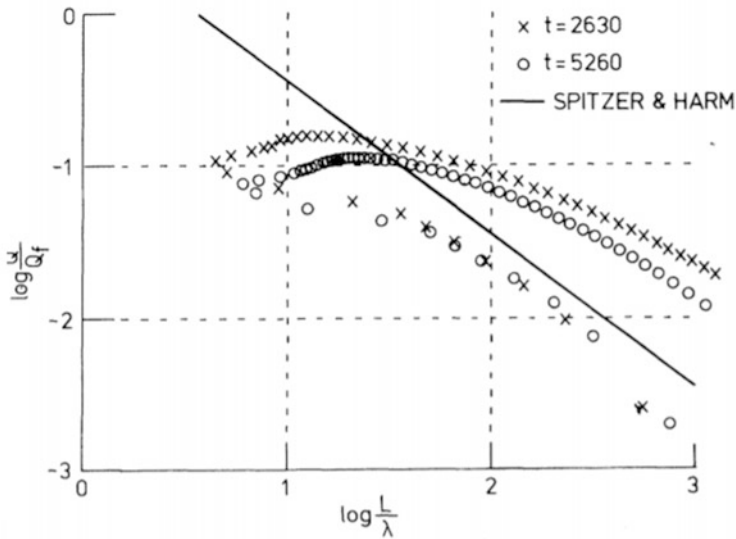

Fig. 6.4 The heat flux of Fokker-Planck simulation normalized with the free streaming flux is plotted at two different times as a function of measured temperature gradient length divided by the local electron mean-free-path. The solid line is the relation of Spitzer-Harm (SH) diffusion. The simulation data are higher than SH flux near the front of the heat flux, while it is automatically limited around f=0.1 to change to the reduced flux in the higher temperature region. This indicate that the local assumption of heat flux defined with the first derivative to space x is not valid. Reprint with permission from Ref. [7]. Copyright 1998 by American Physical Society
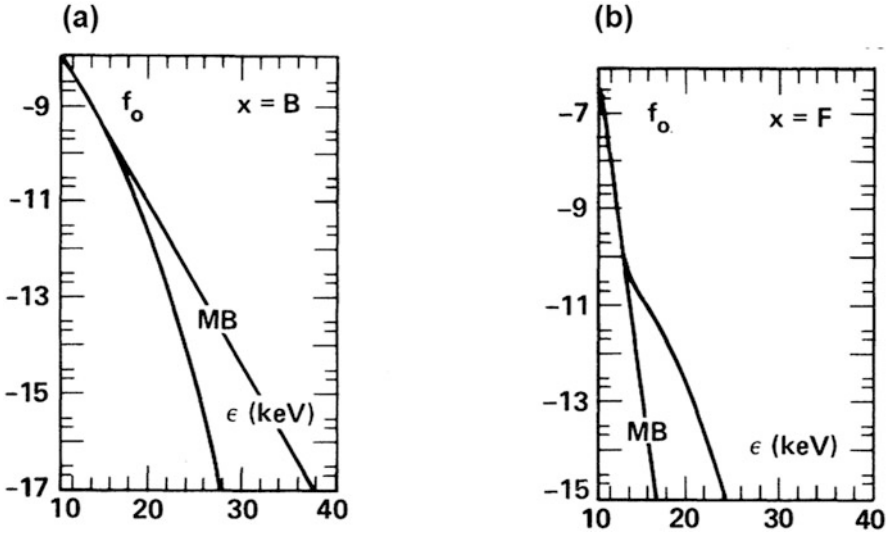
Fig. 6.5 The double functions in Fig. 6.4 stems from the non-Maxwell distribution of $f_0(v)$. The distribution functions obtained by solving FP equation in more relativistic density and temperature profiles are shown. (**a**) and (**b**) are the distribution functions at the laser heated low density region and the heat wave front in the high-density region, near the ablation front, respectively. Reprint with permission from Ref. [9]. Copyright 1998 by American Physical Society

Not only the limitation of the electron heat flux, but also the hysteresis of the heat flux is also seen in Fig. 6.4. Especially, the heat flux is enhanced than SH flux at the heat front region, right region in Fig. 6.3. Enhanced heat flux is due to the high-energy component coming into the cold region from the hotter region, because the mean free path with velocity v is proportional to v^4 and high-energy components freely penetrate in the front region. Such component contributes the preheating of cold region. It is very important if the absorbed laser energy is carried by heat flux, while the high-density and cold region has to be controlled to as cold as possible.

The hysteresis property stems from the non-Maxwell distribution of $f_0(v)$. The distribution functions obtained by solving FP equation in more relativistic density and temperature profiles are shown in Fig. 6.5 [9]. Figures (a) and (b) are the distribution functions at the laser heated low density region and the heat wave front in the high-density region, near the ablation front, respectively. The distribution function near the heating region has less high-energy component than the local Maxwell distribution, therefore the heat flux is reduced than SH model. On the other hand, near the heat front with enhanced high-energy component is produced by electrons coming from the heated region without enough scattering. This enhances the heat flux than SH model in the cold region. This is called **preheating**.

Since FP simulation is time consuming calculation and is not realistic to couple it with hydrodynamic codes. There have been proposed better modeling reproducing almost FP result with simple mathematical models. In what follows, such better models to provide the typical properties of the flux limitation and preheating are reviewed. As summary, the following two characters should be noted.

1. Heat flux is limited in laser, hearting region because of the violation of SH model (flux limitation)
2. Heat flux is higher than SH flux near the heat front region (nonlocal transport)

6.2.5   Flux Limit Properties

Before going to the advanced models for the electron heat flux in laser produced plasma, consider the difference of the heat fluxes mentioned so far from the FP simulation result. The reduction of heat conductivity in FP simulation has been studied by assuming sinusoidal temperature perturbation [10]. In this case, the heat diffusion with SH heat flux is solved numerically to compare to FP simulation result.

$$\frac{3}{2}n\frac{\partial T}{\partial t} = -\frac{\partial}{\partial x}q_{SH}, \quad q_{SH} = -\kappa_{SH}\frac{\partial}{\partial x}T \tag{6.55}$$

The initial condition is

$$T(0,x) = T_0 + \delta T(0)\,exp(ikx) \tag{6.56}$$

From the time progress of heat conduction, it is clear that the relation

$$\delta T(t) \propto exp(-\gamma t) \tag{6.57}$$

is observed. The decay rate is directly related to the heat conduction coefficients for SH model and can be derived for FP simulation as follows.

$$\gamma_{SH} = 2k^2\kappa_{SH}/3n, \quad \gamma_{FP} = 2k^2\kappa_{FP}/3n \tag{6.58}$$

Then, it is possible to define the following normalized value for measuring the flux reduction in FP simulation.

$$\frac{\kappa_{FP}}{\kappa_{SH}} \tag{6.59}$$

The simulation result is plotted with solid circles in Fig. 6.6 [10]. In Fig. 6.6, the solid curve is a fitting curve and the relation is

$$\frac{\kappa_{FP}}{\kappa_{SH}} = \frac{1}{1 + (30k\lambda_e)^{4/3}} \tag{6.60}$$

Further study showed that the FP simulation result can also fit with the following simpler formula [3].
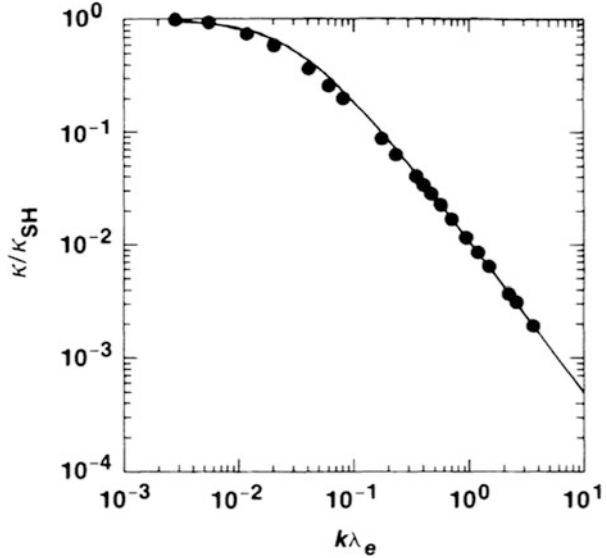
$$\frac{\kappa_{FP}}{\kappa_{SH}} = \frac{1}{1 + 60k\lambda_e} \tag{6.61}$$

For long wavelength perturbation, the heat conductivity is well modeled with SH model, but the conductivity is strongly reduced at short wavelength perturbation. It is informative to compare this relation (6.61) to the case of flux limited heat flux easily calculated to be

$$\frac{\kappa_{FL}}{\kappa_{SH}} = \frac{1}{1 + f^{-1}k\lambda_e} \tag{6.62}$$

It should be noted that the flux limiter $f = 1/60$ (=0.017) well reproduces the FP result. This value of f is consistent to the comparison with the experiment shown in Fig. 6.1.

6.3 Flux-Limit and Nonlocal Models

6.3.1 LMV Nonlocal Model

In an early time, Luciani, Mora, and Virmont (LMV) proposed the following model expression for nonlocal transport [11]. Stationary state is assumed for the heat flux.

$$q_e(x) = \int_{-\infty}^{\infty} q_e(x + \Delta x) W(\Delta x, x) d(\Delta x) \tag{6.63}$$

The **LMV nonlocal heat flux** is given in the form after replacing the variable $x' = x + \Delta x$ and approximating the heat flux in the integral with SH formula (6.10).

$$q_{LMV}(x) = \int_{-\infty}^{\infty} q_{SH}(x')W(x',x)d(x') \tag{6.64}$$

where the **propagator** (**kernel**) of the heat flux is defined [11].

$$W(x,x') = \frac{1}{2\lambda(x')} exp\left(-\left|\int_{x'}^{x} \frac{n_e(x'')}{n_e(x')} \frac{dx''}{\lambda(x')}\right|\right) \tag{6.65}$$

The effective mean free path in the propagator is defined as

$$\lambda = a(\lambda_s \lambda_f)^{1/2}\Big|_{v=v_e}, \quad a = 32 \tag{6.66}$$

where λ_s and λ_f are velocity-averaged mean free paths calculated by scattering and friction given in (6.49) and (6.50), respectively. The coefficient "a" in (6.66) is the adjustable parameter and derived by comparison with FP simulations.

6.3.2   Probability Density of Diffusion

In order to investigate the physical property of the propagator of the heat flux model in (6.64), let us Fourier transform of the LMV heat flux q_{LMV} in a uniform density and constant mean-free-path.

$$q_{LMV}(x) = \int_{-\infty}^{\infty} W(\Delta x)q_{SH}(x + \Delta x)d(\Delta x) \tag{6.67}$$

where we assume for simplicity,

$$W(\Delta x) = \frac{1}{2\lambda} exp\left(-\frac{\Delta x}{\lambda}\right) \tag{6.68}$$

Fourier transformation of the propagator is defined as

$$\Psi(k) = \int_{-\infty}^{\infty} W(x)e^{-ikx}dx \tag{6.69}$$

Carrying out the Fourier transformation of (6.1), we can use of the **convolution integral** in Fourier transformation.

$$G(k)H(k) = \frac{1}{\sqrt{2\pi}} \int_{-\infty}^{\infty} \left[\int_{-\infty}^{\infty} g(x-y)h(y)dy \right] e^{-ikx} dx \qquad (6.70)$$

By use of the convolution relation, (6.67) can be easily transformed to Fourier relation.

$$Q_{LMV}(k) = \Psi(k)Q_{SH}(k) \qquad (6.71)$$

where the Fourier function is defined as

$$Q_{LMV}(k) = \int_{-\infty}^{\infty} q_{LMV}(x)e^{-ikx} dx \qquad (6.72)$$

The Fourier function of the propagator is the same as the heat conductivity ratio and the case of LMV model can be obtained as

$$\frac{\kappa_{LMV}}{\kappa_{SH}} \equiv \Psi(k) = \frac{1}{1 + (k\lambda)^2} \qquad (6.73)$$

where the following relation has been used.

$$\Psi(k) = \frac{1}{2\lambda} \int_{-\infty}^{\infty} e^{-|x|/\lambda - ikx} dx = \frac{1}{2} \left(\frac{1}{1 + ik\lambda} - \frac{1}{-1 + ik\lambda} \right) \qquad (6.74)$$

Although the physical meaning of the LMV model is easily understand and reasonable to be used. However, the flux limit spectrum (means k-dependence) is different from FP calculation shown in (6.61). This is speculated that even with LMV model, the big difference of the mean-free-path on the velocity is not modeled. It suggests that it is better to develop the model for multi-group electron transport, where the heat flux is defined for each velocity component.

In Fig. 6.7 [3], the normalized Fourier functions of the heat conductivity are compared for LMV model and FP result. The LMV model reduces faster than FP result for l/L_T gets to large, too much heat flux is obtained. The other curve AWBS model is from [12] which has improved the LMV model, consequently better modeling.

We have investigated how to improve SH heat conduction model to allow the flux limitation as suggested in experiment and FP simulation. However, even if the flux limitation is reproduced, the electron kinetic effect is also very important to provide the preheating effect. This should be also modeled in an appropriate conduction formula. For this purpose, we need a model allowing the difference of mean free path for difference of velocity of electrons. Let us see more modernized model for heat conduction by electrons.

Fig. 6.7 Two different non-local heat flux models are compared to FP simulation result shown in Fig. 6.6. The integration form of heat flux LMV in (6.64) also reproduces the flux limitation property, while a difference is seen in the figure. AWBS model looks well reproduce FP simulation result. Reprint with permission from Ref. [11]. Copyright 1998 by American Physical Society
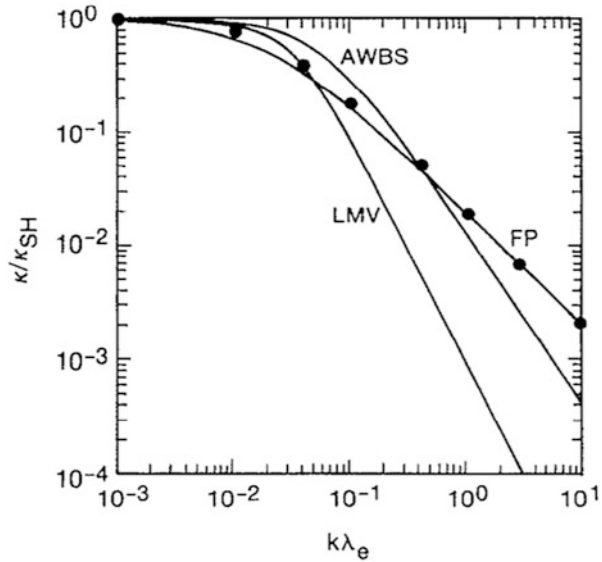
6.4   Comparison with an Experiment

The nonlocal transport model and Fokker-Planck calculations have been compared to measured temperature profiles of electron temperature in laser heated nitrogen gas jet plasma [13]. Gas jet is irradiated with 1ω laser and the heat wave region are irradiated with a short pulse 2ω laser at the same time to measure Thomson scattering and Rayleigh scattering spectra of 2ω lights. The probe beam moves to cover the space of about 2 mm in front of the laser heating plasma region. Simply saying, the principle of Thomson scattering is as follows. The probe beam is scattered by the ion acoustic waves in the plasma and the probe beam is scattered with frequency shift which is the function of the dispersion relation of the ion acoustic wave. Since the ion acoustic wave has its phase velocity proportional to the square root of the electron temperature, the spatial profile of the electron temperature is inferred from the spatial profile of the phase shift [13].

In Fig. 6.8, the experimental data of electron temperature is compared for $t = 0.3$ ns and 1.5 ns. The heating laser has a Gaussian shape with 1.4 ns half width and intensity of $1.5 \times 10^{14} \mathrm{W/cm^2}$. So, $t = 0.3$ ns is at the beginning and $t = 1.5$ ns is almost at the peak intensity. The typical electron density measured by Rayleigh scattering is $10^{19}\,\mathrm{cm^{-3}}$. When the laser intensity is week as $t = 0.3$ ns, the experimental data with error bars are well reproduced with LASNEX and it is almost independent of the flux limiter. At $t = 1.5$ ns, on the other hand, the experimental data differ substantially from LASNEX results with the flux limiter 0.05 and 1.0. Fokker-Planck simulation of 2D SPARK is used to compared to obtain a good agreement with the experimental data. This suggest that LASNEX code does not provide the heat flux penetrating to the deeper region and the flux limit $f = 0.05$ too much prevents the heat loss from the heating region.

Fig. 6.8 Experimental data of electron temperature profiles at two different times (0.3 ns and 1.5 ns). The data are shown with solid squares with error bars. The temperature profile near the peak of laser pulse (t = 1.5ns) is compared to the flux limited diffusion model with f = 1 and 0.05 shown with red and black lines, respectively. The Fokker-Planck simulation result is plotted with the dashed black line. HSR model can also reproduced the data well. Reprint with permission from Ref. [14]. Copyright 1998 by American Physical Society
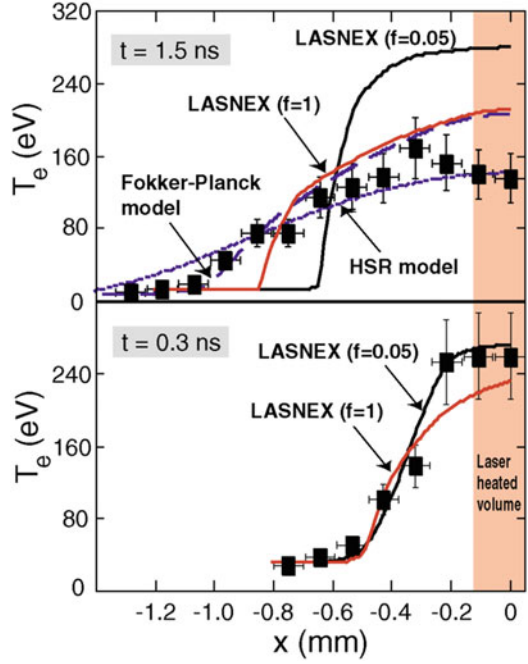
In order to validate a nonlocal model discussed previously with such comparison, the same type of form (6.64) has been calculated. It is called "hot spot relaxation (HSR)" model [14]. In HSR, the kernel W(x', x) is modified from (6.65) so that Fourier spectrum of K/K_{SH} is designed to be

$$\frac{K}{K_{SH}} = \frac{1}{1 + (ak\lambda_e)^{0.9}}, \qquad \lambda_e = \sqrt{Z}\lambda_{ei}, \qquad k\lambda_{ei} \leq 1 \qquad (6.75)$$

where a = 10(Z + 5)/(Z + 12). HSR roughly reproduce Fourier spectrum of FP simulation result shown in Fig. 6.6.

6.5   Multi-group (SNB) Model

The kernel (6.68) is physically well understood and it may give a good model for a single electron group. As we see, it can give the flux-limit property, although slightly different from FP numerical result. It is reasonable to extend it to the case of multi-group electrons, where electron velocity distribution is divided to N group and the propagator is defined as function of the velocity. Then, the preheating by long mean-free-path electrons can be included in the model as well as the flux-limiting property. There have been proposed several methods for such modeling, however, the

difference is mathematical method. Therefore, the idea on how to extend it to the multi-group case is explained for so-called **SNB model** by Schurtz, Nicolai, and Busquet [15].

Before explaining the derivation of SNB model, it is useful to see the comparison of SNB model to FP and SH results. In Ref. [16], the models are compared to the situation relating to the laser plasma. In Fig. 6.9, "Heat bath problem" is shown at $t = 80$ ps after starting with the red curve of the temperature. The black is FP and blue is SNB result. It is well seen that the preheating is well given as that by FP calculation. The heat flux at this point at 10 ps is plotted in Fig. 6.10. The black is SH, red is FP and blue is SNB models, respectively. This result explains the flux limit and preheating well. The peak flux is limited compared to the SH model and the pre-heating in the region for $x > 500$ μm is reasonably predicted by SNB model.

Fig. 6.9 Model simulation of VFP and SNB model starting from the initial temperature distribution plotted with red line. It is shown that SNB model reproduces well the VFP simulation. Reprint with permission from Ref. [17]. Copyright 1998 by American Institute of Physics
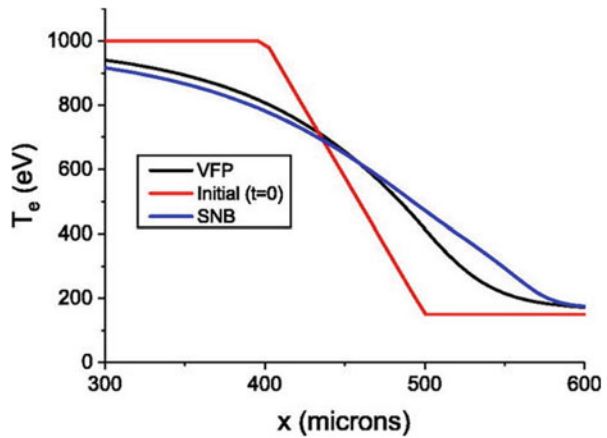
Fig. 6.10 Heat flux distribution at the same time as in Fig. 6.9. The red line is from K2 code of VFP simulation and the blue line is SNB, which reproduces well the VFP result. The black line is from SH heat diffusion model. It is clear that SH overestimates the heat flux and does not show the preheating compared to VFP, while SNB well reproduces these two effects. Reprint with permission from Ref. [17]. Copyright 1998 by American Institute of Physics
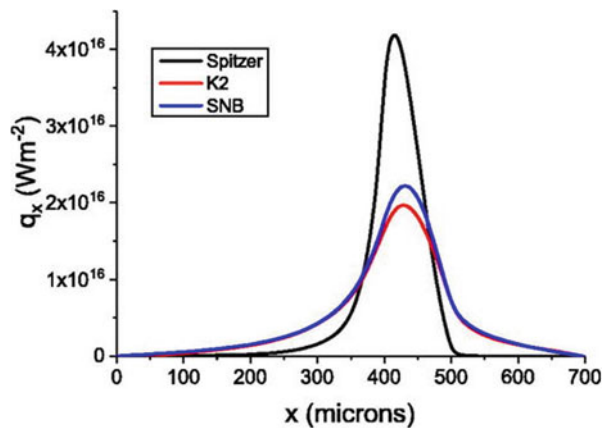
Fig. 6.11 The velocity
dependence of $v^5 f_1$ at the
point of x=500mm at the
time of previous two figures.
Near this point the
preheating by higher
velocity electrons becomes
important in K2 (VFP)
simulation and SNB model
can well reproduce such
preheating as shown with
the blue line. Reprint with
permission from Ref. [17].
Copyright 1998 by
American Institute of
Physics
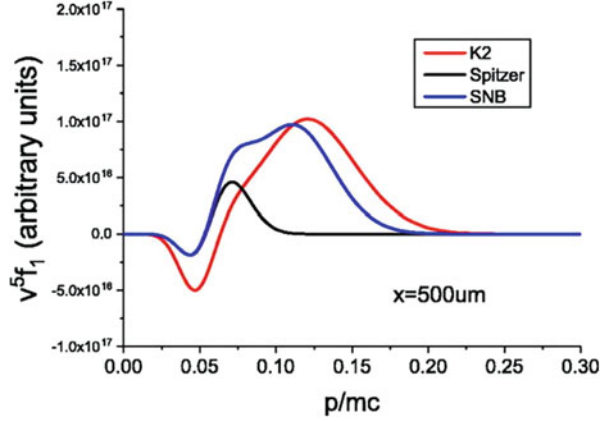
The velocity dependence of heat flux is compared in Fig. 6.11 for SH (black), FP
(red), and SNB (blue) models at the heat front x = 500 μm at 10 ps. The f_1 of SH is
calculated with (6.31) and the sign change around v = 0.05c, and this is less
evaluation of the preheating by high-energy electrons from the high-temperature
region. FP shows enhanced component of heat flux by higher energy electrons, and
this is well reproduced by SNB model.

In SNB model, the electron heat flux is given as the sum of all velocity groups,
consequently the property of long mean free path of high energy electrons are well
reproduced. Let us consider the physics of SNB model. Note that SNB model is now
used widely in modern hydrodynamic simulations.

6.5.1   Derivation of SNB Model

The basic equations for deriving SNB model is the same as (6.17) except for the
collision operator. Assuming scattering frequency without energy change ν_{ei} and
electron-electron thermalize frequency ν_{ee}, the 0th and 1st moment equation to the
angle μ are derived as follows [17, 18].

$$\frac{v}{3}\frac{\partial}{\partial x}f_1 - \frac{eE}{3mv^2}\frac{\partial}{\partial v}\left(v^2 f_1\right) = -2\nu_{ee}\left(f_0 - f_0^M\right) \tag{6.76}$$

$$v\frac{\partial}{\partial x}f_0 - \frac{eE}{m}\frac{\partial}{\partial v}f_0 = -\nu_{ei}f_1 \tag{6.77}$$

Different from SH derivation, SNB model assumes the following form to the
electron distribution function.

$$\begin{aligned} f_0 &= f_0^M + \delta f_0 \\ f_1 &= f_1^M + \delta f_1 \end{aligned} \tag{6.78}$$

The SH has assumed $\delta f_0 = 0$ and $\delta f_1 = 0$. In order to include the flux limit and non-local preheating effects, SNB model derives new equations to obtain the perturbations for δf_0 and δf_1 with reasonable assumption. Since the f_1^M in (6.78) is defined by (6.18), a relation to δf_0 and δf_1 from (6.77) is derived to be.

$$v\frac{\partial}{\partial x}\delta f_0 - \frac{eE}{m}\frac{\partial}{\partial v}\delta f_0 = -\nu_{ei}\delta f_1 \tag{6.79}$$

where E is given by the SH relation (6.21) and by including the density gradient it is give as

$$E = \frac{T_e}{n_e}\frac{\partial n_e}{\partial x} + \gamma\frac{\partial T_e}{\partial x} \tag{6.80}$$

where the coefficient g is a function of the ion charge Z in the form [15].

$$\gamma = 1 + \frac{3(Z + 0.477)}{2(Z + 2.15)} \tag{6.81}$$

The Z-dependence is derived due to the change of ration between ion and electrons in the scattering coefficient ν_{ei} in (6.77).

Define the two mean-free paths for an electron with velocity v in the form.

$$\lambda_{ee} = \frac{v}{\nu_{ee}}, \quad \lambda_{ei} = \frac{v}{\nu_{ei}} \tag{6.82}$$

SNB strategy is to delete the velocity derivative term with an intuitive way. It is clear that the second term at LHS in (6.79) is the acceleration or deceleration by electric field. The high energy electrons are decelerated by the ambipolar electric field E and the return current electrons are accelerated. Since the dynamics of the high-energy electrons is important in the transport modeling, the second term works as an deceleration and it can be modeled as the increase of the collision frequency as [15].

$$\frac{1}{\lambda_{ei}^{(E)}} = \frac{1}{\lambda_{ei}} + \left|\frac{eE}{1/2mv^2}\right| \tag{6.83}$$

Note that (6.83) is not appropriate if the E-field dominantly accelerate electron. In SNB model, the deceleration of high-energy component limiting the heat flux is mainly taken account with (6.83). Equation (6.79) is reduced to the following form.

$$\lambda_{ei}^{(E)}\frac{\partial}{\partial x}\delta f_0 + \delta f_1 = 0 \tag{6.84}$$

In SH derivation, only the relation (6.77) is used to derive the f_1 as in (6.18). However, we have to solve (6.76) at the same time as the second relation for δf_0

and δf_1. In addition, as is explained later, the return current effect is neglected in the formulation and (6.76) is modified to the following relation;

$$\delta f_0 + \frac{\lambda_{ee}}{6} \frac{\partial}{\partial x} \delta f_1 = - \frac{\lambda_{ee}}{6} \frac{\partial}{\partial x} g_1^M \qquad (6.85)$$

The function g_1^M is a modified form of f_1^M to be explained later. Inserting (6.84) into (6.85), it is easy to obtain δf_0 and δf_1 numerically.

In order to know qualitative property of the solutions, discuss about the case with constant mean free paths in space. Then, (6.85) is written in a form;

$$\frac{\partial^2}{\partial x^2} \delta f_0 - \frac{1}{\lambda^2} \delta f_0 = S(x, v)$$

$$S(v, x) = - \lambda_{ei}^{(E)} \frac{\partial}{\partial x} g_1^M \qquad (6.86)$$

$$\lambda = \sqrt{\frac{\lambda_{ee} \lambda_{ei}^{(E)}}{6}}$$

where the source term S is a function of x for a given velocity v in the form and we introduced an effective mean free path $\lambda(v)$. It is easy to formally solve (6.86) in the form.

$$\delta f_0(x, v) = \frac{\lambda(v)}{2} \int_{-\infty}^{\infty} S(x', v) \, exp\left(- \frac{|x - x'|}{\lambda(v)} \right) dx' \qquad (6.87)$$

Let us consider how flux limit and nonlocal preheat are modeled in this SNB transport model. As seen in Fig. 6.6, the flux limit appears when the mean free path becomes long to approach the temperature gradient scale, namely λ/L_T becomes of the order of unity. Let us assume that this condition means the first term becomes larger than the second term in LHS of (6.86). In such condition, we can obtain the following approximate relation from (6.85).

$$\delta f_1 \approx - g_1^M \qquad (6.88)$$

As the result, $f_1 \rightarrow 0$ to result a strong flux limitation from (6.78).

On the other hand, the opposite condition $\lambda/L_T >> 1$ is satisfied especially for the high energy component of electrons. Such component has long mean free path in (6.86) and the hear flux from the heating region propagates to the heat front region.

6.5.2 Multi-group Heat Flux

In SNB model, the heat flux is defined as a sum of multi-group heat fluxes. Let us see the definition of the heat flux by the velocity component (v_{g-1}, v_g), where g is an integer of each group of velocity. Each group g also corresponds to the normalized energy group β_g, where $\beta = mv^2/T_e$.

Since the effect of electric field to prevent the heat flux is taken into account as (6.83), the electric field in (6.18) is neglected and the form (6.30) is more simplified as

$$f_1^M = \frac{\lambda_c(\beta=1)}{L_T}\beta^2(\beta-4)f_0^M \tag{6.89}$$

$$\rightarrow g_1^M = \frac{\lambda_c(\beta=1)}{L_T}\beta^2 f_0^M \tag{6.90}$$

In SNB model, the total heat flux q_e^{SNB} is given as the sum of N groups due to g_1^M and δf_1

$$q_e^{SNB} = \sum_{i=1}^N Q_1^i + Q_2^i \tag{6.91}$$

where

$$Q_1^i = \frac{2\pi m}{3}\int_{v_{i-1}}^{v_i} g_1^M v^5 dv \tag{6.92}$$

$$Q_2^i = \frac{2\pi m}{3}\int_{v_{i-1}}^{v_i} \delta f_1 v^5 dv \tag{6.93}$$

Note that the first term is written also as

$$Q_1^i = q_e^{SH}\frac{1}{24}\int_{\beta_{i-1}}^{\beta_i} \beta^4 e^{-\beta}d\beta \quad \Rightarrow \quad \sum Q_1^i = q_e^{SH} \tag{6.94}$$

The total flux is given by Spitzer-Harm heat flux (6.25) and 1/24 is the normalization factor. By replacing f_1^M with g_1^M, the total heat flux is the same as Spitzer-Harm one, while the maximum in the integral of (6.94) becomes $\beta = 4$. This means the mean free path of electrons carrying the maximum heat is $\lambda = 32\lambda_e$, the recommended value for the LMV model [11].

It should be noted that Q_2^i modify the heat flux due to the electron components with long mean free path as can be guess from the propagator form. This term reduces the heat flux as flux limiter and provides heat flux by electrons of long mean free path, namely pre-heating is given by this new term.

Fig. 6.12 Flux limitation property is compared among three models and VFP simulation with KIPP code. This is the same plot as Fig. 6.6, but for more realistic temperature profile. All three models show good agreement as VFP simulation result. The heat flux is limited dramatically for the case where the temperature gradient scale L_T approached to ten times the electron scattering mean-free-path. Reprint with permission from Ref. [19]. Copyright 1998 by American Institute of Physics
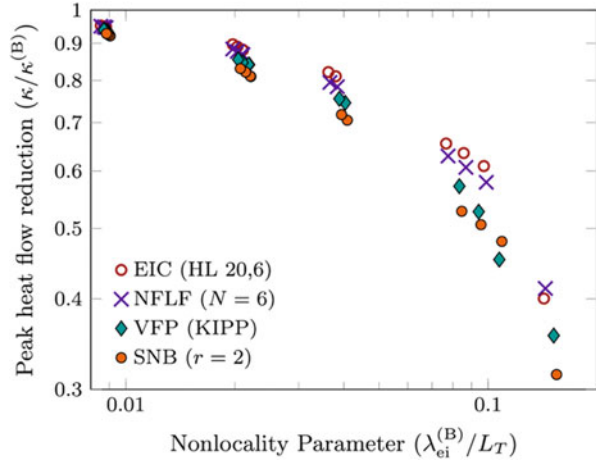
Fourier spectrum of the transport propagator shown in Fig. 6.7 is calculated for SNB model and other models. They are compared in Fig. 6.12 to the other numerical models [18]. The results of VFP code KIPP is shown. Compared to the VFP result, the simple SNB model is found to reproduce the result well. The other data are explained in [18]. Considering the computation time, the SNB is very convenient, especially modeling the effect of flux limit and preheating in hydrodynamic simulation code. Note that r = 2 is a coefficient of modeling electron-electron collision which is approximated with a simple form in (6.76). It is reported that using BGK collision operator with r = 2 gives a good agreement with VFP calculation.

The multi-group diffusion model "SNB model" is widely used in several ICF codes such as Lawrence Livermore National Laboratory's HYDRA, CELIA laboratory's CHIC, CEA's FCI2, DUED (U. Rome), and the University of Rochester Laboratory for Laser Energetics' LILAC and DRACO [18]. It is also applicable to multi-dimensional space codes with magnetic fields [19].

Transport codes are compared in the background hydrodynamics obtained with HYDRA code. Gadolinium hohlraum containing a typical helium gas is heated by laser and the density and temperature profile at t = 20 ns are used as the initial condition of each code. After 5 ps run of simulation codes, the heat flux profiles are plotted in Fig. 6.13 [18]. In Fig. 6.13, "Local" is the heat flux calculated with Braginskii formula, which is equivalent to Spitzer-Harm heat flux. Two models of SNB are shown. It is clear that the SNB model provides well the property of flux limitation near the heating region and preheating character near the heat front as predicted by VFP simulation code IMPACT.
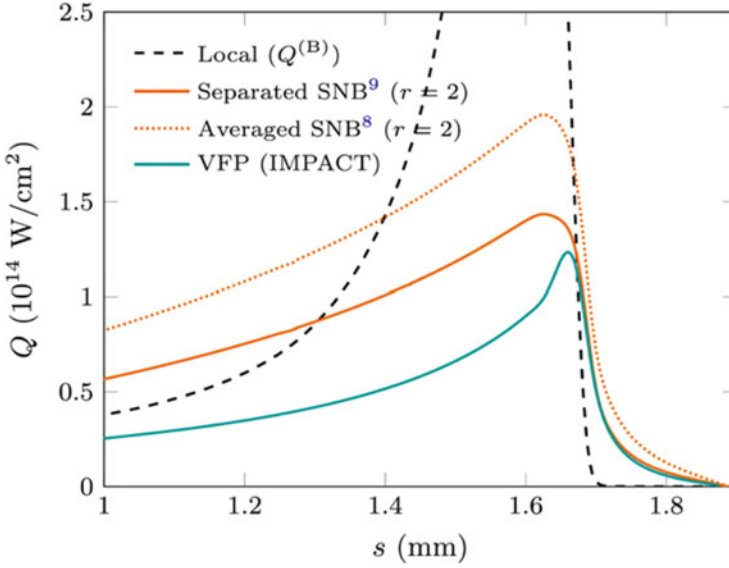
Fig. 6.13 Heat flux distribution near the ablation front of high-Z material. VFP simulation result is shown with green line. It is typical that the maximum of heat flux is limited and the preheating tail is given. The SH extremely over-estimates the heat flux as shown in the dashed line. The model SNB with multi-group is more reasonable and the flux limitation and preheating are well modeled. Reprint with permission from Ref. [19]. Copyright 1998 by American Institute of Physics

6.6   Comparison of SNB Model to Two Different Experiments

By use of Thomson scattering diagnostics, electron distribution functions are measured in a model experiment of aluminum plasma ablating into the vacuum. An aluminum foil is irradiated with six beams 3ω laser with 2 ns pulse width and for the diagnostic probe 2ω laser is used [20]. The five points of ablating plasma are measured for Thomson scattering. In the present case, the scattered spectral shape is used to determine the electron distribution function at each point. The measured electron temperature and density are $1 \sim 1.3$ keV and $0.5 \sim 1 \times 10^{20}$ cm^{-3}, respectively. Speculated density scale lengths are in the range $\lambda_{ei}/L_T = 1.4 \times 10^{-2} \sim 7 \times 10^{-3}$.

In the analysis of Thomson scattering data, the following spectral density function $S(\mathbf{k},\omega)$ of electron plasma contribution is used at high frequency region, where the ion contribution can be neglected. Note that the previous experiment in Chap. 6.4 has used only the ion acoustic wave contribution in low frequency region, and therefore only the information of electron temperature is inferred from Thomson data. The spectral density function by electron plasma is given as [21].

$$S(\boldsymbol{k},\omega) = \frac{2\pi}{k} \frac{f_e(\omega/\boldsymbol{k})}{|\epsilon(\boldsymbol{k},\omega)|^2} \tag{6.95}$$

where $f_e(\omega/\boldsymbol{k})$ is the one-dimensional electron distribution function and $\epsilon(\boldsymbol{k},\omega)$ is the dielectric constant of electron plasma wave.

The Thomson scattering is dominated by the contribution of the plasma waves satisfying the dispersion relation (resonance condition),

$$\epsilon(\boldsymbol{k},\omega) = 0 \quad \Rightarrow \quad \omega(k) = \pm \omega_L(k) + i\gamma_L(k) \tag{6.96}$$

The electron plasma wave is called Langmuir wave with the frequency $\omega_L(k)$. In general, the resonance solution is complex as in (6.96) and the imaginary part $\gamma_L(k)$ is due to wave damping by Landau damping process. It is well known that the **Landau damping** is proportional to a velocity derivative at the resonance speed, $\gamma_L(k) \propto \partial f_e / \partial v$ at $v = \omega_L/k$. By use of these theoretical relations and compare them to Thomson scattering spectra, it is possible to obtain the local electron distribution function in non-Maxwell form. This data also provides the electron density and temperature values at the scattered five points in the experiment.

In Fig. 6.14, the resultant heat flux obtained by the **Thomson scattering** data (TS) is shown with red circles (The detail of TS principle will be discussed in Chap. 9). Spitzer-Harm heat flux is also shown with use of the temperature distribution at the five points as (SH) with blue triangles. In order to check the validity of the nonlocal transport model SNB described in the previous section, a multi-group simulation code has been used for the density and temperature profiles obtained in the experiment. The SNB result is shown with black diamonds. The authors insists that SNB nonlocal transport model cannot reproduce the experimental data and it is about the halfway between SH and the experimental heat flux. I think this concluding remark is too strict for evaluating a robust nonlocal transport model such as SNB. As we have studied in the previous section, SNB guarantees the preheating and flux limit physics, while it is not so strict theoretical model to compare the form of distribution functions.

Fig. 6.14 The heat flux observed experimentally is compared to those from SH diffusion and SNB transport models. Reprint with permission from Ref. [21]. Copyright 1998 by American Physical Society
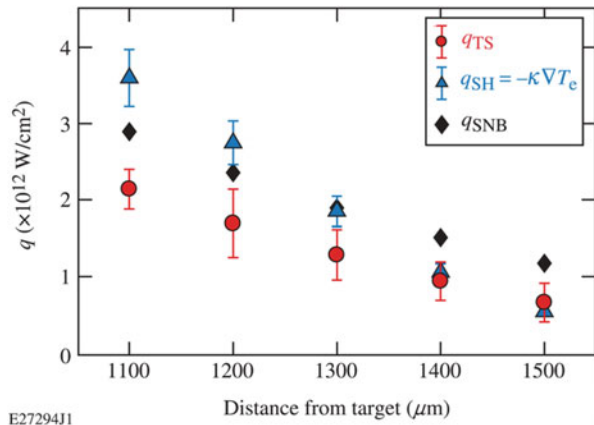
E27294J1

Fig. 6.15 Comparison of the velocity dependent heat flux at the point in the experiment. Three curves are from FP calculation (dashed red curve), Spitzer-Harm (solid blue curve), and SNB (dotted black curve). Reprint with permission from ref. [21]. Copyright 1998 by American Physical Society
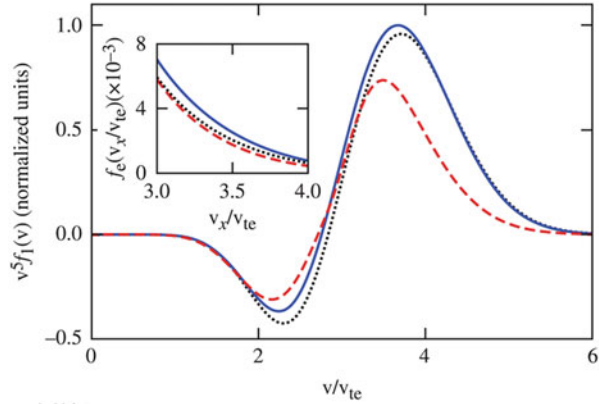
It is also informative to show Fig. 6.15 [20]. The velocity dependent heat flux (6.22) is plotted for one point (1200 μm). Three curves are from FP calculation (dashed red curve), Spitzer-Harm (solid blue curve), and SNB (dotted black curve). It is not so meaningful to compare the distribution function of heat flux. Since the introduction of the function g_1^M instead of Spitzer-Harm f_1^M in (5.15) has no mathematical base and just to avoid too much negative component. So, in general there may be other ways to replace f_1^M to a convenient way for modeling nonlocal transport. The reason why g_1^M is introduced is that it guarantees the preheating effect and the property of flux limit robustly.

It is difficult to say, therefore, that there is not seen an improvement of heat flux in SNB model because it is almost the same as SH, but different from FP result. The validity of SNB should be checked under the condition that the heat flux is strongly inhibited like the flux limit and in the opposite case that the high energy electrons penetrate into cold plasma region. In addition, it is noted that SNB requires to be adjusted about the collisional modeling.

The preheating has been studied in relatively higher density plasma comparing to the experimental data of plastic form plasma with the density near 0.1 g/cm^3 and temperature near 30 eV [22]. As a tool to study such high-density plasma, so-called warm dense matter (WDM), the authors used X-ray Thomson scattering diagnostic to obtain the electron temperature, density, and ionization state by comparing x-ray spectrum with theoretical one, by varying the plasma parameters. The target is made of plastic, gold, aluminum and plastic form layers to observe the preheating effect in the plastic form layer.

In the experiment, preheating of the expanding form plasma was observed and a variety of simulations have been carried out to find the physical source to give preheating to the form region over the high-density plasma region. Even with detail opacity and radiation transport, it was not possible to obtain enough preheating energy flux to the form region. It was finally concluded that about 10% of the free streaming heat flux from the shocked high-density region transfers large amount of heat to preheat the preheat region more than 30 eV as shown in Fig. 6.16 [22]. It is
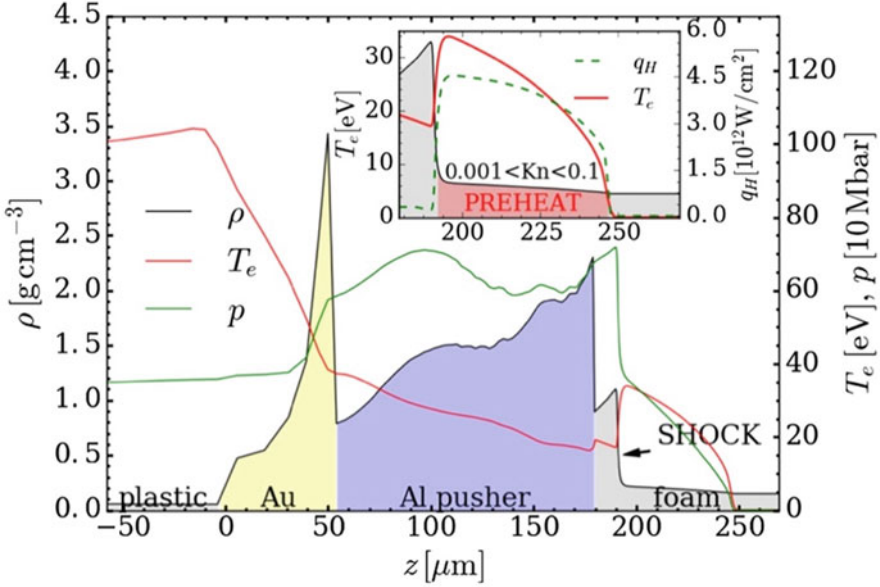
Fig. 6.16 A multi-layered target is heated by laser to find the preheating in the rear side of the target. The enhanced temperature has been measured as preheat in CH foam region in the experiment and computationally reproduced by including non-local transport model. Reprint with permission from Ref. [22]. Copyright 1998 by American Physical Society

surprising to know that the temperature of preheating region is higher than the upstreaming region of the heat flux. It is unphysical in the local thermodynamic equilibrium (LTE) thermodynamics. There should be some unknown physics at the shock front, where the temperature decreases from the front to the rear of the shock front, this means an entropy of plasma decreases by the shock wave. It is not clear why such result is obtained in a nonlocal simulation, while one thing to be clarify is that the contribution of electrostatic field at the shock surface.

As explained in modeling nonlocal transport, it is hard to model the effect of electrostatic field even n one-dimensional system. In SNB model, the electric field is included into an effective mean free path as shown in (6.83) and the electric field is evaluated from the neutral current condition (6.21). Note that there is no density gradient dependence and the force to electrons -eE is the direction of $-\,dT_e/dx$. However, the electrostatic field at the shock front is in general given by the Boltzmann relation;

$$n_e(x) = n_0\, exp\left[e\frac{\phi(x)}{T_e}\right] \quad \Rightarrow \quad e\phi_{01} = T_e\, ln\left(\frac{n_0}{n_1}\right) \tag{6.97}$$

The potential jump at the shock front is more than Te (~20–30 eV) and most of the electrons with energy more than $e\phi_{01}$ are reflected back at the shock front. The evaluation of E field in any non-local transport is difficult issue.

Appendix-C. Fokker-Planck Equation

Vlasov equation is a powerful equation in studying waves, transport, turbulence, and so on from view point of wave-particle interaction and non-Maxwellian plasmas. As mentioned already, Vlasov equation is applicable only for collisionless physics in plasmas. However, collisional effect cannot be neglected in some non-LTE plasmas, especially plasma with strong heat flow and inhomogeneity of physical quantities. Principally, of course, it is required to solve Boltzmann equation of (C.1) with appropriate collision cross section. It is, however, not so easy to solve such differential-integral equation directly. Such collision effect in plasmas is the same as random walk or thermal noise widely seen in the nature. It is easy to use **Fokker-Planck equation** used widely in non-equilibrium statistical mechanics.

Langevin to Fokker-Planck Equation

In order to clarify the intuitive image of the readers to Fokker-Planck equation, it is better to start with a simple one-dimensional **Langevin equation** for a Brownian motion in spatially uniform medium.

$$m\frac{dV(t)}{dt} = -\nu_f mV(t) + mR(t) \qquad (C.1)$$

Here the 1st term in RHS is the frictional force and the 2nd term is a random force。 Such equation is called **stochastic differential equation**. The governing equation to the velocity distribution function P(v,t) defined as ensemble average probability distribution in velocity space is given as follows as will be explained from now.

The ensemble average of any physical quantity of function V is defined by

$$\langle A(V)\rangle = \int_{-\infty}^{\infty} A(v)P(v,t)dv \qquad (C.2)$$

The random force R(t) in (C.1) is Markovian process with Gaussian probability to given as

$$\langle R(t)\rangle = 0, \quad \langle R(t)R(t')\rangle = D\delta(t-t') \qquad (C.3)$$

and the following relation is satisfied.

$$\Delta W = \int_{t}^{t+\Delta t} R(t)dt \qquad (C.4)$$

$$\langle \Delta W \rangle = 0 \tag{C.5}$$

$$\langle \Delta W^2 \rangle = D \Delta t \tag{C.6}$$

Expanding A(V) with Taylor series in velocity, the following relation is obtained

$$A(V(t+\Delta t)) = A(V(t)) + \left.\frac{dA}{dV}\right|_{V=V(t)} \Delta V(t) + \frac{1}{2}\left.\frac{d^2A}{dV^2}\right|_{V=V(t)} \Delta V(t)^2 + \cdots \tag{C.7}$$

Taking the ensemble average of (C.7) yields the following form

$$\langle A(V(t+\Delta t)) \rangle = \langle A(V(t)) \rangle + \left\langle \left.\frac{dA}{dV}\right|_{V=V(t)} \Delta V(t) \right\rangle + \frac{1}{2}$$

$$\times \left\langle \left.\frac{d^2A}{dV^2}\right|_{V=V(t)} \Delta V(t)^2 \right\rangle + \cdots \tag{C.8}$$

Taking finite difference of (C.1) and inserting $\Delta V(t)$ in (C.8) and keeping the term proportional only to the 1st order of Δt, the following equation can be derived finally.

$$\frac{d}{dt}\langle A(V(t)) \rangle = -\nu_f \left\langle V(t)\frac{dA}{dV} \right\rangle + \frac{D}{2}\left\langle \frac{d^2A}{dV^2} \right\rangle \tag{C.9}$$

It is noted that the second term of RHS of (C.9) is remains as the 1st order because of (C.6).

Return to the definition (C.2), (C.9) can be changed to the equation to probability function P(v,t) as follows. The LHS of (C.9) is

$$\frac{d}{dt}\langle A(V(t)) \rangle = \int_{-\infty}^{\infty} A(v)\frac{\partial P(v,t)}{\partial t}dv \tag{C.10}$$

The 1st term of RHS of (C.9) is

$$-\nu_f \left\langle V(t)\frac{dA}{dV} \right\rangle = -\nu_f \int_{-\infty}^{\infty} v\frac{dA}{dv}P(v,t)dv = \nu_f \int_{-\infty}^{\infty} A(v)\frac{\partial}{\partial v}\{vP(v,t)\}dv \tag{C.11}$$

Where partial integral is used with the assumption that $P(\infty,t) = P(-\infty,t) = 0$.

$$\left\langle \frac{d^2A}{dV^2} \right\rangle = \int_{-\infty}^{\infty} \frac{d^2A(v)}{dv^2}P(v,t)dv = \int_{-\infty}^{\infty} A(v)\frac{\partial^2 P(v,t)}{\partial v^2}dv \tag{C.12}$$

The 2nd term of RHS is modified by using the partial difference two times. As the result, (C.9) should be satisfied for any function A(v) only when the condition:

$$\frac{\partial P(v,t)}{\partial t} = \nu_f \frac{\partial}{\partial v}[vP(v,t)] + \frac{D}{2}\frac{\partial^2 P(v,t)}{\partial v^2} \tag{C.13}$$

is satisfied. (C.6) is Fokker-Planck equation.

It should be noted that solving Fokker-Planck equation is exactly the same as calculating an ensemble average for many test particles motioned by Langevin Eq. (C.1). As a simple examples, Fokker-Planck equation is used to study any Brownian motion, white noise in electric circuit, polymer dynamics, etc.

It is useful think about the case of stationary state of (C.13). Then, RHS of (C.13) should vanish and the following relation should be satisfied after integrating it:

$$\frac{dP(v)}{dv} = -\frac{2\nu_f}{D}vP(v) \tag{C.14}$$

This can be easily solved to give

$$P(v) = exp\left(-\frac{\nu_f}{D}v^2\right) \tag{C.15}$$

This is the velocity distribution in the equilibrium state and should be Maxwellian distribution, namely the diffusion coefficient in velocity space given in (C.13) should satisfy the following condition.

$$\frac{D}{2} = \frac{T}{m}\nu_f \tag{C.16}$$

It is very interesting to compare the diffusion coefficient in velocity space (C.16) and that in real space (5.71) which is called Einstein relation. Note that dependence on the collision frequency is opposite. In a very collisional system, the diffusion in velocity space is fast and get to be equilibrium soon, while in the real space it is very slow to diffuse.

In plasmas, collision frequency is a strong function of the particle velocity and in non-LTE plasmas the distribution function is not isotropic in 3-dimensional velocity space. It is, therefore, difficult to directly use Fokker-Planck equation of (C.13). It is now easier, however, to extend the above mathematical derivation from Langevin equation to Fokker-Planck equation. Then, it is clear that the following Fokker-Planck equation can be obtained in 3-diemnsional space of velocity.

$$\frac{\partial P(\mathbf{v},t)}{\partial t} = \frac{\partial}{\partial v_i}\left[\left\langle\frac{\Delta v_i}{\Delta t}\right\rangle P(\mathbf{v},t)\right] + \frac{1}{2}\frac{\partial^2}{\partial v_i \partial v_j}\left[\left\langle\frac{\Delta v_i \Delta v_j}{\Delta t}\right\rangle P(\mathbf{v},t)\right] \tag{C.17}$$

This expression is easily understood that RHS of (C.17) is an extension to 3 dimension of Taylor expansion and the form is derived with the same manner as (C.8), (C.9), and (C.10).

What Fokker-Planck equation says is that any random force in Brownian motion reduces to the combination of the friction term and diffusion term.

It is noted that the probability function P(**v**,t) in (C.17) is the ensemble averaged velocity distribution function in velocity space and it is exactly the same as the velocity distribution function at each real space point as long as the collision is taken place at a point and no change in **r** after each binary collision.

After a long algebra shown in [5], new functions and constant are introduced

$$\Gamma = \frac{Z^2 e^4}{4\pi \varepsilon_0^2 m^2} \ln \Lambda \tag{C.18}$$

$$H(\boldsymbol{v}) = Z_s^2 \left(\frac{m + m_s}{m_s} \right) \int \frac{f_s(\boldsymbol{v}_s)}{g} d\boldsymbol{v}_s \tag{C.19}$$

$$G(\boldsymbol{v}) = Z_s^2 \int g f_s(\boldsymbol{v}_s) d\boldsymbol{v}_s \tag{C.20}$$

Here g is a function of **v** and **v**$_s$ and given in [5]. It is noted that the definition (C.19) and (C.20) are called the **Rosenbluth potentials**. It is well known that the Fokker-Planck equation is reduced to the following form.

$$\left(\frac{\partial}{\partial t} f \right)_{coll} = -\Gamma \frac{\partial}{\partial v_k} \left(\frac{\partial H}{\partial v_k} f \right) + \frac{1}{2} \Gamma \frac{\partial^2}{\partial v_k \partial v_j} \left(\frac{\partial^2 G}{\partial v_k \partial v_j} f \right) \tag{C.21}$$

It is known that the first term of RHS in (C.21) is the dynamical friction and the second one is the diffusion term. The Fokker-Planck equation assumes only the scattering by the binary Coulomb collision, therefore, in the system of two kind of particles like fully-ionized ions and electrons, we have to solve the equation for electron distribution function changing in time by scattering electron-electron(e-e), electron-ion(e-i) and for ion distribution by ion-electron(i-e), ion-ion(i-i). It is noted that in the case of e-e and i-i scattering, (C.7) is a nonlinear equations to the distribution function.

In order to see what happens to a test particle injected from the boundary due to the Coulomb collision in a uniform plasmas, assume the distribution function of the particle is a delta function.

$$f(\boldsymbol{v}, t) = \delta\{\boldsymbol{v} - \boldsymbol{u}(t)\} \tag{C.22}$$

Inserting (C.22) to (C.21) and taking the **v** moment of (C.21) lead the following simple form.

$$\frac{\partial \boldsymbol{u}(t)}{\partial t} = \Gamma \frac{\partial H(\boldsymbol{u})}{\partial \boldsymbol{u}} = -\nu_f(u)\boldsymbol{u} \tag{C.23}$$

The term with G vanish in partial integral process. Equation (C.23) clearly shows that the term H gives the drag force and the frictional coefficient ν_f is calculated. Fokker-Planck equation is more precise equations for the ion stopping discussed in Sect. 4.8. In ion stopping simulation, however, the ionization process should be also included in RHS of (C.21).

Fokker-Planck Equation in Maxwellian Scatterers

It is useful to show the explicit form of Fokker-Planck equation of (C.21) in the case of the distribution of the scatterers is Maxwellian with temperature T_s and mass m_s.

$$f_s(\boldsymbol{v}_s) = f_M(\boldsymbol{v}_s) = n_s \frac{a_s^3}{(\pi)^{3/2}} \exp\left(-a_s^2 v_s^2\right) \tag{C.24}$$

$$a_s^2 = \frac{m_s}{2T_s} \tag{C.25}$$

Here n_s are the number density of the scatterers.

$$x = a_s v \tag{C.26}$$

$$\int_{-\infty}^{\infty} \frac{e^{-y^2}}{|\boldsymbol{y} - \boldsymbol{x}|} d^3 \boldsymbol{y} = \frac{\pi^{3/2}}{x} erf(x) \tag{C.27}$$

The Rosenbluth potentials is given in the flowing form by use of the spherical symmetry in velocity space.

$$erf(x) = \frac{2}{\sqrt{\pi}} \int_0^x e^{-y^2} dy,$$

$$erf(x) = 1 \quad (x \to \infty), \quad erf(x) = \frac{2}{\sqrt{\pi}} x \quad (x \to 0) \tag{C.28}$$

Here erf(x) is an error function defined as

$$H(v) = Z_s^2 \left(\frac{m + m_s}{m_s}\right) a_s n_s \pi^{3/2} \frac{erf(x)}{x} \tag{C.29}$$

The G defined in (C.20) reduces

$$G(v) = \frac{Z_s^2 n_s}{2a_s} \left[\frac{d}{dx} erf(x) + \left(\frac{1}{x} + 2x\right) erf(x)\right] \tag{C.30}$$

It should be noted that since the Maxwell distribution is isotropic in velocity space and depend only on the absolute value of the velocity, H and G reduce to functions only on v as shown in (C.29) and (C.30).

If the distribution function of the scatterers is isotropic in the velocity space, H and G can be given only functions of v. Therefore, the following convenient relations can be obtained.

$$\frac{\partial H}{\partial v_k} = \frac{\partial v}{\partial v_k}\frac{\partial H}{\partial v} = \frac{dH}{dv}\frac{\partial v}{\partial v_k} \tag{C.31}$$

and

$$\frac{\partial^2 G}{\partial v_k \partial v_j} = \frac{\partial^2 G}{\partial v^2} = \frac{d^2 G}{dv^2} \tag{C.32}$$

The v derivative of H and G in (C.31) and (C.32) can be obtained explicitly as

$$\frac{d}{dx}\left(\frac{erf(x)}{x}\right) = -\frac{1}{x^2}erf(x) + \frac{2}{\sqrt{\pi}x}e^{-x^2} = 2\psi(x) \tag{C.33}$$

$$\frac{d^2}{dx^2}\left[\frac{derf(x)}{dx} + \left(\frac{1}{x} + 2x\right)erf(x)\right] = \frac{2}{x^3}\left[erf(x) - \frac{2x}{\sqrt{\pi}}e^{-x^2}\right] = \frac{4}{x}\psi(x) \tag{C.34}$$

Here $\Psi(x)$ is defined as

$$\psi(x) = \frac{1}{2x^2}\left[erf(x) - \frac{2x}{\sqrt{\pi}}e^{-x^2}\right] \tag{C.35}$$

References

1. L. Spitzer, R. Harm, Heat conduction of an electron gas. Phys. Rev. **89**, 977 (1953)
2. R.C. Malone, R.L. MaCrory, R.L. Morse, Indications of strongly flux-limited electron thermal conduction in laser-target experiments. Phys. Rev. Lett **34**, 721 (1975).: Craxton et al., Direct-drive inertial confinement fusion: A review, Phys. Plasmas 22, 110501, Chap. 11 (2015)
3. E.M. Eppeliene, R.W. Short, A practical nonlocal model for electron heat transport in laser plasmas. Phys. Fluids B **3**, 3092 (1991)
4. T.A. Mehlohrn, J.J. Duderstadt, A discrete ordinates solution of the Fokker-Planck equation characterizing charged particle transport. J. Comp. Phys. **38**, 86 (1980)
5. T.J.M. Boyd, J.J. Sanderson, *The Physics of Plasmas* (Cambridge University Press, 2003). Chap. 8
6. M.N. Rosenbluth, W.M. MacDonald, D.L. Judd, Fokker-Planck equation for an inverse-square force. Phys. Rev. **107**, 1 (1957)

7. A.R. Bell, R.G. Evans, D.J. Nicholas, Electron energy transport in steep temperature gradients in laser-produced plasmas. Phys. Rev. Lett. **46**, 243 (1981)

8. A.R. Bell, Non-Spitzer heat flow in a steadily ablating laser-produced plasma. Phys. Fluids **28**, 2007 (1985)

9. J.R. Albriton, Laser absorption and heat transport by non-Maxwell-Boltzmann electron distributions. Phys. Rev. Lett. **50**, 2078 (1983)

10. E.M. Epperlein, Kinetic theory of laser filamentation in plasmas. Phys. Rev. Letts **65**, 2145 (1990)

11. J.F. Luciani, P. Mora, J. Virmont, Nonlocal heat transport due to steep temperature gradients. Phys. Rev. Lett. **51**, 1664 (1983)

12. J.R. Albriton et al., Nonlocal electron heat transport by not quite Maxwell-Boltzmann distributions. Phys. Rev. Lett. **57**, 1887 (1986)

13. G. Gregori et al., Effect of nonlocal transport on heat-wave propagation. Phys. Rev. Lett. **92**, 205006 (2004)

14. V.Y. Bychenkov et al., Nonlocal electron transport in a plasma. Phys. Rev. Lett. **75**, 4405 (1995)

15. G.P. Schurtz, P.D. Nicolai, M. Busquet, A nonlocal electron conduction model for multidimensional radiation hydrodynamics codes. Phys. Plasmas **7**, 4238 (2000)

16. M. Sherlock, J.P. Brodrick, C.P. Ridgers, Testing nonlocal models of electron thermal conduction for magnetic and inertial confinement fusion applications. Phys. Plasmas **24**, 082706 (2017)

17. A. Marocchino et al., Comparison for non-local hydrodynamic thermal conduction models. Phys. Plasmas **20**, 022702 (2013)

18. J.P. Brodrick et al., Testing nonlocal models of electron thermal conduction for magnetic and inertial confinement fusion applications. Phys. Plasmas **24**, 092309 (2017)

19. P.D. Nicolai, J.-L.A. Feugeas, G.P. Shultz, A practical nonlocal model for heat transport in magnetized laser plasmas. Phys. Plasmas. **13**, 032701 (2006)

20. R.J. Henchen et al., Observation of nonlocal heat flux using Thomson scattering. Phys. Rev. Letts. **121**, 125001 (2018)

21. D.H. Froula, S.H. Glenzer, N.C. Luhmann Jr., J. Sheffield, *Plasma Scattering of Electromagnetic Radiation: Theory and Measurement Techniques*, 2nd edn. (Academic, Amsterdam, 2011).; S. H. Glenzer and R. Redmer, X-ray Thomson scattering in high energy density plasmas, Rev. Mod. Phys. 81, 1625 (2009)

22. K. Falk et al., Measurement of preheat due to nonlocal electron transport in warm dense matter. Phys. Rev. Lett. **120**, 025002 (2018)

Chapter 7
Opacity and Radiation Transport

Abstract When an intense laser is irradiated on medium and high Z materials, large amount of energy is converted to x-rays and transported as radiation in plasmas. The same kind of transport equation as the electrons should be solved for the radiation energy spectrum. The tuff issue for the case of non-local electron transport modeling was the inclusion of the effect of electric and magnetic fields. Instead, the photons can be assumed to travel with straight path, while the problem is physical modeling of opacity, especially when the plasma is partially ionized and line radiation transport is important. So, the modeling of spectral opacity and emissivity of partially ionized plasma becomes challenging. It has been studied for a long time in astrophysics regarding the evolution of stars etc. More challenging point in laser plasma is caused by the fact that the plasma is small but high-density, so that the laser plasma is optically thick in some case. With intense lasers, spectral opacity has been studied experimentally and opacity codes have been improved. Finally, neutrino transport in gravitationally-collapsing supernovae is also explained as a topic that the hydrodynamic instability is strongly affected by local and non-local transport by neutrino.

7.1   Radiation Transport

When an intense laser is irradiated on medium or high Z solid targets, substantial amount of absorbed plasma energy is converted to the energy of radiation. In general, the energy rage of such photons is up keV, since the plasma temperature becomes from eV to keV. The fraction of radiation increases as the increase of Z-number of the target material. Even for plastic targets, about 10% of the absorbed energy escaped from the plasma into vacuum as radiation. So, modeling radiation emission, absorption, and transport in laser plasma is very important for time evolution of hydrodynamics.

Let us see how radiation is important in laser-produced plasma. The bremsstrahlung emission from free electrons with ionization degree Z is given in (5.163). Evaluate the cooling time [s] of the plasma roughly as follows.

$$\frac{1}{\tau_c} \sim \frac{J}{n_e T_e} \sim 10^{-7} Z^2 n_i \frac{1}{\sqrt{T_{eV}}} \tag{7.1}$$

where the ion density n_i in cm^{-3} and electron temperature T_{eV} in eV unit. Inserting a typical values of laser plasma and targets, the local radiation cooling time by Bremsstrahlung emission is given as

$$\tau_c \sim 10^{-12} \frac{1}{Z^2} \left(\frac{n_i}{10^{20} cm^{-3}}\right)^{-1} \sqrt{\frac{T_e}{100 eV}} \quad [s] \tag{7.2}$$

This is very short time scale compared to that of hydrodynamics for laser produced plasma and indicates that the radiation transport should be modeled in hydrodynamic codes to evaluate the radiation cooling and heating in (2.108). In addition, radiation absorption and transport are found to be important in analyzing laser produce plasma dynamics.

Note that (7.1) is the cooling time of plasma due to Coulomb interaction of electrons with ions for the case where there is no absorption of radiation in the plasma. It is clear that even hydrogen plasma the cooling time is very short compared to the laser pulse of ns if a solid hydrogen is heated by laser. It is, then, important to solve radiation transport equation in plasma with appropriate opacity and emissivity as a function of radiation frequency. The opacity and emissivity by free electrons are already given in Chap. 5.10. We have to model the opacity and emissivity due to electron transition between bound states and bound and free states. For this purpose, atomic model is required as described in Chap. 5.

Let us consider a modeling of radiation transport with assumption that the spectral opacity and emissivity are given. The basic equation for the radiation transport is almost the same as Fokker-Planck equation except for several difference. It is given as a kinetic equation for radiation energy flux vector I^ν of frequency ν.

$$\frac{1}{c}\frac{\partial}{\partial t} I^\nu(t, \boldsymbol{r}, \boldsymbol{\Omega}) + \boldsymbol{\Omega} \cdot \nabla I^\nu(t, \boldsymbol{r}, \boldsymbol{\Omega}) = \eta^\nu(t, \boldsymbol{r}) - \chi^\nu(t, \boldsymbol{r}) I^\nu(t, \boldsymbol{r}, \boldsymbol{\Omega}) \tag{7.3}$$

In (7.3), $\boldsymbol{\Omega}$ is a direction of radiation propagation, and η^ν and χ^ν are spectral emissivity and opacity, respectively. In (7.3), it is also assumed that the photons propagate straight with the speed of light c and the effect of refraction is neglected, because the photon energy carrying most of energy is in the rage of 100 eV and the cut-off frequency of the photon is higher than the maximum electron density.

Note that it is very hard to solve (7.3) directly, because I^ν is a function of t, $\boldsymbol{r}$, and $\boldsymbol{\Omega}$, totally 6 dimensions. In addition, multi-group transport for photon energy should be solved. In what follows, consider the case of one-dimension in real space. And, let us assume that the photon angle distribution along the direction of non-uniformity is only a function of θ same as in Fig. 6.2. Then, in case of plane geometry (7.3) reduces to

$$\frac{1}{c}\frac{\partial}{\partial t}I^{\nu} + \mu\frac{\partial}{\partial x}I^{\nu} = \eta^{\nu} - \chi^{\nu}I^{\nu} \tag{7.4}$$

It is as follows in spherically symmetric geometry.

$$\frac{1}{c}\frac{\partial}{\partial t}I^{\nu} + \mu\frac{\partial}{\partial r}I^{\nu} + \frac{(1-\mu^2)}{r}\frac{\partial}{\partial \mu}I^{\nu} = \eta^{\nu} - \chi^{\nu}I^{\nu} \tag{7.5}$$

Let us assume that the radiation field is always in steady state for time-varying opacity and emissivity and time derivatives in (7.4) and (7.5) can be neglected. With a typical size of the laser plasma as L, the transit time of photons in plasma is $\Delta t = L/c$ and it is about 3 ps for L = 100 μm. It is a good approximation to neglect this time scale in the plasma produced by ns pulse lasers. Then, (7.4) is rewritten in the form.

$$\frac{d}{d\tau_{\nu}}I^{\nu} + I^{\nu} = S^{\nu} \tag{7.6}$$

where τ_{ν} is **optical depth** and defined as

$$d\tau_{\nu} = \frac{\chi^{\nu}}{\mu}dx = \chi^{\nu}dl \tag{7.7}$$

where dl is a path length of photon propagation. In (7.6), Sn is called **source function** defined as

$$S^{\nu} = \eta^{\nu}/\chi^{\nu} \tag{7.8}$$

It should be noted that the source function is Planck distribution if the plasma matter is in LTE condition, because I^{ν} in (7.3) should be Planck distribution at steady state and in uniform matter in LTE. In laser plasma, however, atomic state is not in LTE in general as discussed in Chap. 5.

It is easy to integrate (7.7) to obtain the solution for the case with a plane geometry with a finite plasma from x = 0 to x = d.

$$I^{\nu}(x) = e^{-\tau_{\nu}(x)}\left(I^{\nu}_{(0,\mu)} + \int_{0}^{x} e^{\tau_{\nu}}S^{\nu}_{(x)}d\tau_{\nu}\right) \qquad \text{for } \mu > 0$$

$$= e^{-\tau'_{\nu}(x)}\left(I^{\nu}_{(d,\mu)} + \int_{x}^{d} e^{\tau'_{\nu}}S^{\nu}_{(x)}d\tau'_{\nu}\right) \qquad \text{for } \mu < 0 \tag{7.9}$$

where τ_{ν} and τ'_{ν} are optical depths integrated as follows.

$$\tau_\nu = \frac{1}{\mu} \int_0^x \chi^\nu dx, \qquad \tau'_\nu = \frac{1}{|\mu|} \int_x^d \chi^\nu dx \qquad (7.10)$$

It is straightforward to extend the above calculation in solving the case of spherical geometry (7.5). Introducing the impact parameter "b" like Coulomb collision in spherical potential, it is easy to formulate the solution.

It is useful to show the angle distribution of radiation flux for the case when an intense laser is irradiated on a gold foil [1]. Based on average ion model to be shown in Chap. 8 spectral emissivity and opacity of gold plasma is calculated with collisional radiative equilibrium assumption for 100 energy group up to 3 keV. The plane target is divided to 120 groups. In Fig. 7.1, a typical angular distribution of spectral integrated radiation flux is shown for four different target positions with normalized intensity at each position. The positions are shown with Lagrangian mesh points. The point i = 120 is the ablating plasma front. Since the optical depth is large in (7.10) for oblique direction $\mu \to 0$, the radiation flux is larger.
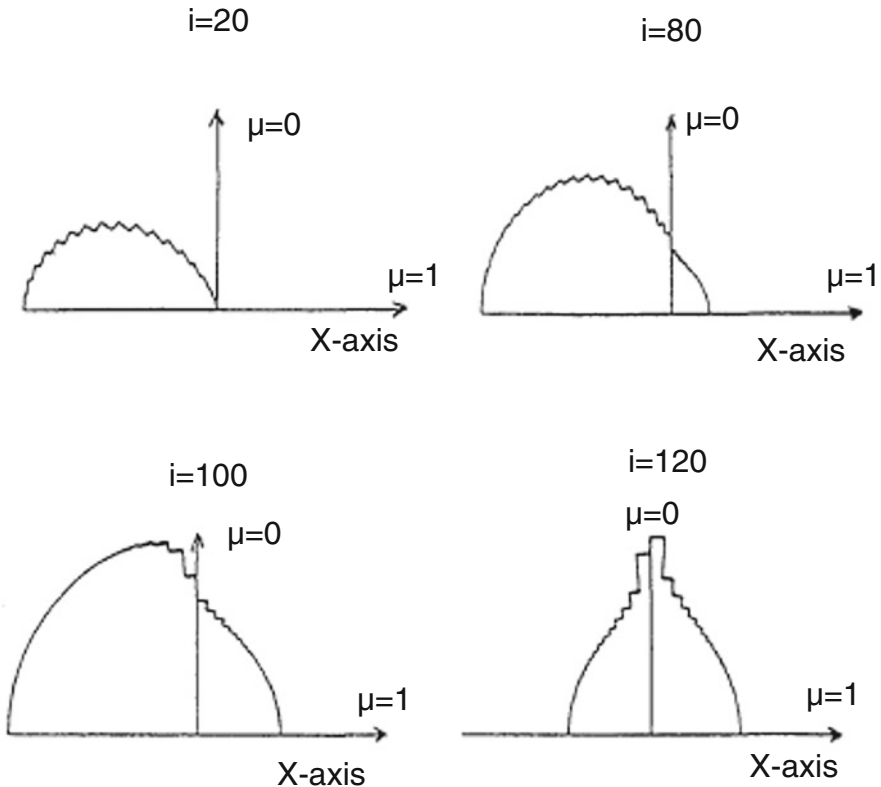
Fig. 7.1 Angular distribution of radiation intensity in gold plasma produced by irradiation of intense laser in plane geometry. The "i" is the mesh number of Lagrangian hydrodynamic simulation

At i = 100 and 80, the radiation is generated inside the heating region and propagates to the rear direction. The radiation generated laser irradiation is penetrated into deep region with a peaking to the normal direction, since the radiation going to the oblique direction is absorbed by the plasma. As the result, near the rear of the gold target i = 20, radiation flux remains around the normal direction.

Different from the electron transport, there is no angle scattering to make the distribution function relatively uniform. It is known that Thomson scattering makes the photon angular distribution uniform, while as is estimated in Vol. 1, it is almost negligibly small compared to the absorption. It is also known that photons are scattered by Compton scattering, while it becomes effective for the photon with energy comparable to mc^2 and it can be neglected. Of course, the emission term in (7.3) is uniform over the angle and it is expected that the photon distribution is rather uniform over angle for optically thick plasma, $\tau_\nu \gg 1$.

It is useful to compare the difference of transport kinetic between electrons and radiations.

1. The propagation velocity is different in electrons (v), while it is the same in radiation (c).
2. The electron orbit is modified by electric field (E), while radiation propagates straight.
3. Electron collision term is a smooth function of electron energy, while the opacity and emissivity vary over orders of magnitude by bound-bound transition effect.
4. Nonlocal transport of electrons approximately adopts Maxwell distribution as local function, while it is meaningless to assume Planck radiation in laser plasma, because the photon filed is far from LTE even the matter is near LTE.
5. The calculation of spectral opacity and emissivity is very hard and we need to use an approximated atomic model so that it is simple but appropriate to the problem.

7.2   Multi-group Diffusion Model for Radiation Transport

It is also fine to expand the angular distribution by Legendre function as in the case of electron transport. It is, however, noted that due to the lucky property of the collision operator we could eliminate the derivative to μ with use of the relation (6.52) and this is the reason why Legendre expansion is used for angular distribution. In the case of radiation, the angular distribution will be considered later after the formulation of angle moments. We derive the equations to the spectral radiation energy density E^ν and radiation flux density $\mathbf{F}^\nu$ as follows. Integrating (7.3) with the angle dΩ, we can obtain the equation for radiation energy density;

$$\frac{\partial}{\partial t}E^\nu + \nabla\mathbf{F}^\nu = 4\pi\eta^\nu - c\chi^\nu E^\nu \qquad (7.11)$$

where E^ν and $\mathbf{F}^\nu$ are defined as

$$E^\nu = \frac{1}{c} \int_{4\pi} I^\nu d\Omega \tag{7.12}$$

$$\boldsymbol{F}^\nu = \int_{4\pi} I^\nu \boldsymbol{\Omega} d\Omega \tag{7.13}$$

where $d\Omega = 2\pi sin\theta d\theta = 2\pi d\mu$. We need the equation to $\boldsymbol{F}^\nu$ and it is derived by integrating (7.3) after scalar product with $\boldsymbol{\Omega}$.

$$\frac{1}{c^2} \frac{\partial}{\partial t} \boldsymbol{F}^\nu + \nabla \boldsymbol{P}^\nu = -\chi^\nu \boldsymbol{F}^\nu \tag{7.14}$$

where we have new function $\boldsymbol{P}^\nu$ defined as

$$\boldsymbol{P}^\nu = \frac{1}{c} \int \boldsymbol{\Omega} \otimes \boldsymbol{\Omega} I^\nu d\Omega \tag{7.15}$$

This corresponds to radiation pressure tensor. In (7.14) the i-th component is

$$(\nabla \boldsymbol{P}^\nu)_i = \frac{\partial}{\partial x_k} P_{ki}^\nu, \quad P_{ki}^\nu = \frac{1}{c} \int \Omega_k \Omega_i I^\nu d\Omega \tag{7.16}$$

Here, let us introduce angular distribution of radiation intensity. For simplicity, consider the plasma is plane geometry and system is one dimension in x-direction in space. The angular distribution is only the function of θ and assume to be given as $\psi^\nu(\theta, x)$. The local radiation intensity is given as

$$I^\nu(t, x, \Omega) = I_0^\nu(t, x)\psi^\nu(\theta, x) \tag{7.17}$$

where $\psi^\nu(\theta, x)$ is normalized as

$$\int_{4\pi} \psi_{(\theta, x)}^\nu d\Omega = 4\pi, \qquad \int_{-1}^{1} \psi^\nu d\mu = 2 \tag{7.18}$$

Then, we obtain the following relation

$$E^\nu = \frac{4\pi}{c} I_0^\nu, \qquad F^\nu = \frac{c}{2} E^\nu \int_{-1}^{1} \psi^\nu \mu d\mu \tag{7.19}$$

The radiation pressure is given as

$$\boldsymbol{P}^\nu = \begin{pmatrix} P^\nu & 0 & 0 \\ 0 & P^\nu & 0 \\ 0 & 0 & P^\nu \end{pmatrix} + \frac{1}{2} \begin{pmatrix} 0 & 0 & 0 \\ 0 & E^\nu - 3P^\nu & 0 \\ 0 & 0 & E^\nu - 3P^\nu \end{pmatrix} \tag{7.20}$$

where the scalar pressure P^ν is related to the energy density in the form.

$$P^\nu = \frac{1}{2} E^\nu \int_{-1}^{1} \mu^2 \psi^\nu d\mu \tag{7.21}$$

Note that for isotropic distribution ($\psi^\nu = 1$), the relation $P^\nu = 1/3E^\nu$ is satisfied and the pressure becomes scalar in (7.20).

Consider a simple case of one-dimensional plane geometry in real space x. Then, all variables become scalar and the following two equations should be solved self-consistently for each group of radiation energy hν.

$$\frac{\partial}{\partial t} E^\nu + \frac{\partial}{\partial x} F^\nu = 4\pi\eta^\nu - c\chi^\nu E^\nu \tag{7.22}$$

$$\frac{1}{c^2} \frac{\partial}{\partial t} F^\nu + \frac{\partial}{\partial x} P^\nu = -\frac{\chi^\nu}{c} F^\nu \tag{7.23}$$

To solve (7.3) as precise as possible in general, we need to solve angular distribution with many freedoms, while we have remained only two lowest moment to μ (μ^0 and μ^1) as shown above. Historically, there have been a variety of trial on how to truncate the higher moment with a proper physical model.

If we have a certain relation between the second moment P^ν and E^ν and F^ν, it is possible to truncate the higher moment equations. For example, (7.21) has a form.

$$P^\nu = f^\nu E^\nu \tag{7.24}$$

where the coefficient f^ν is defined as

$$f^\nu = \frac{1}{2} \int_{-1}^{1} \mu^2 \psi^\nu d\mu \tag{7.25}$$

It is clear that the following relations should be satisfied at two extreme situations.

$$f^\nu = \begin{cases} 1/3 & \psi_\nu = 1 \\ 1 & \psi_\nu = 2\delta(\mu - 1) \end{cases} \tag{7.26}$$

In the diffusion limit as the case of Spitzer-Harm in the electron transport, the angular distribution for all frequency is approximated near unity, namely, $\psi_\nu \approx 1$. Then, the time derivative to F^ν in (7.13) is neglected and $f^\nu = 1/3$ is used to obtain the relation.

$$F^\nu = -\frac{c}{3\chi^\nu} \frac{\partial}{\partial x} E^\nu \tag{7.27}$$

Inserting (7.27) into (7.22), a diffusion type transport equation is obtained.

In the case of further ideal case such as optically thick plasmas, for example, the plasma inside the Sun, the radiation energy distribution is near Planckian. In such a case, solving (7.11) and (7.14) is relatively easy and they are altered to Planck

averaged equation with diffusion term for the radiation temperature T_r [2]. Then, the radiation transport is coupled to hydrodynamic equations relatively easily.

As seen in the electron transport, the diffusion approximation is valid only for the case where a typical scale of change L^ν of each frequency is much longer than the mean free path $l^\nu = 1/\chi^\nu$ in (7.27). Eddington has introduced so-called **Eddington coefficient** to limit the flux of diffusion with the form.

$$F^\nu = \frac{R^\nu}{1 + R^\nu} cE^\nu \tag{7.28}$$

$$R^\nu = \frac{l^\nu}{3} \left| \frac{1}{E^\nu} \frac{\partial}{\partial x} E^\nu \right| \tag{7.29}$$

where the sign of F^ν is of course the negative gradient direction of E^ν. Note that (7.28) is the same property as the flux limited diffusion of electron transport 7.53).

In laser-produced plasmas, it is not realistic in most of cases to assume the plasma is optically thick to all frequency and the radiation energy distribution is far from the Planckian distribution. Therefore, depending on a problem, we have to decide energy grouping and use or produce the spectral opacity and emissivity based on a certain atomic model and ionization model. This is a tuff job as partially discussed in Chap. 5 and will be discussed later about opacity calculation.

Modeling the coefficient f^ν was initially done by Eddington and his model is called **Eddington factor**. Now, it is widely used an improved Eddington factor based on maximum entropy method [3]. Defining R_1 as

$$R_1 = \left| \frac{F^\nu}{cE^\nu} \right| \tag{7.30}$$

Then, a computer fitted functional form of Eddington factor is shown in the for [3].

$$f^\nu = \frac{1}{3} + \frac{0, .01932R_1 + 0.2694R_1^2}{1 - 0.5953R_1 + 0.02625R_1^2} \tag{7.31}$$

It is clear that this Edington factor smoothly change from 1/3 ($R_1 = 0$) to 1 for ($R_1 = 1$). Since (7.31) varied as a function of R_1, it is also called a **variable Edington factor** and widely used in radiation transport simulations.

It is important to note how the Edington factor is calculated in multi-dimensional space. In Fig. 7.2, a simple example is shown in (x, y) two-dimensional space. In the original paper by Minerbo [3], the formulation is for general case to be used for three-dimensional case and it is derived that the Edington factor becomes the following matrix form for each frequency ν.

$$f = \frac{1}{2}\left(1 - \frac{m_2}{m_1}\right)I + \frac{1}{2}\left(3\frac{m_2}{m_1} - 1\right)\frac{F \otimes F}{|F|^2}, \tag{7.32}$$

Fig. 7.2 A computational grid in two-dimensional space and a local heat flux vector of the spectral radiation energy. The numbers identify each zone in the simulation meshes
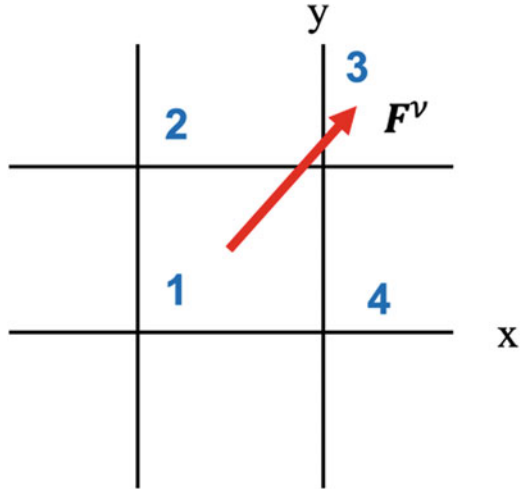
m_1 and m_2 are given in (2.10) in [3]. Note that f is in general a matrix, the first term in RHS in (7.32) is a diagonal term and the second term is a matrix. In Fig. 7.2, for two-dimension, the radiation energy in the numerical discrete zone 1 diffuses to the region 2 and 4 with the matrix in (7.24) with the matrix Edington factor in (7.32). Then, the energy diffuses to the zone 3 from zones 2 and 4. With such two-step diffusion, the energy in zone 1 is transferred to the zone 3 as we expected. For only the case of one-dimension (7.32) tends to a scalar as in (7.31).

7.3 Modeling Spectral Opacity and Emissivity

Radiation transport kinetics is relatively simple compared to the electron transport, because the photon velocity is the speed of light, its orbit is strait, and we can neglect the change of the photon energy by Compton scattering etc. in laser plasmas. However, another difficulty appears in calculating the spectral opacity and emissivity, η^ν and χ^ν. In the case of fully ionized plasma, both are continuous spectra and are given as Bremsstrahlung process shown in Chap. 5.

So, studying radiation phenomena in magnetic confinement fusion plasma, the fuel hydrogens can be assumed to be fully ionized and total emissivity provides the radiation loss from core plasma. This is also the case of very early universe where the space is full of only hydrogen and helium and the ionization and recombination is easy to be studied. It is known that after the recombination at about 400,000 years after the Big Bang, the photons decoupled with the atoms and its Planckian distribution is now observed as Cosmic Microwave Background (CMB) of T = 3 K. However, it is known that re-ionization occurs by ultra-violet photons generated by the first-generation stars after the gravitational attraction. The radiation from each
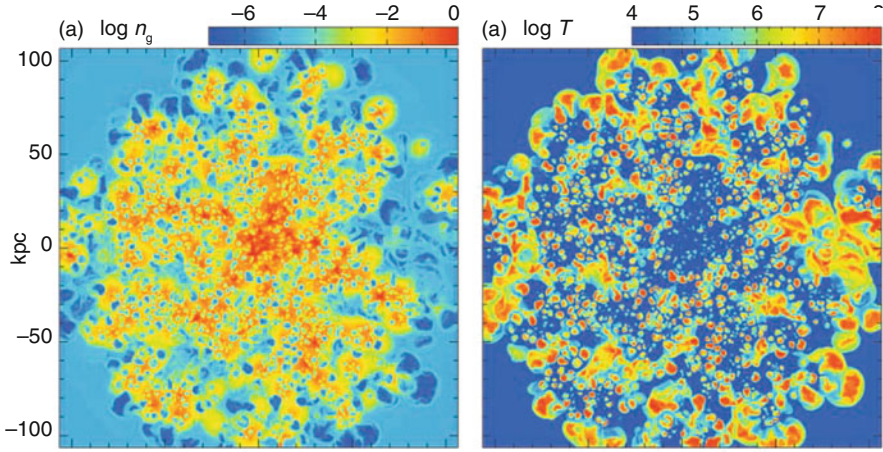
Fig. 7.3 Numerical simulation of radiation transport and star formation in a forming galaxy. Reprinted with permission from Ref. [4]. Copyright by American Astronomical Society

star perturbs the clouds to trigger the formation of new stars. In Fig. 7.3, numerical results at 50 million years on the multiple supernova explosions in a forming galaxy are shown, where (a) the density and (c) temperature distributions are shown over the space of 200 kpc (~0.6 million light years) [4]. Such simulation demands precise treatment of radiation kinetics over full angle and directions.

In solving photo-ionization process, the opacity and emissivity due to the electron transition between bound state to free state should be modeled in the opacity and emissivity. Both spectral properties are reflection of the cross sections discussed in Chap. 5.7. They are continuous spectrum with the edges by the ionization potential. Inclusion of spectral opacity and emissivity of bound-bound transitions is in general hard task. Since the laser can be irradiated any material, especially solid targets with relatively mid-Z to high-Z atoms. Even with intense lasers, they cannot be fully ionized abruptly and radiation transport in partially ionized plasma becomes important as energy transport non-locally.

In Fig. 7.4, emission spectrum is shown for carbon plasma at a temperature of 50 eV and density of 4.3×10^{-3} g/cm^3 [5]. The locations of 1s ionization thresholds of C III, C IV, and C V are indicated by arrows. It is clear that three different codes give almost the same spectra, while the line emissivity spectra are different. Fig. 7.4 suggests that the emitted line radiations are absorbed in plasma even relatively small plasma. If such line transport becomes important in a given plasma, we are demanded to model such line radiation with a reasonable model to grasp the essence of the physics.

As shown in Fig. 7.4, the ionization energies of 1s in different charge states make the emission edges at different energies of photons. Before calculating the spectral emissivity and opacity, we have to calculate the atomic data of all ionization states.
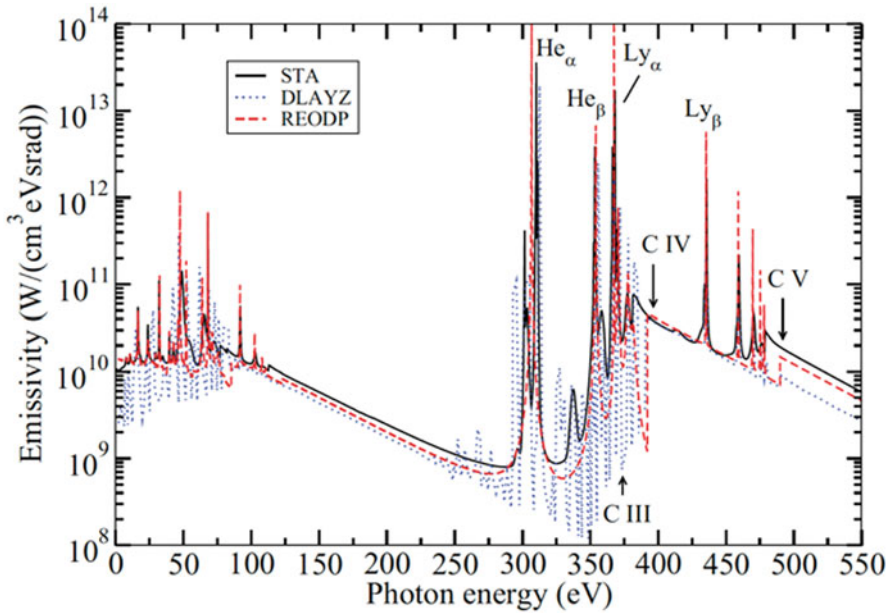
Fig. 7.4 Emission spectra from three different codes are shown for carbon plasma at a temperature of 50 eV and density of 4.3×10^{-3} g/cm^3. Reprint with permission from Ref. [5]. Copyright 1998 by American Physical Society

As shown in Chap. 5.3, there are several precise models to obtain the atomic data for any configurations. Ab initio calculation requires to obtain the distribution of atomic configurations for all charge states. It is clear to carry out such calculation itself very hard task. So, depending on the physics we want to study, some simplification is always recommended.

Assume that we are able to calculate the data base of all configurations of all charge state atoms. Then, we can use **Saha equation** in Sect. 5.2 to obtain the distribution of all configurations of ions in LTE plasma. In Fig. 7.5, the distribution of Si charge states is shown for the cases of temperatures of 100, 50, and 25 eV for silicon dioxide (triangles) and pure silicon (squares) [6]. The density of the plasma is 45 mg cm^{-3}. The ion charge state is calculated with Saha equation and the atomic states of partially ionized silicon ions are modeled with the **detail level accounting (DLA)** where the energy levels are calculated with Hartree-Hock method for many possible configurations as the data base for Saha equation. In Fig. 7.5, it is seen that about 4 ~ 5 different charge states coexist in a state. Most of them are expected to be at the ground state configurations, while the contribution by excited ions cannot be neglected.

In order to see how detail configuration should be included in calculating opacity from such plasma, the opacity spectrum is calculated by including the following configurations to each charge state ion.
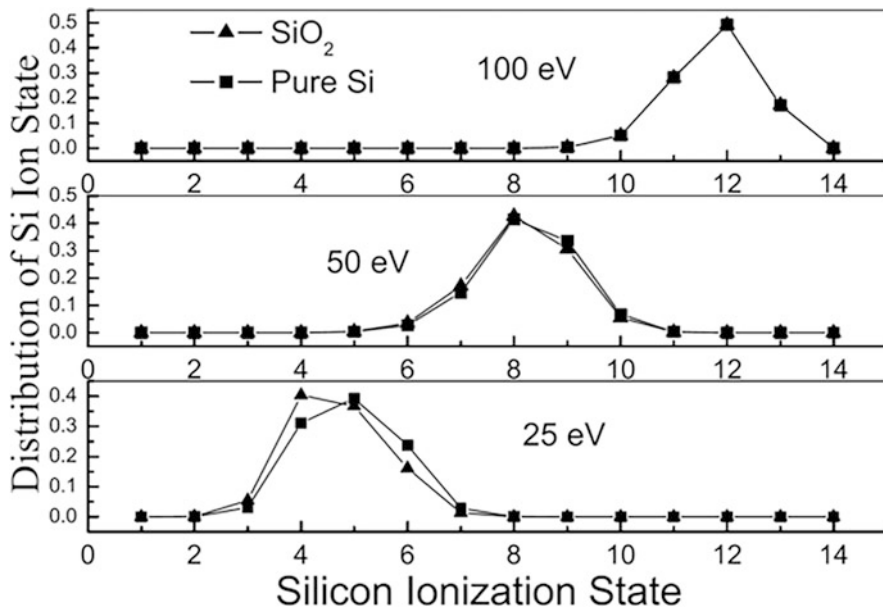
Fig. 7.5 The distribution of Si charge states is shown for the cases of temperatures of 100, 50, and 25 eV for silicon dioxide (triangles) and pure silicon (squares). Reprinted with permission from Ref. [6]. Copyright by American Astronomical Society

$$1s^2 2l^m, \quad 1s^2 2l^{m-1} n'l', \quad 1s^1 2l^{m+1}, \quad 1s^1 2l^m n'l',$$

where $n' < 8$, $l' < n'$ in the DLA calculation. In Fig. 7.6, the resultant opacity spectrum is plotted by varying the maximum of n'. The solid, dashed, dotted, and dash-dotted lines represent models with maximum principal quantum numbers of 8, 6, 4, and 2, respectively. All four models were calculated with the same temperature (56 eV) and density (10 mg/cm^3). The only difference is the number of levels used in each model. From this figure, it is clear that the absorption features become deeper with the inclusion of more levels. However, the absorption changes slightly with increase of n'. For example, in the calculations shown in Fig. 7.6 about 70% of the absorption is attributed to the level n' = 2, and 20% is due to the levels with n' = 3–6. The contributions to the absorption from levels $n' = 7$ and $n' = 8$ are only about 10%, and the contribution from level $n' = 8$ is even less than 5%.

In order to understand which transitions are contributing each spiky spectrum of opacity, consider the calculated transmission spectra of the silicon plasma under almost the same temperature and density as in Fig. 7.6 [7]. In Fig. 7.7, the spectra are shown for the higher photon energy so that the transition is simpler to be explained. The ionization state (Z*) distribution is like that for 50 eV in Fig. 7.5, and most abundant ions are Z* = 6 to 10, corresponding to O, N, C, B, and Be-like silicon, respectively. The transmission (opacity) spectrum due to each charge state silicon is shown in Fig. 7.7. The spectrum of "All ions" is the sum of all from each charge state ions, where the solid line is the theoretical and dotted line is the experimental data [7].

Fig. 7.6 The resultant opacity spectrum with DLA calculation is plotted by varying the maximum of n'. The solid, dashed, dotted, and dash-dotted lines represent models with maximum principal quantum numbers of 8, 6, 4, and 2, respectively. All four models were calculated with the same temperature (56 eV) and density (10 mg/cm^3). Reprint with permission from Ref. [7]. Copyright 1998 by American Institute of Physics
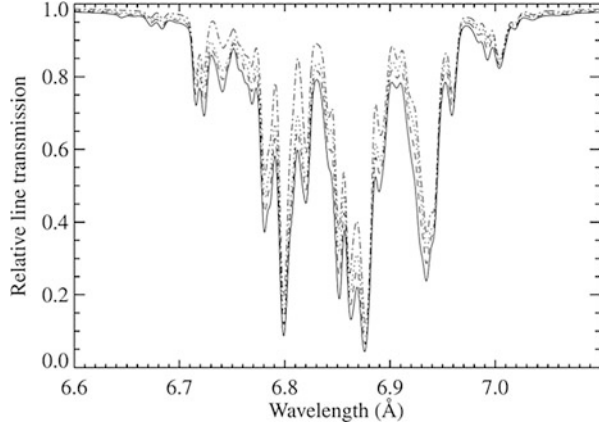
It is informative to know which transitions of ion configurations contribute to each of sharp opacity spectrum. It is seen that the Be, B, and C-like ions make two absorption peaks. It is found that the lower energy part is due to the inner-shell transition in n = 2, while the higher energy is the transition to higher n shell. For example, the dashed line of B-like is the result when the maximum configuration is n = 2 in DLA calculation. Let us see the transitions in B-like ion. The inner shell transition is from the ground state to the following transitions.

$$1s^2 2s^2 2p^1 \rightarrow 1s^2 2s^1 2p^2 \rightarrow 1s^2 2p^3$$
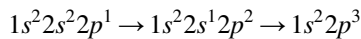
On the other hand, the higher energy peak in C-like ion is given by the transition.

$$1s^2 2s^2 2p^1 nl \rightarrow 1s^2 2s^1 2p^2 \; nl \rightarrow 1s^2 2p^3 nl$$
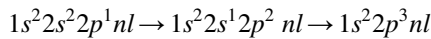
where $n \geq 3$ *and* $l < n$. Such an electron in (n, l) is called a satellite electron which contribute to a small modification of absorption spectrum from the above transition, consequently such transition energy is almost the same position as the lower one of B-like as in Fig. 7.7.

In calculating Figs. 7.6 and 7.7, LTE has been assumed to a uniform plasma heated by thermal radiation generated in a gold cavity heated by intense laser [6]. However, it is not in general to be valid to use LTE assumption, especially laser ablating plasma from medium and high Z targets. Then, some non-LTE distribution should be calculated for charge state distribution of plasma in calculating emissivity and opacity. A better model is **collisional radiative equilibrium** (CRE) model for the case of relatively small plasma characterized by the radiation field is much less compared to Planck radiation. Most of the opacity and emissivity of high-temperature laser plasma and other laboratory plasma probably calculated with charge distribution with CRE model.

Fig. 7.7 Transmission spectra due to different configuration of partially ionized ions. The solid lines are theoretical and the dotted line is experimental. Reprint with permission from Ref. [7]. Copyright 1998 by American Institute of Physics
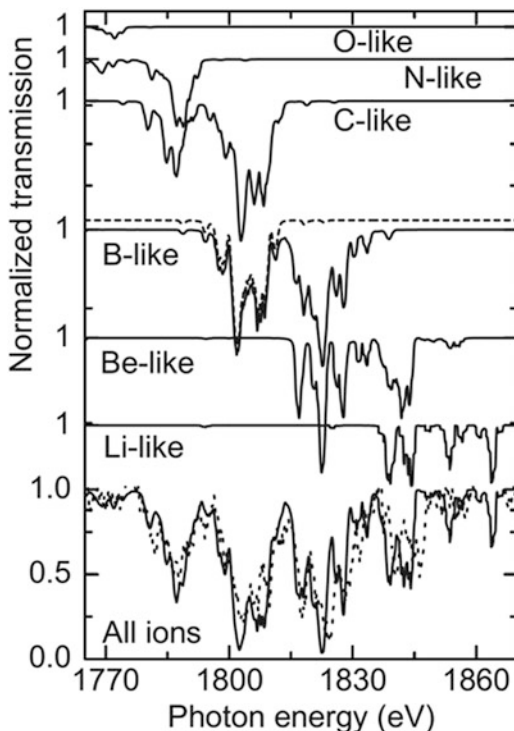
In dense plasmas produced by intense lasers, we can expect the line broadening [8]. the melting of nearby lines to make a kind of band structure. Then, spectral opacity looks easier to model in computer simulation of radiation transport. In Fig. 7.8, the emissivity of carbon plasma with T = 100 eV at five different densities is plotted [5]. It is clear that the lines become broader due to mainly **Stark broadening** effect. It is seen nearby lines melt to finally becomes broad spectrum seen for the density 22.4 g/cm^3. Note that the disappearance of the lines near the ionization edge, say near 500 eV as the density increases is due to the **pressure ionization** effect to be discussed in Chap. 8.

It is useful to see how bound-bound transition opacity is important in plasma even with small number of high-Z atoms. This is the case of the opacity inside the Sun. The sound velocity distribution of the plasma in the Sun has been studied precisely with the helioseismology and its theoretical study requires opacity and self-consistent equation of state [9]. For example, around the boundary of convection and radiation zones roughly characterized with T = 193 eV and $n_e = 10^{23}$ cm^{-3}, the opacity of partially ionized iron is plotted in Fig. 7.9 [10]. It is clear that photo-excitation (red) by bound-bound transition is dominant over 600–1000 eV where the radiation intensity is near peak $h\nu = 2.8$ T ~ 600 eV. In addition, it has fine structure spectra. The photo-ionization (green) by bound-free transition also contributes substantially. The inverse-Bremsstrahlung (blue) by free-free transition is relatively
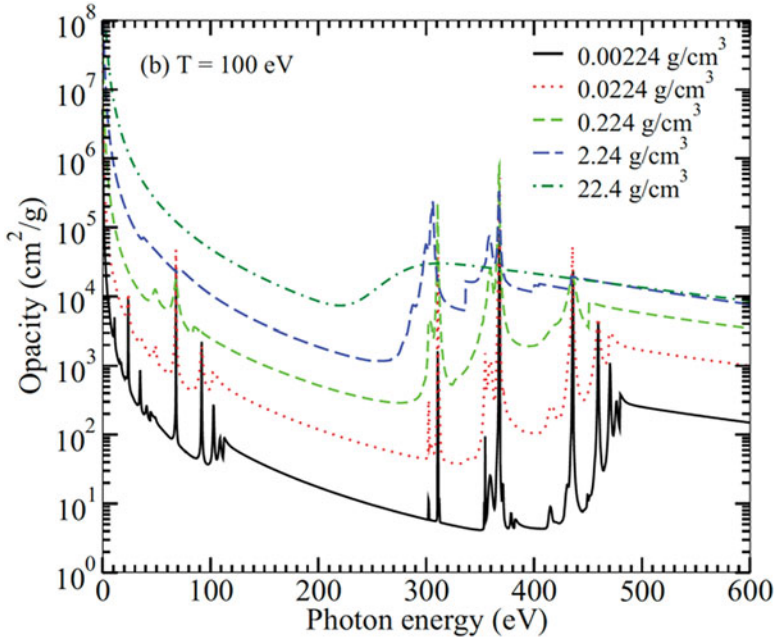
Fig. 7.8 Emission spectrum of carbon plasma at T-100 eV with five different densities are plotted. Reprint with permission from Ref. [5]. Copyright 1998 by American Physical Society

small. In general, we can neglect the effect of scattering (pink) in non-relativistic plasmas.

7.4 Opacity Experiments

Using intense laser or laser-produced or pulse-power produced thermal radiation, spectral transmission **opacity experiment** has been carried out and compared the data to computational results [11]. This is a clear validate and verification research on complicated opacity of high density and high temperature plasmas. Opacity experiment is important not only for radiation transport in laser produced plasma but also for a variety of topics in astrophysics, especially stellar evolutions [9]. Let us briefly see the present status of the opacity experiment and the code comparison.

The stellar interior is characterized with high-density and high-temperature and it is well known that the radiation transport is important to transfer the nuclear fusion energy near the center of a star toward the surface, such as the Sun. The structure of stars strongly depends on the atomic state of the plasma inside the stars. Historically, the opacity has been calculated theoretically, especially using computers. After the progress of intense laser and Z-pinch facilities, a variety of spectroscopic opacity
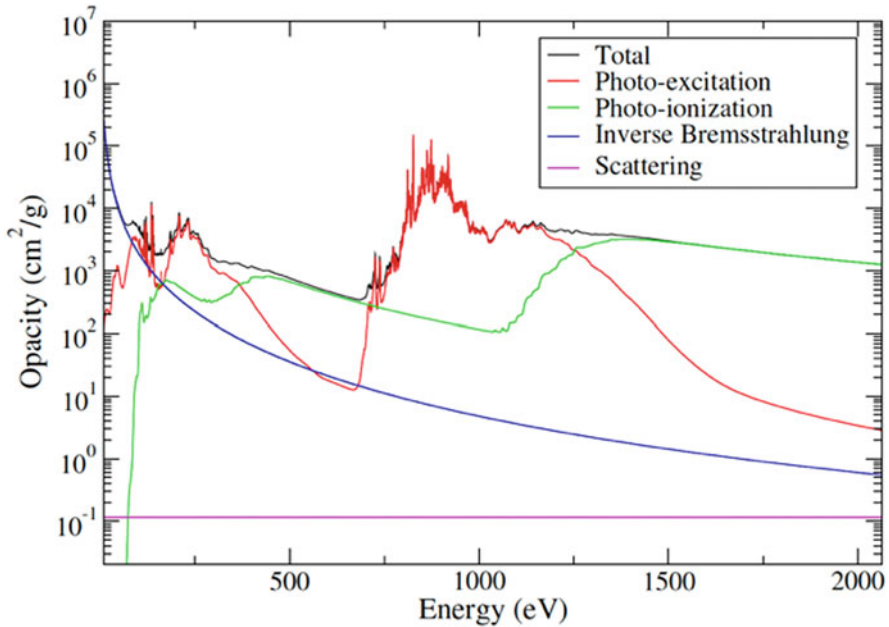
Fig. 7.9 The opacity of the plasma of the Sun around the boundary of convection and radiation zones roughly characterized with $T = 193$ eV and $n_e = 10^{23}$ cm^{-3} [10]

experiments have been performed [12, 13]. Inside of stars, heavy elements like iron are of very small fraction, while it contributes the opacity significantly.

Iron contributes significantly to solar opacity; the relatively large number of bound electrons makes iron more susceptible to model uncertainty of the standard solar model. It is found that opacity model predictions were lower than the opacity data when the temperatures and densities were increased to solar interior values [13].

Precise experiments with Z-facility have been done for Cr, Fe, and Ni to consider the atomic physics causing the lower opacity in Fe plasma [14]. In Fig. 7.10, the experiment setup is shown in (a). Almost Planck radiation of 350 eV radiation temperature is generated by Z-pinch (radiation source) and is irradiated to a plane target with aa half-site opacity sample covered by Be and CH optically thin solids shown in (b). The radiation spectra transmitted through both layers measured by crystal spectrometers are compared to obtain the transmission spectrum to reduce to the spectral opacity. In the experiments, the temperature and electron density measurements result the sample plasma being 180 eV and 3×10^{22} cm^{-3}. In (c), dominant electron configurations of Cr, Fe, and Ni at achieved conditions are shown. Vacancies in the shells are indicated by open circles.

In Fig. 7.11, the experimental opacity is compared to the calculation with OP opacity code. The OP opacity model is widely available and extensively used for solar or stellar models [14]. Comparisons between OP and the measured opacities provide essential clues for model refinements. It is clear in Fig. 7.11 that Cr and Ni opacities are well
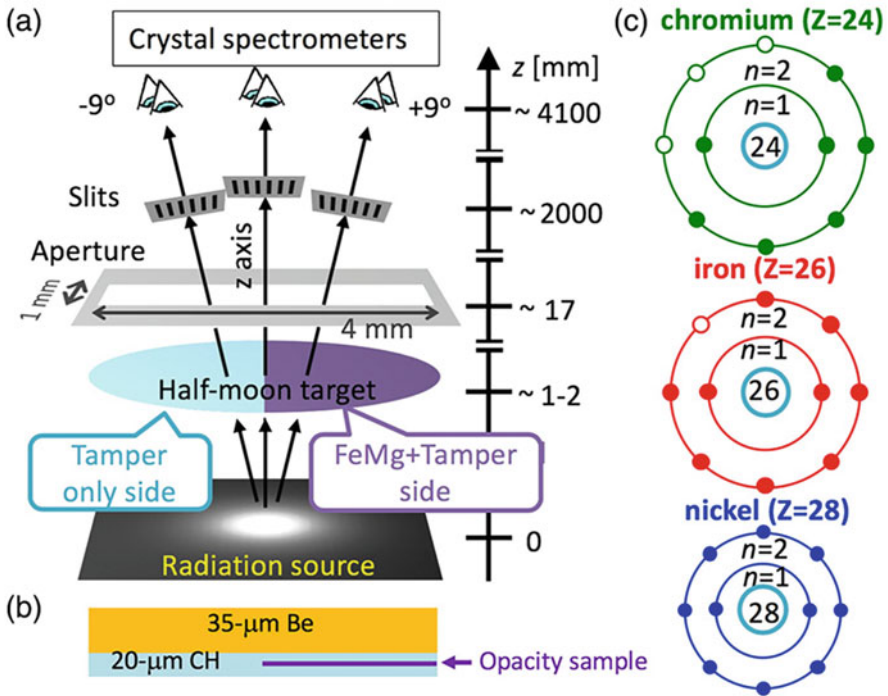
Fig. 7.10 The experimental set up to measure the opacity of chromium, iron, and nickel. Reprint with permission from Ref. [14]. Copyright 1998 by American Physical Society

modeled, while a large discrepancy is seen for Fe. It is about a factor two near 7–8 A region. As seen in Fig. 7.11 (c), Fe ion has open-shell and it is expected there are many lines absorption by the term splitting, which is probably not well included in OP code. The difference of the line positions and line shapes is studied in [14]. It is reported that the other modern atomic codes can improve such discrepancy.

The discrepancy of Fe opacity is very critical especially for astrophysics, because iron is rich abundance in the universe. The higher-than-predicted iron opacity data account for about half the increase needed to resolve the standard solar model discrepancy. This question is critical because, if the data are correct, our understanding of photon absorption in high-density matter must be revised. This would have far-reaching consequences for astrophysics and terrestrial science.

For example, a widely used method to estimate stellar ages depends on opacity, and opacity revisions will therefore lead to substantial changes in the age estimates. Furthermore, if solar composition, opacity, and helioseismology inferences are found to be consistent, the soundness of the **standard solar model** will be reinforced, but the composition and opacity used to model other Sun-like stars must be revised. On the other hand, if observations and solar model inputs cannot be reconciled, possible modifications to the solar model itself would be necessary. A
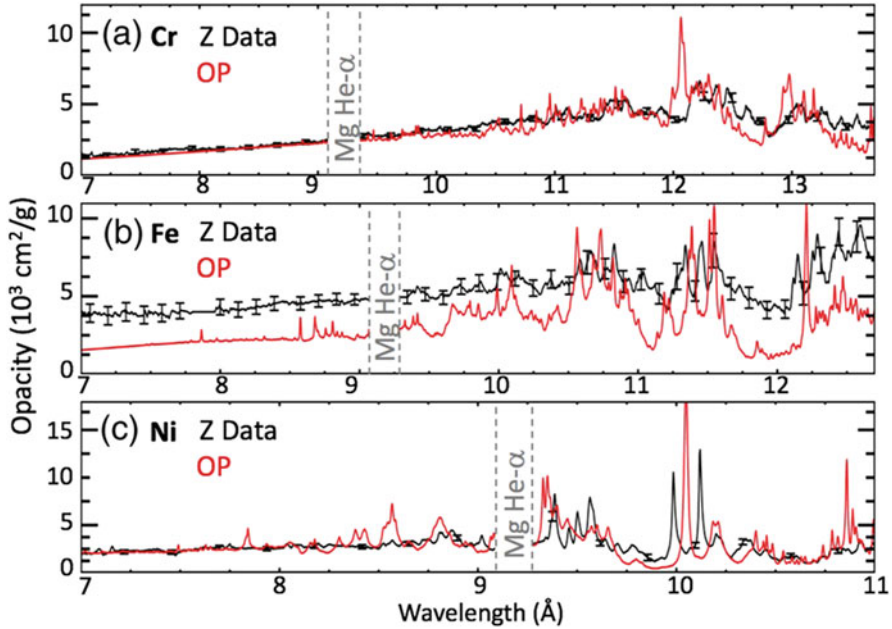
Fig. 7.11 Comparisons between OP opacity code and the measured opacities of three plasma samples. Reprint with permission from Ref. [14]. Copyright 1998 by American Physical Society

new theory, for example, has been proposed to explain the enhanced opacity by taking account of two-photon absorption effect [15].

Of course, the opacity is one of the most important elements to model stellar evolution. The consensus model for a classical nova invokes a binary star system, with accretion from a main-sequence star or evolved giant onto a white dwarf (WD) due to Roche lobe overflow. As hydrogen-rich material is transferred to the WD through an accretion disk, the temperature at the base of the accreted envelope rises until it reaches $\sim 2 \times 10^7$ K, at which point the accreted fuel undergoes fusion via the CNO cycle. A convective zone is born and grows until an optically thick wind is launched, giving rise to the observed classical nova. The launching of the optically thick wind is primarily due to the presence of the iron opacity bump. Accurate opacity of iron is essential to compare observation light cure to a theoretical model [16].

7.5   Radiation Hydrodynamics

The hydrodynamic description of the system consisting of huge number of particles is widely used in many cases from design of air-conditioning to astrophysics, even in cosmology. In laser produced plasmas, they are described in general with two-temperature, one-fluid model as shown in Chap. 2.6. For the fluids being in

LTE with the density ρ, velocity $\mathbf{u}$, and internal energies of the ion fluid ε_i and electron fluid ε_e, (2.105, 2.106, 2.107, and 2.108) should be solved in time and space, where the energy flows to the ion and electrons local fluids are given.

It is convenient to show (7.22) and (7.23) in Lagrangian frame moving with the plasma fluid. By use of (2.105) and (2.106), it is easy to show the equations of radiation in the fluid frame,

$$\rho \frac{d}{dt}\left(\frac{E^\nu}{\rho}\right) + \nabla(\boldsymbol{F}^\nu - \boldsymbol{u}E^\nu) = 4\pi\eta^\nu - c\chi^\nu E^\nu \tag{7.33}$$

$$\frac{\rho}{c}\frac{d}{dt}\left(\frac{\boldsymbol{F}^\nu}{\rho}\right) + \nabla\left(c\mathrm{P}^\nu - \frac{\boldsymbol{u}}{c}\otimes\boldsymbol{F}^\nu\right) = -\chi^\nu \boldsymbol{F}^\nu \tag{7.34}$$

Note that the right-hand-sides in (7.33) and (7.34) are contribution via the coupling with the plasma fluid and they will couple with the equations of energy and momentum of plasma fluid, respectively.

From (2.105), (2.106) and (7.34), the following equation of fluid motion is obtained.

$$\frac{\partial}{\partial t}(\rho\boldsymbol{u}) + \nabla(\rho\boldsymbol{u}\otimes\boldsymbol{u} + \mathrm{P}) = \boldsymbol{S}_r^m \tag{7.35}$$

where $\boldsymbol{S}_r^m$ is the momentum change of the fluid due to the absorption of radiation added to (2.106) as the coupling term in (7.34). The form of $\boldsymbol{S}_r^m$ is derived from 7.34) as

$$\boldsymbol{S}_r^m = \frac{1}{c}\int_0^\infty \chi^\nu \boldsymbol{F}^\nu d\nu \tag{7.36}$$

Note that no momentum change appears due to the radiation emission, because it is assumed to be isotropic. The energy conservation relation to the electron fluid is also obtained after simple mathematics and it is found to be

$$\frac{\partial}{\partial t}\left(\rho\varepsilon_e + \frac{1}{2}\rho u^2\right) + \nabla\left[\rho\boldsymbol{u}\left(\varepsilon_e + \frac{P}{\rho} + \frac{1}{2}u^2\right)\right] = S_r^\varepsilon \tag{7.37}$$

where S_r^ε is the cooling and heating terms due to the radiation. The form of S_r^ε is given from (7.33) as

$$S_r^\varepsilon = \int_0^\infty (c\chi^\nu E^\nu - 4\pi\eta^\nu)d\nu \tag{7.38}$$

When the fluid and radiation are treated as one system, the total momentum and energy conservation relations are obtained from (7.34) and (7.35), and (7.33) and (7.37) as follows, respectively.

$$\frac{\partial}{\partial t}\left(\rho\boldsymbol{u} + \frac{\boldsymbol{F}^R}{c^2}\right) + \nabla\left(\rho\boldsymbol{u}\otimes\boldsymbol{u} + \mathrm{P} + \boldsymbol{P}^{\mathrm{R}}\right) = 0 \qquad (7.39)$$

$$\frac{\partial}{\partial t}\left(\rho\varepsilon_e + \frac{1}{2}\rho u^2 + E^R\right) + \nabla\left[\rho\boldsymbol{u}\left(\varepsilon_e + \frac{P}{\rho} + \frac{1}{2}u^2\right) + \boldsymbol{F}^R + \boldsymbol{q}^e\right] = 0 \qquad (7.40)$$

where E^R, $\boldsymbol{F}^R$, and $\boldsymbol{P}^R$ are spectrum integrated total values of E^ν, $\boldsymbol{F}^\nu$, and $\boldsymbol{P}^\nu$, respectively. For simplicity, the last two terms in RHS in (2.108) are neglected in (7.40). The electron heat flux $\boldsymbol{q}^e$ has been discussed in Chap. 6 and the nonlocal and multigroup flux of SNB given in (6.91) is recommended to be used to evaluate the electron hear flux in a better way, not like Spitzer-Harm diffusion shown in (2.109).

Let us evaluate how important the four radiation terms in (7.39) and (7.40) in the case of laser-produced plasmas. In evaluating each radiation term, it is assumed that the radiation heat flux is important to affect the hydrodynamic energy flux and the following rough relation is applied.

$$F^R \sim O(uP), \quad E^R \sim O\left(\frac{F^R}{c}\right), \quad P^r \sim O\left(E^R\right), \qquad (7.41)$$

where "O" means the order of magnitude. Compare the radiation term to the fluid term in each parenthesis.

$$\frac{F^R}{c^2\rho u} \sim O\left(\frac{u^2}{c^2}\right), \quad \frac{P^R}{P} \sim O\left(\frac{u}{c}\right), \quad \frac{E^R}{\rho\varepsilon_e} \sim O\left(\frac{u}{c}\right) \qquad (7.42)$$

As far as the plasma is non-relativistic fluid, all radiation terms except the radiation heat flux in the energy flux density in (7.40) can be neglected in general.

It is interesting to note the case where the plasma fluid is not non-relativistic while another radiation term(s) become important. For example, inside stars the radiation mean free path is very short and the radiation is almost Planckian distribution. Since the radiation pressure and energy density is proportional to T^4 while the those of plasma particles are in proportion to T, there is critical temperature to a given density that the radiation pressure is comparable to the pressure by the matter. In such a case, we have to keep all radiation terms in radiation hydrodynamic equations. The reason why the above order estimate was wrong inside the stars is as follows. Inside the stars, almost hydrostatic force balance is a good assumption and the assumption $F^R \sim O(uP)$ in (7.41) is not established. The order estimate in such a case is all O(1) in (7.42). Finally noted that the electron heat transport can be neglected in general

inside stars and it is easy to show because the scale of temperature change is much longer than the charged particle means free paths.

7.5.1   Radiation Pressure

In the case of direct laser irradiation to relatively low Z target, the radiation field is far from LTE and the radiation pressure can be neglected. In the case of high-Z target irradiation or radiation confinement by the hohlraum cavity target, it is not so clear if this condition is valid. Evaluate the relation between pressures by matter and radiation within the assumption that radiation temperature is equal to that of the matter. Radiation energy flux S_P and radiation pressure P_P are given as

$$S_P = \sigma T^4 = 1. \times 10^5 T_{eV}^4 \; \left[W/cm^2 \right]$$
$$P_P = \frac{4}{3c} \sigma T^4 = 4.6 \times 10^{-6} T_{eV}^4 \; \left[J/cm^3 \right] \tag{7.43}$$

As already evaluated, about 300 eV Planck radiation gives the flux of 10^{15} W/cm^2. Then, the radiation pressure P_P is about 0.7 Mbar, which is much less than the material pressure as seen in Chap. 3.

It is of course, radiation pressure becomes larger than the plasma pressure for extremely high temperature or low density. Simple evaluation for the balance is

$$2n_e T = \frac{4}{3c} \sigma T^4 \tag{7.44}$$

For the temperature higher as shown in the relation

$$T_{eV} > 3.8 \times 10^{-5} n_e^{1/3}, \tag{7.45}$$

the Planck radiation pressure is higher than the plasma pressure and radiation hydrodynamics is governed not only the radiation energy flux, but also by the radiation pressure to the matters.

In the evolution of stars, there are cases where high temperature Planck radiation propagates to the surface and the atmospheric matters are blown off as stellar wind. This depends on the metallicity of the star and the mass of the stars. It is useful to note that fate of stars as functions of their initial mass and metallicity. Heger et al. has carried out comprehensive and systematic radiation hydrodynamic simulations including the nuclear reactions [17]. In the abstract, the authors wrote as

> How massive stars die—what sort of explosion and remnant each produces—depends chiefly on the masses of their helium cores and hydrogen envelopes at death. For single stars, stellar winds are the only means of mass loss, and these are a function of the metallicity of the star. We discuss how metallicity, and a simplified prescription for its effect on mass loss, affects the evolution and final fate of massive stars. We map, as a function of mass and

metallicity, where black holes and neutron stars are likely to form and where different types of supernovae are produced. Integrating over an initial mass function, we derive the relative populations as a function of metallicity.

One result is shown in Fig. 7.12, where the horizontal axis is the initial mass of single star divided by the mass of the sun and the vertical axis is the metallicity [17]. The metallicity means how much elements heavier than hydrogen and helium exists. The "metal free" is just after the big bang and the gas is made of only hydrogen and helium, while "abundant solar" is the metal distribution inside the sun. It can be regarded the metallicity means the time evolution of Universe. In Fig. 7.12 the final fate of the stars is shown. The starts with mass more than about ten finally explode as supernova type II (core collapse type). Note that the green line shows the boundary where the hydrogen envelope is blowen off by the strong radiation from the inside, radiation pressure and momentum deposition by Thomson scattering. This is the reason why there is the maximum of the mass of stars about 40 observed in our galaxy as seen in Fig. 7.12 as the green boundary.

The radiation pressure and energy transport are critical physics to control the time evolution of brightness of novae [18]. Because an abrupt ignition of nuclear fusion happens on the surface of white dwarfs due to the increase of temperature by accretion, the surface gas is pushed by the radiation and it is observed that the object suddenly starts to increase the light and finally decays. This is called "nova light curve" and its observation data is analyzed with radiation hydrodynamic simulation code.

7.6   Neutrino Transport in Core-Collapse Supernovae

The kinetics of neutrino transport in core-collapse supernova explosion is the most challenging subject as radiation transport numeric. Neutrino propagates at the speed of light as x-rays in plasma, however, the opacity is simpler than the case of photons. The structure of basic equation is the same as (7.3) and the cross section of the matter interaction $\sigma_\nu(\varepsilon_\nu)$ is relatively simple as given to be

$$\sigma_\nu(\varepsilon_\nu) \sim \left(G_F'\right)^2 \varepsilon_\nu^2$$

$$G_F' = \frac{G_F}{(\hbar c)^3} = 5.3 \times 10^{-44} \ \left[cm^2/MeV\right] \tag{7.46}$$

where G_F is Fermi constant. Since the supernova explosion, the most energetic neutrino has the energy of about 10 MeV and the typical absorption cross section $\sigma_\nu \sim 5 \times 10^{-42} \ cm^2$. This extremely small value is due to that fact that the weak interaction force acts by exchange of heavy W and Z-bosons. Before going to discuss the role of neutrino heating, let us estimate the stopping length of neutrino. The column density of neutrino stopping $(\rho l)_\nu$ is roughly evaluated to be
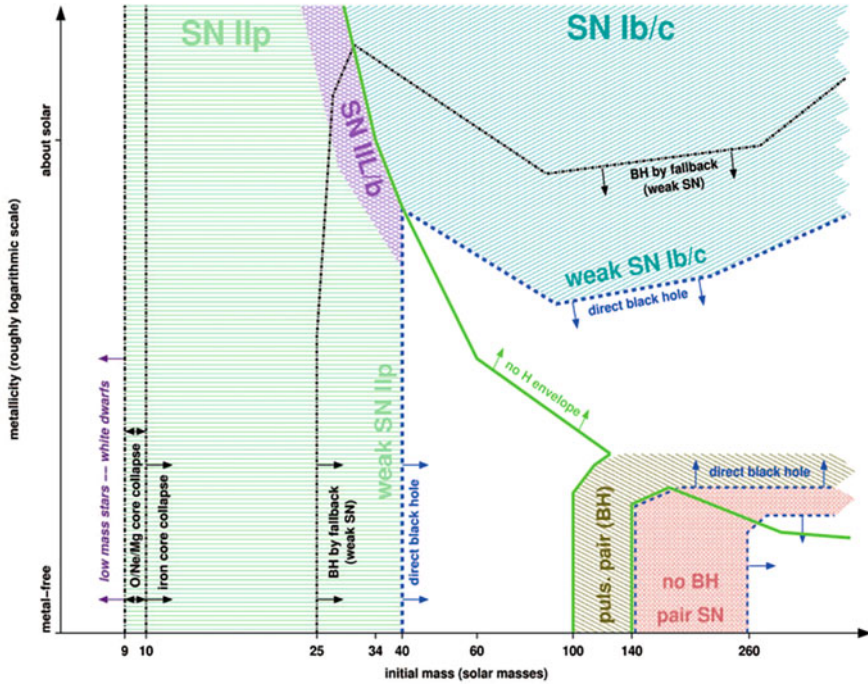
Fig. 7.12 The metallicity dependence of the evolution of stars. The horizontal axis is the initial mass of single star divided by the mass of the sun and the vertical axis is the metallicity. Reprinted with permission from Ref. [17]. Copyright by American Astronomical Society

$$(\rho l)_\nu \sim \frac{m_p}{\sigma_\nu} \sim 4 \times 10^{18} \; \left[g/cm^2\right] \tag{7.47}$$

As we see below, the size of collapsing core is about 100 km, consequently the matter density is of the order of 10^{10} g/cm^3. It is clear that the earth is transparent to neutrino, because the column density of the earth is about 6000 km $\times$ 5.5 g/cm^3 $\sim$4 $\times$ 10^8 [g/cm^2].

It is well-known that the total energy of the neutrino produced by the core-collapse is 10^{53} erg, about 5% of $Mc^2 = 1.8 \times 10^{54}$ *erg* (M: solar mass). Then, only 1% of neutrino energy is absorbed in the core to energize the shock propagation toward the massive star surface. Therefore, it requires very precise analysis of neutrino transport.

Just before the observation of SN1987A, core-collapse supernova explosion has been simulated by Wilson and discussed with Bethe [19]. They obtained the flow diagram in 1-D spherical geometry as shown in Fig. 7.13. The time is second and radius cm units. The iron core of about 1000 km collapses at t = 0 due to the iron dissociation to 13 alpha particles. This nuclear process energy absorption and the pressure drops abruptly to form a proto-neutron star (PNS) of about 10 km. In
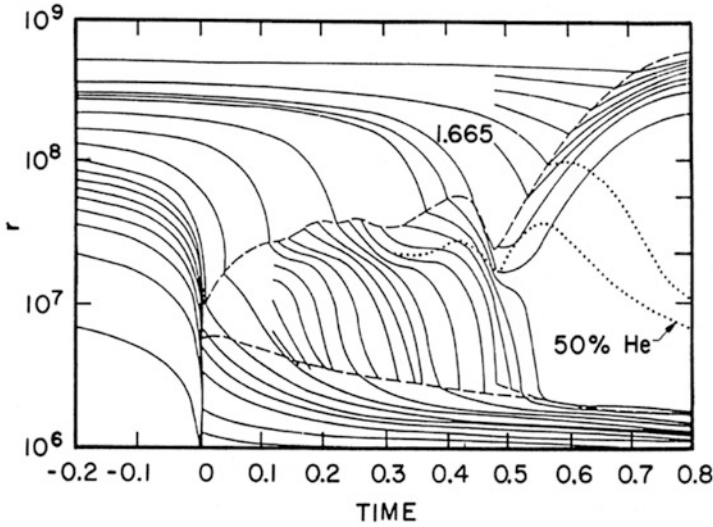
Fig. 7.13 The flow diagram in radius r and time is plotted for gravitational collapsing supernova explosion. The solid lines are flow line indicating time evolution of Lagrangian numerical meshes; the lower dashed curve is the radius of neutrino sphere and the upper one is the out-going shock wave. Reprinted with permission from Ref. [17]. Copyright by American Astronomical Society

Fig. 7.13, the solid lines are flow line indicating time evolution of Lagrangian numerical meshes; the lower dashed curve is the radius of neutrino sphere and the upper one is the out-going shock wave. In the simulation, around 0.48 [s] the **quasi-vacuum region** starts to expand due to the neutrino heating and it is concluded that the shock wave keeps to propagate outward also with neutrino heating. However, it is clear that the quasi-vacuum region accelerates the falling matter outward against the strong gravity is only possible in the constrain of one-dimensional assumption. It is unstable to hydrodynamic instability.

Two years later from the paper of Ref. [19], SN1987A explosion was observed。 The light of the explosion was a physical event for 400 years as a supernova visible to the naked eye. After intensive research on the physics of SN1987A, precise simulations have clarified that two additional physics are critical to modeling supernova explosion. One is the weakening of the shock wave via the iron dissociation at the shock front. Modern simulation has concluded that core-collapse supernova never explodes within one-dimensional geometry; this is due to the fact that the shock wave is weakened by the endothermic effect by the dissociation of falling iron and disappears. The other is the reheating of the core and falling matter via multi-dimensional material mixing is essential to enhance the heating rate by neutrino. Therefore, detail neutrino transport kinetics is required to be simulated in multi-dimensional hydrodynamics.

Typical difficulty of the neutrino transport is schematically shown in Fig. 7.14. Neutrino is generated in proto-neutron-star, where the neutrino is optically thick to

Fig. 7.14 Local to non-local transport model is essential to study the explosion simulation of gravitationally collapsing supernova explosion [Courtesy of K. Sumiyoshi]
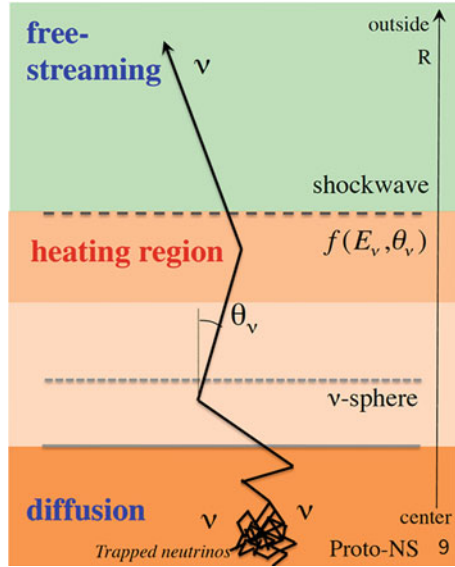
diffuse out from the surface and small fraction of energy of about 1% of the total energy is absorbed by the matter to keep and revival the shock wave to propagate outward. The shock wave is important to disassemble the heavy elements toward the space and only the neutron star remains. The kinetics to continue from optically thick to thin region is challenging subject.

The basic equation of neutrino transport is the same as (7.3) with scattering term on RHS. Therefore, the same modeling as in Chap. 7.2 is shown, for example, in [20]. In [20], three different Edington factors are compared, including (7.32) by Minerbo. The transport kinetics of such discrete ordinate method is compared to that with Monte-Carlo method and it is concluded that a good agreement has been obtained in 1-D and 2-D background hydrodynamic structures. Up to now, it is almost concluded that 1-D never explodes and some of 2-D and 3-D simulations gives explosion, but it is not always.

In order to try to solve Boltzmann equation as precise as possible and carry out simulation with the world-class supercomputer, numerical scheme to solve directly the Boltzmann equation to the neutrino energy distribution function in 3-D geometry in space and neutrino angle has been developed and tested in given static fluid structures [21]. The simulation code has been up-graded to run in the K-computer for carrying out self-consistent 3-D radiation hydrodynamic simulation of core-collapse supernova explosion [22].

One case of core-collapse supernova 3-D simulation has been carried out and reported in [22]. The snap shot of t = 10 ms after the collapse is plotted in Fig. 7.15 [22]. The physical quantities in the iso-surfaces of cut away above the equatorial plane in 3-D are shown. The left is contours of entropy (∼ temperature) and the arrows with color are average velocities. The orange sphere region is shock heated
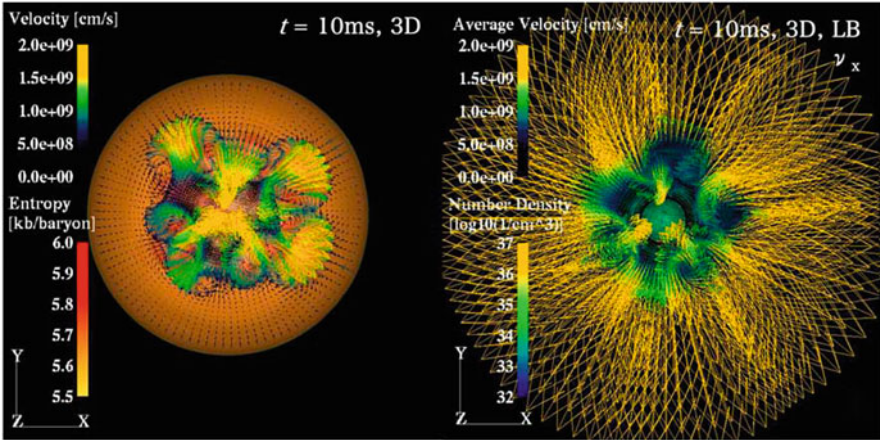
Fig. 7.15 Sophisticated neutrino transport is coupled with three-dimensional hydrodynamic simulation to clarify the physics of supernova explosion. Reprinted with permission from Ref. [22]. Copyright by American Astronomical Society

one and the color boundary is the position of shock wave. Note that fluid explosion velocity reaches almost 10% of the speed of light. The right figure shows a neutrino density contours overlapped with the velocity vectors of local neutrino averaged over the angle; namely, the total neutrino flux velocity of $\langle F/E \rangle$. It is clear that this value ranges from 0 to c place to place. This simulation is not enough to identify the explosion scenario in three-dimensional with precise solver of Boltzmann equation to neutrino. It is expected to clarify the physical condition under which the core-collapse supernova explodes or not by use of the next generation supercomputers. The readers interested in such challenging physics due to neutrino and hydrodynamics can know more in [23] and [24].

References

1. H. Takabe, K. Nishikawa, Computational model for non-LTE atomic process in laser produced plasmas. J. Quanr. Specrrosc. Rad. Transf. **51**, 379–395 (1994)
2. Ya B. Zel'dovich, Yu P. Raiser. Physics of Shock Waves and High-Temperature Hydrodynamic Phenomena, vols. 1 & 2 (Academic Press, New York, 1966 and 67), Chap. 2
3. G.N. Minerbo, Maximum entropy Edington factors. J. Quant. Spectrosc. Radiat. Transf. **20**, 541–545 (1978)
4. M. Mori, M. Umemura, A. Ferrara, The nature of Lya Blobs: Supernova-dominated primordial galaxies. Astrophys. J. **613**, L97–L100 (2004)
5. T.-G. Lee, M. Busquet, et al., Radiative and atomic properties of C and CH plasmas in the warm-dense-matter regime. Phys. Rev. E **98**, 043203 (2018)
6. H.G. Wei et al., Opacity studies of silicon in radiatively heated plasma. Astrophys. J. **683**, 577–583 (2008)

7. Q.-L. Dong et al., Characteristic measurements of silicon dioxide aerogel plasmas generated in a Planckian radiation environment. Phys. Plasmas **17**, 012701 (2010)
8. D. Salzmann, *Atomic Physics in Hot Plasmas* (Oxford University Press, 1998)., Chap. 7
9. N. Vinyoles et al., A new generation of standard solar models. Astrophys. J. **835**, 202 (16pp) (2017)
10. J.C. Pain, F. Gilleron, M. Comet, Detailed opacity calculations for astrophysical applications. MPDI Atoms **5**, 22 (2017). https://doi.org/10.3390/atoms5020022
11. E.S. Dodd et al., Hohlraum modeling for opacity experiments on the national ignition facility. Phys. Plasmas **25**, 063301 (2018)
12. D.B. Sinars et al., Review of pulsed power-driven high energy density physics research on Z at Sandia. Phys. Plasmas **27**, 070501 (2020)
13. J.E. Bailey et al., A higher-than-predicted measurement of iron opacity at solar interior temperatures. Nature **517**, 56 (2015)
14. T. Nagayama, Systematic study of L-Shell opacity at stellar interior temperatures. Phys. Rev. Letts. **122**, 235001 (2019)
15. R.M. More, S.B. Hansen, T. Nagayama, Opacity from two-photon processes. High Energy Density Phys. **24**, 44 (2017)
16. J.R. Lee et al., A search for pulsations in the optical light curve of the Nova ASASSN-17hx. Astrophys J **869**, 7 (8pp) (2018)
17. A. Heger et al., How massive single stars end their life. Astrophys. J. **591**, 288–300 (2003)
18. M. Kato, I. Hachisu, Optically thick winds in nova outbursts. Astrophys. J. **437**, 802 (1994)
19. H.A. Bethe, J.R. Wilson, Revival of a stalled supernova shock by neutrino heating. Astrophys. J. **295**, 14–23 (1985)
20. S. Richers et al., A detailed comparison of multidimensional Boltzmann Neutrino transport methods in core-collapse supernovae. Astrophys. J. **847**, 133 (21pp) (2017)
21. K. Sumiyoshi, S. Yamada, Neutrino transport in three dimensions for core-collapse supernovae I. Static configurations. Astrophys. J. Suppl. Ser. **199**, 17 (32pp) (2012)
22. W. Iwakami, Simulations of the early post-bounce phase of core-collapse supernovae in three-dimensional space with full Boltzmann Neutrino Transport. Astrophys. J. **903**, 82 (24pp) (2020)
23. H.-T. Janka, Neutrino emission from supernovae. *arXiv preprint arXiv:1702.08713* (2017)
24. S. Yamada, Proceedings of the Japan Academy, Ser. B (2024 in press)

Chapter 8
Theoretical Model of Dense Plasmas

Abstract In the dawn of quantum mechanics, scientists had challenged to formulate the equation of many-electron system, such as atom and solid matter, just after the success of Schrodinger equation to explain a hydrogen atom. It is found, however, that a system of multi-electron requires the self-consistent treatment of exchange interaction stemming from Pauli exclusive principle.

In 1930s, Hartree and Fock has derived the equation with use of Slater determinant. It is called Hartree-Fock (HF) equation. This is the equation for many-electron system and if we can solve it, almost exact solution is obtained. However, it was difficult to solve it analytically and numerically. Scientists proposed a variety of approximate theoretical models to solve such many-electron system.

Slater has proposed screened-hydrogenic model (SHM) in 1930. Thomas and Fermi have proposed a statistical model, now called Thomas-Fermi (TF) model. These two models have been widely used, modified, extended, and applied to many purposes even now. Their physical image is very simple and useful as comprehensive understanding of the physics. The examples of applications to the equation of state (EOS) for shock compression (shock Hugoniot) are explained here. Such models can be used to single atom (ion) or statistically averaged ion, so-called average ion model (AIM).

Even with the atomic data are supplied, the ionization potential depression (IPD) is essential to solve Saha equation of ionization population, especially at high-density plasma. Thanks to a rapid progress of computer capability, even HF equation can be solved numerically in some cases. It is very hard to solve, for example, the band structure of condensed matters. Kohn-Sham proposed density-functional theory (DFT) in 1960s. DFT solves one-electron Schrodinger equation for all electrons in the self-consistent potential. It is proved that the self-consistent potential is formulated as a function of only the density profile.

8.1 Introduction

We have studied that the ablation pressure in the rage of 1–100 Mbar can be generated in solid matters, when an intense laser irradiates them. As we will see below, the solid matters are easily compressed and ionization, and the Coulomb interaction energy becomes comparable to the thermal energy of charged particles. If a matter is compressed by keeping low temperature, Fermi degeneracy of free electrons becomes dominant in its pressure. In modern physics of laser produced plasma to be generated from solids, the physics of condensed matters should be studied inter-disciplinary. How to extend the theory and computational methods in the condensed matter physics to the case with finite temperature becomes a challenging subject.

Let us briefly summarized the matter state from solid in room temperature to extremely high-density state. In laser plasmas, special wards, **warm-dense-matter (WDM)** and **high-energy-density plasma (HEDP)** are widely used to show such high-pressure matter states. It is noted that such states are also called as **non-ideal plasma**. The physics of plasma at high-density has been studied for a long time in astrophysics relating to the plasma state inside stars and interior of planets, especially giant planets such as Jupiter. Roughly speaking, it is better to relate WDM to the giant planets and HEDP to the star interior. So, this chapter is strongly related to the evolution of objects in the space and astrophysics. It is noted that HEDP has relatively long history, while WDM became popular in the last two decades.

Physical properties under high-pressure have been also studied as subject of the condensed matter physics from the beginning of quantum mechanism. Most popular topic is **insulator-metal-transition (IMT)** of hydrogen. The IMT was predicted theoretically by Wigner and Huntington in 1935 [1]. Hydrogen is the simplest atom and there have been a lot of theory and computation on IMT. Recently, thanks to the progress of high-pressure technology, it has become a hot topic to demonstrate IMT experimentally. In what follows, the readers must be careful about the definition of IMT, because the **high-pressure physics (HPP)** community tries to demonstrate IMT by keeping the temperature low as the room temperature. Using laser-driven shock waves, the pressure increase also accompanies, in general, the increase of temperature. Any matter can be conductor at high-pressure with high-temperature, because of thermal excitation to produce many free electrons, resulting high-conductivity. This is called **plasma phase transition**.

Since the quantum physics of many-body problem becomes essential to study such high-density plasmas, we need to have basic knowledge of quantum mechanics of many-electron system. In Chap. 5, single atom or ion with multi-electrons has been studied quantum mechanically. In the present chapter, not only modeling single ion but also many-ion system coupled with quantum mechanical wave functions of many electrons are required to be studied.

In Fig. 8.1, progress of supercomputer is shown. It is surprising to know that its computational speed has increased 10,000,000 times in the last 25 years. In the early time to study the many-body problem, it was hard to do it even with such supercomputer,
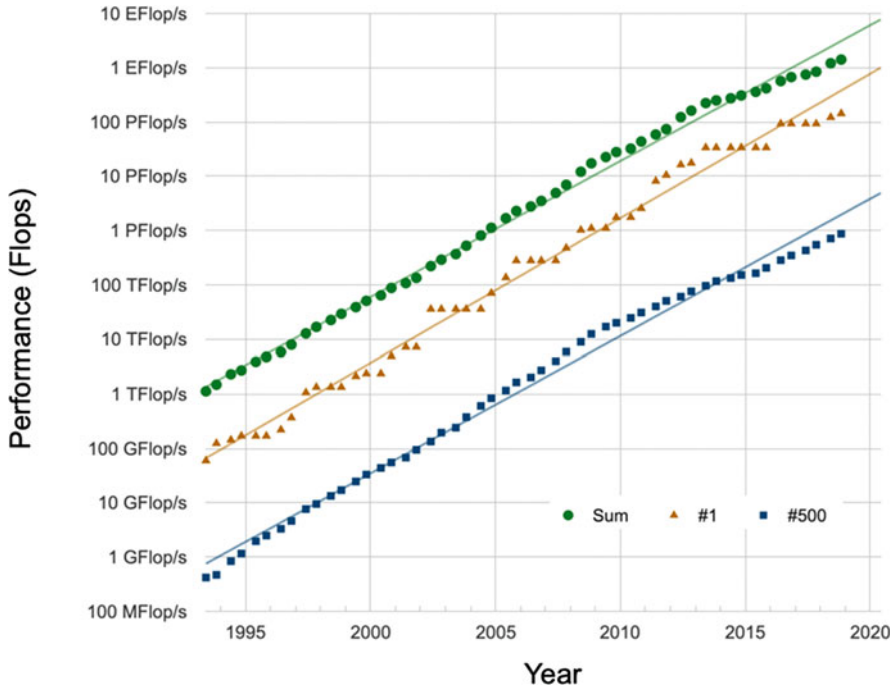
Fig. 8.1 Progress of supercomputer performance (Flops). The orange dots are the performance of the world-top computer the green dots are the sum of top 500 computers. Even the computer of No. 500 shows the performance of blue dots. Over the 25 years from 1995, the seven order of advancement has been achieved. The advancement of the computational speed also has changed the methods to study the plasmas. [From data in www.top500/]

while now it is already the time to challenge a big computing of many-body problems. Before such supercomputing, however, it is important to obtain the sense of physics with simpler models. In the present Chapter, mainly single ion models developed in early stage of quantum mechanics are explained. Then, it is explained how to solve "ab-initio" models of the real high-density plasma system.

8.2 Variety of Physical States of Dense Plasmas

8.2.1 Molecule and Solid

In the book by Kittel [2], the table of **bulk modulus** is given for many solid states. The bulk modulus B is the pressure defined at solid density and room temperature as

$$B = \rho \frac{\partial P}{\partial \rho} \tag{8.1}$$

The bulk modulus indicates how high pressure is necessary to compress the solid material to increase its density two times. For example, H (0.002), C (4.43), Al (0.722), Fe (1.68), and Au (1.73), where the numbers are the bulk modulus in Mbar unit.

With the bulk modulus data of the solid matters, intense laser can be used to perform experiments to study the physical properties of matters at densities higher than solids. In addition to the laser ablation pressure, such high-pressure physics has been also promoted with use of static pressure to generated in a tiny area by **diamond anvil cell (DAC)**, which is shown later in this chapter. This is complementary to the laser ablation pressure method because DAC can increase the pressure to about one Mbar keeping the temperature as low as enough to avoid temperature effect on the physical property of matter. It is noted that a single shock compression by the ablation pressure increases both of density and temperature. To study almost adiabatic compression, it is required to use a shaped pulse with continuous increase of the laser intensity as discussed in Chap. 4, which is the same technology required for the high-gain target implosion for laser implosion.

Let us consider a molecular bonding solid the simplest of which is the hydrogen solid at low temperature. A hydrogen molecule is formed by **covalent bonding** and the bonding force is due to the **exchange interaction energy** same as the para-helium electron configuration shown in Chap. 5. At room temperature, the hydrogen molecule is in gas state. The potential energy of the center of mass of two hydrogen atoms is given in Fig. 8.2 as a function of the distance of two hydrogen nuclei. In Fig. 8.2, two potential profiles are plotted for U_A with the case of two electrons with the same spins and for U_S of the case with opposite spins. U_S and U_A represent symmetric and anti-symmetric bonding, respectively. Two electron spins are the same as para-helium and ortho-helium configurations as studied in Chap. 5.

Fig. 8.2 A famous hydrogen molecule eigen-energy as the function of the molecular nuclei distance (r). Depending upon the combination of both spins, symmetric state U_s with opposite spins becomes bound state, while anti-symmetric case U_A with the same spins is not bound state because of the Pauli exclusive principle
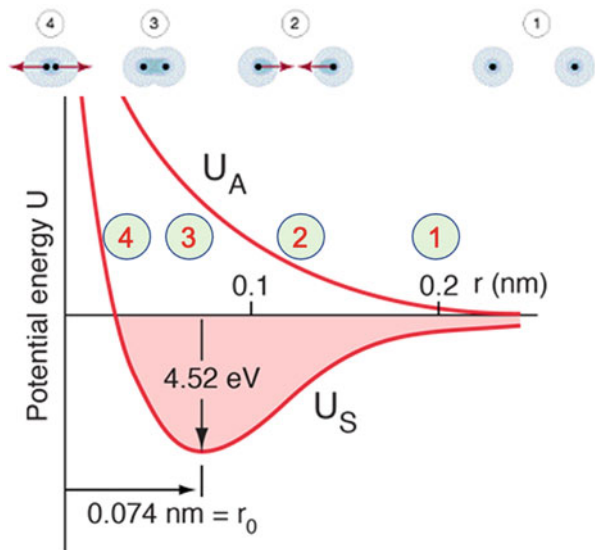
Exchange interaction is negative only for the case with the opposite spin pair, therefore, the molecule bonding is possible only for the opposite spin pair. Such covalent bonding force is strong and the dissociation energy is 4.52 eV. It suggests that high-temperature is demand to dissociate the molecule thermally.

This potential energy U(r) at T = 0 is the total energy of the hydrogen molecule, and the force F(r) to compress of the system is given as

$$F = -\frac{\partial U}{\partial r} \tag{8.2}$$

Note that the force vanishes at the equilibrium radius of the bottom of the potential as indicated at $r = r_0$ (*state* 3) in Fig. 8.2, and it is attractive for the larger distance, the states 1 and 2, and repulsive at shorter distance state 4 in Fig. 8.2. This force can be converted to the pressure for the solid with many molecules. If the average volume of one molecule is give as V, U is nothing without the internal energy of the average molecule of the thermodynamic system. By use of the relation of thermodynamics, we obtain the pressure P and the force of the molecule surface in the forms

$$dU = -PdV \implies P = \frac{\partial U}{\partial V} \implies 4\pi r^2 P = F \tag{8.3}$$

This pressure is called **elastic pressure** and **cold pressure**.

The potential energy of the molecular bonding has been modeled with **Lenard-Jones potential**.

$$U(r) = 4\varepsilon \left[\left(\frac{\sigma}{r}\right)^{12} - \left(\frac{\sigma}{r}\right)^{6} \right] \tag{8.4}$$

Then, the minimum energy is $-\varepsilon$ at $r = 2^{1/6}\sigma$.

8.2.2   High-Pressure Cold Matters

Let us call the high-pressure state of condensed matter at room temperature or less as high-pressure cold condense matter or simply **high-pressure cold matter (HPCM)** in this Chapter. In Fig. 8.3, a conceptual diagram of the change of states and physical phenomena are shown. Decreasing the temperature of hydrogen gas, hydrogen liquid and solid is formed at very low temperature 14 K. The binding between the molecules is not covalent bonding, but the **dipole-diploe interaction** schematically shown in Fig. 8.4. The electron cloud in each molecule shifts so that each molecule has dipole moment of charge. This bonding is week compared to the covalent bonding. Such force is called **Van der Waals force** and it is also modeled with Lenard-Jones potential force in (8.4) with appropriate parameters ε and σ.
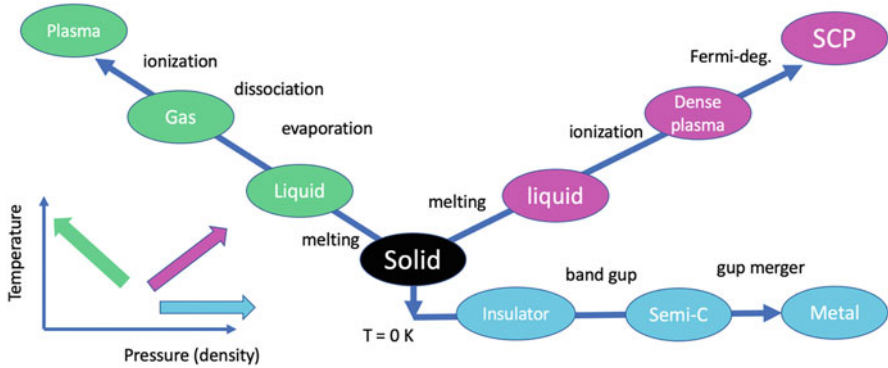
Fig. 8.3 Schematic diagram of temperature and density showing the phase transitions in the different regions produced by intense laser irradiation on solid materials. The ablating plasma with green color finally becomes ideal plasma expanding to the vacuum. The shock compression of solid change the state of matter to strongly coupled plasma as shown in red. In HPP, metallic hydrogen has been studied by applying high-pressure without increase of temperature. This study is shown with blue lines and the point is compression without heating
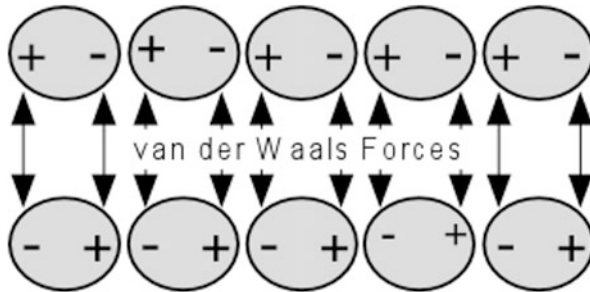
Fig. 8.4 Schematics of solid or liquid hydrogen bonding. The electron cloud in hydrogen molecule shifts from the center symmetry induces the dipole field to attract the other molecules via dipole interaction. In low temperature limit, they can stay as solid via this van der Waals force

8.2.3   Pressure Ionization

Using the DAC, the matter state changes as the light bule marks in Fig. 8.3, where the temperature is kept low enough. Initially, the solid hydrogen is insulator because all electrons are bounded in their parent molecules. In the word of the band theory of the solid-state physics, the electrons are all in the valence band and cannot move nonlocally. The insulator has a large band gap, and the Fermi energy is in the forbidden region as shown in Fig. 8.5. With increase of the density of the solid hydrogen, so-call **pressure ionization** mechanism becomes important. The pressure ionization makes the ionization potential depressed, and the matter state alters to semiconductor and conductor as schematically shown in Fig. 8.5.
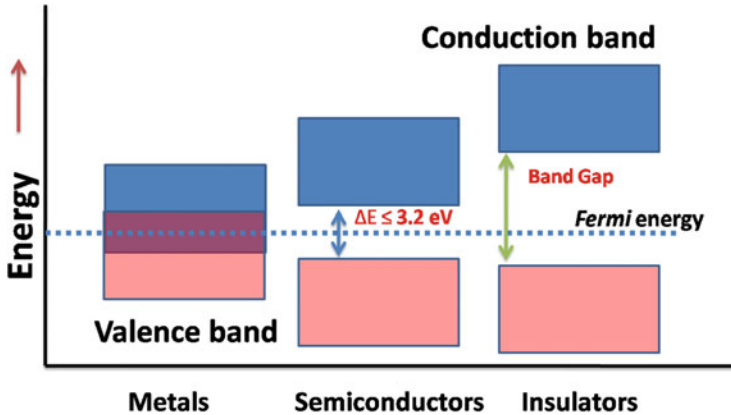
Fig. 8.5 A picture showing the difference of three state of normal solid matters. In the band theory, the system has valence band and conduction band. Many materials in solid state are classified to three, metal, semiconductor, and insulator. Metal has free electrons in the conduction band. The conduction and valence bands are separated by a gup, while it is called the semiconductor if the band gap is smaller than 3.2 eV. For the case with more wide energy gap and no electrons in the conduction band, it is insulator
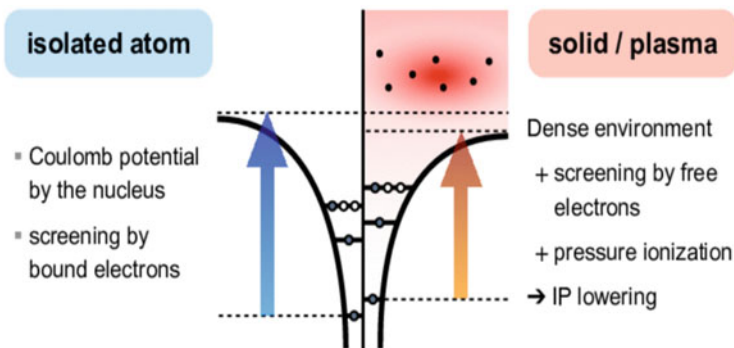
Fig. 8.6 If any atom is isolated and no effects by free electrons and nearby atoms, the energy levels of all bound electrons are affected only by the Coulomb forces by the nucleus and the other bound electrons. In solid materials and dense plasmas, the free electrons running in the atom shields the Coulomb field also the potential of the surrounding ions decrease the ionization potential. This is called pressure ionization and ionization potential lowering

Let us explain the mechanism of the pressure ionization for a simple case regarding one atom in high-density after the dissociation of molecular state. As shown on the left in Fig. 8.6, the isolated atom in neutral state has bound electrons in the grand state. The potential field can confine all bound electrons. However, with the increase of the density, the Coulomb field by nearby nuclei works to weaken the force by the central nucleus and the overlapping of the Coulomb field changes the free state energy lower than the isolated case. In addition, the free electron density at the atomic shells becomes high to shield the nuclear Coulomb potential.

As the result, the energy levels of the upper state electrons shift, and it also be broadened by the nearby nuclei and free electron fields. Many-body problem should be solved for a system made of N nuclei with N×Z electrons. Of course, it is possible to extend **Hartree-Fock method** explained in Chap. 5.3 to many-atom system formally. However, it is almost impossible to solve such many-body problem staring from total Hamiltonian to obtain the total wave function of electrons for a given positioning of all nuclei. Some challenge for solving approximated wave functions in each five-atom system has been carried out, where so called discreate-variational Xα method is used to obtain total electron wave function as shown later.

Several methods have been developed to find approximated electron quantum states. There are two broad classes of methods, wavefunction-based and density-based and each of these classes are further subdivided into different approaches. These two methods are.

1. **Wavefunction-based methods:** An explicit form for the wavefunction is written down and observables are calculated using this wavefunction. Examples are Hartree-Fock method and para-potential method as already shown in Chap. 5. More simplified para-potential method, **screened-hydrogenic model (SHM)** will be explained soon below. In laser produced plasmas, SHM has been widely used to make data base of thermodynamic quantities in wide range of density and temperature by including the pressure ionization effect. This idea was initially proposed by Slater in 1930.
2. **Density-based methods:** The focus is shifted from the wavefunction to the electronic density. The wavefunction is not written explicitly. Examples are **Thomas-Fermi approximation** and **density-functional theory (DFT)**. In laser produced dense plasma, computer simulation based on the density functional theory has been used by coupling with **molecular dynamic simulation** for ion motion. Such simulation is called *Ab initio* **simulation**.

The high-pressure physics experiment with use of DAC can keep the temperature low enough to study the physics of condense matter at higher density than solid. The long-standing challenge is the demonstration of metallic hydrogen experimentally. Recent apparent progress on this topic is given later. In addition, finding of superconductivity in hydrogen under extremely high pressure is also reported.

The insulator metal transition of hydrogen is also very important in planet science. It is expected that the inside of giant planets such as the Jupiter and Saturn are made of hydrogen in metallic state. Like the dynamo-effect inside our Earth, a strong magnetic field can be generated by the dynamo motion in the Jupiter. Magnetic field on the Earth stems from the convective motion of melted iron inside. Since the hydrogen metal may have higher conductivity than the melted iron, roughly speaking, stronger magnetic field may be expected for the Jupiter case. About 20 times stronger magnetic field has been observed near the surface of the Jupiter, and it is predicted with the high-conducting metal of hydrogen inside the Jupiter. So, the high-pressure physics is important to study the physics of interior of giant planets, many of which have been found as outer-solar planets recently.

8.2.4   Warm Dense Matter

In Fig. 8.7, shown is the density and temperature diagram in logarithmic scale of the regions of warm dense matters (WDM) and high energy-density plasma (HED). Note that there is no common clear definition of both states of WDM and HEDP. In addition, it is also difficult to clearly define the deference of matter and plasma. Roughly speaking, the physics of high-energy density is relatively simpler than the physics of warm dense matter, because almost no idealistic theory is applicable to describe the physical property of the warm dense matter. Since the temperature is higher in HEDP compared to the WDM, HEDP is strongly related to the physics of the evolution of stars as shown in Fig. 8.7, where the evolutional paths of the Sun and a star with 60 times solar mass are plotted. In contrast, the WDM can be said to be the physics of the evolution of planets, especially giant planets as shown in Fig. 8.7, where the giant planet such as Jupiter and brown dwarf are plotted. The central core of laser fusion implosion is located above the center of the Sun.

The physics of warm dense matter is a frontier between condensed matter and plasma physics. Here the density goes around the solid density and the temperature varies from 0.1 to 100 eV. In this regime, matter is mostly degenerate, strongly coupled, and non-ideal. WDM is an interdisciplinary research field bridging
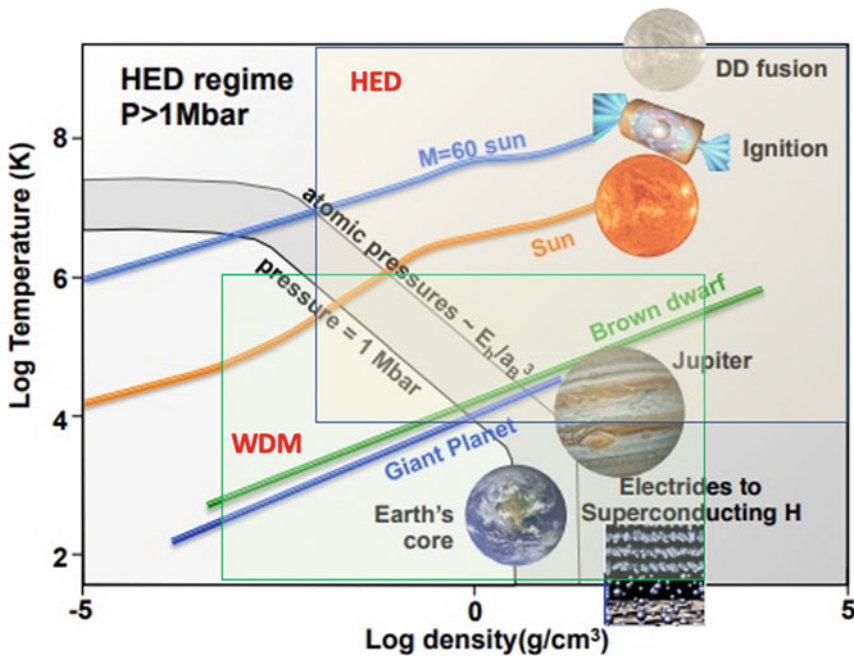
Fig. 8.7 Density and temperature diagram in logarithmic scale of the region of HED (high-energy-density) and WDM (warm dense matter), while this zoning is very ambiguous and no clear boundary in general. Reprinted with permission from Ref. [1]. Copyright by National Academies Press
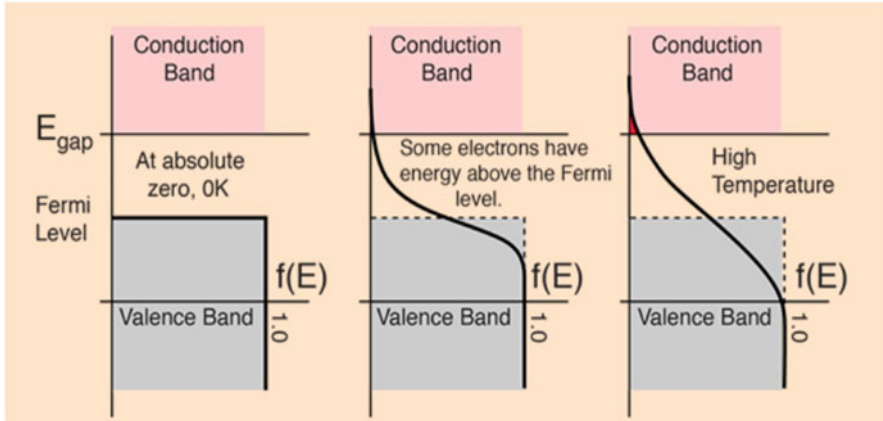
Fig. 8.8 Any materials in the state of insulator at cold temperature can show the property of conductor by the increase of the high-energy tail of Fermi distribution of electrons. Such change to metal from insulator by heating is called plasma phase transition

high-pressure physics community and laser-plasma community, where the former has grown from the condense matter physics historically. From the theory point of view, one must deal with *ab initio* calculations such as **quantum molecular dynamics (QMD)** which work well at low temperatures (T < 1 eV) and density functional theory for electrons.

Different from T = 0 case, the system of many particles is not in the grand state quantum mechanically. Atoms are ionized not only by the pressure ionization, but also by the thermal ionization as shown in Fig. 8.8. Free electrons are not completely degenerated and thermal excitation produces the free electrons in conduction band. In such case with thermal excitation of the system, the electron quantum system is calculated by assuming the nuclei are fixed in time. This is called the **Born-Oppenheimer approximation**. Another way of stating this approximation is that the time scale of the motion of electrons is much shorter than the nuclei and thus the response time of the electrons to any change in the positions of the nuclei is considered immediate, namely quasi-steady-state response of electrons can be assumed. The motion of all nuclei is treated as classical Coulomb interaction system given by the electron charge distribution. This simulation is QMD.

8.2.5 High-Energy Density Plasma

When matters are compressed to the direction of the red marks in Fig. 8.3, the electron degeneracy is important even if the thermal energy of electrons are a few or several times larger than the Fermi energy. The main fusion fuel of DT should be compressed under its temperature as low as possible for the high gain fusion energy production to be discussed in Vol. 3. Such partially degenerate high-density matter is

also a target of our research. More high-density characterizing the inside of compact objects in Universe, then, **strongly coupled plasma (SCP)** should be studied. In SCP, the ion-ion Coulomb charge interaction becomes important with relatively uniform electron density background.

While there is no definitive threshold of being in the high-energy density regime, perhaps a rough measure would be material at pressures of around one megabar, which is a quantity whose units are energy per unit volume ~1 Mbar (10^5 J/cm^3). For example, material at a density of 0.01 g/cm^3 and heated to 100 eV is at 1 Mbar. A temperature of 100 eV corresponds to about 10^7 J/g for hydrogen.

Roughly speaking, most of the theoretical models and numerical methods used for describing WDM can be extended to HEDP. It can be said that HEDP is simpler than WDM from theoretical modeling point of view. Special case of HEDP is, for example, the matter at the center of white dwarfs. Electrons are almost completely degenerate and the ions are moving like inside the sea of electrons. Such case is modeled by **one-component plasma (OCP)** and the ion-ion Coulomb correlation is studied in the uniform electron density.

8.2.6 Ion Sphere and Average Ion Models

The concept of ion sphere model has been widely used to describe the atomic state and thermo-dynamic property of the WDM and HEDP. In this model, the **ion sphere radius** R is defined by a simple relation.

$$\frac{4}{3}\pi R^3 n_i = 1 \tag{8.5}$$

Assume that this ion sphere shown in Fig. 8.9 is not a real ion, but this sphere represents the statistically averaged ion sphere. Therefore, it gives any physical properties of the statistical averaged ions. When the physical properties stemming from the statistical distribution around this averaged state, it is required to do additional study. For example, line broadening is obtained only when the statistical distribution of ion-ion distance fluctuation is given. It is noted that many physical properties such as equation of state is approximated with the ion sphere model as shown below.

Such kind of modeling is called **average-ion-model (AIM)** in plasma. It is also called **average-atom model (AAM)**. The combination of AIM and SHM have been intensively used to make data base for radiation hydrodynamic codes for laser-produced plasmas. Assuming that the ion sphere is a micro-thermodynamic system of plasma, it is possible to obtain the thermodynamic property, pressure, and internal energy as functions of density and temperature.

To provide an easy image of AIM in statistical physics, it is a good example to compared to the fluid modeling of the plasma. The plasma is defined with velocity distribution function and the best way to study the physics of plasma is to start with

Fig. 8.9 A cartoon of the
ion sphere model and its
radius. Simplest modeling
of atoms in high density is to
treat an average atom with
radius R as isolated atomic
system
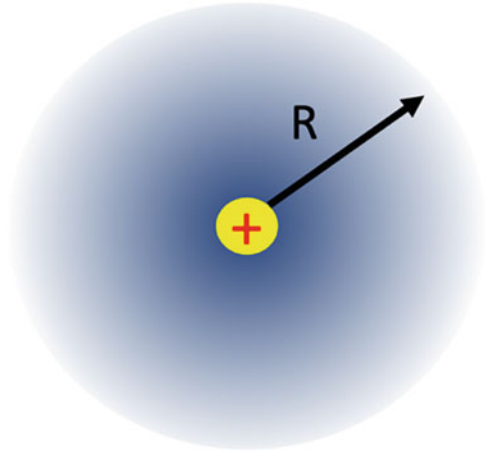
Vlasov equation. However, most of plasma can be described with fluid approxima-
tion. The fluid approximation is a mathematical model to reduce the freedom of
statistical system. So, the reader not familiar with such atomic physics can regard
that AIM is a kind of fluid model in plasma kinetic theory.

In the case of local thermodynamic equilibrium (LTE), it is possible to obtain the
Helmholtz free energy F for given (V, T), where the volume V is regarded as the
volume of the ion sphere defined in (8.5).

$$\varepsilon = F + TS \tag{8.6}$$

$$S = -\frac{\partial F}{\partial T} \tag{8.7}$$

$$P = -\frac{\partial F}{\partial V} \tag{8.8}$$

It is in general possible to separate F into three components,

$$F = F_c(V) + F_e(V, T) + F_i(V, T) \tag{8.9}$$

This free energy F should be the same as F in (8.2) at T = 0. Therefore, $F_c(V)$ is
determined by the molecular bonding and Coulomb repulsion or any bonding at
T = 0 as in Fig. 8.2.

Once the free electrons appear as metallic state shown in Fig. 8.5 due to the
pressure ionization by compression, the free electrons contribute to the free energy to
give Fermi pressure. As we discuss later, Coulomb interaction energy becomes
important in some case of WDM, the Coulomb interaction energy with the nearby
ions should also be included in $F_c(V)$. How to model $F_e(V, T)$ and $F_i(V, T)$ are the
main subject of the equation of states in WDM as will be seen later.

Historically, the quantum state of high-density matters has been studied by two different approaches. In the band theory, appearance of forbidden zone of a free electron in solid is clear, for example, by solving one-dimensional Schrodinger equation of an electron in a periodic potential. One example of simple theory is **Kronig-Penny model**. The other approach is mostly based on the ion sphere model. As already mentioned, there are two ways to study; namely, one is electron density-based theoretical method and the other is wave-function based method. They have been developed to obtain the free energy by electrons F_c and F_e in (8.9)

In the present Chapter, Thomas-Fermi theory is explained at first as the simplest theory for the density-based method. How sophisticated theory can be commonly used to study WDM and HEDP depends on the progress of experimental facility and diagnostics as well as computer technology. Precision diagnostics and well-defined laser experiments have recently demanded so-called *ab-initio* simulation as precise as possible to solve many-body system realized in experiments. ***Ab initio* calculations** are computations of electronic orbitals with no other hypotheses than Coulomb interactions between all electrons and nuclei with electrons obeying Fermi statistics with the Pauli exclusion principle.

Computer simulation of **molecular dynamics (MD)** is used for dense plasma instead of **particle-in-cell (PIC)** simulation in relatively low density high-temperature plasma. MD is originally used to solve the ion dynamics with effective potential such as Lenard-Jones potential in (8.3). Most popular example is dynamic simulation of protein folding in water molecule heat bath. On the other hand, the electron distribution in condense matters has been studied with **density functional theory (DFT)** for given positioning of all nuclei. The rapid progress of computing shown in Fig. 8.1 has made it possible to combine MD and DFT to know time evolution of WDM, where MD is replaced with *ab-initio* QMD.

The second method, wavefunction-based model, can give us more detail information of the electron quantum state. However, as already mentioned in Chap. 5, Hartree-Fock method can be formulated, while it is almost impossible to solve it in many-body problem. Wave-function based method results, for example, the property due to the quantum shell structure of bond electrons. In Fig. 8.10, the ionization energy needed to reach charge state Z from charge state Z-1 of a copper ion is plotted, where the color-coding indicates the valence electron shell of state Z-1. K, L, M, and N shells represent the quantum sates with the principal quantum number n = 1, 2, 3, and 4, respectively. The jump of the values in Fig. 8.10 is due to the shell structure of the wave functions. The Thomas-Fermi model cannot reproduce such shell-dependent property.

In the ion-sphere model, if we can have **self-consistent spherical potential** V(r) in the ion sphere (r < R), it is easy to solve one-electron Schrodinger equation.

$$\left[-\frac{\hbar^2}{2m} \nabla^2 + V(r) \right] \psi_i = E_i \psi_i \tag{8.10}$$

Fig. 8.10 The ionization energy needed to change the charge state Z from the charge state Z-1 of a copper atom. The color-coding indicates the valence electron shell of state Z-1. K, L, M, and N shells represent the quantum sates with the principal quantum number n = 1, 2, 3, and 4, respectively
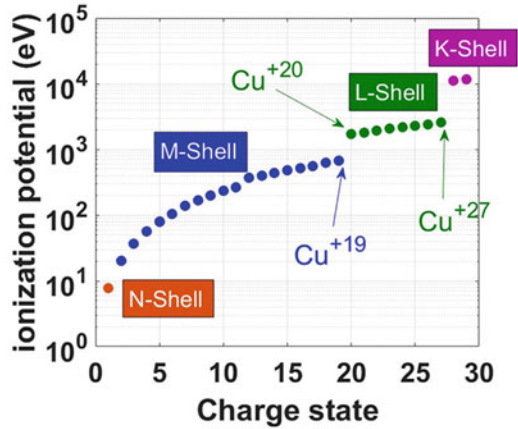
where ψ_i and E_i are the electron wave function and eigen-energy for a quantum state "i", respectively. It is easy to solve (8.10) numerically for a given consistent potential V(r), while to find the V(r) is a tuff job. Note that V(r) should consist of

$$V(r) = V_{ie} + V_{ee} + V_{ex} \tag{8.11}$$

where V_{ie} is Coulomb interaction energy with nuclear charge, V_{ee} is the electron-electron Coulomb interaction energy, and V_{ex} is the exchange interaction energy. The Hartree-Fock method is solved iteratively to obtain the total wave function in Slater matrix and all interaction energies are included consistently. However, new theoretical model is required for each of three potentials in (8.11) once Schrodinger equation is reduced to one electron equation.

In the present Chapter, we look back the para-potential method to give a consistent potential screened by many electrons in an atom. Based on the fundamental property of hydrogen atom, the method to fit the binding energy of each electron in multi-electron ion-sphere is explained. This is called s**creened hydrogen model (SHM)** and has been widely used to obtain the thermodynamic property in laser-plasma.

It is noted that AIM gives only the physical quantity averaged over many statistical configurations is obtained. However, it is shown that how we can obtain the statistical spread of each configuration, such as charge distribution and energy shift of line emission due to the difference of the number of electrons in the same shell, is obtained by use of SHM in laser plasma as to be explained.

8.2.7   Band and Band Gap

It is better to see why bands and band gaps appear in dense-matters as quantum effect. The electrons in an atom occupy atomic orbitals, each with its own individual energy level. When two or more atoms combine to form a molecule, their atomic

orbitals overlap. In Fig. 8.11, the energy states of electrons are shown as the s-state and p-state when the interatomic distance is large, that is, the atom is an isolated atom. In the case of hydrogen molecule in Fig. 8.2, it is shown that the s-state becomes to have two energy levels because of the Pauli's exclusion principle as U_S and U_A. In a molecule, Pauli's exclusion principle states that no two electrons can have the same quantum number. Therefore, when two identical atoms combine to form a diatomic molecule, each atomic orbital splits into two molecular orbitals with different energies.

This means once the overlapping of two electron wave functions takes place at a certain interatomic distance in Fig. 8.11, the separation of the energy level of the s-state appears as well as the p-state. The electrons in the previous atomic orbitals can occupy the new orbital structure without having the same energy. Similarly, when N identical atoms are assembled to form solid, such as crystal lattice, the electron orbitals overlap over many nuclei. Due to the Pauli exclusion principle, the wave functions of two electrons cannot overlap with the same quantum number, so the atomic orbitals are split into N individual orbitals, each with different energy. This is indicated on the left in Fig. 8.11, where the band in high-density with the interatomic distance "a" is made of many of different energy levels.

Because the number of atoms in a macroscopic solid is so large ($N \sim 10^{22}$), the number of orbitals is also very large, and therefore the energies are very closely spaced. The energy of the adjacent levels is on the order of 10^{-22} eV. Since the energies of adjacent levels are very close, they can be considered as a continuum, or energy band. The formation of such bands is mostly a feature of the outermost electrons (valence electrons) of the atom, which are involved in chemical bonding
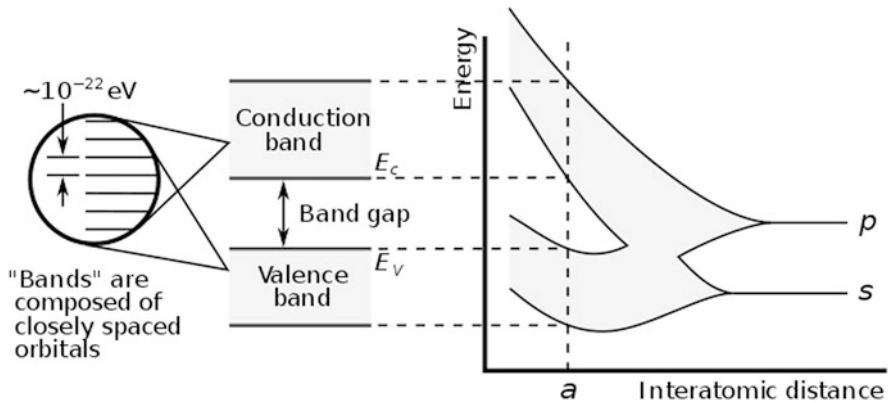
Fig. 8.11 On the right, the energy level structure change by the decrease of the interatomic distance is plotted. For the case where the atomic distance is large, the atom is isolated and fine discrete energy levels are defined. As the distance decreases, the many electrons from the surrounding atoms makes different eigen energy state like the case of hydrogen molecule in Fig. 8.2. At the solid density (radius a) or higher density, the band structure is formed. Since the band structure is formed by many electrons in the dense state, there are roughly the number of eigen states by all electrons 10^{22} cm^{-3} in unit volume in solid as shown at the left

and electrical conduction. Since the inner electron orbitals do not overlap as much, their bands are very narrow.

The band gap is the energy range that remains uncovered by any of the energy bands due to their finite width. The width of a band depends on the degree of overlap of the atomic orbitals from which the band originates. The width of two adjacent bands is insufficient to cover the full energy range. For example, the bands associated with core orbitals (such as 1s electrons) are very narrow due to the small overlap of adjacent atoms. As a result, the band gap between the core bands tends to be large. In the higher bands, the bands become progressively wider at higher energies due to the overlap of relatively large orbitals, and the band gap disappears at higher energies.

8.3 Screened Hydrogen Models

The wave quantum mechanics is found to give the precise quantum state of hydrogen atom thanks to the discovery of **Schrodinger equation** in 1926. Then, many peoples tried to extend one-electron Schrodinger equation to atoms with multi-electrons, including partially ionized atoms. In 1927, the next year, Hartree introduced so-called **Hartree method** to solve N-electron wave function in an atom. In 1930, Slater and Fock independently pointed out Hartree method did not satisfy the principle of anti-symmetry of the wave function required by the Pauli exclusive principle for Fermion electrons. In 1935, Hartree reformulated the method more suitable. Now, **Hartree-Fock method** with the wave function of the determinant of Slater matrix is widely used as very precise basic equation for multi-electron system.

Even with Hartree-Fock equation proposed in 1930s, it is almost impossible to solve it analytically and very time-consuming calculation was demanded to apply even atoms with a small number of electrons. Historically, the birth and rapid progress of computational capability has been required to solve Hartree-Fock equation. Therefore, a variety of models have been proposed in the early time by neglecting some physics elements due to multi-electron effect. By focusing on the Coulomb shielding effect in the multi-electrons bounded in an atom or ion, Slater proposed a method to obtain the eigen energy of multi-electron atom. This is the basic idea of the **Screened Hydrogen Model (SHM)** described in this section. Note that this model is still used widely after the improvement of the screening constants.

The historical development of the SHM is reviewed briefly by Smithwick in [3]. Let me borrow his sentence. The SHM is an alternative and simple approach that uses the one-electron wavefunctions of the hydrogen atom for each electron of a multi-electron atom by substituting an effective nuclear charge Z_i for the value of Z. Agreement with experimental energies can be obtained by varying Z_i with screening parameters. The SHM provides a starting point for semi-empirical calculations involving complex atomic or molecular systems.

The SHM was first used in 1930 by Slater who approximated the energies of electrons in 1s and 2s/2p orbitals as $E_i = (Z_i)^2 \frac{1}{2n^2}$ in atomic units. Z_{1s} (for $n_i = 1$) equals Z – 0.30 when two 1s electrons were present and both Z_{2s} and Z_{2p} (with $n_i = 2$) equals Z – 1.70−0.35 ($N_{2S} + N_{2P} - 1$) when two 1s electrons were present. The Slater 1 s wave function was the same as the hydrogen 1 s wave function with Z_{1S} substituted for Z. The Slater 2s and 2p wave functions both had the same value of $Z_{2S} = Z_{2P}$ substituted for Z and the same radial part of the hydrogen-like 2p wave function but with 2s or 2p angular parts. Numerous molecular orbital calculations were based on Slater wave functions. Layzer and Kregar each calculated screening parameters and electron energies with series functions in powers of Z.

The calculation of the properties of dense plasmas at high temperatures is an important application of the SHM that involves the determination of the energies of atoms and ions across the periodic table. The Dirac equation is an alternative form of the SHM that includes relativistic corrections for each electron. A closer agreement between experimental and calculated electron energies is expected to lead to improved predictions of plasma properties.

It is in general hard to solve *ab-initio* model such as Hartree-Fock equation in high-density plasma because it is not clear how to model the pressure ionization in Hartree-Fock method. If we have appropriate radial potential V(r) for modeling the ion sphere in any density and we can obtain reasonable wave functions to calculate not only the thermodynamic functions, the free energy F(ρ,T), but also oscillator strengths of line radiations etc. Then, it is convenient for installing equation of state and opacity in simulation codes. Note that equation of state can be modeled with statistically averaged atomic state, while the opacity, especially line radiation opacity, calculation needs the variance distribution from the average atom state.

Here, only the average ion model (AIM) is discussed to obtain the equation of state such as pressure and internal energy in dense plasma. They are used in modeling in hydrodynamic simulation for laser produced plasma. This AIM is a robust model to obtain the eigen energy of any ionization state of any atom, based on the quantum theory of hydrogen atom. The energy is given by taking account of the Coulomb charge screening in multi-electron bound atom or ion.

8.3.1   Screened Hydrogen Model (SHM)

By using SHM improved by More [4], the energy of an electron in an eigen state n (the principal quantum number) is given to be

$$E_n = -I_H \left(\frac{Z_n}{n}\right)^2 + E_n^0 \qquad (8.12)$$

Where I_H is the Rydberg constant (13.6 eV). In (8.12), Z_n is the effective nuclear charge seen by the electron in the state n and E_n^0 is the screening effect by the

electrons outside the orbit of the electron in the state n. In (8.12), the Z_n and E_n^0 are given to be

$$Z_n = Z - \sum_{m<n} \sigma_{n,m} P_m - \frac{1}{2} \sigma_{n,n} P_n \tag{8.13}$$

$$E_n^0 = \frac{1}{2} \frac{e^2}{r_n} \sigma_{n,n} P_n + \sum_{m>n} \frac{e^2}{r_m} \sigma_{m,n} P_m \tag{8.14}$$

where σ_{nm} is the screening constants proposed by More so that the ionization potentials of a variety of atoms are well reproduced compared to those obtained by solving Hartree-Fock Slater equation [5]. In (8.13) and (8.14), Z is the ion nuclear charge and P_n (P_m) is the number of electrons in the eigen-state n (m). In (8.14), r_n (r_m) is the effective orbit radius of the electron with the quantum number n (m) and defined as

$$r_n = a_B \frac{n^2}{Z_n} \tag{8.15}$$

where a_B is the Bohr radius.

The well-known relations of the hydrogen-like ions are explicitly used to obtain the energy E_n. The relation of SHM has an advantage for the consistency condition;

$$\frac{\partial}{\partial P_n} E_{ion} = E_n \tag{8.16}$$

where E_{ion} is the total energy of the bound electrons in the ion and is defined as

$$E_{ion} = -\sum_n I_H \left(\frac{Z_n}{n}\right)^2 \tag{8.17}$$

Since the electron-electron interaction energy should not be doubly counted, the following relation is required in the model.

$$E_{ion} \neq \sum_n E_n \tag{8.18}$$

It is convenient to use another expression of E_n^0 and Z_n in (8.13) and (8.14).

$$Z_n = Z - \sum_{m \leq n} \sigma_{nm}^{AM} P_m \tag{8.19}$$

$$E_n^0 = \sum_{m>n} \sigma_{nm}^{AM} P_m \tag{8.20}$$

Table 8.1 Screening constants σ_{nm}^{AM} defined in (8.21) as a table of matrix [n, m]. The number 1–10 is this table shows "n". This means the screening effect to an electron in the n-sate by the m-state electron is large for n > m, while it is relatively small for n < m as easily understood from the spread of wave functions

n= 1	2	3	4	5	6	7	8	9	10
0.3125	0.9380	0.9840	0.9954	0.9970	0.9970	0.9990	0.9990	0.9999	0.9999
0.2345	0.6038	0.9040	0.9722	0.9979	0.9880	0.9900	0.9990	0.9999	0.9999
0.1093	0.4018	0.6800	0.9155	0.9796	0.9820	0.9860	0.9900	0.9920	0.9999
0.0622	0.2430	0.5150	0.7100	0.9200	0.9600	0.9750	0.9830	0.9860	0.9900
0.0399	0.1597	0.3527	0.5888	0.7320	0.8300	0.9000	0.9500	0.9700	0.9800
0.0277	0.1098	0.2455	0.4267	0.5764	0.7248	0.8300	0.9000	0.9500	0.9700
0.0204	0.0808	0.1811	0.3184	0.4592	0.6098	0.7374	0.8300	0.9000	0.9500
0.0156	0.0624	0.1392	0.2457	0.3711	0.5062	0.6355	0.7441	0.8300	0.9000
0.0123	0.0493	0.1102	0.1948	0.2994	0.4222	0.5444	0.6558	0.7553	0.8300
0.0100	0.0400	0.0900	0.1584	0.2450	0.3492	0.4655	0.5760	0.6723	0.7612

where σ_{nm}^{AM} is the screening constant introduced in [6]. There is a simple relation with Kronecker δ.

$$\sigma_{mn}^{AM} = \sigma_{mn}\left(1 - \frac{1}{2}\delta_{mn}\right) \tag{8.21}$$

The matrix table of σ_{mn}^{AM} is given in Table 8.1 [6].

It is important to know that the above formulation to obtain the well-approximated energy of bound electrons can be used to any given configuration with integer n. Then, we can use the SHM for **detailed configuration accounting (DCA)** for all possible configurations. If we can model the transition cross sections of electron collision and photon processes as described in Chap. 5, even the photo-ionizing non-LTE plasma atomic process can be studied reasonably by solving the rate equations of all possible detail configurations within SHM as shown, for example, in [7].

8.3.2 Average Ion of SHM

In the case of the average atom model, the above relations to SHM are extended by assuming that the number of electrons in the n-shell is not the real number but the statistically averaged non-integer number. Of course, the relation $P_n/g_n \leq 1$ should be satisfied, where g_n is the number of states of the eigen state n.

Assume the **local thermodynamic equilibrium (LTE)** condition. The electrons in an averaged ion are separated to the bound electrons and free electrons. The energy distribution of the bound electrons is assumed to be governed by Fermi-Dirac distribution.

$$P_n = g_n \left[1 + exp \left(\frac{E_n + \Delta U - \mu}{T_e} \right) \right]^{-1} \tag{8.22}$$

where μ is the chemical potential and ΔU is the energy shift due to the **continuum lowering** as schematically shown in Fig. 8.6. To derive the continuum lowering has been performed relating to the ion state inside stars in astrophysics. Recently, it has become possible to clarify the continuum lowering experimentally to verify such theories. Here, we adopt the continuum lowering expression in high-density limit of **Steward-Pyatt model** [8].

$$\Delta U_{SP} \approx \frac{3}{2} \frac{Z^* e^2}{4\pi\varepsilon_0 R_0} \tag{8.23}$$

Note that More details are given in the next section.

We also assume that the free electrons are also in LTE, therefore, the number of free electrons per an ion is given to be

$$Z^* = \frac{1}{2\pi^2 n_i} \left(\frac{2mT_e}{\hbar^2} \right)^{3/2} I_{1/2}(\mu/T_e) \tag{8.24}$$

$$I_{1/2}(x) = \int_0^\infty \frac{y^{1/2}}{1 + exp(x - y)} dy \tag{8.25}$$

The chemical potential μ is determined so that the charge neutrality condition is satisfied.

$$Z = Z^* + \sum_n P_n \tag{8.26}$$

Assuming a certain value of the maximum of n (n_{max}) and using (8.12) and (8.26), we can obtain the statistically averaged population P_n for given density and temperature.

It is not trivial to model an appropriate value of n_{max}. The maximum value is not given as a discrete value because we are dealing with statistically averaged atomic condition and some physical model of pressure ionization sis required for modeling of this problem. A model of the pressure ionization to SHM has been studied in [9], where it is modeled by decreasing the number of states in the upper bound levels.

$$g_n = \frac{2n^2}{1 + \left(a \frac{r_n}{R_0} \right)^b} \tag{8.27}$$

The fitting constants a and b have been chosen as a = 3 and b = 4 to correspond to Thomas-Fermi result [10]. In (8.23), the pressure ionization is determined by the
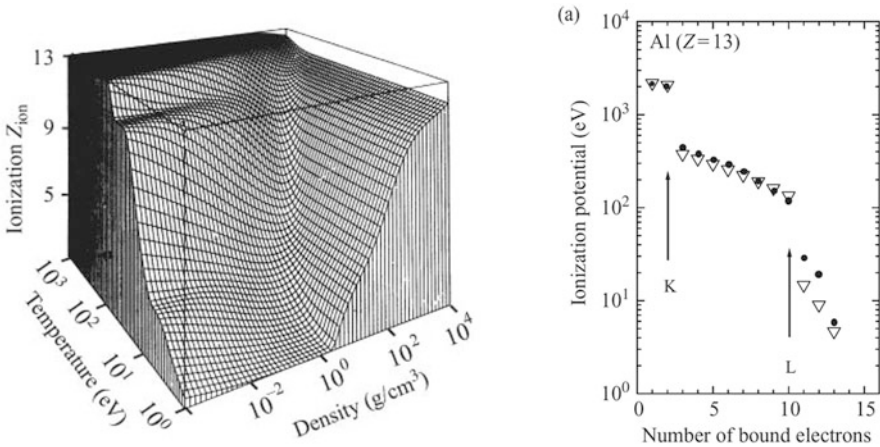
Fig. 8.12 (**a**) The charge state of aluminum as a function of temperature and density calculated by SHM for AIM. In high-temperature and low density, the ionization is due to thermal effect and shell structure is clearly seen. In the low temperature and high density, the pressure ionization increases the number of free electrons [6]. (**b**) The ionization potential of an isolated aluminum atom calculated with SHM (black dots). For comparison, the same data are also shown with precise method, Hartree-Fock calculation (triangles). Reprinted with permission from Ref. [6]. Copyright 1998 by Oxford University Press

electron orbit radius divided by the ion spere radius. It is intuitively reasonable that the bound state disappears abruptly for the electron orbit overlaps the orbits of nearby bound electrons.

In Fig. 8.12a, the charge Z^* as function of density and temperature is plotted for the case of aluminum ($Z = 13$) at high density plasma state [6, 9]. The shell structure is obtained for thermal ionization and pressure ionization is clear with increase of density. Note that the change of P_n, $- E_n$, and Z_n due to the temperature increase at density 0.1 g/cm^3 in Fig. 8.12a is shown in [10] as well as the case of gold, where $n_{max} = 5$ and 10 are assumed for aluminum and gold, respectively.

In Fig. 8.12b, the ionization potential energy is also plotted without the pressure ionization effect, namely for an isolated aluminum atom. Energy jump due to shell structure of K-shell and L-shell is well reproduced by SHM (black dots) same as the result of Hartree-Fock calculation (triangles) [10].

8.3.3   Screened Hydrogen Model with (n, ℓ)

The SHM has been extended to include angular momentum dependence in AIM. It is well-known that the degeneracy of the angular momentum quantum number ℓ at each principal quantum state n is accidental in case of hydrogen or hydrogen-like atom, where the potential is exactly proportional to 1/r. In the case of multi-electron

bound atom, binding energy of each ℓ-state in the same n-shell has different values and no degeneracy appears. So, depending on how precise atomic model is required, inclusion of n and ℓ in SHM is natural.

A self-consistent model based on a nonrelativistic screened-hydrogenic model (SHM) with ℓ-splitting has been developed to calculate the **equation of state (EOS)** of matter in local thermodynamic equilibrium [11]. This model takes account of the quantum subshell effect to go beyond the simple semiclassical and statistical Thomas-Fermi approach to obtain the electronic properties. The whole model is fast, robust, and reasonably accurate over a wide range of temperatures and densities. New screening constants are given in [11, 12]. In this case, the total energy of bound electrons is given in the same form as (8.17)

$$E_{ion} = - I_H \sum_k \left(\frac{Z_k}{n_k} \right)^2 \tag{8.28}$$

where $k = \{n, \ell\}$ and the energy sprit by ℓ is included in Z_k in the form same as (8.13).

$$Z_k = Z - \sum_j \sigma_{j,k} \left(1 - \frac{\delta_{jk}}{D_k} \right) P_j \tag{8.29}$$

where j also represents the configuration $j = \{n, \ell\}$ and the energy split by ℓ comes from the ℓ dependence of the set of the screening constant ($\sigma_{j,\ k}$) and the integer degeneracy of subshell k as follows.

$$D_k^0 = 2(2\ell_k + 1) \tag{8.30}$$

The screening constant ($\sigma_{j,\ k}$) are calculated by fitting over a large data basis containing nonrelativistic ionization potentials and excitation energies calculated using the Superstructure code and the multi-configuration Dirac–Fock code [12]. Note that additional assumption is also adopted in [11].

In [11], the fractional occupation number (P_k) is not given by Fermi-Dirac distribution, but it is calculated so that the electric Helmholtz free energy per average ion of the plasma (F_e) becomes minimum at fixed density and electron temperature.

$$F_e = F_{bound} + F_{free} + F_{ion-sphere} \tag{8.31}$$

In (8.31), F_{bound} is free energy of the average ion subsystem in the bound state given by SHM, F_{free} is the free energy of homogeneous free electron gas, and $F_{ion-sphere}$ is the contribution by the continuum lowering.

The free energy of the bound electrons is given with E_{ion} in (8.28) as

$$F_{bound} = E_{ion} - TS_{bound} \tag{8.32}$$

According to Boltzmann law on the entropy, S_{bound} is the sum of all bound state as

$$S_{bound} = -k_B \sum_k \left[P_k ln \left(\frac{P_k}{D_k} \right) + (D_k - P_k) ln \left(\frac{D_k - P_k}{D_k} \right) \right] \tag{8.33}$$

where the decrease of the number of states by pressure ionization effect given in (8.23) is also modeled and D_k is reduced from D_k^0 in (8.30).

It is too much to repeat the description in [11] and let us see the resultant **shock Hugoniot** relation with EOS derived by this SHM. The density jump of a single shock wave is plotted in Fig. 8.13 and compared to the present SHM, QEOS, and experimental data [11]. The QEOS is an EOS model widely used in laser plasma study [13] and the electron EOS is based on Thomas-Fermi model described in the next section. The QEOS is given by separating the total free energy as in (8.9) and the cold and ion components are given with so-called **Cowan model.**

In Fig. 8.13, EOS consisting of SHM for electron component and Cowan model for ion is shown as SHM-QEOS and the cases of three different coefficients of the ionization potential lowering given in (8.20) with different constants are plotted
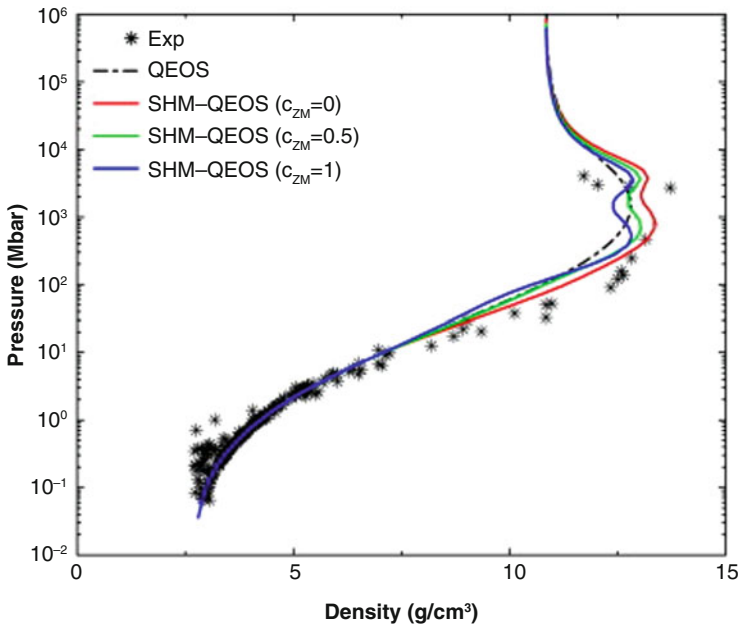
Fig. 8.13 Shock Hugoniot data of aluminum from an experiment (*) and the present SHM with different coefficients and the original QEOS data. Reprint from Ref. [11]. Copyright 2012, with permission from Elsevier
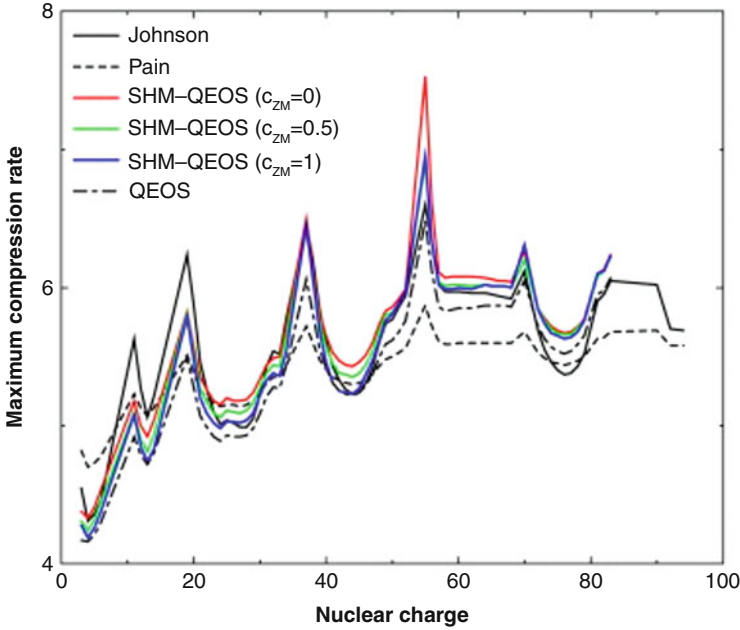
Fig. 8.14 The maximum compression rate as a function of different atomic elements (nuclear charge). As seen in Fig. 8.13, all solids have the maximum compression rate characterized by the atomic shell structure. The present SHM results are compared to other theoretical data. Reprint from Ref. [11]. Copyright 2012, with permission from Elsevier

[11]. It is clear that all provides almost the same Hugoniot curve and the scattered experimental data are well explained. Just a qualitative difference is that QEOS does not give the shell effect of electron orbits, while the SHM predicts the effect.

The effect of shell in atom is emphasized or clearly observed in Fig. 8.14, where the maximum compression ratio is plotted for all atomic number Z [11]. All curves are theoretical prediction and the simple current SHM can reproduce the prediction with more complicated calculation by Johnson and Pain.

Let us consider that physics giving the oscillating structure in Figs. 8.13 and 8.14. In the case where the ionization happens in the shock surface region, a part of shock compression energy is used for ionization. This is regarded that the freedom of the thermodynamic system increased. As shown in Chap. 3, the density ration of strong shock wave is a function of the freedom of the gas, and the increase of the number of freedom N results the increase of compression ratio. The increase of the density ratio more than four $(=2.712 \times 4 = 10.8 \text{ g/cm}^3)$ in Fig. 8.14 is due to this ionization effect. In the limit of the strong shock wave, the ratio reduced to the value of four, because the ionization energy is relatively small compared to the shock pressure work.

The periodic structure seen in Fig. 8.14 is also due to the ionization energy loss in the compression. The first peak is for Na (Z = 11), K (=19), and so on. They are transition metal with one electron in the outer shell. In the case when the shock is strong to ionized this electron, the high-density compression is observed.

8.4   Thomas Fermi Model for an Ion Sphere

To consider the physical property of compressed matters, a variety of theoretical models have been proposed to calculate the statistically averaged density distribution as consistently as possible. One of the convenient ways to calculate the electron density distribution for a system with a nucleus at the center and the surrounding electrons is **Thomas-Fermi (TF) model** as studied in early time of modern physics [14]. The TF model is still widely applied in many quantum systems, even to a hydrogen atom since it is very easy to solve numerically and provides approximate electron density profile in a compressed atom.

Although it is easy to solve computationally at the present, it is interesting to know that R. Feynman wrote how to do numerical calculation before the computer was invented [15]. About forty wives of scientists gather in a classroom and follow Feynman's instructions to turn the hand-cranked calculators, dividing the work among them and producing numerical values. He writes the results on the blackboard as the wives obtained in the numerical calculations. Although the TF model is not so complicated as seen below, it was difficult to solve without such human power before the computer era.

The basic equation to be solved is Poisson equation to the potential $\phi(r)$,

$$\varepsilon_0 \frac{1}{r^2} \frac{d}{dr}\left(r^2 \frac{d}{dr}\phi\right) = -Ze\delta(r) - en_e(r) \qquad (8.34)$$

where $n_e(r)$ is the radial distribution of electron density around the nucleus with charge Z. It is assumed that the electron density is given by Fermi-Dirac statistics.

$$n_e(r) = \int \frac{2}{\hbar^3} f_{FD}(r,p)d^3p = \frac{8\pi}{\hbar^3} \int_0^\infty p^2 f_{FD}(r,p)dp \qquad (8.35)$$

where $f_{FD}(r,p)$ is the **Fermi-Dirac distribution**.

$$f_{FD}(r,p) = \frac{1}{1 + exp\left\{\frac{p^2/2m - e\phi - \mu}{T}\right\}} \qquad (8.36)$$

It is clear that above equations are enough to determine the density profile $n_e(r)$, once the charge neutral sphere radius R_0 is given and the chemical potential is determined so that the charge neutrality is satisfied in the ion sphere. In the limit ($\mu \to -\infty$), the electron density (8.35) tends to the **Boltzmann distribution** for a given electric potential ϕ. Due to this reason, the TF model is an extension of classical **Debye-Hueckel model** to Fermion gas. Boltzmann distribution cannot be used in the case of high-density plasma, and the simple **Debye shielding model** should be replaced by TF model.

8.4.1 Screened Electron Density Distribution

Introducing x and y defined as

$$x = \frac{p^2}{2mT}, \quad y = \frac{e\phi + \mu}{T} \tag{8.37}$$

The electron density (8.35) is given in more simple form:

$$n_e(r) = \frac{1}{2\pi^2}\left(\frac{2m}{\hbar^2}\right)^{3/2}\int_0^\infty \frac{x^{1/2}}{1 + exp(x - y)}\,dx \tag{8.38}$$

It is more convenient to solve (8.34) with assumption that the radial function of potential is given like

$$\phi(r) = \frac{Ze}{4\pi\varepsilon_0 r}Y(r) \tag{8.39}$$

Then, (8.34) can be reduced to the second order differential equation to Y(r).

In high-density plasmas, the ion-ion Coulomb coupling is strong and it is good approximation to introduce the ion sphere defined in (8.5) and set the boundary $R = R_0$ here. It is also assumed that the same amount of charge is filled by electrons to make charge neutral in the ion sphere. Then, the problem to solve (8.34) becomes an eigen-value problem to the boundary conditions:

$$Y(0) = 1, \tag{8.40}$$

$$\frac{d}{dr}\phi(r = R_0) = 0 \tag{8.41}$$

Since we assumed the form (8.39), the first term on RHS in (8.34) disappears. After rewriting (8.34) to the equation to Y(r), we obtain a second order nonlinear differential equation to Y(r). It is recommended to solve the equation to Y(r) by integrating from both boundaries. Such numerical method is called **shooting method** and the eigen value μ starting with a trial value at the beginning should be converged to the value so that both solutions integrated from the center $r = 0$ and from the boundary $r = R_0$ continuously match at a given fixed matching point.

In Fig. 8.15, the electron radial density profile obtained by the TF model is shown for an isolated neutral argon atom, where R_0 is infinity. The resultant radial density distribution is compared to that obtained by the **Hartree method** described in Chap. 5. It is noted that the Hartree method solves Schrodinger equation to all wave functions for the bounded N electrons by including the Coulomb interaction. Although the exchange interaction is not included in this Hartree method, it is much better calculation than TF model. It is seen in Fig. 8.15 that electron density distribution obtained by such simple TF model is good enough in this case compared to that obtained by the Hartree method. Big difference is that the Hartree method can
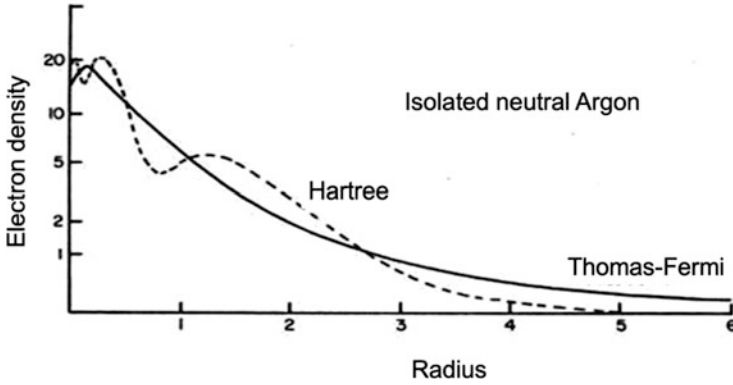
Fig. 8.15 The electron density radial distribution of isolated neutral argon atom obtained by Thomas-Fermi model and more precise Hartree method. Since the Hartree method solve the wave functions and the shell structures are seen

include the effect of shell structure by filling states with different principal quantum numbers. TF cannot reproduce such quantum shell effect.

In the present TF model in high density and/or high temperature, it may be possible to divide the electrons into the bound and free components. There are two ways for the definition of the fraction of free electron component in the ion sphere as follows.

$$f_{free} = \frac{4\pi}{Z} \int_0^{R_0} n_e \left(\frac{p^2}{2m} - e\phi(r) \geq 0 \right) r^2 dr \tag{8.42}$$

$$f_{free} = \frac{4\pi}{3Z} R_0^3 n_e(R_0) \tag{8.43}$$

The first one (8.42) is the case regarding the electrons with positive energy are the free electron, while the second one (8.43) simply regards the free electron density is equal to the density at the boundary of the ion sphere.

8.4.2 Fitting Formula of TF Results

Many scientists have developed approximate fitting formulae for the numerical result of Thomas-Fermi model. One of the best is the formula derived by R. M. More [4] to be shown here. This can be applied any materials with different atomic and charge numbers. As mentioned by More, Thomas-Fermi equation has a kind of self-similarity to the hydrogen case ($Z = 1$ and $A = 1$). It is well-know that Thomas-Fermi data such as electron pressures P_e, and internal energy ε_e of plasma with Z and A can be reproduced once we have the data of the hydrogen case. At first, the plasma

density and electron temperature should be converted to the equivalent physical quantities for the hydrogen plasma.

$$\rho_1 = \frac{\rho}{AZ}, \quad T_1 = \frac{T}{Z^{4/3}} \tag{8.44}$$

More has shown that the charge state of any material at any density and temperature obtained with the numerical result of TF model can be reproduced by the following fitting formula.

$$Z^*(\rho, T) = Z \frac{x}{1 + x + \sqrt{1 + 2x}} \tag{8.45}$$

where x is a function of (ρ_1, T_1) [4].

Inserting this x into (8.45), the effective charge predicted by TF model is very precisely given. The resultant of effective ionization charge for $Z = 1$ and $A = 1$ is shown in Fig. 8.16. The density and temperature correspond to ρ_1 and T_1 and it is easy to obtain the charge state with the relation (8.44) for any elements.

It is clearly seen in Fig. 8.16 that for a given density and/or temperature, the ionization increases with the temperature and/or density, respectively. The former tendency is thermal ionization and common even in low density plasma, while the
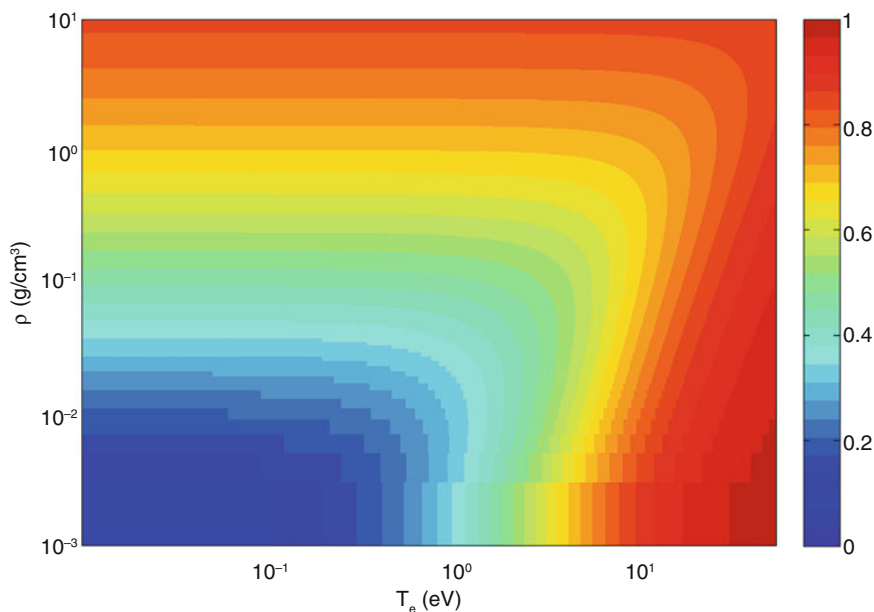
Fig. 8.16 Thomas-Fermi model has self-similarity solution, and all data of different Z number can be produced with use of the solution for hydrogen. Figure shows the ionization charge as a function of density and temperature by use of the fitting formula (8.45)

latter is typical for the high-density plasma. Since the number of states for the bound state decreases with the increase of density, many electrons must be in the free state. This indicate that Fermi energy of the electrons increases with the density and the plasma becomes Fermi degenerate state. So, in the dense plasma with low temperature and high density, Fermi degeneracy of electrons becomes important.

8.4.3 Property of Thomas-Fermi Results

The effective charge Z^* increases with the increase of density even at $T = 0$. Such ionization is called **pressure ionization**, because high density means the distance of nearby two ions makes a joint potential as schematically shown with the solid line in Fig. 8.17, and the **ionization potential depression (IPD) (lowering)** (χ) due to the overlapping of Coulomb potential allows the bound electrons in the higher-energy levels to be free. The pressure ionization is due to the depression of the ionization energy level by overlapping the potential of the nearby ions.

This has a very important information, since the depression of the ionization energy level means most of the upper-bounded discreet energy states with a large principal number should be eliminated in the partition function of (5.5). In solving the **Saha equation** of (5.14), most difficult point is the evaluation of the function of u_ζ and $u_{\zeta + 1}$. These values change dramatically depending on how the maximum quantum state can be regarded to be the bound states, since the number of states dramatically increases in the upper state as a single atom.

However, the physics image will change in the case of finite temperature, where the ions are moving due to thermal motion. In such case, it is better to obtain the probability for the nearest neighbor two ions. This is a problem of statistical physics, and it is informative to see the case of **Debye potential** for the ideal plasma. The

Fig. 8.17 The image of pressure ionization is shown by overlapping the potential profile of two isolated ions (dotted lines) and the potential by summing both (solid lines). The decrease of interatomic distance by imposed high pressure depresses the ionization energy level as the solid line
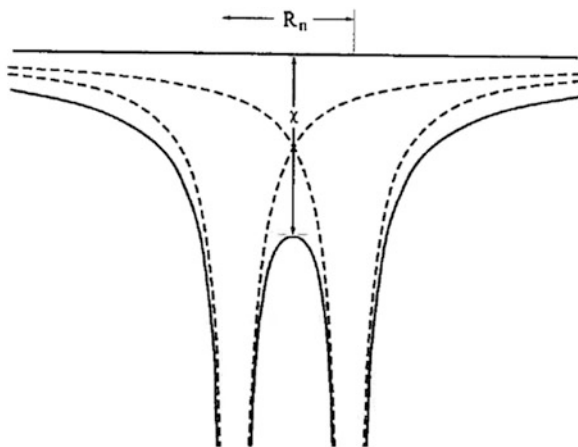
probability of another ion comes to the radius r of the central ion is given by the following Boltzmann distribution

$$f(r) = e^{-\frac{Ze}{T}\phi(r)} = exp\left(-\frac{Z^2e^2}{4\pi\varepsilon_0 Tr}e^{-k_D r}\right) \tag{8.46}$$

Let us introduce the two dimensionless values.

$$\Gamma_{ii} = \frac{Z^2e^2}{4\pi\varepsilon_0 TR_0} \tag{8.47}$$

$$x = \frac{r}{R_0} \tag{8.48}$$

where Γ_{ii} is called **ion-ion coupling parameter** and R_0 is the ion-sphere radius. Then, (8.46) is rewritten as,

$$f(x) = exp\left(-\frac{\Gamma_{ii}}{x}e^{-\frac{R_0}{\lambda_D}x}\right) \tag{8.49}$$

The condition of the ideal plasma requires the parameter Γ_{ii} is much smaller than unity. It is useful to see the radial structure of this probability. It is clear from (8.49) that $f(x)$ tends to zero near r = 0 and two ions repel each other via Coulomb repulsive force. At far distant point $f(x) = 1$ and this function is monotonically increase with the radius. It is very reasonable and coincides with our intuitive image.

Most of bound electrons with orbit radius more than R_0 as an isolated atom will be continuum in such many-body system. In case of hydrogen, the average orbit r_n of a s-state wave function is given in (5.26).

$$r_n = a_B \frac{n^2}{Z} \tag{8.50}$$

It is easy to calculate the critical ion density whose orbit radius of the principal quantum state n satisfies the condition.

$$\frac{4\pi}{3}r_n^3 n_i = 1 \quad \rightarrow \quad n_i = 3 \times 10^{22}\frac{Z^3}{n^6} \ [1/cm^3] \tag{8.51}$$

This approximately gives the critical principle number for pressure ionization. It is written also for hydrogen as

$$\rho_n = 0.05\frac{1}{n^6} \ [g/cm^3] \tag{8.52}$$

At high-density plasma, such lowering is very essential.

At the same time, the number of states of free electrons is also decreases as increase of density. It is useful to know that the number of free electron states per unit volume is given to be

$$N(E) = 2 \int_0^E g(k)dk = \frac{1}{3\pi} \left(\frac{2m}{\hbar^2} \right)^{3/2} E^{3/2} \tag{8.53}$$

where N(E) is the number of states of free electron to the energy of E. It should be noted that the energy obtained by setting $N = Zn_i$ is **Fermi energy**. The number of free electron states per ion is also decrease in proportion to the inverse of ion density for a given energy E. This means that increase of density, the pressure ionization decreases the number of bound electrons, while the number of states of free electrons also decreases with the increase of density. Then, the required pressure of compression will increase due to Fermi degeneracy of free electrons.

It is noted that TF model would be good enough for many problems even for contemporary subjects. The potential profile obtained by TF model can be used for an approximate potential for one electron Schrodinger equation. If you calculate the electron energy-states in the TF potential, it approximately reproduces the electron shell-structure (1s, 2s, 2p, 3s, 3p but then 4s comes before 3d. . .) of the periodic table of Mendeleev chart. It also correctly predicts how that structure is changed for high-charge ions.

TF is simple because it is one equation for all the electrons. The more accurate methods (Hartree or Hartree-Fock) have a separate differential equation for each electron, so it is 26 equations for Fe. Actually, of course, only 13 because the two spins (up and down spin) have almost the same potential, same equation.

Historically, the TF model has been extended to include another physical effect as shown in Chap. 6 in Ref. [16]. For example, the extension to molecules such as a hydrogen bonding shown in Fig. 8.2. The attractive force by the exchange interaction has been included as Thomas-Fermi-Dirac model, where the exchange potential is modeled as a function of local density. The density divergence near the central nuclear charge has been eliminated by Thomas-Fermi-Dirac-Weizsacker model. These models have been developed before commonly use of the computer, but it is informative to know how quantum mechanical equation should be simplified by use of such models. As the progress of computing, the following direct calculation of multi-electron and many-body system has become more popular.

8.5   Density Functional Theory for Multi-electron Interacting System

We have studied the structure of atoms by assuming the ion sphere model. The electron density distribution or the wave function of each electron have been solved based on simple models derived from quantum mechanics. In the case of high-

density plasma, it is essential to consider the statistical properties of many electrons whose wavefunctions spread over many nuclei. The nuclei also move slowly by the Coulomb force due to neighboring ions and surrounding electrons. It is natural to study such system with many charged particles by solving so-called "*ab-initio*" problem. The *ab-initio* calculation means to solve the many-body problem quantum-mechanically as exact as possible by starting from multi-electron Schrodinger or Dirac equations, for example, the **Hartree-Fock (HF) equation** mentioned in Chap. 5 gives us the exact solution of the grand state of the many-electron system [16, 17]. To solve HF equation directly, however, faces numerical difficulty even with the supercomputer, and the **density functional theory (DFT)** based on the HF theory is widely used for the *ab-initio* calculation.

The rapid progress of supercomputer has made it possible to solve such complicated problem in a reasonable CPU time. As shown in Fig. 8.1, it is surprising to know the progress of CPU time, for example, from the fastest supercomputer in the world ***Earth simulator*** in 2002 to now ***Fugaku*** in 2020 [18]. Their speeds are respectively 40 TF and 400 PF, namely 10,000 times progress in CPU over the last 18 years in Japan (the world). Computer scientists are always demanded to challenge new and more *ab-initio* methods according to the progress of computer capability.

Note, however, that if we would like to solve the N electron system with M classical nuclei like fixed points in space, Schrodinger equation for N electron system becomes a problem to solve it in 3N space dimension in three-dimensional real space, for example, in HF theory. Of course, challenges to solve HF equation by integrating over 3N space by use of Monte Carlo method has been carried out like a **quantum Monte Carlo (QMC)** [19].

More flexible numerical method, on the other hand, has been widely used mainly in the solid-state physics. In this method, Schrodinger equation for N electrons is independently solved as one-electron problem in an effective potential given as a function of the local electron density. This is called **density functional theory (DFT)**, which results from the work of Hohenberg, Kohn and Sham [16]. This method has been applied also to atoms and molecules. In laser-produced warm dense plasmas, DFT has been extended to the system with finite temperature, for example, as reviewed in [20].

The simulation codes of DFT have been developed with different numerical schemes. They have been compared as code-comparison for the case of solids at T = 0 in [21]. It is surprising to know that many codes gave almost the same results with good accuracy. Here, after a brief explanation of the Hartree-Fock theory, the basic equation of DFT is derived for the case of finite temperature.

8.5.1 Hartree-Fock Theory of Multi-electron System

In Sect. 5.3, how to study the quantum state of single atom with multi electrons has been discussed. In the case of Helium atom, anti-symmetry of the total electron wave function is required to provide not only Coulomb interaction but also the exchange

interaction between two electrons. When a system has N_n nuclei and N electrons, the total Hamiltonian of the system is given in the form for **Born-Oppenheimer approximation**, where nuclei are fixed.

$$H_H = \sum_{i=1}^{N} H_{H,i} \tag{8.54}$$

where $H_{H,\,i}$ is one-electron Hamiltonian indicated with "i" for the case when the wave functions of the other electrons are given.

$$H_{H,i} = -\frac{\hbar^2}{2m}(\nabla_i)^2 - \frac{e^2}{4\pi\varepsilon_0}\sum_{k=1}^{N_n}\frac{Z_k}{|\boldsymbol{r_i}-\boldsymbol{R_k}|} + \frac{e^2}{4\pi\varepsilon_0}\sum_{j\neq i}^{N}\frac{1}{|\boldsymbol{r_i}-\boldsymbol{r_j}|}|\psi_j|^2 \tag{8.55}$$

Assume the total wave function Ψ is given as the product of single electron, namely, Ψ has the form.

$$\Psi_H(\boldsymbol{r}_1, \boldsymbol{r}_2, \ldots \boldsymbol{r}_N) = \psi_1(\boldsymbol{r}_1)\psi_2(\boldsymbol{r}_2)\cdots\cdots\psi_N(\boldsymbol{r}_N) \tag{8.56}$$

This assumption is called the **Hartree approximation**. Note that the subscripts of the wave functions are independent number of the subscripts of the positions. The Schrodinger equation for $\psi_i(\boldsymbol{r}_i)$ is shown as

$$H_{H,i}\psi_i(\boldsymbol{r}_i) = \varepsilon_i\psi_i(\boldsymbol{r}_i) \quad \text{for } i = 1, \ldots N \tag{8.57}$$

where ε_i is the eigen value of the i-th electron and Coulomb interaction energy with the other electrons is consistently included. Since (8.57) is a nonlinear equation and is required to be solved iteratively by a numerical method so that the numerical solution is self-consistent. The solution of (8.57) has no exchange interaction between the electrons. The formulation should take account of the property of Fermion of the electron.

It is known that the total wave function of the Fermion gas should be anti-symmetry. Namely, the exchange of two electrons in the system should change the sign of the total wave function. A simple form of (8.56) is not acceptable as Fermion gas. The anti-symmetric total wave function is given by the following Slater determinant. It also should include the freedom of the electron spin, up or down (denoted with "s"). For simplicity, the coordinate including the spin (**r**, s) is shown as **x** in what follows.

$$\Psi_{HF}(\boldsymbol{x}_1, \boldsymbol{x}_2, \ldots \boldsymbol{x}_N) = \frac{1}{\sqrt{N!}}\begin{vmatrix} \psi_1(\boldsymbol{x}_1) & \cdots & \psi_N(\boldsymbol{x}_1) \\ \vdots & \ddots & \vdots \\ \psi_1(\boldsymbol{x}_N) & \cdots & \psi_N(\boldsymbol{x}_N) \end{vmatrix} \tag{8.58}$$

This is called **Hartree-Fock approximation**. Then, the Schrodinger equation for the i-th electron is given as the same form, but the Hamiltonian becomes differential and integral operator $\mathcal{F}$ [16].

$$E_{HF} = \langle \Psi_{HF} | H | \Psi_{HF} \rangle = \sum_{i=1}^{N} H_i + \frac{1}{2} \sum_{i=1}^{N} \sum_{j=1}^{N} \left(J_{ij} - K_{ij} \right) \qquad (8.59)$$

where H_i, J_{ij}, and K_{ij} are defined as

$$H_i = \int \psi_i^*(\boldsymbol{x}) \left[-\frac{\hbar^2}{2m} \nabla^2 - \frac{e^2}{4\pi\varepsilon_0} \sum_{k=1}^{N_n} \frac{Z_k}{|\boldsymbol{r} - \boldsymbol{R}_k|} \right] \psi_i(\boldsymbol{x}) d\boldsymbol{x} \qquad (8.60)$$

$$J_{ij} = \frac{e^2}{4\pi\varepsilon_0} \iint |\psi_i(\boldsymbol{x_1})|^2 \frac{1}{|\boldsymbol{r}_1 - \boldsymbol{r}_2|} |\psi_j(\boldsymbol{x_2})|^2 d\boldsymbol{x}_1 d\boldsymbol{x}_2 \qquad (8.61)$$

$$K_{ij} = \frac{e^2}{4\pi\varepsilon_0} \iint \psi_i^*(\boldsymbol{x_1}) \psi_j(\boldsymbol{x_1}) \frac{1}{|\boldsymbol{r}_1 - \boldsymbol{r}_2|} \psi_j^*(\boldsymbol{x_2}) \psi_i(\boldsymbol{x_2}) d\boldsymbol{x}_1 d\boldsymbol{x} \qquad (8.62)$$

Note that all integrals result real values and $J_{ij} \geq K_{ij} \geq 0$. The J_{ij} is **Coulomb integral** representing the Coulomb repulsive force between all two electrons in the system. On the other hand, the K_{ij} is the **exchange integral** and stems from the force due to the exclusive principle of Fermion particles. The exchange energy is purely quantum mechanical one and it appears because we have adopted the total wave function in the form Slater determinant to guarantee its anti-symmetry. It is important to note the fact that both energies look unphysical interaction for the case of $j = i$, while this unphysical case is excluded for the total energy in (8.59) since

$$J_{ii} = K_{ii} \qquad (8.63)$$

We adopt (8.63) for extending to the density functional formulation to be discussed soon.

Same as the Hartree approximation, we must adopt the wave functions $\psi_i(\boldsymbol{r})$ orthogonal, and then the following N coupled Schrodinger equation is obtained for the i-th single wave function.

$$\widehat{\mathcal{F}}(\boldsymbol{x})\psi_i(\boldsymbol{x}) = \sum_{j=1}^{N} \varepsilon_{ij} \psi_j(\boldsymbol{x}) \qquad (8.64)$$

where $\widehat{\mathcal{F}}$ is **Hartree-Fock Hamiltonian**.

$$\widehat{\mathcal{F}}(\boldsymbol{x}) = -\frac{\hbar^2}{2m} \nabla^2 - \frac{e^2}{4\pi\varepsilon_0} \sum_{k=1}^{N_n} \frac{Z_k}{|\boldsymbol{r} - \boldsymbol{R}_k|} + \widehat{g}(\boldsymbol{x}) \qquad (8.65)$$

In (8.64), ε_{ij} is the eigen-value derived in matrix. (8.64) is called **Hartree-Fock equation.**

On the right-hand side of (8.65), the first term the kinetic energy, the second term is Coulomb interaction with all nuclei, and the third term is integral operator due to the Coulomb and exchange interaction of the i-th electron with all other electrons in the system. It is given in the form.

$$\widehat{g}(\boldsymbol{x}) = \widehat{j}(\boldsymbol{x}) - \widehat{k}(\boldsymbol{x}) \tag{8.66}$$

where the Coulomb coupling operator and exchange interaction operator are given to be

$$\widehat{j}(\boldsymbol{x})\psi_i(\boldsymbol{x}) = \frac{e^2}{4\pi\varepsilon_0} \sum_{j=1}^{N} \int |\psi_j(\boldsymbol{x}')|^2 \frac{1}{|\boldsymbol{r} - \boldsymbol{r}'|} \psi_i(\boldsymbol{x}) d\boldsymbol{x}' \tag{8.67}$$

$$\widehat{k}(\boldsymbol{x})\psi_i(\boldsymbol{x}) = \frac{e^2}{4\pi\varepsilon_0} \sum_{j=1}^{N} \int \psi_j^*(\boldsymbol{x}')\psi_i(\boldsymbol{x}') \frac{1}{|\boldsymbol{r} - \boldsymbol{r}'|} \psi_j(\boldsymbol{x}) d\boldsymbol{x}' \tag{8.68}$$

A new eigen value ε_i defined as follows is obtained by integrating (8.65) after the product with ψ_i^*.

$$\varepsilon_i \equiv \varepsilon_{ii} = \langle \psi_i | \widehat{\mathcal{F}} | \psi_i \rangle = H_i + \sum_{j=1}^{N} \left(J_{ij} - K_{ij} \right) \tag{8.69}$$

Then, the total energy is given as

$$E_{HF} = \sum_{i=1}^{N} \varepsilon_i - V_{ee} \tag{8.70}$$

$$V_{ee} = \frac{1}{2} \sum_{i,j=1}^{N} \left(J_{ij} - K_{ij} \right) \tag{8.71}$$

It is easily verified that the total wave function given in Slater determinant results the following form for two location probability after integration by $\boldsymbol{x}_3, \cdots \boldsymbol{x}_n$ space.

$$\mathrm{n}(\boldsymbol{x}_1, \boldsymbol{x}_2) = \frac{1}{N(N-1)} \sum_{k,l}^{N} |\psi_k(\boldsymbol{x}_1)|^2 |\psi_l(\boldsymbol{x}_2)|^2 - \psi_k^*(\boldsymbol{x}_1)\psi_k(\boldsymbol{x}_2)\psi_l^*(\boldsymbol{x}_2)\psi_l(\boldsymbol{x}_1) \tag{8.72}$$

The probability of two electrons at the same place and with the same spin $\boldsymbol{x}_1 = \boldsymbol{x}_2$ becomes null.

8.5.2   Kohn-Sham Density Functional Theory (DFT)

Kohn-Sham theory provides the exact solution for the grand state of the system with many electrons and many nuclei by solving the following eigen-value problem of each electron. Then, the exchange effect due to the spin is modeled in the effective potential as a function of density. It starts to solve the single electron Schrodinger equation with the effective Hamiltonian derived by Kohn-Sham, $H_{KS}(\boldsymbol{r})$.

$$H_{KS}(\boldsymbol{r})\varphi_i(\boldsymbol{r}) = \varepsilon_i \varphi_i(\boldsymbol{r}) \tag{8.73}$$

where **Kohn-Sham Hamiltonian** is given in the form

$$H_{KS}(\boldsymbol{r}) = -\frac{\hbar^2}{2m}\nabla^2 + V_{KS}(\boldsymbol{r}) \tag{8.74}$$

On RHS in (8.74), the first term is the kinetic energy of electron and the second term is the effective potential which is only the function of the electron density defined by

$$n(\boldsymbol{r}) = \sum_{i=1}^{N} |\varphi_i(\boldsymbol{r})|^2 \tag{8.75}$$

It is assumed that KS potential is given as a function of density

$$V_{KS}(\boldsymbol{r}) = f[n(\boldsymbol{r})] \tag{8.76}$$

It is important to note that the effective potential (Kohn-Sham) potential $V_{KS}(\boldsymbol{r})$ is common to all N electrons, so the eigen-energy ε_i and eigen-function $\varphi_i(\boldsymbol{r})$ can be obtained by solving (8.73) as a single electron system. The orthogonality of all wave functions is certified. In solid-state physics, it is enough to obtain the N electron configuration after solving (8.73) for N wave functions from the lowest energy state. However, in the case of dense plasmas, it is required to solve many wave functions including excited states because of thermal excitation of electrons.

For the case where the computational system is assumed to have N_n nuclei and N electrons, the KS potential is given in the form:

$$V_{KS}(\boldsymbol{r}) = V_{ne}(\boldsymbol{r}) + V_H(\boldsymbol{r}) + V_{xc}(\boldsymbol{r}) \tag{8.77}$$

where $V_{ne}(\boldsymbol{r})$ is Coulomb potential to the i-th electron by the nuclei and given as

$$V_{ne}(\boldsymbol{r}) = -\frac{e^2}{4\pi\varepsilon_0}\sum_{j=1}^{N_n}\frac{Z_j}{|\boldsymbol{r} - \boldsymbol{R}_j|} \tag{8.78}$$

where Z_j and $\boldsymbol{R}_j$ are the nuclear charge and position of the j-th nucleus. The second term on RHS in (8.77) is the **Hartree potential** by all electron at the point $\boldsymbol{r}$.

$$V_H(\boldsymbol{r}) = \frac{e^2}{4\pi\varepsilon_0} \int d^3\boldsymbol{r}' \frac{n(\boldsymbol{r})}{|\boldsymbol{r} - \boldsymbol{r}'|} \tag{8.79}$$

The third term in (8.77) stands for the potential giving the force stemming from the **exchange and correlation (xc) energy** among N electrons. In DFT, both energies are represented with E_{xc} as a function of only the electron density $n(\boldsymbol{r})$. Then, $V_{xc}(\boldsymbol{r})$ in (8.77) is defined by the functional derivative.

$$V_{xc} = \frac{\delta E_{xc}}{\delta n(\boldsymbol{r})} \tag{8.80}$$

It is better to say that if the exchange-correlation (xc) energy E_{xc} is derived as a function of the local density exactly, Kohn-Sham density functional theory is exact. This exchange-correlation energy E_{xc} is not only these two energies, but it represents all energy left in (8.77) stemming from multi-electron system. It is hard job to correctly formulate the **xc energy,** and it is usually defined approximately.

In solving DFT with computers, many numerical schemes have been developed. This is reported as code comparison in [21]. Typical numerical issue in calculating all wave functions with (8.73) appear from the fact that some electron wave function changes smoothly far from any nuclei, while it changes rapidly near a nucleus due to the deep Coulomb potential.

8.5.3   Density Functional Theory for Finite Temperature System

The Kohn-Sham theory has been applied to the case of solids, where total electrons are in the ground state. In the case of finite electron temperature ($T \neq 0$), we must extend the Kohn-Sham theory so that the electrons are excited thermally to have a finite probability at the higher energy levels. Then, it is reasonable to assume that the electron energy distribution is given by Fermi-Dirac distribution f_{FD}.

$$f_{FD}(\varepsilon_i) = \frac{1}{exp[(\varepsilon_i - \mu)/T]} \tag{8.81}$$

where μ is the chemical potential. With the factor two of spin freedom, the electron density is given as

$$n(\boldsymbol{r}) = 2 \sum_{i=1}^{N} f_{FD}(\varepsilon_i)|\varphi_i(\boldsymbol{r})|^2 \tag{8.82}$$

The unknown chemical potential μ is determined to satisfy the electron number conservation relation:

$$N = 2 \sum_{i=1}^{N} f_{FD}(\varepsilon_i) \tag{8.83}$$

After solving the above relations with one-electron Schrodinger Eq. (8.73) iteratively, the self-consistent density and each eigen-energy give the total energy of the electrons E in the system.

$$E = \sum_{i=1}^{N} f_{FD}(\varepsilon_i)\varepsilon_i - \frac{1}{2} \frac{e^2}{4\pi\varepsilon_0} \int d^3\mathbf{r} \int d^3\mathbf{r}' \frac{n(\mathbf{r})n(\mathbf{r}')}{|\mathbf{r} - \mathbf{r}'|} + E_{xc}$$
$$- \int d^3\mathbf{r} V_{xc}(\mathbf{r})n(\mathbf{r}) \tag{8.84}$$

where the first term is the sum of eigen energies of N electrons as single electron. Since this term double counts the Coulomb interaction energy among multi-electrons, the second term is needed in (8.84).

In (8.84), the total exchange energy for each electron is defined by the following integral.

$$E_{xc} = \int d^3\mathbf{r}\varepsilon_{xc}(\mathbf{r})n(\mathbf{r}) \tag{8.85}$$

It is very hard subject to derive the local exchange-correlation energy $\varepsilon_{xc}(\mathbf{r})$ as a function of the local density $n(\mathbf{r})$ [22]. In the form (8.84), the xc energy is also double counted and the fourth term is required.

In the actual computation, the coupled equations are solved iteratively so that the numerical result becomes self-consistent.

In [20], **density functional theory with molecular dynamics (DFT-MD)** has been developed to solve the problem including the ion motion. New formulation of the xc energy for finite-temperature hydrogen has been derived and its effect has been discussed in WDM. Using the Kohn-Shan approach, the xc energy of the system, $\varepsilon_{xc}(\mathbf{r})$, is replaced by the xc free energy $f_{xc}(\mathbf{r})$ within the local density approximation (LDA) based on parametrized path integral Monte Carlo data for the **uniform electron gas (UDG)** at warm dense matter conditions [20].

In the UDG, Slater has derived the following simplest form of the xc energy as a function of density for solids [16]:

$$\varepsilon_{xc}(\mathbf{r}) = an^{1/3}, \qquad a = -\frac{3}{4}\left(\frac{3}{\pi}\right)^{1/3} \tag{8.86}$$
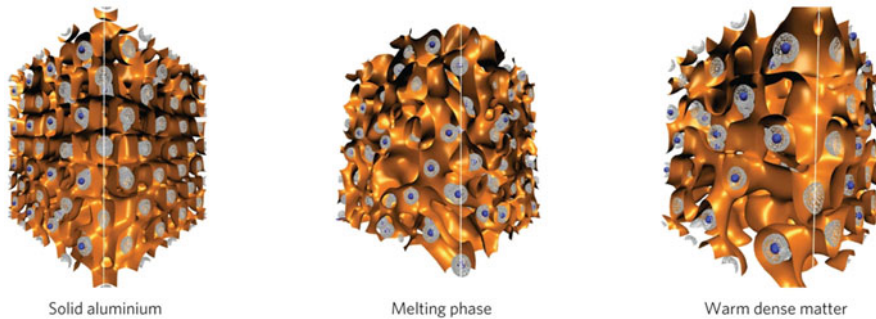
Fig. 8.18 The density surface distribution for given density in three different stage in laser compression of solid aluminum. The simulation is carried out with time-dependent density functional theory (TDDFT). Reprinted by permission from Macmillan Publisher Ltd: ref. [23], Copyright 1993

This simplest form has been used for many cases. The intensive works have focused on the improvement of the density functional form of the xc energy as general form for the grand state in solids. In the case of WDM system with finite temperature, the research to formulate the xc energy is still challenging subject [22].

In Fig. 8.18, three snap shots of time-dependent density functional theory simulations of the formation of WDM are shown This is the result of TDDFM based on DFT-MD to the following experiment [23].

Two 4.5 J laser beams were used to irradiate 50-µm-thick Al foils (initial density of $\rho = 2.7$ g/cm^3) coated with 2-µm-thick perylene. The laser beams were absorbed by the perylene, heating the material, and two counter-propagating multi-Mbar shock waves were launched into the solid aluminum by ablation pressure. Within 0.5 ns, the laser power rose to a power that was constant over time, with an intensity of 35 TWcm^{-2}. Each laser operated at 527 nm and was spatially smoothed over a focal spot of 60 µm to launch strong shocks.

The left is solid state, the middle is melting phase, and the right is WDM state. In the figure, the ions (blue) abandon their lattice positions. Although core electrons (grey) remain mostly unchanged, the delocalized conduction electrons (represented by orange iso-surfaces) are disturbed from the very regular structure in the lattice.

8.5.4   Time Dependent DFT

Numerical method, of course, changes in solving the **time dependent DFT (TDDFT)**. The basic equation to be solved is now the following **time-dependent Schrodinger equation**.

$$i \frac{\partial}{\partial t} \varphi_i(\boldsymbol{r}, t) = H_{KS}(\boldsymbol{r}, t) \varphi_i(\boldsymbol{r}, t) \tag{8.87}$$

The Kohn-Sham Hamiltonian is given with the same form (8.74) as functions of the time-dependent density $n(\boldsymbol{r}, t)$. The density is defined by (8.82). If we use the finite dereference method to the time integration, the iteration should be carried out to keep the consistency of Kohn-Sham theory at each time step.

At first, consider that case of very fast phenomena seen when an ultra-short laser pulse irradiate gas with atom or molecule. Even in such a case of single atom or molecule, DFT is useful to obtain the spectrum of **higher-harmonic generation (HHG)** due to nonlinear oscillation of electrons in the gas. In Chap. 2 (Volume-1), the **multi-photon ionization** process has been discussed. When an intense laser is irradiated with the intensity less than dominant ionization process, the bound electrons oscillate in the potential by nuclei and this un-harmonic oscillation causes the emission of many harmonic radiations.

As shown in [24], the time dependent potential by the laser electric field $V_L(\boldsymbol{r}, t)$ is given under the dipole approximation.

$$V_{KS}(\boldsymbol{r}) \Rightarrow V_{KS}(\boldsymbol{r}, t) + V_L(\boldsymbol{r}, t) \tag{8.88}$$

where

$$V_L = E_0 f(t) \sin(\omega t) \boldsymbol{r} \cdot \boldsymbol{\alpha} \tag{8.89}$$

where the peek electric field is E_0 and the structure of laser envelope is f_0 and $\boldsymbol{\alpha}$ is the unit vector showing the laser polarization. Note that (8.87) is applicable only in the non-relativistic case. In the ultra-intense and relativistic laser case, Schrodinger equation should be replaced by Dirac equation and the potential V_L should include the force by magnetic field of laser.

It is useful to see TDDFT simulation applied for the HHG from the He atom as shown in Fig. 8.19 [24]. Note that the solid line is obtained from the simulation and the squares represent experimental data. It is concluded that even atomic or molecular gas system, DFT results reasonable HHG spectrum being able to explain the corresponding experiment.

More complicated case where laser is irradiated to solid and other has been carried out. The time-dependent simulation code is now available as an open source (name SALMON) in our community [25].

8.5.5   Quantum Molecular Dynamics (QMD)

To study a long-time evolution of WDM, it is necessary to solve the motion of nuclei consistently. It is reasonable to assume that since the mobility of electrons is much
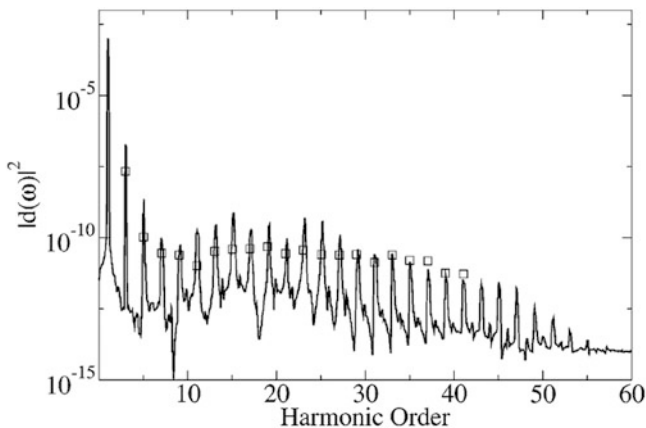
Fig. 8.19 The higher-harmonic generation (HHG) is clearly seen by the post process of the dipole moment spectral analysis with total wave functions obtained from TDDFT. Reprinted with permission from Ref. [24]. Copyright by Annual Review Journal

larger than that of nuclei, DFT is applicable to given positions of nuclei at each time step. The motion of a nucleus k is governed by the following equation of motion.

$$M_k \frac{d}{dt} \boldsymbol{v}_k = - \nabla_k [E_e(\boldsymbol{R}_k) + V(\boldsymbol{R}_k)] \tag{8.90}$$

where M_k, $\boldsymbol{v_k}$, and $\boldsymbol{R}_k$ are the mass, velocity, and position of a nucleus k. $E_e(\boldsymbol{R}_k)$ is the total electron energy at the point $\boldsymbol{R}_k$ calculated by DFT for electron system. In addition, the nucleus k is affected the Coulomb force by the other nuclei whose potential energy is given as

$$V(\boldsymbol{R}_k) = \frac{e^2}{4\pi\varepsilon_0} \sum_{j=1}^{N_n} \frac{Z_k Z_j}{|\boldsymbol{R}_k - \boldsymbol{R}_j|} \tag{8.91}$$

Since the force to nuclei is given at each time step by quantum mechanical method DFT, it is QMD and different from the classical molecular dynamics (MD) where usually the force is given by Lenard-Johns type potential shown in (8.4).

In Fig. 8.19, three snap shots of time dependent DFT simulation are already shown [23]. This is the case of DFT-QMD simulation. Do not confuse that TDDFT for (8.87) is the time-dependent simulation of electron dynamics for fixed nuclei and the time step is very short, while the DFT-QMD is the time evolution of ion motions with time step much longer than the previous case. It is, of course, easy to extend TDDFT to follow the motion of nuclei, but the problem is the time-consuming computation time.

References

1. E. Wigner, H.B. Huntington, On the possibility of a metallic modification of hydrogen. J. Chem. Phys. **3**, 764 (1935). National Science Council, Frontier in High Energy Density Physics, The National Academies Press (2003).
2. C. Kittel, *Introduction to Solid State Physics*, 8th edn. (Wiley, 2005)
3. R.W. Smithwick, Application of the screened Hydrogenic model to light atoms. Comput. Chem. **9**, 131 (2021)
4. R.M. More, *Pressure Ionization, Resonance and the Continuity of Bound and Free states*, Advances in Atomic and Molecular Physics, vol 21 (Academic Press, 1985), p. 305
5. R.M. More, Electron energy levels in dense plasmas. J. Quant. Spectrosc. Radiat. Transf. **27**, 345–357 (1982)
6. S. Atzeni, J. Myer-ter-Vehn, *The Physics of Inertial Fusion* (Oxford Science Publication, 2004), p. 327
7. F. Wang et al., Calculation of photoionized plasmas with a detailed-configuration-accounting atomic model. J. Phys. Soc. Jpn. **78**, 064301 (2009)
8. J.C. Stewart, K.D. Pyatt Jr., Lowering of ionization potentials in plasmas. Astrophys. J. **144**, 1203 (1966)
9. G.B. Zimmerman, R.M. More, Pressure ionization in laser-fusion target simulation. J. Quant. Spectrosc. Radiat. Transfer **23**, 517–522 (1980)
10. G.D. Tsakiris, K. Eidmann, An approximate method for calculating Planck and Rosseland mean opacities in hot, dense plasmas. J. Quant. Spectrosc. Radiat. Transf. **38**, 353 (1987)
11. G. Faussurier, C. Blancard, P. Renaudin, Equation of state of dense plasmas using a screened-hydrogenic model with ℓ-splitting, High Energy Density Phys. 4 (2008) 114–123
12. G. Faussurier, C. Blancrad, A. Decoster, New screening coefficients for the hydrogenic ion model including ℓ-splitting for fast calculation of atomic structure in plasmas, J. Quant. Spectrosc. Radiat. Transfer. **58**, 233–260 (1997)
13. R.L. More et al., A new quotidian equation of state (QEOS) for hot dense matter. Phys. Fluids **31**, 3059 (1988)
14. R.P. Feynman, N. Metropolis, E. Teller, Equations of state of elements based on the generalized Fermi-Thomas theory. Phys. Rev. **75**, 1561 (1949)
15. R.P. Feynman, *Surely You're Joking, Mr. Feynman!* (Adventures of a Curious Character, 1997)
16. R.G. Parr, W. Yang, *Density-Functional Theory of Atoms and Molecules* (Oxford University Press, 1989)
17. B.H. Bransden, C.J. Joachain, *Physics of Atoms and Molecules* (Lomgman Group, 1983)., Chap. 7
18. S. Kudo, K. Nitadori, T. Ina, T. Imamura, Prompt Report on Exa-Scale HPL-AI Benchmark. In *2020 IEEE International Conference on Cluster Computing (CLUSTER)*, 2020, pp. 418–419, https://doi.org/10.1109/CLUSTER49012.2020.00058
19. J.M. Thijssen, *Computational Physics*, 2nd edn. (Cambridge University Press, 1999)., Chap 5
20. M. Bonitz et al., Ab initio simulation of warm dense matter. Phys. Plasmas **27**, 042710 (2020)
21. K. Lejaeghere et al., Reproducibility in density functional theory calculation of solids. Science **351**, 1415 (2016)
22. K. Ramakrishna, T. Dornheim, J. Vorberger, Influence of finite temperature exchange-correlation effects in hydrogen. Phys. Rev. B **101**, 195129 (2020)
23. L. Fletcher, H. Lee, T. Döppner, et al., Ultrabright X-ray laser scattering for dynamic warm dense matter physics. Nature Photon **9**, 274–279 (2015). https://doi.org/10.1038/nphoton.2015.41
24. M.A.L. Marques, E.K.U. Gross, Time-dependent density functional theory. Annu. Rev. Phys. Chem. **55**, 427 (2004)
25. A. Yamada, K. Yabana, Multiscale time-dependent density functional theory for a unified description of ultrafast dynamics: Pulsed light, electron, and lattice motions in crystalline solids. Phys. Rev. B **99**, 245103 (2019)

Chapter 9
Physical of Warm Dense Matters

Abstract Continuous progress of compute capability, DFT has been used to study complicated physics of warm-dense matter (WDM) to compared to a variety of experimental results in laboratories obtained by compression and heating of solids with intense lasers. The phase transition of insulator-metal of hydrogen is now hot topics in high-pressure physics (HPP). Advancement of laser technology and diagnostics have made such challenging subjects as precision science.

In twenty-first century, x-ray free electron laser (XFEL) facilities have been constructed as users' facility. XFEL is new method to precision diagnostics of dense matters via x-ray Thomson scattering (XRTS). For bridging the experiment and theory to analyze XRTS data, Chihara formulated scattering spectra by decomposing three dynamical structure factors (DSF). Now, time-dependent DFT (TDDFT) is also solved with supercomputer to apply laser-matter interaction in quantum world.

In this chapter, whole stories and models are explained and some examples are explained regarding the application to analyze experimental data obtained with intense lasers and XFEL.

9.1   Shock Dynamic Compression and Equation of State

A static compression method to study the thermodynamic property of compressed matters was explained in Chap. 8, where a study of the metallic hydrogen with a **diamond anvil cell (DAC)** is described. Such static mechanical compression of matters is useful tool for study of the properties of matters at low temperature, and such study is called **high-pressure physics.** The extremely high pressure up to 5 Mbar is achieved at the present day. Since the property of metal is defined at the temperature of the null Kelvin, DAC would be a good device to study such high-pressure physics for the condensed matter physics.

As the readers see here, on the other hand, it is possible to compress matters to pressure higher than the static methods with DAC by use of intense lasers. The ablation pressure loaded on solid sample surface generates shocks during the time comparable to the laser pulse duration, namely order of 10^{-9} s (~ns). Although it is

very short time, the time need to change from the initial state to the shocked state is shorter than the laser pulse and thermodynamic equilibrium relation can be used in general even in the case where phase transition happens at the shock front.

The achievable pressure depends on the laser intensity and its wavelength as shown in Chap. 3. Most of the recent experiments use the intensity less than several 10^{14} W/cm^2 and laser wavelength of 0.35 μm, and the experimental range covers the pressure up to 100 Mbar. In general, the physical quantities of equation of state are derived using Ranking-Hugoniot (RH) relation. The curve obtained from the RH relation is called the **Hugoniot curve** as shown in Chap. 3. This topic is well described in the textbook by Zel'dovich and Raizer [1]. The experiments to obtain the Hugoniot curve of a variety of solid materials at extremely high pressure have been done with high-explosive or nuclear underground test. The theory and experiment before the 1960s are well described in Chapter XI-2 in the book [1].

In general, the pressure of matters is divided into three components as Helmholtz free energies in (8.9).

$$P(V,T) = P_c(V) + P_i(V,T) + P_e(V,T) \tag{9.1}$$

where $V = 1/\rho$ is the specific volume. In what follows, we use both of V and the mass density ρ for convenience. The $P_c(V)$ is the **cold pressure** of matters at temperature equal to zero. This pressure is the target in the study by use of DAC. In the shock compression, the temperature also increases as the density, and the Hugoniot curve also depends on the thermal pressure by the motion of nuclei, namely ions $P_i(V,T)$, and the contribution by thermal electrons $P_e(V,T)$. The ion pressure includes the contribution by phonons and ion thermal motion. The Debye theory is famous at low temperature condensed matters [2].

It is better to see one example for the case of a solid at the initial state. In the book [1], the case of solid lead is shown, and its data are shown in Table 9.1. The solid lead is compressed by the pressure up to 4 Mbar and its density increases to 2.2 times the solid density. It is clear in Table 9.1 that even with heating by a shock wave up to about 2.3 eV, the cold pressure is predominant in (9.1), while the internal energy looks distributed almost equally to the three components; namely, equal energy partition. Mostly the compressed state is kept by the cold pressure in (9.1), consequently, to know $P_c(V)$ is very important.

Table 9.1 Parameter behind a strong shock wave in lead. Pressure, energy, and temperatures are in the units of Mbar, eV, and eV, respectively. Reprinted with permission from ref. [1]. Copyright by Cambridge University Press

ρ/ρ_0	P	P_c	P_i	P_e	P_c/P	$\varepsilon - \varepsilon_0$	ε_c	T
1.3	0.25	0.21	0.03	0.0005	0.84	0.25	0.15	0.09
1.5	0.65	0.51	0.14	0.0063	0.78	0.96	0.47	0.30
1.7	1.33	0.95	0.34	0.038	0.71	2.42	0.96	0.74
1.9	2.25	1.56	0.56	0.127	0.69	4.71	1.63	1.29
2.1	3.36	2.33	0.73	0.290	0.69	7.75	2.48	1.92
2.2	4.01	2.77	0.93	0.415	0.69	9.65	2.97	2.28

Progress of technology of pressure-drivers and diagnostics has led the experiments to a laboratory scale and precise data are now available experimentally. The diagnostics is essential ingredient for such research, but we don't describe the details of the diagnostics and limit in this book only to explain its physical principle.

9.1.1   Theoretical Base for Shock Equation of State

Assume that the physical quantities in front of a shock, ρ_0, P_0 and ε_0 are known in (3.10, 3.11, and 3.12). Introducing the shock velocity, U_s, and compressed matter velocity, U_p, which is equal to the piston velocity in the laboratory frame, we can replace u_0 and u_1 with them.

$$U_s = u_0, \quad U_p = u_0 - u_1 \tag{9.2}$$

If we can obtain these velocities experimentally, we can solve (3.10, 3.11, and 3.12) to obtain the physical quantities in the shock compressed region,

$$
\begin{aligned}
\rho_1 &= \rho_0 \frac{U_s}{U_s - U_p} \\
P_1 &= P_0 + \rho_0 U_s U_p \\
\varepsilon_1 &= \varepsilon_0 + \frac{1}{2}(P_1 - P_0)\left(\frac{1}{\rho_0} - \frac{1}{\rho_1}\right)
\end{aligned}
\tag{9.3}
$$

With given values of U_s and U_p for single-shock dynamics, the thermodynamic state after the shock passage are given by (9.3). This curve of density vs pressure is called the **Hugoniot curve**.

In general, for the case of high-pressure applied to the solid or liquid samples, it is possible to neglect the initial values of P_0 and ε_0 in (9.3) and we obtain

$$
\begin{aligned}
P &= \rho_0 U_p^2 \left(1 - \frac{V}{V_0}\right) \\
\varepsilon &= \frac{1}{2} P V_0 \left(1 - \frac{V}{V_0}\right)
\end{aligned}
\tag{9.4}
$$

where the suffix "1" is omitted for simplicity. The cold components must be given by the integral:

$$\varepsilon_c = -\int_{V_0}^{V} P_c dV \tag{9.5}$$

Fig. 9.1 Pressure-Volume
(P-V) diagram with
adiabatic relation P_c and
Hugoniot relation PH, when
the initial volume V_{0c} is
compressed to the volume
V. Since the shock wave
accompanies the increase of
entropy by altering flow
kinetic energy to the thermal
energy at the shock front,
the compressed matter has
extra internal energy O-A-B
compared to that for the case
of adiabatic compression.
Reprinted with permission
from ref. [1]. Copyright by
Cambridge University Press
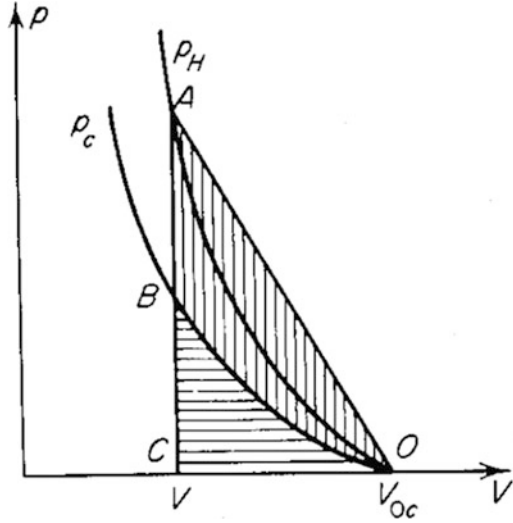
Plotting the Hugoniot cure for P ($=P_H$) and the cold curve P_c as functions of the
specific volume V with use of (9.4) in Fig. 9.1, it is clear graphically that

1. The increase of the internal energy by shock is given by the area of the triangle of
   O-A-C from (9.4).
2. The energy increase of the cold component is given by the area of O-B-C shaded
   by the horizontal lines as defined in (9.5).
3. The increase of the thermal energy by shock is the area of O-A-B shaded by the
   vertical lines.

Let us evaluate the energy given to the kinetic flow energy K in the shocked region.
K is easily obtained from (9.2) and (9.4) that

$$K = \frac{1}{2} U_p^2 = \frac{1}{2} PV_0\left(1 - \frac{V}{V_0}\right) \quad \Rightarrow \quad K = \varepsilon \tag{9.6}$$

It is surprising that the shock wave gives equally its energy to internal and kinetic
energies regardless the strength of shock wave. The total energy given to the
compressed materials is

$$E = \varepsilon + K = P(V_0 - V) \tag{9.7}$$

It is informative to confirm whether E is the mechanical work done by the piston,
W. The mechanical work W done by the piston per unit time is

$$\frac{dW}{dt} = PU_p = P(V_0 - V)J_0 \tag{9.8}$$

where J_0 is the mass increase in the shocked region per unit time,

$$J_0 = \rho_0 u_0 \tag{9.9}$$

Therefore, the energy given to the unit mass by the shock wave, E, is the same as the mechanical power given to the unit mass.

If we can obtain many Hugoniot curves starting from different initial conditions, say different initial densities or initial pressures, we can obtain the thermodynamic quantities $\varepsilon(P,V)$ in a wide range as a table or fitting formula. Then, we can solve the hydrodynamic energy equation by altering LHS of (2.22) to the form.

$$\frac{d\varepsilon}{dt} = \frac{\partial\varepsilon}{\partial P}\bigg|_V \frac{dP}{dt} + \frac{\partial\varepsilon}{\partial V}\bigg|_P \frac{dV}{dt} \tag{9.10}$$

However, still the temperature is unknown. Recently, the temperature is also measured experimentally by measuring the radiation emission from the shocked region. It is simple that the compressed matters are optically thick and the radiation emission is assumed to be Planck radiation and the observed photons in appropriate energy is used to obtain the temperature T(V,P).

Even if the temperature data are also obtained, the thermodynamic consistency should be checked. If not, there should be some miss assumption mentioned already. In the early time of research, the temperature was not be able to be detected, but we have to derive the temperature T(P, V) in order to determine the equation of state. In such case, we can obtain the temperature from P and ε data as follows.

Start with the first law of thermodynamics.

$$d\varepsilon = TdS - PdV \tag{9.11}$$

Assume that the internal energy ε is obtained as a function of density and pressure from experimental Hugoniot data, the following relation should be satisfied in LTE.

$$d\varepsilon = \frac{\partial\varepsilon}{\partial V}\bigg|_P dV + \frac{\partial\varepsilon}{\partial P}\bigg|_V dP \tag{9.12}$$

Eliminating (9.11) with (9.12) to obtain the following relation to T,

$$TdS = \left\{ P + \frac{\partial\varepsilon}{\partial V}\bigg|_P \right\} dV + \frac{\partial\varepsilon}{\partial P}\bigg|_V dP \tag{9.13}$$

Equation (9.13) can be modified by dividing it with dS as

$$T = \left\{ P + \frac{\partial\varepsilon}{\partial V}\bigg|_P \right\} \frac{\partial V}{\partial S}\bigg|_P + \frac{\partial\varepsilon}{\partial P}\bigg|_V \frac{\partial P}{\partial S}\bigg|_V \tag{9.14}$$

This can be also written with use of **Maxwell relation** [2].

$$T = \left\{ P + \frac{\partial \varepsilon}{\partial V}\bigg|_P \right\} \frac{\partial T}{\partial P}\bigg|_S - \frac{\partial \varepsilon}{\partial P}\bigg|_V \frac{\partial T}{\partial V}\bigg|_S \qquad (9.15)$$

In order to solve (9.14) or (9.15) to obtain T(V,P), we need to know the entropy S=S(V,P). This can be done from (9.11) with dS = 0 for a constant S_i.

$$\varepsilon(V, S_i) = - \int P(V, S_i)dV \qquad (9.16)$$

Solving (9.16) as implicit unknown for S_i, we obtain the so-called iso-entropy (adiabatic) curve. Once the iso-entropy relation is also obtained, the temperature is given from (9.11) in the form

$$T = \frac{\partial \varepsilon}{\partial S}\bigg|_V \qquad (9.17)$$

Then, we have obtained all thermodynamic quantities. It is better to check the thermodynamic consistency (2.37) is satisfied and how much the error bar is. It is noted that in the case where phase transitions happen, be careful to the fact that some derivatives may diverge. For example, the volume change under a constant pressure in the 1st order phase transition.

9.1.2   Shock EOS Experiments

Let us see a modern method of diagnostics widely used in laser shock experiments. The measurement of a shock wave and piston velocities are carried out with use of the Doppler shift of the irradiating laser for diagnostic purpose. In Fig. 9.2a, a schematics of a typical shock experiment with intense laser is shown, where Omega EP laser stands for laser irradiation from the left [3]. The sample of compression experiment is shown as TATB and the other target materials are for clear imaging of shock propagation in the target.

By measuring the Doppler shift of the reflected laser of diagnostic for VISAR, the piston velocity is observed. Shock velocity is observed by measuring the time interval of Dt between the shock arrival and exist in the TATB layer as shown in Fig. 9.2b. At the same time, measuring the self-emission spectrum from the shock region, the temperature is inferred.

It is noted that the materials are optically thin for the laser for the diagnostic coming from the left in Fig. 9.2, but optically thick to the spectrum in the self-emission of the shocked material. In case of hydrogen sample, the diagnostic laser is chosen to be visible light and the emission is chosen ultra-violet. Shock Hugoniot experiment for metal materials, we can extend the above method, too. The details of
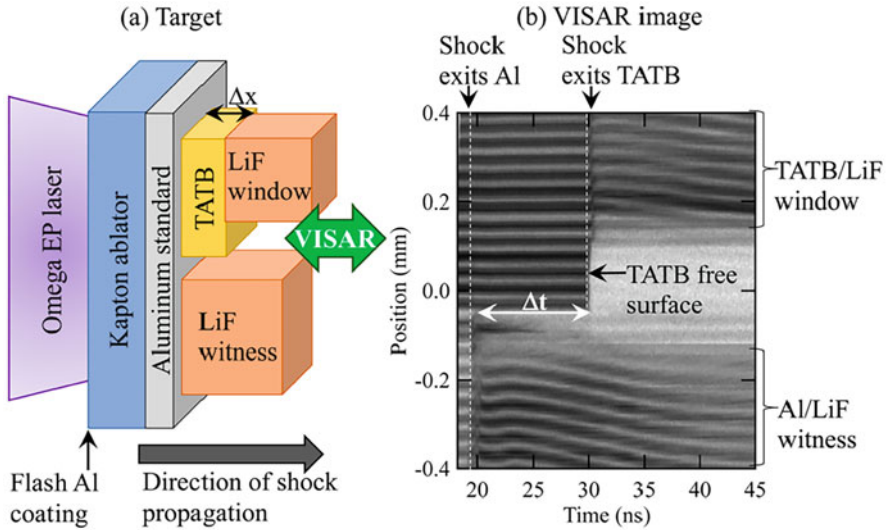
Fig. 9.2 (**a**) A typical target structure set-up of EOS experiment with intense lasers. The right (**b**) is data of VISAR showing the timing of shock passage [3]. Reprint with permission from ref. [3]. Copyright 1998 by American Institute of Physics

the diagnostic system called VISAR and VOP is well explained in a review paper [4].

Modern shock experiments are done with gas gun, Z-pinch or laser facilities [5]. In the case of Z-pinch and some case of lasers, soft x-ray source generated by such drivers has been used, since the radiation is smooth flux to the ablator of targets to generate planer shocks. By use of such shock Hugoniot experiments, the pressure and density curves are obtained experimentally as already shown in Fig. 8.13.

9.1.3 Shock Experimental Results

Even if the band gap of compressed matters is wide enough in the shock experiments as indicating the gap of insulator in Fig. 8.8, they can show the properties of metal, namely **insulator-metal transition (IMT)** is observed in shock experiments. It is easy to understand the physics, because the band gap disappears by the shock compression as shown in Fig. 8.5. This is purely insulator-metal transition to be discussed later. At the same time, however, the Fermi-Dirac distribution of the electrons expands the electron distribution to higher energy levels and some fraction of electrons can freely run in the conduction band, when the matter is heated by the shock wave to the temperature where the thermal energy is comparable or larger than the band gap energy.

Experimental result of the insulator-to-metal transition of fluid molecular hydrogen was initially reported by the experiment with gas gun [6]. High shock pressures are generated by impact of a hypervelocity impactor accelerated by a gas gun onto the front surface of aluminum sample holder. The experiment is designed so that a shock wave reverberating hold between Al_2O_3 anvils to compress liquid H_2 or D_2 to pressures of 0.93–1.8 Mbar. Thanks to the multi-shock compression, the temperature is kept at a few 0.1 eV, roughly 10 times lower than a single shock case at the same pressure. In this experiment, electric conductivities are measured. It is measured that the resistivity decreases almost 4 orders of magnitude from 0.9 to 1.4 Mbar and then plateaus to 1.8 Mbar.

This pressure 1.4 Mbar for insulator-to-metal transition is very low compared to the static experiment result 5 Mbar by another static method. Shock compression is also used to clarify the critical pressure to change the insulator to metal in fluid deuterium at relatively low temperature. The experimental data are plotted in Fig. 9.3 in Ref. [7] to find the phase transition boundary curve, where the black solid line inferred by experimental data is the **plasma phase transition**. It is easily understood such phase transition from the images combined both of Figs. 8.5 and 8.8. The boundary with the black open circles means the points where the band gap becomes about 2 eV, almost semiconductor.

There have been published many experimental data for many materials. In Fig. 9.3, many of experimental Hugoniot data of deuterium are compared to calculated curves [8]. This is the present status of shock compression experiments, where still error bars are not so small and several different theoretical models of equation of state (EOS) look relatively well explain the experimental data.

Fig. 9.3 Many experimental data of solid deuterium Hugoniot curves compared to a variety of theoretical curves. Reprint with permission from ref. [8]. Copyright 1998 by American Physical Society
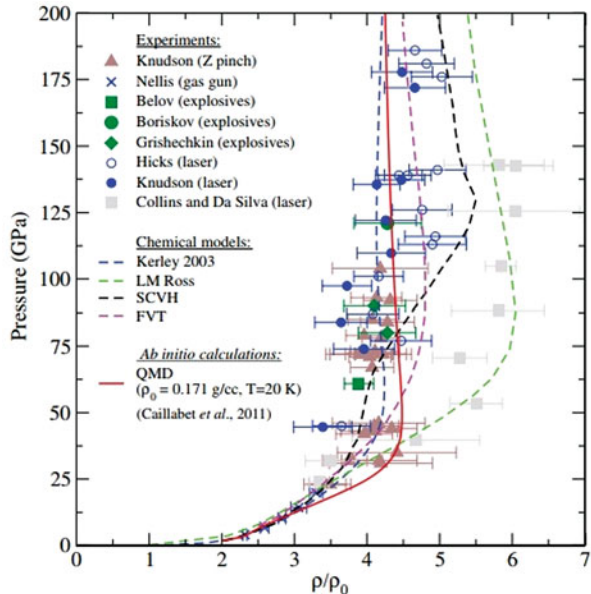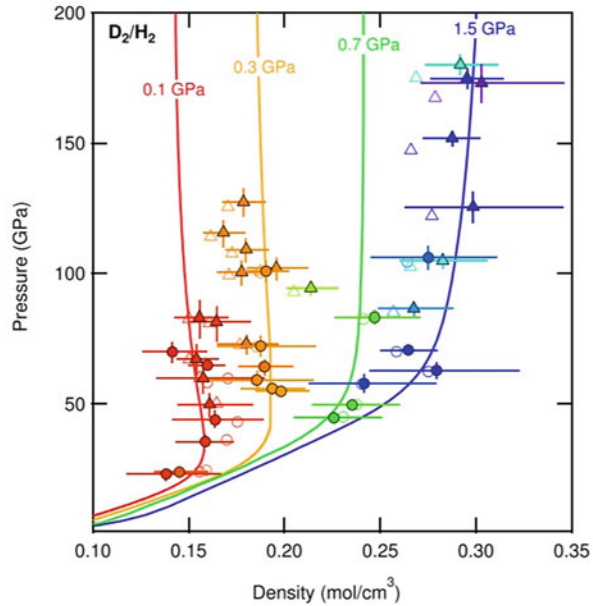
It was already mentioned that to obtain the dense matter EOS in a wide range, we
must get experimental data by changing the initial condition of density and/or
pressure. Using the shock wave transmitting from the quartz reference plate, the
Hugoniot curves of the different initial density and pressure can be obtained
[9]. Since we know the details of the shock Hugoniot of quartz, the shock com-
pressed state of the fluid hydrogen is evaluated with the initial parameters of shock
experiment. In Fig. 9.4, the experimental data are plotted for hydrogen and deute-
rium for four different initial pressures (density), 1 kbar (0.029 mol/cm^3), 3 kbar
(0.044 mol/cm^3), 7 kbar (0.061 mol/cm^3), and 15 kbar (0.079 mol/cm^3) [9]. The
corresponding solid lines are theoretical ones from density-functional-theory with
molecular dynamics (DFT-MD) methods. It is seen that small change of the initial
pressure and density alters the Hugoniot curve substantially.

9.2 Equation of State of Hydrogen at High Pressure

The compressible fluid dynamics becomes important to study and apply the dynam-
ics of plasmas produced by intense lasers, because the energy flux (W/cm^2) is
extremely high on the surface of the matters irradiated by such lasers and the
pressure over 1 Mbar (100 GPa) is easily generated as shown in Chap. 3. Any
solid matters are highly compressed and heated under one million atmosphere
pressure. To know the dynamics of such plasmas, realistic **equation of state
(EOS)** should be prepared before any hydrodynamic analysis.
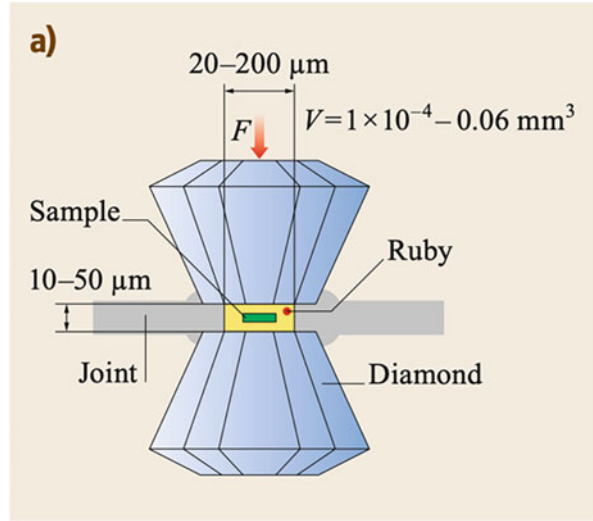
Here, a brief review of the equation of state (EOS) for the liquid or solid hydrogen is given since most of the important physics are included in the case of hydrogen. Such high-pressure properties of the matters have been studied in the community of **high-pressure physics** for a long time and the standard technique to produce high-pressure has been done with **Diamond Anvil Cell (DAC)** method.

The DAC uses two diamonds as shown in Fig. 9.5 to apply high pressure to a small sample sandwiched by two diamonds with help of mechanical pressure to them [10]. With advancement of technology, the maximum pressure approached to about 5 Mbar (500 Gpa). It is noted that DAC can compress matters while keeping the sample temperature low enough. So, it cannot be used to obtain experimental data for the wide range of matter temperature at high-pressure. Note that the laser shock wave method has appeared as an alternative way to study the high-pressure physics in higher pressure region.

The physics of molecular bonding of the hydrogen gas was explained already. It is well known that the hydrogen becomes molecular solid at extremely low temperature. The phase diagram of hydrogen at high pressure is shown in Fig. 9.6 [11]. Compared to Figs. 9.4 and 9.6 is more precisely in high-pressure and low-temperature region, based on the recent theoretical results reported in [12]. Hydrogen has four different solid states at very low temperature. At the atmospheric pressure it is normal molecular solid (Solid I), but it changes the lattice structure at high pressure to Solid I, II, and III [13]. The physics in such low temperature region is out of the present textbook and the readers can obtain the image of the lattice structures drawn in [13].

Insulator to metal transition of hydrogen at high pressure is very fundamental in the condense matter physics. Over 80 years ago Wigner and Huntington predicted that if solid molecule hydrogen was sufficiently compressed in the $T = 0$ K limit, the
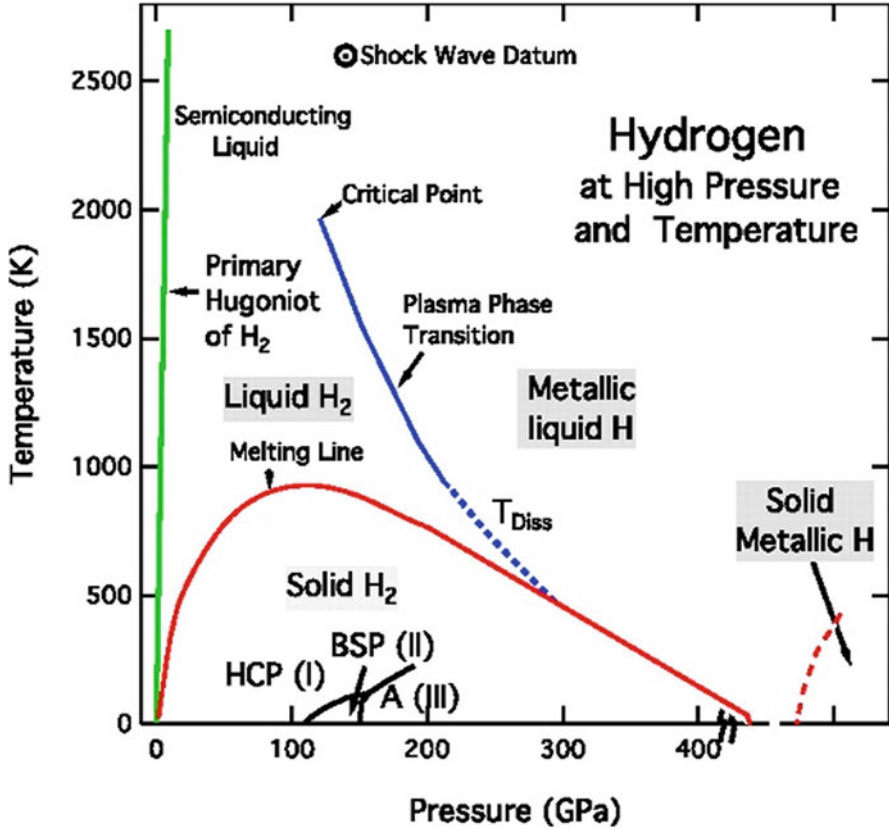
Fig. 9.6 Phase diagram of hydrogen at high pressure and relatively low temperature. The melting boundary is shown with red curve, and the boundary of plasma phase transition is shown with blue curve. The critical point is the triple-phase point. It is predicted that the solid metallic hydrogen appears at high-pressure under very low temperature as shown with red dot line. Reprinted with permission from ref. [11]. Copyright by PNAS

molecules would dissociate to form atomic **metal hydrogen (MH)** [14]. In this famous old paper, the authors calculated the electron wave functions with Slater matrix in so-called **Wigner-Sitz cell**. It is concluded that the total electron state become in free state to form metallic hydrogen at pressure of 0.25 Mbar (25 Gpa).

9.2.1   Insulator Metal Transition

Before talking about the **insulator-metal transition (IMT)** at high-pressure, let us remember the definition of materials. The solid materials are classified as metals, semiconductors, and insulators at T = 0 K based on the **band gap theory** as

schematically shown in Fig. 9.4. The bands in quantum energy levels are classified as valence and conduction bands. Electrons in the valence band cannot move and all electrons in the insulators are in the valence band. On the other hand, electrons in the conduction band can easily move in the materials and the metals have enough electrons in the conduction band. The semiconductors are in the middle. If the insulators have energy gap over which electrons easily jump up to the conduction band with absorption of photon energy of the ultra-violet component of wavelength 400 nm (~3.2 eV), the materials are defined as semiconductors.

In the case of insulators, electrons are filled in the density of state below Fermi-energy as explained in Fig. 8.5, and the band gap is wide not allowing electrons in the conduction band. It is, however, noted that the band gap is a function of the average atomic distance of the matters, and it changes as the matters are compressed as shown in Fig. 8.11. In the metals, enough electrons are in the energy level higher than the Fermi energy level, which is the zero energy in the case of an atomic energy. When a condensed matter is compressed and the energy levels of the bands change so that the electrons located in the valence band becomes free, the compressed matters show the properties of metals thanks to such free electrons. This is a rough explanation of the IM transition of hydrogen at high pressure for the temperature $T = 0$ case.

As increase of the pressure of hydrogen sample, the semiconductor state appears where external ultra-violet photons are absorbed at the sample surface. Then, after the metal transitions the photons are reflected almost completely by the free electron plasma current near the surface. These two phenomena are regarded the evidence of IM transition at high-pressure. This transition is shown above 4 Mbar in Fig. 9.6.

It is also suggested from Fig. 9.6 that at high pressure lower than the critical value of the MI transition, substantial free electrons in the conduction band can be supplied if the temperature of the matters are increased by $k_B T > \Delta E$, where ΔE is the energy of the gap. Such transition from insulator to metal at relatively high temperature in the compressed matter is studied by Zel'dovich and Landau [15]. Such phase transition is plotted with blue line as **plasma phase transition** in Fig. 9.6. In this case, the hydrogen phase changes from the solid to liquid insulator and then to metallic liquid as shown in Fig. 9.6.

9.2.2 Computational Studies

There are many computational methods to obtain the band structures and electron density structures in high-pressure regime based on quantum many-body problem. Simply saying, it is numerical modeling to solve many electrons Hartree-Fock equation in many nuclei, say more than 10^{20} electrons should be solved consistently as shown in Chap. 8.5. It is impossible even with supercomputers in near future.

One trial for the compressed matters in an early time has been done with so-called discrete-variational Xα method (DX- Xα) [16]. They considered clusters with a crystal structure of neon. Solving many wave functions for one set of nucleus and

Fig. 9.7 Computational result of eigen-energies of totally 13 neon nuclei are compressed with 10 × 13 (=130) electrons. Total wave functions have 130 energy levels. At far interatomic distance, the energy levels of each isolated atom is obtained, while as decrease of the distance, they are separated and makes band structure [16]. Reprint with permission from ref. [16]. Copyright 1998 by American Physical Society
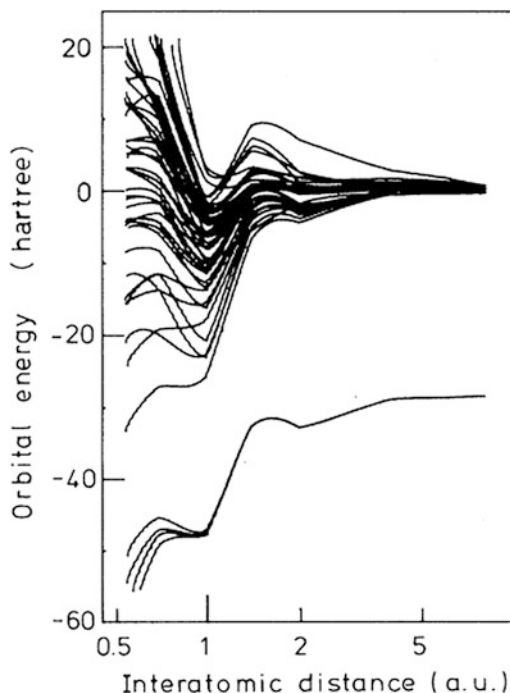
electrons with appropriate boundary conditions and they are used for the base functions for variational methods for total wave functions of all electrons in the cluster. Numerical atomic basis orbits are solutions of the one-electron wave equation containing the spherically symmetric potential

$$V(r) = V_C + V_{ex} + V_W \qquad (9.18)$$

Here V_C is the Coulomb potential due to the nucleus and direct part of the inter-electronic interaction. V_{ex} is the Slater exchange potential, which is of local assumption and proportional to the (density)$^{1/3}$ as shown in (15.4.33). V_W is a model potential of the wall corresponding to the ion sphere.

In Fig. 9.7, the energy levels of all electrons in 13 neon nuclei are plotted as functions of interatomic distance normalized by Bohr radius. All electrons energy levels tend to those of a single atom for the case where the atomic distance is large. With decrease of the distance the ground state energy decreases thanks to the potential of the neighbor nucleon, but the energy levels of the states whose wave functions are wider and affected by the other electrons are spread as already pointed out schematically in Fig. 8.11. It is noted that most of the electrons at the upper energy levels are free electrons and they are jumping around the cluster. They can be regarded as free electrons and the energy levels of the free state are speculated going down in Fig. 9.7 as the density increases. There are finite number of eigen states in Fig. 9.7, because of finite number of the base functions in the computation.
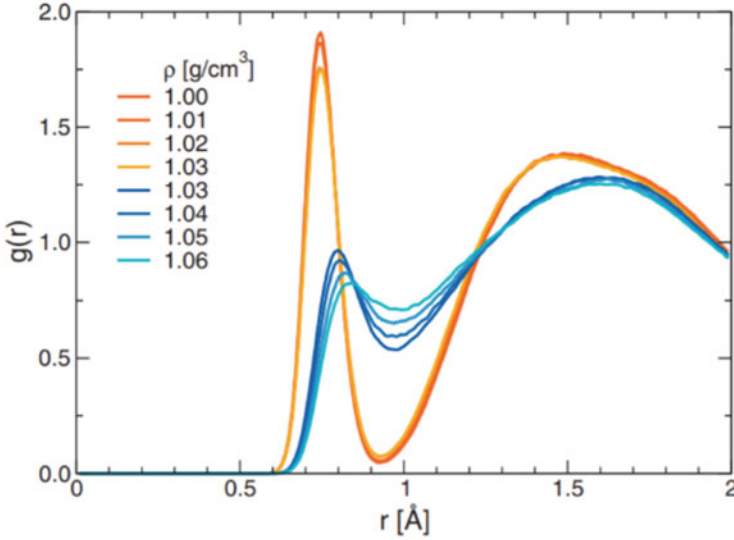
Fig. 9.8 The phase transition is clearly observed computationally. The radial distribution function is the radial distribution of probability of the surrounding nuclei. From orange to blue lines, the increase of the density changes the probability dramatically. Reprint with permission from ref. [18]. Copyright 1998 by American Physical Society

More precise calculations have been done with ab initio **molecular dynamics (MD)**, **quantum Monte Carlo (QMC)** and **density functional theory (DFT)**. Computations have been done for hydrogen at pressure up to several Mbar and temperature above the melting line up to 1500–2000 K. The **first-order phase transition** in liquid hydrogen, between a low conductivity molecular state and a high conductivity atomic state has been observed. The phase transition is characterized by the abrupt change of **electric conductivity** and the **radial distribution function**, which are derived consistently from the computational results [42, 43].

In Fig. 9.8, it is very clear that the phase transition dramatically happens at the density around 1.03 g/cm^3 as the proton-proton radial distribution function (pair-correlation function) g(r) in blue changes to that in red [18]. In the computation, the density is changed with a constant temperature 700 K, isotherm. It is seen in Fig. 9.8 that the pair function before the phase transition behaves like a lattice, while once the phase transition happens the ordered structure disappears, and protons are located randomly in such metallic state.

In Fig. 9.9, the resultant electric conductivities are shown for the case of four different temperatures [19] and three temperatures [17]. The abrupt increase of the conductivity is seen at high pressure and such phase transitions happen at lower pressure at higher temperature. These transitions correspond to the plasma phase transition in Fig. 9.6. Such insulator-metal transition can be experimentally observed by detecting abrupt change of reflectivity of probing laser light from the pressured sample.
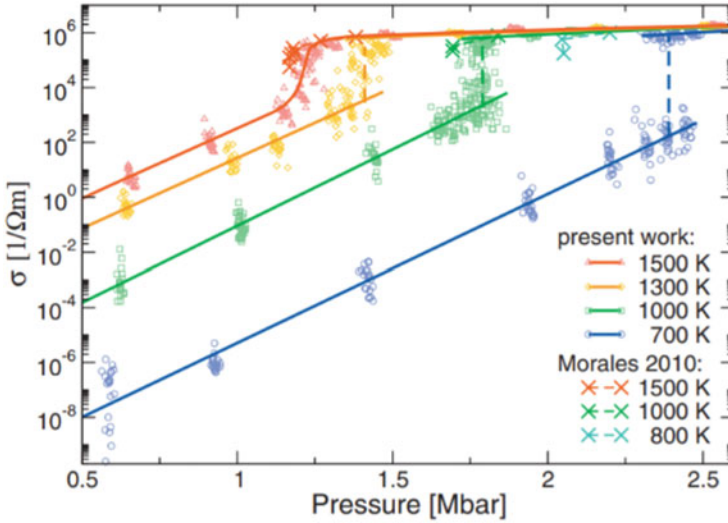
Fig. 9.9 Pressure dependence of electric conductivity at given temperatures. The phase transition is clearly observed. Reprint with permission from ref. [18]. Copyright 1998 by American Physical Society

9.2.3   Experimental Evidence of Insulator Metal Transition

As mentioned before, the hydrogen metal state appears at more pressure than that at which the band structure becomes of semiconductor. With optical measurement of solid hydrogen at T = 100 K under the pressure of 300, 306, 311, and 316 GPa with DAC, the transmission spectra show photon absorption edge and its photon energy decreases as the pressure increases [20]. Since the photons of visible light are completely absorbed by the hydrogen, it is called **black hydrogen**. In this experiment, the technical maximum pressure was 320 Gpa, but the data extrapolate to the higher pressure, consequently indicating the prediction that the metal hydrogen should be observed at about 450 GPa when the gap closes.

It is reported that the Wigner-Huntington insulator-metal transition predicted in 1935 was experimentally observed with the diamond anvil cell (DAC) [21]. Production of the metallic hydrogen has been a great challenge to condense matter physics and applications. At a pressure of 495 GPa hydrogen is found to become metallic with reflectivity as high as 91%. This critical pressure is about 10 times higher than the value predicted by Wigner-Huntington about 80 years ago, while it was near the value predicted by the extrapolation of the photon absorption edge mentioned above at15 years ago. Comparison with a theoretical model on reflectance inferred the plasma frequency of about 33 eV at T = 5.5 K, which corresponds to the free electron density of $7 \sim 9 \times 10^{23}$ cm^{-3}. This number is consistent with the value of estimated atom number density. This accomplishment is regarded to the production of Wigner-Huntington transition to the atomic metallic hydrogen in the laboratory [21].

9.3   Radial Distribution Function and Strongly Coupled Plasma

9.3.1   Interaction Energy in Ideal Plasma

As explained in Chap. 2 in Volume 1, the **Debye shielding** is given for the ideal plasma in the form.

$$\rho(r) = -\frac{1}{4\pi}k_D^2\frac{q}{r}\,exp(-k_Dr) \tag{9.19}$$

where $q = Ze$ or $= -e$ for the central charge of ion or electron, respectively. Then the Coulomb interaction energy of such Debye shielded charged particle can be obtained as

$$\int \rho(r)\frac{q}{4\pi\varepsilon_0 r}d\boldsymbol{r} = -\frac{q^2k_D}{4\pi\varepsilon_0} \tag{9.20}$$

Summing up two cases of an ion at the center and the electron at the center, and dividing by two for avoiding double counting, the following total energy density of plasma particles is obtained

$$E_{tot} = E_{kin} + E_{int} = \frac{3}{2}(n_i + n_e)T - \frac{1}{8\pi}k_D^3 T \tag{9.21}$$

The Coulomb interaction due to Debye potential is attractive force for both of ion and electron because the interaction energy of the second term of RHS in (9.21) is negative.

The ratio of the interaction energy to thermal energy is a dimensionless parameter proportional to the plasma Λ defined as

$$\Lambda = 4\pi n\lambda_D^3 \tag{9.22}$$

where $n = n_i = n_e$ is assumed for simplicity and λ_D is the Debye length. The Λ is roughly equal to the number of particles in the **Debye sphere**, which is required to be much larger than unity for the ideal plasma. For hydrogen plasma the energy ration is

$$\frac{E_{kin}}{E_{int}} = 24\pi n\lambda_D^3 = 3\Lambda \tag{9.23}$$

The plasma Λ is nothing without the ration of both energies and it approaches the unity as the increase of the interaction energy. It is noted that as Coulomb logarithm approaches unity, the collisional coefficients based on Debye shielding model

becomes not applicable and some new theory is required. The plasma Λ is also related to the **ion-ion coupling parameter** Γ_{ii} defined in the form:

$$\Gamma_{ii} = \sqrt[3]{3}\Lambda^{-2/3} \tag{9.24}$$

It is important to study the physical properties of such **strongly coupled plasma** to study the physics near the centers of stars and giant planets. Even in the industrial application of plasma or planet formation with accretion disk in Universe, for example, so-called **dust plasma** plays important role in the evolution of system. In case of such dusty plasma, the coupling parameter Γ_{ii} approaches to unity even though the plasma number density is very low compared to the solid density. The dusty plasma is made of many giant particles whose charge is thousands of the elementary charge, namely an effective Z of each cluster of particles is very large. In such case, plasma becomes strongly coupled even if the density is not so high.

In addition, it is useful to enumerate the reason why Debye shielding model is violated near the Coulomb logarithm near unity:

1. The interaction energy of the order of kinetic energy means $T \approx e\phi$ in Deby theory and Taylor expansion cannot be used in this case.
2. In such condition, the number of charged particles in Debye sphere with radius λ_D is only a few particles and the statistical assumption like Boltzmann distribution cannot be used in deriving (9.19).

In such strongly coupled plasma, Rutherford scattering, and Debye shielding cannot be used to obtain the transport coefficients due to Coulomb scattering in plasma.

9.3.2   Strongly Coupled Plasmas

The radial probability function of neighboring ions has been given statistically in (9.19). As we see above, however, it is not a good approximation with Debye shielding, and we must ask more precise study. In case of high-density and relatively low temperature plasma, the electron Fermi energy is high and spatially uniform density distribution of electron can be a good assumption. Such plasma is called **one component plasma (OCP)** and its ion **radial distribution function** and related physics have been studied, for example, by S. Ichimaru [22].

In Fig. 9.10, the radial distribution function g(r) calculated by Monte Carlo method is shown for different ion coupling parameter Γ_{ii} from 0.1 to 140 [23]. For the case of a small Γ_{ii} showing week coupling, the distribution is like that suggested by (9.19). With the increase of the ion coupling parameter, the probability inside the ion sphere is going to vanish and large coupling makes the function overshoot outside the ion sphere radius. In this case the neighbor ions can frequently approached around the sphere the radius of which is the value of the peak in Fig. 9.11. It is known that at the coupling parameter around 178, the liquid-solid
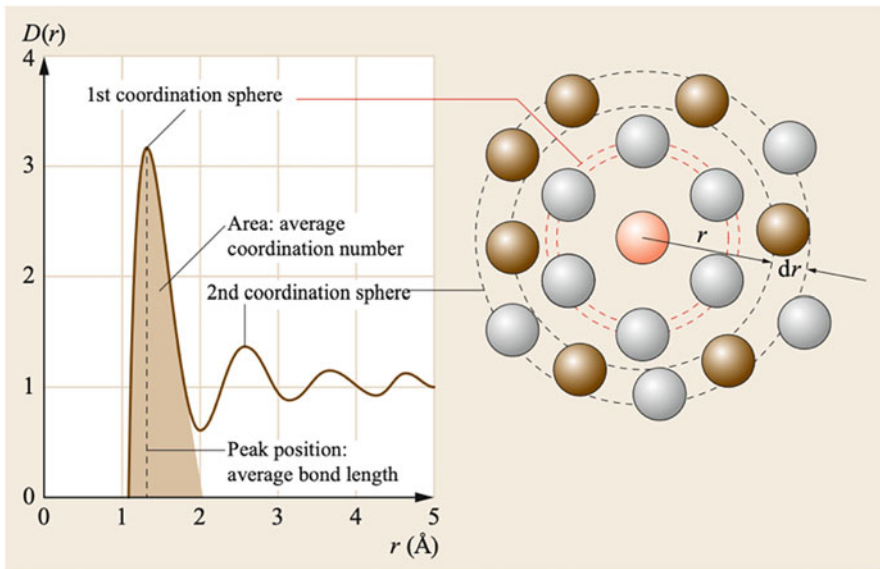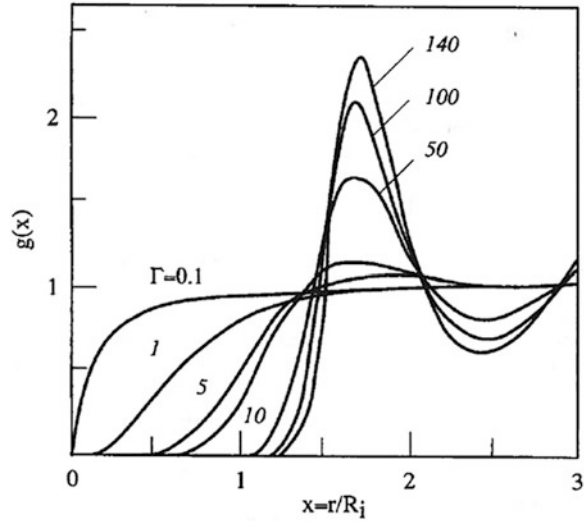
Fig. 9.11 Image of a snap shot of the most probable ion configurations suggested by an example of
radial distribution function. Reprint from ref. [23] with kind permission from Springer Science +
Business Media

phase transition is observed in such OCP. This phase transition is called **glass phase transition** because the ions make lattice structure in a short distance, but it like an amorphous and no crystal structure is observed over a long distance.

Such strongly coupled plasma has been studied to know the physics inside of white dwarfs, giant planets, and so on. To know the ion distribution, for example, inside of the white dwarfs, where electron strongly degenerates and OCP is good approximation. The precise radial distribution function is very interesting to know the fusion reaction due to the overlapping of two ions wave functions at an extremely high density such as the center of white dwarf characterized by the density 10^9 g/cm^3. In addition, the surface of neutron stars is also in such strongly coupled plasma state.

The classical statistical Monte Carlo is applicable to ion-ion coupling, but it is doubtful to apply to the centered ion and electrons interaction. This is because electrons must be treated quantum mechanically. One possibility is to use the density-functional method explained in Chap. 8.4. To know the physics simpler, however, the electron density profile obtained after solving Thomas-Fermi model is widely used for the electron radial distribution function around the centered ion. Therefore, using the electron density profile or electrostatic potential around the central ion, the transport coefficients can be calculated by use of the effective Coulomb logarithm explained later in this chapter.

9.4   Quantum Scattering of Electrons in Coulomb Field

In high density near the solid density, the scattering analysis should be done quantum mechanically. For example, the de Broglie wavelength of electron with kinetic energy equal to that of the 1s state of Hydrogen atom is about Bohr radius 0.5Å. This is the same order of the average ion distance near solid density. If the charge density distribution statistically averaged around each ion can be obtained by some method, the differential cross section of Coulomb scattering can be calculated based on Schrodinger equation for one particle as shown in Chap. 5. It is noted that the following non-relativistic derivation can extend to the relativistic case in replacing the wavenumber of electron wave function with the momentum vector for relativistic collision.

As was discussed in Chap. 5, **Born approximation** is the basic method on such scattering problem. Born approximation is widely used, not only atomic physics, but also nuclear physics to study charge distribution inside nucleus, including quarks. In nuclear physics, relativistic scattering should be considered because injected electron energy is in the rage of 100 MeV, but here the impinging electron energy is in the rage of 1–100 eV and non-relativistic treatment is enough.

When the density distribution screening the central charge q is assumed to be given as a function of the radial coordinate r, the potential V(r) can be obtained by solving the Poisson equation.

$$\varepsilon_0 \nabla^2 V(r) = -q\delta(r) - \rho_{sc}(r) \tag{9.25}$$

For a given potential and no change of the charge around the point charge, one electron Schrodinger equation reduces to a simple equation for scattering problem:

$$\left\{ -\frac{\hbar^2}{2m} \nabla^2 + V(r) - E \right\} \psi(\boldsymbol{r}) = 0 \tag{9.26}$$

This can be written in the form

$$\left(\nabla^2 + k_0^2 \right) \psi = \frac{2m}{\hbar^2} V \psi \tag{9.27}$$

Where k_0 is the wavenumber of the incident electron wave defined to be

$$k_0^2 = \frac{2mE}{\hbar^2} \tag{9.28}$$

9.4.1 Born Approximation

Here the scattering is elastic one and no energy change happens, namely the energy E in (9.26) should be kept constant. The homogeneous solution of (9.27) for $V = 0$ is the plane wave being incident to the target and its solution is

$$\psi = \psi_0 = exp(i\boldsymbol{k}_0 \cdot \boldsymbol{r}) \tag{9.29}$$

In solving (9.27) mathematically to obtain a formal solution, it is very useful to know that LHS of (9.27) is **Helmholtz equation**. Using **Green function** to the Helmholtz homogeneous term, (9.27) can be given in the following integral equation form.

$$\psi(\boldsymbol{r}) = \psi_0(\boldsymbol{r}) - \frac{2m}{\hbar^2} \int \frac{e^{ik_0|\boldsymbol{r}-\boldsymbol{r}'|}}{4\pi|\boldsymbol{r}-\boldsymbol{r}'|} V(\boldsymbol{r}') \psi(\boldsymbol{r}') d\boldsymbol{r}' \tag{9.30}$$

where $\psi_0(\boldsymbol{r})$ is the general solution of the homogeneous equation of (9.27) in neglecting RHS and homogeneous solution is the incident wave (9.29). Of course, (9.30) is not the final solution of (9.27), but it should be noted that (9.30) gives us the exact solution when the interaction potential V(r) is given. It is possible to solve (9.30) with use of computer, then the well-known iteration method will be used starting from an appropriate initial solution. It is reasonable to start with solution obtained by Born approximation which will be described below. The solution of Born approximation is good enough in many cases as will be explained later.

In calculation of the scattering by the central charge, we would like to know the wave function after the scattering. This means the coordinate $\mathbf{r}$ in (9.30) can be assumed to be very far from the central region where the potential V(r) is large enough and cannot be neglected in the integral (9.30). Namely, if r > > r' then the following approximation can be used.

$$|\mathbf{r} - \mathbf{r}'| \approx \sqrt{(\mathbf{r} - \mathbf{r}')^2} = \sqrt{r^2 - 2\mathbf{r} \cdot \mathbf{r}' + r'^2} \approx r - \mathbf{r} \cdot \mathbf{r}'/r$$

$$\frac{1}{|\mathbf{r} - \mathbf{r}'|} \approx \frac{1}{r|1 - \mathbf{r} \cdot \mathbf{r}'/r^2|} \approx \frac{1}{r}\left(1 + \frac{\mathbf{r} \cdot \mathbf{r}'}{r^2}\right) \approx \frac{1}{r} \qquad (9.31)$$

This is the first order expansion to the small value r'/r. In the solution the scattered direction is $\mathbf{r}/r$ and its wave number is equal to k_0 because of **elastic scattering**, we can introduce the scattered wavenumber $\mathbf{k}_1$ as follows.

$$\mathbf{k}_1 = k_0 \frac{\mathbf{r}}{r} \qquad (9.32)$$

It is noted that the first order term of (9.31) is important in the exponential term but can be neglected in the denominator of the integral. Inserting (9.31) in the exponential term in (9.30) and using the scattered wave momentum (9.32), (9.31) is written to be

$$\psi(\mathbf{r}) \rightarrow e^{i\mathbf{k}_0 \cdot \mathbf{r}} + \frac{e^{ik_0 r}}{r} f(\theta) \quad (r \rightarrow \infty) \qquad (9.33)$$

$$f(\theta) = -\frac{m}{2\pi\hbar^2} \int e^{-i\mathbf{k}_1 \cdot \mathbf{r}'} V(\mathbf{r}') \psi(\mathbf{r}') d\mathbf{r}' \qquad (9.34)$$

$$\theta = \frac{1}{k_0^2} \mathbf{k}_0 \cdot \mathbf{k}_1 \qquad (9.35)$$

In many cases, we assume that the potential in (9.34) is spherically symmetric [V(**r**) = V(r)] and the scattering is axially symmetric and scattering angle depends only the angle θ made by the incident direction and scattered direction as defined in (9.35). It is informative to rewrite (9.34) in the following form for the amplitude of **scattered wave**,

$$f(\theta) = -\frac{m}{2\pi\hbar^2} \phi|V|\psi$$
$$\phi(\mathbf{r}) = e^{i\mathbf{k}_1 \cdot \mathbf{r}} \qquad (9.36)$$

where $\phi(\mathbf{r})$ is the plane wave of the incident electron wave function.

The Born approximation can be used if the scattered wave component of the second term of (9.33) is much smaller than the incident component of the first term of (9.33). Then, the perturbation theory can be used to assume that the wave function

in the second term of (9.33) can be replaced with that shown in (9.29). The following relation is obtained

$$f(\theta) = -\frac{m}{2\pi\hbar^2} \int e^{i\boldsymbol{q}\cdot\boldsymbol{r}'} V(r') d\boldsymbol{r}' \qquad (9.37)$$

Where the following the wave vector made of the incident and scattered wave vectors is introduced.

$$\boldsymbol{q} = \boldsymbol{k}_0 - \boldsymbol{k}_1 \qquad (9.38)$$

Its absolute value is easily calculated with use of (9.32) as follows.

$$
\begin{aligned}
q = |\boldsymbol{k}_0 - \boldsymbol{k}_1| &= \sqrt{k_0^2 + k_1^2 - 2k_0 k_1 \cos\theta} \\
&= k_0 \sqrt{2(1 - \cos^2\theta)} = 2k_0 \sin(\theta/2)
\end{aligned}
\qquad (9.39)
$$

It should be noted that (9.37) is proportional to the Fourier transformation of the scattering potential V(r) with respect to the wave vector defined in (9.38). For the spherically symmetric potential, (9.37) can be written

$$f(\theta) = -\frac{m}{\hbar^2} \int_0^\infty r'^2 \, dr' \int_0^\pi \sin\theta' d\theta' \, exp(iqr' \cos\theta') V(r') \qquad (9.40)$$

After integration to the angle, (9.40) become the following simple form

$$f(\theta) = -\frac{2m}{\hbar^2 q} \int_0^\infty r' V(r') \sin(qr') dr' \qquad (9.41)$$

where q is given in (9.39).

9.4.2   Differential Cross Section

As is defined in (9.33) the function $f(\theta)$ is clear to provide the differential scattering cross section in the form.

$$\frac{d\sigma}{d\Omega} = |f(\theta)|^2 \qquad (9.42)$$

Let us calculate the scattering cross section for the case of the Debye potential given in (5.7). Inserting (5.7) to V in (9.41) and using the formula

$$\int_0^\infty exp(-ax)\, sin(bx)dx = \frac{b}{a^2 + b^2} \tag{9.43}$$

(9.41) reduces to the following form.

$$f(\theta) = -\frac{meQ}{2\pi\varepsilon_0\hbar^2}\frac{1}{q^2 + k_D^2} \tag{9.44}$$

Since q is given in (9.39), the following differential scattering cross section is obtained for the Debye potential

$$\frac{d\sigma}{d\Omega} = |f(\theta)|^2 = \left(\frac{Ze^2}{4\pi\varepsilon_0 E_0}\right)^2 \frac{1}{\left[4sin^2(\theta/2) + (k_D/k_0)^2\right]^2} \tag{9.45}$$

In deriving (9.45), the charge of the central scatter is assumed $Q = Ze$ and the following relation is used

$$E_0 = \frac{\hbar^2 k_0^2}{2m} \tag{9.46}$$

where E_0 is the kinetic energy of the incident electron. In the limit of **Rutherford scattering**, Debye screening is not considered, namely $k_D \to 0$. In this limit, the well-known differential cross section is obtained.

$$\frac{d\sigma}{d\Omega} = \left(\frac{Ze^2}{8\pi\varepsilon_0 E_0}\right)^2 \frac{1}{sin^4(\theta/2)} = \frac{b_0^2}{(1 - cos^2\theta)^2} \tag{9.47}$$

Here the impact parameter b_0 is used. The Rutherford scattering differential cross section is exactly reproduced using Quantum mechanical Born approximation derived in (9.47).

Then, the total cross section of the scattering by Rutherford formula is calculated by changing as $x = 1 - cos\,\theta$ and the total cross section by Coulomb scattering is given to be

$$\sigma_C = \int \frac{d\sigma}{d\Omega}(1 - cos\,\theta)d\Omega = 2\pi b_0^2 \int_{x_{min}}^1 \frac{1}{x}dx \tag{9.48}$$

In (9.48), the term in the second eq. $1 - cos\,\theta$ is a weight factor to the contribution of the cross section since the scattering with the angle of θ can change the initial momentum to the fraction of $1 - cos\,\theta$. Thanks to this contribution, a simple integration shown in the last term in (9.48) is obtained.

$$\sigma_C = 2\pi b_0{}^2 \, ln(1/x_{min}) \tag{9.49}$$

To avoid infinity by accumulation of small angle scattering in Rutherford model, the minimum angle scattering is introduced, namely

$$x_{min} = \theta_{min}{}^2/2 \tag{9.50}$$

How to evaluate the minimum angle in the present model is same as the minimum impact factor introduced in previous section. The Debye shielding is very important for converging the integral. A simple evaluation of the minimum angle should be given by the following evaluation

$$\theta_{min} \approx \frac{\left(\frac{Ze^2}{4\pi\varepsilon_0\lambda_D^2} \frac{\lambda_D}{v} \right)}{mv} \tag{9.51}$$

Where the scattering to the electron by the central charge is calculated up to the radius of Debye length. Taking an average energy of the plasma electron as $mv^2 \approx T$, (9.51) can be approximated as

$$\theta_{min} \approx \frac{1}{4\pi n\lambda_D^3} = \frac{1}{\Lambda} \tag{9.52}$$

Where Coulomb log defined in (9.22) is used. Finally, the total cross section of electrons scattering by Coulomb field in plasma is obtained as

$$\sigma_C = 4\pi b_0{}^2 \, ln(\Lambda) \tag{9.53}$$

The simply evaluated cross section in Volume 1 is obtained after more precise calculation starting from Rutherford differential cross section given in (9.47).

Finally, note that with use of computer, it is possible to solve the exact solution of (9.25) and (9.27) for the case of thermodynamic equilibrium condition, for example, assuming Fermi-Dirac distribution. This is the next step after the above Born approximation and the incident wave is also modified by the Coulomb potential of the ventral charge. This is called distorted wave method.

9.4.3   Density Distribution and Form Factor

From (9.41) the differential scattering cross section can be obtained provided that the potential structure by the screening charge distribution is given. Mathematically more convenient if (9.41) is an integration of the density profile instead of the potential obtained solving Poisson equation. By use of Green function theorem,

this purpose has been accomplished. The **Green theorem** to volume integral with Laplacian operator is given

$$\int_V dV \left(A\nabla^2 B - B\nabla^2 A\right) = \oint_S d\mathbf{S} \cdot (A\nabla B - B\nabla A) \qquad (9.54)$$

Where A and B are arbitrary functions defined in space. If the volume is taken so that the integrand of RHS sufficiently disappears on the integral surface, RHS vanishes in the surface integration. When any combination of two scalar functions A and B satisfies this condition, LHS of (9.54) always vanishes for the infinite volume integral, namely

$$\int_V dV A\nabla^2 B = \int_V dV B\nabla^2 A \qquad (9.55)$$

By use of (9.55) to the integral (9.37), the following relation is obtained.

$$\int e^{i\mathbf{q}\cdot\mathbf{r}} V(\mathbf{r}) d\mathbf{r} = -\frac{1}{q^2} \int e^{i\mathbf{q}\cdot\mathbf{r}} \nabla^2 V(\mathbf{r}) d\mathbf{r} \qquad (9.56)$$

Then, (9.56) and Poisson equation

$$\nabla^2 \left[\frac{V(\mathbf{r})}{e}\right] = -\frac{1}{\varepsilon_0}\rho(\mathbf{r}) \qquad (9.57)$$

gives the following surprising relation to the integrand of (9.37)

$$\int e^{i\mathbf{q}\cdot\mathbf{r}} V(\mathbf{r}) d\mathbf{r} = \frac{e}{\varepsilon_0 q^2} \int e^{i\mathbf{q}\cdot\mathbf{r}} \rho(\mathbf{r}) d\mathbf{r} \qquad (9.58)$$

$$f(\theta) = -\frac{m}{2\pi\hbar^2} \frac{e}{\varepsilon_0 q^2} \int e^{i\mathbf{q}\cdot\mathbf{r}} \rho(\mathbf{r}) d\mathbf{r} \qquad (9.59)$$

It is easily found that the integration of (9.58) is Fourier transformation of the charge density distribution around the scattering center charge.

Let us examine how the differential scattering cross section defined by (9.42) and (9.37) is conveniently reduces to Rutherford scattering case with use of (9.53). Inserting the charge density as $Ze\delta(\mathbf{r})$ in (9.59) the following relation is obtained.

$$f(\theta)^2 = \left(\frac{Ze^2 m}{2\pi\hbar^2\varepsilon_0}\right)^2 \frac{1}{q^4} \qquad (9.60)$$

It is easily seen that using (9.39), (9.60) reproduced Rutherford scattering given in (9.47).

9.4.4   Form Factor and Nucleus Charge Experiment

Introducing the concept of form factor of electron scattering by the screened Coulomb field around the nucleus with charge Ze, (9.59) gives the following definition to the differential scattering cross section

$$\frac{d\sigma}{d\Omega} = \left(\frac{d\sigma}{d\Omega}\right)_{Rutherford} |F(q)|^2 \tag{9.61}$$

Where F(q) is called **form factor** defined as

$$F(q) = \int e^{i\boldsymbol{q}\cdot\boldsymbol{r}} \rho_N(\boldsymbol{r}) d\boldsymbol{r} \tag{9.62}$$

F(q) has been widely used to study the charge distribution of nucleus in nuclear physics experiment. The density distribution in (9.62) is normalized one so that its volume integral becomes equal to unity.

$$\rho_N(\boldsymbol{r}) = \frac{1}{Ze} \rho(\boldsymbol{r}) \tag{9.63}$$

It should be noted that the form factor.

If mono-energetic electron beam is available and strongly coupled plasma can be kept for a long time, experimental data of the scattering can be used to obtain the density distribution around the central charge. Through such experiment the angular distribution of the differential scattering cross section is obtained and the experimental data of angular distribution of scattering is compared with that given in (9.61). Then, the form factor obtained experimentally can be used to determined statistically averaged radial density distribution through the inverse-Fourier transform

$$\rho_N(\boldsymbol{r}) = \frac{1}{(2\pi)^3} \int e^{-i\boldsymbol{q}\cdot\boldsymbol{r}} F(\boldsymbol{q}) d\boldsymbol{q} \tag{9.64}$$

Once the density distribution is obtained, the effective Coulomb collision cross section will be used to calculate the revised transport coefficients in wide range of plasma parameter. However, it has not been done in plasma, because it is difficult to maintain such plasma for a long time so that enough scattering data are available.

In the beginning of nuclear physics, Rutherford used alpha particles to study inside the atom and he found vary rare scattering of large angle from a foil target. He derived the Rutherford scattering differential cross section shown in (9.47) and concluded that the radial spread of the nucleus is smaller than 10^{-12} cm. However, proton or such alpha particles are not convenient to study the charge distribution of nucleus, because they interact with nuclear force, and they also have inner structures.

Electron is more convenient because it has no internal structure and Coulomb interaction is most dominant compared to another forces.

The study of charge distribution of nucleus with form factor has been done with 500 MeV electron beam accelerated by LINAC in Stanford University in the early 1950s. In the case of nuclear physics scattering, beam electrons are highly relativistic, and we must follow this case.

Example of form factor F(q) obtained in early experiments are plotted in Fig. 9.12 where electron beam of energy from 150 to 300 MeV was impinged and solid circles are experimental data for three different nuclei. Note that the axis of q is given in the unit of momentum with relation $p = \hbar q$ and the momentum is given in the unit of (energy)/c. In this case, instead of Rutherford scattering, **Mott scattering formula** is used. In Mott formula additional physics due to spin and magnetic interaction is added to Rutherford formula.

For convenience to the readers, the density distribution and its form factor is shown in Fig. 9.13 for several different density distributions.

Is it possible to do the same kind of experiment for the ions in plasma? Can we, however, obtain the form factor to infer the electron density distribution around

Fig. 9.12 The form factor F(q) obtained in early experiments. The electron beam of energy from 50 to 300 MeV was impinged and solid circles are experimental data for three different nuclei
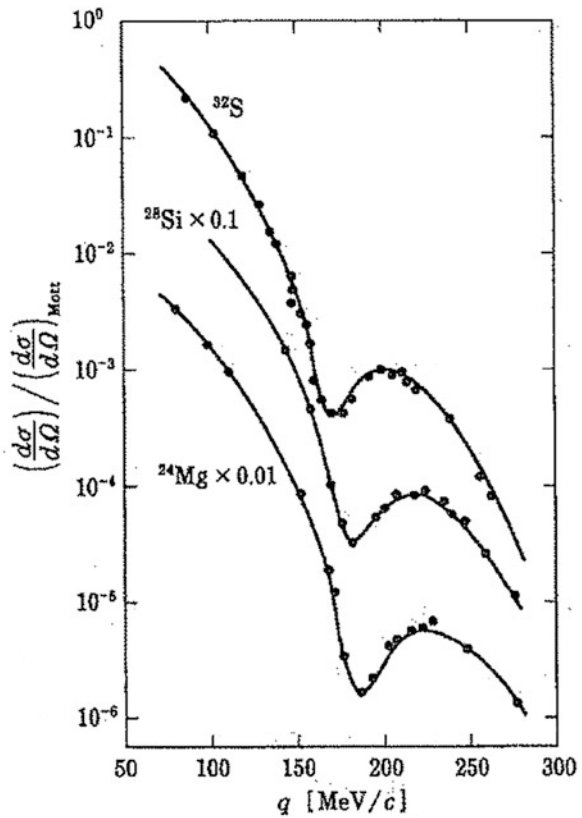
Fig. 9.13 The charge
distributions of nuclei
obtained with the
experimental data of form
factors
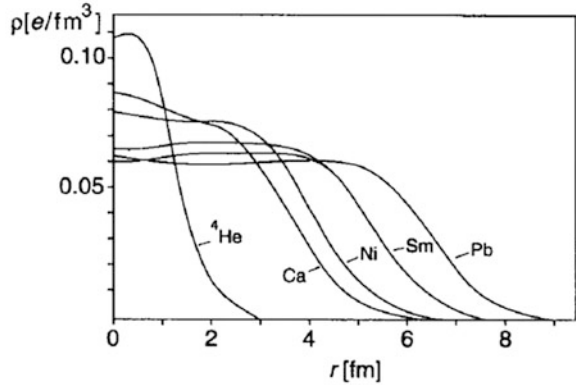
an ion? It is possible of atoms at a fixed position, namely solid-state matters, molecules, etc. It is difficult to apply it for experiment in the case of plasmas in which the ions are moving with thermal velocity. In the future, however, very short pulse electron beam and its diagnostic technique are developed, the form factor of the screened ions can be experimentally studied.

It is useful to note that the density distribution of very small scale of plasmas is now experimentally studied with x-ray pulse from XFEL, which is called **Small-Angle X-Ray Scattering** (**SAXS**) [24]. The principle and mathematics are the same as described above. The difference is that X-ray beam is used instead of the electron wave packets and the charge distribution is replaced by the x-ray refraction index determined by the electron density distribution.

SAXS has been developed as a particularly suitable technique to characterize structure and form factors of colloidal systems in solution and therefore to probe nanometer-scale structure. The combination of microfluidics and SAXS provides a powerful tool to investigate phase transitions at different molecular levels and relevant timescales. This method can be a new one to study the density structure of dense plasmas produced by ultra-intense lasers.

9.5   Coulomb Log Λ in Dense Quantum Plasmas

We should think about the minimum angle of scattering to avoid divergence in (9.42). It is also important to discuss about why we need to exclude the contribution from large angle scattering more than $\theta = 90$ degree to total scattering cross section in (9.48). In a large angle scattering, it is not appropriate to use classical mechanics, because the kinetic energy of impact electron is less than the Coulomb interaction energy. Born approximation of quantum scattering is not applicable either. Therefore, the integral equation of (9.30) should be solved directly. Of course, such calculation has been carried out using computer, however, it is easily understood that this contribution is negligible as far as the plasma is ideal $\Lambda \gg 1$. This is the reason way there is also limitation of analysis based on Rutherford formula.

Such quantum deflection contribution has been studied, and the following modified formula is proposed [25]

$$ln(\Lambda) = \frac{1}{2} \, ln \left[1 + \left(\frac{b_{max}}{b_{min}} \right)^2 \right] = \frac{1}{2} \, ln \left(1 + \frac{\lambda_D^2}{b_0^2 + \lambda_{dB}^2} \right) \qquad (9.65)$$

where electron **de-Broglie wavelength**

$$\lambda_{dB} = \frac{\hbar}{\sqrt{mT}} \qquad (9.66)$$

has been introduced to take account of quantum deflection near head-on collision. The modified form in (9.65) is reasonable because it guarantees a positive value of the Coulomb log for a strongly coupled plasmas. In addition, the quantum diffraction effect is modeled in the last term in (9.65).

The better fitting formula for the Debye length including the quantum diffraction effect is also obtained by solving Schrodinger equation directly. The modified Debye length is given in (9.65) with the form

$$\lambda_D \rightarrow \lambda_D \, exp \left\{ \frac{1.65 - 0.4 ln\Lambda}{(ln\Lambda)^{0.65} + 1} \right\} \qquad (9.67)$$

where $ln\Lambda$ evaluated in (9.65) is installed in (9.67). The Debye length re-calculated in (9.67) is used to obtain the fitting formula to the Coulomb logarithm.

This modified Coulomb logarithm has been compared to another theoretical and computational results in Fig. 9.14 [25]. In Fig. 9.14, the fitting formula of (9.65) and (9.67) is plotted with the line (T-M) for the classical case, where de Broglie correction is neglected to compare with the more precise computation of molecular dynamics (MD). The diamond symbols are MD results and the red line is the fitted curve to the MD result. It is seen that the good agreement is obtained with MD results. The blue and orange dashed curves are the theoretical results based on perturbation methods 50].

In the MD simulation, quantum effect is not included. The green lines are two theory cases with the de Broglie cut included. Then, the denominator in (9.65) will be increased and the value of Coulomb log decreased as shown in Fig. 9.14. It is noted that the horizontal axis is the coupling parameter defined to be

$$g = b_0/\lambda_D. \qquad (9.68)$$

In Fig. 9.14, MD simulation has been carried out with the parameters in the gray region in the upper figure, from weekly coupled plasma g = 0.003 to strongly coupled plasma with g = 20, where the other formulae are calculated with fixed temperature of T = 500 eV. More details are given in the reference.
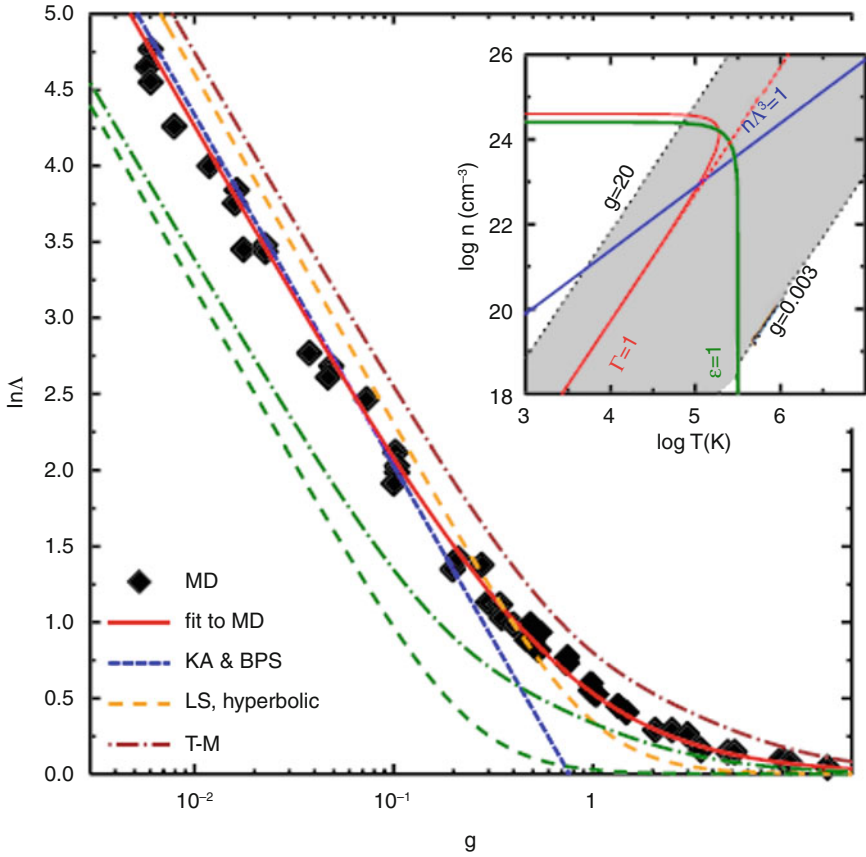
Fig. 9.14 The effective Coulomb log derived by taking account of strongly coupled quantum effect at high-density plasma. Reprint from ref. [25]. Copyright 2012, with permission from Elsevier

It is important to note that in the region of large g, Coulomb log approaches zero and it means that running electrons are almost not scattered by the ion charges to provide high conductivity. This is a general property of the dense Quantum plasmas. In such a case, dominant conduction is attributed to the electrons with Fermi energy. The conductivity, for example, the inside of white dwarfs is very high due to the above reason.

9.6 Density Fluctuation and Dynamic Structure Factor

So far, most of the plasmas have been assumed to have constant density in space. If the electron density is completely uniform as well as the charge is also smeared out uniformly, any photons are not scattered from such mathematically idealized

plasmas. The ion individuality and electron density fluctuation are subject to Thomson scattering and incident electromagnetic waves are scattered, when the cut-off frequency of plasma is lower than the incident electromagnetic wave frequency $\omega_{cr} < \omega$, where ω is the incident wave frequency and ω_{cr} is the cut-off (critical) frequency of the plasma with free electron density n_e. The **cut-off electron density** n_{cr} is given as

$$n_{cr} = \frac{\varepsilon_0 m}{e^2} \omega^2, \qquad n_{cr} = 10^{27} (\hbar\omega_{keV})^2 \left[1/cm^3 \right] \qquad (9.69)$$

Note that the cut-off density of x-rays is higher than most of electron density of solids.

In measuring the plasma density and temperature, optical diagnostics have been used with use of scattered spectra of laser probe from a local point of plasma. This is common methods used for a variety of plasmas. Depending on the density of plasma, infrared to X-ray coherent light sources are used in laser plasmas.

In this book, it is not mentioned in detail about the optical probe of plasma for relatively low-density plasma such as ablating plasma generated by intense lasers. Since the optical probe measurement, the plasma density should be lower than the cut-off density of plasmas. In addition, the photon number of the optical probe should be large enough so that clear signal of the scattered photons is detected.

For the case of measuring the high-energy density plasmas and warm-dense matters, the optical method demands higher-cut-off density probe. If the matter is at rest such as solid, molecule and so on, then x-rays from synchrotron radiation source (SRS) has been widely used to study the electron density distribution due to the Thomson scattering, the physics of which has been shown in Volume 1. The principle is simple. The electrons irradiated by the optical probe oscillate by the electric field of x-rays and emit the electromagnetic waves with the same frequency. Since the brightness of the synchrotron radiation is relatively low as shown in Fig. 9.15 [26] a long-time exposure is required.

Since the electron density distribution fluctuates in HEDP or WDM with thermal velocity and phase velocity of collective motion, on the other hand, brighter x-ray source with short pulse is required for diagnostics of them. As shown in Fig. 9.15, the relatively large facilities of **x-ray free-electron lasers (XFEL)** have been constructed in US (LCLS: https://lcls.slac.stanford.edu/), Japan (SACLA: http://xfel.riken.jp/), Europe (European XFEL: xfel.eu). XFELs are also characterized by high-repetition rate pulses, typically 10 HZ. In addition, each pulse consists of many ultra-short pulses. It is 2–100 fs in European XFEL with about 10^{10} photons in 25 keV x-ray operation and 10^{12} photons for 5 keV.

The ultra-short pulse allows to take snap shots of the scattered x-ray signal in high-density plasma with finite temperature. Not only the snap shots, but the frequency of the plasma waves is also high enough to obtain the oscillation frequencies of such collective modes in dense plasmas. As shown in Chap. 2, the electron plasma wave and ion acoustic wave are typical collective modes in plasmas without external magnetic field. The scattered x-ray spectra can be related to the plasma
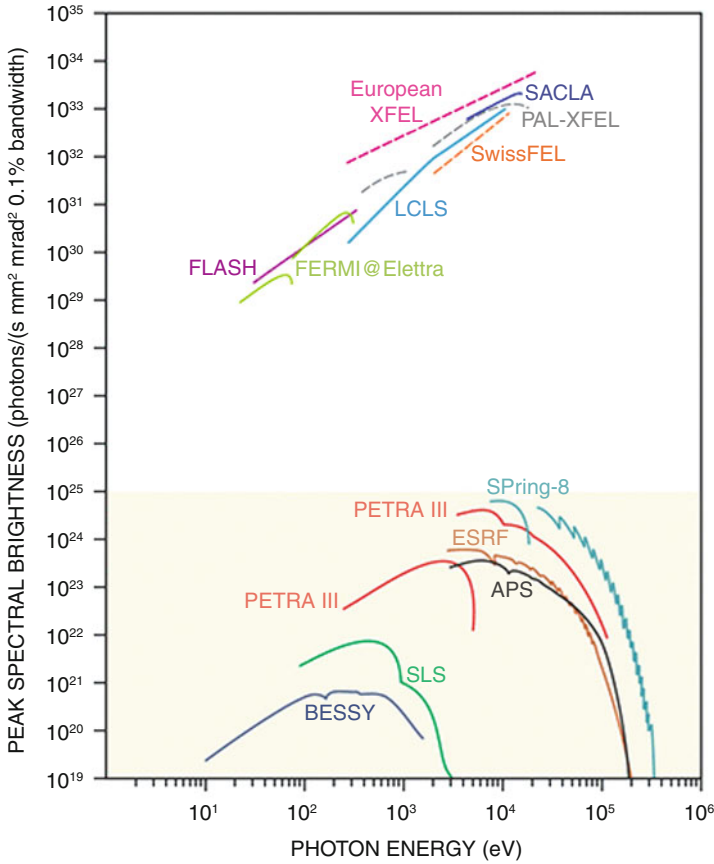
Fig. 9.15 Brightness of photon sources as a function of photon energy (eV). The synchrotron radiation source has been used widely as x-ray source like shown as Spring-8 etc., while XFEL source is monoenergetic and brighter x-ray source such as LCLS etc. Reprint with permission from ref. [26]. Copyright 1998 by American Physical Society

parameters of density and temperature via comparing to the wave theory of plasmas. Note that the damping process and non-Maxwellian effects also affect the profile of the scattered x-ray spectra, and the kinetic theory of plasma waves and Landau damping to be described in Volume 4 should be applied to the theoretical study.

9.6.1   X-Ray Scattering Diagnostics

In Fig. 9.16, a typical configuration of WDM experiment is shown [27]. The drive laser is irradiated on the target to compress and heat the target material, where the
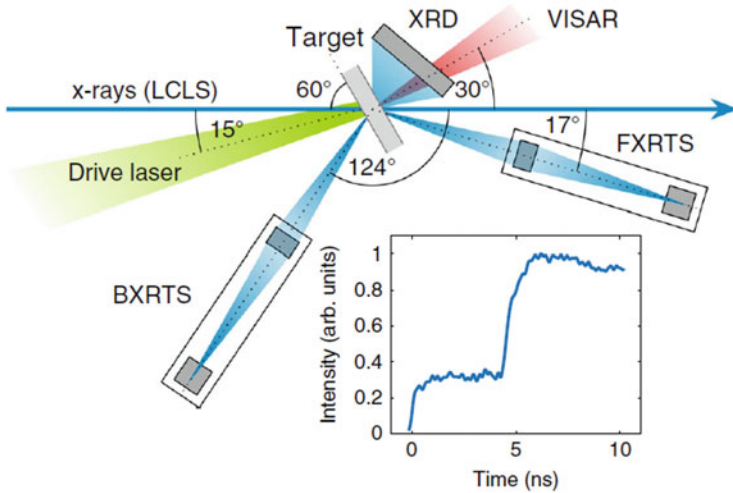
Fig. 9.16 A typical configuration of WDM experiment. The drive laser is irradiated on the thin foil target to compress and heat the target material. The laser intensity profile is shown in the inset figure as two step intensity for pre-compression and main compression. Then, a LCLS XFEL is injected to the compressed WDM. Reprinted by permission from Macmillan Publisher Ltd: ref. [27], copyright 1993

laser intensity profile is shown in the inset figure as two step intensity for pre-compression and main compression. Then, a LCLS XFEL is injected to the compressed WDM. The **x-ray diffraction (XRD)** and forward x-ray Thomson scattering (FXRTS) and backward one (BXRTS) were measured.

In any plasmas, Thomson scattering is induced by two different processes. They are called **non-collective scattering** and **collective scattering**. Thomson scattering in linear and nonlinear cases discussed in Volume 1 corresponds to the non-collective scattering. The scattering of light due to a single electron has been considered. When XFEL is irradiated to a test sample matter, the non-collective scattering is observed as total sum of the scattered x-ray from all electrons in XFEL interacting region.

Since strongly coupled plasmas such as WDM, ion-ion pair corelates via Coulomb force and the pair correlation function as shown in Fig. 9.11, has a characteristic distance as the case for the coupling parameter larger than unity. This means that each scattered x-ray with phase information from each electron cloud overlaps on the imaging plate. This interference makes the image to reflect the information of ion-ion pair correlation. This is the case of non-collective scattering used for XRD imaging.

This is the case of conventional XRD method been used historically to study the atomic structure of crystal and so on. With use of XFEL, coherent and bright x-ray beam can be used to apply the conventional XRD with higher resolution. In addition, the pulse duration of XFEL is very short enough to obtain the pair correlation

function even for plasmas such as WDM where ion thermal velocity is small enough to obtain a snap shot with XFEL pulse.

It has been studied in Volume 1 that an incident laser interacts with waves in plasmas to make the plasma waves unstable and the frequency-shifted scattered light is produced. This is called **parametric instability** due to non-liner ponderomotive force of intense lasers in plasmas. For example, laser is scattered by electron plasma wave, it is called as **stimulated Raman scattering**. Note that Raman has found the scattering for the case without instability, and it is called **Raman scattering**.

The same physical phenomenon as Raman scattering is now clearly observed in high-density plasma thanks to bright-coherent XFEL source. The scattering of incident x-ray with the plasma wave due to plasma collective physics corresponds to the collective scattering. In plasma without external magnetic field, electron plasma wave sand ion acoustic waves are spontaneously induced by thermal fluctuation and decay due to Coulomb collision and Landau damping. The dispersion relations of the waves and the damping rates are functions of plasma temperature and density if assuming Maxwell distribution functions. With such scattering spectra, plasma density and temperature can be measured for WDM.

As will be clear with plasma kinetic theory in Volume 3, the plasma waves have relatively long-life time when their wavelength is longer than the Debye length.

$$k\lambda_{De} < 1 \tag{9.70}$$

For separating which the non-collective or collective Thomson scattering is dominant from plasma scattering, the nondimensional parameter α is introduced [28, 29].

$$\alpha = \frac{1}{k\lambda_{De}} \tag{9.71}$$

The collective scattering can be used for high-energy x-ray beam $\alpha > 1$. Note that XFEL wavenumber k in (9.71) should be replaced by the wavenumber of the plasma waves scattering x-rays. It is approximately acceptable because of the following consideration.

As has been shown in Fig. 9.17 (also see Fig. 4.6 in Volume 1), three waves have to satisfy the **matching condition.**

$$\omega_0 = \omega_s + \omega \quad \boldsymbol{k}_0 = \boldsymbol{k}_s + \boldsymbol{k} \tag{9.72}$$

where $(\omega_0, \boldsymbol{k}_0)$, $(\omega_s, \boldsymbol{k}_s)$, *and* $(\omega, \boldsymbol{k})$ represent the incident, scattered and plasma waves, respectively.

In the case without extra explanation, it is assumed that the vectors $\boldsymbol{k}_0$ and $\boldsymbol{k}_s$ have finite angle and the wavenumber of the plasma waves also has roughly the same absolute values as $\boldsymbol{k}_0$ and $\boldsymbol{k}_s$.

It is informative to calculate Debye length of plasma λ_{De} and the wavelength of x-ray from XFEL, λ_X.
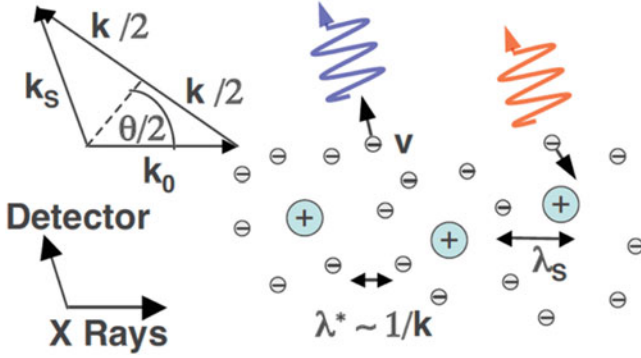
Fig. 9.17 Schematics of the incident (X Rays, k_0), and the scattering (Detector, k_s) and the plasma mode (k) satisfying (9.72). The scattered lights are blue shift and red sifts by the electron thermal motions. Reprint with permission from ref. [29]. Copyright 1998 by American Physical Society

$$\lambda_{De} = 0.74 \left(\frac{T_{eV}}{n_{20}} \right)^{\frac{1}{2}} \quad [nm]$$

$$\lambda_X = 1.2 \left[(\hbar \omega)_{keV} \right]^{-1} \quad [nm] \tag{9.73}$$

where n_{20} is the electron density in unit of 10^{20} cm^{-3}.

9.6.2   Dynamical Structure Factor (DSF)

So far, the physical reason for Thomson scattering has been explained. It is better to explain the theory of the Thomson scattering from plasma with use of **dynamical structure factor (DSF)** $S(k, \omega)$. The definition of DSF is given as

$$S(k, \omega) = \frac{1}{2\pi V} \int_{-\infty}^{\infty} dt \langle \rho_k(t' + t) \rho_{-k}(t') \rangle \, exp(i\omega t) \tag{9.74}$$

Where Fourier decomposed density fluctuation $\rho_k(t)$ is defined to be,

$$\rho_k(t) = \int_{-\infty}^{\infty} dr [n(r, t) - n_0] \, exp(-i k \cdot r) \tag{9.75}$$

The electron density perturbation at a given time $n(r, t) - n_0$ consists of thermal noise and the enhanced fluctuation by the resonance in plasma, namely electron and ion waves. The DSF sheds light on the oscillation frequency of the waves in plasma. Namely, DSF $S(k, \omega)$ has all information of the density fluctuation in the plasma.

In addition, the **structure factor (SF)** $S(k)$ is defined with DSF as follows.

$$S(k) = \frac{1}{N}\left\langle |\rho_k(t)|^2 \right\rangle = \int_{-\infty}^{\infty} S(k, \omega)d\omega \tag{9.76}$$

This SF is related to the **pair (radial) distribution function** $g(r)$ given in Fig. 9.10.

$$g(r) = 1 + \frac{1}{n}\int_{-\infty}^{\infty} \frac{dk}{(2\pi)^3}[S(k) - 1]\,exp(i k \cdot r) \tag{9.77}$$

Note that the position r is a vector in $g(r)$, while the electron cloud is spherically symmetric around the nucleolus, consequently $g(r)$ is only a function of radius.

The differential scattering cross section defined as fraction of the scattered x-ray to the angle θ between the incident and scattered X-rays per solid angle Ω and the frequency interval $\Delta\omega$ of $\omega = \omega_i - \omega_s$ is given in the form [29, 30].

$$\frac{\partial^2 \sigma}{\partial\omega\partial\Omega} = \sigma_T \frac{\omega_s}{\omega_0}\frac{1}{2}\left(1 + cos^2\theta\right)S(k, \omega) \tag{9.78}$$

$$k = |k_0 - k_s| = 2\omega_0\,sin(\theta/2)/c$$

This indicates that we can evaluate the plasma parameters from Thomson scattering spectrum, if we have the theory relating to the DSF $S(k, \omega)$ as a function of the plasma parameters such as temperature and density. Note that if the data quality is very fine, electron distribution function can be determined from the scattered spectrum within some assumption.

In general, DSF consist of three terms, namely

1. Peaked density profile by bound electros and free electrons forming Debye shielding around each nucleus. They move with ion motion, but the ion thermal velocity is very small so that Doppler shift by the ion motion can be neglected. The form factor of the bound and Debye shielding electron distribution and the ion-ion pair correlation function determines the structure factor and it can be regarded as elastic scattering ($\omega = 0$). Let us write this component as the elastic component, $S_{elas}(k)$.
2. The longitudinal collective motions in plasma have the density structure according to the dispersion relation of the plasma waves. They are the electron plasma wave and ion acoustic wave as discussed in Chap. 2. Including the case of WDM, the dispersion relation with strongly coupling and quantum effects are used for the electron plasma wave [20, Chap. 2 in Ref. 18]. Since they have the frequencies of electron and ion plasma frequencies, the frequency shifts are observed. They are collective mode and in-elastic scattering. Let us write this as the collective component, $S_{collec}(k, \omega)$.

3. Another inelastic component in DSF is related to the photoionization of x-ray by a bound electron, the physics of which has been discussed in Chap. 5. In the present case, the process is not absorption of x-ray photon by a bound electron, but the process is inelastic photo absorption by the bound electron. Let us write it as $S_{be}(k, \omega)$.

It is shown by J. Chihara that the total DSF can be written in the form [31, 32].

$$S(k, \omega) = S_{elas}(k) + S_{collec}(k, \omega) + S_{be}(k, \omega) \tag{9.79}$$

$$S_{elas}(k, \omega) = [f(k) + q(k)]^2 S_{ii}(k) \tag{9.80}$$

$$S_{collec}(k, \omega) = Z_f S_{ee}^0(k, \omega) \tag{9.81}$$

$$S_{be}(k, \omega) = Z_b \int d\omega' S_{ce}(k, \omega - \omega') S_s(k, \omega') \tag{9.82}$$

where $f(k)$ and $q(k)$ are the form factor of bound electrons and Debye shielding free electrons, and $S_{ii}(k)$ is the ion-ion pair correlation function. Z_f and Z_b are the numbers of free and bound electrons in the statistically averaged ion. The real spectra of $S_{ee}^0(k, \omega)$ by one free electron is discussed soon.

9.6.3   Elastic Scattering (X-Ray Diffraction: XRD)

In 1914, von Laue observed these diffraction patterns by irradiating metal with X-rays. Braggs and his son also developed his X-ray crystallography in 1915. Each person's achievements have come to fruition in each year as the Nobel Prize in Physics.

With the advent of X-ray scattering technology in recent years, it has become possible to measure the physical characteristics of high-density plasma and use it for research on high-energy density physics.

When the parameter α in (9.71) is small enough by inserting the parameters in (9.73), Coherent-XRD image can be obtained to provide the ion-ion pair correlation. In Fig. 9.16, the image on XRD is the scattered x-ray intensity image in two-dimensional plate (say, x and y). Since the electrons are located randomly and the scattered x-ray is a snapshot for a few femto-second, the scattering image is like the scattered electron de-Broglie wave image discussed previously. This is the non-collective Thomson scattering method.

The x-ray is an electromagnetic wave and its propagation and scatter in electron density are given by the following equation from Maxwell equations.

$$c^2 \nabla^2 E + \left(\omega^2 - \omega_{pe}^2\right) E = 0 \tag{9.83}$$

where the electron plasma frequency is only a function of the electron density:

$$\omega_{pe}^2 \propto n_e(\boldsymbol{r}, t) \tag{9.84}$$

Comparing (9.83) with Schrodinger equation for quantum electron scattering (9.26), the mathematics of electron scattering in each potential field can be directly applied to the analysis of coherent XRD image. In the case of x-ray scattering by the electron cloud around a central ion, the potential in (9.26) is replaced as

$$V(r) \iff -n_e(r) \tag{9.85}$$

In the case of x-ray scattering, Coulomb potential by the central ion should be neglected, namely, it is enough to neglect the term due to Rutherford scattering in (9.61). It is noted that in WDM many electrons are still in bound state in each ion, but the bound electrons also contribute to Thomson scattering with the incident frequency as far as the absolute value of binding energy is smaller than the x-ray photon energy.

Therefore, the forma factor $F(q)$ is used to obtain the electron density profile. The foam factor is also used in identifying a single gold nano-scale particles of size from 10 nm to 80 nm in water solution. The conventional small-angle x-ray scattering (SAXS) has been used to reproduce the electron density profile in the gold by reproducing with the resultant form factor [33]. SAXS is now widely used to measure a time evolution of clumpy density structure in WDM, for example, the growth of ripple amplitude of a surface unstable to Rayleigh-Taylor instability [24].

As a typical experiment, liquid iron scattering measurement with XRD is explained. In this study, the experiment measured the density of liquid iron at pressures up to 116 GPa and 4350 K via static compression using a **laser-heated diamond-anvil cel**l (LH-DAC) [34].

In studying the physics of planets' inside, it is required to know the physical property of main component of dense metallic cores of planets. This is not only true for Earth, but also for Mercury and Mars, which are expected to have partially molten cores. Density (ρ) and longitudinal sound velocity (VP) are the primary observables of Earth's liquid outer core.

Therefore, laboratory measurements of these properties at high pressure are of great importance to understand Earth's and other planets' core composition and behavior. While determination of density for crystalline materials under high pressure and temperature (P-T) is relatively straight-forward by in situ x-ray diffraction.

The density of liquid iron has been determined via static compression experiments following an innovative analysis of diffuse scattering from liquid [34]. The longitudinal sound velocity was also obtained to 45 GPa and 2700 K based on inelastic x-ray scattering measurements. Combining these results with previous shock-wave data, we determine a thermal equation of state for liquid iron.

In Fig. 9.18, ion-ion pair correlation function is obtained as the radial distribution function [34]. The scattered intensity in the x-y plane at the rear of the liquid iron is shown in Fig. 9.18a, where the scattered angle is used to obtain the scattered wavenumber Q (nm^{-1}). By assuming the spherically symmetric electron cloud
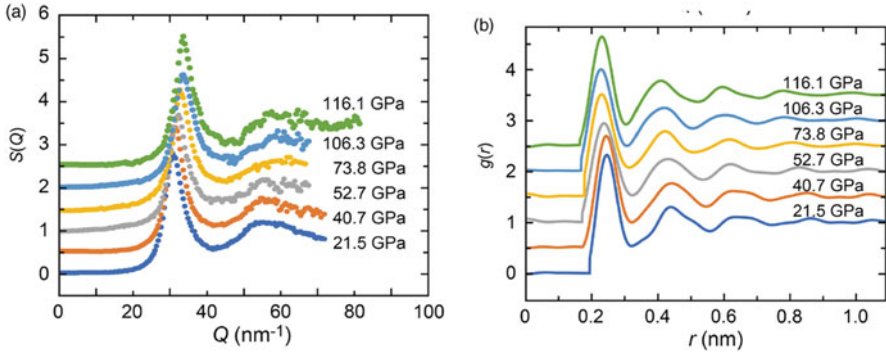
Fig. 9.18 (**a**); Scattered wavenumber dependence of form factors by elastic scattering of XRD for iron at high pressures produced by DAC. (**b**); The form factor is inverse-transformed with Fourier method to convert the radial distribution functions. The reduce of the first peak of the radial distribution give the density compressed with high pressure. Reprint with permission from ref. [34]. Copyright 1998 by American Physical Society]

distribution around each ion core, the date (a) can be transformed to the radial distribution function shown in Chap. 9.3.

In Fig. 9.18b, the **radial distribution function** (ion-ion correlation function) $g(r)$ is shown. It is clearly seen the over-shooting oscillation profile is seen indicating that the liquid iron is strongly coupled plasma as shown in Fig. 9.10. Note that low frequency density perturbation due to acoustic wave in the ion liquid has also observed in the spectrum of the scattered x-ray with angle $Q = 3$ [nm^{-1}].

9.6.4 Collective Thomson Scattering

It is complicated calculation is required to understand the physics behind Thomson scattered x-ray spectra from WDM where plasma waves are excited and damping. The detail derivation of general relativistic case has been given in the book [28] or a review paper [29]. Here, we try to explain the basic physics affecting the scattered spectra from WDM with a finite temperature.

Recall the simple formula of Thomson scattering by an electron oscillating without initial velocity. Thomson scattering cross section σ_T defined as

$$\sigma_T = \frac{8\pi}{3} r_e^2, \quad r_e = \frac{e^2}{4\pi\varepsilon_0 mc^2} \tag{9.86}$$

where r_e is the electron classical radius and they are given as

$$\sigma_T = 67 \left[\text{fm}^2\right], \quad r_e = 2.8 \left[\text{fm}\right]. \tag{9.87}$$

The scattered power by a single electron to the angle θ made by the incident and scattered directions is given as

$$\frac{dP_s}{I_i d\omega d\Omega} = \frac{3}{16\pi}\sigma_T \cos^2\theta\delta(\omega - \omega_i) \tag{9.88}$$

Note that the scattering cross section is independent of incident electromagnetic wave frequency. In (9.88), I_i, ω_i, and P_s are incident intensity and frequency and scattered power. To observe bright scattering photons, total large number of electrons and bright light source are key technology.

From an electron located at $\boldsymbol{r} = \boldsymbol{r}_j(t)$ is oscillated by the incident XFEL with its acceleration $\boldsymbol{\alpha}_j$ in the form, where we assume the XFEL is linearly polarized in the vector $\boldsymbol{E}_i$ direction.

$$\boldsymbol{\alpha}_j = -\frac{e}{m}\boldsymbol{E}_i \sin\{\omega t - \boldsymbol{k}\cdot\boldsymbol{r}_j(t)\} \tag{9.89}$$

So, the angle θ in (9.89) is the angle of the vector $\boldsymbol{E}_i$ and the vector $\boldsymbol{R} - \boldsymbol{r}_j(t)$, where $\boldsymbol{R}$ is a fixed point of the diagnostic window at a far from the plasma. Since the angle θ is also the electron position dependent and write as θ_j below.

In the case of incoherent light source, (9.89) can be applicable by taking the summation to all electrons. For the coherent photon source, the interferometry of the scattered photons from different electrons become important and it has an essential information for Thomson scattering diagnostic. For this purpose, it is necessary to obtain the retarded electric and magnetic fields at the observation point $\boldsymbol{R}$ as sum of all electrons at $\boldsymbol{r} = \boldsymbol{r}_j(t)$.

Such complicated calculation is shown in [28]. Here we limit the description qualitatively and show the formula of the scattered spectrum. It is easy to know that the delta-function of (9.89) becomes Gaussian spectrum because the thermal motion of electrons leads to Doppler shift of the scattered spectrum. This means the spread of the scattered spectrum has the information of electron temperature. In addition, propagating waves inside the plasma gives the shift of the scatted spectrum as shown in (9.72).

In WDM, plasma waves are spontaneously indued and decay due to damping. A simple damping oscillation model is

$$\frac{d^2}{dt^2}X + \gamma\frac{d}{dt}X + \omega_0^2 X = 0 \tag{9.90}$$

Then, an approximate solution is

$$X(t) \quad \propto \quad exp[i(\omega - \omega_0)t - \gamma t] \tag{9.91}$$

Laplace transformation gives the Lorentzian spectrum.

$$X(\omega) \quad \propto \quad \frac{\gamma}{(\omega - \omega_0)^2 + \gamma^2} \tag{9.92}$$

It is natural to assume that there will be two peaks with shifts from the incident frequency at $\omega = \omega_i \pm \omega_P$. The wave number $\boldsymbol{k}_P$ is uniquely determined by the relation (9.72). These two peaks are easily understood from the following mathematics of the trigonometric formula. As already derived in (4.6.5) in Volume 1, the source term to generate scattering electromagnetic waves in plasma is given as

$$\left(\omega_s^2 - c^2 k_s^2 - \omega_{pe}^2\right) E_s = -\omega_{pe}^2 cos\theta \delta n_P E_i \tag{9.93}$$

where the suffix "i, s, p" represents the physical quantities shown in (9.72).

Use (9.72) so that incident and scattered electromagnetic field satisfies the dispersion relation, LHS in (9.93) vanishing, the following relation is obtained to RHS with the sinusoidal plasma wave and incident wave.

$$\begin{aligned}
\delta n_P E_i &\propto sin(\omega_i t - \boldsymbol{k}_i \cdot \boldsymbol{r}) \, sin\left(\omega_P t - \boldsymbol{k}_p \cdot \boldsymbol{r}\right) \\
&\propto sin\left\{(\omega_i - \omega_P)t - \left(\boldsymbol{k}_i - \boldsymbol{k}_p\right) \cdot \boldsymbol{r}\right\} \\
&+ sin\left\{(\omega_i + \omega_P)t - \left(\boldsymbol{k}_i + \boldsymbol{k}_p\right) \cdot \boldsymbol{r}\right\}
\end{aligned} \tag{9.94}$$

Under the matching condition of (9.72), the first term in RHS of (9.94) becomes the source to generate the scattering electromagnetic wave resonantly, because the dispersion relation in LHS in (9.93) is satisfied. This low frequency component is called **Stokes line** in the cases of Raman scattering.

On the other hand, the second term in (9.94) generates higher frequency component of the scattered electromagnetic wave. As will see below, this component can be observed for the case with high temperature plasma. It is called **anti-Stokes line** in the Raman scattering.

For the case where the plasma wave is the electron plasma wave (Bohm-Gross wave) given in (11.7.17), it is possible to measure the electron density. In addition, the spread of the scattered light is related to the damping process shown in (9.92); consequently, it is also possible to determine the thermal spread of the electron distribution function or electron temperature, because the damping by the electron Landau damping or Coulomb collision damping is a function of electron temperature.

To predict the scattered wave intensity, it is necessary to know the electron density fluctuation symbolically written as δn_P in (9.93). The density fluctuation in plasma is determined by the balance between the thermal excitation of the fluctuation and the dissipation process. It is well known that the **fluctuation-dissipation theory** provides the fluctuation spectrum.

Dynamic structure factor (DSF) of the collective modes in plasma $S_{collec}(k, \omega)$ is related to the **plasma dielectric function** $\varepsilon(k, \omega)$ by use of the fluctuation-dissipation theory [28].

$$S_{collec}(k, \omega) = \frac{\epsilon_0 \hbar k^2}{\pi e^2} \frac{1}{1 - exp(\hbar\omega/T_e)} Im\left[\frac{1}{\epsilon(k,\omega)}\right] \qquad (9.95)$$

$\epsilon(k, \omega)$: longitudinal plasma dielectric function

For example, when a simple fluid model with a constant dissipation rate γ is used to derive the dielectric function of plasma wave as derived in Chap. 2, the dielectric function of a plasma $\epsilon(k, \omega)$ is easily obtained by regarding X in (9.90) as electrostatic field.

$$\epsilon(k, \omega) = 1 - \frac{\omega_{pe}^2}{\omega^2} - i\frac{\gamma}{\omega}$$

The imaginary part of $\epsilon(k, \omega)$ has the Lorentzian form (9.92). Weaker the damping, stronger the peak intensity of scattering, and the width of the DSF of such collective scattering becomes wide as the damping increases.

In addition, the detail balance relation for $\hbar\omega \gg T_e$ yields the following relation

$$S_{collec}(-k, -\omega) = exp(-\hbar\omega/T_e)S_{collec}(k, \omega) \qquad (9.96)$$

This relation says that the up-shift scattering is much weaker than the lower-shift scattering. On the other hand, in the ideal plasma $\alpha \gg 1$, the plasma temperature is much higher than the photon energy $\hbar\omega \ll T_e$, the up-shift component in (9.94) is almost the same as the down-shift component.

$$S_{collec}(-k, -\omega) = S_{collec}(k, \omega) \qquad (9.97)$$

This is the case of the optical diagnostics of laser produced plasmas and magnetically confined plasmas, and the in-elastic scattering by the collective plasma wave modes in (9.94) appears in both sides of the original photon energy as we see later.

9.6.5   Plasma Diagnostics with Optical Thomson Scattering

Optical probe for measuring the plasma parameters of laser produced plasma in ablating region, relatively lower density than the solid, has been used for diagnostics. For example, the higher-harmonic laser is used for such diagnostic to study the plasma generate by more powerful fundamental frequency lasers [Chap. 5 in Ref. 53].

In this case, the laser produced plasma is lower density and higher temperature compared to WDM and the condition $\alpha \gg 1$ is satisfied. Therefore, the atomic and Debye electron cloud is too small to scatter the optical probe and the most of the scattering is due to the collective-inelastic scattering, the second term in RHS in (9.94).

In Fig. 9.19, typical spectra of the collective DSF are shown [35]. In Fig. 9.19, the three density cases are plotted with different temperature and different incident photon energy.

Case (a)   The incident probe is laser with its wavelength $\lambda = 532nm$ ($\hbar\omega = 2.3eV$), the plasma density is 10^{19} cm^{-3}. This is a typical case of diagnosing laser-produced ablation plasma with the second harmonic light probe. The frequency is normalized by the plasma frequency ω_{pl}. In this case, $\hbar\omega_{pl} = 0.117eV$. The colors of lines correspond to different plasma temperatures. $T_e = 200, 600,$ *and* 3000 *eV* for black (a1), red (a2), and blue (a3), respectively. Both side intensities are the same, because $\hbar\omega/T_e \ll 1$. The width of the both spectra become wider as increase of temperature, because the damping of the plasma wave becomes higher due to Landau damping.

Case (b)   This figure is the case with TS light source is $\lambda = 4.13$ nm ($\hbar\omega = 30eV$), so-called EUV light source. In this case, $\hbar\omega_{pl} = 1.17eV$. The colors of lines correspond to different plasma temperatures. $T_e = 0.8, 2.0,$ *and* $8.0eV$ for black (c1), red (c2), and blue (c3), respectively. The

Fig. 9.19 Theoretical spectra of DSF, S_{ee}^0, for the collective scattering by the electron plasma wave. Figure (**a**) is the case of ablating plasma with relatively low density and optical Thomson scattering. With the increase of the electron temperature increases from a1 to a3, the damping effect is enhanced to make the structure broad. Figure (**b**) is the scattering of EUV light from higher density plasma. The asymmetry of the structure appears reflecting the relation (9.96). Figure (**c**) is x-ray scattering near solid density. Note that the amplitude decreases from (**a**) to (**c**) drastically. Reprint with permission from ref. [35]. Copyright 1998 by American Physical Society
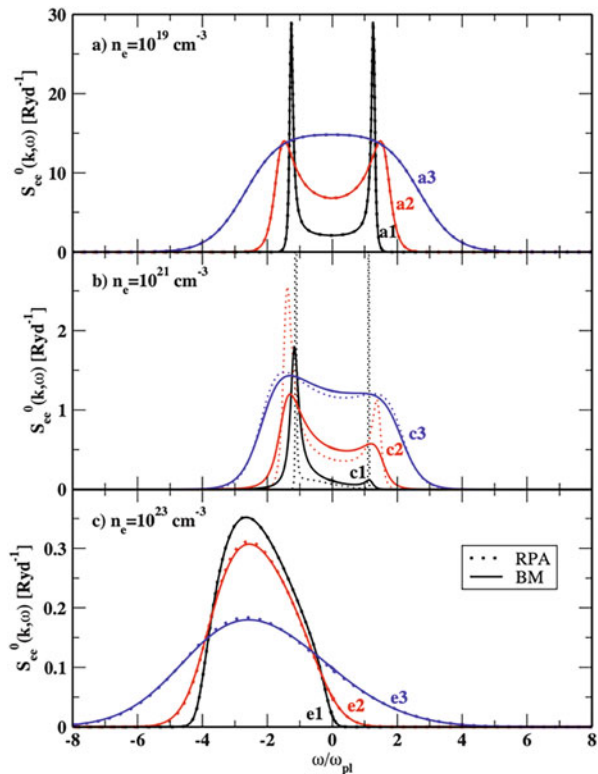
asymmetry of Stokes and anti-Stokes lines appears in the case of (c1) with $\hbar\omega/T_e$=2. Although the anti-Stokes line increases as the temperature increases, the scattered spectra become broader due to the increase of Landau damping effect. In addition, the coupling parameter Γ is almost unity in these three cases, therefore the fluctuation amplitude per one free electron $S_{ee}^0(k,\omega)$ in (9.81) is relatively small compared to the case a). Note that the spread of a3 and c3 looks same in the normalized frequency means the damping in c3 is about ten time larger than a3.

Case (c)   For the case of x-ray probe with λ=0.26 nm ($\hbar\omega$=4.77 keV), the even the high-density plasma is transparent to the x-ray, since the cut-off density of 10^{23} cm^{-3} is $\hbar\omega_{pl} = 11.7eV$, much lower than the x-ray photon energy. The colors of lines correspond to different plasma temperatures. $T_e = 0.5,\ 3.0,\ and\ 13.0eV$ for black (e1), red (e2), and blue (e3), respectively. In most of the case, $\hbar\omega/T_e > 1$ and the anti-Stokes lines disappears. In such WDM situation, the Fermi energy contributes to the plasma wave dispersion relation and the peak of the resonance is shifted near $\omega \approx 2\omega_{pl}$. In addition, the fluctuation amplitude per one free electron $S_{ee}^0(k,\omega)$ in (9.81) becomes smaller compared to the above two cases. This means extremely bright x-ray source such as XFEL is dispensable for such weak signal measurement.

With increase of coupling parameters from the top to bottom in Fig. 9.19, the intensity of DSF per one free electron becomes weaker since the collective motion of free electrons are prohibited by Coulomb interactions in strongly coupled plasma.

9.6.6   WDM Experiment with XRTS Diagnostics

As the integrated experiments, all three contributions in (9.79) are identified to be used to measure the temperature, density, and ionization degree. Let us see two examples of laser shocked WDM experiments for the case of strongly coupled plasma in the region of $\alpha < 1$. In such case with x-ray source, the wavelength of x-ray is shorter than the Debye length and the x-ray is refracted by the Debye shielding electron cloud. So, the elastic scattering by the atomic and Debye cloud foam factors in (9.80) becomes important.

Before the completion of XFEL facilities, laser-generated hard x-ray line emissions have been applied to the x-ray Thomson scattering diagnostics of dense plasmas. Here, one example using NIF laser is reported with 1.1 MJ hohlraum implosion of a spherical CH solid with 1.15 mm radius [36]. The line x-rays are produced by another laser beams irradiating on zinc solid and the helium-like ions of Zn emitting 9.0 keV photon energy is used for TS x-ray scattering source.

The x-ray spectrum from XRTS data have been fitted with theory of DSF explained above. The best fit of the WDM scattering zone averaged temperature and charge state of carbon ions are concluded that [36].

$$\langle T \rangle = 86 \pm 20 eV, \quad \langle Z_C \rangle = 4.92 \pm 0.15,$$

while an integrated radiation-hydrodynamic code HYDRA results

$$\langle T \rangle = 109 eV, \quad \langle Z_C \rangle = 4.40,$$

In the analysis of XRTS spectrum, it is shown that the fraction of the elastic scattering to the total one is 0.24, while this ratio from HYDRA simulation is 0.35. Such a difference suggested some improvement of the ionization model in HYDRA compared to XRTS data, because the collective scattering is proportional to the number of free electrons.

The HYDRA simulations have been carried out with two different ionization lowering models. One is Thomas-Fermi model and the other is Stewart-Pyatt mode. How to theoretically model the ionization potential lowering will be discussed next section and it is concluded that both models cannot well predict the pressure ionization of WDM [36]. It is insisted that XRTS can be a precise diagnostics of modeling high-pressure effects in WDM.

Along with such experiments, XFELs are now widely used to study the plasma properties in WDM compressed by intense lasers. In Fig. 9.20, x-ray spectrum of incident XFEL with photon energy of 8 keV scattered from WDM is shown [37]. The target is a solid aluminum foil and the scattered spectrum before the compression, aluminum solid state, is shown with bule line. The elastic scatter component around 8 keV and a peak at lower energy is observed.

Aluminum at room temperature (blue line) is metal and three electrons from each atom are not in the bound state. It is a kind of plasma with free electrons with the Fermi energy. The plasma wave in such quantum plasma provides the peak of the collective mode on the left as seen in Fig. 9.20. This is due to the collective contribution to DSF shown in (9.81).

The experimental result obtained by Thomson scattering from the laser-compressed aluminum WDM is shown with gray spiky line "single shot signal". With use of theoretical models of DSF in (9.79), it is concluded that the shift of the peak by the plasma wave is due to the density compression of 2.3 times the solid density, and a factor 2.8 over the cold scattering peak at energy 8 keV is due to the heating to 1.75 eV. Of course. Thomson scattering spectra are a function of scattered angle from the incident X-ray direction. Fig. 9.20 is obtained at the angle of 13 degree from XFEL incident direction, corresponding to FXRTS in Fig. 9.16. In the present WDM, the ionization energy of the bound electrons is higher than the plasma temperature. The ionization is not affected by laser compression and $Z_f = 3$ does not change by the shock wave.

In Fig. 9.20, the collective (inelastic) scattering component spectrum is shown with three humps with green, red, and purple colors. As shown in the box in the
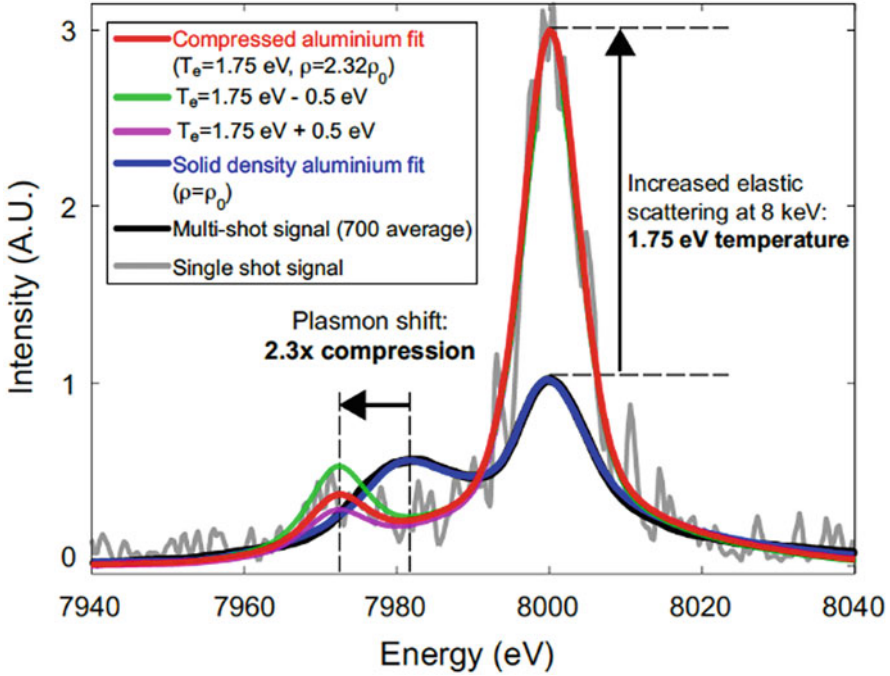
Fig. 9.20 XRTS spectra from aluminum foil before compression (blue) and after compression (red). The profile of the low energy hump by the collective scattering by plasma wave changes as green and pink by changing the electron temperature slightly. The shift of this peak position gives the compressed density. Reprinted by permission from Macmillan Publisher Ltd: ref. [37], copyright 1993

figure, the difference among three is the difference of assumed electron temperature, $T_e = 1.75–0.5$ eV, 1.75 eV, and $1.75 + 0.5$ eV, respectively. The increase of the electron temperature leads to the enhancement by the plasma wave damping by Landau damping, causing the decreases of the peak amplitude. Note that the peak of the spectrum hump of the collective mode is very sensitive to the electron temperature.

In Ref. [38], sensitivity to the theoretical model to the elastic scattering in (9.80) is discussed in detail. In the elastic component in (9.80), the atomic form factor $f(k)$ does not change after the shock compression, while it is pointed out that the Debye screening form factor $q(k)$ is very sensitive to the temperature. Taking account of the Debye shielding effect of each atom, the increase of the scattered x-ray peak at 8 keV is evaluated due to the increase of the temperature to 1.75 eV. Of course, note that the increase or decrease of the elastic scattering component is a function of the scattering angle and the above statement is not universal.

Throughout the Thomson scattering, the decomposition of DSF shown in (9.79) proposed by J. Chihara has been used as a standard model. The Chihara formula has

been compared to the DSF spectra directly obtained from the time-dependent density-functional-theory (TD-DFT) [39]. It is informative to cite this conclusion and copy it here.

The authors presented a method for the direct calculation of the DSF for warm dense matter, independent of Chihara decomposition, by applying real-time TDDFT to configuration drawn from thermal Mermin DFT-MD calculations. Comparison of the result s with state-of-the-art models applied within the Chihara picture illustrates some subtle differences between the two, though it generally supports the use of the Chihara formalism as an inexpensive alternative to the very detailed and computationally intensive TDDFT calculations.

9.7 Ionization Potential Depression (Continuum Lowering)

It has been clear that the ionization degree is very sensitive in Thomson scattering spectra. In high-density plasmas, the pressure ionization and resultant ionization potential lowering is important physics to determine the ionization degree, and transport phenomena stemming from mainly the free electrons. As mentioned in Saha LTE ionization model, the ionization potential lowering is essential to determine the number of free electrons.

The evaluation of the lowering of ionization potential which is also called **ionization potential depression (IPD)** and **continuum lowering** has been studied from the beginning of modern plasma physics in application to statistical mechanics [40] and astrophysics [41]. Let us cite them as "EK" and "SP" theoretical models simply below. More than last 50 years, SP model has been widely used to study dense plasmas. In the first experiment possible to study with XFEL, however, demonstrated that EK theoretical model well explain solid density plasma experiment [42].

In this experiment, the x-ray photon absorption edge by the bound-free photoabsorption has been measured from WDM irradiated by XFEL. However, more precise atomic model with detail configuration has been studied about the energy state of K-shell electrons [43]. This pointed out the change of K-shell electron energy as the ionization proceeds and the above conclusion has not been confirmed. With more detail atomic code, the experimental data of [42] has been analyzed again to clarify the improvement of the atomic model [44].

Let us see the basic theory of IPD and discuss the experimental data with XFEL.

9.7.1 Theoretical Models

In SP model, they proposed to use Thomas-Fermi model to the spherically symmetric potential around the centered ion as explained previously to be used as statistically averaged potential. Different from the ion-sphere model, the boundary should be taken to the infinite radius and the effect of neighboring ions is also included to

the Thomas Fermi model. The electrons in bound state and free states are assumed to be in Fermi-Dirac distribution and ions are classical as given in Boltzmann distribution.

Then, SP has modified the Poisson equation mathematically to the following form with changing variables as

$$y = \frac{e\phi}{T}, \quad x = \frac{r}{\lambda_D} \tag{9.98}$$

where the Debye length is contributed by both of electrons and ions, while it is assumed that both have the same temperature T. Then, the Poisson equation with replacement of electron density with Fermi-Dirac distribution can be reduced to the following form.

$$\frac{1}{x}\frac{d^2}{dx^2}(xy) = \frac{1}{Z+1}\left\{\frac{F(y-\alpha)}{F(-\alpha)} - exp(-Zy)\right\} \tag{9.99}$$

where

$$\alpha = \frac{\mu}{T} \tag{9.100}$$

and F is so-called Fermi-Dirac integral defined to be

$$F(\eta) = \int_0^\infty \frac{t^{1/2}}{e^{t-\eta}+1} dt \tag{9.101}$$

Finally, (9.99) should be solved to satisfy the following two boundary conditions.

$$y(\infty) = 0, \quad xy \rightarrow \frac{Ze^2}{(4\pi\varepsilon_0}\lambda_D T) \quad (x \rightarrow 0) \tag{9.102}$$

The normalized chemical potential α is an eigen value obtained so that the solution should satisfy the boundary conditions (9.102).

In SP paper, they have solved (9.99) numerically for wide range of density and temperature. At the same time, SP also obtained approximate solutions in the inner and outer region and tried to match the both functions to obtain the depressed ionization energy. Then, SP modified the function so that it can well reproduce the numerical results. The resultant formula of IPD by SP can be given in the following form.

$$\Delta U_{SP} = \frac{3}{2}\frac{Ze^2}{4\pi\varepsilon_0 a}\left\{(1+X^3)^{2/3} - X^2\right\} \tag{9.103}$$

where a is the ion sphere radius and X and a are both defined to be

$$X = \frac{\lambda_D}{a}, \quad \frac{4\pi}{3} a^3 n_i = 1 \tag{9.104}$$

It is useful to know the physical image of (9.103). The ionization potential depression compared to the case of isolated ion is given with (9.103) and its high temperature limit, $X >> 1$,

$$\Delta U_{SP} \approx \frac{Ze^2}{4\pi\varepsilon_0 a} \frac{1}{X} = \frac{Ze^2}{4\pi\varepsilon_0} \frac{1}{\lambda_D} \tag{9.105}$$

In such ideal plasma, the potential is shielded by the Debye shielding effect. This potential can be Taylor expanded near the centered ion ($r << \lambda_D$) as

$$U_{DH} \approx \frac{Ze^2}{4\pi\varepsilon_0 r}\left(1 - \frac{r}{\lambda_D}\right) \qquad (a << r << \lambda_D) \tag{9.106}$$

The second term is the depressed ionization potential and is the same as that by SP.

In the opposite limit for strongly coupled plasma with $X << 1$, (9.103) is reduced to

$$\Delta U_{SP} \approx \frac{3}{2} \frac{Ze^2}{4\pi\varepsilon_0 a} \tag{9.107}$$

This limiting case is also easily understood as follows. In strongly coupled plasma, the ion-sphere model is good image, and we assume the situation that the electron density is very high because of Fermi energy and the charge neutrality within the ion sphere (IS) is reasonable. Then, the potential inside the sphere can be expressed as

$$U_{IS} = \frac{Ze^2}{4\pi\varepsilon_0 r} - f(r) = 0 \quad at \ r = a \tag{9.108}$$

Where the function f(r) is the potential contribution by electron density. This gives us the ionization potential depression f(a), which is the same as (9.107) except the factor 3/2.

The second formula, although their work was earlier historically by Ecker and Kroll [40], is given in the following form:

$$\Delta U_{EK} = \frac{Ze^2}{4\pi\varepsilon_0} g \tag{9.109}$$

$$g = \begin{cases} 1/\lambda_D & for \quad n_i < n_{cr}/(1+Z) \\ 1/a \times C(1+Z)^{1/3} & for \quad n_i > n_{cr}/(1+Z) \end{cases}$$

$$n_{cr} = \frac{3}{4\pi} \left(\frac{T}{Z^2 e^2} \right)^3$$

In (9.109), C is originally a function of density and temperature, but C = 1 is found to give a good agreement with recent experimental data.

9.7.2 Experimental Evidence of IPD

There have been a lot of experimental study on the theory of IPD, but it was very difficult to measure IPD directly, especially in dense plasma. The first IPD experiments have carried out with XFEL laser at SLAC, Stanford Univ. [45]. In these experiments, a monochromatic x-ray pulse of well-defined photon energy is focused to spots of $\sim$10 μm^2 on thin foils of various materials. Typical intensities achieved are on the order of 10^{17} Wcm^{-2}, sufficient to heat the irradiated regions to temperatures exceeding 100 eV on femtosecond timescales, and to drive resonant and non-linear atomic processes. The intense x-ray pulse can drive x-ray photoionization of inner-shell electrons, provided the photon energy is higher than the shell's ionization edge, and bound-bound transitions leading to excited atomic configurations, if the resonance energies are within the bandwidth of the x-ray pulse. Recombination into the core holes created by this interaction produces strong x-ray emission that has been spectrally resolved to identify ionization edges

In Fig. 9.21, in the vertical axis, the emitted photon intensity spectrum from heated aluminum plasma is plotted as a function of the photon energy between 1470 eV to 1670 eV [44]. The image is obtained after many shots of XFEL by changing the photon energy of XFEL pulses. The data are shown for the irradiation of XFEL with photon energy from 1470 eV to 1800 eV, which is shown in the horizontal axis. The strong intensities of about eight lines are clearly seen with the threshold FEL photon energy increasing from low energy to higher energy. These lines are identified due to the electron transition 2p-1s of partially ionized aluminum atom. The FEL photons are predominantly absorbed by K-shell electrons as explained in Chap. 5, if the FEL photon energy is higher than the threshold energy of bound-free transition as shown in Fig. 9.21 for the case of iron.

Just after a hole is generated in the K-shell, another electron fulfills the hole to emit the line radiation. One possible process is radiative transition of bound electron from L-shell to K-shell and this line emissions are observed and shown in Fig. 9.21. The energy gap between L-shell and K-shell changes as ionization stage changes in the aluminum atom. As the ionization stage change from Al-IV stage to Al-XI, its gap increases as shown by the line positions in the horizontal axis of Fig. 9.21. Therefore, the threshold XFEL energy gives us the information of energy depth of K-shell electron measured from the real free energy state which is determined by plasma effect.

Fig. 9.21 Varying the photon energy of XFEL, the x-ray emission spectra have been measured to evaluate the ionization potential depression (IPD). The experimental data are compared to simulation with two different ionization potential depression theoretical models. Reprinted by permission from Macmillan Publisher Ltd: ref. [44], copyright 1993
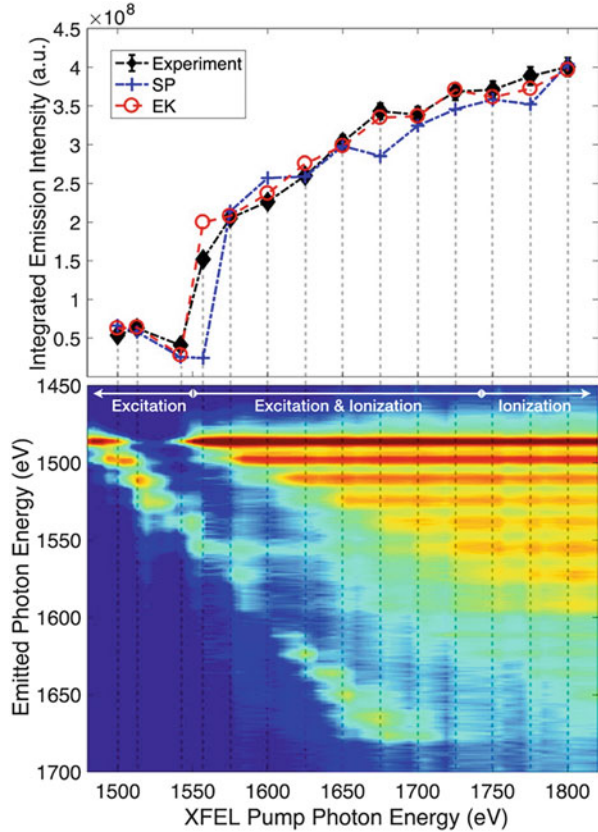
The integrated emission intensity is plotted in the above in Fig. 9.21, and compered to computational results with two different ionization potential depression models. It is found that both theoretical models well reproduce the present experimental result [44].

In Ref. [46], another analysis of the possibility is reported to obtain highly precise measurements of the ionization potential depression (IPD) in dense plasmas with spectrally resolved x-ray scattering. In this method, the advantage is that the electron temperature and the free electron density are simultaneously determined. So, more precise study is expected. A proof-of-principle experiment at the LCLS probing isochorically heated carbon samples, demonstrates the capabilities of this method and motivates future experiments at x-ray free electron laser facilities.

In Fig. 9.22, the experimental data of XRTS spectrum are shown with blue dots. The spectrum is analyzed theoretically with Chihara decomposition formula. A model fit to the scattering spectrum using the Chihara decomposition and assuming local thermal equilibrium provides a stable fit giving $Te = 21.7$ eV, $Z = 1.71$, and an IPD of 24 eV. The model fit total spectrum is plotted in red in Fig. 9.22 showing a good agreement with the XRTS data. It is mentioned that looking at the absolute

Fig. 9.22 The ionization potential depression is determined experimentally from XFEL Thomson scattering measurement. Reprint from ref. [46] with permission from Institute of Physics, (Courtesy of D. Kraus)
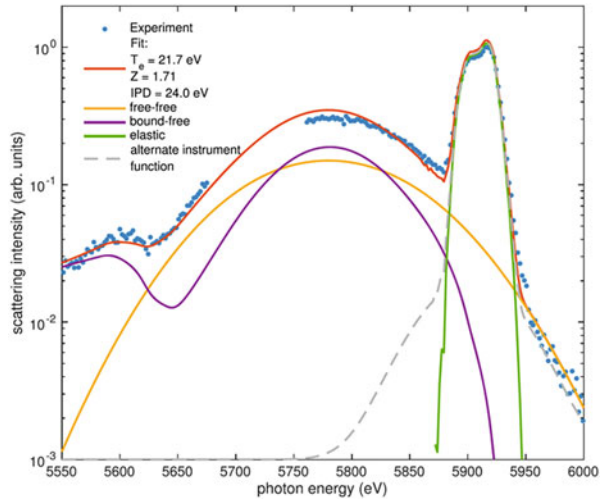
value of the IPD obtained from the fit (24 eV) is in very good agreement with the Stewart–Pyatt prediction for the best fit plasma parameters (25.3 eV) and does not agree with modified Ecker–Kroell (47.7 eV). It is noted that before such XFEL facility, there was no way to check the theoretical model with precise experimental way, while XFEL has made such comparison possible to motivate better modeling of the ionization potential depression (IPD).

References

1. Ya. B. Zel'dovich, Yu. P. Raizer, *Physics of Shock Waves and High-Temperature Hydrodynamic Phenomena* (Dover Publisher, 2002)
2. W. Griener et al., *Thermodynamics and Statistical Mechanics* (Springer, 1995)
3. M.C. Marshall et al., Shock Hugoniot measurements of single-crystal 1,3,5-triamino-2,4,6-trinitrobenzene (TATB) compressed to 83 GPa. J. Appl. Phys. **127**, 185901 (2020)
4. K. Falk, Experimental methods for warm dense matter research. High Power Laser Sci. Eng. **6**, E59 (2018). https://doi.org/10.1017/hpl.2018.53
5. S.T. Weir, S&TR, LLNL, 12 October/November, 2018
6. S.T. Weir et al., Metallization of fluid molecular hydrogen at 140 GPa (1.4 Mbar). Phys. Rev. Lett. **76**, 1860 (1996)
7. P.M. Celliers et al., Insulator-metal transition in dense fluid deuterium. Science **361**, 677 (2018)
8. J.M. McMahone et al., The properties of hydrogen and helium under extreme conditions. Rev. Mod. Phys. **84**, 1607 (2012)
9. S. Brygoo et al., Analysis of laser shock experiments on precompressed samples using a quartz reference and application to warm dense hydrogen and helium. J. Appl. Phys. **118**, 19 (2015)
10. R.P. Dias, I.F. Silvera, *Metallic hydroge*n. J. Phys. Condens. Matter **30**, 254003 (2018)
11. I. Silvera, The insulator-metal transition in hydrogen. PNAS **29**, 12743 (2010)
12. M.A. Molares, Towards a predictive first-principles description of solid molecular hydrogen with density functional theory. Phys. Rev. B **87**, 184107 (2013)
13. G.J. Ackland, Bearing down on hydrogen. Science **348**, 1429 (2015)

14. E. Wigner, H.B. Huntington, On the possibility of a metallic modification of hydrogen. J. Chem. Phys. **3**, 764 (1935)

15. V.E. Fortov, I.V. Lomonosov, Ya B Zeldovich and equation of state problems for matter under extreme conditions. Physics-Uspekhi **57**, 219 (2014)

16. K. Fujima et al., Analysis of the electronic properties of extremely condensed matter by the discrete-variational Xα method: Application to cold dense neon plasma. Phys. Rev. A **32**, 3585 (1985)

17. M.A. Morales et al., Evidence for a first-order liquid-liquid transition in high-pressure hydrogen from ab initio simulations. PNAS **107**, 12799 (2010)

18. W. Lorenzen et al., First-order liquid-liquid phase transition in dense hydrogen. Phys. Rev. B **82**, 195107 (2010)

19. W. Lorenzen et al., Metallization in hydrogen-helium mixtures. Phys. Rev. B **84**, 235109 (2011)

20. P. Loubeyre et al., Optical studies of solid hydrogen to 320 GPa and evidence for black hydrogen. Nature **416**, 613 (2002)

21. R.P. Dias, I.F. Silera, Observation of the Wigner-Huntington transition to metallic hydrogen. Science **355**, 715 (2017)

22. S. Ichimaru, *Statistical Physics of Dense Plasmas* (Taylor & Francis Group, LLC, 2019)

23. S.G. Brush, H.L. Sahlin, E. Teller, Monte Carlo study of a one-component plasma. I. J. Chem. Phys. **45**, 2102 (1966)

24. T. Kluge et al., Observation of ultrafast solid-density plasma dynamics using femtosecond X-ray pulses from a free-electron laser. Phys. Rev. X **8**, 031068 (2018)

25. J. Vorberger and D O Greicke, Comparison of electron–ion energy transfer in dense plasmas obtained from numerical simulations and quantum kinetic theory High Energy Density Phys., 10, 1–8, March (2014).

26. Brighter and faster: The promise and challenge of the x-ray free-electron laser, Phys. Today, 1 July (2015). Page 26

27. S. Frydrych, J. Vorberger, N.J. Hartley, A.K. Schuster, K. Ramakrishna, A.M. Saunders, T. van Driel, R.W. Falcone, L.B. Fletcher, E. Galtier, E.J. Gamboa, S.H. Glenzer, E. Granados, M.J. MacDonald, A.J. MacKinnon, E.E. McBride, I. Nam, P. Neumayer, A. Pak, K. Voigt, M. Roth, P. Sun, D.O. Gericke, T. Döppner, D. Kraus, Demonstration of X-ray Thomson scattering as diagnostics for miscibility in warm dense matter. Nat. Commun. **11**, 2620 (2020)

28. D.H. Froula et al., *Plasma Scattering of Elecromagnetic Radiation* (Elsevier, Amsterdam, 2011)

29. S.H. Glenzer, R. Redmer, X-ray Thomson scattering in high energy dense plasmas. Rev. Mod. Phys. **81**, 1625 (2009)

30. R. Thiele et al., Plasmon resonance in warm dense matter. Phys. Rev. E **78**, 026411 (2008)

31. J. Chihara, Interaction of photons with plasmas and liquid metals photo absorption and scattering. J. Phys. Condens. Matter **12**, 231 (2000)

32. J. Chihara, Difference in X-ray scattering between metallic and non-metallic liquids due to conduction electrons. J. Phys. F **17**, 295 (1987)

33. C.-F. Huang et al., XFEL coherent diffraction imaging for weakly scattering particles using heterodyne interference. AIP Adv. **10**, 055219 (2020)

34. Y. Kuwayama et al., Equation of state of liquid ion under extreme conditions. Phys. Rev. Letts. **124**, 165701 (2020)

35. G. Gregori et al., Theoretical model of x-ray scattering as a dense matter probe. Phys. Rev. E **67**, 026412 (2003)

36. D. Kraus et al., X-ray scattering measurements on imploding CH spheres at the National Ignition Facility. Phys. Rev. E **94**, 011202(R) (2016)

37. L.B. Fletcher et al., Ultrabright X-ray laser scattering for dynamic warm dense matter physics. Nat. Photonics **9**, 274–279 (2015)

38. L. B. Fletcher et al., Supplementary information of Ref [37]

39. A.D. Baxzewski et al., X-ray Thomson scattering in warm dense matter without Chihara decomposition. Phys. Rev. Lett. **116**, 115004 (2016)

40. G. Ecker, W. Kröll, Lowering of the ionization energy for a plasma in thermo-dynamic equilibrium. Phys. Fluids **6**, 62–69 (1963)

41. J.C. Stewart, K.J. Pyatt, Lowering of ionization potentials in plasmas. Astrophys. J. **144**, 1203–1211 (1966) [8]

42. O. Ciricosta et al., Direct measurements of the ionization potential depression in a dense plasma. Phys. Rev. Lett. **109**, 065002 (2012)
43. C.A. Iglesias, A plea for a reexamination of ionization potential depression measurements. HEDP **12**, 5–11 (2014)
44. M.F. Kasim, J.S. Wark, S.M. Vinko, Validating continuum lowering models via multiwavelength measurements of integrated X-ray emission. Sci. Rep. **8**, 6276 (2018)
45. S.M. Vinko et al., Creation and diagnosis of a solid-density plasma with an X-ray free-electron laser. Nature **482**, 59–62 (2012)
46. D. Kraus et al., Characterizing the ionization potential depression in dense carbon plasmas with high precision spectrally resolved x-ray scattering. Plasma Phys. Control. Fusion **61**, 014015 (2019)

Index